# Tephrochronology of the Greenland ice-cores and the North Atlantic Region during Marine Isotope Stage 4.

**Abbott, Peter Michael**

# Tephrochronology of the Greenland Ice-cores and the North Atlantic Region during Marine Isotope Stage 4

**Peter Michael Abbott**

Submitted to the University of Wales in fulfilment of the requirements for the Degree of Doctor of Philosophy

Swansea University

2010

# Abstract

The occurrence of several high-magnitude abrupt climatic changes during the last glacial period (~120-10 ka BP) was first recognised within the Greenland deep ice-core records. Subsequent identification of similar climatic variations has demonstrated the potential global significance of these events. Three of these millennial-scale events occurred during Marine Isotope Stage (MIS) 4 (~79-59 ka BP), a period characterised by cooler global temperatures. An understanding of the forcing mechanisms and the environmental responses to these events is currently unattainable due to chronological uncertainties and the inability to precisely synchronise disparate records. Tephrochronology, however, has the potential to facilitate high-precision ice-marine correlations by tracing isochronous horizons between different sequences spanning this period. This potential is demonstrated through the construction of the first tephrochronological framework for MIS 4 within the North Atlantic region. Fourteen cryptotephra horizons are identified within the NGRIP and GRIP ice-cores and the MD04-2822 marine core. Both major and trace element compositions are presented for these previously unknown tephra horizons and form the backbone of this framework. In addition, high-precision, independent age estimates have been assigned to the horizons identified within the ice-core sequences.

This framework represents a significant first step towards the regional and potentially hemispheric synchronisation of MIS 4 climatic archives. As well as providing the first evidence for the activity of Icelandic volcanic systems during MIS 4, this framework also demonstrates the widespread dispersal of basaltic-trachybasaltic products from the Jan Mayen volcanic region and potentially the deposition of Japanese volcanic material over Greenland. In addition, investigations of laser ablation inductively coupled plasma mass spectrometry have demonstrated that reliable trace element characterisations can be obtained from tephra shards ~20 μm in diameter, which opens up new possibilities for the incorporation of this technique in distal tephra studies.

# Declaration

This work has not previously been accepted in substance for any degree and is not being concurrently submitted in candidature for any degree.

Signed . ..... (candidate)

Date ....29/03/11.....

STATEMENT 1

This thesis is the result of my own investigations, except where otherwise stated. Where correction services have been used, the extent and nature of the correction is clearly marked in a footnote.

Other sources are acknowledged by footnotes giving explicit references. A bibliography is appended.

Signed .. ..... (candidate)

Date .....29/03/11.....

STATEMENT 2

I hereby give consent for my thesis, if accepted, to be available for photocopying and for inter-library loan, and for the title and summary to be made available to outside organisations.

Signed ... ..... (candidate)

Date ....29/03/11.....

# Acknowledgements

Firstly, I would like to express my sincere thanks to **Dr Siwan Davies** for her supervision of my PhD studies. Without her help and support and the opportunities she provided for me this project would not have been possible.

Thanks to **Dr Nick Pearce** at Aberystwyth University for his supervision, access to the LA-ICP-MS system and much needed advice regarding the trace element data.

Many thanks to all at the Centre for Ice and Climate, Niels Bohr Institute, University of Copenhagen for making me most welcome during my extended visits to the Institute. Particularly **Inger Seierstad** for all her help with making me feel settled in the city and for entertaining me for many long hours in the freezer! Also, thanks to **Dr JP Steffensen** for supervising my work in Copenhagen and **Dr Anders Svensson** for regularly providing me with updated ice core ages.

I would like to thank **Dr Bill Austin** and **Fiona Hibbert** from the University of St Andrews for providing me with access to the MD04-2822 marine core and for aiding my interpretation of the tephra record.

Thanks to **Professor Stefan Wastegård** from Stockholm University for providing tephra samples for analysis and for responding to my many data requests.

Thanks to **Dr David Steele** and **Dr Chris Hayward** for their assistance during my visits to the NERC Tephrochronology Analytical Unit at the University of Edinburgh.

Finally, I would like to thank all of my family and friends, in Swansea and beyond, for their help and support over the course of my PhD studies.

Financial assistance for this project was provided by the Natural Environment Research Council (NER/S/A/2005/13417).

# Table of Contents

# List of Figures

# List of Tables

# 1. Introduction

## 1.1 Scientific Rationale

### 1.1.1 Dansgaard-Oeschger Events and the Potential Application of Tephrochronology

Since the recovery of the first Greenland ice-cores in the 1960s, several high-magnitude abrupt climatic changes are known to have punctuated the last glacial period (~120-11.65 ka BP) (see Johnsen et al., 1992; Dansgaard et al., 1993; GRIP Members, 1993; Grootes et al., 1993; Dansgaard, 2004; Johnsen et al., 2001; NGRIP Members, 2004; Walker et al., 2009). In total, 25 of these so-called Dansgaard-Oeschger (DO) events have been recognised between the end of the last interglacial and the start of the Holocene (figure 1.1; NGRIP Members, 2004). Similar rapid climatic transitions have since been identified in the North Atlantic region as well as at many sites further afield, e.g. Santa Barbara Basin, California, Hulu Cave, China, and Cariaco Basin, Venezuela (e.g. Bond et al., 1993, 1997; Behl and Kennett, 1996; Schulz et al., 1998; Genty et al., 2003; EPICA Community Members, 2006; Peterson and Haug, 2006; Wang et al., 2006; Martrat et al., 2007).Three of these millennial-scale events (DO 18, 19 and 20) occurred during the Marine Isotope Stage (MIS) 4 period and are thought to be characterised by abrupt warmings of up to 16 °C followed by gradual cooling back into stadial conditions (Lowe and Walker, 1997; Lang et al., 1999; NGRIP Members, 2004; Landais et al., 2005). MIS 4 was first defined using marine oxygen isotope records that document past ice-volume changes. It was a distinct period of cooler global temperatures within the last interglacial to glacial transition during which mid-latitude ice sheets increased in volume and there was an associated lowering in eustatic sea levels (Shackleton, 1987). Overall, the understanding of MIS 4 is limited as past studies of the last glacial period often focus solely on MIS 2 and 3 as they are within the limits of the radiocarbon dating technique.

Changes in the mode of thermohaline circulation due to iceberg discharges and freshening of surface waters in the North Atlantic Ocean are known to coincide with the DO events and ice-rafted debris deposits in marine cores is associated with their termination (Alley and Clark, 1999; Stocker, 2000; Hemming, 2004; Landais et al., 2004), however, the mechanisms forcing these discharges remain uncertain.

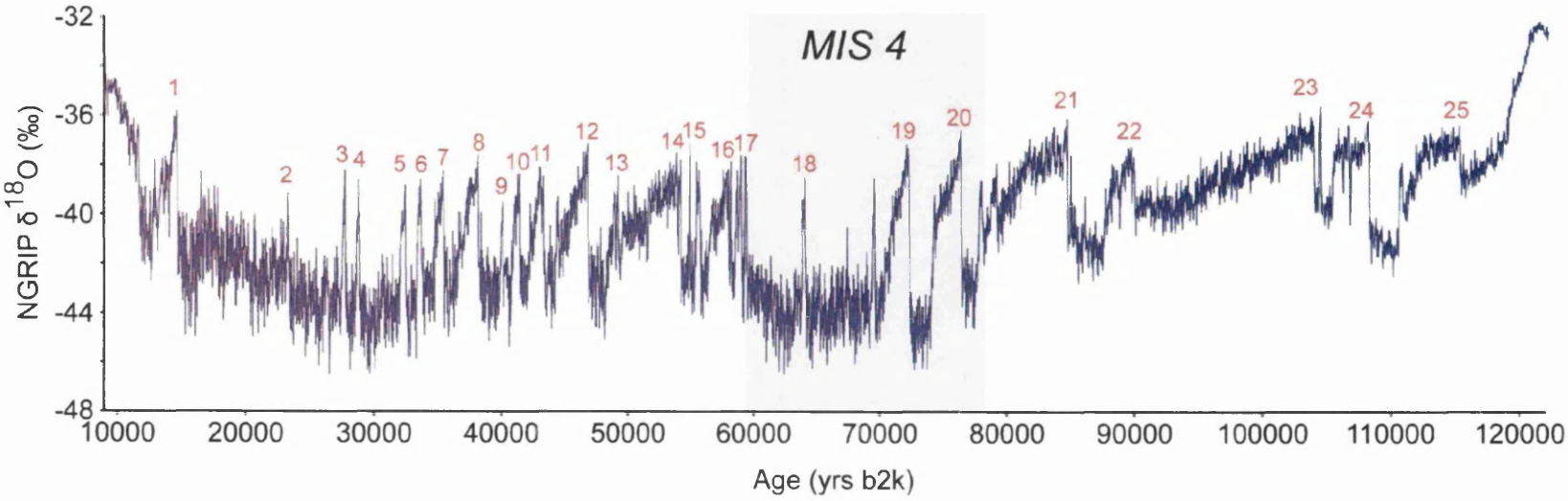


**Figure 1.1:** The oxygen isotope ratio profile for the NGRIP ice-core with the 25 Dansgaard-Oeschger events between 10 and 120 kyr b2k marked. Data for the oxygen isotope profile from NGRIP Members (2004). Timescale from A. Svensson (pers. comm., 2008) counted down to 60 yrs b2k and modelled from 60 yrs b2k to the base of the core. The timescale is referenced to 2000 AD "b2k". Any references to BP ages use 1950 AD as the reference point which is the reference point that is used for radiocarbon ages and many previous ice-core chronologies. Isotopic values are expressed in ‰ with respect to Vienna Standard Mean Ocean Water (V-SMOW).

Synchronisation of palaeoclimatic records retaining DO signals will increase the understanding of the rate, relative timing and environmental responses to these events. However, synchronisation of records from disparate locations and different depositional realms throughout this period has been hampered by the limitations of dating techniques. This constrains the creation of independent timescales for different sequences and a full assessment of the causal mechanisms for DO events is yet to be achieved.

One of the few techniques that has the potential for addressing this issue is tephrochronology. The identification of volcanic tie-lines between different palaeoclimatic sequences, provides an unprecedented opportunity for the high-precision correlation of archives from different depositional environments (Lowe, 2001; Turney et al., 2004; Lowe et al., 2008). The correlation of tephra horizons between sequences relies on the distinct geochemical fingerprints of different horizons and their deposition within disparate sequences is assumed to be geologically instantaneous. Identification of these time-synchronous horizons holds much promise for the synchronisation of ice and marine cores within the North Atlantic region. Particularly due to the high eruptive frequency of the Icelandic volcanic systems and widespread dispersal of eruptive products. To date, this potential has been demonstrated through the identification of key tephra horizons common to both the Greenland ice-core and North Atlantic marine records, e.g. Vedde Ash, Saksunarvatn Ash, Fugloyarbanki Tephra, Faroe Marine Ash Zone III and North Atlantic Ash Zone II (Kvamme et al., 1989; Austin et al., 1995; Grönvold et al., 1995; Ram et al., 1996; Zielinski et al., 1997; Eiríksson et al., 2000; Rasmussen et al., 2003; Mortensen et al, 2005; Wastegård et al., 2006; Davies et al., 2008; Svensson et al., 2008). However, only five tie-lines are currently available for the synchronisation of marine and ice-core records and very little work has focused on the identification of tephra horizons during the last glacial period. The potential of applying tephrochronology during MIS 4 is yet to be fully explored and no eruptions occurring during MIS 4 have been previously identified in North Atlantic sequences (figure 1.2). It is likely that this has resulted from the lack of focus on MIS 4 within previous studies because evidence from ice-core records suggests that this period was characterised by active volcanism (figure 1.3). For the potential of tephrochronology to be realised a framework of tephra horizons deposited during this period is required. This framework will act as a template to facilitate the future synchronisation of records of the MIS 4 period.

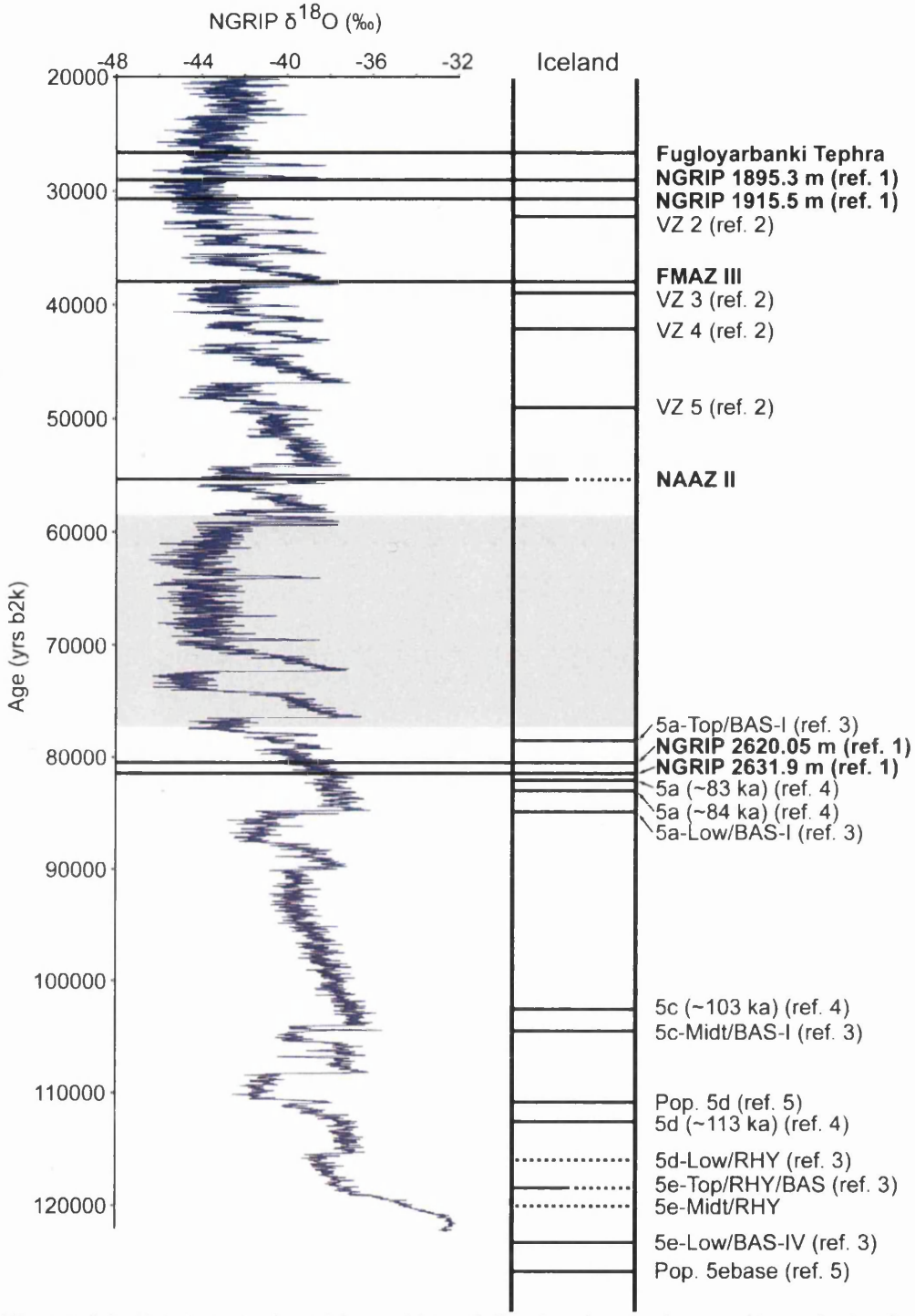


**Figure 1.2:** Relative stratigraphic position of distal tephra horizons with an Icelandic origin deposited within the Greenland ice-cores or North Atlantic marine sequences during the MIS 2 to MIS 5e climatic periods with reference to the NGRIP oxygen isotope ratio stratigraphy. Horizons in bold and traced across to the isotope record have been identified within the NGRIP ice-core. Grey shaded area is the period of study within this project. Solid lines = basaltic composition; Dotted lines = rhyolitic composition; Line combination = bimodal composition. Multiple references for Fugloyarbanki Tephra, FMAZ III, NAAZ II and 5e-Midt/RHY detailed in text. Ref. 1 = S. Davies (unpublished); Ref. 2 = Lackschewitz and Wallrabe-Adams (1997); Ref. 3 = Wastegård and Rasmussen (2001); Ref. 4 = Lacasse et al. (1998); Ref. 5 = Fronval et al. (1998). Isotopic values are expressed in ‰ with respect to V-SMOW.

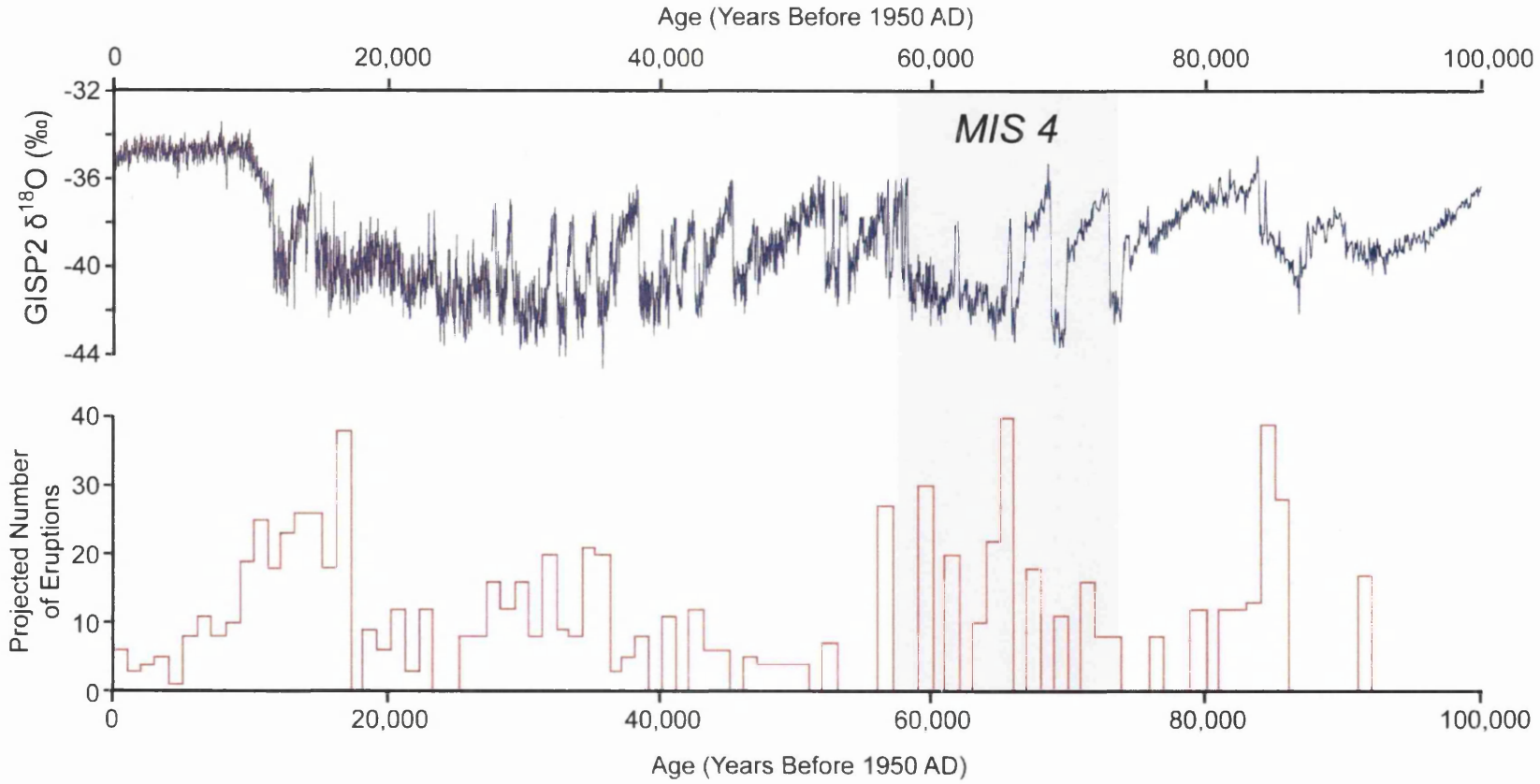


**Figure 1.3:** Oxygen isotope ratio record for the GISP2 ice-core compared to the projected number of volcanic eruptions per millennium that produced a volcanic sulphate signal greater than or equal to 75 ppb. Oxygen isotope data from Grootes and Stuvier (1997) and volcanic data adapted from Zielinski et al. (1996a). Isotopic values are expressed in ‰ with respect to V-SMOW.

The Greenland ice-cores NGRIP and GRIP represent an unprecedented archive for the development of this framework due to the available high-resolution chemostratigraphy for the NGRIP core and the high-precision chronologies being developed for both cores. The chemical records have a critical role in the identification of cryptotephra horizons in the ice-cores as elevated sulphate concentrations may indicate the presence of volcanic material. Whilst, the high-precision chronologies will enable independent ages to be assigned to any cryptotephra horizons that are identified. These age estimates and detailed geochemical characterisations for each tephra horizon will form the backbone of this framework. The construction of a tephrochronological framework for MIS 4 will subsequently enable target intervals within other records from the North Atlantic region to be investigated for the presence of coeval tephra horizons. These investigations should focus on high-resolution records retaining a clear DO event signal such as the MD04-2822 marine core extracted from the Rockall Trough area that will be investigated within this study.

Constructing a tephrochronological framework for MIS 4 relies on the characterisation of the geochemical composition of tephra horizons to trace volcanic events between sequences. The major element geochemistry can provide a distinct fingerprint for different eruptions. However, recent studies have suggested that in some instances these characterisations do not always adequately discriminate between the products of different volcanic eruptions (Davies et al., 2004; Pyne-O'Donnell et al., 2007). This has led to calls for techniques that characterise the trace element composition of individual shards to be employed, as they may prove to be more discriminatory and a larger suite of elements will be available for comparisons to be made between horizons (Turney et al., 2004). Laser ablation inductively coupled plasma mass spectrometry (LA-ICP-MS) holds much promise for the trace element characterisation of individual shards (Pearce et al., 1999; Pearce et al., 2004a), however as yet this technique has not been widely employed within tephrochronological studies in the North Atlantic region. In addition, the spatial resolution of LA-ICP-MS systems has up until now restricted its application within the study of cryptotephra horizons in ultra-distal locations, such as the Greenland ice-cores. Recent advances in LA-ICP-MS systems, however, with shorter wavelength lasers being coupled to high-resolution mass spectrometers, now provides the opportunity for reliable trace element characterisations to be obtained from small (~20-40 μm diameter) shards deposited in these locations (Pearce et al., 2007). The use of LA-ICP-MS will help to determine if the characterisation of the trace element composition of horizons strengthens correlations made previously based on major

element analysis and if it permits the geochemical discrimination of horizons with similar major element compositions.

## 1.2 General Objectives and Aims

The overall objectives of this study are to create the first tephrochronological framework for the MIS 4 period within the North Atlantic region and to test the capabilities of a new LA-ICP-MS system within the study of tephra horizons deposited in distal locations. The general aims of this project are:

- to use the high-resolution chemostratigraphy for the NGRIP ice-core and direct ice sampling methods to detect cryptotephra horizons within the MIS 4 section of this record.

- to trace any horizons identified within the NGRIP record in the GRIP ice-core record by chemical synchronisation of the two sequences and direct ice sampling.

- to investigate whether any tephra horizons identified within the ice-cores can be traced in the MIS 4 section of the MD04-2822 marine core.

- to geochemically fingerprint each horizon by major and trace element analysis for identification of coeval horizons from the different sequences and to determine potential volcanic sources.

- to assess the potential of the new LA-ICP-MS system for distal tephra studies. An experimental methodology will be applied to determine the optimal operating conditions for this system and to assess whether this technique can be used for discrimination purposes.

# 2. Towards a Tephrochronological Framework For MIS 4 in the North Atlantic Region

## 2.1 Defining Marine Isotope Stage 4 (~79-59 ka BP) in the Marine Records

MIS 4 was first identified as a climatic period within the pioneering work of Emiliani (1955). Building on the work of Urey (1948), Emiliani analysed the ratio of the oxygen isotopes $^{18}O$ and $^{16}O$ in $CaCO_3$ obtained from pelagic foraminifera within Atlantic, Caribbean and Pacific Ocean deep-sea cores (Emiliani, 1955). A similar pattern of down-core variations in oxygen isotope ratios could be identified within all cores. These down-core, i.e. temporal, variations were interpreted as resulting from fluctuations in ambient water temperature that caused isotopic fractionation of the water contributing to the isotopic signal of the foraminifera (Emiliani, 1955). The long records of oxygen isotope ratio variations were split into climatic stages and Emiliani (1955) established a convention for labelling these stages, following a system introduced by Arrhenius (1952). Warm, isotopically light interglacial periods were labelled with odd numbers and cold, glacial periods, which are isotopically heavy, were assigned even numbers. These climatic stages are numbered from the top-down with stage 1 representing the present interglacial and are referred to as marine isotope or oxygen isotope stages.

Since Emiliani (1955) the worldwide occurrence of these variations has been recognised and Hayes et al. (1976) demonstrated that they closely match the orbital variations central to the theory of climate change that was developed through the pioneering work of James Croll, George Murphy and most famously Milutin Milankovitch, after whom the cycles are named (Croll, 1875; Murphy, 1876; Milankovitch 1941; Patience and Kroon, 1991). The stacking of records from around the globe and subsequent tuning of this record to the predicted Milankovitch variations led to the creation of the SPECMAP age model, which provided ages for the climatic variations recorded in the marine sediments (see Imbrie et al., 1984; Pisias et al., 1984; Martinson et al., 1987).

Figure 2.1a shows the SPECMAP oxygen isotope profile from the last interglacial to the present. When the nomenclature for the MIS stages was first defined MIS 3 was mistakenly interpreted as representing an interglacial stage. However, together with the MIS 5 substages and MIS 4 this period represents a climatic oscillation during the

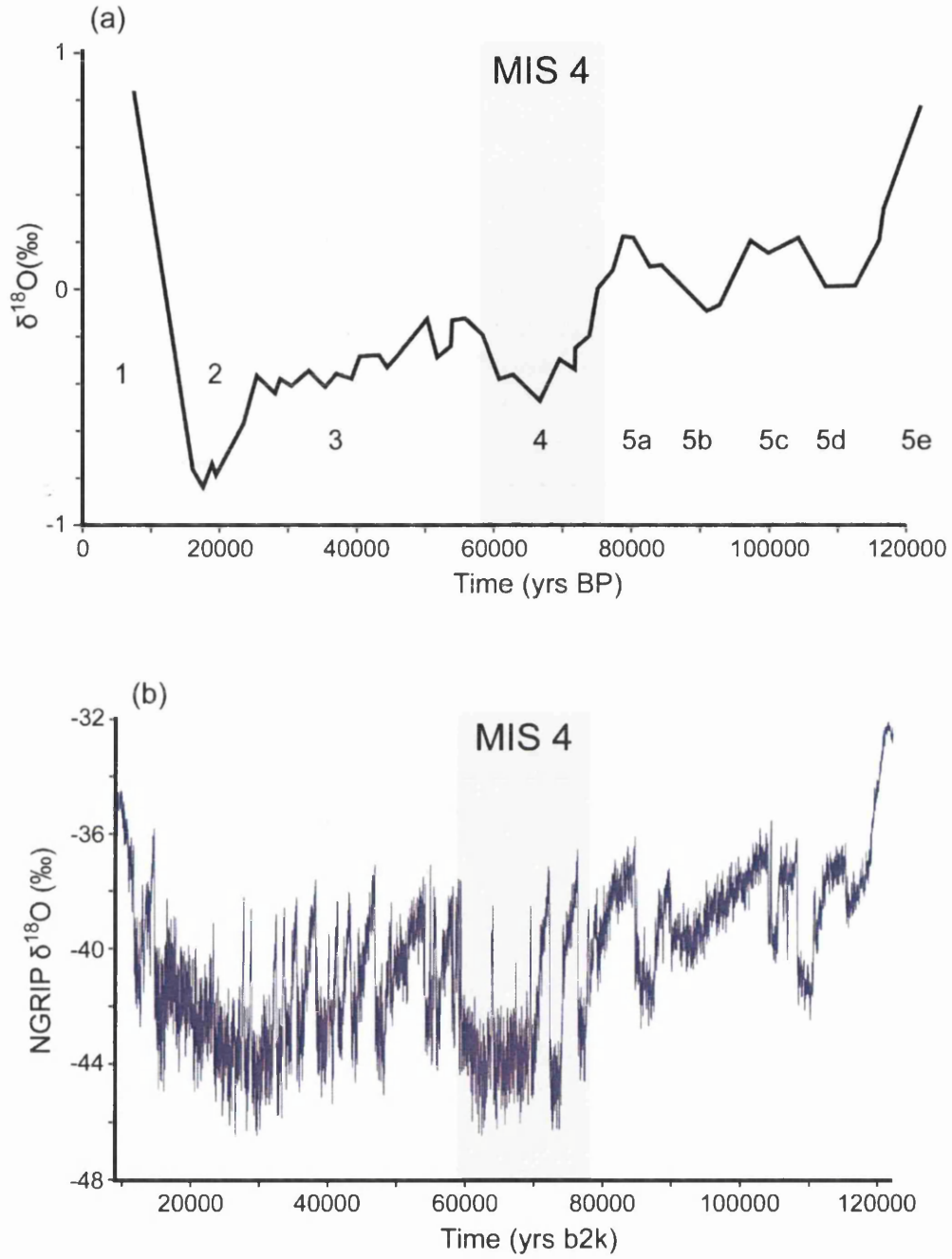


**Figure 2.1:** (a) SPECMAP marine chronostratigraphy for the past 120 kyr from a stacked marine oxygen isotope record (adapted from Gibbard and Van Kolfschoten (2004) and Martinson et al. (1987)). BP timescale referenced to 1950 AD (b) The oxygen isotope ratio profile for the NGRIP ice core from 10-120 kyr b2k. Data for the oxygen isotope profile from NGRIP Members (2004). Timescale from A. Svensson (pers. comm., 2008) counted down to 60 yrs b2k and modelled from 60 yrs b2k to the base of the core. The timescale is referenced to 2000 AD "b2k".

transition from full interglacial (MIS 5e) to full glacial conditions (MIS 2). This error resulted from the higher resolution of records for the MIS 5e-1 period which occurs because more recent, near-surface sediments have undergone less compression (Patience and Kroon, 1991). Therefore, MIS 4 does not represent a period of full glacial or interglacial conditions but does represent a distinct climatic period of cooler global temperatures occurring during the last interglacial to glacial transition.

Emiliani (1955) initially interpreted the oxygen isotope ratio variations as the result of fluctuations in ambient water temperature. However subsequent research, (e.g. Shackleton, 1967; Shackleton and Opdyke, 1973), identified the growth and decay of the Pleistocene ice sheets, as the principal control on the oxygen isotope variations (Imbrie et al., 1984). The marine isotope record indicates that MIS 4 represented a period of growth of mid-latitude ice-sheets with global land ice-volume being 68 % of that during the last glacial maximum (Shackleton, 1987). This resulted in a large fall in eustatic sea level, with levels falling by more than 60 m between MIS 5a and 4, to a level 75 m below the present day (Shackleton, 1987). Variability within methane records from the NGRIP ice-core also indicates that the growth of the mid-latitude ice sheets caused significant wetland and hydrological changes during MIS 4 (Chappellaz et al., 2003).

The construction of the marine isotope stratigraphy during the 1950s and 1960s significantly improved the understanding of glacial/interglacial cycles during the Quaternary period. However, the subsequent retrieval of high-resolution ice-cores from the Greenland Ice Sheet demonstrated that superimposed on these low resolution fluctuations were abrupt millennial-scale variations in climate. These so-called Dansgaard-Oeschger events occurred throughout the period from MIS 5e to MIS 2 with three occurring during MIS 4 (figure 2.1b).

The resolution of the climate signal recorded within the Greenland ice-cores has led to them being regarded as significant climatic stratotypes for the Holocene and last glacial periods, to which a multitude of climate records from sites in the North Atlantic region and from around the globe have been compared (Rohling et al., 2003; Clement and Peterson, 2008; Lowe et al., 2008).

## 2.2 Greenland Ice-cores and Dansgaard-Oeschger Events during MIS 4

The drilling of deep ice-cores in Greenland started during the 1960s with the retrieval of the Camp Century core and since then numerous other ice-cores, extending back through the last glacial cycle, have been recovered (Dansgaard, 2004; Johnsen et al., 2001). Significant technological advances allowed two new deep ice-cores to be drilled in central Greenland during the early 1990s, the European funded Greenland Ice-core Project (GRIP) and the American led Greenland Ice Sheet Project (GISP2). Both of these projects aimed to retrieve a high-resolution record of the last glacial period and ice from the last interglacial period (Eemian, MIS 5e) (GRIP Members, 1993). The GRIP ice-core was retrieved from the highest point of the Greenland Ice Sheet (72.58°N, 37.64°W, 3,238m a.s.l.) and the GISP2 core 28 km to the west (72.59°N, 37.64W) (figure 2.2).

Investigations of the oxygen isotope profile for the GRIP ice-core revealed that due to deformation of ice at the base of the core, attributed to flow over bedrock, an undisturbed record for the Eemian period had not been retrieved (Alley et al., 1995). As a consequence a new drill site 325 km north-northwest of GRIP (75.10°N, 42.32°W, 2921m a.s.l.; figure 2.2) was selected and between 1996 and 2003 the 3,085 m long NGRIP core was extracted (Dahl-Jensen et al., 1997, 2002; NGRIP Members, 2004). This core extends back to 123 kyr BP and preserves a complete record of MIS 4, however a complete record of the Eemian period is yet to be recovered in Greenland (NGRIP Members, 2004).

All ice-cores recovered from Greenland have revealed the occurrence of repeated rapid warming events during the last glacial period, which are commonly referred to as the Dansgaard-Oeschger (DO) events or cycles (figure 2.3). These events have been identified within the stable oxygen isotope ratio records from the ice, a proxy for ice-surface air temperatures over Greenland (Johnsen et al., 2001). In addition, recognition of similar changes in the chemical records from the cores supports the proposition that these were significant climatic events that resulted in large–scale atmospheric changes (Mayewski et al., 1997; Yang et al., 1997). The DO events were first numbered from the GRIP ice-core record with 24 events being recognised during the last glacial period (Johnsen et al., 1992; Dansgaard et al., 1993). A 25$^{th}$ DO event was recognised within

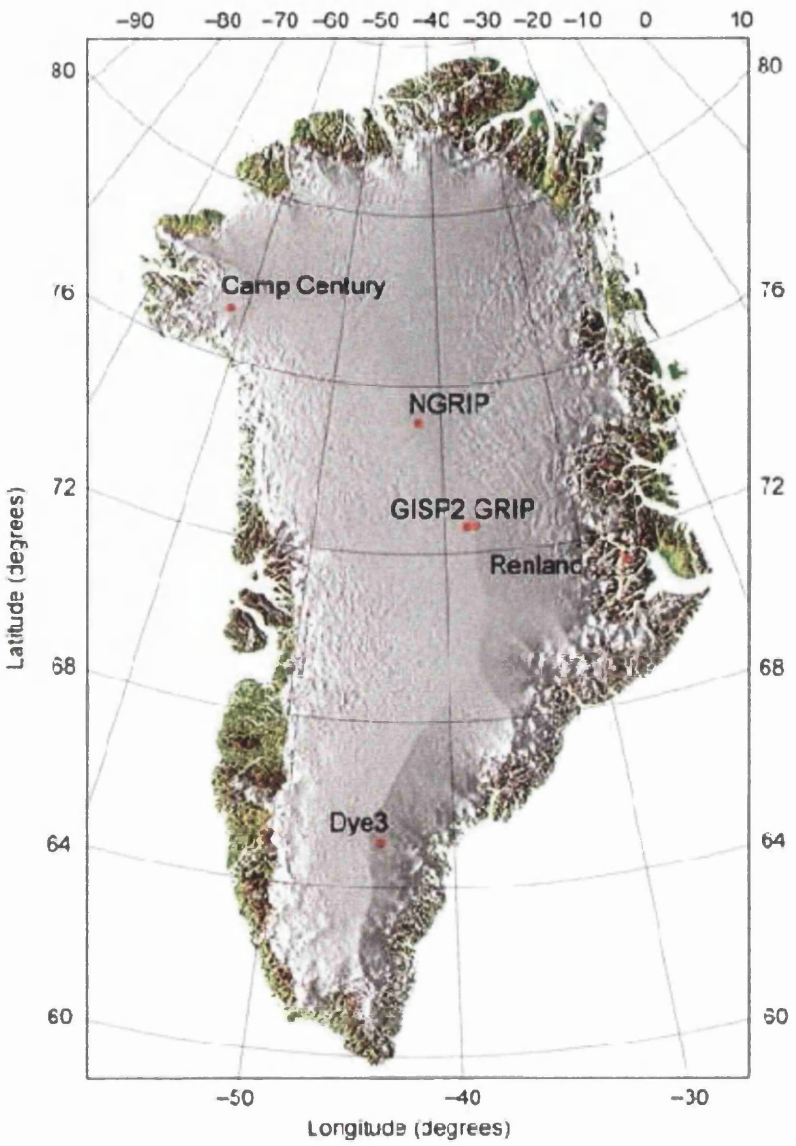


**Figure 2.2:** Map of Greenland showing the location of the deep ice core drilling sites (from NGRIP Members, 2004).

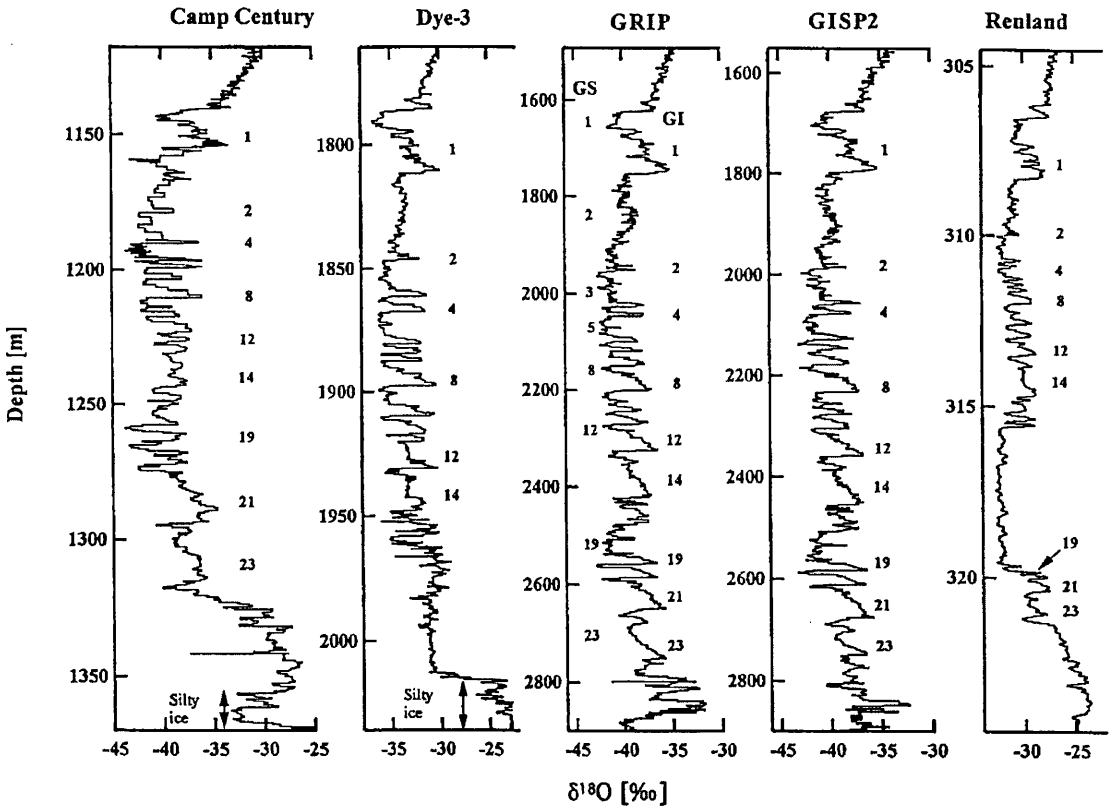


**Figure 2.3:** Continuous stable oxygen isotope profiles along five Greenland deep ice-cores (locations shown on figure 2.2) (from Johnsen et al., 2001). Less negative oxygen isotope ratios indicate warmer surface temperatures over Greenland. Isotopic values are expressed in ‰ with respect to V-SMOW.

the NGRIP oxygen isotope record; this weak DO event occurred during the inception of the last glacial period (figure 1.1; NGRIP Members, 2004).

The records indicate that these abrupt warming events, with temperature increases of up to 16°C, occurred within less than 100 years and were then followed by an interstadial period (Landais et al., 2005; Clement and Peterson, 2008). Gradual cooling then occurred over several hundred years until temperatures returned to pre-warming, stadial levels (Lang et al., 1999). Analysis of the timing of these events has revealed that they generally recur with a periodicity of ~1,500 years (Grootes and Stuvier, 1997; NGRIP Members, 2004; Clement and Peterson, 2008). However, some events were "skipped" and intervals of 3,000 and 4,500 years between the onset of events occurred. Overall, this has led to suggestions that the events are triggered by a forcing mechanism with a cycle of ~1,500 years (Rahmstorf, 2003).

The wider significance of these events as regional and potentially global mass reorganisations of the climate system has been demonstrated by the identification of millennial scale climate fluctuations in numerous marine and continental records from the North Atlantic region and many other key climate records from around the world (North Atlantic records: e.g. Bond et al., 1993, 1997; Rasmussen et al., 1997; Elliot et al., 1998, 2002; Antoine et al., 1999; Van Kreveld et al., 2000; Genty et al., 2003; Martrat et al., 2007; Global records: e.g. Behl and Kennett, 1996; Charles et al., 1996; Chen et al., 1997; Schulz et al., 1998; Hendy and Kennett, 2000; Peterson et al., 2000; Wang et al., 2001; Altabet et al., 2002; Benson et al., 2003; Hughen et al., 2004; Ortiz et al., 2004; Yuan et al., 2004; EPICA Community Members, 2006; Peterson and Haug, 2006; Wang et al., 2006). In general, the DO events are more defined within Northern Hemisphere records while millennial scale climate variations in Southern Hemisphere records appear to have teleconnections to DO events, but warming events are in anti-phase to the Northern warmings.

During MIS 4, the period under investigation in this study, three DO events are recorded within the Greenland ice-cores, 18, 19 and 20, and temperature increases of 11, 16 and 11°C (± 2°C) respectively have been calculated for these periods (Figure 2.4; Landais et al., 2004b). These surface temperature changes were estimated using the isotopic composition of air trapped within the NGRIP ice-core and the thermal diffusion of nitrogen and argon (see Severinghaus and Brook, 1999; Goujon et al.

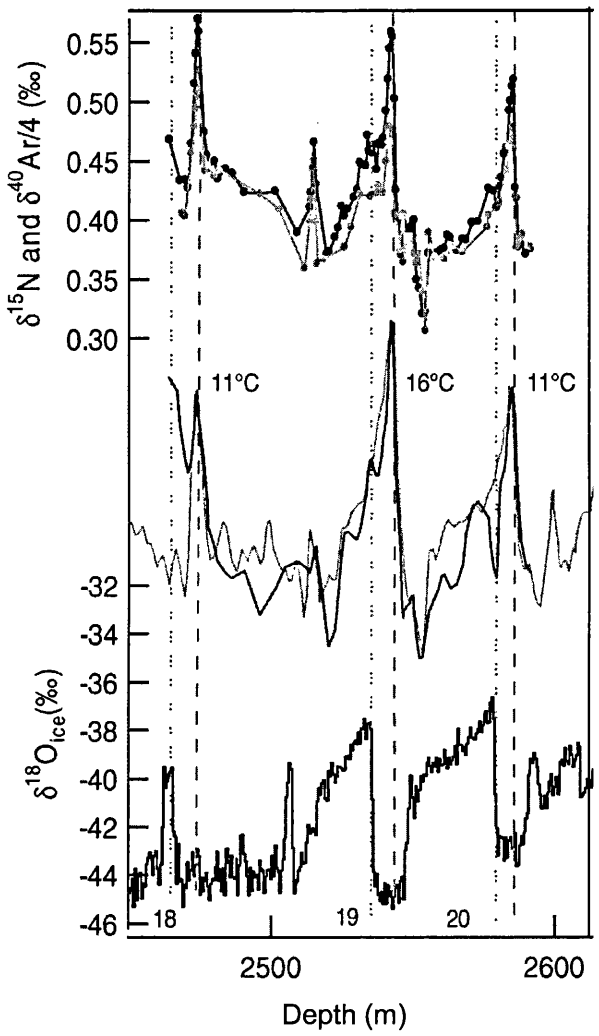


**Figure 2.4:** Temperature reconstructions for DO 18, 19 and 20 in the NGRIP ice-core. Top: $\delta^{15}N$ (black) and $\delta^{40}Ar$ (grey) records. Middle: $\delta^{15}N_{excess}$ smoothed over a three point running mean (black) and modelled (grey) with temperature increases of 11, 16 and 11℃ for D-O 18, 19 and 20. Bottom: $\delta^{18}O_{ice}$ on the NGRIP ice core. Adapted from Landais et al. (2005).

2003; Landais et al., 2004a, b; Landais et al., 2005). The temperature change inferred for DO 19 is consistent with a similar reconstruction for this event from the GRIP core by Lang et al. (1999). Overall, these reconstructions highlight the high magnitude of the rapid warming events over Greenland during the MIS 4 period.

Climatic changes correlated to these three DO events have also been identified within proxy records from North Atlantic marine sequences including MD04-2822, a marine core extracted from the Rockall Trough area that will be explored within this study (chapter 7).

## 2.3 Determining the Mechanisms Controlling Dansgaard-Oeschger Events

DO events have been widely related to shifts in the mode of thermohaline circulation (THC) within the North Atlantic region, caused by freshwater inputs from abrupt iceberg discharges freshening the source of North Atlantic Deep Water (e.g. Rooth, 1982; Broecker et al., 1985; Alley and Clark, 1999; Stocker, 2000; Landais et al., 2004a; Knutti et al., 2004). The rapid warming events represent the resumption of the THC and the transportation of heat from the tropics to the high-latitudes (Clement and Peterson, 2008). Unlike the orbitally-forced, long-term climatic variations recorded in the marine sediments the mechanisms forcing the freshwater discharges are unknown and many hypotheses exist. Some attribute them to processes internal to the climate system, including the systematic failure of the Greenland Ice Sheet due to a MacAyeal type binge-purge process (MacAyeal, 1993; Van Kreveld et al., 2000) or deep-water oscillations induced by changes in Southern Ocean sea-ice extent and ice sheet surges in the North Atlantic (Maslin et al., 2001). However, other mechanisms have been suggested including atmospheric transport of freshwater (Broecker, 2000), volcanism (Bay et al., 2004) and the external forcing of variations in solar activity (van Geel et al., 1999; Braun et al., 2005, 2008).

Precise dating and synchronisation of palaeoclimatic records retaining DO signals will allow the relative timing and rate of environmental responses to the climate shifts recorded in sequences from different environments and geographical locations to be determined. Once this is established the various hypotheses of the mechanisms forcing

these events and the processes that propagate their climatic impact globally can be tested. By examining if they could have plausibly caused the changes and relative timings observed in the global palaeoclimate records (Clement and Peterson, 2008). Improved understanding of the mechanisms forcing these rapid climate events will also help to determine how the climate system, notably the mode of THC, will respond to future climatic perturbations (Clark et al., 2002; Timmermann and Menviel, 2009). The synchronisation of palaeoclimatic records from the North Atlantic region is key to improving the understanding of the mechanisms controlling the DO events. Because, firstly, the Greenland ice-cores preserve the most high-resolution record of these events, secondly, outside of the Greenland ice-cores, North Atlantic marine sequences are the archives that most consistently preserve a DO signal (Voekler and workshop participants, 2002) and thirdly, changes in ocean circulation within this region are seen as the key driver of these events.

One of the major limitations constraining the determination of the relative timing of the environmental responses to DO events is an inability to date sequences retaining a DO signal precisely through the creation of independent timescales (Clement and Peterson, 2008). Absolute dating of ice cores on calendar timescales has been achieved through visual layer counting, however, ice flow modelling or tuning to orbital parameters is required once compaction has eliminated this layering (Clement and Peterson, 2008). Dating of marine and terrestrial records relies on radiocarbon dating; this limits the absolute dating of sequences retaining DO signals because the calibration of the radiocarbon timescale to absolute timescales beyond 26 ka BP is highly debated (e.g. Kitagawa and van der Plicht, 2000; van der Plicht et al., 2004; Fairbanks et al., 2005; Hughen et al., 2006) and sequences can only be radiocarbon dated back to ~45-50 ka BP (Bird et al., 1999; Clement and Peterson, 2008). Below this depth timescales are often created through synchronisation to orbital parameters or tuning to ice cores or other high-resolution records, which introduces circularity in determining the relative timing of climatic events (Clement and Peterson, 2008).

It has been widely suggested that tephrochronology is one of the few techniques that offers the potential to synchronise records from different depositional environments through the definition of time-synchronous tie-lines; particularly within the North Atlantic region due to the relatively high productivity of the Icelandic volcanic region (e.g. Lowe et al., 2001, 2008; Turney et al., 2004). The precise correlations between sequences this technique creates can then be used to test hypotheses regarding non-synchronous

or synchronous responses to climatic variations (Lowe, 2001). The potential for tephrochronology to determine the relative timing of DO events in North Atlantic sequences was demonstrated by Davies et al. (2008). With the stratigraphic position of the Fugloyarbanki Tephra, widespread within North Atlantic marine records, in the NGRIP record suggesting that temperature changes related to DO event 3 were synchronous between the depositional realms (Davies et al., 2008). However, until now very little work has focused on synchronising North Atlantic archives of the MIS 4 climatic period and a framework of volcanic events during this period is currently not available.

## 2.4 Constructing a Tephrochronological Framework for MIS 4

### 2.4.1 Principles of Tephrochronology

The term tephra derives from the Greek word for ash, τεφρα, and was first introduced by Thorarinsson (1944) and later redefined by Thorarinsson (1974) as a collective term for all airborne volcanic ejecta, including both air-fall and pyroclastic flow material (Haflidason et al., 2000). Tephra can be classified based on its size, and this forms the basis of the nomenclature of Fisher (1961), which divides tephra into blocks and bombs (>64 mm), lapilli (2-64 mm) and ash (<2 mm). The ash component of tephra can be transported over thousands of kilometres from a source volcano prior to deposition, therefore, this size fraction is the main focus of distal tephrochronological studies. Following deposition tephra can be preserved within a wide range of environments, e.g. marine, lacustrine, terrestrial and ice sheet/glacier sequences, that represent useful palaeoclimatic archives (e.g. Lacasse and Garbe-Schönberg, 2001; Turney et al., 1997; Mortensen et al., 2005).

If horizons are correlated between sequences they can act as time-synchronous tie-lines because their deposition is assumed to be geologically instantaneous and a tephrostratigraphy can be defined. The synchronicity in the deposition of horizons means that if a tephra horizon can be dated within one sequence that age can be applied to all other occurrences of that particular horizon, thus forming a tephrochronology (Walker, 2005). The dating of horizons is not essential for them to act as time-parallel markers for synchronisation.

Early tephrochronological studies relied on correlating tephra horizons based on the physical and visual properties of shards, such as colour, morphology and refractive indices. However, such features are not diagnostic of individual eruptions, as similar characteristics can be produced by eruptions from the same volcanic centre or centres with similar lithologies (Turney et al., 2004). In addition, some non-volcanic materials have similar visual and physical properties to tephra shards, e.g. opaline silica (Turney et al., 2004). The characterisation of the mineral assemblages within a tephra horizon has been used for correlation (Shane, 2000). However, due to preferential deposition the mineralogical composition of a horizon can vary with distance from source (Sparks et al., 1997), some material can be dissolved in acidic environments (Hodder et al., 1991) and there may not be significant variation in the mineralogy of horizons from the same centre (Turney et al., 2004). Therefore a more comprehensive and discriminatory characterisation of tephra horizons is required; the geochemical characterisation of juvenile glass shards fulfils these criteria (Davies et al., 2002). In addition, glass shards are the ash component transported the furthest from a volcano following an eruption thus forming the major constituent of distal tephra horizons.

The geochemical composition of glass shards formed during a volcanic eruption is related to the bulk geochemistry of magma and the character of the volcanic eruption (Barker, 1983; Davies et al., 2002). As a consequence the geochemistry of glass shards can vary between both volcanic centres and individual eruptions from the same centre. In some instances, however, there may be significant overlap in the geochemical composition of shards produced during separate eruptions and only subtle differences in geochemistry may be apparent.

Correlation of horizons using geochemical evidence is the main technique used within tephrochronological studies, however, where possible correlations should be additionally supported by stratigraphic information regarding the horizons (Pearce et al., 2008b). More extensive details regarding the geochemical characterisation of glass shards within tephra horizons are provided in section 2.5.

Tephra horizons can be dated through the direct dating of the volcanic material using radiometric techniques such as argon isotope (e.g. Ton-That et al., 2001) or fission track dating (e.g. Bigazzi et al., 2005). Ages can also be obtained for horizons indirectly through the dating of sediments related to the tephra horizon, for example using

radiocarbon or luminescence dating (e.g. Haflidason et al., 2000; Toms et al., 2004), or via the position of the horizon within an annually banded sequence such as a varved lake sequence or an ice-core (e.g. Wulf et al., 2004; Grönvold et al., 1995). The dating of horizons is crucial if tephrochronology is to be used for the refinement of chronologies for climatic archives.

Tephrochronological studies have been carried out in many geographical regions including Northern Europe (e.g. Haflidason et al., 2000; Van Den Bogaard and Schminke, 2002), Mediterranean Europe (e.g. Di Vito et al., 1999), East Africa (e.g. Brown et al., 1992), North America (e.g. Ortega-Guerrero and Newton, 1998), South America (e.g. Toms et al., 2004), New Zealand (e.g. Froggatt, 1983), Greenland (e.g. Grönvold et al., 1995), Antarctica (e.g. Basile et al., 2001), Japan (e.g. Machida, 1999) and oceanic regions through the study of deep-sea sediments (e.g. Hunt and Najman, 2003). Formerly, these studies focussed on the recognition of visible horizons of tephra and thus were restricted to areas proximal to volcanic sources or where local conditions promote intensified shard accumulation, e.g. meteorological (strong winds and precipitation) or sedimentological (sediment focusing into lakes) (Mangerud et al., 1986; Turney et al., 2004). This situation changed within the late 1990s with the recognition of tephra horizons invisible to the naked eye within many sequences. The discovery of these horizons was a consequence of the development of new techniques to identify and extract tephra shards from sediment sequences (e.g. Dugmore, 1989; Rose et al., 1996; Turney, 1998).

### 2.4.2 Cryptotephrochronology

The horizons invisible to the naked eye are composed of low concentrations of shards and/or shards of a small size and were initially referred to as microtephras (e.g. Lowe and Turney, 1997). This terminology implies that either the horizon is thin or composed of small shards, which may be the case for many 'microtephra' horizons, however, it is not a general rule. Lowe and Hunt (2001) recommended the use of the term cryptotephra, derived from the Greek word to hide *(kryptein)*, which expresses the concealed nature of these horizons and has no size-related connotations (Turney et al., 2004). The term cryptotephra will be adopted throughout this study.

The identification of cryptotephra horizons has greatly increased the spatial extent over which tephrochronology can be applied through the extension of the known

geographical range of products of different volcanic regions. For example, the known range of the Icelandic Vedde Ash (10,300 $^{14}$C yr BP) has been extended to Scotland (Lowe and Turney, 1997), Scandinavia (Wastegård et al., 1998), the Netherlands (Davies et al., 2005a), northwest Russia (Wastegård et al., 2000) and the Alps (Blockley et al., 2007). In addition, cryptotephra studies have identified previously unrecognised tephra horizons that do not have visible equivalents in a proximal setting, such as the Borrobol Tephra (12,300 $^{14}$C yr BP). This horizon, which is believed to have an Icelandic provenance, has been identified in cryptotephra form at sites within Scotland (Turney et al., 1997; Ranner et al., 2005), southern Sweden (Davies et al., 2003) and marine sediments from the North Iceland Plateau (Eiríksson et al., 2000).

Since their discovery the majority of intensive cryptotephra studies have focused on terrestrial sequences (e.g. Davies, 2002), however it has also been demonstrated that they can be identified in both ice-core (e.g. Mortensen et al., 2005) and marine sequences (e.g. Kristjánsdóttir et al., 2007). Early work using chemical records from Greenland ice-cores identified cryptotephra horizons as variations in these proxies can be related to volcanic eruptions and can be used to identify sections of ice that may contain tephra shards (e.g. Palais et al., 1992; Fiacco et al., 1994).

### 2.4.3 Chemical Records of Volcanism from the Greenland Ice-cores

An advantage of ice-cores over both marine and terrestrial archives is that while they can all preserve tephra from volcanic eruptions, only ice-cores simultaneously preserve a record of the aerosols ejected during volcanic eruptions (Zielinski et al., 1997). Aerosols and gases such as sulphur compounds (S and $SO_2$), chlorine (Cl), hydrogen (H) and fluorine (F) are emitted during volcanic eruptions. When they combine with hydroxyl (OH) and water ($H_2O$) in the atmosphere they form acidic compounds including hydrogen chloride (HCl), hydrogen fluoride (HF), hydrogen sulphate ($H_2SO_4$), and hydrogen sulfide ($H_2S$) (Chalmas, 2004; Textor et al., 2004). These gases are transported within the stratosphere to the poles, before sedimentation into the troposphere and eventual deposition via snowfall or dry deposition (Zielinski, 2000).

The past deposition of acidic gases on the ice sheet has been reconstructed from ice-cores using the electrical conductivity method (ECM). ECM is a proxy for the acidity (pH) of ice and was used in the earliest ice-core reconstructions of volcanic activity (e.g. Hammer, 1980; Hammer et al., 1980). These reconstructions focused on the historical time period and distinct acidity peaks were attributed to known historical

eruptions, using ice-core chronologies to date their timing (e.g., Tambora AD 1815, Laki AD 1783). Since then many records have been created based on the ECM record of various Greenland ice-cores (e.g. Taylor et al., 1992; Clausen et al., 1997).

Subsequently past volcanic activity has been reconstructed by measuring the sulphate ($SO_4^{2-}$) concentrations in ice, which is a direct measure of the hydrogen sulphate ($H_2SO_4$) component of the aerosol record (Herron, 1982; Mayewski et al., 1993; Zielinski et al., 1996). Sulphate concentrations may be enhanced by the scavenging of $SO_4^{2-}$ through adsorption onto tephra particles within the volcanic cloud (Rose, 1977).

A 110,000 yr continuous record of volcanically produced sulphate from the GISP2 record was compiled by Zielinski et al. (1996a). Through empirical orthogonal function decomposition, a form of multivariate analysis, it was possible to isolate sulphate variations due to volcanic activity from other potential sulphate contributions, e.g. dimethylsulfide (DMS) and continental salts (Zielinski et al., 1996a). Their work suggested that during the past 110,000 years a minimum of 838 volcanic eruptions loading the atmosphere with a similar amount of sulphur to large historical eruptions occurred (e.g. Krakatau (1883) and Katla (1918)). In particular, several millennia within MIS 4 can be identified as having a high number of eruptions, higher than some millennia during deglaciation (figure 1.3).

Zielinski et al. (1997) identified three periods of continuous volcanic activity within the GISP2 record at 6000-17,000, 27,000-36,000 and 79,000-85,000 yr BP. The most recent of these periods spans the final stages of deglaciation and the two later periods occurred over climate transitions, during which growth of the mid-latitude ice-sheets occurred and eustatic sea levels fluctuated during all of these periods (Zielinski et al., 1997). This supports the suggestion that increased isostatic crustal stresses induced by climatically forced changes in the volume of continental ice sheets and associated changes in eustatic sea levels can act to increase volcanic activity (e.g. Matthews, 1969; Rampino et al., 1979; Kyle et al., 1981; Nakada and Yokose, 1992; Rampino and Self, 1993; Jull and McKensie, 1996; Zielinski, 2000). This theory is particularly relevant during MIS 4 because records of glacioeustatic sea level change (e.g. Mayewski et al., 1997) and marine oxygen isotope records (e.g. Shackleton, 1987) suggest that significant ice sheet growth occurred during this period.

The record of sulphate from the NGRIP ice-core, measured using continuous flow analysis (CFA), is the highest resolution record available from Greenland. This

technique provides chemical records at an effective resolution of between 10 and 25 mm (full description of technique in section 3.2.2). The record currently encompasses the MIS 4 climatic period as it has been collected on the core from 1404 m depth to the base of the core, which equates to the last glacial period between ~10 to 110 ka BP. Distinct peaks in sulphate are considered to be the most reliable indicators of volcanic eruptions within ice-core records (Bigler et al., 2007) and therefore could act as a guide to the potential location of cryptotephra horizons within the NGRIP record. This potential was demonstrated by Mortensen et al. (2005) who utilised CFA sulphate records for the NGRIP ice-core to identify cryptotephras horizons within the Last Glacial Termination time period (see section 2.4.4.1). This sulphate record is central to the development of a tephrochronological framework for MIS 4 in this study.

### 2.4.4 Tephra Horizons Previously Identified Within the Greenland Ice-cores and Potential Volcanic Source Regions

Various studies have identified, extracted and geochemically analysed tephra horizons contained within ice-cores extracted from the Greenland Ice Sheet (table 1.1). This work has mainly focused on visible horizons (e.g. Grönvold et al., 1995; Zielinski et al., 1997) or cryptotephra horizons related to significant volcanic signals with an assumed origin based on the geological record (e.g. Fiacco et al., 1994; Hammer et al., 2003). However, the potential to identify numerous new horizons through the intensive study of specific time periods has recently been demonstrated (Mortensen et al., 2005). The volcanic sources of all these previously identified eruptions can act as a guide to the potential sources of tephra horizons deposited over Greenland during MIS 4.

The summary table of horizons previously identified within the Greenland deep ice-cores highlights that the dominant source of volcanic material extracted thus far is the Icelandic volcanic region (table 1.1). However, material erupted from other volcanic regions has been identified and literature sources suggest that other regions could be potential sources of tephra deposited over Greenland. Figure 2.5 illustrates both the volcanic regions from which previously identified tephra have been sourced and suggested potential source regions.

**Table 2.1:** Summary of tephra horizons previously identified within Greenland deep ice cores. The discovery of tephra related to Ash Zone 2 in the Dye 3 core by Ram and Gayley (1991) is excluded as it was derived from a disturbed section of the core. Nine additional cryptotephra horizons identified by Mortensen et al. (2005) between 1506.26 and 1628.25 m were not included as they were not correlated to known deposits. The major oxide geochemistry of the majority of these additional horizons suggests an Icelandic origin, however the possibility that they are derived from other sources (e.g. Alaska, Japan, and Cascades volcanic regions) is not ruled out. All ages are referenced to 1950 AD.

| Ice Core Age AD/BC/yr BP | Core | Correlated with other deposits | Eruption/Horizon | Source | References |
|---|---|---|---|---|---|
| 1982 AD | Dye 3 | Yes | El Chichón | Chiapas, Mexico | de Angelis et al. (1985) |
| 1912 AD | NGRIP | Yes | Katmai | Alaska | Pilcher (pers com, 2005) |
| 1783 AD | GISP2 | Yes | Laki | Lakagigar, Iceland | Fiacco et al. (1994) |
| 1602± 1AD | GISP2 | No | Unknown | Unknown | de Silva and Zielinski (1998) |
| 1479AD | GISP2 | Attempted | Mt. St. Helens Wn Tephra | Washington State, USA | Fiacco et al. (1993) |
| 1362 AD | GISP2 | Yes | Öræfajökull | Öræfajökull, Iceland | Palais et al. (1991) |
| 1362 AD | NGRIP | Yes | Öræfajökull | Öræfajökull, Iceland | Pilcher (pers com, 2005) |
| 1259 AD | GISP2 | No | Unknown | Unknown | Palais et al. (1992) |
| 938 ± 4 AD | GISP2 | Yes | Glass A- Eldgjá Glass B- Unknown | Eldgjá-Katla, Iceland | Zielinski et al. (1995) |
| 871± 2 AD | GRIP | Yes | Settlement layer | Veidivötn, Torfajökull, Iceland | Grönvold et al. (1995) |
| 877± 4 AD | GISP2 | Yes | Settlement layer | Veidivötn, Torfajökull, Iceland | Zielinski et al. (1997) |
| 1623 ± 36 BC | GISP2 | No | Unknown | Unknown | Zielinski and Germani (1998a) |
| 1645 ± 7 BC | GRIP | Attempted | Thera | Santorini | Hammer et al. (2003) |
| 7627 ± 150 years BP | GISP2 | Yes | Mount Mazama | Crater Lake, Oregon | Zdanowicz et al. (1999) |
| 10180 ± 60 years BP | GRIP | Yes | Saksunarvatn Ash | Grimsvötn, Iceland | Grönvold et al. (1995) |
| 10325 ± 205 years BP | GISP2 | Yes | Saksunarvatn Ash | Grimsvötn, Iceland | Zielinski et al. (1997) |

| Ice Core Age AD/BC/yr BP | Core | Correlated with other deposits | Eruption/Horizon | Source | References |
|---|---|---|---|---|---|
| 10428 ± 60 years BP | NGRIP | Yes | Saksunarvatn Ash | Grimsvötn, Iceland | Mortensen et al. (2005) |
| 11980 ± 80 years BP | GRIP | Yes | Z-1 (Ash Zone, Vedde, Skógar) | Katla, Iceland | Grönvold et al. (1995) |
| 12252 ± 86 years BP | NGRIP | Yes | Z-1 (Ash Zone, Vedde, Skógar) | Katla, Iceland | Mortensen et al. (2005) |
| ~12660 years BP | NGRIP | Yes | Tv-1 (I-THOL-2) | Grimsvötn, Iceland | Mortensen et al. (2005) |
| 26760 years BP | NGRIP | Yes | Fugloyarbanki | Iceland | Davies et al. (2008) |
| ~29085 years BP | NGRIP | No | NGRIP 1895.3 m | Katla, Iceland | Davies (unpublished) |
| ~30510 years BP | NGRIP | No | NGRIP 1915.5 m | Katla, Iceland | Davies (unpublished) |
| ~52000 years BP | GRIP | Yes | Z-2 (Ash Zone 2) | Kirkjufell, Torfajökull, Katla, Iceland | Grönvold et al. (1995) |
| 52682 ± 5000 years BP | GISP2 | Yes | Z-2 (Ash Zone 2) | Kirkjufell, Torfajökull, Katla, Iceland | Zielinski et al. (1997) |
| ~75400 years BP | GRIP | No | Unknown | Katla, Iceland | Grönvold et al. (1995) |
| ~76500 years BP | GRIP | No | Unknown | Unknown | Grönvold et al. (1995) |
| ~77500 years BP | GRIP | No | Unknown | Katla, Iceland | Grönvold et al. (1995) |
| ~80150 years BP | NGRIP | No | NGRIP 2620.05 m | Iceland | Davies (unpublished) |
| ~80985 years BP | NGRIP | No | NGRIP 2631.9 m | Katla, Iceland | Davies (unpublished) |

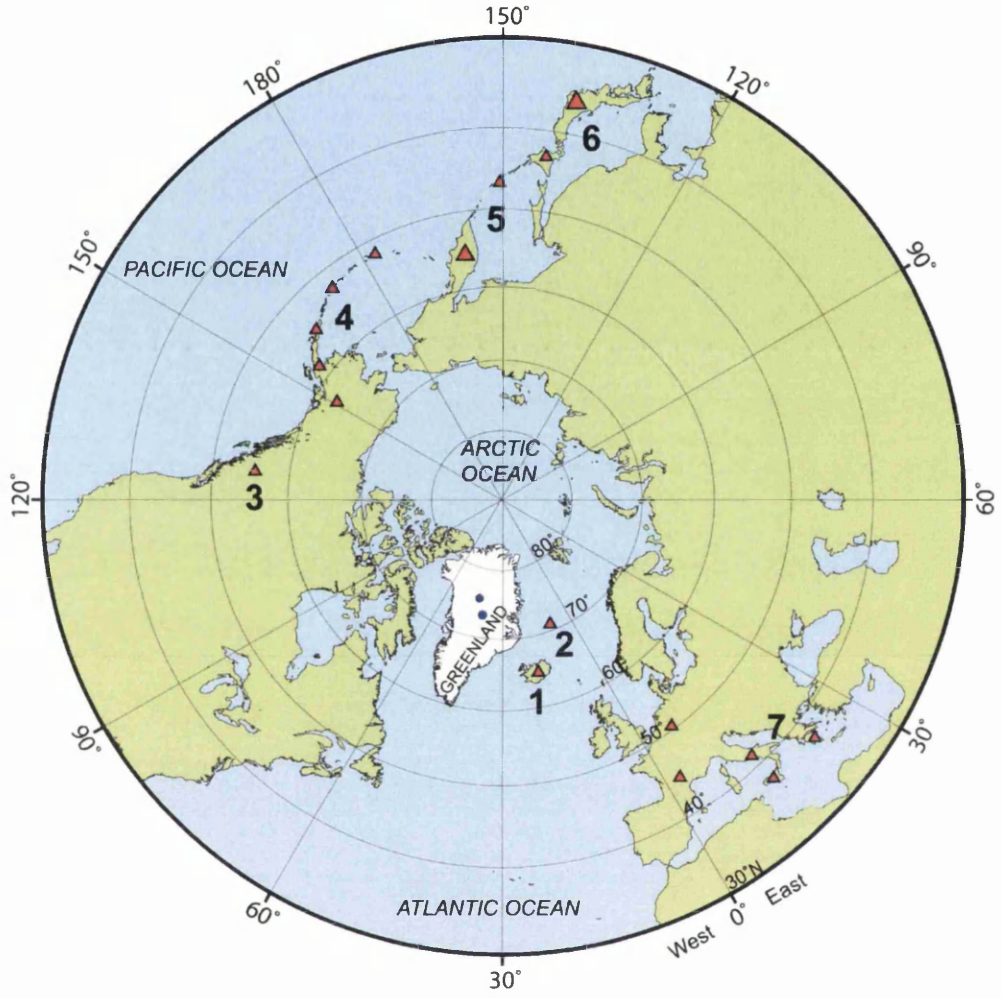


**Figure 2.5:** Volcanic regions with the potential to deposit tephra horizons within the North Atlantic region. Volcanic regions: 1: Iceland; 2: Jan Mayen; 3: Cascades; 4: Alaska-Aleutian Islands; 5: Kamchatka-Kurlie Islands; 6: Japan; 7: Mediterranean Europe.

### 2.4.4.1 Iceland and Jan Mayen

The dominant source of the tephra horizons summarised in table 1.1 is Iceland, which is not unexpected due to its close proximity to Greenland and high eruption frequency during the Late Quaternary. It is generally assumed that the transport of tephra shards from Iceland to Greenland occurs via a northwesterly dispersal within the troposphere, however the transport mechanisms are not fully understood and it may be possible that a circumarctic pathway exists (Mortensen et al., 2005). This is due to the prevailing westerly winds that exist at high altitudes over Iceland (Lamb, 1972).

Several of the key Icelandic tephra horizons found extensively in North Atlantic marine and Northern European terrestrial sequences have been identified within the Greenland ice-cores. For example, the Vedde and Saksunarvatn Ash, have both been identified in visible and cryptotephra form in marine and terrestrial sequences from the North Atlantic region (e.g. Lacasse et al., 1995; Wastegård et al., 1998; Wastegård et al., 2001). In addition, horizons previously identified within marine sediments such as North Atlantic Ash Zone 2 (Z-2) and the Fugloyarbanki Tephra have been identified within the ice-core records forming important chronostratigraphic tie-lines between the sequences and demonstrating that it is possible to trace horizons between depositional environments during the glacial period. However, to date little work has focused on the identification of tephra horizons within the MIS 4 sections of the ice-cores.

The most intensive study of cryptotephra horizons within the NGRIP ice-core was completed by Mortensen et al. (2005) who focused on the identification of horizons within the Last Glacial Termination. Within this study 12 horizons were identified that contained multiple shards, three of these could be linked to known Icelandic eruptions (see table 1.1) and the major element chemistry of the other horizons mainly point towards an Icelandic origin. However other sources (e.g. Cascades, Alaska, Japan) are not entirely ruled out for some of the horizons. Overall, this study demonstrated the dominance of Iceland as a source of volcanic horizons within the Greenland ice-cores and the value of intensively studying specific time periods within the cores as many eruptions not previously identified in the geological record were isolated.

At present no horizons that can be definitively linked to a Jan Mayen source have been identified, however, it should not be ruled out as a potential source as it is the volcanic region with the closest proximity to the Greenland ice-core deep drilling sites (figure 2.5; region 2).

### 2.4.4.2 North America

At present four tephra horizons have been identified within Greenland ice-cores that have been attributed to North American volcanic regions; two from Alaska and two from the Cascades volcanic region (regions 3 and 4 on figure 2.5). The westerly jet stream that dominates high altitude atmospheric circulation between 30 to 70°N provides a plausible pathway along which tephra from these volcanic regions could be transported prior to deposition over Greenland (Fiacco et al., 1994; Lamb, 1972).

It has been reported that tephra shards are present within the NGRIP ice-core within the 1912 AD layer and can be reliably correlated to the Katmai eruption from Alaska, which occurred during that year (Pilcher, pers com, 2005). At present this data has not been published therefore an assessment of the robustness of this correlation based on major element geochemistry is not possible. The second tephra horizon that may potentially derive from an Alaskan source is a horizon identified within the GRIP core dated to 1645 ± 7 BC. It has been suggested that this tephra was derived from the Aniakchak volcano (Pearce et al., 2004b) although, the provenance of this horizon has been widely debated and will be discussed further in section 2.4.4.4.

Zdanowicz et al. (1999) provides evidence for the identification of material within the GISP2 ice-core that can be related to the Mount Mazama eruption which occurred within the Cascades volcanic region. This correlation is based on major element similarities between tephra shards identified within the cores and proximal deposits, and is supported by the similarity between the calibrated radiocarbon age for the eruption (7545-7711 cal yr BP) and ice-core age for the horizon (7627 ± 150 yr BP) (Zdanowicz et al., 1999). Fiacco et al. (1993) attributed tephra shards in the 1479 AD layer of the GISP2 ice-core to the volcanic eruption that formed the Mount St. Helens Wn tephra (1479-1480 AD). However, geochemical differences between the material identified within the ice-core and proximal deposits from this eruption indicate that this correlation is questionable.

### 2.4.4.3 Northwest Pacific Rim

At present no tephra horizons from volcanic regions around the Northwest Pacific Rim (Japan, Kurile Islands, Kamchatka; regions 5 and 6 on figure 2.5) have been identified

within Greenland ice-cores, however, they are often suggested as possible sources of rhyolitic horizons not correlated to known deposits. For example it has been suggested that a Japanese volcano is the potential source of shards present within the ~1604 AD layer of the GISP2 ice-core (de Silva and Zielinski, 1998). In addition, Mortensen et al. (2005) suggested that some horizons within the Last Glacial Termination section of NGRIP could have originated from these sources. Transport of shards prior to deposition on Greenland could occur within the high altitude westerly jet stream, see section 2.4.4.2, and within the transport pathway shown to transport continental dust from East Asia to Greenland during the last glacial phase (Svensson et al., 2000).

#### 2.4.4.4 Mediterranean Europe

The possibility that tephra from a volcanic eruption occurring within Mediterranean Europe has been deposited on the Greenland Ice Sheet is widely debated and concerns the potential deposition of the products of an eruption of the Thera (Santorini) volcano, Greece, during the second millennium BC (Warren, 1984).

Zielinski and Germani (1998a) identified and geochemically characterised tephra particles from the GISP2 ice-core related to a large sulphate spike within a layer corresponding to 1623 ± 36 BC. This date relates well to a 1628/1627 BC age for the Santorini eruption inferred from climatic perturbations recorded in tree ring sequences (Baillie and Munro, 1988). However, geochemical characterisations of this material does not relate to proximal deposits from the Santorini eruption or other large volcanic eruptions known to have occurred at the time (Zielinski and Germani, 1998a; Vogol et al., 1990). This led Zielinski and Germani (1998a) to suggest that the shards were derived from an eruption undocumented in the geologic record, potentiality from Kamchatka, Alaska or an equatorial source. Manning (1998) and Schmid et al. (2000) both challenged this conclusion and suggest that the material does relate to the Santorini eruption; however the evidence they present does not fully support this claim (Zielinski and Germani, 1998b).

The debate regarding the age of the Santorini eruption recommenced when Hammer et al. (2003) found tephra shards within a layer of the GRIP ice-core corresponding to 1645 ± 7 BC. These shards were analysed for their major element composition using an analytical scanning electron microscope and trace element composition using secondary ion mass spectrometry. Based on both of these characterisations and a

comparison to data from proximal deposits, Hammer et al. (2003) concluded that the GRIP shards originated from the Santorini eruption. However, Eastwood et al. (2004) highlighted that there are large analytical errors on the data presented in Hammer et al. (2003) and compositional differences with proximal deposits for many elements (e.g. $SiO_2$, FeO, MgO and some trace elements). The correlation made by Hammer et al. (2003) was also challenged by statistical comparisons presented in Kennan (2003). Based on new analyses of the major and trace element composition of proximal deposits an alternative source for the horizon, the Aniakchak volcano in Alaska, was proposed by Pearce et al. (2004b). This proposition has not been fully accepted and debate regarding the origin of this horizon has continued (e.g. Denton and Pearce, 2008; Vinther et al., 2008).

Evidence for material from another Mediterranean volcanic eruption, the 79 AD Vesuvius eruption, within both the GRIP and Dye 3 cores is referred to by Hammer et al. (2003). However, this claim is currently unsubstantiated because detailed geochemical information relating to this discovery has not been published.

Therefore, there is no conclusive evidence for the deposition of tephra horizons produced by eruptions within Mediterranean Europe over the Greenland Ice Sheet. As a consequence this will only be considered as a potential source if the geochemistry of a horizon does not relate to deposits of more proximal volcanic regions.

#### 2.4.4.5 Low Latitude Eruptions

The deposition of products of low latitude eruptions on the Greenland Ice Sheet and the existence of bipolar tephra horizons appears to have been demonstrated by the work of Palais et al. (1990, 1992). This work identified rhyolitic shards with comparable geochemical compositions from approximately coeval positions within ice-cores from both poles. The tephra shards were related to a strong sulphuric peak dated to ~1259 AD that has been recorded in ice-cores from Greenland, Antarctica and Arctic Canada (e.g. Zielinski, 1995; Langway et al., 1988; Fisher and Koerner, 1988). Langway et al. (1988) suggested that this eruption occurred close to the equator in the Northern Hemisphere based on a comparison of the ratio of sulphur deposition from this eruption in Greenland and Antarctica to the deposition of total-beta radioactivity from nuclear-bomb tests (Palais et al., 1992).

At present, a volcanic source for this horizon has not been identified as suggested eruptions from Mexican and New Zealand volcanic sources have been ruled out based on chronological issues (see Buckland et al., 1997; Lowe and Higham, 1998; Oppenheimer, 2003). Oppenhemier (2003) suggests that strong candidate provinces could be the tropical island arcs, such as Indonesia, Melanesia, Polynesia and Micronesia. These centres offer the potential to conceal the 10-30 km diameter crater that Oppenheimer (2003) proposes was created during this eruption.

## 2.4.5 Tephrochronology of Potential Source Regions During MIS 4

### 2.4.5.1 Iceland

Due to the high productivity of the Icelandic volcanic region and the dispersal of ash from eruptions over a wide geographical extent numerous previous studies have identified tephra horizons within ice, marine and terrestrial sequences from the North Atlantic region covering the last glacial cycle (figure 1.2; e.g. Bramlette and Bradley, 1941; Ruddiman and Glover, 1972; Kvamme et al., 1989; Sjøholm et al., 1991; Grönvold et al., 1995; Lacasse et al., 1996b; Ram et al., 1996; Lackschewitz and Wallrabe-Adams, 1997; Fronval et al., 1998; Lacasse et al. 1998; Haflidason et al., 2000; Lacasse and Garbe-Schönberg, 2001; Wastegård and Rasmussen, 2001; Rasmussen et al., 2003; Wallrabe-Adams and Lackschewitz, 2003; Austin et al., 2004; Wastegård et al., 2005; Wastegård et al., 2006; Svensson et al., 2008; Davies et al., 2008; S. Davies, unpublished).

However, this assessment of previously identified horizons highlights a gap in the overall tephrochronological framework for the MIS 4 period (figure 1.2). The paucity of North Atlantic tephra horizons identified during the MIS 4 period is likely to be due to a lack of focus on this period within previous studies. Because, the identification of tephra horizons within MIS 2, 3 and 5 sequences indicates that Icelandic volcanic regions were active throughout the last glacial period and produced widespread horizons.

### 2.4.5.2 Other Potential Source Regions

An inspection of the tephrochronological records from other sources regions, identified as potential contributors of tephra horizons to the Greenland ice-core records, reveals evidence for some volcanic activity during MIS 4.

The most significant eruption occurring during the study period is the low latitude eruption of Toba, Sumarta (71,000-73,000 ± 5000 yr BP) (Zielinski, 2000; Schulz et al., 2002). This eruption may have been the greatest single eruption within the Quaternary, however, Oppenheimer (2002) suggests it had a limited global, climatic impact. Zielinski et al. (1996b) identified a large volcanic signal at 71,000 ± 5000 yr BP between DO 20 and 19 within the GISP2 core and attributed this to the Toba eruption. This inference was supported by the presence of the Toba tephra horizon between two interstadial events correlated to DO 19 and 20 recorded within sediment cores from the Arabian Sea (Schulz et al., 2002). This tephra horizon was widely dispersed over the Indian Ocean and continent and has been well characterised geochemically for both its major and trace element composition (Westgate et al., 1998; Song et al., 2000). It has been suggested that a double peak in sulphate at 2548 m depth within the NGRIP chemostratigraphy represents the deposition of aerosols from the Toba eruption on the Greenland Ice Sheet (S.J. Johnsen, *pers. comm.*, 2006).

The Japanese volcanic regions were highly active during the last glacial cycle, and may have deposited horizons during MIS 4 (Aoki and Machida, 2006). However, the chronostratigraphic control on these horizons is insufficient to attribute any to deposition during MIS 4. The K3 tephra horizon, believed to have been sourced from the Nemo Volcano, Onekotan Island, Kurile Islands was identified within the MIS 4 section of a marine core from the Sea of Okhotsk by Gorbarenko et al. (2002). At present, no volcanic horizons of an MIS 4 age erupted from North American volcanic regions have been identified.

### 2.4.6 Assigning Ages to Tephra Horizons in the Greenland Ice-cores

A distinct advantage of utilising the NGRIP and GRIP ice-cores within the construction of a tephrochronological framework is that a common timescale for both cores, Greenland Ice-core Chronology 2005 (GICC05), has been complied and this can be used to assign ages to any identified horizons. These high-precision ages can then be assigned to any occurrences of these tephra horizons within other sequences thus improving the dating of these sequences, which is crucial to using tephrochronology to determine the mechanisms controlling the DO events.

The GICC05 chronology has been developed back to 60 ka BP for the NGRIP core using a multi-parameter approach, which relies on the identification and counting of

annual cycles within oxygen isotope ratios and concentrations of chemical species (e.g. sodium, calcium, ammonium, nitrate and sulphate) measured using CFA (Andersen et al, 2006; Rasmussen et al., 2006; Svensson et al., 2006, 2008; Vinther et al., 2006). This chronology is being transferred to the GRIP ice-core using common reference horizons (Rasmussen et al., 2008; see section 3.2.3.2). The chronologies developed using these counting techniques have a high precision, for example GICC05 has an error of approximately 1.3 ka at 60 ka BP, which is unprecedented in comparison to other ice-core timescales (Svensson et al., 2008). This counted chronology will be extended through the MIS 4 period, however, at present the timescales are extended past 60 ka BP using ice-flow models (A. Svensson, *pers. comm.*, 2008).

### 2.4.7 Tracing Horizons in North Atlantic Marine Sediments

Following the construction of a tephrochronological framework for the Greenland ice-cores the tracing of these horizons into North Atlantic marine sediments is the next crucial step towards synchronising palaeoclimatic records for the MIS 4 period. The ability to identify volcanic horizons in these records has been demonstrated previously and they form a significant component of the tephrochronological framework for the last glacial period (figure 1.2). The most notable of these horizons is North Atlantic Ash Zone II (NAAZ II) which is a significant marker horizon within MIS 3 records. This horizon was first identified by Bramlette and Bradley (1941) and was later described by Ruddiman and Glover (1972) (Wastegård et al., 2006). Material related to the components of this ash zone has a widespread distribution within the North Atlantic and was transported throughout the area by ice-rafting processes (e.g. Kvamme et al., 1989; Lacasse et al., 1996; Haflidason et al., 2000; Austin et al., 2004). Material with a similar composition to this ash zone has been identified within the GRIP, GISP2 and NGRIP ice-cores (Grönvold et al., 1995; Ram et al., 1996; Svensson et al., 2008). Other notable widespread marine deposits are Faroe Marine Ash Zone (FMAZ) III (~33 $^{14}$C ka BP) and the Fugloyarbanki Tephra (~23 $^{14}$C ka BP; also referred to as FMAZ II). Both of these basaltic horizons have been identified within a series of marine cores from the Faroe Islands region and the Fugloyarbanki Tephra has also been identified within marine cores from the Reykjanes Ridge and the Labrador Sea (Lackschewitz and Wallrabe-Adams, 1997; Rasmussen et al., 2003; Wastegård et al., 2006). In addition, a widespread MIS 5 horizon, 5e-Midt/RHY, was deposited during the middle of the MIS 5e sub-stage (~124 ka BP) and has been identified in various marine cores from the Norwegian and Greenland Seas and a terrestrial site in the Faroe Islands (e.g.

Sjøholm et al., 1991; Fronval et al., 1998; Lacasse and Garbe-Schönberg, 2001; Wallrabe-Adams and Lackschewitz, 2003; Wastegård et al., 2005).

The major difference between horizons identified in North Atlantic marine sediments and the Greenland ice-cores is that different transportation processes can be responsible for the deposition of horizons in the marine environment. As well as being deposited via direct airfall, horizons can be deposited via ice-rafting of both sea ice and icebergs calved from Icelandic ice sheets (Austin et al., 2004). Ice-rafting of volcanic material can result in material larger than expected being deposited at distal sites and the focus of previous studies, on the identification of tephra horizons with grain sizes larger than 150 μm in diameter, has biased studies towards the identification of ice-rafted horizons (e.g. Wastegård and Rasmussen, 2001; Rasmussen et al., 2003; Wastegård et al., 2006).

The development of density separation techniques for the identification of deposits of fine ash less than 80 μm in diameter has revolutionised the identification of cryptotephra deposits in terrestrial sequences (e.g. Turney, 1998; Zillén et al., 2002; Davies et al., 2005; Koren et al., 2008). The application of this technique to the study of cryptotephra horizons in marine cores has been limited. However, its successful application has been demonstrated by Lowe et al. (2007) who used density separation to identify fine ash deposits in marine cores from the Southern Adriatic. The use of this technique within the investigation of North Atlantic marine sequences may lead to the identification of fine ash material and tephra horizons that would have been overlooked using the techniques exploited in previous studies. The likelihood that any identified horizons were deposited via primary airfall is greater for smaller particles sizes and their effectiveness as chronostratigraphic markers is greater relative to ice-rafted deposits due to their stratigraphic integrity.

## 2.5 Geochemical Characterisation of Tephra Horizons

### 2.5.1 Major Element Characterisation

A wide range of analytical techniques have been used to geochemically characterise the major element composition of glass shards in tephra horizons. Some utilise bulk samples of shards such as X-ray fluorescence (XRF; e.g. Norddahl and Haflidason, 1992), instrumental neutron activation analysis (INAA; e.g. Schmid et al., 2000) and

inductively coupled plasma mass spectrometry (ICP-MS; Eastwood et al., 1999) (Turney et al., 2004). However, bulk samples are vulnerable to contamination from other material, such as phenocrysts and detritus, and the samples sizes required may be greater than can be extracted from distal and cryptotephra horizons (Shane, 2000; Pearce et al., 2004). Thus, grain-discrete methods that analyse the geochemical composition of individual glass shards are favoured because they circumvent the problems of contamination and sample size, while offering higher analytical precision (Turney et al., 2004). At present the most widely used technique is electron probe micro-analysis (EPMA), which was developed during the 1960s (Smith and Westgate, 1969) and measures the major element composition of individual tephra shards.

### 2.5.2 Electron Probe Micro-Analysis (EPMA)

EPMA measures the major element composition of a tephra shard by analysing the energy of X-rays produced when it is bombarded by an electron beam. The energy of the X-rays produced by each major element is unique and the intensity of production is proportional to the amount of the element present within the shard (Hunt and Hill, 1993). Therefore, by measuring the X-rays produced during bombardment it is possible to determine the composition of the shard (Hunt and Hill, 1993).

There are two types of EPMA, Energy Dispersive Spectrometry (EDS) and Wavelength Dispersive Spectrometry (WDS), which differ in the way they measure the X-rays produced. During EDS X-rays of all energies are measured simultaneously whereas in WDS they are measured individually and sequentially via the tuning of the spectrometer to only one wavelength at a time (Reed, 2005; Davies et al., 2002). The sequential measurement of X-rays in WDS offers a higher analytical precision and allows closer monitoring of the mobility of alkalis during analysis (Hunt and Hill, 1993). Other advantages of WDS are that there is less dead time after the arrival of an X-ray pulse during which the system does not respond to further pulses. In addition, morphological distortion of readings, a common problem in EDS analysis, is reduced as samples are polished to a flat surface for analysis (Hunt and Hill, 1993; Reed, 1993). Polishing samples can also remove post-depositional shard-surface alteration and hydration, which could produce spurious analyses, and removes scratches and cracks, which could induce absorption of X-rays by the sample and reduce the amount of X-rays reaching the spectrometers (Hunt and Hill, 1993). These factors make EPMA by WDS the standard method utilised within tephrochronological studies despite

requiring a longer counting time and higher beam current than EDS (Hunt and Hill, 1993; Turney et al., 2004).

Despite being the standard analytical technique, the treatment of data produced within EPMA analysis is strongly debated. Analyses of major oxides produced using EPMA are reported as percentages of sample weight. The sum of the oxide percentages (total oxides) for individual analyses rarely equals 100% due to the relative influence of a range of factors. These include the water content of shards, the presence of unmeasured elements such as phosphorous, fluorine or chlorine, small inaccuracies introduced during sample preparation and individual shard characteristics, such as shard wall thickness, structure and impurities (Froggatt, 1983; Turney et al., 2004).

Two conventions exist for the treatment of data with low analytical totals. Firstly, to discard any totals below 95 % and utilise the raw data and secondly to accept all data with totals greater than 90 % and normalise the data to 100 %, i.e. a volatile-free anhydrous basis (Froggatt, 1992; Hunt and Hill, 1993; WoldeGabriel et al., 2005; Pearce et al., 2008b). The first convention is typically followed within north European tephra studies, while the second is in common use in most other areas where tephrochronological studies are undertaken, e.g. East Africa, North America and New Zealand.

The main argument for not normalising data and rejecting low totals is that they are due to poor point selection, inappropriate probe conditions or the analysis of altered shards (Hunt and Hill, 1993). The normalisation of data may mask the quality of data, extend the range of elements for particular tephras and potentially create false correlations (Hunt and Hill, 1993; Pollard et al., 2006). Whereas, others argue that normalising data to 100% is required because the degree of shard hydration (water content) is the dominant control on total oxide values and is related to the environment of deposition for a particular horizon, not formation processes (Froggatt, 1992; Pearce et al., 2008b). It is possible for a shard to contain 10 % water without geochemical alteration taking place, therefore, tephra shards from a particular eruption deposited in disparate environments may have different water contents but not be geochemical altered. Normalising will permit geochemical comparisons of the deposits in the different environments and enhance the data by making outliers easier to identify and reduce the dispersion of data (Pearce et al., 2008b). Within this study major element analyses from horizons will be normalised to 100 %; the use of this convention is justified in section 3.5.2.1.

### 2.5.3 Is EPMA an Adequate Characterisation Technique?

A limitation of solely using major oxide composition data is that in some instances it is not possible to adequately discriminate between tephras produced from the same volcano or different volcanic centres (Haflidason et al., 2000). This may cause problems if horizons are deposited within a short space of time and stratigraphic or chronological differences cannot be used to confidently discriminate between the horizons. An example of this is provided by the Borrobol Tephra that was sourced from Iceland and was first identified in Scottish lake sediments close to the initial warming of Greenland Interstadial-1 (Allerød) (Turney et al., 1997). Subsequent investigations identified a horizon with an identical major element composition in a Swedish lake sequence, however, high-resolution $^{14}C$ ages and the pollen stratigraphy imply that this horizon was deposited later than the Borrobol tephra in Scotland (Davies et al., 2004). This led Davies et al. (2004) to question whether they represent two separate eruptions with the same major element geochemistry. Further studies have also proposed that two eruptions with 'Borrobol'-like geochemistry occurred closely spaced in time (Pyne-O'Donnell et al., 2007). Additional geochemical discrimination methods could be used to determine if the horizons represent the products of one or two volcanic events. The current proliferation in tephrochronological studies and continual identification of new tephra horizons means this issue will become more pertinent within future studies.

It has been widely recommended that the relative proportions of minor, trace and rare earth elements within tephra shards may prove to be more discriminatory than major oxide characterisations (Turney et al., 2004). Wilson (1989) has shown that different tectonic settings can have distinctive trace element signatures and Pearce et al. (2008b) highlighted that magmatic processes can cause subtle and difficult to detect differences in major element concentrations but induce significant changes in trace element composition. Therefore, the analysis of the trace element composition of tephra horizons could be used to improve characterisations, help to discriminate between horizons or strengthen correlations by providing concentration data for an additional 20-30 elements (Pearce et al., 2004a).

### 2.5.4 Trace Element Characterisation

Trace elements are elements present within geological material with concentrations of less than 0.1 % or 1000 parts per million (ppm) (Davies, 2002; Rollinson, 1993). During

trace element analysis a large suite of elements can be measured; a sub-set of which is the rare earth elements (REEs). The REEs are a series of elements with atomic numbers between 57-71 (La-Lu) which are the most useful trace elements and are important for the understanding of igneous petrology (Rollinson, 1993). Typically low atomic number REEs such as La and Ce are referred to as the light rare earths (LREE) and high atomic number REEs such as Er and Yb are referred to as heavy rare earths (HREE).

Initial work on characterising the trace element composition of tephra deposits used methods such as XRF (e.g. Lacasse et al., 1995), instrumental neutron activation analysis (INAA) (e.g. Paterne et al., 1986) and atomic absorption spectrophotometry (AAS), which all rely on the analysis of bulk samples. However, these methods cannot be applied to the study of distal and cryptotephra horizons due to the relatively large volume of material required (~0.25-3 g) (Davies, 2002). Techniques such as proton induced X-ray emission (PIXE, e.g. Fraser, 1995) and ion microprobe analysis (e.g. Hinton, 1995) have been developed and could be utilised for grain-specific trace element analysis as these techniques both provide excellent spatial resolution and very low detection limits. However, they have proven to be slow and very expensive and currently have not been applied widely to the analysis of single tephra shards (Pearce et al., 2004a).

One method that provides considerable potential for trace element analysis of distal tephra horizons is ICP-MS. This technique was developed during the early 1980s and gained recognition during the late 1980s for the analysis of the trace elements of dissolved bulk samples, and is currently a widely used geochemical characterisation tool (Pearce et al., 2004a). Two ICP-MS methods are available for the analysis of tephra horizons, solution nebulisation and laser ablation, but only the latter is able to undertake single-grain analyses (Pearce et al., 2004a). The application of solution nebulisation ICP-MS to the geochemical characterisation of small volumes of tephra shards and cryptotephra horizons has been explored previously (see Davies, 2002). It was found that solution nebulisation can be used to analyse small volumes of shards, however inaccuracies are introduced when samples <20 µg are analysed due to errors relating to weight measurement (Davies, 2002).

Therefore, when studying cryptotephra horizons yielding a small amount of volcanic material, the ability to gain single-grain analyses makes laser ablation ICP-MS the most suitable technique for trace element characterisation.

### 2.5.5 Laser Ablation Inductively Coupled Plasma Mass Spectrometry (LA-ICP-MS)

During LA-ICP-MS, material is ablated from the surface of a shard using a laser before being fed into a mass spectrometer for the relative proportions of different elements to be ascertained (see section 3.5.3 for full description). The first LA-ICP-MS devices were developed during the late 1980s (e.g. Gray, 1985; Arrowsmith, 1987) and utilised infrared laser systems coupled to an ICP-MS to achieve a spatial resolution of ~150 µm (Pearce et al., 2004a). The modification of laser systems during the 1990s to use ultraviolet wavelengths (e.g. 266 nm or 213 nm) improved laser absorption and stabilised ablation, allowed spatial resolution to be improved to approximately 30 µm (Pearce et al., 2007). Coupled with improvements in ICP-MS sensitivity, to maintain acceptable detection limits (see Pearce et al., 1999, 2007), it became possible to use LA-ICP-MS to analyse single tephra shards of ~40 µm in diameter (Pearce et al., 2007). Calibration strategies that utilise analyses of reference materials, such as the National Institute for Standards and Technology soda lime silicate glasses NIST 610 and 612, and the concentration of an element within shards previously determined using EPMA have been developed to allow absolute trace element concentrations to be calculated (Perkins and Pearce, 1995; Pearce et al., 1996; see section 3.5.3.3). The use of characterisations of single tephra shards by these LA-ICP-MS systems within tephrochronological studies has subsequently been demonstrated (Bryant et al., 1999; Pearce et al., 1999; Shane et al., 1999; Westgate et al., 2008). For example, Pearce et al. (2008b) utilised trace element characterisations of silicic tephra beds within the Auckland region, New Zealand to support earlier correlations based on major element characterisations. In addition, the characterisations provided information regarding the petrogenetic evolution of rhyolitic volcanism in the Taupo Volcanic Zone. Despite this success the application of LA-ICP-MS to the analysis of volcanic horizons deposited within ultra-distal locations such as the Greenland ice-cores, where tephra shards are typically less than 30 µm in diameter, has to date proved problematic (e.g. Davies et al., 2005b).

However, recent developments in ICP-MS instrumentation have enhanced sensitivity and lowered background counts, which could potentially improve analytical precision and lower detection limits allowing smaller glass shards to be analysed (Pearce et al., 2007). In particular when these ICP-MS systems are coupled with shorter wavelength laser systems, 193 nm instead of 266 nm, which are more efficient due to greater laser

absorbance permitting more controlled ablation of tephra shards (Gonzalez et al., 2002; Pearce et al., 2007). The potential of using these new systems for the analysis of small shards from cryptotephra horizons deposited within distal locations was highlighted by Pearce et al. (2007) but is yet to be explored (see chapter 4).

## 2.6 Geochemical Characteristics of the North Atlantic Volcanic Regions

It has been highlighted that of the potential source regions the most likely sources of horizons present within both the Greenland ice-cores and North Atlantic marine sequences are the Icelandic and Jan Mayen volcanic regions. It was also highlighted that the key method for the correlation of horizons is robust geochemical characterisation, however it is also important if tephra horizons are to improve the knowledge of the volcanic history of source regions. The geochemistry of distal tephra deposits are controlled by processes at the volcanic source and thus have direct relations to the composition of proximal deposits. Therefore, an understanding of the nature of the two key volcanic regions of Iceland and Jan Mayen and the geochemical characteristics of the material they produce is required.

### 2.6.1 Icelandic Volcanism

Volcanic systems within Iceland produce material ranging in composition from basaltic to silicic, with rhyolitic material being the dominant silicic rock type (Lacasse and Garbe-Schönberg, 2001). The general form of Icelandic volcanic systems is a central volcano, which erupts both basaltic and rhyolitic products, with an associated fissure swarm that only produces basaltic material (Larsen and Eiríksson, 2008). In total, thirty-two volcanic systems have been defined in Iceland based on petrological differences in their erupted material (Jakobsson, 1979; Gudmundsson, 2000). Geographically the volcanic systems are grouped into rift zones and flank zones. The rift zones represent the subaerial continuation of the Mid-Atlantic rift across Iceland and active rifting occurs within these areas (Jónasson, 2007). The flank zones are areas off the main rift zones where no active rifting is observed (Lacasse and Garbe-Schönberg, 2001). Two rift zones have been defined, the western rift zone (WRZ) and the eastern rift zone (ERZ), and three flank zones, the western, southern and eastern flank zones (WFZ, SFZ and EFZ). The location of these zones and the major volcanic systems that fall within them are marked on the map in figure 2.6.

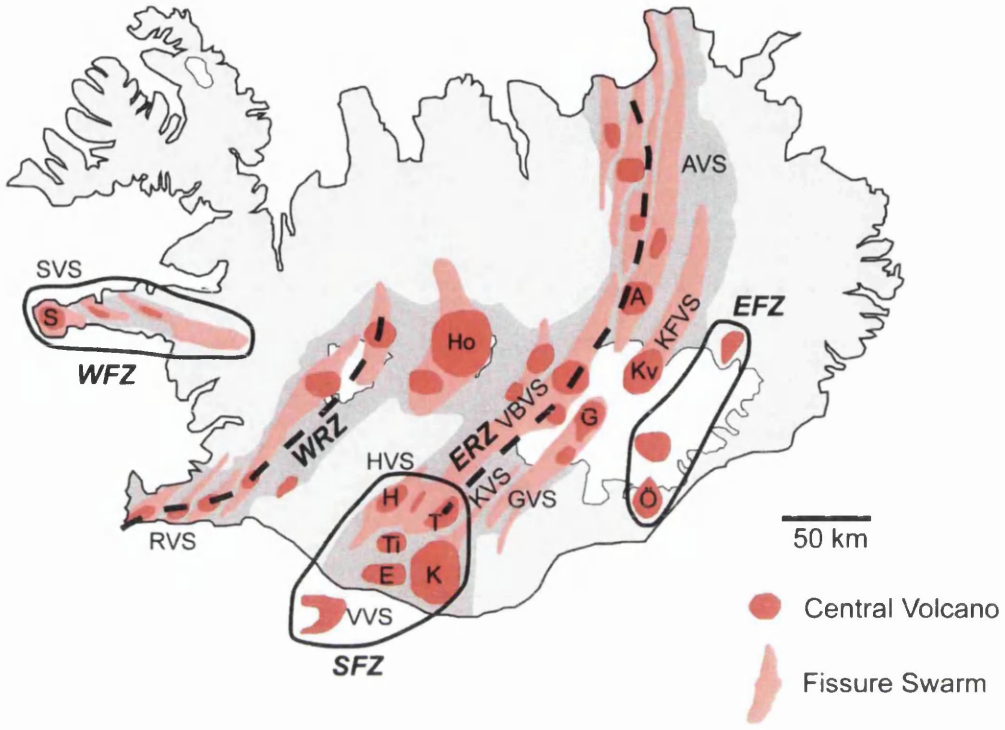


**Figure 2.6:** Major volcanic systems and central volcanoes of Iceland adapted from Jónasson (2007) and Larsen and Eiríksson (2008). Dashed lines represent the crests of the ERZ and WRZ. Solid lines indicate the location of the flank zones. Dark grey shading indicated areal extent of rocks erupted since the Brunhes magnetic epoch (<800 ka). Volcanic systems marked are the Snæfellsnes volcanic system (SVS), Reykjanes volcanic system (RVS), Askja volcanic system (AVS), Kverkfjöll volcanic system (KFVS), Veidivötn-Bárdarbunga volcanic system (VBVS), Hekla volcanic system (HVS), Katla volcanic system (KVS), Grímsvötn volcanic system (GVS) and Vestmannaeyjar volcanic system (VVS). Central volcanoes marked are Snæfellsjökull (S), Askja (A), Hofsjökull (Ho), Bárdarbunga (B), Kverkfjöll (Kv), Grímsvötn (G), Hekla (H), Torfajökull (T), Tindfjallajökull (Ti), Eyjafjallajökull (E), Katla (K) and Öræfajökull (Ö).

The geochemical composition of the material produced by the volcanic systems of Iceland fall into three rock suites, tholeiitic, transitional alkaline and alkaline (figure 2.7). All of the rock suites contain material across the compositional range from basaltic to rhyolitic, however, basaltic material is predominately erupted from the Icelandic centres (Jakobsson et al., 2008). Tholeiitic and alkali suites can be distinguished based on the lower alkali ($K_2O$ and $Na_2O$) content of the tholeiitic material, with only a minor overlap between the suites for some basaltic material (figure 2.7a). Alkali values for the transitional alkali material lie between the other two rock suites, with high overlaps apparent for basaltic material. Figure 2.7b also illustrates the differences between the compositions of the series, and emphasises the high-Ti contents of the Icelandic basalts. The three series can also be differentiated using other major oxides such as $Al_2O_3$, which has a higher concentration in alkali and transitional basalts than tholeiitic material, and CaO which is highest in the tholeiitic series and lowest in alkali material (Hemond et al., 1993; Jakobsson et al., 2008).

The volcanic systems producing material with affinities to these three rock suites can be grouped geographically. The volcanic systems in the rift zones produce tholeiitic (sub-alkali) material. Alkali material is produced in the systems of the WFZ and the Vestmannaeyjar system, which is part of the SFZ. The remaining systems within the SFZ and the systems of the EFZ produce material with a transitional alkali composition (Jakobsson, 1972, 1979). At the central volcanoes these compositions are paralleled in both the rhyolitic and basaltic products, i.e. volcanoes producing tholeiitic basalts also produce tholeiitic rhyolites (McGarvie, 2009).

In addition to the overall differences between the rock suites geochemical variability can be observed between the products of individual volcanic systems and compilations of analyses from individual centres, such as those of Jakobsson (1979) and Jakobsson et al. (2008), can be used in attempts to deduce the volcanic source of distal tephra horizons.

### 2.6.2 Jan Mayen Volcanism

Jan Mayen is a 54 km long volcanic island located on the Mid Atlantic Ridge 750 km NNE of Iceland (figure 2.8). Two volcanic systems approximately 25 km in length are present on the island. Firstly the northern part of the island consists of Beerenberg, a single large stratovolcano which last erupted in 1970, and secondly the southern part of

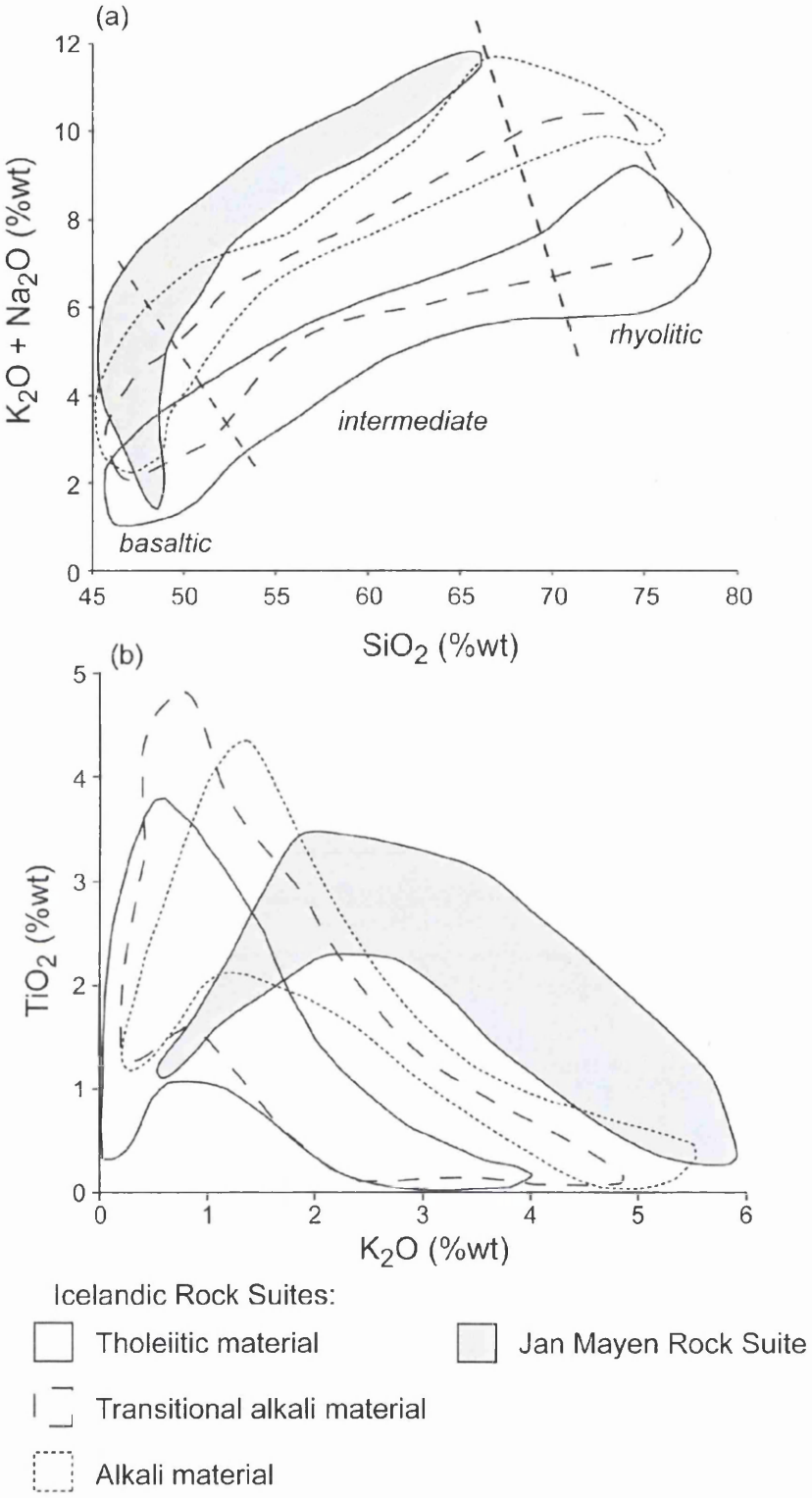


**Figure 2.7:** (a) $K_2O$ + $Na_2O$ vs. $SiO_2$ and (b) $TiO_2$ vs. $K_2O$ compositional variation diagrams for whole rock analyses of material from the three Icelandic rock suites and the Jan Mayen rock suite. Adapted from Jakobsson et al. (2008). Data for the Jan Mayen rock suite from Imsland (1984) and Maaløe et al. (1986). The approximate location of the division lines between basaltic, intermediate and rhyolitic material are shown.

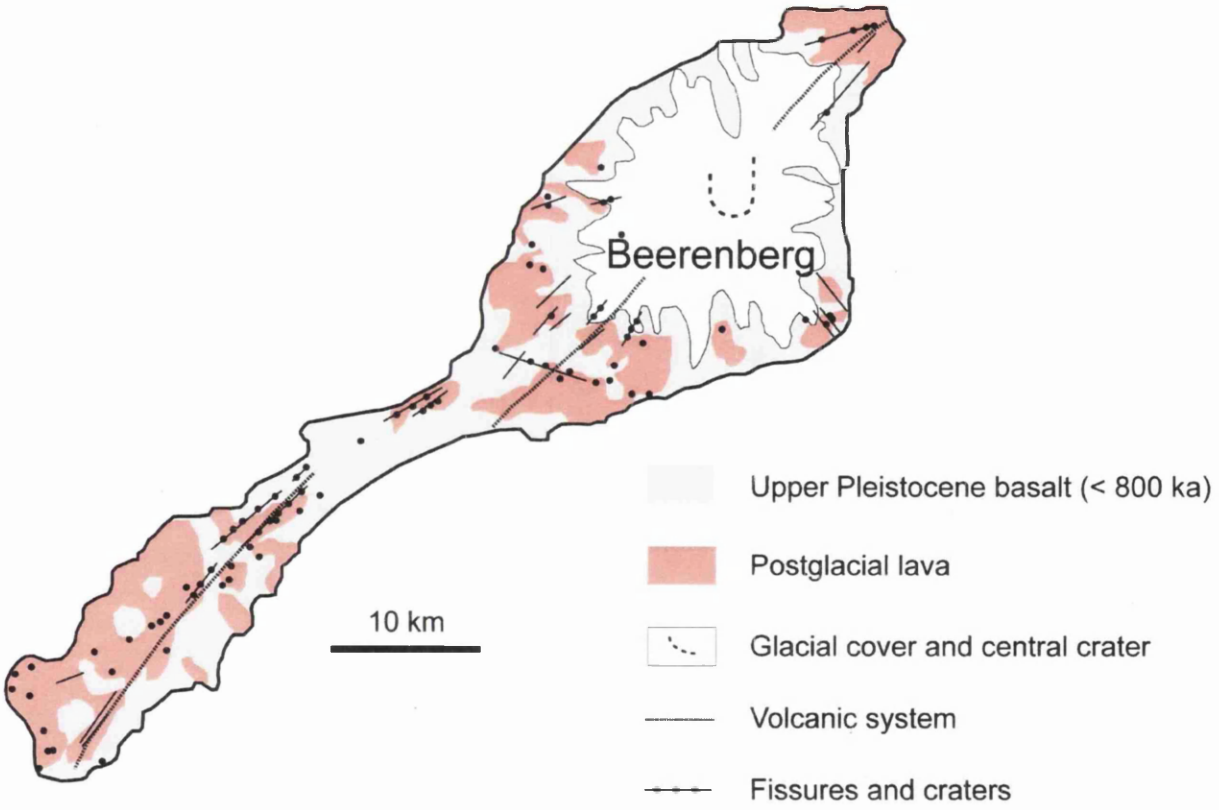


**Figure 2.8:** Volcanic systems and central volcano of the Jan Mayen island. Adapted from Lacasse and Garbe-Schönberg (2001) and Maaløe et al. (1986) both of which were adapted from the map of Imsland (1978).

the island is characterised by numerous small volcanoes aligned along NE trending fissures (figure 2.8; Maaløe et al., 1986; Lacasse and Garbe-Schönberg, 2001).

Major element geochemistry can be used to distinguish Jan Mayen volcanic material from material produced by the Icelandic volcanic systems (figure 2.7). Jan Mayen material generally displays higher total alkali values, particularly for intermediate material, and lower $TiO_2$ and CaO concentrations. There is some overlap on the total alkali versus silica plot for basaltic material (figure 2.7a), however it is possible to distinguish between these products using the $K_2O$ concentration of the material (figure 2.9). Jan Mayen basaltic products have distinctly higher concentrations of $K_2O$ (~0.6-4%wt) than Icelandic basaltic material (<1%wt). Due to the high potassium content the rock suite of Jan Mayen is classified as potassic alkaline and trachybasaltic material is the most common rock type found on the island (Imsland, 1984; Maaløe et al., 1986).

The explosive nature of Jan Mayen and its potential for contributing tephra horizons to North Atlantic records was demonstrated by Chambers et al. (2004) which describes the discovery of four tephra horizons with the distinct geochemical signature of Jan Mayen products within a Holocene lacustrine record from the Aran Islands, western Ireland. In addition, Lacasse and Garbe-Schönberg (2001) reported evidence for eight major explosive eruptions from the Jan Mayen volcanic system within marine sediments covering the last 6 Ma.

### 2.6.3 Trace Element Characteristics of the Icelandic and Jan Mayen Rock Suites

The determination of the trace element composition of rocks from Iceland and Jan Mayen is limited in comparison to the analysis of their major element composition. However, some studies have used techniques such as XRF and INAA to determine the concentrations of certain trace elements within proximal material. An understanding of these characterisations is crucial for relating the trace element characterisations of distal material to potential sources.

For both the Icelandic and Jan Mayen provinces the REE elements, or a sub-set of the more abundant REEs, were the trace elements most regularly measured in early studies aiming to characterise the composition of the main igneous rock suites within both regions (figure 2.10; e.g. O'Nions et al., 1976; Óskarsson et al., 1982; Maaløe et

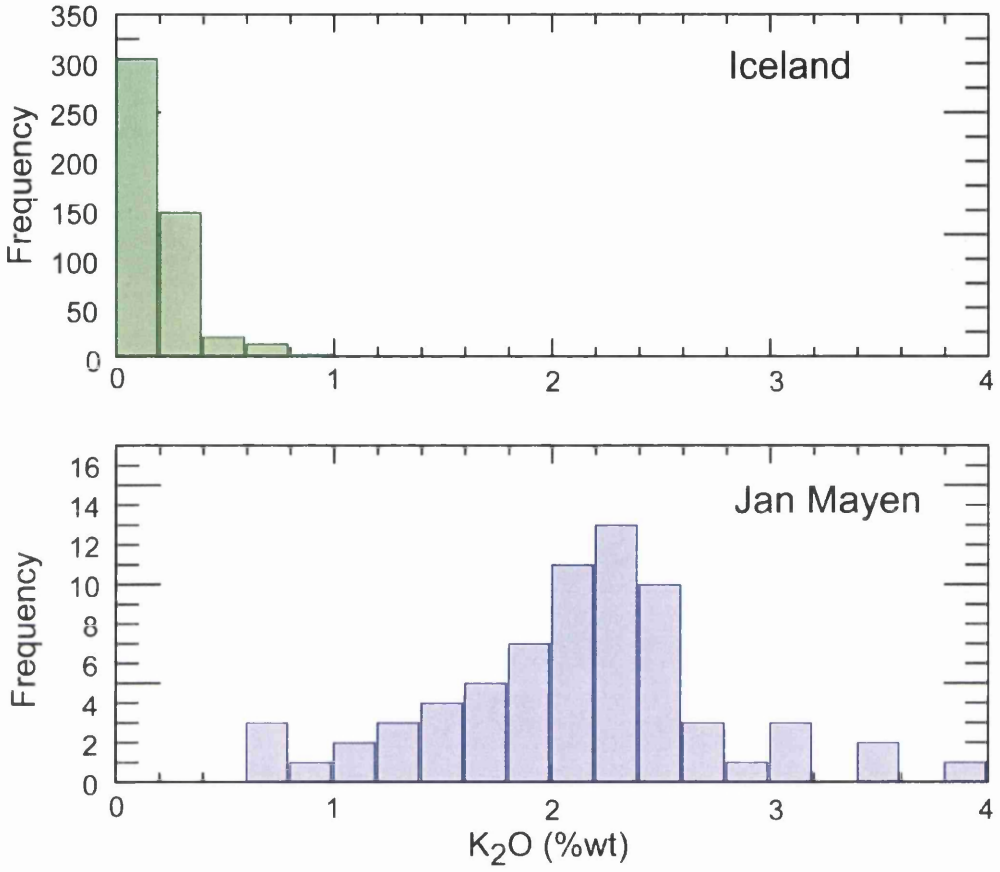


**Figure 2.9:** Frequency distributions of the $K_2O$ concentrations of rocks from Iceland and Jan Mayen with a $SiO_2$ concentration of 46-52 %wt. 489 whole rock analyses from supplementary data provided with Jakobsson et al. (2008). 69 whole rock analyses for Jan Mayen material from Imsland (1984).

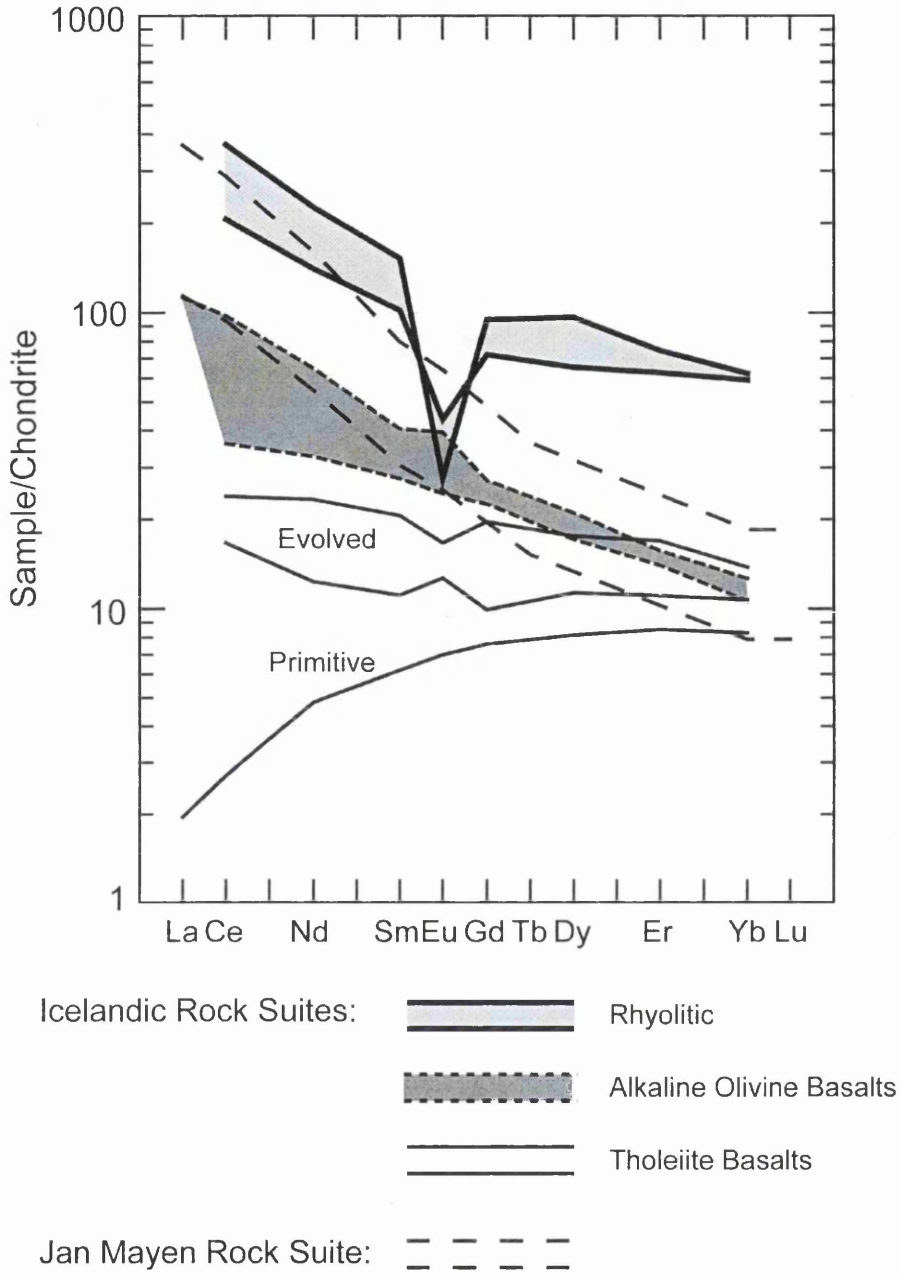


**Figure 2.10:** Chondrite-normalised REE patterns for Icelandic and Jan Mayen proximal volcanic deposits (modified from Óskarsson et al., 1982; Maaløe et al., 1986; Lacasse et al., 1996). Analyses for Icelandic fields taken from O'Nions and Grönvold (1973) and O'Nions et al. (1973, 1976) analyses for Jan Mayen field taken from Maaløe et al. (1986). La, Tb and Lu not measured in the analyses of Icelandic material and Gd, Dy and Er not measured in the analyses of Jan Mayen material. Chondrite compositions from Sun and McDonough (1989).

al., 1986). These characterisations were based on the analysis of proximal material with the most distinct major element geochemistries and the REE characterisations presented in Figure 2.10 can be regarded as end-member compositions for the different suites. Figure 2.10 shows that the evolved rhyolitic rocks from Iceland display the highest concentration of REEs with enrichment of the LREEs and a strong negative Eu anomaly, caused by fractional crystallisation of plagioclase during evolution (Óskarsson et al., 1982). The alkaline basalts have lower REE concentrations than the rhyolitic material, but display relatively enriched LREEs and there is some evidence for the earlier Eu enrichment of the alkaline material (Óskarsson et al., 1982). The evolved tholeiites have a flat profile and are depleted in LREEs compared to the alkaline basalt material, however both of these suites have comparable concentrations of HREEs. The less evolved tholeiites show a distinct depletion in the LREEs (Óskarsson et al., 1982). O'Nions and Grönvold (1973) suggested that the differences in trace element abundance could be due to a range of factors including chemical variability of source material, variable crystalline fractionation of parent magmas, different degrees of partial melting and wall-rock reactions in magma chambers. Characterisations of Jan Mayen material are also included on figure 2.10 and compared to the Icelandic basaltic suites the Jan Mayen trachybasaltic material is enriched in LREEs with a steeper profile, but has similar concentrations for the HREEs.

Subsequent studies by Meyer et al. (1985) and Hemond et al. (1993) collated large amounts of rare earth element data from rocks within the neovolcanic (<700,000 yr old) region of Iceland (figure 2.11). Data from Hemond et al. (1993) were grouped based on rock type and figure 2.11a compares this information to the end member compositions defined by the earlier studies. The analyses from Hemond et al. (1993) display a general agreement with the end-member compositions defined by the earlier studies and the analyses all fall within the envelope for REE compositions of Icelandic material. The one exception to this agreement is that REE concentrations for the evolved tholeiitic material are generally higher than the earlier studies suggest, this may be indicative of more varied source material.

Meyer et al. (1985) grouped the data based on volcanic system and Figure 2.11b shows that analyses from rift zone areas such as Langjökull, Thingveller and Bárdarbunga-Grímsvötn were found to have flatter REE profiles characteristic of the tholeiitic material produced within these regions. The flank zone centres of Hekla and Katla maintain the steeper profile which was earlier defined as being characteristic of alkali basaltic material. Analyses from the rift zone areas are more variable than from

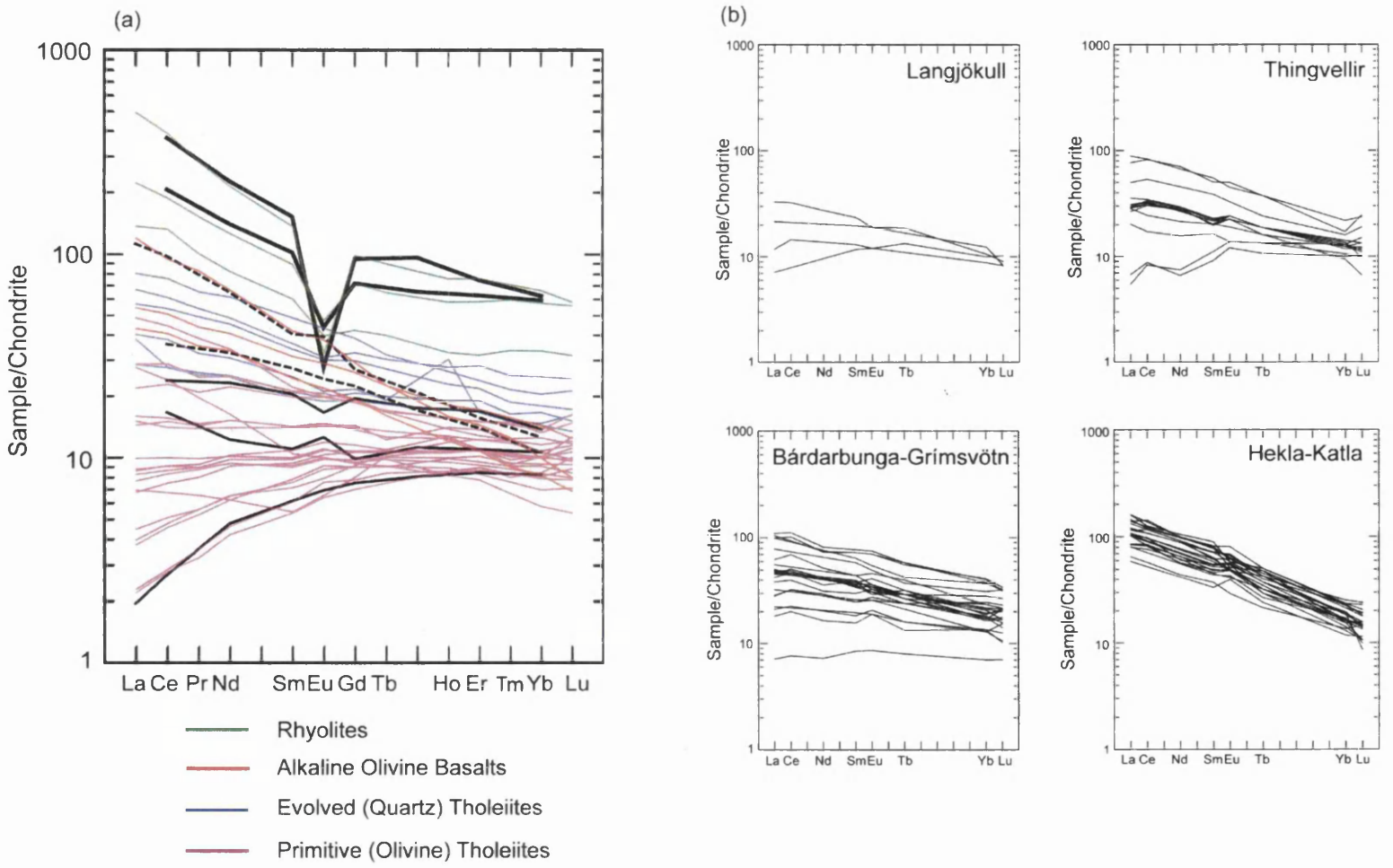


**Figure 2.11:** (a) Comparison between end-member REE characterisations for Icelandic volcanic material defined by Óskarsson et al. (1982), see figure 2.10, and REE analyses of Icelandic material grouped by rock type presented in Hemond et al. (1993). (b) REE element profiles for material related to four Icelandic volcanic centres from Meyer et al. (1985).

the flank zone, which Meyer et al. (1985) attributed to differences in melting conditions between the two zones. A feature of many of the REE profiles from both the rift and flank zones is a positive Eu anomaly, an indicator of enrichment of this element within the volcanic material (figure 2.11; Óskarsson et al., 1982).

The analysis of the trace element composition of distal tephra horizons erupted from the Icelandic and Jan Mayen volcanic centres is scarce in comparison to the major element characterisation of these horizons. Limited work on the characterisation of individual shards has been conducted and also on the analysis of tephra horizons deposited during the last glacial period. Studies conducted previously have focused on the analysis of horizons within long-term marine records of volcanism, for example, Lacasse et al. (1996a) utilised INAA to analyse the trace element composition of bulk ash samples from a 5 Ma-old marine core from the Iceland Plateau. In general, these past studies have demonstrated that the shapes of the REE patterns from the characterisations of distal deposits are comparable to those from proximal deposits of both the Icelandic and Jan Mayen volcanic regions (Lacasse et al., 1996a; Lacasse and Garbe-Schönberg, 2001; Wallrabe-Adams and Lackschewitz, 2003).

# 3. Methodology

## 3.1 Introduction

To construct a tephrochronological framework for the North Atlantic region during the MIS 4 climatic periods samples were taken from three cores extracted from three sites within the region. The GRIP and NGRIP ice-cores were retrieved from the centre of the Greenland Ice Sheet between 1989 and 1993 and 1996 and 2003 respectively. The marine core MD04-2822 was taken from the Rockall Trough area of the North Atlantic Ocean during 2004 (figure 3.1). The following sections provide information on (1) the cores themselves, (2) the sampling strategies employed, (3) the tephra extraction methods used, (4) the methods used to determine the geochemistry of the tephra shards and (5) the graphical and statistical methods used to compare geochemical datasets.

## 3.2 Tephra Analysis of the Greenland Ice-cores

### 3.2.1 Ice-cores under Study: NGRIP and GRIP

Access was granted to the archive sections of two deep ice-cores, NGRIP and GRIP, which are currently stored at and curated by the Niels Bohr Institute, University of Copenhagen. These cores were selected for analysis as they represent key high-resolution records for the last glacial period, chemical records from the cores may indicate the presence of cryptotephra horizons and chronologies currently being developed for the cores can be used to assign ages to any tephra horizons (see chapter 2). These cores are archived in a coldhouse at -26 °C in an attempt to preserve them in the same condition as when they were extracted from the ice sheet. Both cores were split into 55 cm length segments during the in-field processing of the cores and these segments are commonly referred to as ice-core bags. These bags are numbered consecutively from the top down, and the depth of the base of a bag in metres can be calculated by multiplying the bag number by 0.55. Continuous high resolution chemical records have previously been obtained for a large part of the NGRIP ice-core, and these will form the basis of the strategy for the sampling of the core. Along the length of the core the electrolytical meltwater conductivity (ECM) was measured in the field on a cleaned horizontal core surface (Dahl-Jensen et al., 2002). The ECM of ice-cores is a

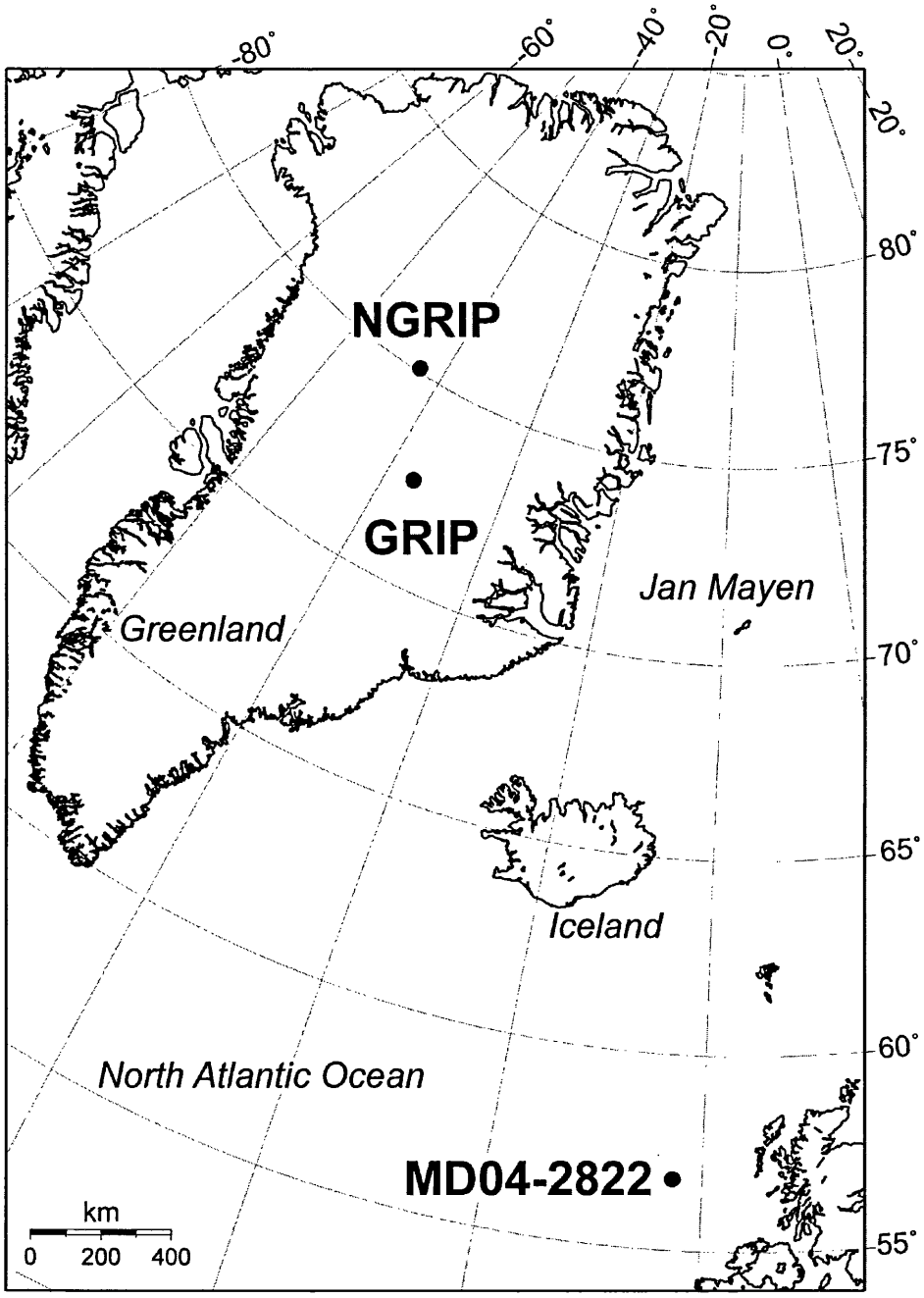


**Figure 3.1:** Location map of the core sites for the two ice-cores (NGRIP and GRIP) and the marine core (MD04-2822) utilised within this study.

standard technique that has been performed since the early 1980s (Hammer, 1980). A recently developed technique, continuous flow analysis (CFA), was also used to measure variations in the concentration of chemical species along the glacial section of the core during the 2000 field season and this represented its first use on ice-cores from Greenland. The CFA technique is described in section 3.2.2. The NGRIP ice-core provided the initial focus within this project as the high-resolution chemical records were used as a guide to the potential location of cryptotephra horizons.

An ECM record was also obtained for the GRIP ice-core along with a limited amount of chemical information for some sections of the core which will aid in devising a sub-sampling strategy.

### 3.2.2 Continuous Flow Analysis of the NGRIP Ice-core

During CFA subsections of the core (3.1 × 3.1 × 165 cm) were melted continuously on a gold coated melting plate within a cold lab (-20 °C). The melting device is designed so that water melted from the outer part of the subsection is discarded and only water from the inner part (2.0 ×2.0 cm) is retained for analysis (Röthlisberger et al., 2000). This process prevents any contamination from the drilling fluid, the handling of the ice-cores or the atmosphere affecting the CFA results. The meltwater from the inner part of the subsection was continuously pumped into a warm lab (+20 °C), where it was split into separate flows and fed into a number of analysis systems. These analysis systems used fluorescence or absorption spectrometric methods to determine sulphate ($SO_4^{-2}$), nitrate ($NO_3^-$), calcium ($Ca^{2+}$), sodium ($Na^+$), ammonium ($NH_4^+$), formaldehyde (HCHO) and hydrogen peroxide ($H_2O_2$) concentrations for the section of the NGRIP ice-core covering the last glacial period (10-110 ka BP) (Bigler, 2004). Full descriptions of the individual detection systems can be found in Röthlisberger et al. (2000). The accuracy of the CFA systems were tested regularly by the measurement of blank water samples between each ice sample and standard solutions of known concentration at regular intervals (Bigler, 2004). The dataset produced is near-continuous for all species with occasional short gaps. These occur around core breaks, where ice was removed for decontamination, and when problems were experienced with individual detection systems (Rasmussen et al., 2006). The concentration records have a 1 mm resolution, however the effective resolution of the data, i.e. the shortest separation over which two peaks in the dataset can be resolved, is between 10 and 25 mm (Andersen et al., 2006).

### 3.2.3 Identification of Ice-core Bags for Tephra Analysis

#### 3.2.3.1 NGRIP

Within this study the sampling strategy for the NGRIP ice-core was based on three distinct criteria. Firstly, bags containing visible horizons were selected, secondly bags containing distinct chemical signals potentially related to volcanic eruptions and thirdly the continuous sampling of bags from ice-core sections covering rapid climatic changes related to the DO events was also undertaken.

During the drilling of the NGRIP ice-core the position of visible horizons potentially composed of tephra were identified via visual inspection of the core. Past studies have shown that tephra horizons can be visually identified within the Greenland ice-cores (e.g. Grönvold et al., 1995; Davies et al., 2008). Therefore ,records from the in-field processing of the core were consulted to determine the position of any visible bands.

The importance of sulphate concentrations in ice-cores acting as an indicator of the deposition of volcanic aerosols was highlighted in section 2.4.3. As a consequence, bags containing distinct peaks in sulphate, exceeding set thresholds, were selected for sampling. To account for climatically driven variations in sulphate concentrations between interstadial and stadial periods two thresholds were used. These were 180 ppbw for the warmer, interstadial periods which are characterised by lower sulphate levels and 800 ppbw for the higher sulphate levels during the cooler, stadial periods.

In addition to the sulphate record the ECM record from certain sections of the core was investigated. The ECM record provides a measure of the acidity of the ice-core and has also been used to reconstruct past volcanic activity (Hammer et al., 1980; Clausen et al., 1997). However, use of this volcanic proxy has been restricted mainly to the Holocene period due to the effect that increased dust deposition of up to two orders of magnitude during the glacial period has on the record (Svensson et al., 2000). Alkaline dust contained within the ice-core can weaken or obliterate the ECM record because it acts to neutralises the ice (Bigler et al., 2007). Dust levels also vary between the interstadial and stadial periods that characterise the ice-core climate record from the last glacial period (Ruth et al., 2002, 2003). Lower dust levels during the interstadial periods mean that the ECM record is affected less by neutralisation. Thus, the ECM record from the interstadial periods during MIS 4 was inspected for any distinct peaks

potentially related to volcanic eruptions. Any bags containing ECM peaks unrelated to sulphate peaks exceeding the set thresholds were sampled.

The final sampling criteria employed was the continuous sampling of ice-core bags over some of the rapid climate transitions apparent within the oxygen isotope record of MIS 4. It was not feasible to continuously sample the entire ice-core section relating to the MIS 4 period, however, the past discovery of some cryptotephra horizons within ice-cores without an associated chemical signal (e.g. Davies et al., 2008) suggests that some horizons may be overlooked if sampling was focused solely on distinct sulphate and ECM peaks. Ice sections covering rapid climate transitions were continuously sampled because the effectiveness of tephra horizons as tie-lines, to aid the determination of the relative timing of rapid climatic changes, is increased if they fall on or near these transitions.

#### 3.2.3.2 GRIP

The main aim of sampling the GRIP ice-core was to determine if any tephra horizons identified within the NGRIP record could be traced between the cores, and act as time-synchronous tie-lines between the sequences. The sections to be sampled were selected with the aid of a chemical synchronisation method developed by the Centre for Ice and Climate at the University of Copenhagen. This synchronisation method, outlined in Rasmussen et al. (2008), relies on using distinct peaks in the volcanic indicators of acidity (ECM and DEP) and where available sulphate and calcium concentration as tie-points between the cores. To define tie-points the chemical peaks have to be assumed to be synchronous and the robustness of these synchronisations can be assessed through the identification of tephra horizons within both cores. The geochemical signature from glass shards in the horizons can be used to demonstrate that peaks relate to the same eruption.

This synchronisation method was used to define depths within the GRIP record potentially relating to tephra horizons identified in the NGRIP core. Bags from these sections were continuously sampled. The length of the sampled section was dependant on the strength of the correlation around that period, determined by the number of tie points that had been identified, with longer sections being sampled where less tie points had been defined.

### 3.2.4 Development of Sub-Sampling Strategies for Ice-core Bags

Following the selection of bags for sampling it was necessary to determine how to subsample the 55 cm segments of ice at a high-resolution. The strategies developed for the subsampling of ice from each bag were unique due to the variable nature of chemical signals recorded in the high-resolution chemostratigraphy. For example, peaks in sulphate concentrations exceeding the thresholds are not consistent in form or length and some bags may contain multiple peaks in sulphate concentration. Despite this variability a set of general guidelines were established to ensure that the nature of sampling was consistent between bags.

#### 3.2.4.1 Bag Sampling Guidelines

The first criteria was to sample across the whole peak in sulphate concentration taking either one sample or multiple samples over wide peaks or peaks with apparent structure. A minimum sampling length of 3 cm was maintained over these peaks. Higher resolution samples, i.e. 1 cm, could have been taken, however, this would have resulted in a relatively large amount of sample loss as ~1 mm of ice is lost when a band saw is used to cut down pieces of ice. Sample loss could have an adverse effect within this study due to the low concentration of tephra shards present in the ice-cores and the possible thin nature of the cryptotephra horizons. A 3 cm minimum was deemed to provide an appropriate compromise between restricting sample loss and maintaining a high-resolution of sampling.

The second guideline was to take 5 cm samples above and below any samples related to distinct sulphate peaks. If a chemical peak was located within the top or bottom 5 cm of a bag these samples were taken from bags above or below the bag containing the main sulphate or ECM peak. These samples were taken to ensure that any potential leads and lags between the deposition of tephra and the deposition of the volcanic aerosols are identified. This could be important in determining the source of tephra particles because synchronous deposition of tephra and aerosols is expected if both were transported in the troposphere. While a delay in the deposition of aerosols of the order of months is expected if they were transported in the stratosphere and the tephra in the troposphere, which is possible for an explosive low latitude eruption (Vinther et al., 2006). Within this time period 5 cm of ice represents approximately 5 years of deposition, therefore encompassing the expected duration of any potential offset.

The third guideline was to sample any additional chemical signals within all the bags potentially related to volcanic eruptions that did not exceed the prescribed thresholds. This will restrict the need to resample bags in further investigations, which is necessary due to the limited amount of ice available and the need to preserve the remaining ice for future investigations using other proxies.

Often within the bags selected for periods of continuous sampling no distinct chemical signals were apparent, therefore these guidelines were not followed. In these cases 3 samples were taken from the bags with samples taken between the bag depths of 0-20, 20-40 and 40-55 cm. This strategy provides a balance between determining the stratigraphic position of any horizons to a high degree and minimising the number of samples to be inspected for tephra content. This strategy was also used during the sampling of the GRIP ice-core as there is a limited amount of chemical information available from which a more detailed sampling strategy can be defined.

Figure 3.2a illustrates the application of these guidelines to the creation of a sampling strategy for the NGRIP ice-core bag 4632. Sample 1 was taken as the sulphate peak exceeds the 800 ppbw threshold, two samples (2 and 3) were taken over the other period of high sulphate levels in the bag as two distinct peaks are apparent and samples 4 and 5 were taken to account for any leads or lags between aerosol and tephra deposition. The remainder of the bag, sample 6, was not sub-sampled further as no significant sulphate peaks were identified within this section.

### 3.2.5 Direct Ice-core Sampling

Ice-core sampling took place in a cold workroom (-18 °C) attached to the main storage freezer at the University of Copenhagen. All samples from the NGRIP core were taken from the archive segments of the core, which had not been sampled or accessed since they were collected in Greenland during the 2000 field season. Samples from the GRIP ice-core were taken from working segments previously sampled for other studies.

To sample the ice-core bags a 1 cm strip was cut off the side of each 55 cm segment using a band saw (figure 3.2b and 3.3). This strip was then cut down into sub-samples, according to the sampling strategy devised for the particular bag. These sub-samples were placed into individual sample bottles before being melted at room temperature.

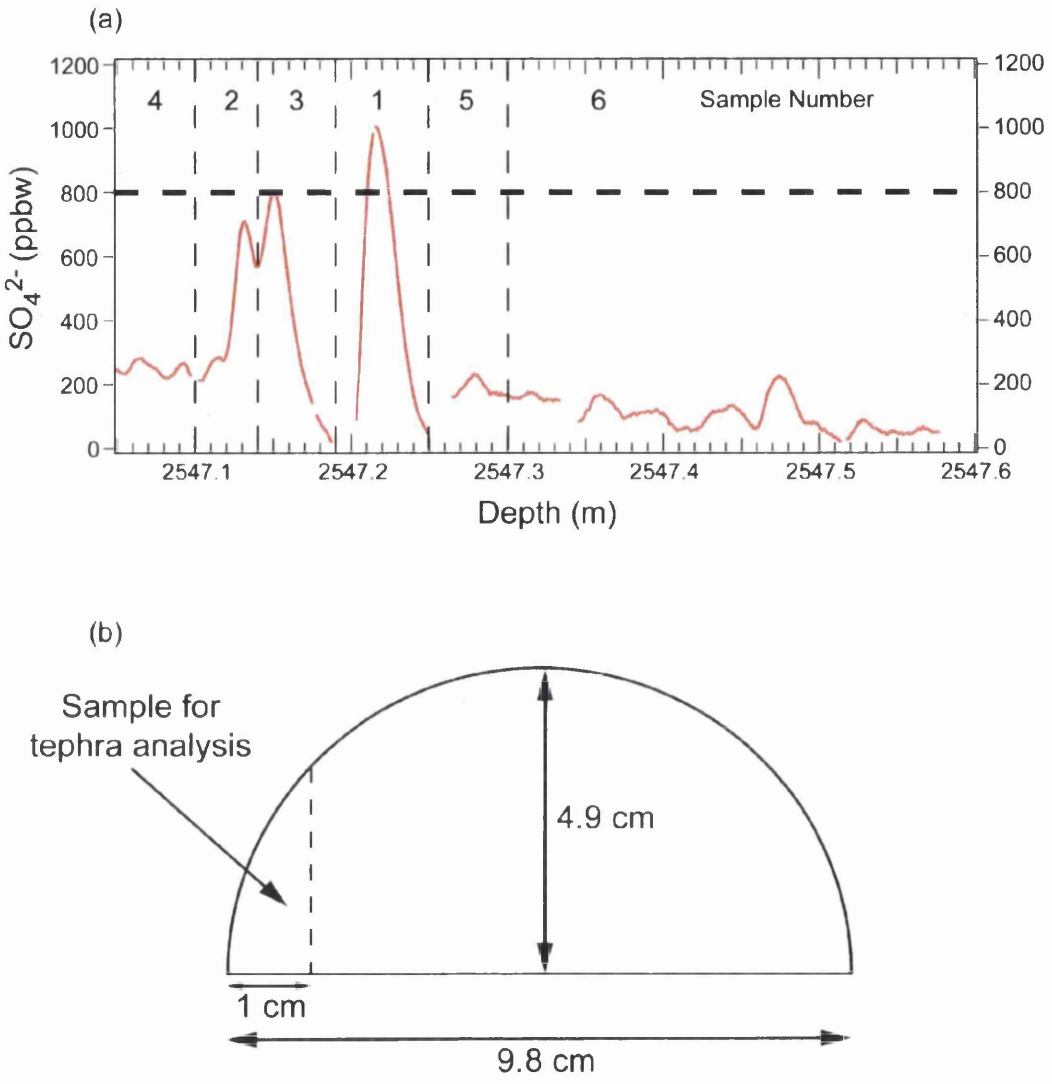


**Figure 3.2:** (a) Continuous flow analysis sulphate record for NGRIP bag 4632 (2547.05-2547.6 m) with the sub-sampling strategy for the six samples taken from the bag indicated. Horizontal black dashed line indicates the sulphate peak selection threshold. (b) Cross-section of an ice-core segment with the section removed for tephra analysis illustrated.

1. 1 cm wide strip of ice removed from the edge of the ice core bag (55 cm segment) to be sampled (picture 1).

2. 55 cm strip subsampled according to the sampling strategy devised from the CFA records (picture 2).

3. Samples placed in plastic bottles and melted at room temperature (picture 3).

4. Water samples transferred to centrifuge tubes and centrifuged for 5 mins at 2500 rpm to isolate any particulate matter. Repeated until all the water was centrifuged.

5. Sample bottles washed with distilled water and centrifuged three times.

6. Material evaporated on a hotplate into a 1 cm × 1 cm pencil square drawn onto a frosted slide (28 × 48 mm).

7. Sample covered with epoxy resin and heat cured for 3 hours at 60°C to embed the material.

Picture 1

Picture 2

Picture 3

**Figure 3.3:** Summary of methods for the sub-sampling of ice-core material and the preparation of samples for tephra concentration counts and geochemical analysis.

Once the samples had melted the water was transferred into 15 ml centrifuge tubes, before being centrifuged at 2500 rpm for 5 minutes to concentrate any particulate material in the base of the tube. Excess water was discarded and this process repeated if the volume of the melted water from the subsample exceeded 15 ml. Each sample bottle was then washed with distilled water that was transferred to the corresponding centrifuge tube and centrifuged at 2500 rpm for 5 minutes. Excess water was discarded and this washing procedure was repeated two further times to ensure that all material had been transferred from the sample bottles to the centrifuge tubes. This process is summarised in figure 3.3 (steps 1-5).

### 3.2.6 Processing of Ice-core Samples

To assess the number of tephra shards within the ice-core sub-samples the particulate material within them was mounted in epoxy resin on microscope slides. This method was employed to allow tephra shard concentrations to be assessed in addition to being the first stage in preparing samples for geochemical analysis. Consequentially, it was unnecessary to resample sections of ice containing a high concentration of tephra shards to gain material for geochemical analysis. This was preferable due to the limited amount of core material available and the time required to resample core sections.

Prior to the mounting of material on to microscope slides one side of the 28 × 48 mm slides was frosted using silicon carbide powder mixed with distilled water. This frosting increases the surface area of the slide to which epoxy resin can bond. The sample details, i.e. sample/bag number and depth of sample, were etched onto the unfrosted side of the microscope slides using a diamond pen. All slides were cleaned by placing them in acetone-filled beakers within an ultrasonic bath for 5 minutes, before being rinsed in acetone and placed on to a hotplate. This ensures that all potentially contaminating material, such as excess silicon carbide powder, is removed from the slide.

An approximately 1 × 1 cm box was drawn with a pencil on the frosted side of each slide; into which the contents of the corresponding centrifuge tube was pipetted and left to evaporate on a hotplate. The inside of each centrifuge tube was then washed 3 times with distilled water and the water was transferred on to the microscope slide after each wash for evaporation, to ensure that all of the particulate material has been transferred onto the microscope slide. Once all of the water had evaporated, the

sample was covered in epoxy resin and left to set on the hotplate for approximately 3 hours at 60°C. This process is summarised in figure 3.3 (steps 6-7). Following the preparation of slides the concentration of tephra shards within the samples was ascertained using optical microscopy (see section 3.4).

## 3.3 Tephra Analysis of North Atlantic Marine Core MD04-2822

The marine core MD04-2822 is stored at the University of St Andrews and proxy records from the core were used to determine which section of the core relates to the MIS 4 climatic period (see section 7.2.1). The period of interest, 2200-2380 cm, was subsampled at a 1 cm resolution during January 2008. Full descriptions of the core and the determination of the period of interest are provided in chapter 7. This core was selected for analysis because it preserves a high-resolution record of the MIS 4 period and a significant number of proxy records are being collected from the core, which can be compared to ice-core proxies. In addition, it lies on a different dispersive pathway from Iceland, i.e. SE as opposed to NW, thus any horizons common to both depositional environments would have a widespread dispersion within the North Atlantic region making them effective horizons for future tracing.

### 3.3.1 Procedure for Processing Marine Samples

A rigorous extraction method was required to determine whether tephra shards were present within these marine samples and a procedure modified from those described in Turney (1998), Davies (2002) and Blockley et al. (2005) was employed (figure 3.4). The various stages of this procedure aim to isolate tephra shards from the host material by systematically removing different components of the sediment.

From each 1 cm sample selected for analysis 2 g of sediment was freeze dried using a Thermo Savant Freeze Dryer. Freeze drying was carried out so that shard concentrations could be worked out relative to the dry weight of the sample. If wet sample weight was used some bias could be introduced to shard concentrations if there was variations in the water content of the marine material. From each sample 0.5 g of the freeze dried sediment was ashed in a muffle furnace for 2 hours at 550 °C to remove any organic material and then left in dilute (10%) hydrochloric acid (HCl) overnight to remove any carbonate material. The samples were then sieved through 80 µm and 25 µm nylon mesh to isolate the 25-80 µm fraction of the sample; the typical

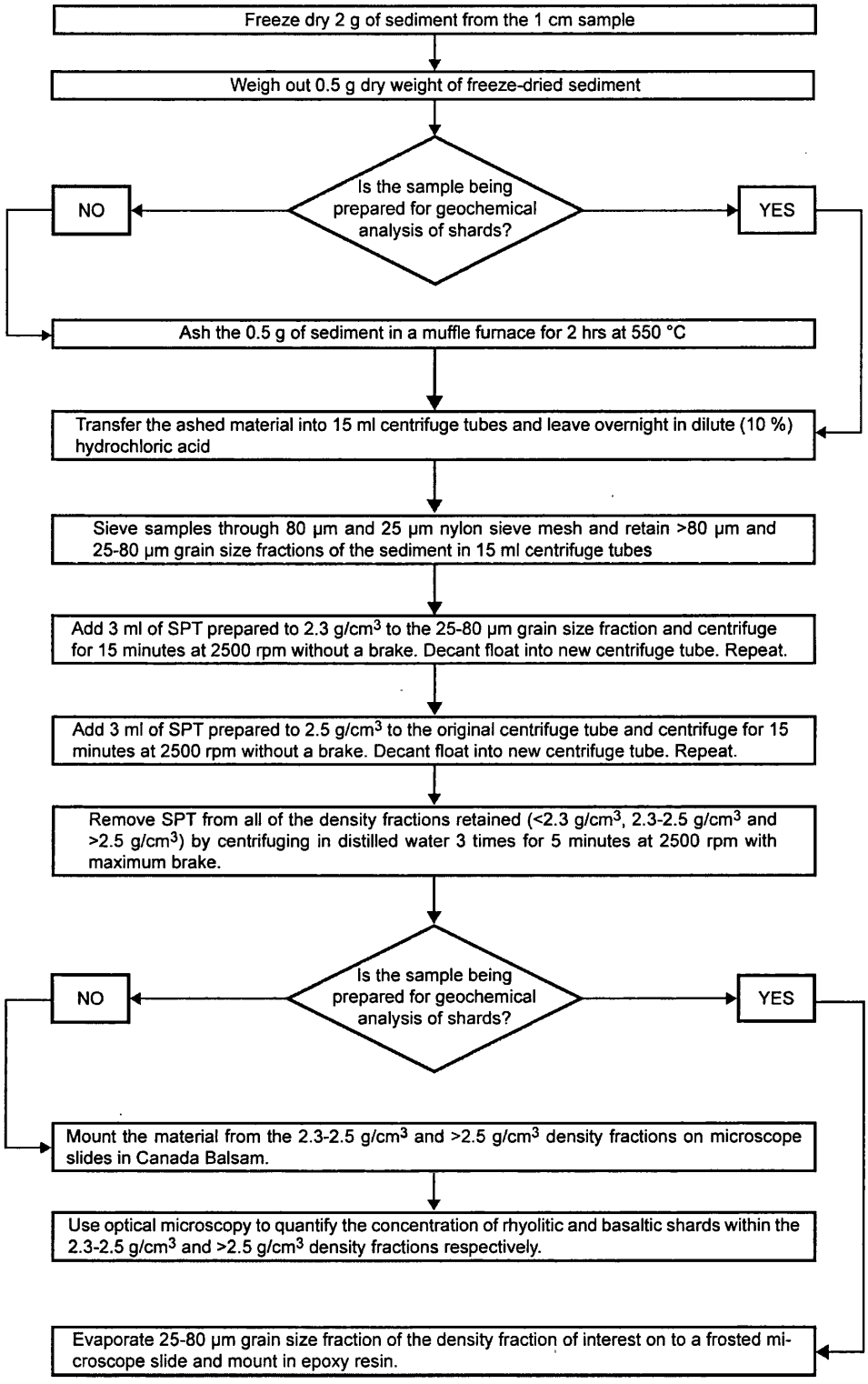


**Figure 3.4:** Flowchart of the procedures used to prepare material from the marine core samples for shard concentration quantification and geochemical analysis. Modified from Turney (1998), Davies (2002) and Blockley et al. (2005).

size of tephra shards found within distal settings. The material less than 25 μm in diameter was discarded, while the material greater than 80 μm diameter was retained for possible future analysis.

Density separation of the material within the 25-80 μm grain size fraction was then carried out using the heavy liquid sodium polytungstate (SPT). With the material being separated into three density fractions isolating material with densities of <2.3 g/cm$^3$, 2.3-2.5 g/cm$^3$ and >2.5 g/cm$^3$. This further isolates tephra shards from the host sediment as rhyolitic material has a typical density of between 2.3 and 2.5 g/cm$^3$ and basaltic material a density greater than 2.5 g/cm$^3$. Biogenic material such as diatoms has a density less than 2.3 g/cm$^3$ so is therefore removed from the samples containing tephra shards. Minerogenic material has a typical density greater than 2.5 g/cm$^3$ and is therefore retained within the density fraction containing basaltic material.

The material from the 2.3-2.5 g/cm$^3$ and > 2.5 g/cm$^3$ fractions were evaporated on to microscope slides and mounted using the mounting media Canada Balsam. The concentration of glass shards within each sample was then quantified through the identification of shards, using the criteria described in section 3.4. Samples with distinct peaks in shard concentration were selected for further analysis with shards from these samples being prepared for geochemical characterisation.

When samples were being prepared for the shards to be geochemically analysed a slightly altered procedure was used with two significant modifications (figure 3.4). Firstly, the samples were not ashed to remove organic components and secondly the samples were mounted in epoxy resin not Canada Balsam. The ashing stage was avoided because heating of tephra shards above 350 °C is known to alter the geochemistry of shards through alkali mobilisation (Davies, 2002). This step was not replaced with an acid digestion phase, which has previously been employed to replace ashing, because it has been found that this procedure could have a significant effect on the geochemistry of tephra shards (Blockley et al., 2005). It should be noted that when samples were processed for geochemical analysis it appeared that the ashing procedure was unnecessary for the samples prepared for concentration counts due to low levels of organic matter within the core material. Therefore the ashing phase could be excluded from future studies reducing the time required to process samples.

Material from the density fraction containing tephra shards to be geochemically analysed was mounted on frosted 28 × 48 mm microscope slides in epoxy resin using the method summarised in section 3.2.6.

## 3.4 Identification of Tephra Shards Using Optical Microscopy

The presence of juvenile glass tephra shards within both the ice and marine core samples was assessed using a high-powered (×100) light microscope. Volcanic glass shards can be identified based on their physical characteristics such as colour, shape, morphology, and the presence of vesicles and mineral inclusions. However some shards can look very similar to minerogenic and biogenic material; in these cases the optical properties of the material can be used for discrimination.

The first optical property to be used was the behaviour of tephra shards when viewed under polarised light. Rapid cooling of magma during the formation of the glass component of tephra means that little or no crystallisation of the mineral phase occurs (Fisher and Schminke, 1984). Therefore volcanic glass shards have a non-crystalline structure, whereas mineralogical material commonly has a crystalline structure. When volcanic glass shards are viewed under cross-polarised light with polarising lens below and above the sample the plane-polarised light is unaffected by the non-crystalline structure of the shards and they will extinguish. In contrast, the plane-polarised light will be refracted by the crystalline structure of mineralogical material. Thus, light will be transmitted through the polarising lens above the sample and the material will appear bright.

The second optical property that can be utilised is dependant on the refractive index (RI) of the material in which the shards are mounted. The Becke line is a bright halo of concentrated refracted light that appears around a particle due to a difference in refractive indices between the particle and the mounting medium. If the microscope is defocused by increasing the distance between the sample and the objective the Becke line will move into the material with a higher refractive index (RI) (Enache and Cumming, 2006).

The two mounting media used within this study, epoxy resin and Canada Balsam, both have a RI of ~1.55. While rhyolitic shards tend to have a RI around 1.5 and crystalline minerals have a RI greater than 1.55. Therefore, when mounted in either epoxy resin or

Canada Balsam resin the Becke line will move outwards from rhyolitic shards and into crystalline materials, and thus can be used to discriminate between these two types of material. Basaltic material tends to have a RI higher than 1.55 therefore the Becke line moves into these shards when the stage is defocused.

## 3.5 Geochemical Analysis of Tephra Shards

### 3.5.1 Preparation of Slides for Geochemical Analysis

Samples from both the ice and marine cores containing glass shards requiring geochemical analysis were mounted in epoxy resin on microscope slides. To prepare shards for geochemical analysis a flat, polished section through the centre of the shards has to be achieved. This is required to reduce the effect that morphological distortion could have on WDS readings, remove post-depositional shard-surface alteration and hydration and remove scratches, which could induce absorption of X-rays by the sample and reduce the amount of X-rays reaching the spectrometers (Hunt and Hill, 1993; Reed, 1993).

The first stage of preparation was to grind away the majority of the epoxy resin over the sample using silicon carbide paper until a flat surface approximately 30-40 μm thick was achieved. At this thickness the majority of the shards within a sample are sectioned or near the surface; if not samples were ground further until a sufficient number of shards was exposed. The surface of the resin was then polished on a Logitech CL50 polishing machine using 6 μm and 1 μm diamond suspension, with both grades being used for approximately 30 minutes, until a mirror finish was achieved on the surface. The quality of the sections and the polish were checked using reflected light microscopy.

After being washed in distilled water the slides were cleaned by immersing them in petroleum sprit and placing them in an ultrasonic bath for 10 minutes. This removed any material, such as diamond suspension, or grease that may have adhered to the slides. A carbon coat was then evaporated on to the surface of the samples prior to geochemical analysis of the shards, to prevent charging under the electron bombardment which takes place during EPMA analysis (Reed, 2005).

### 3.5.2 Electron Probe Micro-Analysis

EPMA of the glass shards using wavelength dispersive spectrometry (WDS) took place at the NERC Tephrochronology Analytical Unit based at the School of GeoSciences, University of Edinburgh. A Cameca SX100 electron microprobe with five vertical wavelength dispersive spectrometers was used to gain oxide values for 10-11 major elements from individual shards. The oxides measured were $SiO_2$, $TiO_2$, $Al_2O_3$, FeO (total), MnO, MgO, CaO, $Na_2O$, $K_2O$ and $P_2O_5$. In addition the concentration of Cl within some shards was measured. The operating conditions used were an accelerating voltage of 10 kV, a beam current of 10-20 nA and a beam spot size of 4-5 μm. A ZAF correction was used to correct for the matrix effects of atomic number, X-ray absorption and secondary fluorescence (Reed, 2005). The microprobe was calibrated through the analysis of pure metal, silicate and synthetic oxide standards. Three secondary standards (TB1G, Lipari and BCR2g) were analysed at regular intervals during the analysis period to monitor for any drift in the analyses and to assess the precision and accuracy of the glass analyses. Average oxide values from all analyses of the standards over the analysis period and the expected values for the standards are shown in appendix 1.

The sectioned glass shards to be analysed were identified using a combination of transmitted and reflected light in an optical microscope system and backscatter electron imaging. During analysis each shard was numbered and its position on the slide and the size and shape of the sectioned areas were carefully recorded. This meant that it was possible to relocate the shards during LA-ICP-MS analysis, which is crucial if trace element concentrations are to be gained (see section 3.5.3.3).

#### 3.5.2.1 Major Element Data Normalisation

The two conventions regarding the treatment of EPMA data were introduced in section 2.5.2. Within this study the convention of the normalisation of data to 100% was followed. The normalisation of data was of particular importance in chapter 7 and the analysis of geochemical data from marine tephra shards, as the majority of the analyses gained had total oxide values less than 95% and thus would have been rejected if the alternative convention was in use. The normalisation of data also facilitated comparisons to published data only reported in a normalised form. In addition to comparisons with rock classification schemes, such as the total alkalis

versus silica (TAS) classification of Le Maitre et al. (1989) and the alkali-tholeiitic division line defined by MacDonald and Katsura (1964), which were defined using normalised datasets. One of the main arguments for not normalising data is that it masks any poor quality analyses, however, in general normalisation had the effect of reducing the variation within the main geochemical populations and further emphasising any outlying values.

Additionally, it is conventional to calculate trace element concentrations on an anhydrous basis, so normalisation of the major element data produces fully anhydrous characterisations of shards.

Throughout the subsequent chapters all of the major element geochemical data presented on figures and in tables will be normalised data, and total oxide values are the pre-normalised values. All of the raw unnormalised data for tephra shards analysed within this study are presented in the appendices.

### 3.5.3 Laser Ablation Inductively Coupled Plasma Mass Spectrometry

#### 3.5.3.1 LA-ICP-MS System and Operating Conditions

A LA-ICP-MS system located at the Institute for Geography and Earth Sciences, Aberystwyth University was used, and the work was conducted over three analytical periods. A Coherent GeoLas 193 nm Excimer laser coupled to a Thermo Finnigan Element 2 high resolution sector mass spectrometer was used; the high potential for this system in characterising small, ~ 20 µm diameter, tephra shards was described in Pearce et al. (2007). The instrumental conditions were consistent between the first two analysis periods, however prior to the third run instrument sensitivity (i.e. cps/ppm) had been improved because of experience gained in use. The impact these improvements had will be discussed in section 4.2.

The laser system produces a homogenised beam that normally ablates circular, flat-bottomed craters into tephra shards. A flat-bottomed ("top-hat") crater profile reduces the risk of tunnelling through shards during analysis; an issue often encountered with older systems where laser energy has a Gaussian distribution and is concentrated at the centre of the beam producing conical craters (Pearce et al., 2007). During this study the 193 nm laser was pulsed at a frequency of 5 Hz with an energy at the sample

of 10 J/cm$^2$ and typically a beam diameter of 14 µm. These conditions were selected because they provide a constant signal to the mass spectrometer and sufficient energy to ablate material from the shard surface, while preserving the shards for long enough for analysis to take place. The choice of 14 µm as the typical beam diameter was governed by the size of the glass shards that were being analysed. However for some small shards or shards with a small sectioned area a 6 µm beam diameter was employed. The quality of the data produced during these analyses and their comparability to analyses gained using a 14 µm beam diameter is discussed in section 4.3.

### 3.5.3.2 Analysis of Samples, Gas Blanks and Reference Material

During analyses the beam was moved across the exposed surface of the shard; so that the laser beam did not 'tunnel' through the shard and ablate underlying resin and moving the beam over the sample ensures that fresh, unheated material is ablated. This minimises the effect of element fractionation and the effect of variations in the size of ablated material as the laser changes focus during analyses when the beam is static (Pearce et al., 2008).

During an analysis the microparticulate material ablated from the shard surface is carried into the plasma for ionisation in a stream of argon gas before being drawn into the mass spectrometer. When a laser beam diameter of 14 µm was being used the detectors within the mass spectrometer scanned the mass range of the elements being measured 16 times leading to an analysis time of ~42 seconds. This number of passes was reduced to 8 for the 6 µm analyses due to the shorter lifespan of the smaller shards under the laser and thus the shorter signal produced by the shards.

A suite of 34 elements was measured during the first and second analytical periods (table 3.1). In the final analytical period only 30 elements were measured with Ti, Ni, V and Cr not being analysed. In the initial analysis period these elements were found to be unreliable with negative concentrations often being recorded and poor lower limits of detection. This was a result of high background counts for these elements within the LA-ICP-MS system, for example high Ni blanks were recorded because the directional cones used within the mass spectrometer are made of nickel.

**Table 3.1:** Elements measured during LA-ICP-MS analysis and the isotopes and isotope abundances. Isotopes selected to avoid saturation of detector and where possible reduce the potential influence of polyatomic interference.

| Element | Symbol | Isotope used for analysis | Isotope Abundance (%) |
|---|---|---|---|
| Silicon | Si | 29 | 4.67 |
| Calcium | Ca | 43 | 0.14 |
| Scandium | Sc | 45 | 100 |
| Titanium | Ti | 47 | 7.3 |
| Vanadium | V | 51 | 99.8 |
| Chromium | Cr | 52 | 83.8 |
| Cobalt | Co | 59 | 100 |
| Nickel | Ni | 60 | 26.1 |
| Rubidium | Rb | 85 | 72.2 |
| Strontium | Sr | 88 | 82.6 |
| Yttrium | Y | 89 | 100 |
| Zirconium | Zr | 90 | 51.5 |
| Niobium | Nb | 93 | 100 |
| Caesium | Cs | 133 | 100 |
| Barium | Ba | 138 | 71.7 |
| Lanthanum | La | 139 | 99.9 |
| Cerium | Ce | 140 | 88.5 |
| Praseodymium | Pr | 141 | 100 |
| Neodymium | Nd | 143 | 12.2 |
| Samarium | Sm | 147 | 15.0 |
| Europium | Eu | 153 | 52.2 |
| Gadolinium | Gd | 158 | 24.8 |
| Terbium | Tb | 159 | 100 |
| Dysprosium | Dy | 163 | 24.9 |
| Holmium | Ho | 165 | 100 |
| Erbium | Er | 166 | 33.6 |
| Thulium | Tm | 169 | 100 |
| Ytterbium | Yb | 174 | 31.8 |
| Lutetium | Lu | 175 | 97.4 |
| Hafnium | Hf | 178 | 27.3 |
| Tantalum | Ta | 181 | 99.9 |
| Lead | Pb | 208 | 52.4 |
| Thorium | Th | 232 | 100 |
| Uranium | U | 238 | 99.3 |

During the analysis of tephra shards additional measurements are taken before and after sample analyses are acquired. Firstly, the background levels of elements within the system are determined by the systematic acquisition of measurements when no sample is being ablated, i.e. a gas blank. Secondly, analyses are made of a calibration standard. The reference material used within this study was NIST SRM 612 a synthetic-soda-lime silicate glass produced by the National Institute of Standards and Technology. This glass has been spiked with 61 trace elements to a concentration of approximately 40 ppm (Pearce et al., 2004a). The working concentrations for 50 elements within this material were complied from new analyses and published data and reported in Pearce et al. (1997). These working concentrations were used for

calibrations within this study. Sets of five gas blanks and five analyses of NIST 612 were taken before and after the analysis of tephra shards from a horizon and the averages were used to determine the magnitude of instrumental drift during the analytical period.

### 3.5.3.3 Calculation of Trace Element Concentrations

The results gained from the mass spectrometer are reported in average counts per second (cps) for each element and a series of calculation steps are required to convert the readings into parts per million concentration data. Firstly, the background count levels of elements within the system have to be subtracted from the readings using the gas blank measurements. The drift between the average gas blanks measurements prior to and subsequent to the analysis period are assumed to be linear.

The blank subtracted counts rates for each element are then ratioed to the count rates for an internal standard isotope that has been determined previously for each shard by EPMA. An internal standard is used because the amount of ablated material can vary between analyses of the samples and of the calibration standard (Pearce et al., 2007). In this study $^{29}Si$ was primarily used as the internal standard; however some datasets were additionally ratioed to an alternative internal standard, $^{43}Ca$. The potential use of Ca isotopes for internal standardisation will be explored in section 4.4. Normalised major oxide values were used so the trace element concentration data is calculated on an anhydrous basis.

To gain trace element concentration data from these ratios the following equation was used:

$$C^{el}_{unk} = C^{el}_{rm} / (CPS^{el}_{rm} / CPS^{I.S.}_{rm}) \times (CPS^{el}_{unk} / CPS^{I.S.}_{unk}) \times (C^{I.S.}_{unk} / C^{I.S.}_{rm})$$

Where C = concentration, el = analyte element, I.S. = element used as internal standard, rm = in the reference material, unk = in the sample being analysed and CPS = counts per second (Perkins and Pearce, 1995)

This equation can also be expressed as:

Concentration = slope of calibration × (analyte counts/internal standard counts) × correction factor for differences in internal standard

(from Pearce et al., 2007)

The averages of the measurements of the NIST 612 reference material taken before and after the tephra shard analyses were used to calculate the calibration slope and the correction factor (drift) over the analytical period. This equation was used to calculate the concentration of all elements for the tephra shards analysed during this study.

#### 3.5.3.4 Identification of Outliers

Following the calculation of trace element concentrations for each of the horizons the datasets were inspected to identify any outlying analyses which should be removed from further analysis and the calculation of averages for horizons. Manual scanning of the data, biplots and REE profile diagrams were all used to identify these outliers and approximately 5 % of the analyses were excluded. Explanations for outlying values include the analysis of micro-inclusions of minerals such as zircon and plagioclase, which can be found within tephra shards, or the analysis of some resin along with the tephra shard (Pearce et al., 2004a).

## 3.6 Graphical Representation of Geochemical Data

For both major and trace element concentrations biplots have been used to illustrate and compare the datasets produced to one another and to published analyses. In addition, data collected from the LA-ICP-MS system, in particular the rare earth elements (REEs) is presented on chondrite normalised multi-element, spider diagrams generated using the IGPET program (Carr, 2008). These plots are commonly used within the analysis of this data because REE are the trace elements most commonly measured within volcanic material (see section 2.5.4).

The abundances of REE elements within natural samples are highly variable due to the different stabilities of atomic nuclei; in general REE with even atomic numbers are more stable and more abundant than REE with odd atomic numbers (Rollinson, 1993).

Therefore a composition versus abundance plot for REE concentrations will have a zig-zag pattern (Rollinson, 1993). To smooth out this abundance variation REE concentrations from samples are normalised to a common reference standard such as the REE concentrations of a chondritic meteorite or primitive mantle sample (Rollinson, 1993; Sun and McDonough, 1989). The normalised data for samples is then presented on a concentration versus atomic number diagram, with the concentrations expressed as the logarithm of value (Rollinson, 1993). The reference standard used for normalisation can have a distinct effect on the REE profiles produced, therefore to maintain consistency only the standard of Sun and McDonough (1989) will be used when REE data is presented during this study.

## 3.7 Statistical Analysis of Geochemical Data

During this study two statistical techniques were used to facilitate comparisons between geochemical data sets and support the qualitative methods of biplots and REE profiles. The similarity coefficient was used as a measure of similarity between datasets and the statistical distance method was used to assess if significant differences occur between datasets.

### 3.7.1 Similarity Coefficient

Similarity coefficients are calculated using the equation below:

$$d_{(1,2)} = \frac{\sum_{k=1}^{n} R_k}{n}$$

Where $d_{(1,2)}=d_{(2,1)}$ is the similarity coefficient for the comparison between samples 1 and 2, k is the element number, n is the number of elements, $R_k = X_{k1}/X_{k2}$ if $X_{k2} \geq X_{k1}$ or $X_{k2}/X_{k1}$ if $X_{k1}>X_{k2}$, $X_{k1}$ is the concentration of element k in sample 1 and $X_{k2}$ is the concentration of element k in sample 2 (from Borchardt et al., 1972; Hunt et al., 1995).

This coefficient was used to calculate similarity between datasets of major elements. Only elements with concentrations greater than 1 %wt were used because the lower precision of low concentration elements could have a large effect on the calculated coefficients (Hunt et al., 1995). Calculated similarity coefficients range between 0.6 and

1, with values closer to 1 indicating more similarity in the datasets (Hunt et al., 1995). Beget et al. (1992) suggests that similarity coefficient values between 1 and 0.95 indicate that the samples are identical, values between 0.95 and 0.90 show that the datasets are not identical but are likely to originate from the same volcanic source and values below 0.90 occur because there is no relation between the tephra horizons. These thresholds will be referred to in this study.

### 3.7.2 Statistical Distance Function

The statistical distance between samples, calculated using the equation below, was developed by Perkins et al. (1995, 1998) to assess the differences between geochemical datasets using the Euclidian distance between samples.

$$D^2 = \sum_{k=1}^{n} (x_{k1} - x_{k2})^2 / (\sigma_{k1}^2 + \sigma_{k2}^2)$$

Where n is the number of elements used in the comparison, $x_{k1}$ and $x_{k2}$ are the average concentration of the kth element in the two samples being compared and $\sigma_{k1}$ and $\sigma_{k2}$ are the standard deviations on the average values for kth element within the two samples (Pearce et al., 2008a).

$D^2$ has a chi-squared distribution amongst compositionally identical samples (Perkins et al., 1995) therefore chi-squared test critical values can be used for the hypothesis testing of calculated $D^2$ values. The calculated $D^2$ values are compared to critical values at the 99% confidence level, which are given in table 3.2 where the degrees of freedom are the number of elements used in the comparison.

If the calculated $D^2$ value is greater than the critical value then the null hypothesis, that the samples are identical can be rejected, and the samples are considered different at the 99 % confidence level. If the calculated $D^2$ value is less than the critical value then the samples are not considered to be different, however they can also not be considered to be the same (Pearce et al., 2008a). Low $D^2$ values can suggest that a correlation exists but it is not statistically valid. The main reason for this is that two datasets can have the same mean and standard deviation values but different trends in the individual data values, which can be assessed using biplots of element concentrations.

**Table 3.2:** Critical values at the 99% confidence level used to test statistical distance values for degrees of freedom between 5 and 15.

| Degrees of Freedom | Critical Value at the 99% confidence level |
|---|---|
| 5 | 15.09 |
| 6 | 16.81 |
| 7 | 18.48 |
| 8 | 20.09 |
| 9 | 21.67 |
| 10 | 23.21 |
| 11 | 24.73 |
| 12 | 26.22 |
| 13 | 27.69 |
| 14 | 29.14 |
| 15 | 30.58 |

This technique has recently been applied to both major element (e.g. Hillenbrand et al., 2008) and trace element datasets (e.g. Pearce et al., 2008a). Within this study it will be used to compare both major element and trace element data.

When major element datasets are being compared oxides with an average composition greater than 0.1 % were compared. In general this meant for comparisons of datasets from basaltic material concentrations for 10 oxides were compared ($SiO_2$, $TiO_2$, $Al_2O_3$, FeO (total), MnO, MgO, CaO, $Na_2O$, $K_2O$ and $P_2O_5$), and for comparisons of rhyolitic material 7 oxides were compared with MnO, MgO and $P_2O_5$ being excluded.

Pearce et al. (2008a) used 15 elements during their statistical distance calculations on trace element datasets (Rb, Sr, Y, Zr, Nb, Ba, La, Ce, Nd, Sm, Eu, Yb, Hf, Th and U). These elements were selected because they include elements from across the mass range measured during LA-ICP-MS. However there was a slight bias to using lighter elements because their greater abundance means the determinations of their concentration are more precise and standard deviations are lower. A bias towards heavier, less abundant elements could have an influence on $D^2$ values as high standard deviations could make samples appear compositionally closer (Pearce et al., 2008a). Within this study the same suite of elements was used during comparisons, with the exception that Ba was excluded. This was due to increased uncertainty in the determination of the concentration of this element.

# 4. The Potential Application of Trace Element Analysis to Distal Tephrochronology within the North Atlantic Region

## 4.1 Introduction

In section 2.5.4, the potential use of grain-specific determinations of the trace element composition of volcanic glass shards was emphasised along with the need to increase the spatial resolution of these techniques to permit the analysis of shards identified within distal locations. This chapter explores the application of a new LA-ICP-MS system to the analysis of tephra shards from distal sequences within the North Atlantic region. Material from tephra horizons identified within the Greenland ice-cores, GRIP and NGRIP, and various marine cores within the region was utilised within this analysis.

The first section of this chapter assesses the quality of the data that has been gained (section 4.2). Before subsequent sections explore four key issues regarding the LA-ICP-MS procedures and the application of trace element analysis of tephra shards within tephrochronological studies conducted on sequences from the North Atlantic region.

To assess the LA-ICP-MS procedures that were utilised it will first be determined if the spatial resolution of the system can be enhanced through an assessment of data gained using a 6 μm laser beam diameter (section 4.3) and secondly, the use of different elements as internal standards for calibration will be explored (section 4.4). This will allow procedural recommendations for the future use of this system within distal tephrochronological studies to be made.

The key tephrochronological issues that will be explored are (1) whether trace element characterisations reinforce the correlation of tephra horizons previously based on major element characterisations (section 4.5) and (2) whether trace element characterisations can help to distinguish between tephras with similar major element compositions (section 4.6).

In total material from 24 tephra horizons was analysed using LA-ICP-MS, 16 of these horizons were identified within this study and the remaining 8 have been provided for

analysis by Dr Siwan Davies and Professor Stefan Wastegård. Within sections 4.2 and 4.3 arbitrary labels have been assigned to the tephra horizons because the geographic and stratigraphic context of the horizons is not required for the analysis (table 4.1).

## 4.2 Assessing the Quality of the LA-ICP-MS data

### 4.2.1 Accuracy

A potential means to assess the accuracy of the trace element data gained within this study would have been to analyse homogenous synthetic or natural glass secondary standards during the analytical period and compare the results gained to certified trace element concentrations for these materials. A similar procedure is used when the major element composition of tephra shards is determined. However, at present this is not possible because there are very few reference materials which have a certified homogenous trace element composition and none are certified at the microanalytical scale being used within this study (Pearce et al., 2004a).

Another potential method for verifying the results would be to compare them to trace element compositions gained for the studied horizons using other methods such as ion microprobe analysis. This method was used by Pearce et al. (2007) to assess the accuracy of measurements of the Santorini and Aniakchak tephras, by comparing LA-ICP-MS, ion probe and solution ICP-MS measurements of these tephras. The trace element characterisations from the different methods were very similar, thus demonstrating the accuracy of the LA-ICP-MS technique. However, it was not possible to make similar comparisons in this study because this represents the first time that the trace element composition of these horizons has been determined. Therefore it is not possible to make a full assessment of the accuracy of the data within this chapter.

### 4.2.2 Analytical Precision and Instrument Sensitivity

The analytical precision for a set of analyses can be measured as the percentage relative standard deviation (standard deviation/average*100) from a series of analyses of a glass standard or from individual shards within a tephra horizon. For analyses of homogeneous glasses analytical precision improves with increasing element concentration. Analyses of the NIST 614, NIST 612 and NIST 610 reference materials,

**Table 4.1:** Summary table of information regarding horizons utilised within sections 4.3 and 4.4 to assess the LA-ICP-MS procedures utilised within this study. The actual horizons to which these labels relate are given in appendix 2.

| Horizon Label | Depositional Environment | | Geochemistry | Si and Ca Internal Standard Used | 14μm and 6μm analyses gained? |
|---|---|---|---|---|---|
| | Ice-core | Marine Core | | | |
| Horizon A | | × | Rhyolitic | | |
| Horizon B | | × | Rhyolitic | | |
| Horizon C | | × | Rhyolitic | | × |
| Horizon D | | × | Rhyolitic | | × |
| Horizon E | | × | Rhyolitic | | × |
| Horizon F | × | | Basaltic | × | |
| Horizon G | × | | Basaltic | × | × |
| Horizon H | × | | Basaltic | × | |
| Horizon I | × | | Basaltic | × | |
| Horizon J | × | | Basaltic | | × |
| Horizon K | × | | Basaltic | × | × |
| Horizon L | × | | Basaltic | × | × |
| Horizon M | × | | Basaltic | × | |
| Horizon N | × | | Basaltic | × | |
| Horizon O | × | | Basaltic | | × |
| Horizon P | × | | Basaltic-andesitic | | |
| Horizon Q | × | | Rhyolitic | | × |
| Horizon R | × | | Basaltic | × | |
| Horizon S | × | | Basaltic | × | × |
| Horizon T | × | | Basaltic | × | |
| Horizon U | × | | Basaltic | × | × |
| Horizon V | × | | Basaltic | | × |
| Horizon W | | × | Basaltic | × | |
| Horizon X | | × | Basaltic | × | |

which have nominal concentrations of 1, 50 and 500 ppm respectively, demonstrate this relationship (figure 4.1; Pearce et al., 2004a).

One of the factors affecting the precision of analyses made using the LA-ICP-MS system is the instrument sensitivity. The sensitivity of the system can be estimated from the counts per second recorded by the mass spectrometer per part per million element concentration for analyses of the glass standard NIST 612. Calculating the sensitivities for the three analytical periods over which analyses were made within this study showed that the sensitivity was consistent between the first and second periods. However, it increased by a factor of ~1.75 for the third period due to improvements made to the tuning of the mass spectrometer prior to this period. An assessment of analyses of NIST 612 made during the three runs showed that the increase in sensitivity did improve precision, with the precision on the NIST 612 glass varying between 2-10 % during the first two runs and only varying between 2-7 % during the final run. These precisions are within the range Pearce et al. (2007) expected when describing the potential of this new system.

Figure 4.2 illustrates the relationship between analytical precision and element concentration for average analyses, using a 14 µm beam diameter, of basaltic tephra horizons made during the three analysis periods. During periods 1 and 2 the precision for the majority of elements ranges between 20 and 70 %, while during run three the precision ranges between 15 and 50 %. The slight improvement in precision during the third period can be attributed to increased instrument sensitivity during this run; if it is assumed that the sample heterogeneity is the same in all the horizons of basaltic material. For all of the horizons the relationship of better analytical precision with increasing element concentration (figure 4.2) can be observed, however it is weaker than within the homogenous references glasses.

The precisions for the horizons imply that there is a wide range of concentrations for each element that was analysed and this range is greater than the analytical errors estimated from the NIST 612 analyses. This can be attributed to greater heterogeneity in the composition of individual basaltic shards from the studied horizons relative to the NIST 612 reference glass. Another factor for the worsening precision is the use of a 14 µm beam diameter for the sample analyses compared to a 30 µm beam for the NIST 612 analyses. This means that ~4.5 times less material is being fed into the mass spectrometer during a sample analysis.

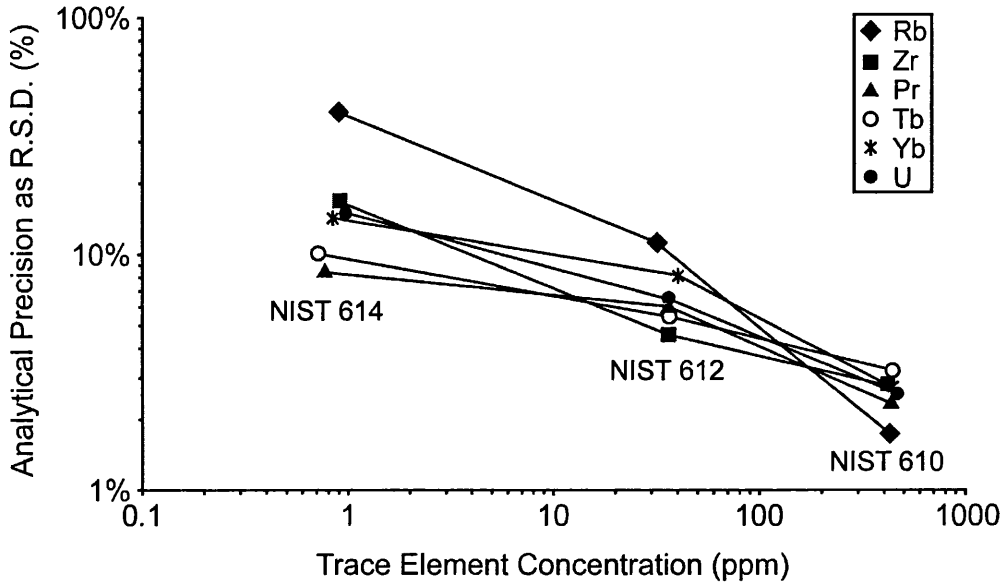


**Figure 4.1:** Concentration of selected elements within NIST 614, 612 and 610 against the analytical precision (as the relative standard deviation) determined from 5 repeat LA-ICP-MS analyses at 1 mJ and 5 Hz (adapted from Pearce et al., 2004).

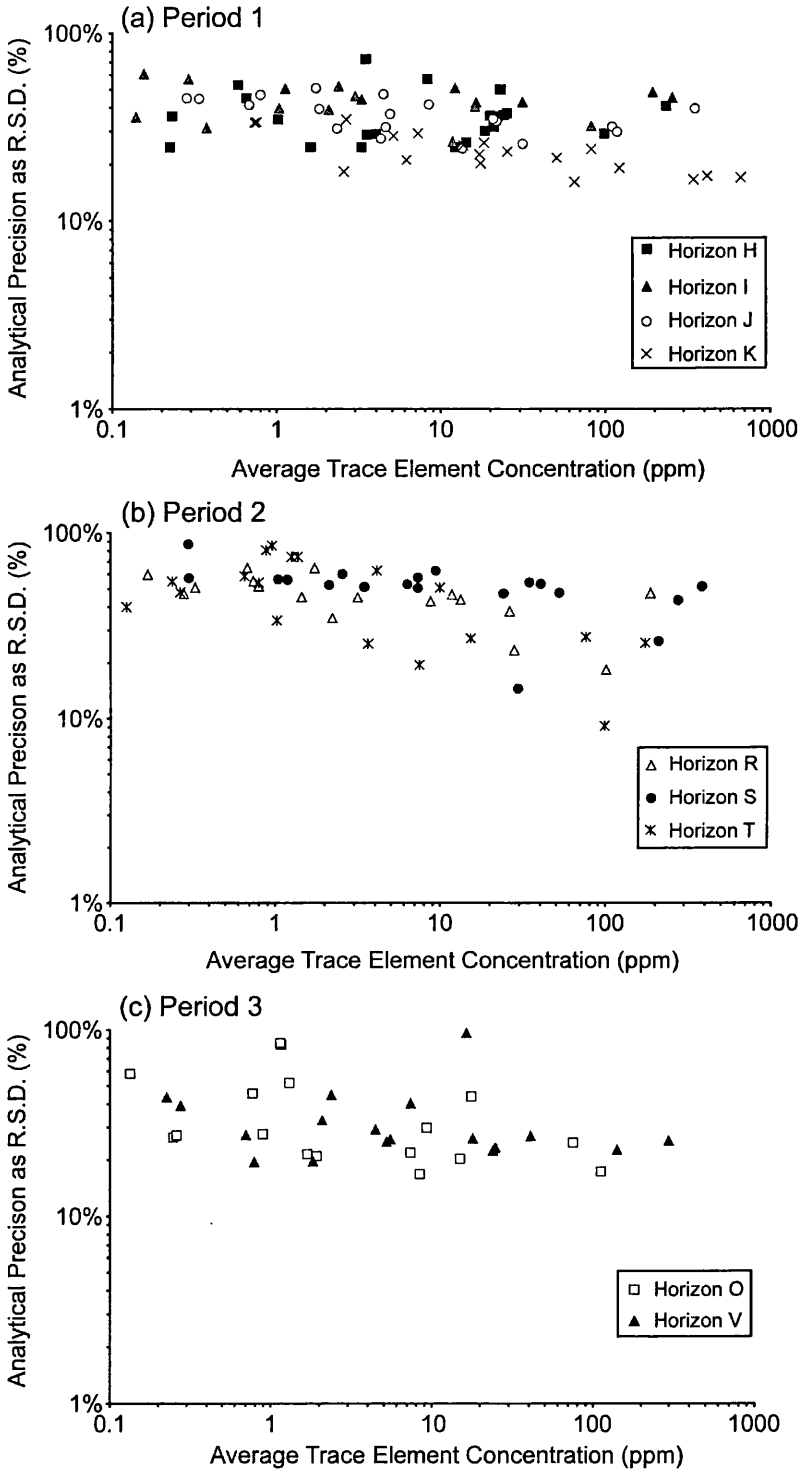


**Figure 4.2:** Analytical precision and average trace element concentration for basaltic tephra horizons analysed during the three analytical periods. Average concentrations calculated from individual shard analyses within each horizon and analytical precision is the relative standard deviation for these averages.

The precision of analyses of four rhyolitic horizons made during the third run ranges between ~5-25 % (figure 4.3); which implies that the rhyolitic material was more heterogeneous than the basaltic material. As with the basaltic horizons the worse precision compared to the reference glass analyses is due to the use of a smaller laser beam diameter and greater heterogeneity between individual shards.

### 4.2.3 Lower Limits of Detection

Theoretical lower limits of detection (LLD) provide a measure of how the LA-ICP-MS system is responding (i.e. cps/ppm) and the ratio between signal and background counts (Pearce et al., 2007). LLD were calculated using the average of five NIST 612 glass analyses and five gas analyses at the start of each day of analysis. They were calculated as 3 times the standard deviation of the gas blank analyses multiplied by the ratio between element concentration and counts per second for the average of each element from the NIST 612 analyses. These analyses were made using a 30 µm laser beam diameter, whereas analyses of samples were made using a 14 µm beam diameter. To compensate for the difference in the volume of material ablated during a single laser pulse using the different beam diameters the LLD calculated from the NIST 612 analyses were multiplied by 4.5.

The LLD for the sample analyses range between 0.01 and 1 ppm and were reasonably consistent between the three runs. These LLD are comparable to those for former LA-ICP-MS systems operating at a spatial resolution of ~25 µm (Pearce et al., 2004a). LLD increase with decreasing beam size, therefore the consistency in LLD between the systems can be attributed to the improvements in the sensitivity of ICP-MS instrumentation. Higher values were observed for the elements excluded prior to the third run (Ti, Ni, V and Cr) because of the high instrument blanks at these masses, this was also a cause of high LLD for Ba and Pb.

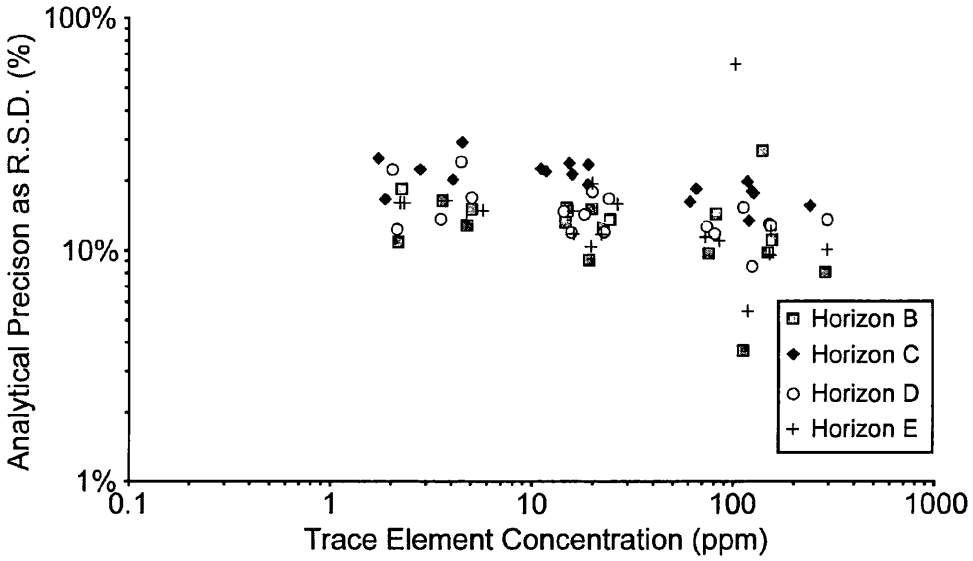


**Figure 4.3:** Analytical precision and average trace element concentration for four rhyolitic tephra horizons analysed during the third analytical period. Average concentrations calculated from individual shard analyses within each horizon and analytical precision is the relative standard deviation for these averages.

## 4.3 Testing the Spatial Resolution of the LA-ICP-MS System

### 4.3.1 Introduction

Increases in the number of cryptotephra studies being undertaken in the North Atlantic region has resulted in the identification of cryptotephra horizons at increasingly distal sites (see section 2.4.2). Including the Greenland ice-cores investigated within this study, which are 1500 km from the nearest potential volcanic source of tephra horizons. An additional example is provided by the widespread Vedde Ash as this horizon has recently been described in two lake sequences in Switzerland and Southern Germany, ~2500 km south east of its Icelandic source (Blockley et al., 2007).

In general there is a decrease in the maximum size of atmospherically transported volcanic particles, deposited following an eruption with increasing distance from the volcanic source (Lacasse et al., 1996). Thus, the identification of tephra horizons at increasingly distal sites will result in the isolation of smaller tephra shards than previously encountered. As geochemical composition is the key tool for the correlation of tephra horizons over long distances, the analytical techniques used to geochemically characterise individual shards have to be capable of producing reliable data at the smallest possible spatial resolution. Thus, facilitating the robust characterisation of these more distal horizons.

Earlier it was highlighted that the new LA-ICP-MS system, operating with a 14 µm beam diameter, produces analyses with a similar precision and LLD as past systems that operated with a ~25 µm diameter laser beam (section 4.2). This indicates that the improvement in spatial resolution should not have significantly affected the reliability of trace element characterisations. The aim of this section is to investigate whether it is possible to further improve the spatial resolution and gain reliable trace element characterisations from individual tephra shards analysed using a laser beam diameter of 6 µm and the current tuning setup of the LA-ICP-MS system. This will determine if the new system can be used in tandem with EPMA, which has a spatial resolution of 5 µm (section 3.5.2), to gain major and trace element characterisations from distal tephra horizons where the size of shards restricts the maximum shard section that can be obtained to ~10 µm in diameter.

To achieve this during the LA-ICP-MS analysis of tephra horizons within this study, in addition to analysing shards with a 14 µm laser beam diameter, selected shards were analysed using a 6 µm diameter laser beam. The shards analysed with a 6 µm laser beam were either small or only partly exposed during preparation for geochemical analysis, leaving only a small section of the shard exposed for analysis. All of the shards had been previously analysed using EPMA to allow internal standardisation of the data. To assess the reliability of the analyses made using a 6 µm beam diameter, sets of analyses from horizons where data has been gained from shards using both a 14 µm and 6 µm beam diameter are compared both qualitatively and quantitatively using the statistical distance function. Before an assessment is made of the overall potential for utilising a 6 µm diameter beam in future studies.

### 4.3.2 Comparison of 14 µm and 6 µm Beam Diameter Trace Element Characterisations

In total analyses from twelve distal horizons were investigated, from which a minimum of 5 analyses of shards were acquired using a 6 µm laser beam diameter (table 4.2). Both the 14 µm and 6 µm analyses from individual horizons were conducted during the same analysis window, i.e. the sample was not removed from the sample chamber between the analyses. Therefore variations in instrument conditions between analytical windows can be excluded as an influence on intra-sample variability.

Another potential source of intra-sample variation of trace element concentrations is major element geochemical differences between the sets of shards analysed with the different laser beam diameters. The two sets of shards from each horizon represent geochemical sub-populations of the overall geochemical composition of the horizon. To rule major element geochemical differences out as a source of intra-sample variation it has to be ensured that the sub-populations have comparable compositions.

For all twelve horizons the major element composition of the two sub-populations were compared using both the similarity coefficient and statistical difference methods (table 4.2). The high similarity coefficient values (all $\geq 0.964$) and low $D^2$ values (all $\leq 2.48$) for the comparisons strongly suggests there are no major differences between any of the sub-populations. Therefore, major element geochemical differences can be ruled out as a cause of any trace element contrasts between analyses acquired using the 6 µm or 14 µm beam diameters on shards from the same horizon.

**Table 4.2:** Tephra horizons used to analyse the spatial resolution of the LA-ICP-MS system. Critical values at the 99% confidence interval for $D^2$ are 18.48 for the major element comparisons and 27.69 for the trace element comparisons. SC = Similarity Coefficient. ME = Major elements; TE = Trace elements.

| Tephra Horizon | No. 14 µm analyses | No. 6 µm analyses | Major Elements - SC | $D^2$ - 14 to 6 µm ME analyses | $D^2$ - 14 to 6 µm TE analyses |
|---|---|---|---|---|---|
| Horizon C | 13 | 8 | 0.983 | 0.69 | 14.6 |
| Horizon D | 14 | 8 | 0.975 | 0.66 | 23.0 |
| Horizon E | 11 | 7 | 0.991 | 1.51 | 16.3 |
| Horizon G | 17 | 5 | 0.987 | 0.59 | 23.8 |
| Horizon J | 14 | 5 | 0.964 | 2.01 | 7.44 |
| Horizon K | 14 | 5 | 0.969 | 2.03 | **116.1** |
| Horizon L | 14 | 5 | 0.974 | 1.90 | 22.0 |
| Horizon O | 5 | 9 | 0.977 | 2.48 | 22.4 |
| Horizon Q | 9 | 5 | 0.977 | 0.51 | 19.3 |
| Horizon S | 11 | 5 | 0.986 | 0.49 | 15.4 |
| Horizon U | 6 | 5 | 0.989 | 1.61 | **40.8** |
| Horizon V | 11 | 8 | 0.977 | 1.16 | 21.7 |

The chondrite-normalised REE element profiles of the individual 6 µm and 14 µm analyses and the averages for each horizon are plotted in figures 4.4 and 4.5 respectively. These profiles provide an initial inspection of the analyses because they allow concentration data for 14 trace elements to be inspected.

The most obvious difference between the sets of analyses is the greater variation within the concentrations of the 6 µm analyses, which can be observed for all of the horizons. This variation is less pronounced for the lighter REEs, e.g. La, Ce, Pr and Nd, than the heavier REEs. The greatest consistency between the 6 µm and 14 µm analyses is for horizons C, D, and E; which can be observed on both figures 4.4 and 4.5. The 6 µm analyses from these horizons also show the least amount of variation and the most consistency between the profiles. The only exception is that Eu concentrations are consistently higher in the 6 µm analyses for all three horizons. This is probably a result of polyatomic interference from $^{137}Ba^{16}O$, which has the same mass as $^{153}Eu$ the Eu isotope measured during these analyses, as high background levels of Ba were observed when these samples were being run.

For the nine other horizons REE profiles from the two sets of analyses all show some degree of overlap, however the magnitude of this overlap varies between horizons. For example horizons G, J and Q show a high degree of overlap between the sets of analyses relative to the low levels of overlap between the datasets for horizons K, L, S and U (figure 4.4). Despite this variation in overlap between horizons the average trace

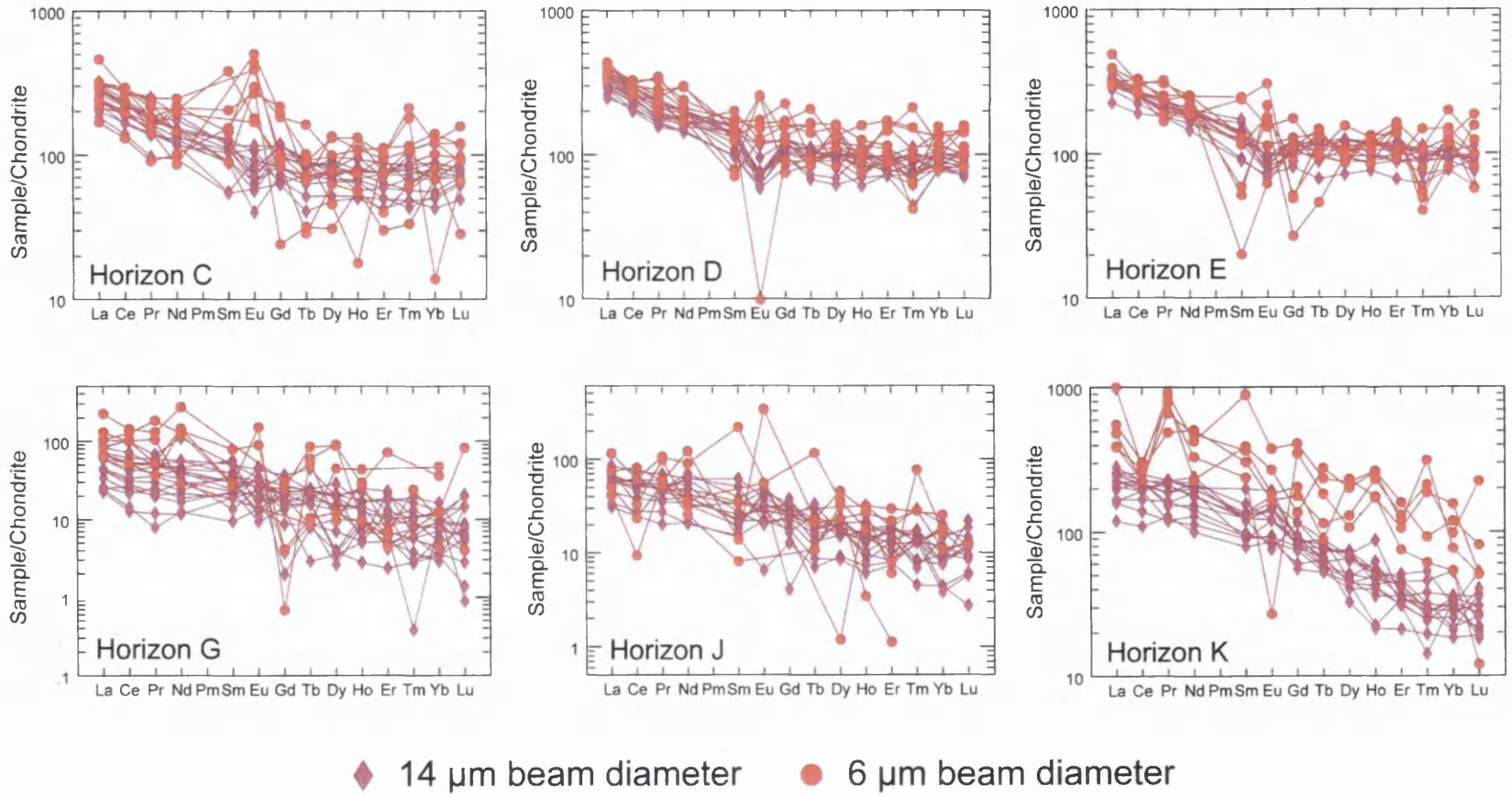


**Figure 4.4:** Chondrite-normalised REE profiles for individual shards gained from 12 tephra horizons where tephra shards were analysed using either a 14 µm or 6 µm laser beam diameter. No outlying 6 µm analyses have been removed. Chondrite composition from Sun and McDonough (1989).

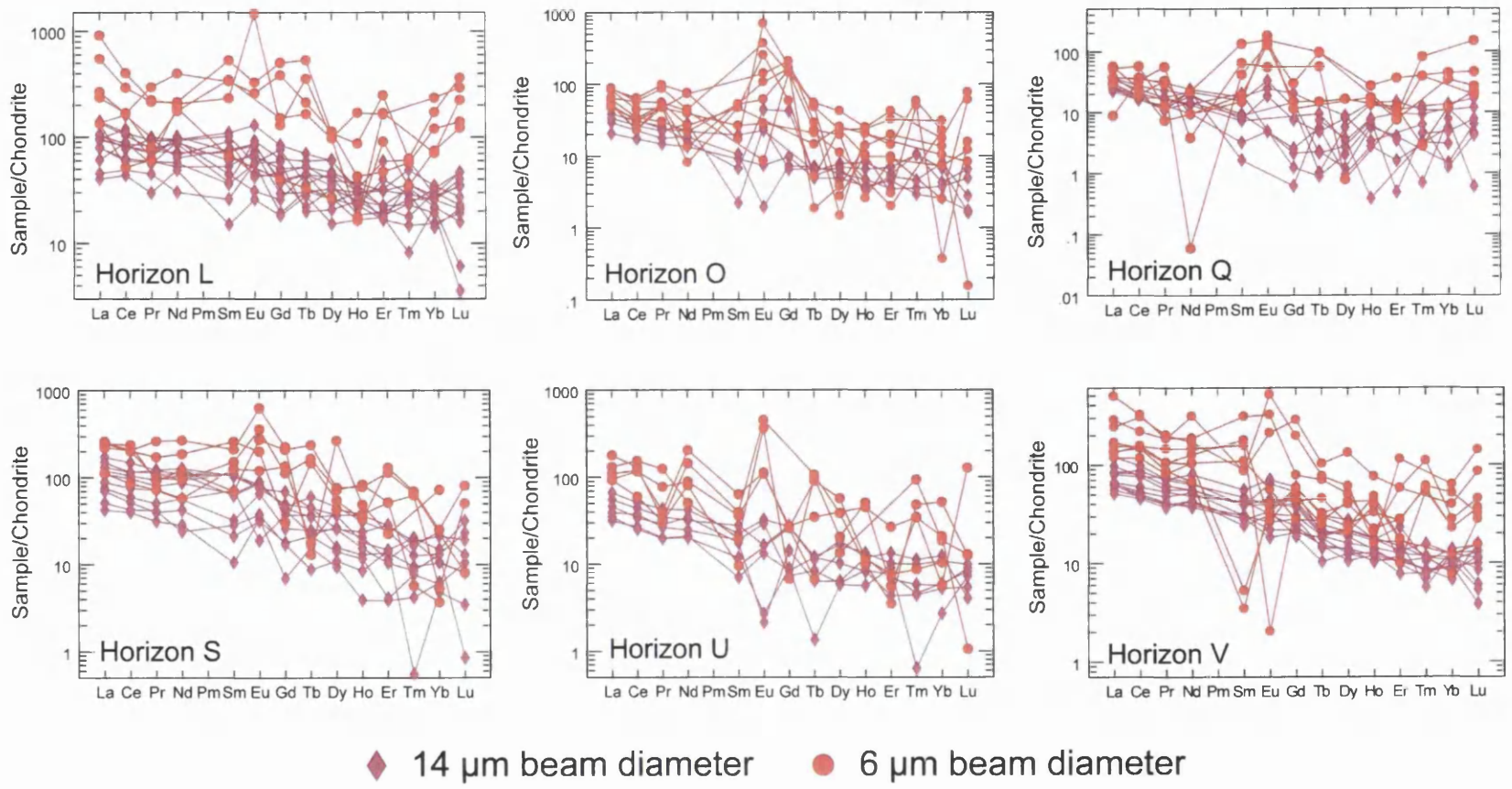


**Figure 4.4:** continued.

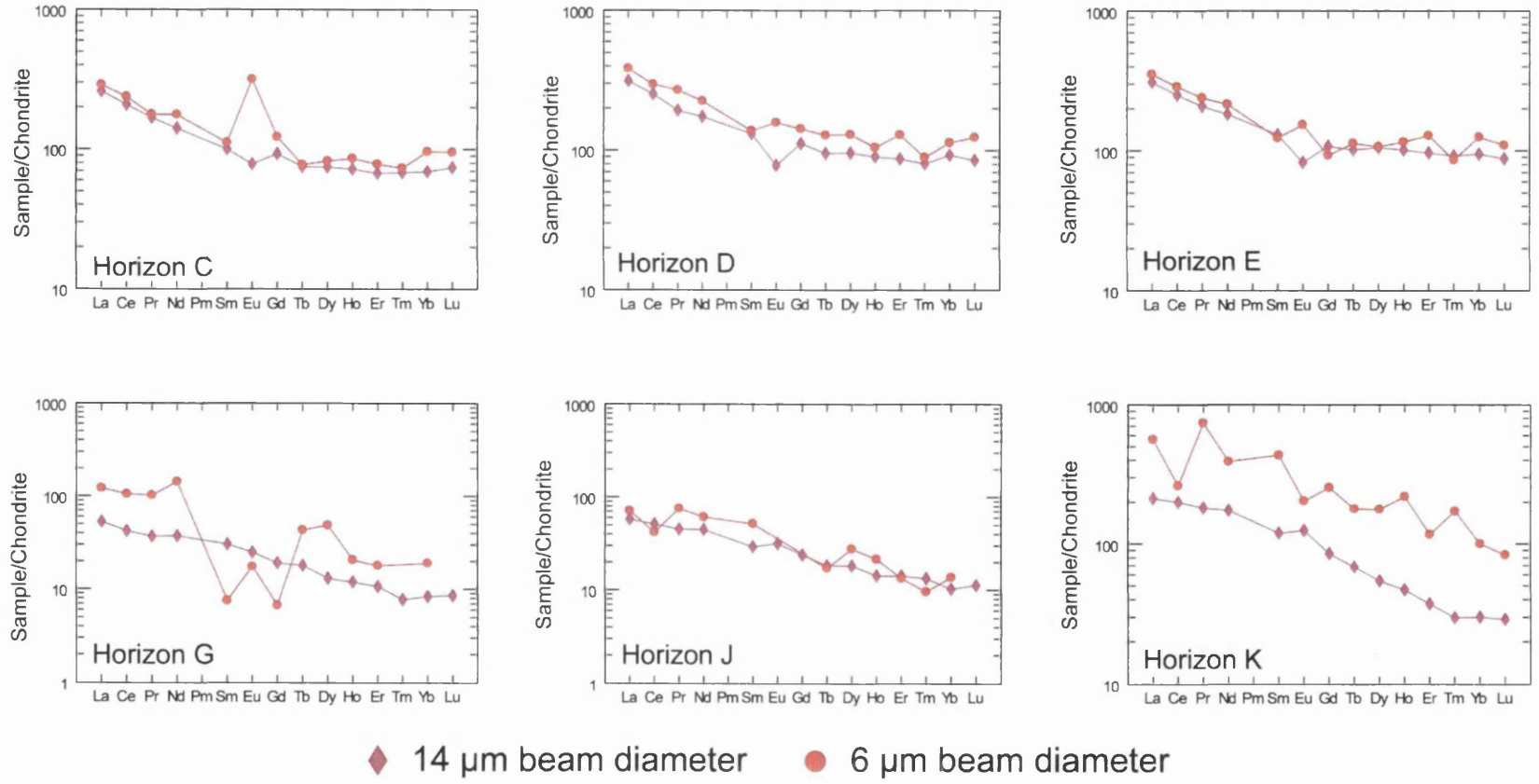


**Figure 4.5:** Average chondrite-normalised REE profiles for 12 tephra horizons from which tephra shards were analysed using either a 14 µm or 6 µm laser beam diameter. Chondrite composition from Sun and McDonough (1989).

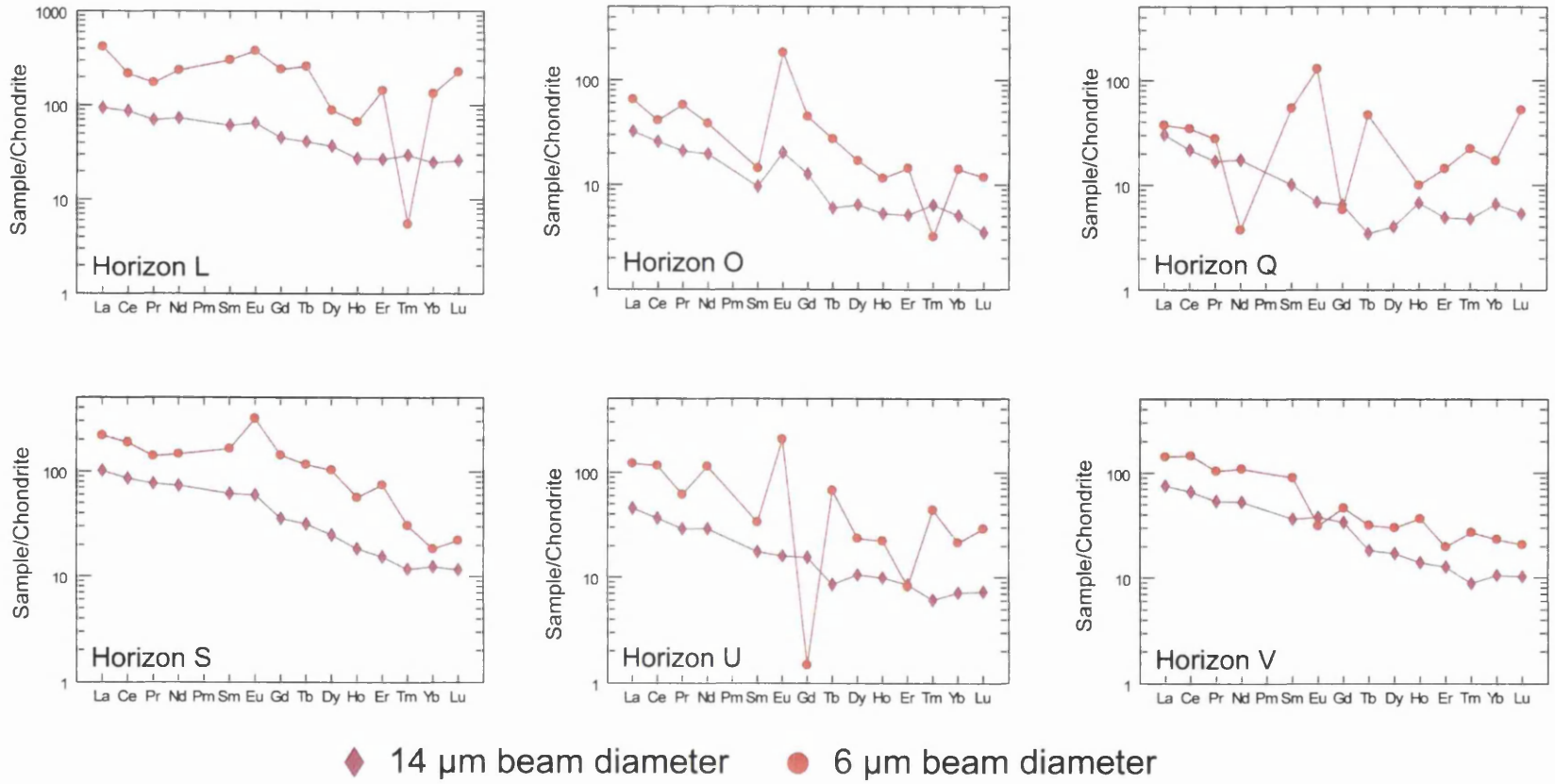


**Figure 4.5:** continued.

element concentrations calculated for the 6 µm analyses tend to be higher than those calculated for the 14 µm analyses for all horizons (figure 4.5).

Biplots of trace element data from four of the horizons (C, V, U and K) are shown in figures 4.6 and 4.7. These horizons were selected as examples that demonstrate the different relationships observed between the 14 µm and 6 µm datasets. The biplots for horizon C show that the trace element characterisation of the horizon using a 6 µm beam diameter for analyses is indistinguishable from the characterisation gained using a 14 µm beam diameter, supporting the observations from the REE profiles. For horizon V the analyses made using a 14 µm beam diameter are more tightly clustered and less variable than the 6 µm beam diameter data and there is no overlap between the geochemical fields of the analyses. However, within figures 4.6 (d) and (e) the analyses appear to fall along the same element ratio trend lines. For the other two horizons (U and K) large scale differences exist between the two datasets. But it can be observed that the concentrations calculated for the 6 µm analyses are more variable and exceed those for the 14 µm analyses, consistent with the observations made from the REE profiles.

The differences between the two trace element datasets from each of the twelve horizons were assessed using the statistical difference function with the concentrations of 14 elements across the mass range being compared (table 4.2). This analysis did identify the major differences observed between the datasets for horizons U and K as the $D^2$ values for both these horizons exceed the critical value. However, $D^2$ values for some horizons displaying distinct qualitative differences did not exceed the critical value, e.g. horizon V, and thus were not identified as being statistically different. This may be due to the impact that the high variability in the 6 µm data analyses has when calculating the $D^2$ value. The equation to calculate $D^2$, section 3.7.2, is sensitive to high standard deviations and erroneously low $D^2$ values may be produced when highly variable datasets are being compared.

### 4.3.3 Assessing the Optimal Beam Diameter

The main impact that reducing the size of the laser beam has is to drastically decrease the volume of material ablated during an analysis. Reducing the diameter of the laser beam from 14 µm to 6 µm reduces the amount of material ablated during each laser

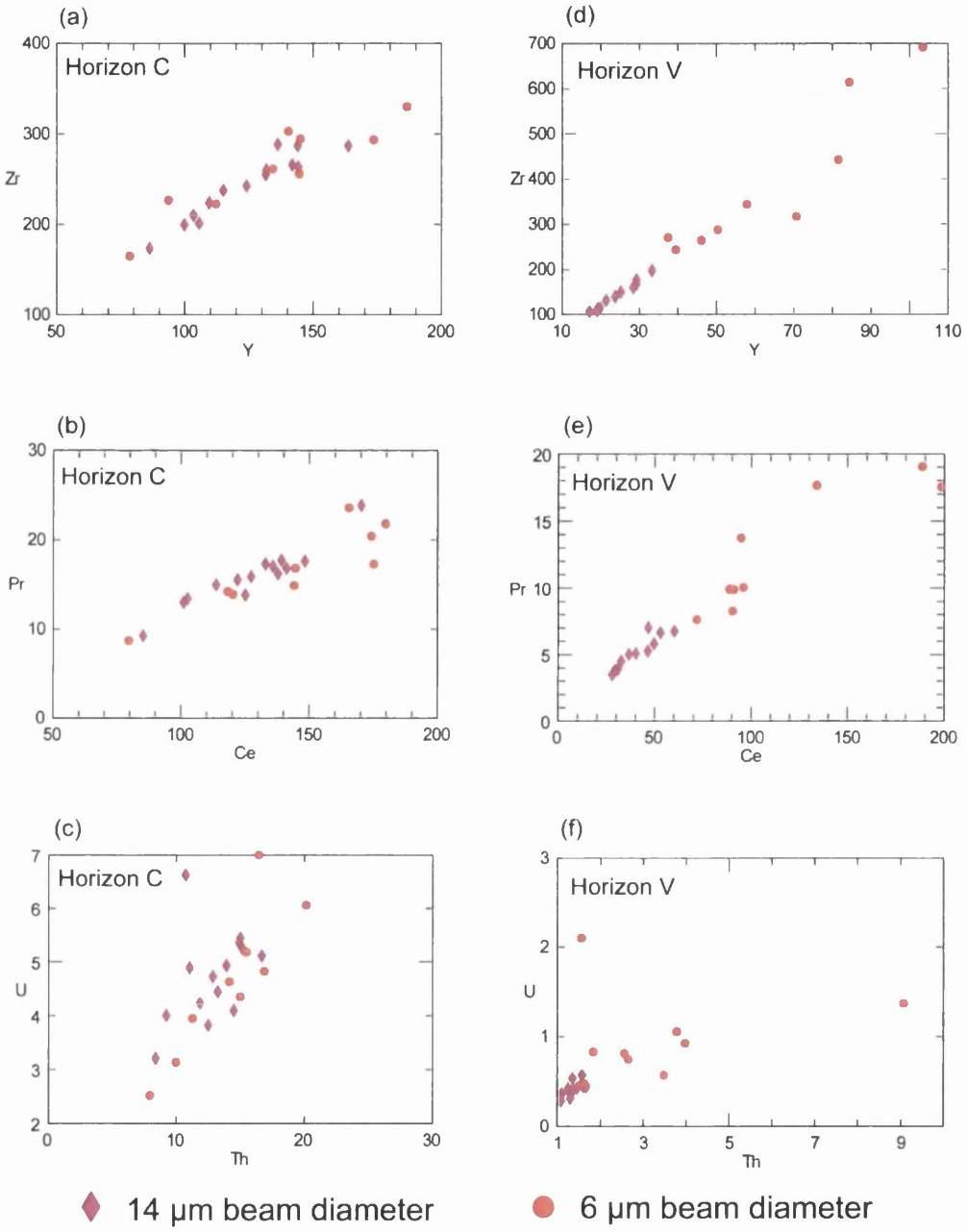


**Figure 4.6:** Compositional variation diagrams of trace element concentration data gained using either a 14 µm or 6 µm laser beam diameter from (a, b, c) horizon C (d, e, f) and horizon V. All concentrations in ppm.

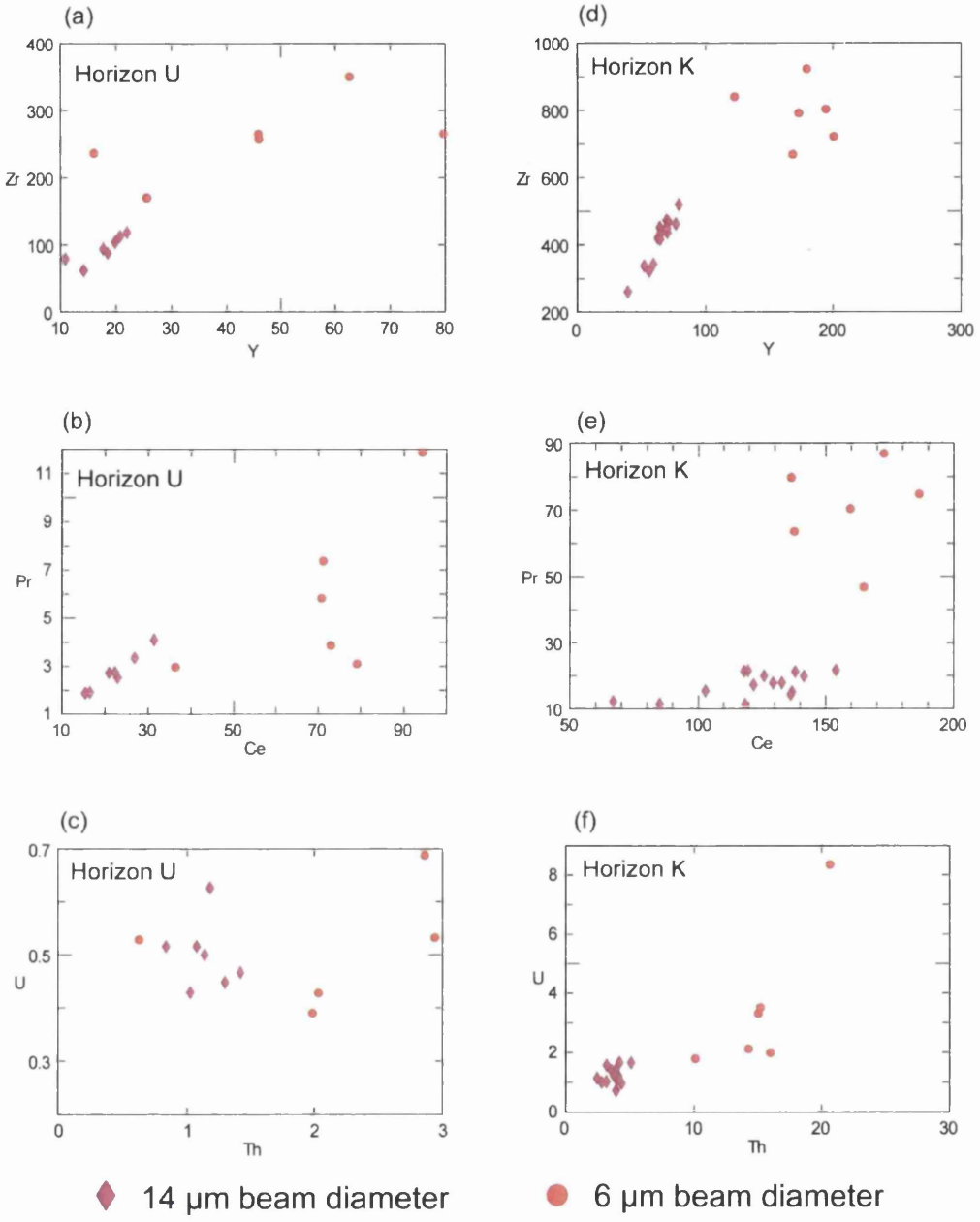


**Figure 4.7:** Compositional variation diagrams of trace element concentration data gained using either a 14 µm or 6 µm laser beam diameter from (a, b, c) horizon U and (d, e, f) horizon K. All concentrations in ppm.

pulse by approximately 5.5 times. As far less material is being fed into the mass spectrometer lower average counts per second are recorded for each element. The precision of trace element determinations are related to count rates; with worse precision observed when count rates are lower due to statistical counting errors. The error introduced due to counting statistics is related to the square root of the number of counts, therefore the relative error will be higher for the analyses using the 6 µm beam than the 14 µm beam. This introduces more variability into the 6 µm data and explains the greater spread of results observed within these datasets (figure 4.4). Statistical counting errors are also the cause of the greater variability within the heavier REEs than the lighter REEs. The heavier REEs are less abundant within the tephra shards, thus lower, less precise counts are recorded for these elements during analyses.

Of particular importance is the effect that reducing the volume of material being fed into the mass spectrometer has on the count rates for $^{29}Si$ as this isotope was used as the internal standard for both the 14 µm and 6 µm analyses. To assess the effect count rates of the internal standard have on calculated concentration data the ratio of Si counts from a sample analysis and the background Si counts can be compared to the calculated concentrations. As an example, if the Si count signal from an analysis was 40000 cps and the background Si counts 20000 cps the ratio would be 2.0. Ratios are lower for the 6 µm analyses as the reduced amount of sample material ablated during those measurements produces lower count rates. This ratio is considered instead of absolute sample count rates to remove the effect that instrument sensitivity variations have on background signals.

In general the calculated concentrations were found to decrease approximately exponentially with increasing ratio between sample and background counts; until they stabilised past a threshold where Si count rates do not have an influence on calculated trace element concentrations (figure 4.8). This relationship can be observed on figure 4.9, which illustrates the ratios and calculated concentrations for six elements from four example horizons. From the plots in figure 4.9 and an inspection of data from other horizons it appears that once the ratio between sample and background count rates for the 6 µm analyses exceeds ~0.8-0.9, the Si count rates have a negligible influence on the calculated concentrations.

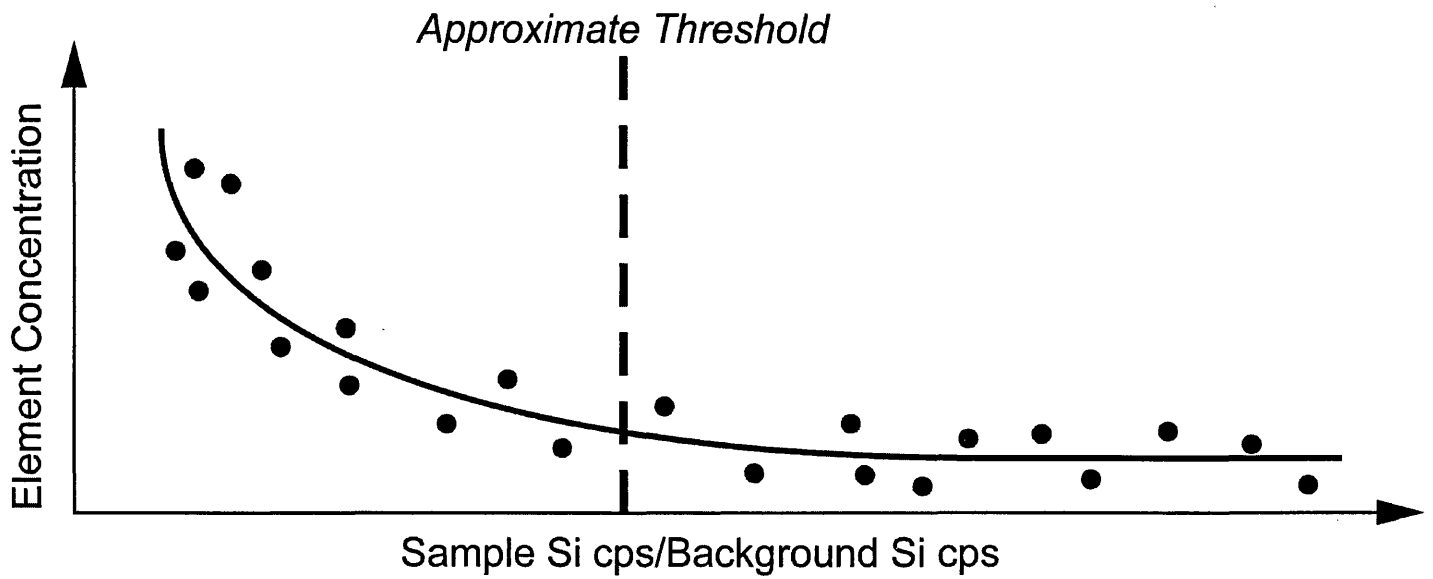


**Figure 4.8:** Schematic representation of the relationship between element concentration and the ratio between sample and background Si counts per second for analyses using the LA-ICP-MS system.

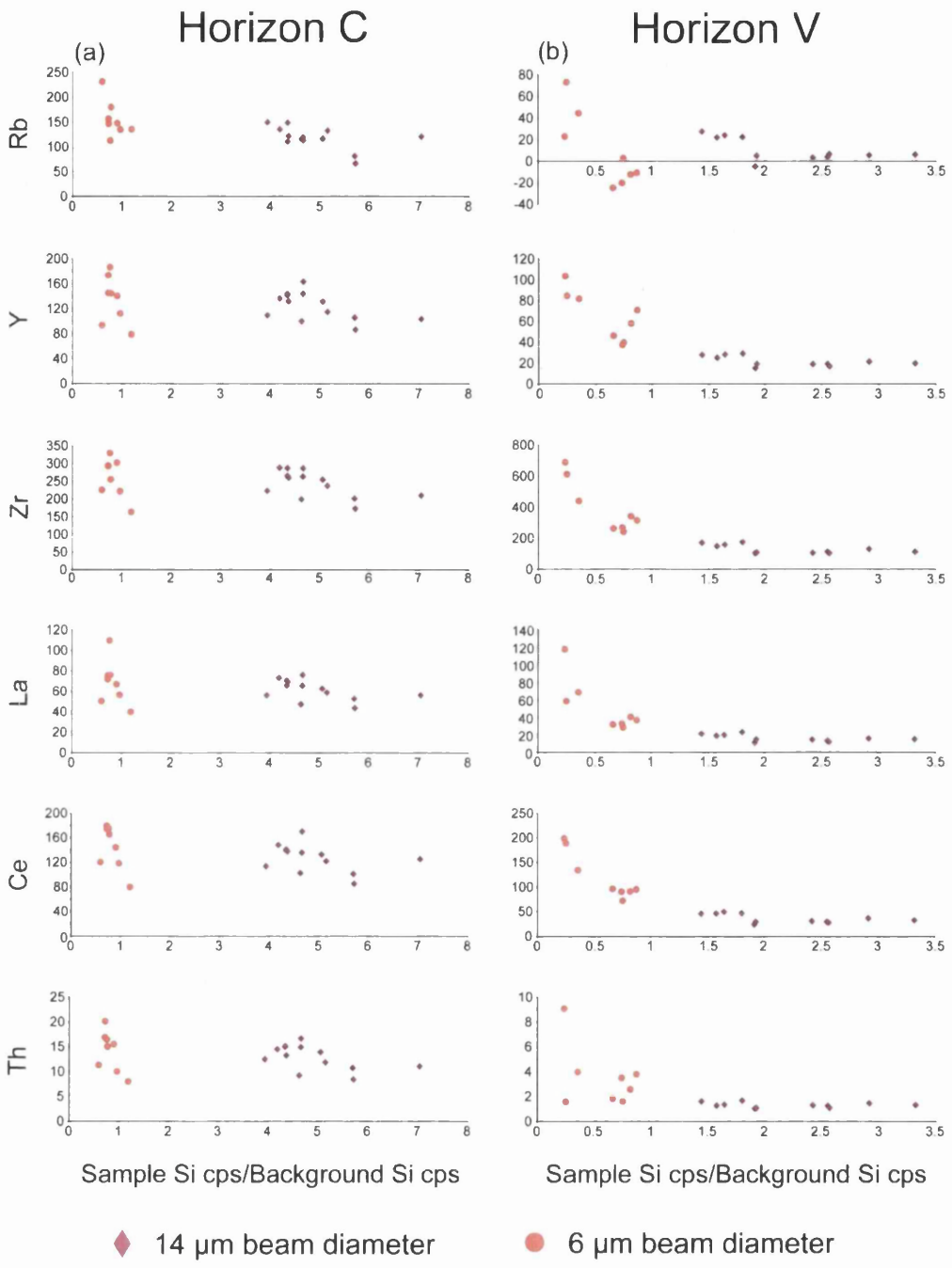


**Figure 4.9:** Element concentrations versus the ratio between sample to background Si counts per second for the elements Rb, Y, Zr, La, Ce and Th for (a) horizon C (b) horizon V (c) horizon U and (d) horizon K. All concentrations in ppm.

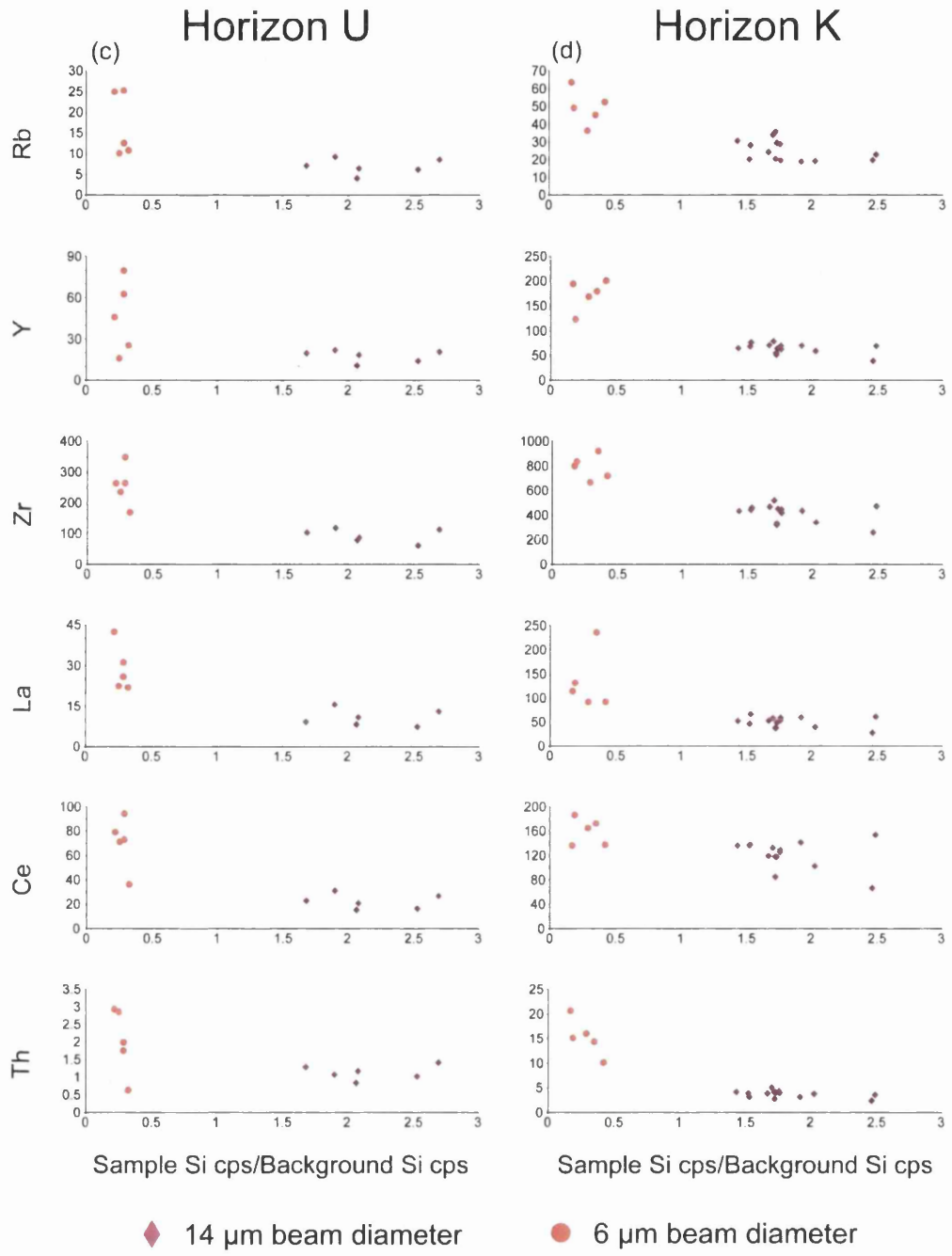


**Figure 4.9:** continued.

The overall relationship is most closely approximated in the data from horizon V as a consequence of the wide range of ratios for the 6 μm analyses from this horizon (figure 4.9b). The similarities in the trace element concentrations between the 14 μm and 6 μm analyses for horizon C occur because the ratios for the analyses using a 6 μm beam diameter are approximately greater than the threshold (figure 4.9a). Whereas for horizons U and K the large differences between the concentrations from the sets of analyses occur because the count rates for the 6 μm analyses are much less than the threshold value (figure 4.9c and d).

Table 4.3 summarises the average ratios between sample and background counts for all twelve horizons. These ratios show that the horizons which were found to have high similarities between the sets of analyses, such as C, D and E have ratios for the 6 μm analyses close to the threshold (0.77-0.90) whereas 6 μm analyses from the horizons that displayed high differences, such as L, U, S and K had the lowest ratios (0.24-0.29), far below the threshold value.

**Table 4.3:** Average ratio between sample counts and background counts for 6 μm and 14μm analyses from the 12 studied horizons.

| | Average Sample/Background Si Counts Ratio | |
|---|---|---|
| Tephra Horizon | 14 μm Analyses | 6 μm Analyses |
| Horizon C | 4.91 | 0.83 |
| Horizon D | 4.62 | 0.77 |
| Horizon E | 6.37 | 0.90 |
| Horizon G | 1.87 | 0.31 |
| Horizon J | 2.25 | 0.34 |
| Horizon K | 1.82 | 0.29 |
| Horizon L | 1.76 | 0.26 |
| Horizon O | 4.01 | 0.79 |
| Horizon Q | 2.66 | 0.61 |
| Horizon S | 1.49 | 0.24 |
| Horizon U | 2.16 | 0.28 |
| Horizon V | 2.19 | 0.59 |

Overall, the potential for this system to gain reliable trace element data from tephra shards using a 6 μm laser beam diameter has been demonstrated, however to consistently achieve this it has been shown that the ratio of the sample counts to background counts for Si has to be improved. This is easier when rhyolitic material rather than basaltic material is being analysed, because of the higher Si concentrations within the shards. But could also be achieved if the sensitivity of the system is further improved, or potentially the laser energy and frequency is increased.

The count ratios on analyses using a 10 µm beam diameter may exceed the threshold for reliable element concentrations. However, this was not investigated within this study because the major goals were to gain characterisations of the horizons using a 14 µm beam and to test the limits of the system using a 6 µm beam and only a limited amount of material was available for most horizons.

## 4.4 Selection of an Internal Standard for the Analysis of Basaltic Material

### 4.4.1 Introduction

In section 3.5.3.3 it was highlighted that knowledge of the concentration of at least one element within a tephra shard is required to calculate trace element concentrations for that shard. Concentrations of both $SiO_2$ and CaO are determined using EPMA and can be analysed during LA-ICP-MS, thus both could be used as an internal standard. The majority of grain-specific studies using LA-ICP-MS have focused on the analysis of rhyolitic material for which CaO is not an appropriate internal standard. Because, its concentration is low (~1 %wt) within rhyolitic glass compared to that of $SiO_2$ (~>70 %wt) (Pearce et al., 2004a). Only a few grain-specific studies of basaltic tephra deposited within distal localities have been conducted, e.g. Davies et al. (2005b), when because of the higher CaO concentrations within this material (~8-14 %wt) there is the potential to use Ca isotopes as an internal standard.

The increased sensitivity of the new LA-ICP-MS system raises the potential issue of saturation of the detectors from $^{29}Si$ atoms, which may make it unusable as an internal standard. In these situations and when basaltic material is being analysed the use of a lower abundance isotope of Ca as an internal standard would allow trace element concentrations to be calculated. However, it first has to be established whether trace element concentrations calculated using Ca as an internal standard are directly comparable to those using Si. For this analysis there are no reference values for the horizons, therefore it is assumed that the Si standardised data is 'correct' because it has a higher concentration within the analysed material and the $^{29}Si$ isotope used is more abundant than the $^{43}Ca$ isotope. Despite being the most abundant calcium isotope $^{40}Ca$ was not used as the internal standard due to potential interference of $^{40}Ar$ from the carrier gas.

### 4.4.2 Comparison of Trace Element Data Calculated Using Different Internal Standards

Trace element concentrations from 14 μm laser beam diameter analyses of shards from 12 basaltic horizons were calculated using $^{43}Ca$ as an internal standard in addition to being calculated using $^{29}Si$ as the internal standard (table 4.4). Additionally analyses from two horizons, horizons W and X, where a 20 μm beam diameter was utilised were calibrated using both of the isotopes.

Figure 4.10 displays chondrite-normalised average REE profiles for six of the horizons that were analysed. These horizons were selected because they illustrate the differing relationships that are apparent between the Si and Ca standardised datasets for individual horizons. In all cases the REE profiles from both sets of data follow the same patterns, with some horizons having indistinguishable profiles for the two sets of data (horizons L and W). However, offsets of differing magnitude can be observed between the datasets from other horizons. For example, for horizons F and M the Si standardised trace element concentrations consistently exceed the Ca standardised data, whereas for horizons I and K the Ca standardised trace element concentrations consistently exceed the Si standardised concentrations. The biplots in figure 4.11 demonstrate that these relationships also exist within the concentrations of trace elements lighter (Zr, Y) and heavier (Hf, Th) than the REEs.

**Table 4.4:** Average ratio between 29 average trace element concentrations calculated using $^{29}Si$ and $^{43}Ca$ as an internal standard. Horizons ordered based on the ratio between the concentrations from each dataset. Critical value for $D^2$ at the 99 % confidence level of 29.14.

| Tephra Horizon | Ratio Between Si and Ca I.S.ed trace element concentrations | | $D^2$ |
|---|---|---|---|
| | Average | S.D. | |
| Horizon F | 1.48 | 0.03 | 24.28 |
| Horizon M | 1.34 | 0.08 | 17.84 |
| Horizon S | 1.17 | 0.03 | 1.61 |
| Horizon X | 1.17 | 0.01 | 11.18 |
| Horizon G | 1.16 | 0.06 | 1.24 |
| Horizon W | 0.99 | 0.02 | 0.06 |
| Horizon L | 0.97 | 0.04 | 0.06 |
| Horizon N | 0.86 | 0.05 | 0.83 |
| Horizon K | 0.79 | 0.01 | 9.30 |
| Horizon U | 0.75 | 0.04 | 5.10 |
| Horizon T | 0.75 | 0.02 | 15.12 |
| Horizon R | 0.74 | 0.02 | 9.37 |
| Horizon H | 0.71 | 0.07 | 4.28 |
| Horizon I | 0.59 | 0.03 | 10.10 |

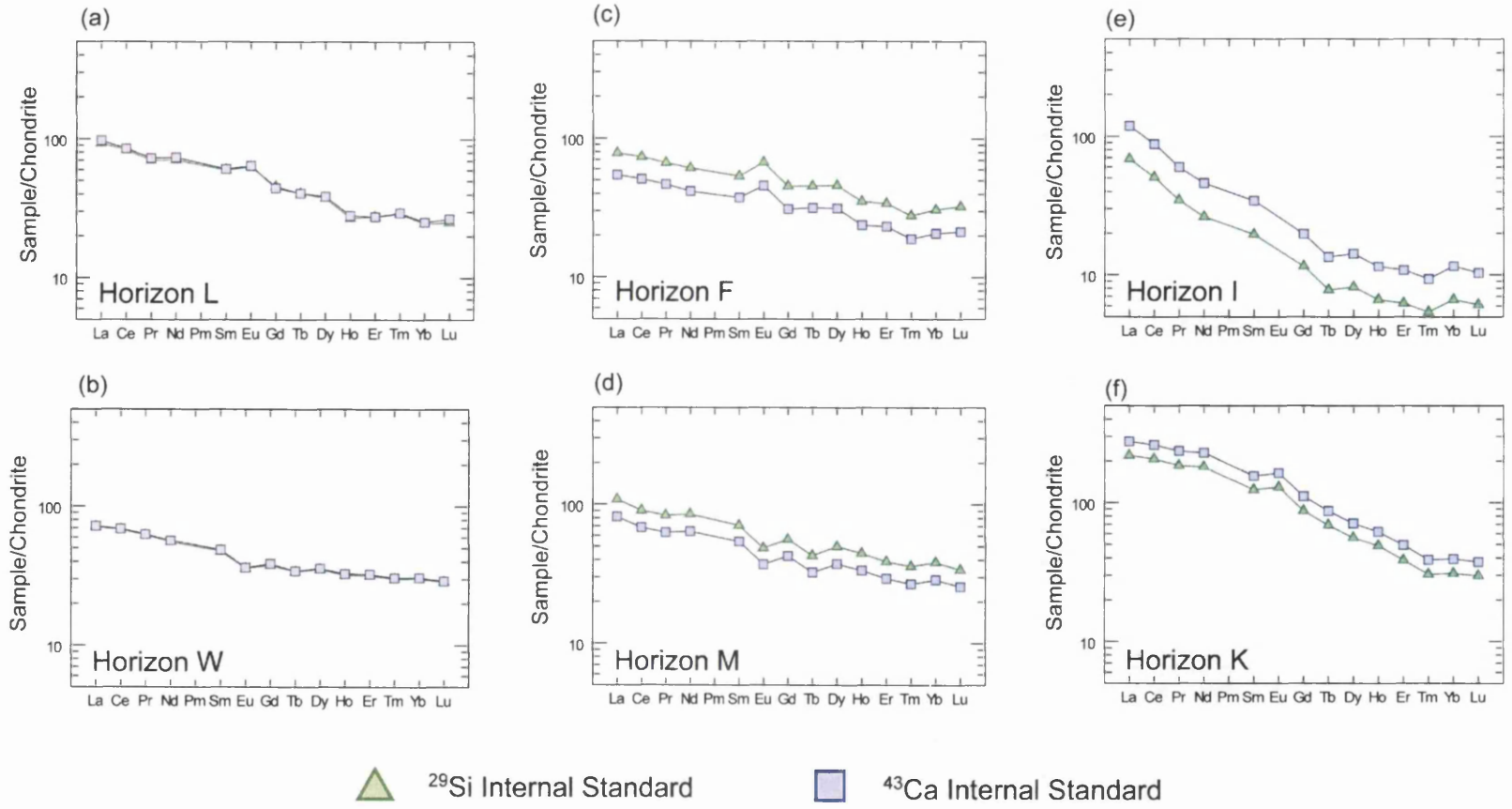


**Figure 4.10:** Chondrite-normalised average REE profiles for six tephra horizons with trace element concentrations calculated using both Si and Ca as an internal standard. Chondrite composition from Sun and McDonough (1989).

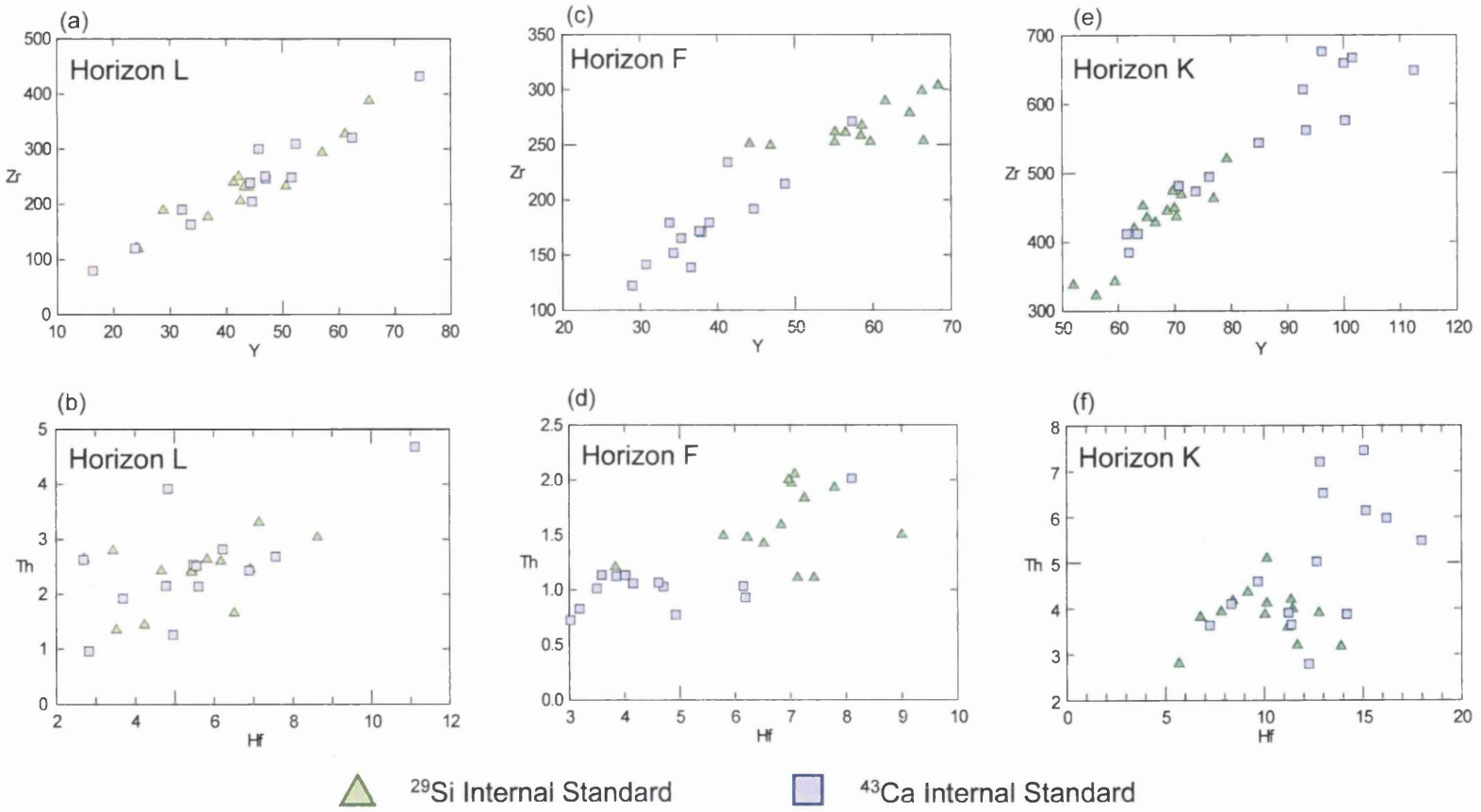


**Figure 4.11:** Compositional variation diagrams for tephra horizons (a and b) Horizon L, (c and d) Horizon F and (e and f) Horizon K using trace element concentrations calculated using both Si and Ca as an internal standard. All concentrations in ppm.

For each horizon the magnitude of offset between the two sets of data can be quantified by averaging the ratios between average trace element concentrations from the Si and Ca standardised datasets (table 4.4). These ratios show that there is a wide range of offsets (1.48-0.59) between horizons; however, the low standard deviations show that the offset ratios are consistent between elements within individual horizons.

The difference between the Si standardised and Ca standardised datasets for each horizon was statistically compared using the statistical distance function (table 4.4). None of the $D^2$ values exceed the critical value of 29.14 at the 99% confidence level, therefore for all of the horizons the Si standardised and Ca standardised datasets cannot be regarded as statistically different. This test does suggest that the datasets could be correlated, especially horizons with exceptionally low $D^2$ values such as W and L, however it was shown earlier that clear differences exist between the datasets from some horizons. As with the comparisons between the 14 µm and 6 µm beam diameter data in section 4.3.2 the high variability and consequent high standard deviations for the analyses from basaltic material appears to have a strong influence on the $D^2$ values of comparisons.

### 4.4.3 Analysis of the Offsets between Si and Ca Internally Standardised Datasets

It was shown in section 4.3.3 that reducing the beam diameter for analyses has a large affect on the count rates for both the internal standard and all other analyte elements. Count rates will also be affected when an element less abundant within the samples is used as an internal standard. For the studied horizons the sample count rates for $^{29}Si$ were approximately 25 to 45 times greater than those for $^{43}Ca$. The ratio between the sample counts and background counts for the analyses were also much lower for $^{43}Ca$ than $^{29}Si$ (table 4.5). As a consequence one would expect reduced precision within the concentrations calculated using Ca as an internal standard due to statistical counting errors. However, this does not explain the variability in the offsets observed as no direct relationships can be identified between the count ratios and the magnitude of the offset between the Si and Ca standardised trace element concentrations.

**Table 4.5:** Average ratios between sample and background count rates for analyses standardised using $^{29}Si$ and $^{43}Ca$ as an internal standard. Horizons ordered based on the ratio between the concentrations from each dataset.

| Tephra Horizon | Average Sample/Background Count Ratios | |
|---|---|---|
| | $^{29}Si$ | $^{43}Ca$ |
| Horizon F | 1.40 | 0.66 |
| Horizon M | 2.07 | 0.75 |
| Horizon S | 1.48 | 0.43 |
| Horizon X | 4.22 | 1.46 |
| Horizon G | 1.87 | 0.70 |
| Horizon W | 4.16 | 1.29 |
| Horizon L | 1.76 | 0.36 |
| Horizon N | 1.34 | 0.36 |
| Horizon K | 1.82 | 0.33 |
| Horizon U | 2.16 | 0.45 |
| Horizon T | 2.76 | 0.67 |
| Horizon R | 2.56 | 0.91 |
| Horizon H | 2.32 | 0.67 |
| Horizon I | 3.31 | 0.68 |

The most likely explanation for the offsets is a greater susceptibility of the Ca count rates to variations in background signals within the system during an analysis window. Drift in the background signals is assumed to be linear between the average of a set of gas blank analyses taken prior to analyses being made from a sample and the average of a set of gas blanks measured afterwards. Deviations of the background signals from this linear trend could have an impact on the gas corrected count rates and lead to over or under estimation of element concentrations. If the drift correction underestimates the actual background element levels for the internal standard blank subtracted sample count rates will be too high. Consequentially the calculated trace element concentrations will be underestimated and systematically negatively offset from the actual concentrations. The reverse situation of a systematic positive offset in calculated concentrations will occur if the background levels are overestimated.

Any over or under estimation of backgrounds signals will have a relatively greater impact when Ca count rates are blank corrected than Si count rates as background Ca forms a greater percentage of the overall counts for the element during a sample analysis than background Si (table 4.6). The potential impact is also greater when smaller beam sizes are utilised as less material is ablated and sample count rates are lower for both $^{29}Si$ and $^{43}Ca$. Which explains why this issue has not been encountered during previous studies utilising larger beam size diameters, where the gas blank forms a far smaller proportion of the count rates during a sample analysis.

**Table 4.6:** Average percentage of counts per second during the analysis of individual shards from horizons that originated from the gas blank within the LA-ICP-MS system. Horizons in italics were analysed using a 20 µm laser beam diameter.

| Tephra Horizon | $^{29}Si$ | $^{43}Ca$ |
|---|---|---|
| Horizon F | 42 % | 60 % |
| Horizon M | 33 % | 57 % |
| Horizon S | 40 % | 70 % |
| *Horizon X* | *19 %* | *41 %* |
| Horizon G | 34 % | 59 % |
| *Horizon W* | *19 %* | *44 %* |
| Horizon L | 37 % | 74 % |
| Horizon N | 43 % | 73 % |
| Horizon K | 36 % | 75 % |
| Horizon U | 30 % | 69 % |
| Horizon T | 27 % | 60 % |
| Horizon R | 28 % | 52 % |
| Horizon H | 30 % | 60 % |
| Horizon I | 23 % | 59 % |

This issue could be circumvented through more regular acquisition of gas blank analyses. This would improve the calculation of the counts per second from sample analyses (blank subtracted count rates) as more appropriate gas subtractions would be made if non-linear background variations were occurring. Subsequent investigations have experimented with analysing glass blanks prior to each sample analysis and have shown that this can reduce systematic offsets and improve accuracy (N. Pearce, *pers. comm.*, 2009). In addition the variability of data gained from horizons is reduced; implying that the precision of the analyses are also improved (N. Pearce, *pers. comm.*, 2009).

Overall, the results presented here show that for this new system when a 14 µm laser beam is utilised, the use of $^{43}Ca$ as an internal standard produces more variable concentration data compared to concentration data calculated using $^{29}Si$ as an internal standard. This variability was probably caused by unaccounted for variations in background counts within the system, which have more of an impact when these small beam diameters are being used and when lower concentration elements are utilised as internal standards. Therefore it is recommended that the higher concentration isotope of $^{29}Si$ is used as the internal standard within the calculation of trace element concentration data for basaltic tephra shards. If it is only possible to calculate concentrations using $^{43}Ca$ as the internal standard then the consistency in ratios shown in table 4.4 implies that comparisons should only be made between the ratios of element concentrations. As the raw concentration data alone is potentially inaccurate and may yield incorrect interpretations.

Background variability may have also introduced offsets to absolute concentrations calculated using $^{29}Si$ as the internal standard. As a consequence when horizons analysed within this study are being compared in later sections and consistent offsets are observed, consideration will be given to the ratios between the trace elements as they are unaffected by the misestimation of background element levels.

## 4.5 Comparison of the Trace Element Signatures of Widespread Tephras Correlated by Major Elements

### 4.5.1 Introduction

Within section 1.1.1 it was highlighted that at present five tephra horizons can be traced between Greenland ice-core and marine sequences. These horizons have previously been correlated based on the major element characterisation of individual shards within deposits, their relative chronostratigraphic position and independent dating of sequences. The following sections will test the correlation of two of the present North Atlantic region ice-marine tie-lines, the Saksunarvatn Ash and Fugloyarbanki Tephra, through single-grain LA-ICP-MS analysis of ice and marine occurrences of both tephra horizons (figure 4.12). Similarities in trace element composition between occurrences will increase the robustness of these correlations. Whereas, differences could indicate that the occurrences within the different depositional environments represent the products of two closely spaced volcanic eruptions producing material with similar major element geochemical compositions. These horizons also provide a contrast between a horizon deposited during an interglacial period (Saksunarvatn Ash) and one deposited during a glacial period (Fugloyarbanki Tephra).

### 4.5.2 Saksunarvatn Ash

The Saksunarvatn Ash was first identified by Mangerud et al. (1986) as a visible horizon at the type site of Lake Saksunarvatn on the Faroe Islands, where it was deposited following an eruption of the Icelandic Grimsvötn/Kverkfjöll volcanic system (Haflidason et al., 2000). This horizon has been discovered at other terrestrial sites in northern Europe (e.g. Birks et al., 1996) and within various North Atlantic marine cores (e.g. Sjøholm et al., 1991; Eiríksson et al., 2000). In addition, Grönvold et al. (1995)

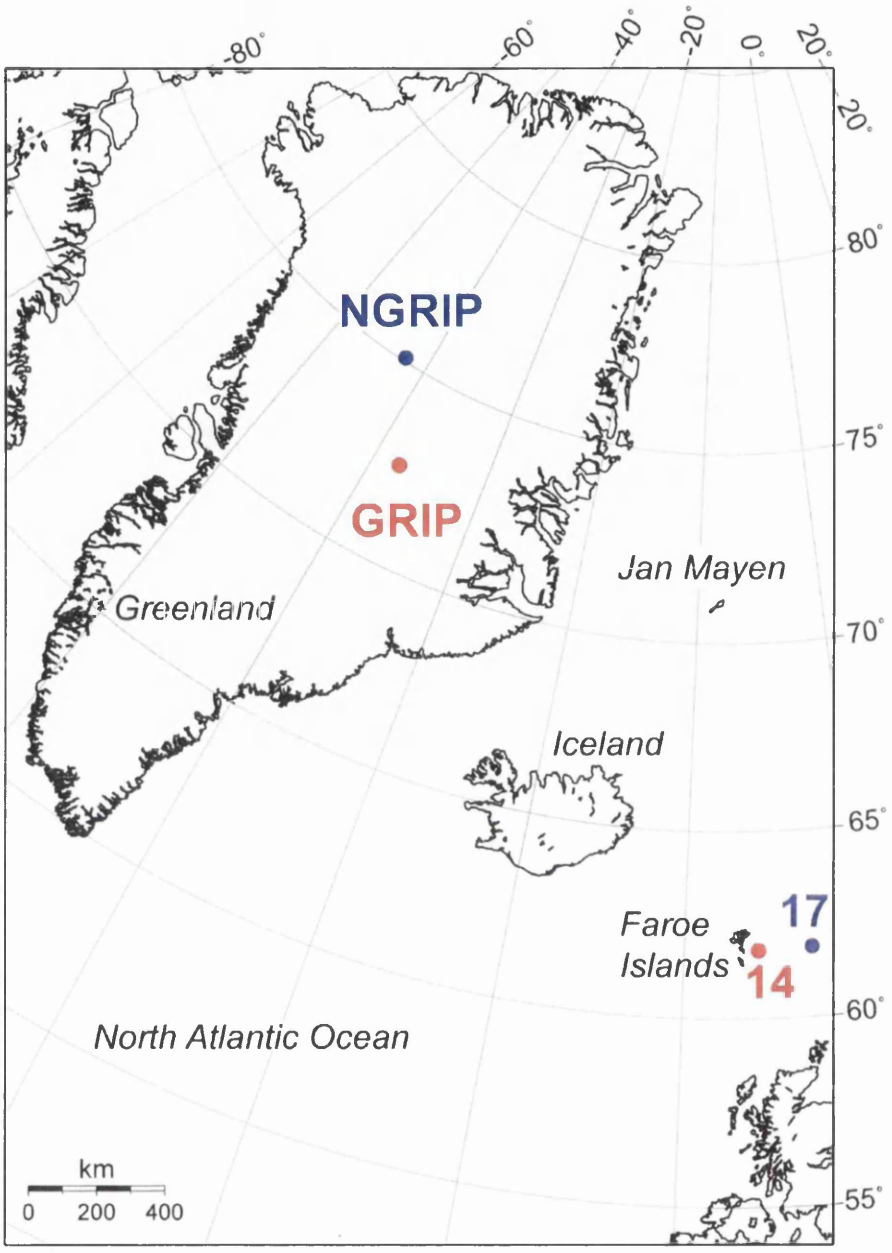


**Figure 4.12:** Depositional locations of the Saksunarvatn Ash (red) and Fugloyarbanki Tephra (blue) occurrences analysed using LA-ICP-MS.

reported that tephra shards found at a depth of 1528.61 m within the GRIP ice-core were correlated to the Saksunarvatn Ash and its discovery in the NGRIP ice-core was reported by Mortensen et al. (2005). Thus this tephra horizon can be regarded as an important stratigraphic marker within the North Atlantic region. The Saksunarvatn Ash was deposited during the early Preboreal climatic period and has been dated in terrestrial sequences to 9000 ± 100 $^{14}$C yrs BP (Björck et al., 2001) and the latest ice-core age for this horizon is 10347 ± 45 yr b2k based on the GICC05 time-scale (Rasmussen et al., 2006).

Recent research on Icelandic lake sediments has called into question the nature of the Saksunarvatn Ash following the identification of three ash horizons of Saksunarvatn age with similar major element geochemistry deposited within a 120 year period (Johannsdottir et al., 2005, 2006). Therefore the distal tephra horizons that have all been attributed to one eruption, based on major element geochemistry, could be the products of a single eruption or different eruptions with varying dispersal pathways. Greater characterisation of occurrences correlated to the Saksunarvatn Ash using trace element analysis may provide evidence to support one of these scenarios.

Glass shards previously correlated to the Saksunarvatn Ash and identified within a marine core and an ice-core were analysed for their trace element composition. The shards from the marine occurrence of the Saksunarvatn Ash were found at a depth of 185 cm in the LINK 14 marine core from the Sandoy Trough, east of the Faeroe Islands (figure 4.12; Nielsen et al., 2007; Rasmussen et al., submitted). Material from the Saksunarvatn Ash deposit found at a depth of 1528.61 m within the GRIP ice-core was also analysed.

The major element compositions of tephra shards from both occurrences were reacquired using EPMA to facilitate relocation of the shards during LA-ICP-MS analysis (table 4.7; figure 4.13). Figure 4.13 compares these analyses to a geochemical field for other horizons correlated to the Saksunarvatn Ash and reported in Birks et al. (1996), Dugmore and Newton (1997), Wastegård et al. (2001) and Andrews et al. (2002). All of the analyses from the LINK 14:185 and the GRIP 1528.61 m deposits fall within the extensive field defined by analyses of the other deposits. There is a high similarity between the LINK 14:185 and GRIP 1528.61 m analyses, with a similarity coefficient value of 0.975, and the geochemical fields for both sets of analyses overlap on all the compositional variation diagrams (figure 4.13).

**Table 4.7:** Summary of normalised major oxide and trace element data for glass shards from the GRIP 1528.61 m and LINK 14:185 tephra horizons. Mean and 1 standard deviations are shown. Total oxides are raw values prior to normalisation. All major elements expressed as percentage weight. All trace element concentrations expressed as ppm. Total iron is expressed as FeO. n = number of shards analysed. The complete dataset of unnormalised data is provided in appendix 2.

| | Saksunarvatn Ash | |
|---|---|---|
| | GRIP 1528.61 m | LINK 14:185 |
| n | 22 | 12 |
| $SiO_2$ | 50.21 (0.24) | 49.72 (0.25) |
| $TiO_2$ | 2.93 (0.16) | 3.15 (0.18) |
| $Al_2O_3$ | 13.19 (0.19) | 12.93 (0.13) |
| FeO | 13.85 (0.42) | 14.56 (0.31) |
| MnO | 0.25 (0.07) | 0.25 (0.05) |
| MgO | 5.85 (0.52) | 5.73 (0.14) |
| CaO | 10.31 (0.35) | 10.25 (0.19) |
| $Na_2O$ | 2.58 (0.14) | 2.61 (0.13) |
| $K_2O$ | 0.44 (0.03) | 0.45 (0.03) |
| $P_2O_5$ | 0.39 (0.05) | 0.36 (0.05) |
| Total Oxides | 95.53 (0.35) | 97.68 (0.69) |
| n | 11 | 9 |
| Sc | 52.8 (11.2) | 33.3 (5.98) |
| Rb | 13.7 (3.98) | 11.4 (3.18) |
| Sr | 311 (33.8) | 365 (269) |
| Y | 58.7 (8.00) | 44.6 (4.60) |
| Zr | 268 (20.5) | 201 (15.5) |
| Nb | 24.8 (3.92) | 19.1 (1.69) |
| Ba | 164 (33.3) | 107 (18.9) |
| La | 18.7 (1.69) | 17.5 (2.00) |
| Ce | 45.8 (7.79) | 43.9 (4.64) |
| Pr | 6.41 (0.99) | 6.12 (1.32) |
| Nd | 28.4 (6.09) | 26.7 (2.70) |
| Sm | 7.97 (1.78) | 7.55 (0.98) |
| Eu | 3.99 (0.93) | 2.35 (0.21) |
| Gd | 9.45 (1.54) | 8.27 (1.68) |
| Tb | 1.71 (0.34) | 1.38 (0.22) |
| Dy | 11.6 (1.88) | 9.39 (0.85) |
| Ho | 1.99 (0.43) | 1.89 (0.25) |
| Er | 5.75 (1.38) | 5.52 (1.02) |
| Tm | 0.73 (0.13) | 0.83 (0.16) |
| Yb | 5.24 (1.13) | 5.40 (0.56) |
| Lu | 0.85 (0.30) | 0.79 (0.13) |
| Hf | 6.79 (1.29) | 6.09 (0.95) |
| Ta | 1.59 (0.38) | 1.52 (0.25) |
| Th | 1.64 (0.33) | 1.79 (0.23) |
| U | 0.45 (0.13) | 0.92 (0.64) |

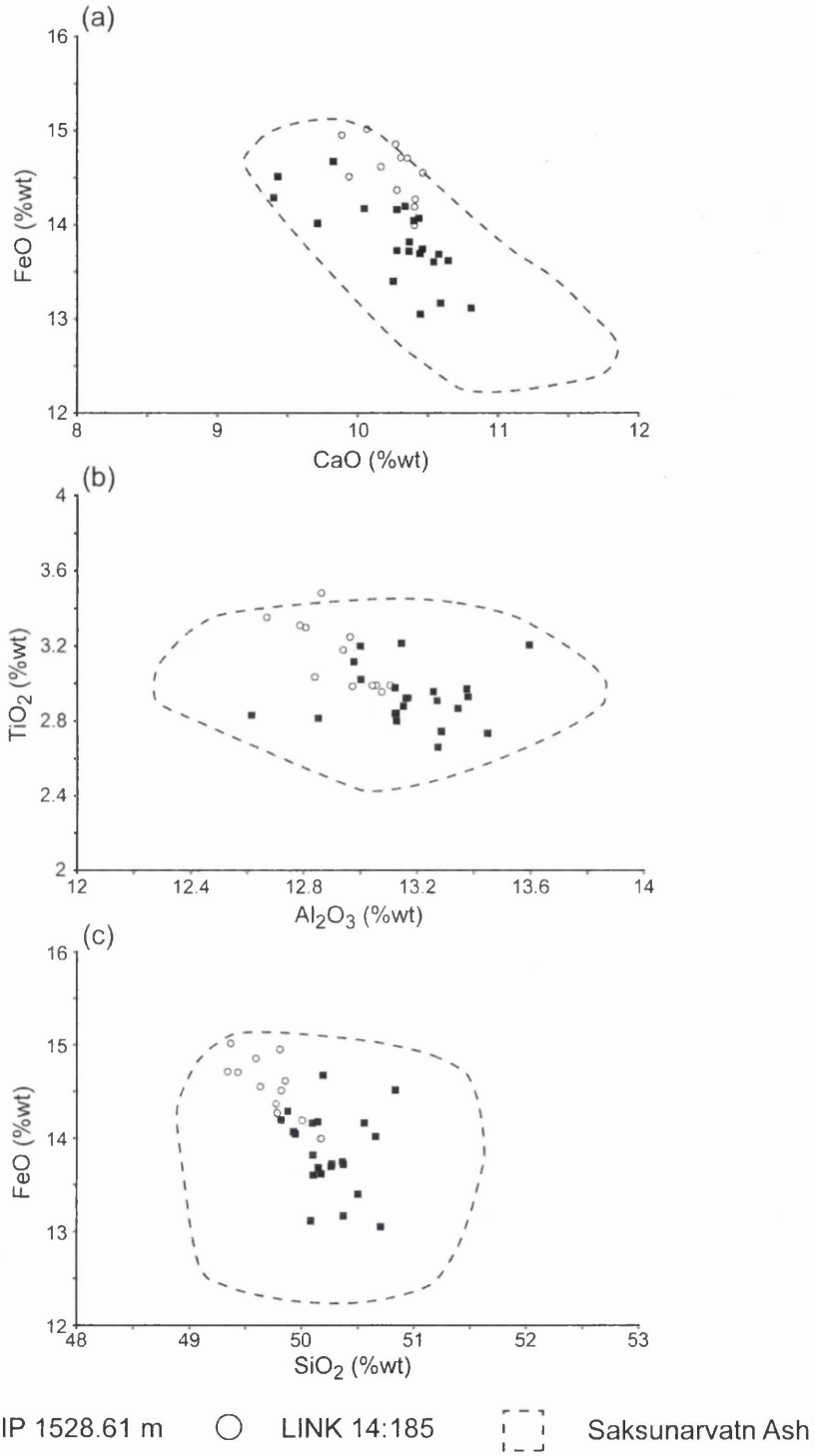


**Figure 4.13:** (a) CaO vs. FeO (b) $Al_2O_3$ vs. $TiO_2$ and (c) $SiO_2$ vs. FeO compositional variation diagrams for analyses of GRIP 1528.61 m and LINK14:185 compared to geochemical fields for the Saksunarvatn Ash. Geochemical field for the Saksunarvatn Ash defined using geochemical analyses from occurrences of the tephra described in Birks et al. (1996), Dugmore and Newton (1997), Wastegård et al. (2001) and Andrews et al. (2002).

Nine individual shards from the LINK 14:185 horizon and eleven shards from the GRIP 1528.61 m horizon were analysed for their trace element composition (table 4.7). The REE profiles for these analyses are shown in figure 4.14 along with the average REE profiles for the two horizons (figure 4.14c). The average profiles show that there are strong similarities between the horizons in the concentrations of the lighter and heavier REEs, however differences are apparent for the middle REEs, such as Eu, Gd, Tb and Dy. The concentrations of the middle REEs within GRIP 1528.61 m exceed those from LINK 14:185, however these differences may be due to polyatomic interference, i.e. the peak in Eu. The biplots in figure 4.15 support the observation of similarities in the concentration of certain elements within the shards from each horizon, e.g. figures 4.15a and b. However, some subtle geochemical differences can be observed; most notably there is a difference in Y and Zr concentrations between the horizons, despite the Y/Zr ratio remaining approximately constant (figure 4.15f). This offset in absolute concentrations is a real geochemical difference between the horizons and cannot be attributed to gas blank misestimation. If these horizons had identical compositions and either one or both had been affected by gas blank misestimation such offsets would have been observed when any element pairs were compared on biplots and on the REE diagrams. Therefore, these horizons represent deposits from different eruptive events. The difference in Y and Zr concentrations, but consistency in Y/Zr ratio between the horizons can be attributed to fractional crystallisation within the source magma chamber between the eruptive events. Because, this process will increase the concentration of these incompatible elements within the residual magma at the source region without affecting the ratio between them (Rollinson, 1993).

The statistical distance between the two horizons has a $D^2$ value of 15.3 when 14 elements are compared. This does not exceed the critical value for the comparison of 29.14 at the 99 % confidence level, thus the observed differences between the horizons is not statistically significant. However, this may be a result of the geochemical differences between the horizons only being apparent for some elements and the relative heterogeneity of the characterisations.

This has represented the first attempt to obtain trace element signatures for distal occurrences of the Saksunarvatn Ash. The major element similarities between the horizons suggests it is very likely they are derived from the same eruptive source, however, the subtle trace element differences that can be observed suggests that the two horizons were not produced during the same eruptive phase. They may represent different phases with differing dispersal pathways and could be related to the proximal

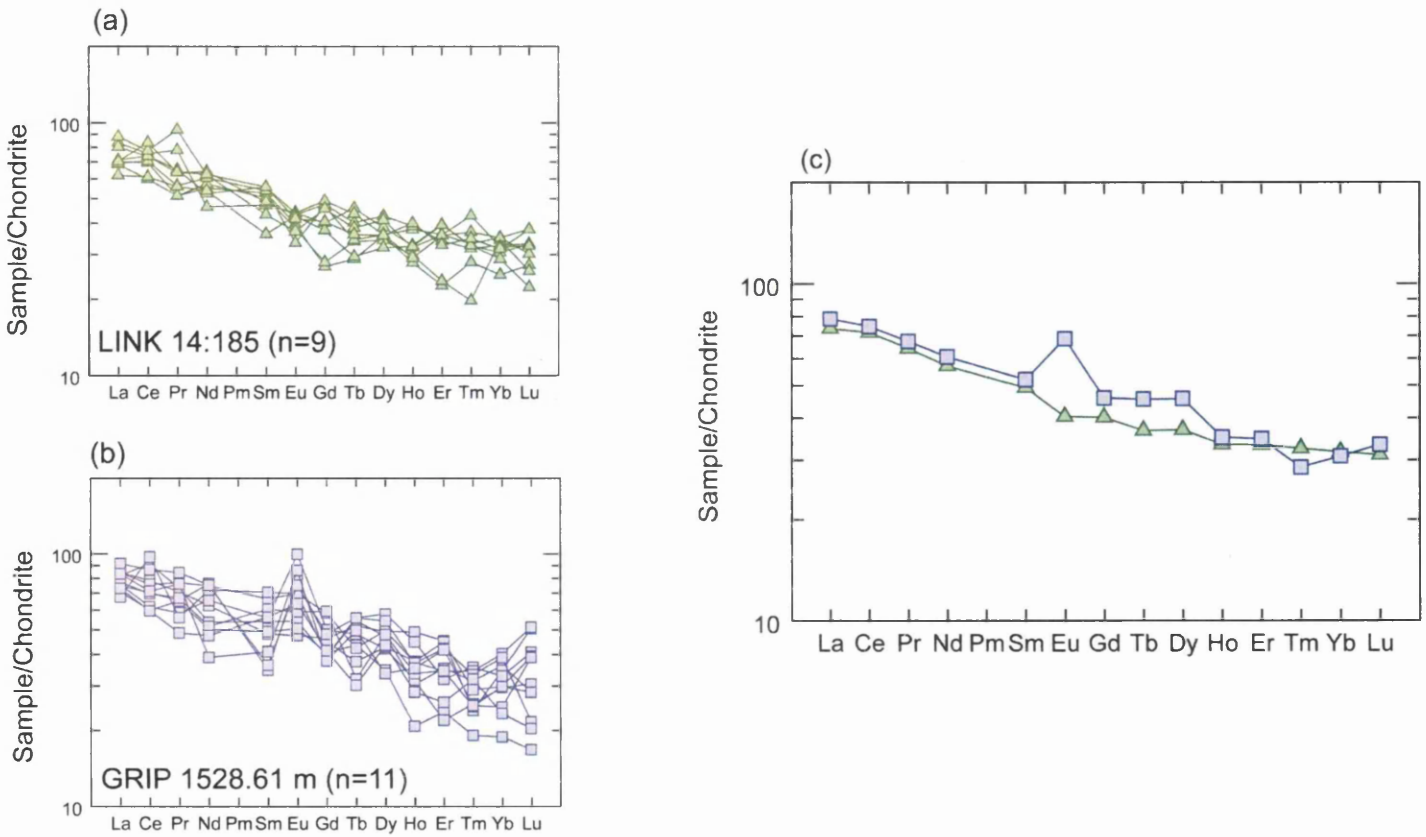


**Figure 4.14:** Chondrite-normalised REE profiles of individual shards from (a) LINK 14:185 and (b) GRIP 1528.61 m. (c) Average REE profiles for the two horizons. Chondrite compositions from Sun and McDonough (1989).

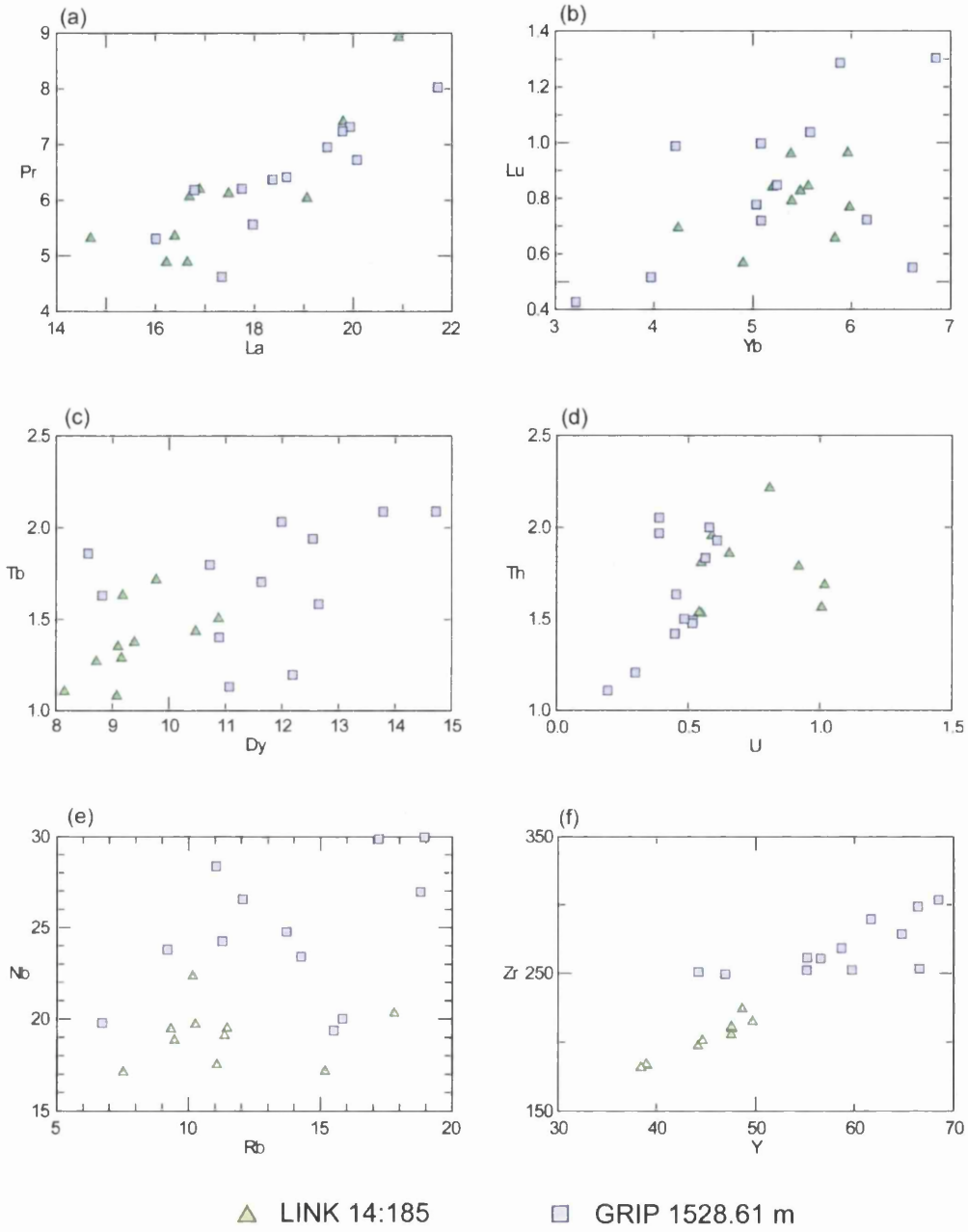


**Figure 4.15:** Compositional variation diagrams displaying trace element concentrations for tephra shards within LINK 14:185 and GRIP 1528.61 m. Concentrations in ppm.

deposits described by Johannsdottir et al. (2005, 2006). The identification of these trace element differences suggests that the GRIP 1528.61 m and LINK 14:185 horizons cannot be correlated and act as a tie-line between the ice and marine sequences. Further investigation of other horizons attributed to the Saksunarvatn Ash is required to determine the geographical extent of the deposition of these two different eruptive phases and if the phase identified within the GRIP ice-core can be identified within any marine sequences. This investigation could also be extended to terrestrial sequences containing material attributed to the Saksunarvatn Ash.

### 4.5.3 Fugloyarbanki Tephra

The Fugloyarbanki Tephra, also referred to as Faroe Marine Ash Zone II (FMAZ II), has been identified in many marine cores from the Faroe region where it has been described as a visible horizon ranging in thickness from 2 to 10 cm (Rasmussen et al., 2003; Wastegård et al., 2006). This horizon originates from the Icelandic Hekla-Vatnafjöll volcanic system and was deposited following DO event 3 following the warmest part of the interstadial (~22,900-23,300 $^{14}$C years BP) (Wastegård et al., 2006). The significance of this horizon increased following its identification as a visible horizon in the NGRIP ice-core (Davies et al., 2008). The ice-core age of this horizon is 26470 ± 390 yr b2k based on the GICC05 time-scale and it was deposited shortly after DO event 3 (Andersen et al., 2006; Svensson et al., 2006; Davies et al., 2008).

The marine occurrence of the Fugloyarbanki Tephra analysed here was reported in Wastegård et al. (2006) and was identified at a depth of 633-635 cm in the LINK 17 core extracted from the Faeroe-Shetland Channel (figure 4.12). Fugloyarbanki Tephra shards found in the NGRIP ice-core between 1848.0 and 1848.1 m depth form the ice-core occurrence (Davies et al., 2008). As with the Saksunarvatn Ash the major element composition of shards was reanalysed.

Figure 4.16 shows biplots of the new major element data from the two samples LINK 17:634 and NGRIP 1848 m. From these plots two populations can be identified within the major element geochemistry of the tephra shards of NGRIP 1848 m; with bimodality occurring within the concentrations of elements, such as $SiO_2$, $K_2O$ and CaO (table 4.8). The population with lower $SiO_2$ concentrations is dominant within the analyses and it occupies a field coincident with analyses from shards within LINK 17:634; these new analyses are comparable to the Fugloyarbanki Tephra analyses

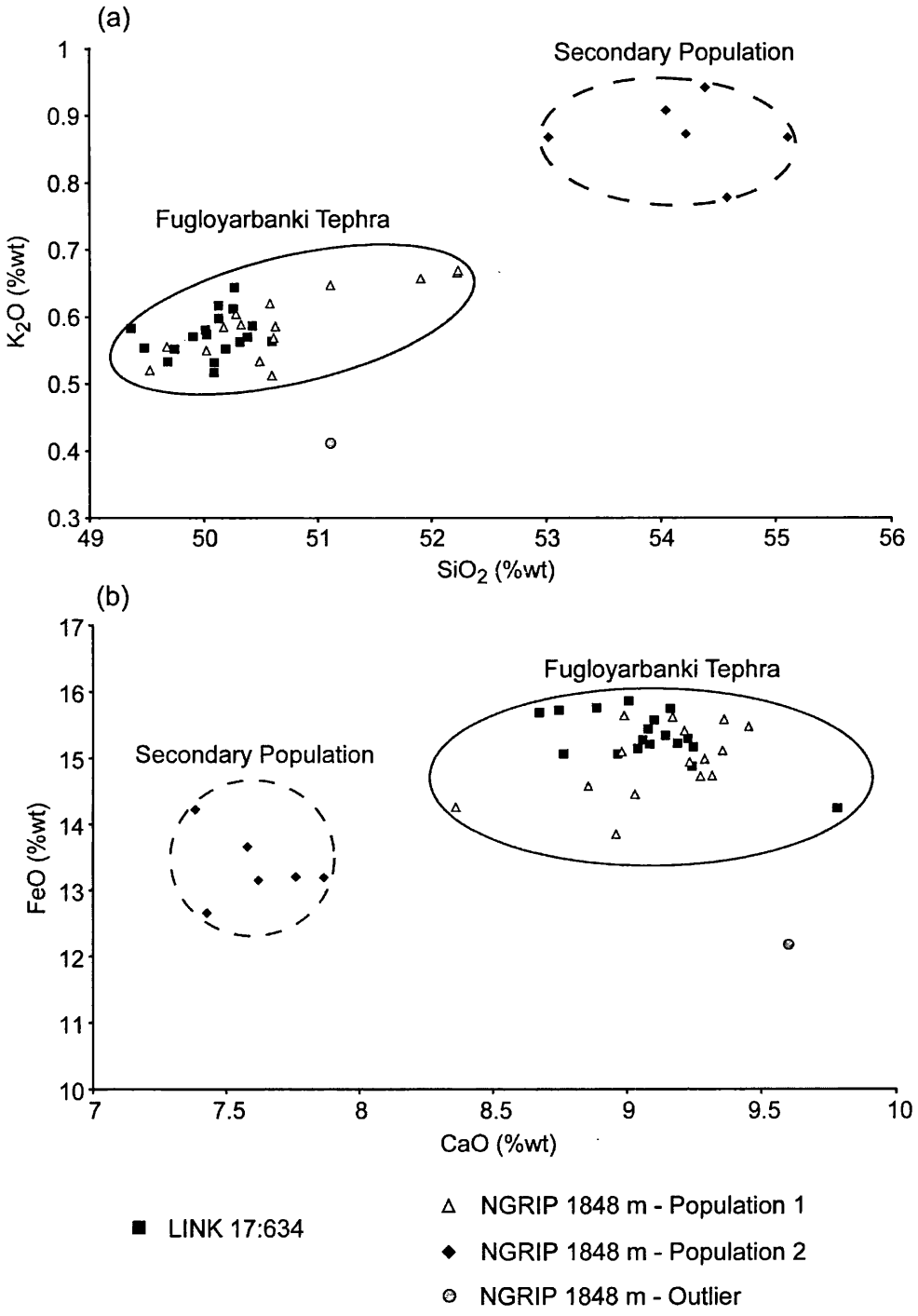


**Figure 4.16:** (a) $SiO_2$ vs. $K_2O$ and (b) CaO vs. FeO compositional variation diagrams for analyses of tephra shards from LINK 17:634 and NGRIP 1848 m.

**Table 4.8:** Summary of normalised major oxide and trace element data for glass shards from the NGRIP 1848 m and LINK 17:634 tephra horizons. Mean and 1 standard deviations are shown. Total oxides are raw values prior to normalisation. All major elements expressed as percentage weight. All trace element concentrations expressed as ppm. Total iron is expressed as FeO. n = number of shards analysed. The complete dataset of unnormalised data is provided in appendix 2.

| | Fugloyarbanki Tephra | | |
|---|---|---|---|
| | NGRIP 1848 m Population 1 | NGRIP 1848 m Population 2 | LINK 17:634 |
| n | 15 | 6 | 18 |
| $SiO_2$ | 50.69 (0.84) | 54.23 (0.70) | 50.06 (0.33) |
| $TiO_2$ | 3.69 (0.13) | 3.15 (0.16) | 3.86 (0.12) |
| $Al_2O_3$ | 12.57 (0.17) | 12.98 (0.22) | 12.63 (0.25) |
| FeO | 14.96 (0.54) | 13.35 (0.53) | 15.32 (0.39) |
| MnO | 0.26 (0.06) | 0.22 (0.05) | 0.25 (0.06) |
| MgO | 4.67 (0.23) | 3.49 (0.07) | 4.81 (0.45) |
| CaO | 9.12 (0.27) | 7.61 (0.19) | 9.08 (0.25) |
| $Na_2O$ | 2.92 (0.12) | 3.39 (0.10) | 2.94 (0.12) |
| $K_2O$ | 0.59 (0.05) | 0.87 (0.05) | 0.57 (0.03) |
| $P_2O_5$ | 0.52 (0.05) | 0.72 (0.06) | 0.49 (0.03) |
| Total Oxides | 98.11 (0.65) | 98.35 (0.79) | 98.58 (0.65) |
| n | 5 | 4 | 17 |
| Sc | 36.2 (6.07) | 25.3 (6.37) | 42.0 (6.57) |
| Rb | 21.5 (8.56) | 23.8 (3.81) | 16.8 (5.44) |
| Sr | 254 (24.0) | 285 (38.5) | 251 (23.5) |
| Y | 55.6 (7.42) | 71.5 (8.93) | 52.1 (4.89) |
| Zr | 297 (24.8) | 375 (49.2) | 248 (22.2) |
| Nb | 26.4 (3.52) | 36.8 (5.17) | 25.8 (2.82) |
| Ba | 213 (44.3) | 263 (39.5) | 143 (20.0) |
| La | 22.3 (2.28) | 29.8 (4.10) | 21.1 (2.66) |
| Ce | 48.5 (4.45) | 63.9 (7.94) | 51.0 (4.83) |
| Pr | 6.72 (0.75) | 9.50 (0.88) | 7.17 (0.68) |
| Nd | 34.1 (7.94) | 47.0 (11.0) | 33.2 (3.47) |
| Sm | 9.80 (0.54) | 12.2 (3.04) | 8.85 (1.16) |
| Eu | 2.71 (0.77) | 2.95 (0.40) | 2.96 (0.41) |
| Gd | 10.2 (0.96) | 13.3 (1.71) | 11.1 (2.25) |
| Tb | 1.34 (0.44) | 1.94 (0.45) | 1.61 (0.25) |
| Dy | 11.1 (2.25) | 14.5 (4.48) | 10.9 (1.21) |
| Ho | 2.10 (0.39) | 3.05 (0.47) | 2.07 (0.33) |
| Er | 5.68 (1.54) | 7.37 (0.58) | 5.97 (0.98) |
| Tm | 0.75 (0.19) | 1.13 (0.20) | 0.88 (0.15) |
| Yb | 5.69 (0.87) | 7.54 (2.00) | 5.08 (0.88) |
| Lu | 0.89 (0.59) | 0.83 (0.18) | 0.89 (0.30) |
| Hf | 8.77 (1.36) | 9.26 (1.77) | 7.00 (0.78) |
| Ta | 1.85 (0.24) | 2.47 (0.83) | 2.04 (0.29) |
| Th | 1.92 (0.46) | 2.75 (0.42) | 2.31 (0.43) |
| U | 0.58 (0.10) | 0.83 (0.13) | 0.70 (0.14) |

presented in Wastegård et al. (2006) and Davies et al. (2008). The secondary population shows similarities to two analyses reported in Davies et al. (2008) as outliers; but not to secondary populations associated with some North Atlantic occurrences of the Fugloyarbanki Tephra (Rasmussen et al., 2003; Wastegård et al., 2006). The identification of six individual shards with a contrasting geochemistry to the dominant population suggests that they are not outliers, but form part of a significant secondary population. Statistical distance calculations on the three populations, table 4.9, support the observations from the biplots in figure 4.16 that the dominant population of NGRIP 1848 m is correlated to the LINK 17:634 analyses because of the low $D^2$ value of 2.17. These calculations also demonstrate that the differences between the secondary population of NGRIP 1848 m and the other two populations are statistically significant as both of the $D^2$ values exceed the critical value.

**Table 4.9:** Statistical distance comparison between average major element compositions of populations from the LINK 17:634 and NGRIP 1848 m tephra horizons. Critical value for $D^2$ of 23.21 at the 99 % confidence level.

| | LINK 17:634 | NGRIP 1848 m Pop 1 | NGRIP 1848 m Pop 2 |
|---|---|---|---|
| LINK 17:634 | 0.0 | | |
| NGRIP 1848 m Pop 1 | 2.17 | 0.0 | |
| NGRIP 1848 m Pop 2 | **124** | **100** | 0.0 |

Trace element analyses were gained from 17 shards from LINK 17:634, 5 shards from the dominant population of NGRIP 1848 m and 4 shards from the secondary population. The average trace element concentrations of the separate populations are provided in table 4.8. REE profiles of all the analyses and the average profiles for the three populations are shown in figure 4.17.

Large differences can be observed between the average REE concentrations of the second population from NGRIP 1848 m and the two populations attributed to the Fugloyarbanki Tephra; with the concentrations of REEs within this population commonly exceeding those within the other two populations. The profiles from the two Fugloyarbanki Tephra populations display strong similarities, particularly for the light REEs La, Ce, Pr and Nd. The low number of analyses on shards from population 1 of NGRIP 1848 m may account for the variations between the profiles for the heavier REEs. These elements will suffer from more analytical noise because of their lower abundances and more analyses would provide a smoother profile.

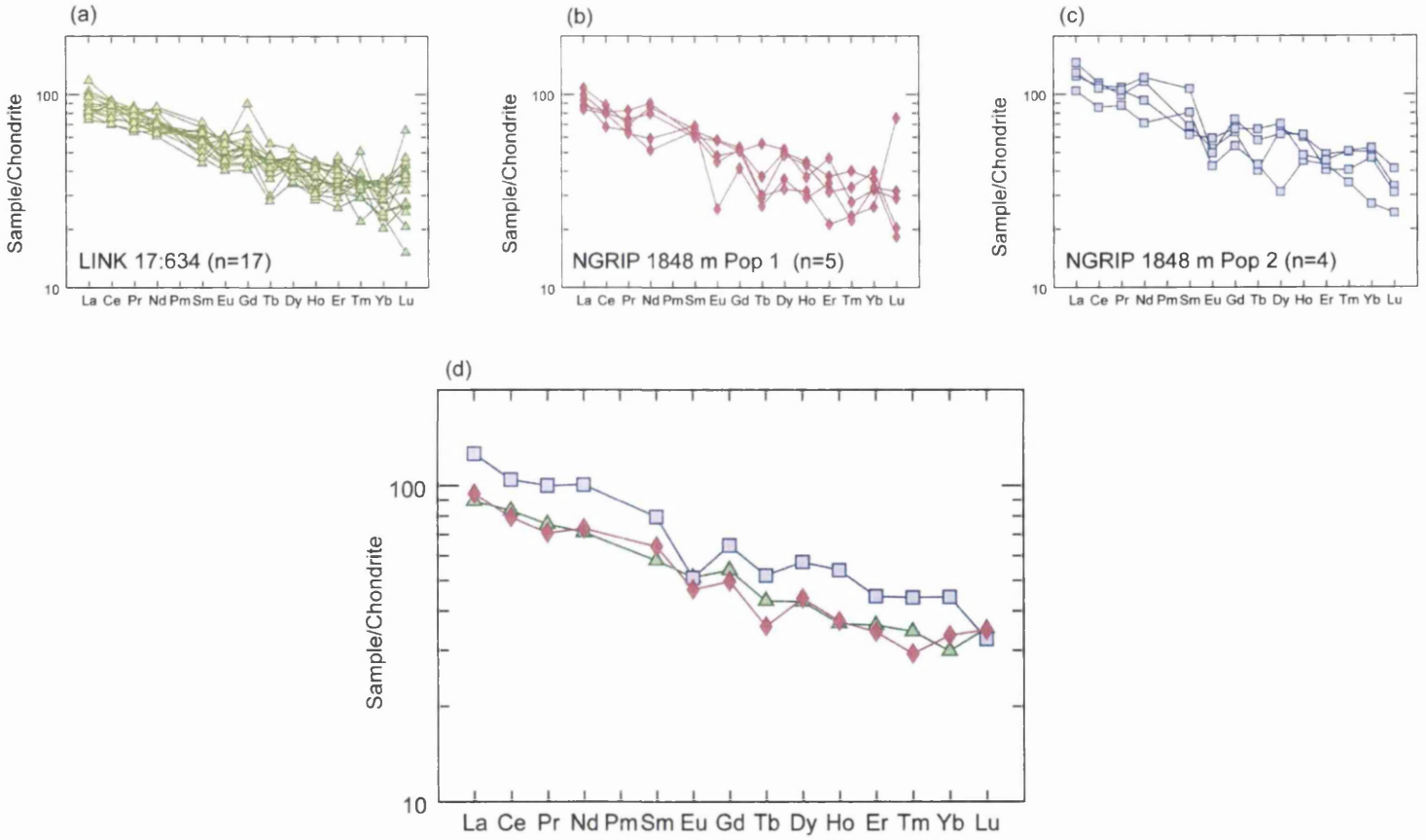


**Figure 4.17:** Chondrite-normalised REE analyses of single shards from (a) LINK 17:634 (b) Population 1 of NGRIP 1848 m (c) Population 2 of NGRIP 1848 m. (d) Chondrite-normalised average REE profiles of the three sets of analyses. Chondrite compositions from Sun and McDonough (1989).

The trace element similarities between the Fugloyarbanki Tephra horizons are also observed in figure 4.18, with analyses from the two populations falling consistently within the same fields and on similar ratio trend lines. Therefore, based on the trace element geochemical evidence the material from the LINK 17:634 horizon and the dominant population of NGRIP 1848 m are the products of the same eruptive event.

The differences between the trace element geochemistry of the secondary population of NGRIP 1848 m and the other two populations are emphasised by figure 4.18 as analyses from all the populations are only coincident on the U versus Th compositional variation diagram. Statistical distance function analysis on the trace element data does not provide statistical evidence for these differences, as the $D^2$ values for the comparisons between the populations do not exceed the critical value (table 4.10). However, it is likely that this is due to the impact that high standard deviation values have on $D^2$ values.

**Table 4.10:** Statistical distance comparison between average trace element compositions of populations from the LINK 17:634 and NGRIP 1848 m tephra horizons. 14 element concentrations utilised. Critical value for $D^2$ at the 99 % confidence level of 29.14.

| | LINK 17:634 | NGRIP 1848 m Pop 1 | NGRIP 1848 m Pop 2 |
|---|---|---|---|
| LINK 17:634 | 0.0 | | |
| NGRIP 1848 m Pop 1 | 5.8 | 0.0 | |
| NGRIP 1848 m Pop 2 | 25.5 | 18.9 | 0.0 |

These trace element results provide further evidence to support the correlation of these two tephra deposits, previously correlated based on major element geochemistry. Despite the depositional sites falling on different depositional pathways, i.e. NGRIP lies NW of the Icelandic source and LINK 17 lies SE, material from the same eruption appears to have been transported to both sites. Overall, this increases the robustness of the correlation of the Fugloyarbanki Tephra between the ice and marine sequences and its use as a time-synchronous tie-point. The secondary population, present only in the NGRIP sample, may represent the products of an Icelandic eruption approximately coeval to the Fugloyarbanki Tephra that was not dispersed in a SE direction.

It was reported in Wastegård et al. (2006) that other deposits of the Fugloyarbanki Tephra were analysed for their REE composition by Bäckström (1998) and were found to have identical compositions. However, the results of these analyses were not presented in a form appropriate for comparison to the characterisations presented in this section.

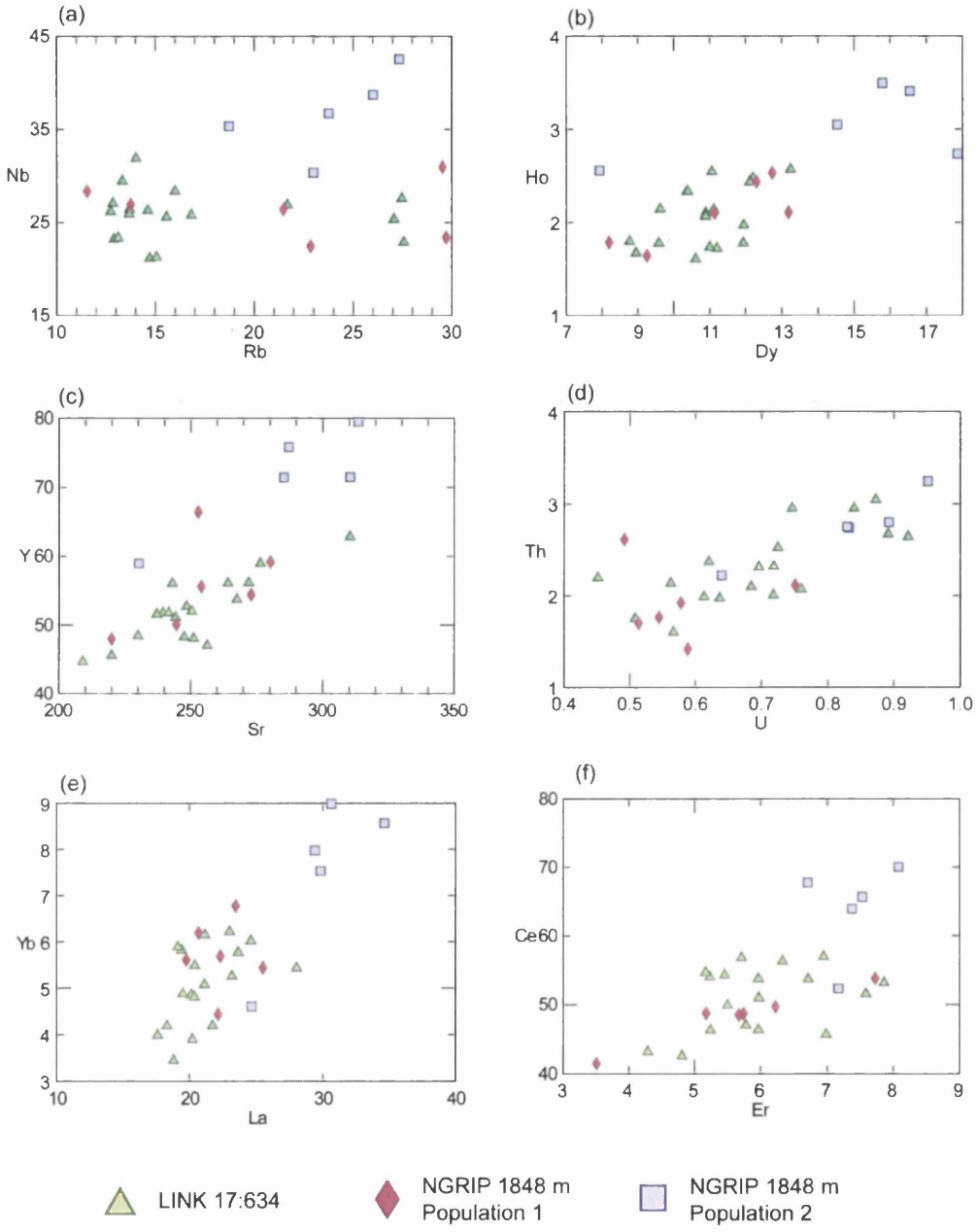


**Figure 4.18:** Compositional variation diagrams displaying trace element concentrations for analyses of tephra shards from LINK 17:634 and NGRIP 1848 m. Concentrations in ppm.

## 4.6 Comparison of the Trace Element Signatures of Distal Occurrences of the Products of the Katla Volcanic System

### 4.6.1 Introduction

It was highlighted in section 2.5.3 that one of the major issues currently affecting tephrochronology is the inability to discriminate between tephras based solely on major element geochemistry. In particular, several previously unknown cryptotephras with similar geochemical compositions have been identified in the ice-cores (Davies, unpublished; this study), demonstrating the high productivity of some volcanic centres. Katla, in particular, has been a very productive centre (Óladóttir et al., 2008). This 80 km long system, located in the Southern Flank Zone of Iceland (figure 2.6), consists of a central volcano and a fissure swarm (Óladóttir et al., 2008). The Katla system was one of most productive volcanic centres during the Holocene period and its activity is dominated by explosive basaltic eruptions, which have produced numerous widespread tephra horizons (Jakobsson, 1979; Óladóttir et al., 2008). The major element geochemistry of Katla horizons erupted during the Holocene has been well studied and strong similarities in major element geochemistry between eruptions have been observed (Óladóttir et al., 2008). However, Katla products can be easily distinguished from the products of other systems as they are characterised by high $TiO_2$ values, typically >4 % (Lacasse et al., 2007; Larsen and Eiríksson, 2008). Only a few studies have ascertained the trace element composition of tephra horizons produced by the Katla system. For example, Sigmarsson et al. (2005, 2008) analysed the composition of some Holocene horizons and it is suggested that temporal variations in composition can be identified. The results presented in this section represent one of the first attempts to characterise the trace element composition of Katla horizons deposited during the last glacial period.

The Katla system was active throughout the last glacial period (Jakobsson, 1979); however few proximal archives spanning this period are available. The Greenland ice-cores have the potential to provide the best record of Katla volcanism throughout this period as they are the most resolved, continuous distal archive for the last glacial period.

The LA-ICP-MS system was used to analyse the trace element composition of four previously identified cryptotephra horizons from the Katla system found within either

the NGRIP or GRIP ice-cores (S. Davies, unpublished). In addition, one Katla-sourced horizon identified in this study, NGRIP 2574.55 m, was analysed. Full details of this horizon and its correlation to a Katla source are provided in section 5.4.6. These horizons have all been correlated to a source from the Katla volcanic system due to the high $TiO_2$ values measured from the individual shards (table 4.12). Table 4.11 provides a summary of information on the samples and the stratigraphic position of the horizons within the two ice-cores are shown in figure 4.19. Horizons will be referred to by the basal depth of the samples containing the tephra shards (table 4.11).

**Table 4.11:** Summary of the ice samples containing tephra horizons sourced from the Katla volcanic region. Approximate ages derived from the GICC05 timescale for the two cores (A. Svensson, *pers. comm.*, 2009)

| Ice Core | Bag Number | Depth Interval (cm) | Depth of Sample Top (m) | Depth of Sample Base (m) | Approximate Age (yr b2k) |
|---|---|---|---|---|---|
| GRIP | 3121 | 7-8 | 1716.07 | 1716.08 | 14010 |
| NGRIP | 3446 | 45-55 | 1895.2 | 1895.3 | 29135 |
| NGRIP | 3483 | 0-40 | 1915.1 | 1915.5 | 30560 |
| NGRIP | 4681 | 49-55 | 2574.49 | 2574.55 | 76160 |
| NGRIP | 4786 | 5-15 | 2631.8 | 2631.9 | 81035 |

## 4.6.2 Major Element Characterisations

Major element analyses were made of individual shards to facilitate internal standardisation within the calculation of trace element concentrations and to assess the compositional similarities between horizons.

These horizons are suitable for the assessment of trace element variations between separate eruptions with similar major element geochemical compositions because clear stratigraphic differences imply that none of these horizons are the products of the same eruption (figure 4.19). Despite the close temporal separation of some horizons, such as the ~1400 years between the deposition of NGRIP 1895.3 m and NGRIP 1915.5 m. In addition, broad major element geochemical similarities can be observed in figure 4.20. Only one statistical distance function comparison displays a statistically significant difference (table 4.13) and the majority of the similarity coefficient comparisons exceed the threshold of 0.95 defined by Beget et al. (1992) as indicating that the tephra horizons are geochemically identical (table 4.14). Therefore, only a limited amount of discrimination can be made between the horizons based on the major element characterisations of the horizons provided here.

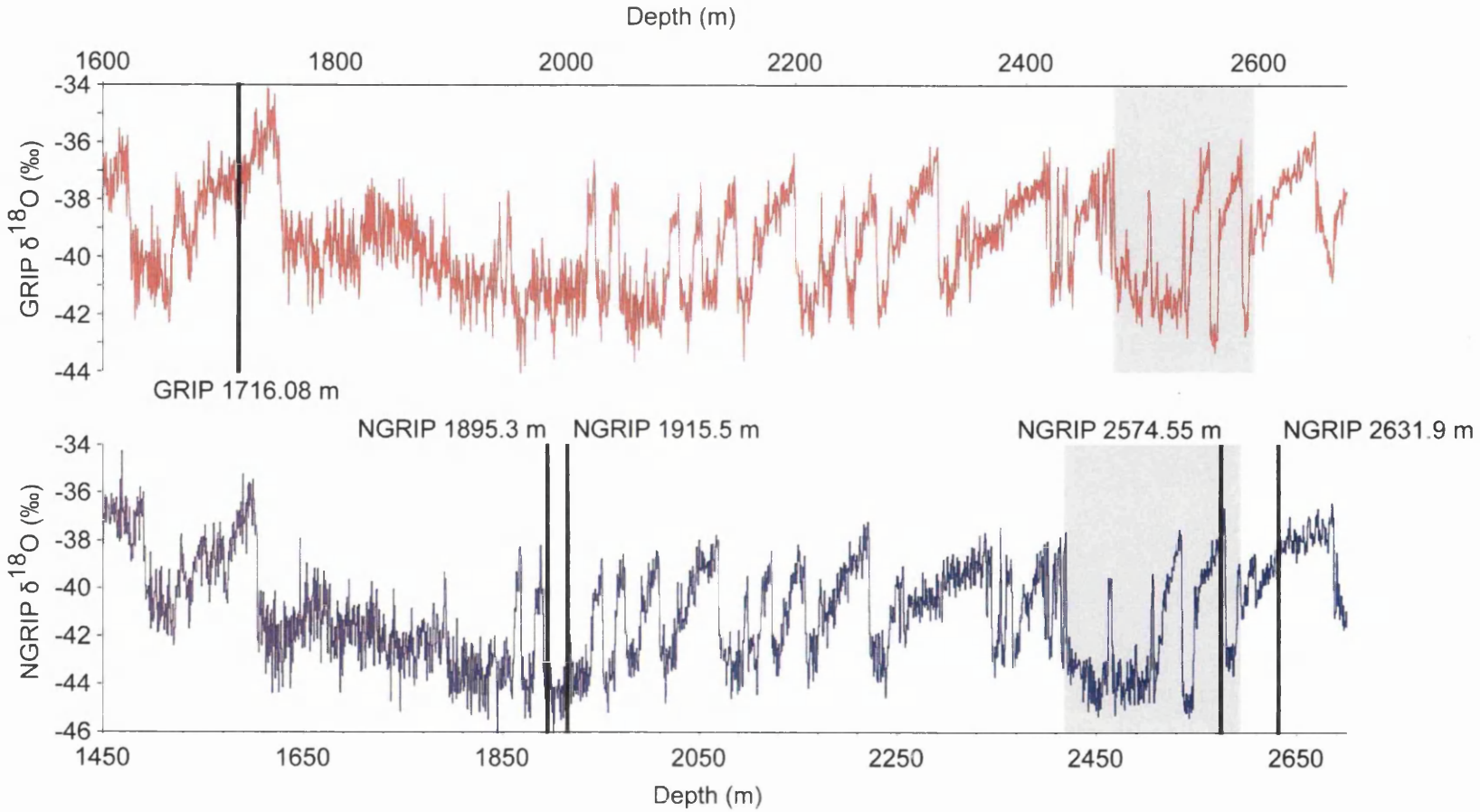


**Figure 4.19:** Stratigraphic position within the GRIP and NGRIP ice-cores of the five tephra horizons sourced from the Katla volcanic region analysed for their trace element composition using the LA-ICP-MS system. Grey shaded areas mark the stratigraphic position of the MIS 4 period within each core. Isotopic values are expressed in ‰ with respect to V-SMOW.

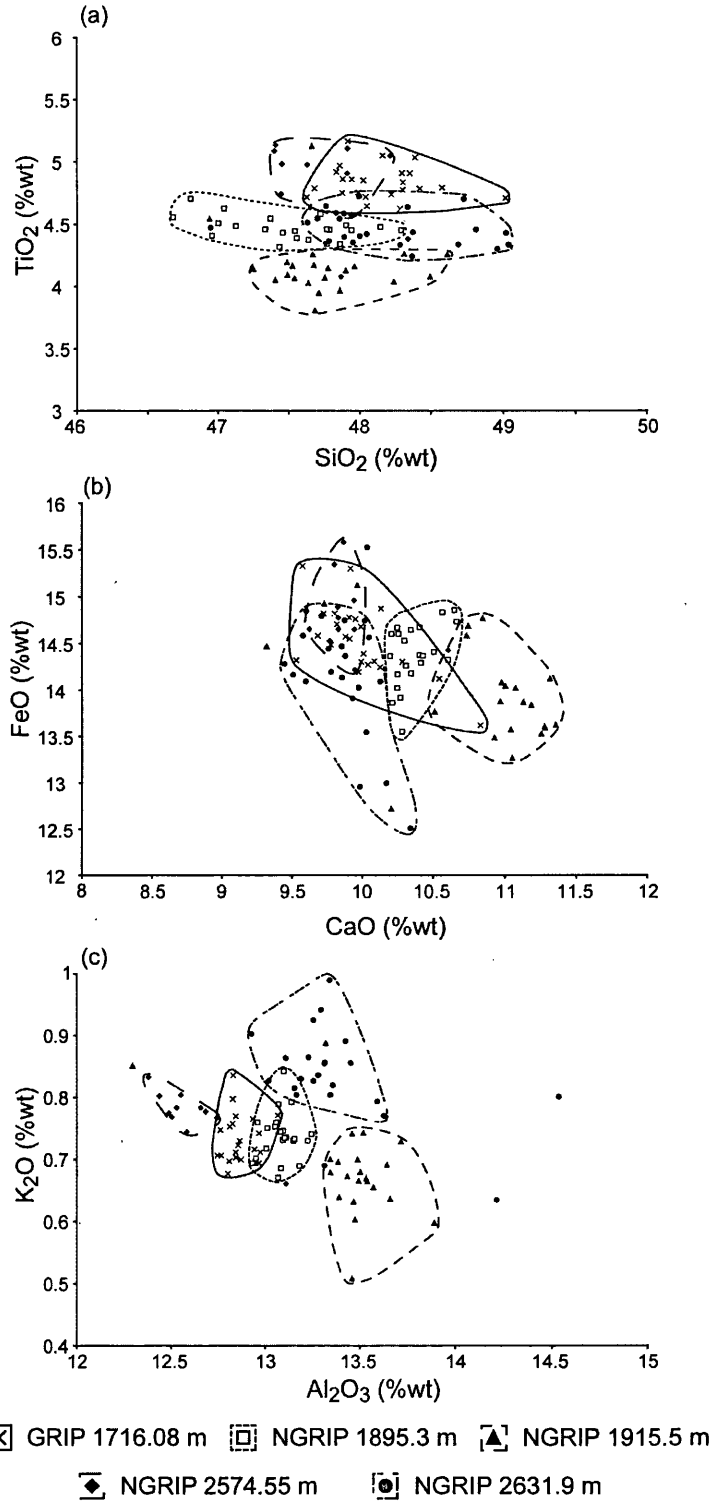


**Figure 4.20:** Geochemical data from five tephra horizons identified within the NGRIP and GRIP ice-cores and produced by the Katla volcanic region compared on (a) $SiO_2$ vs. $TiO_2$ (b) CaO vs. FeO and (c) $Al_2O_3$ vs. $K_2O$ compositional variation diagrams.

**Table 4.12:** Summary of normalised major oxide and trace element data for glass shards from five tephra horizons sourced from the Katla volcanic system identified within either the NGRIP or GRIP ice-cores. Mean and 1 standard deviations are shown. Total oxides are raw values prior to normalisation. All major elements expressed as percentage weight. All trace element concentrations expressed as ppm. Total iron is expressed as FeO. n = number of shards analysed. The complete dataset of unnormalised data is provided in appendix 2.

| | GRIP 1716.08 m | NGRIP 1895.3 m | NGRIP 1915.5 m | NGRIP 2574.55 m | NGRIP 2631.9 m |
|---|---|---|---|---|---|
| n | 23 | 22 | 22 | 11 | 23 |
| $SiO_2$ | 48.13 (0.31) | 47.51 (0.43) | 47.75 (0.39) | 47.77 (0.33) | 48.17 (0.52) |
| $TiO_2$ | 4.83 (0.13) | 4.47 (0.09) | 4.17 (0.26) | 4.82 (0.34) | 4.47 (0.13) |
| $Al_2O_3$ | 12.83 (0.21) | 13.08 (0.08) | 13.45 (0.29) | 12.61 (0.20) | 13.38 (0.36) |
| FeO | 14.53 (0.38) | 14.59 (0.32) | 13.98 (0.58) | 14.79 (0.39) | 14.07 (0.87) |
| MnO | 0.24 (0.07) | 0.23 (0.06) | 0.22 (0.07) | 0.25 (0.04) | 0.22 (0.06) |
| MgO | 5.24 (0.27) | 5.51 (0.07) | 5.70 (0.44) | 5.02 (0.13) | 5.09 (0.29) |
| CaO | 9.98 (0.29) | 10.37 (0.15) | 10.81 (0.55) | 9.91 (0.25) | 9.96 (0.52) |
| $Na_2O$ | 2.91 (0.24) | 2.99 (0.15) | 2.74 (0.39) | 3.16 (0.12) | 3.07 (0.22) |
| $K_2O$ | 0.73 (0.05) | 0.74 (0.04) | 0.68 (0.08) | 0.77 (0.04) | 0.83 (0.08) |
| $P_2O_5$ | 0.59 (0.04) | 0.52 (0.04) | 0.50 (0.07) | 0.83 (0.31) | 0.75 (0.05) |
| Total Oxides | 95.55 (0.79) | 98.50 (0.38) | 98.52 (0.59) | 97.05 (0.58) | 98.93 (0.65) |
| | | | | | |
| n | 16 | 14 | 5 | 6 | 12 |
| Sc | 17.7 (7.52) | 23.3 (10.3) | 9.86 (7.16) | 9.75 (5.85) | *5.38 (15.3)* |
| Rb | 22.8 (3.77) | 30.9 (12.3) | 17.7 (7.75) | 6.95 (1.84) | 29.0 (7.10) |
| Sr | 243 (107) | 382 (195) | 112.6 (19.5) | 198 (51.4) | 298 (75.7) |
| Y | 18.1 (8.67) | 25.5 (12.5) | 8.41 (1.42) | 17.7 (4.26) | 24.1 (5.41) |
| Zr | 174 (41.2) | 201 (52.0) | 75.1 (18.7) | 94.0 (21.8) | 142 (32.4) |
| Nb | 17.0 (8.57) | 22.2 (13.6) | 6.74 (0.83) | 13.8 (4.47) | 22.9 (5.18) |
| Ba | 189 (20.5) | 158 (23.4) | *924 (1035)* | 89.6 (15.2) | 192 (95.8) |
| La | 12.7 (5.61) | 16.9 (7.52) | 7.37 (1.61) | 10.8 (3.12) | 18.1 (4.73) |
| Ce | 26.2 (14.1) | 34.3 (15.1) | 15.1 (3.06) | 22.3 (6.10) | 40.8 (11.0) |
| Pr | 3.49 (1.68) | 4.67 (2.12) | 1.92 (0.40) | 2.75 (0.86) | 5.18 (1.30) |
| Nd | 17.5 (11.2) | 21.5 (13.1) | 9.30 (2.77) | 13.6 (4.02) | 24.9 (5.79) |
| Sm | 4.64 (2.15) | 5.32 (3.89) | 1.30 (0.68) | 2.70 (1.14) | 5.48 (1.42) |
| Eu | 1.49 (0.64) | 1.13 (1.37) | 1.16 (0.97) | 0.93 (0.75) | 2.37 (1.06) |
| Gd | 3.87 (2.02) | 4.05 (2.95) | 1.15 (0.97) | 3.21 (1.94) | 7.38 (2.97) |
| Tb | 0.66 (0.37) | 0.47 (0.47) | 0.25 (0.07) | 0.32 (0.16) | 0.70 (0.19) |
| Dy | 3.29 (2.08) | 4.36 (1.64) | 1.68 (0.36) | 2.70 (1.47) | 4.43 (1.29) |
| Ho | 0.69 (0.36) | 0.74 (0.38) | 0.26 (0.07) | 0.56 (0.17) | 0.79 (0.15) |
| Er | 1.80 (1.05) | 2.11 (1.09) | 0.89 (0.25) | 1.40 (0.51) | 2.09 (0.68) |
| Tm | 0.21 (0.13) | 0.25 (0.19) | 0.13 (0.08) | 0.15 (0.10) | 0.23 (0.10) |
| Yb | 1.40 (0.69) | 1.65 (0.81) | 0.77 (0.05) | 1.21 (0.62) | 1.82 (0.36) |
| Lu | 0.22 (0.16) | 0.37 (0.19) | 0.10 (0.05) | 0.18 (0.06) | 0.28 (0.11) |
| Hf | 3.87 (1.13) | 4.59 (1.42) | 1.93 (0.49) | 1.89 (0.57) | 3.32 (0.86) |
| Ta | 0.91 (0.43) | 1.34 (0.55) | 0.51 (0.25) | 0.80 (0.24) | 1.51 (0.56) |
| Th | 0.98 (0.39) | 1.80 (1.28) | 1.15 (0.26) | 1.14 (0.21) | 1.39 (0.20) |
| U | 0.32 (0.14) | 0.61 (0.29) | 0.31 (0.09) | 0.50 (0.07) | 0.40 (0.09) |

Difficulties in distinguishing between tephra horizons may also arise when comparing datasets from different EPMA instruments if variations in operating conditions have affected characterisations. Major element similarities will also inhibit the discrimination of tephra horizons deposited closely spaced in time, particularly if only one horizon is identified within a low-resolution sequence. Within these situations trace element geochemistry has the potential to be more discriminatory that major elements.

**Table 4.13:** $D^2$ values for statistical distance comparisons between the average major element geochemical compositions of the five Katla tephra horizons. Critical value for $D^2$ of 21.67 at the 99% confidence level.

| | GRIP 1716.08 m | NGRIP 1895.3 m | NGRIP 1915.5 m | NGRIP 2574.55 m | NGRIP 2631.9 m |
|---|---|---|---|---|---|
| GRIP 1716.08 m | 0.0 | | | | |
| NGRIP 1895.3 m | 11.7 | 0.0 | | | |
| NGRIP 1915.5 m | 13.6 | 5.26 | 0.0 | | |
| NGRIP 2574.55 m | 3.98 | **22.4** | 17.0 | 0.0 | |
| NGRIP 2631.9 m | 13.4 | 18.3 | 14.5 | 6.28 | 0.0 |

**Table 4.14:** Similarity coefficients for comparisons between the major element compositions of the Katla five tephra horizons.

| | GRIP 1716.08 m | NGRIP 1895.3 m | NGRIP 1915.5 m | NGRIP 2574.55 m | NGRIP 2631.9 m |
|---|---|---|---|---|---|
| GRIP 1716.08 m | 1.000 | | | | |
| NGRIP 1895.3 m | **0.968** | 1.000 | | | |
| NGRIP 1915.5 m | 0.937 | **0.957** | 1.000 | | |
| NGRIP 2574.55 m | **0.975** | **0.955** | 0.916 | 1.000 | |
| NGRIP 2631.9 m | **0.967** | **0.969** | 0.946 | **0.967** | 1.000 |

### 4.6.3 Trace Element Characterisations

The REE profiles for the analyses of individual shards within the five Katla tephra horizons are shown on figure 4.21. This figure demonstrates that differing levels of heterogeneity can be observed within the trace element data, for example both GRIP 1706.08 m and NGRIP 1895.3 m display a relatively high level of heterogeneity in comparison to the other three horizons. The differing levels of heterogeneity between trace element characterisations of horizons will be discussed in section 8.3.4.2.

The average profiles for the five horizons are shown on figure 4.22a and there is a general coherency between the gradients of the profiles with all of them displaying a relatively gentle slope from the LREEs to the HREEs. One exception is the peak in Eu observed for NGRIP 1915.5 m, probably caused by polyatomic interference from BaO (see section 4.3.2), however if excluded the profile gradient for this horizon is comparable to those from the other horizons. The consistency in REE profiles indicates that REE ratios will be similar for all of the horizons.

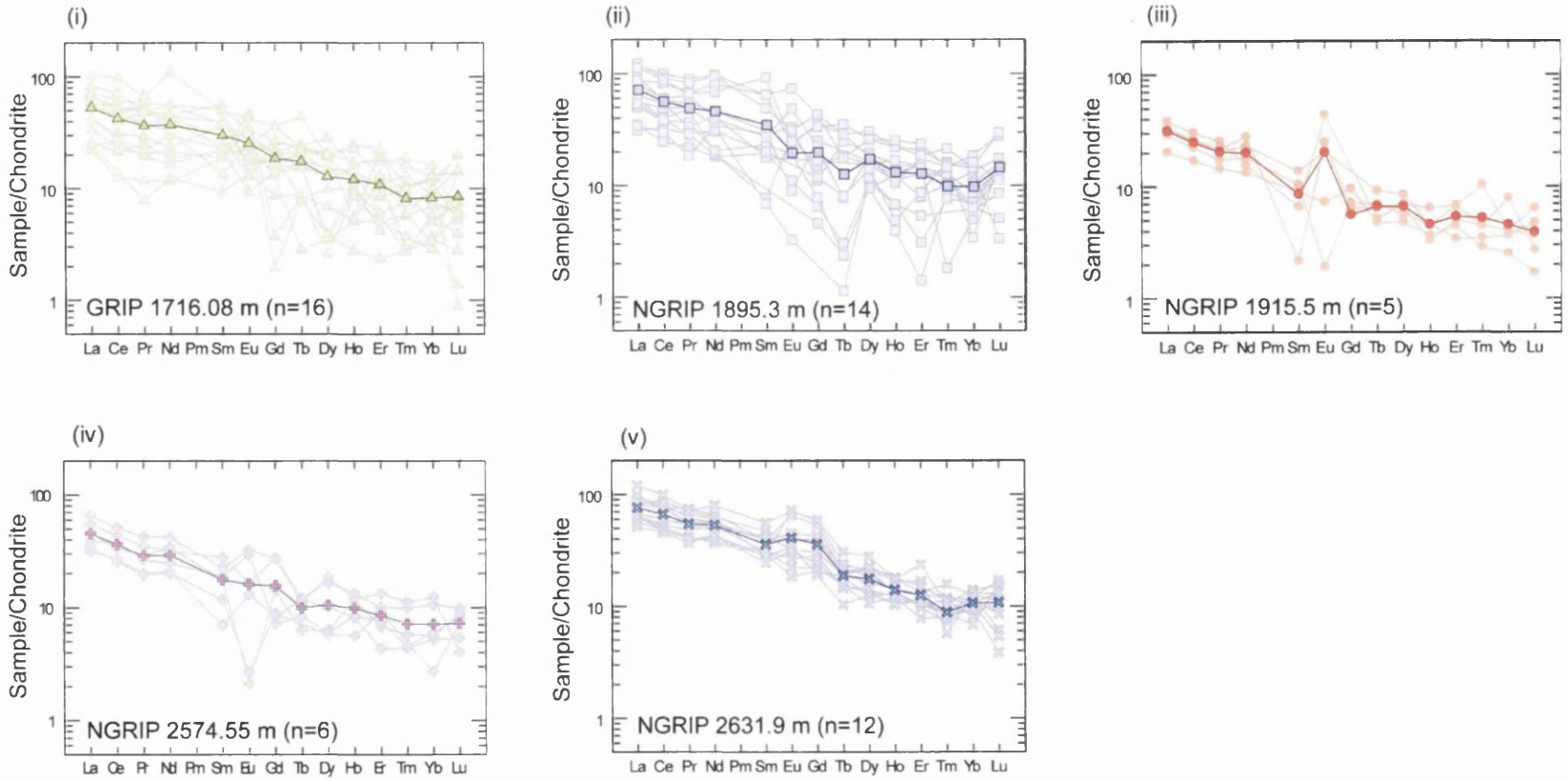


**Figure 4.21:** Individual chondrite-normalised REE profiles for shards from five tephra horizons identified within the Greenland ice-cores which are all the products of eruptions of the Katla volcanic system. Average profiles for the horizons are highlighted. Chondrite values from Sun and McDonough (1989).

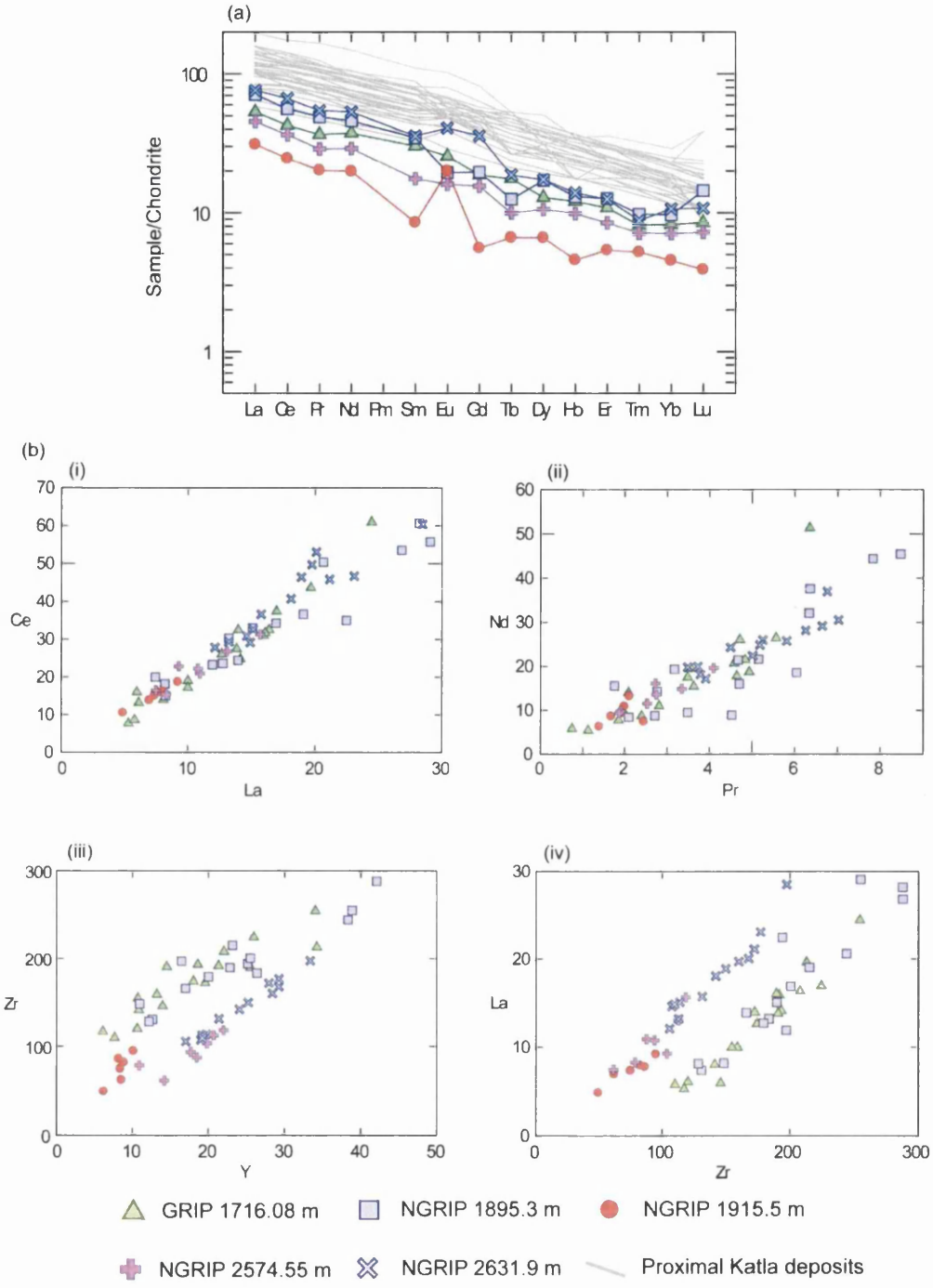


**Figure 4.22:** (a) Average chondrite-normalised REE profiles for ice-core Katla horizons compared to characterisations of proximal Katla deposits reported in Meyer et al. (1985) and Lacasse et al. (2007). (b) Comparisons between trace element geochemical data from individual shards within the Katla horizons on (i) La vs. Ce (ii) Pr vs. Nd (iii) Y vs. Zr and (iv) Zr vs. La compositional variation diagrams.

Characterisations of material proximal to the Katla volcanic system are also shown on figure 4.22a. The gradient of the REE profiles for the horizons from the ice-cores are very similar to the proximal deposits and fall within a narrow compositional range; which is a key feature of proximal Katla products (Lacasse et al., 2007). However, the absolute concentrations of REEs within the distal tephra horizons are offset towards lower concentrations relative to the proximal characterisations. This offset in absolute concentrations may be a consequence of the use of different methods and instrumentation for the acquisition of the trace element data or issues related to gas blank misestimation.

Individual trace element analyses show that for some element pairs an overall similarity in trace element composition between all of the horizons can be observed. For example, in figure 4.22b (i) and (ii) all of the analyses fall along the same linear covariant trends for the element pairs La-Ce and Pr-Nd. However, for other element pairs including Y-Zr and Zr-La the horizons fall along different ratio trend lines, which allows the horizons to be discriminated from one another. This is shown in figures 4.22b (iii) and (iv) which demonstrates that the horizons can be split into two groups, the younger GRIP 1706.08 m, NGRIP 1895.3 m and NGRIP 1915.5 m horizons and the older NGRIP 2574.55 m and NGRIP 2631.9 m. The occurrence of different trace element covariance trends between horizons may be indicative of temporal variations in conditions within the source magma chamber and magmatic processes.

A likely explanation for the trace element differences is that replenishment of the magma chamber below Katla, i.e. an input of more primitive and less evolved magma, occurred between the eruptions producing NGRIP 2574.55 m and NGRIP 1915.15 m (N. Pearce, *pers. comm.*, 2009). Small-scale variations in the average major element concentrations for the horizons appear to support this (figure 4.23). Over time, there is a decrease in $Al_2O_3$, CaO and MgO within each group resulting from fractional crystallisation of plagioclase feldspar and clinopyroxene in the magma chamber; but the rise in concentrations between the NGRIP 2574.55 m and NGRIP 1915.5 m horizons indicates that the magma has become more primitive, probably by replenishment with a new batch of mantle derived material. A difference in trace element composition of the magma chamber prior and subsequent to this replenishment thus explains the difference in incompatible elements ratios such as Zr/Y between the groups. Incompatible elements are not incorporated into crystallising mineral phases in any quantity, and thus, during fractional crystallisation their concentrations increase in the residual magma, but their ratios remain constant

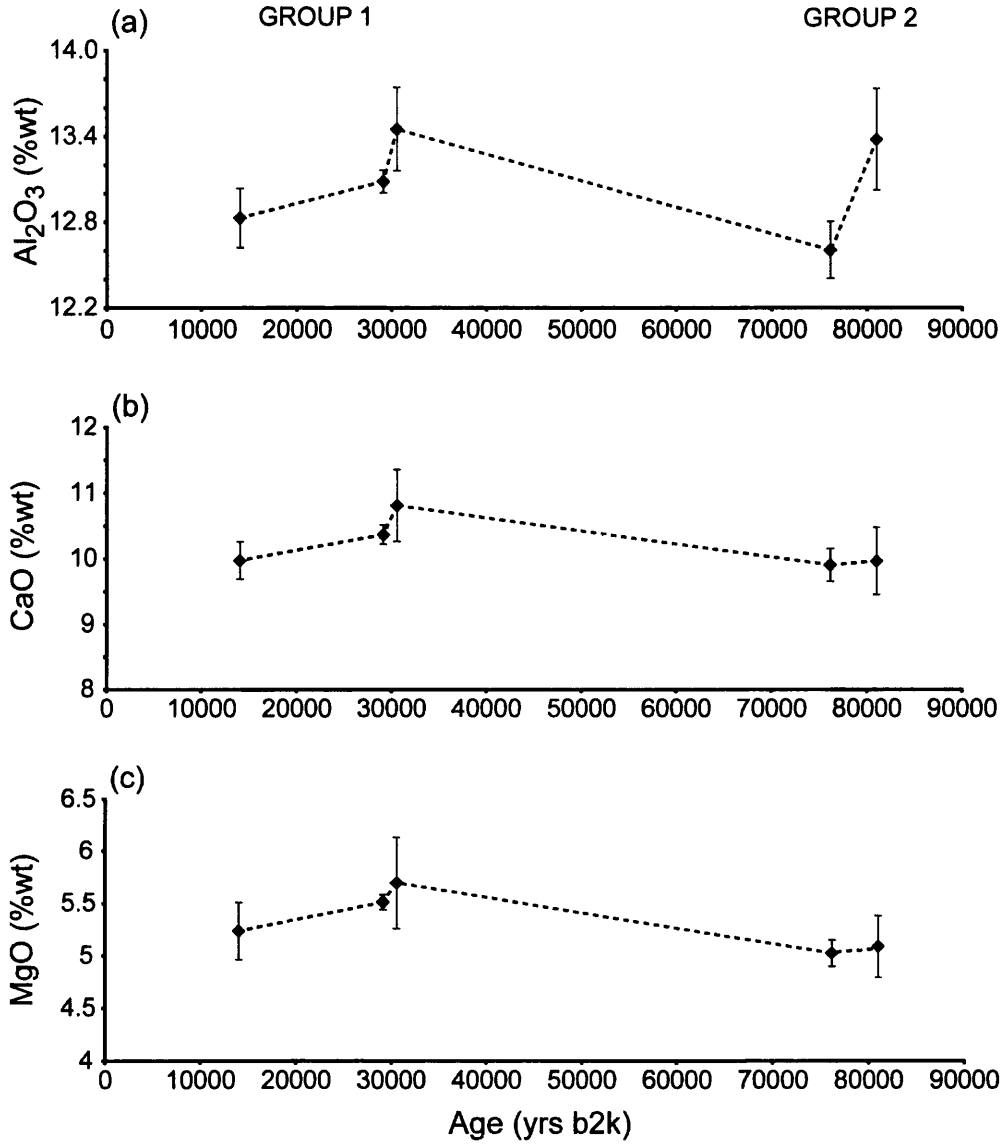


**Figure 4.23:** Temporal variation of mean (a) $Al_2O_3$ (b) CaO and (c) MgO major oxide concentrations within five tephra horizons sourced from the Katla volcanic system during the last glacial period. Error bars are one standard deviation of the average values shown in table 4.12. Ages derived from the GICC05 timescale for the two cores (Svensson, *pers. comm.*, 2008).

(Rollinson, 1993). The sensitivity of incompatible element concentrations to melting, however, means that different batches of magma from the same general source region, may have different incompatible element ratios but similar major element compositions (Rollinson, 1993).

This process explains why horizons within the two groups can be discriminated from one another. However, it also needs be ascertained whether within these general, temporal groupings trace element differences between horizons can be identified. Geochemical discrimination of these closer spaced horizons is of greater importance within tephrochronological studies.

#### 4.6.3.1 Group 1: GRIP 1716.08 m, NGRIP 1895.3 m and NGRIP 1915.5 m

The heterogeneity displayed within the analyses of shards from GRIP 1706.08 m and NGRIP 1895.3 m results in relatively extensive geochemical fields on the biplots in figure 4.24, and high overlaps between the horizons can be observed. In addition, the analyses from NGRIP 1915.5 m generally fall within the fields for both the GRIP 1706.08 m and NGRIP 1895.3 m horizons. For horizons with large overlaps differences in ratio trends can sometimes be used to distinguish between the horizons. However, as can be seen on the Sr-Y, Nb-La and Ce-La biplots in figure 4.24 the linear covariance between the element pairs is comparable for each horizon. The similarities in the ratios between trace elements for all three horizons are also shown on the ratio-ratio biplots in figure 4.25. As a consequence it is not possible to confidently distinguish between these three horizons based on their trace element compositions. This may be due to no fractional crystallisation or magma melting occurring within the Katla magma chamber between the eruptions producing these horizons.

#### 4.6.3.2 Group 2: NGRIP 2574.55 m and NGRIP 2631.9 m

Biplots of analyses from the two horizons identified as the second group on figure 4.22 demonstrate that there are minimal overlaps between the geochemical fields for the horizons due to the higher concentration of trace elements within NGRIP 2631.9 m relative to NGRIP 2574.55 m (figure 4.26). However, the linear covariance for some of the element pairs appears to follow approximately the same ratio trend lines. These observations suggest that the horizons may have similar compositions and the offset

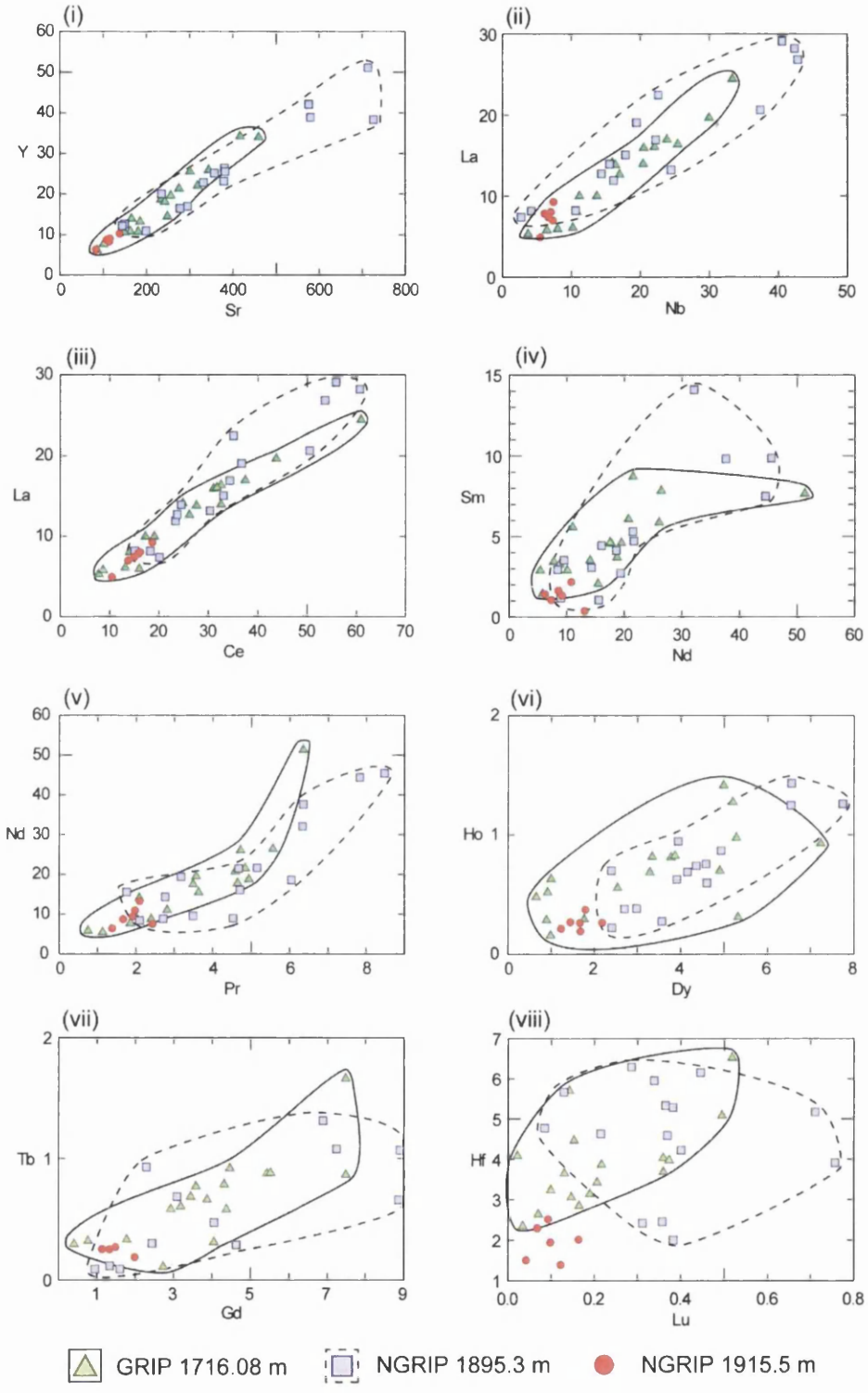


**Figure 4.24:** Compositional variation diagrams for selected trace elements from individual shards within the GRIP 1716.08 m, NGRIP 1895.3 m and NGRIP 1915.5 m tephra horizons.

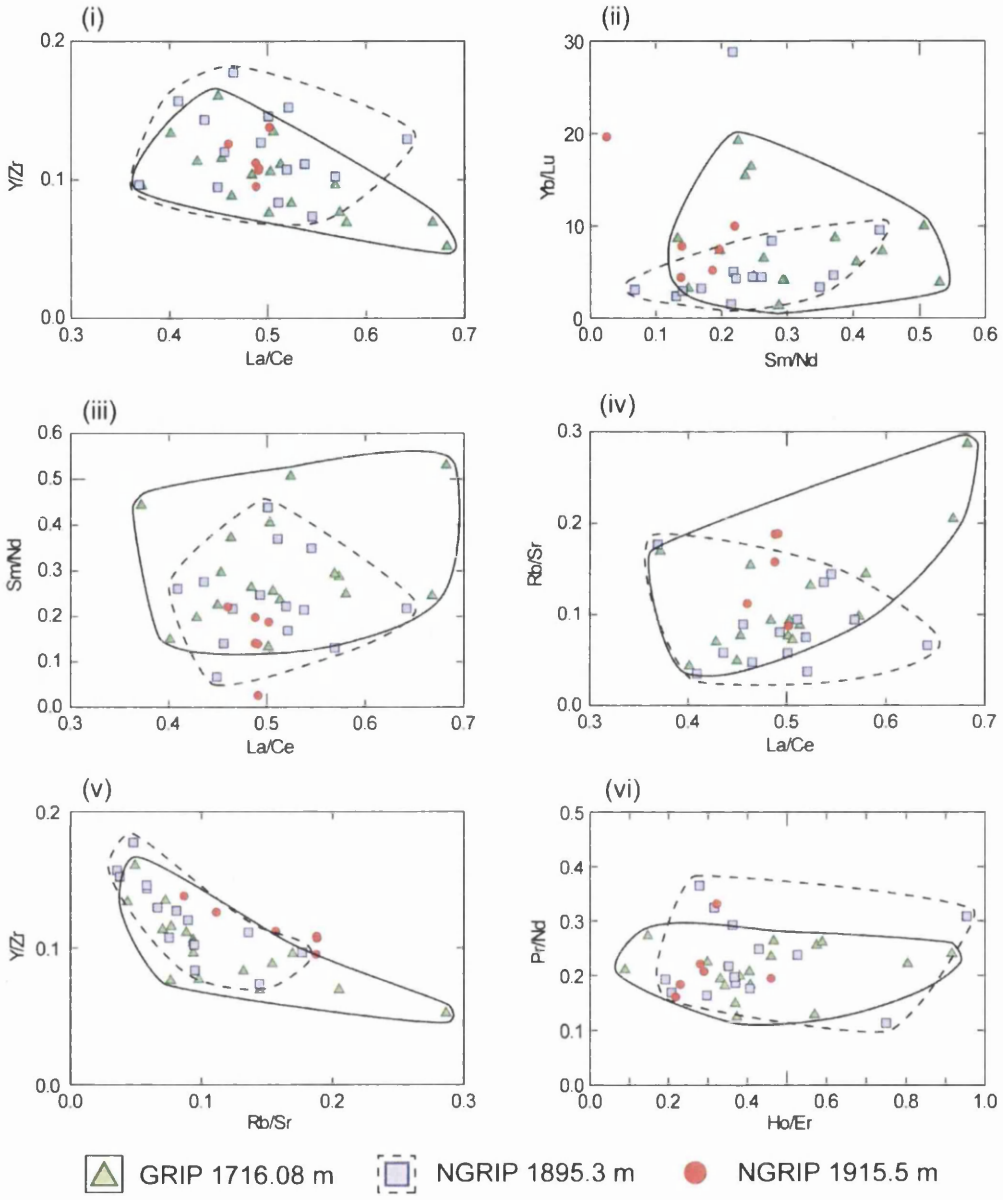


**Figure 4.25:** Trace element ratio-ratio diagrams for analyses of individual shards from the GRIP 1716.08 m, NGRIP 1895.3 m and NGRIP 1915.5 m tephra horizons.

has been introduced by the effect of misestimation of gas blank levels on absolute trace element concentrations. Therefore trace element ratios for the horizons were compared as these would be unaffected by the misestimation. Figure 4.27 illustrates that while some ratios cannot be used to discriminate between the horizons (figures 4.27 i-iv) others such as Y/Zr and Th/Nb distinctly differ between the horizons (figures 4.27 v-viii). Thus, although gas blank misestimation may have affected the calculation of trace element concentrations for these horizons, geochemical differences between the horizons can still be identified using the ratios between the trace elements. The observed ratio differences may have been caused by a small degree of mantle melting within the source region between the eruptive events (Rollinson, 1993).

### 4.6.3.3 Trace Element Statistical Distance Comparisons

The statistical distance function was utilised to assess the discriminations between these horizons. The average concentration of 14 elements within each horizon was compared with only one statistically significant difference, between the NGRIP 1915.5 m and NGRIP 2631.9 m horizons, identified (table 4.15). This appears to contradict the qualitative evidence, but may be due to the trace element differences only being apparent for certain elements and the high heterogeneity, and consequent high standard deviation values, for some of the horizons.

**Table 4.15:** $D^2$ values for statistical distance comparisons between the average trace element geochemical compositions of the five Katla tephra horizons. 14 elements utilised within the comparisons. Critical value for $D^2$ of 29.14 at the 99% confidence level.

| | GRIP 1716.08 m | NGRIP 1895.3 m | NGRIP 1915.5 m | NGRIP 2574.55 m | NGRIP 2631.9 m |
|---|---|---|---|---|---|
| GRIP 1716.08 m | 0.0 | | | | |
| NGRIP 1895.3 m | 3.41 | 0.0 | | | |
| NGRIP 1915.5 m | 16.7 | 21.4 | 0.0 | | |
| NGRIP 2574.55 m | 22.5 | 14.7 | 18.6 | 0.0 | |
| NGRIP 2631.9 m | 5.14 | 3.63 | **57.1** | 19.8 | 0.0 |

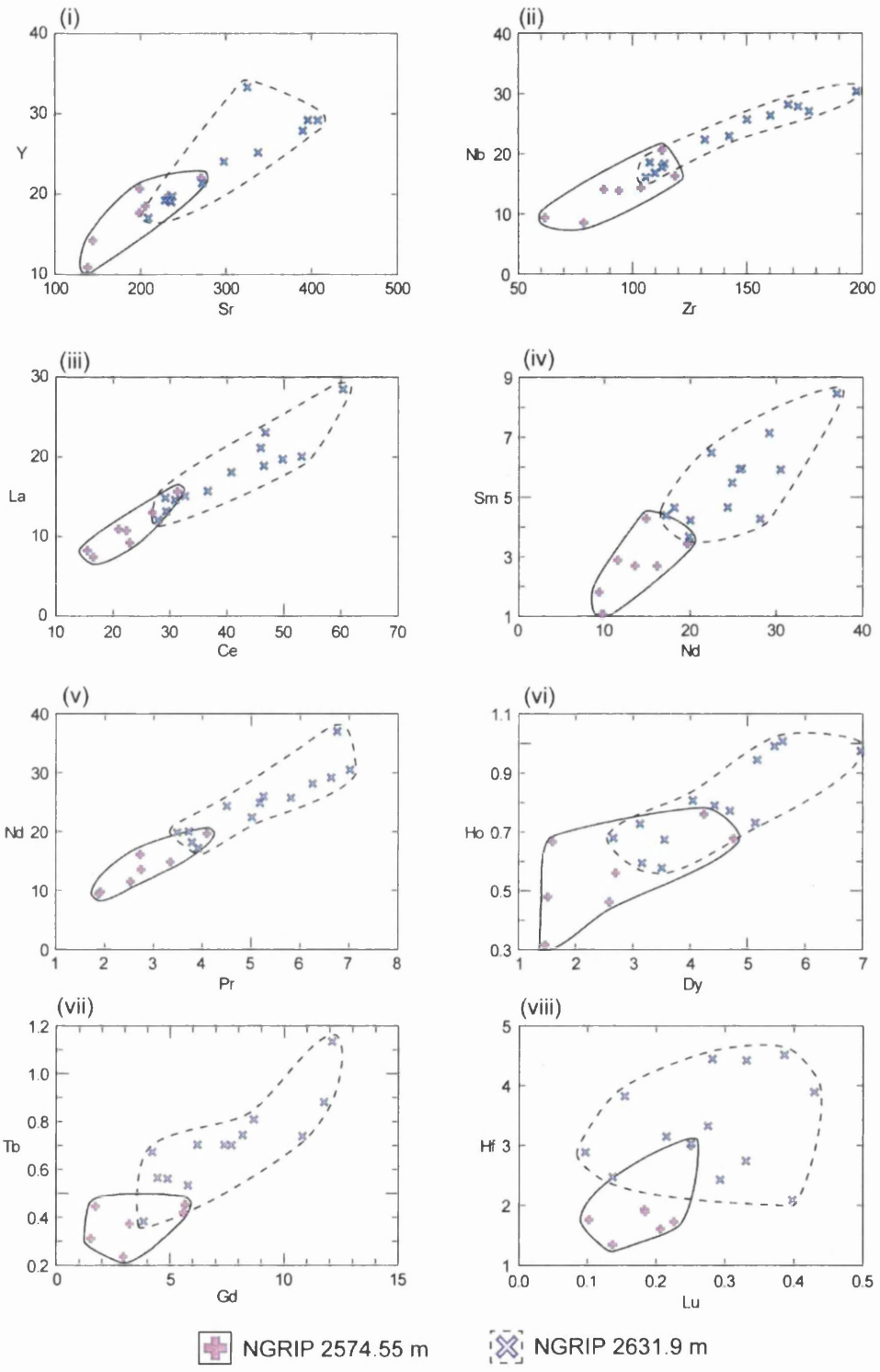


**Figure 4.26:** Compositional variation diagrams for selected trace elements from individual shards within the NGRIP 2574.55 m and NGRIP 2631.9 m tephra horizons.

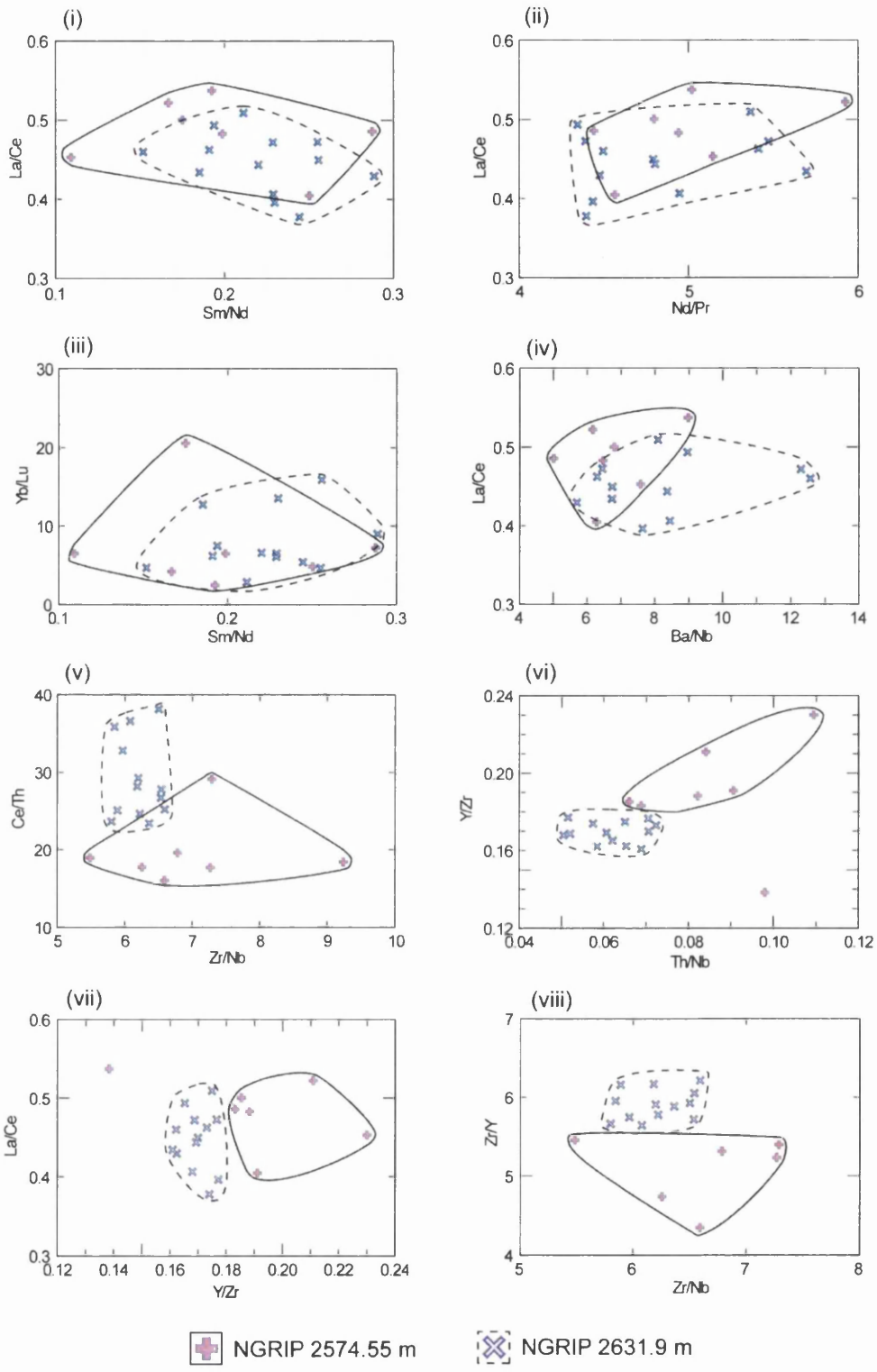


**Figure 4.27:** Trace element ratio-ratio diagrams comparing individual analyses of shards from the NGRIP 2574.55 m and NGRIP 2631.9 m tephra horizons.

### 4.6.4 Summary

The analysis presented in the preceding sections provides mixed evidence for the potential use of trace elements to distinguish between the products of the Katla volcanic system. There are broad temporal variations in the trace element composition of horizons produced by the Katla volcanic system, due to magma chamber replenishment, which allowed the horizons to be grouped based on differences in the linear covariance of incompatible elements. Within these groupings it was only possible to discriminate between the NGRIP 2574.55 m and NGRIP 2631.9 m horizons within group 2; these horizons were deposited with a temporal separation of ~5000 years. Within group 1 it was not possible to discriminate between GRIP 1706.08 m and NGRIP 1895.3 m, which were deposited with a ~1425 year separation, as these horizons have very similar trace element compositions.

The use of statistical distance comparisons to provide statistical evidence for the differences observed on biplots appears to be strongly influenced by the high variability within the datasets, and demonstrates that this technique can provide misleading results in the absence of a qualitative comparison of datasets.

## 4.7 Chapter Summary

Within this chapter it has been demonstrated that:

- The precision and lower limits of detection for trace element analyses gained using the new LA-ICP-MS system and a 14 μm beam diameter are comparable to those for older systems operating at a lower spatial resolution.

- There is the potential to improve the spatial resolution of the new LA-ICP-MS system further, through the use of a 6 μm laser beam diameter, however the sensitivity of the system would have to be improved to increase the ratio between sample counts and background counts.

- The internal standardisation of datasets using either Si or Ca as an internal standard produced variable offsets in calculated trace element concentrations. These offsets can be attributed to misestimation of background element levels within the LA-ICP-MS system ascertained through the analysis of gas blanks.

•The comparison of trace element signatures for horizons previously correlated based on major element compositions has increased the robustness of the correlation of two occurrences of the Fugloyarbanki Tephra. However, trace element differences between two horizons attributed to the Saksunarvatn Ash indicate they do not relate to the same eruptive event, which calls into question the use of these deposits as chronostratigraphic markers.

•Incompatible trace element ratios such as Y/Zr can be used to distinguish between the products of the Katla volcanic system and to identify magmatic evolution events such as magma chamber replenishment. However, some horizons do have highly similar trace element compositions and the ability to discriminate between eruptions may be limited by the timing of magmatic changes in the source region.

•Throughout this chapter it has been shown that the statistical distance function has deficiencies when the trace element datasets created within this study are compared, due to the high variability of the data and subtle trace element differences between horizons.

# 5. Tephrochronology of Marine Isotope Stage 4 within the NGRIP Ice-core

## 5.1 Introduction

Within section 1.2 the principle aim of this study, to create a tephrochronological framework for the MIS 4 period in the North Atlantic region, was outlined and emphasised the important role of the NGRIP ice-core within the construction of this framework. This chapter presents detailed descriptions of horizons identified during this study within the MIS 4 section of the NGRIP record.

Section 5.2 details how the sampling strategies described within section 3.2.3 were applied to the sampling of the NGRIP ice-core. A summary of general information relating to the tephra horizons that have been identified is provided in section 5.3.2, before each individual horizon is described and the major and trace element characterisations of the horizons are outlined (section 5.4). Both of these characterisations for each horizon have been compared to proximal volcanic deposits; firstly, to ascertain if source volcanic regions can be determined for the horizons and secondly, to explore the reliability of the trace element characterisations made within this study. In addition, similarity coefficient comparisons have been made to the geochemistry of the horizons forming the present MIS 2-5e tephrochronological framework (appendix 6). This will determine if mutual sources can be identified for the horizons and permit an assessment of the relevance of the horizons identified within this study to the volcanic history of source areas throughout the MIS2-5e period.

## 5.2 Sub-sampling of the NGRIP ice-core

The NGRIP sampling strategy was based on three criteria:

1. Visible bands

    -During the drilling campaign three bags from the MIS 4 section of ice were recorded as containing visible bands and these bags were all subsampled.

2. Distinct chemical signals

    -84 bags were selected for sub-sampling based on the position of distinct chemical peaks (sulphate and ECM) in the ice.

3. Continuous sampling over climatic transitions

-Ice spanning 5 high-magnitude and rapid climate transitions was sampled continuously. The selected warming and cooling transitions are the most distinct climatic events during this period and have all been recognised within other climatic archives such as the marine core MD04-2822 investigated within this study. In addition, the transition between the DO 20 interstadial period and the subsequent stadial period is believed to be when the Toba super eruption occurred (see section 2.4.5.2). To sample over these periods ice was taken from 73 ice-core bags.

The location of the 161 selected ice-core bags with reference to the NGRIP oxygen isotope record are shown on figure 5.1. Using the guidelines set out in section 3.2.4.1 they were sub-divided into 891 individual samples and the tephra content of each of these samples was assessed (appendix 3).

## 5.3 Tephra Horizons within the NGRIP Ice-core

### 5.3.1 Visible Horizons

Four visible bands within bags 4438, 4506 and 4547 (figure 5.2) did not contain any tephra shards and thus do not represent visible tephra horizons. A likely explanation for the formation of these visible bands is the presence of a high level of impurities, which can promote the formation of bubbles within the ice (Svensson et al., 2005).

Chemical records for these bags reveal that each visible band correlates with either a peak in microparticle concentration or a gap in the record which is indicative of saturation of the detector used to measure microparticle concentration (figure 5.3). These peaks in microparticle concentration are mirrored in the $Ca^{2+}$ concentration records for the bags. This suggests that the impurity causing the visible bands to form is dust and the high levels could be attributed to short term increases in the atmospheric transport of dust to the ice sheet. Therefore, no visible tephra horizons can be identified within the MIS 4 section of the NGRIP ice-core.

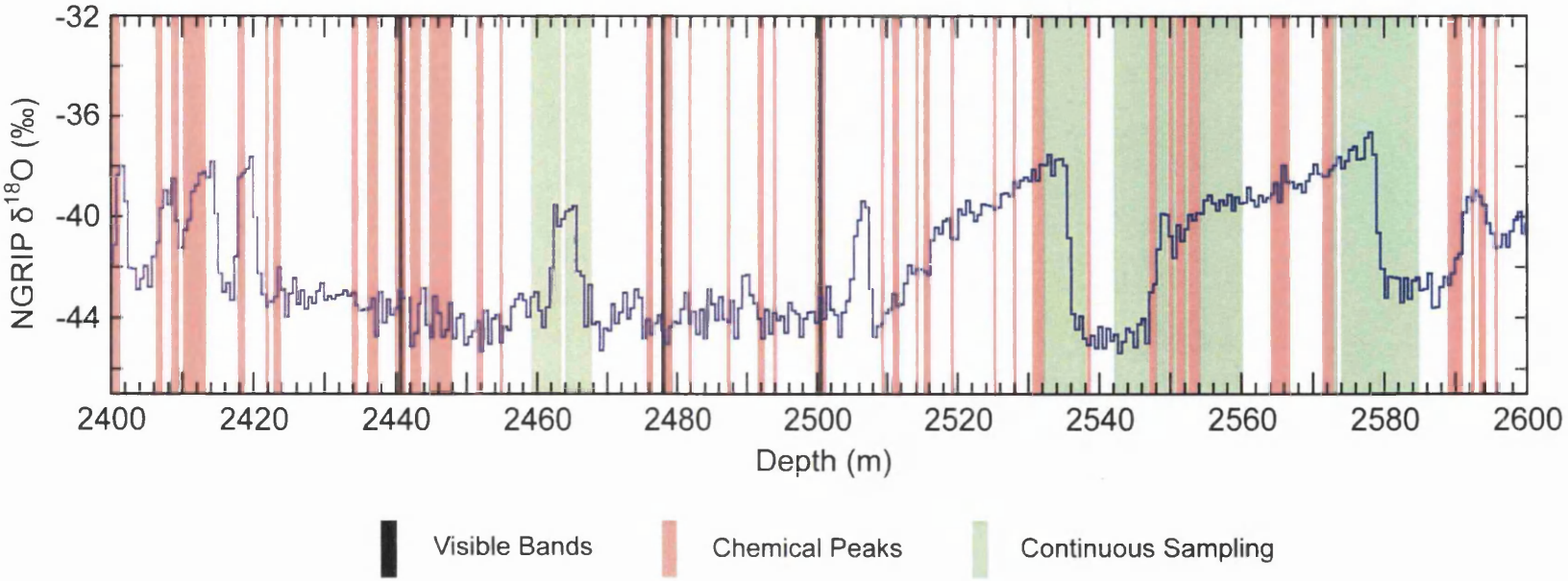


**Figure 5.1:** Stratigraphic position of ice-core bags from the NGRIP ice-core sampled during this study with reference to the oxygen isotope record for the core. Isotopic values are expressed in ‰ with respect to V-SMOW.

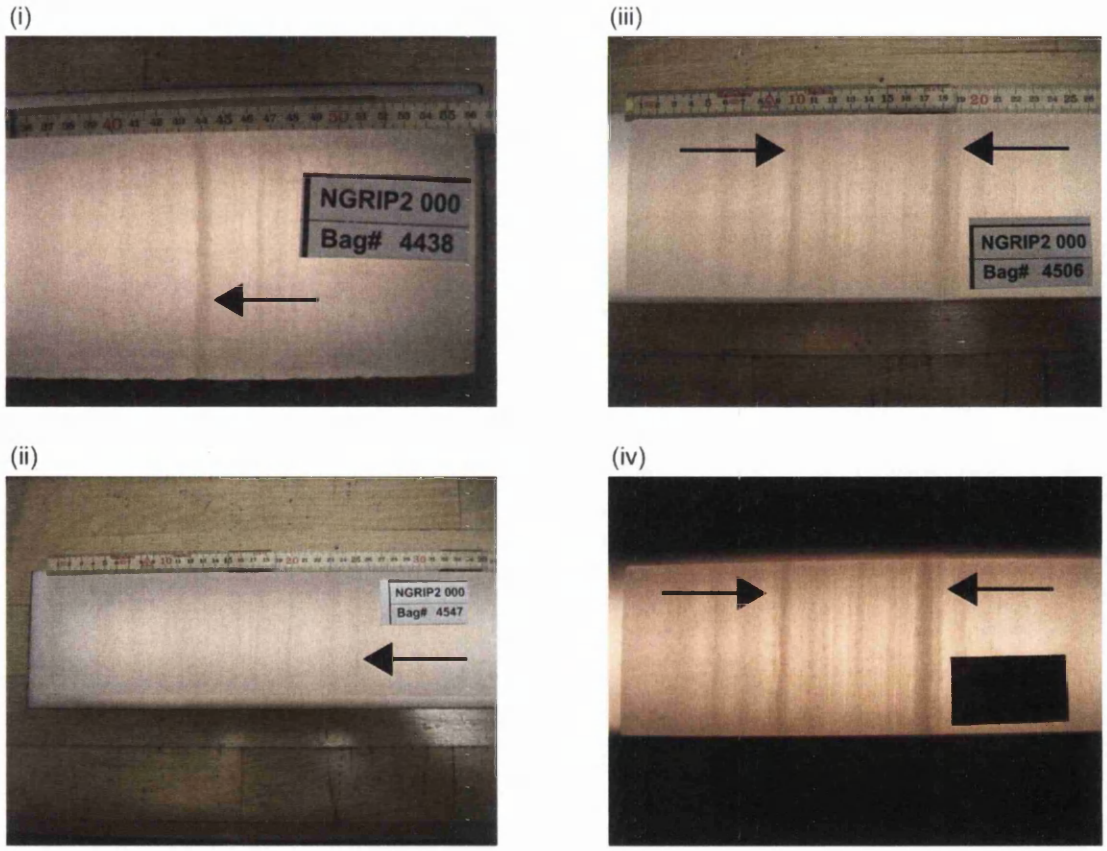


**Figure 5.2:** Photographs of visible bands within ice-core bags (i) NGRIP 4438 (ii) NGRIP 4547 and (iii and iv) NGRIP 4506 identified during the drilling of the NGRIP ice-core as potentially relating to visible tephra horizons. Photographs were taken over a light box during the subsampling of the ice-core. Black arrows indicate the position of the visible bands.

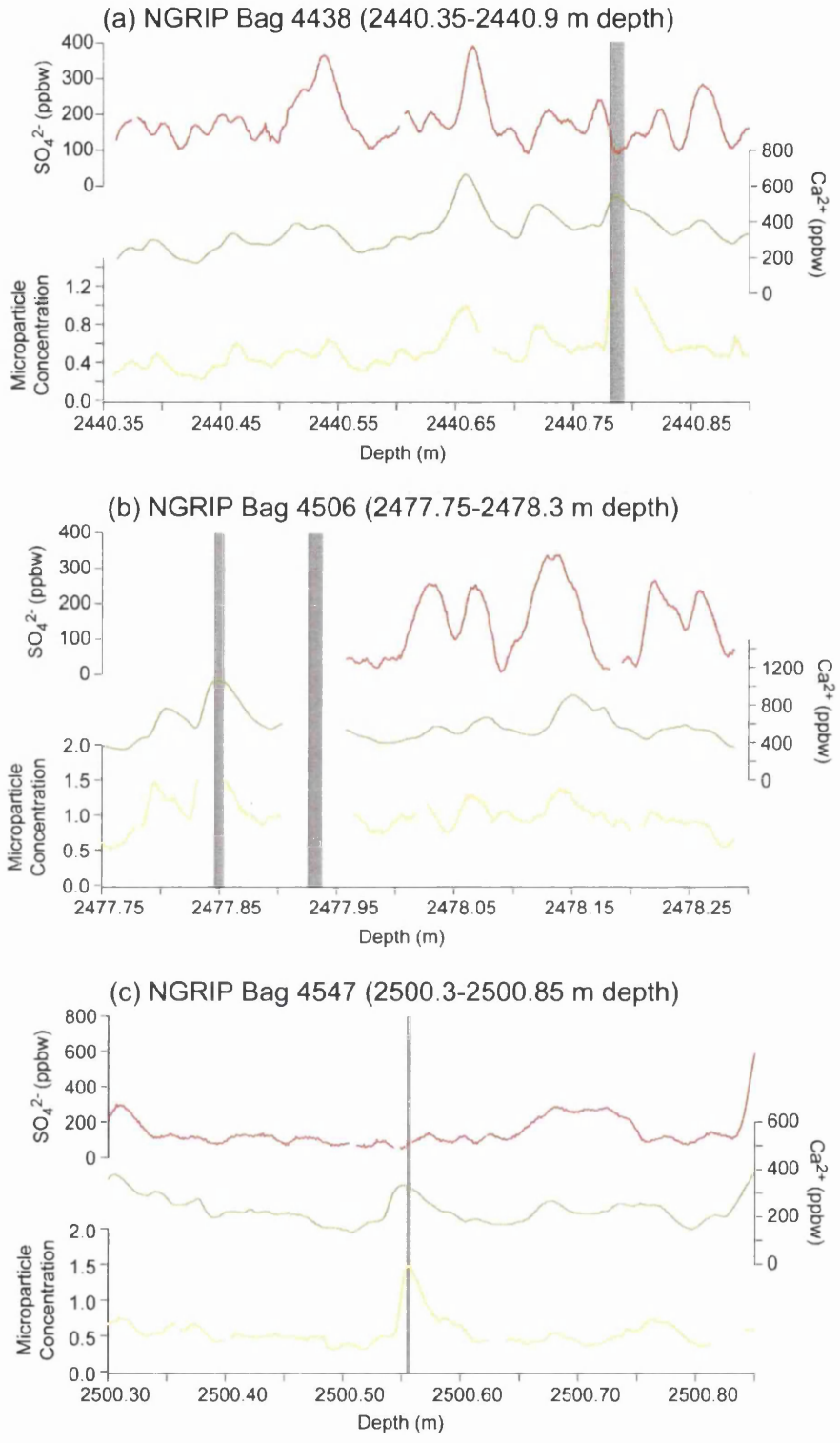


**Figure 5.3:** High-resolution sulphate, calcium and dust concentration records for NGRIP ice-core bags identified during drilling as containing visible bands. Microparticle concentration is measured as particles ($\times 10^6$) per ml).

### 5.3.2 Cryptotephra Horizons

Six of the samples, chosen due to the presence of distinct chemical peaks or for continuous sampling, were found to contain a significant number (>20) of glass shards (figure 5.4). Other samples were found to contain background levels of tephra with low concentration of shards (<4) (appendix 3). These samples were not processed for geochemical analysis, because the classification of such a low concentration of shards as horizons is questionable and the amount of material was insufficient to provide a full geochemical characterisation. The horizons outlined here were defined based on the high concentration of shards relative to background levels and a homogenous geochemical signal from the shards.

The stratigraphic position of the six cryptotephra horizons with respect to the NGRIP oxygen isotope record is shown in figure 5.5a. Figure 5.5b illustrates the position of the individual horizons relative to the high resolution sulphate record. The tephra horizons are referred to by the basal depth of the ice sample in which the layers were found (table 5.1) and table 5.2 presents the average major and trace element compositions of all of the NGRIP horizons.

**Table 5.1:** Summary of the ice samples from the MIS 4 period of the NGRIP ice-core containing a significant number of tephra shards.

| Bag Number | Depth Interval (cm) | Depth of Sample Top (m) | Depth of Sample Base (m) |
|---|---|---|---|
| 4439 | 18-24 | 2441.08 | 2441.14 |
| 4439 | 34-38 | 2441.24 | 2441.28 |
| 4464 | 20-25 | 2454.85 | 2454.9 |
| 4548 | 0-5 | 2500.85 | 2500.9 |
| 4634 | 0-20 | 2548.15 | 2548.35 |
| 4681 | 49-55 | 2574.49 | 2574.55 |

The major element data for all horizons is displayed on a total alkali versus silica (TAS) plot (figure 5.6) so that the material can be classified according to the nomenclature for volcanic rocks of Le Maitre et al. (1989). Figure 5.7 provides an inset of the TAS plot focusing on analyses from basaltic and basaltic andesitic material. Included on this plot is the division line between tholeiitic and alkaline basalts defined by MacDonald and Katsura (1964) based on analyses of Hawaiian volcanic material. This will aid in the classification of any Icelandic basaltic material as tholeiitic analyses will plot below this line, alkaline analyses will plot above the line and transitional alkali basalts will fall close to the division line (Meyer et al., 1985; Jakobsson et al., 2008).

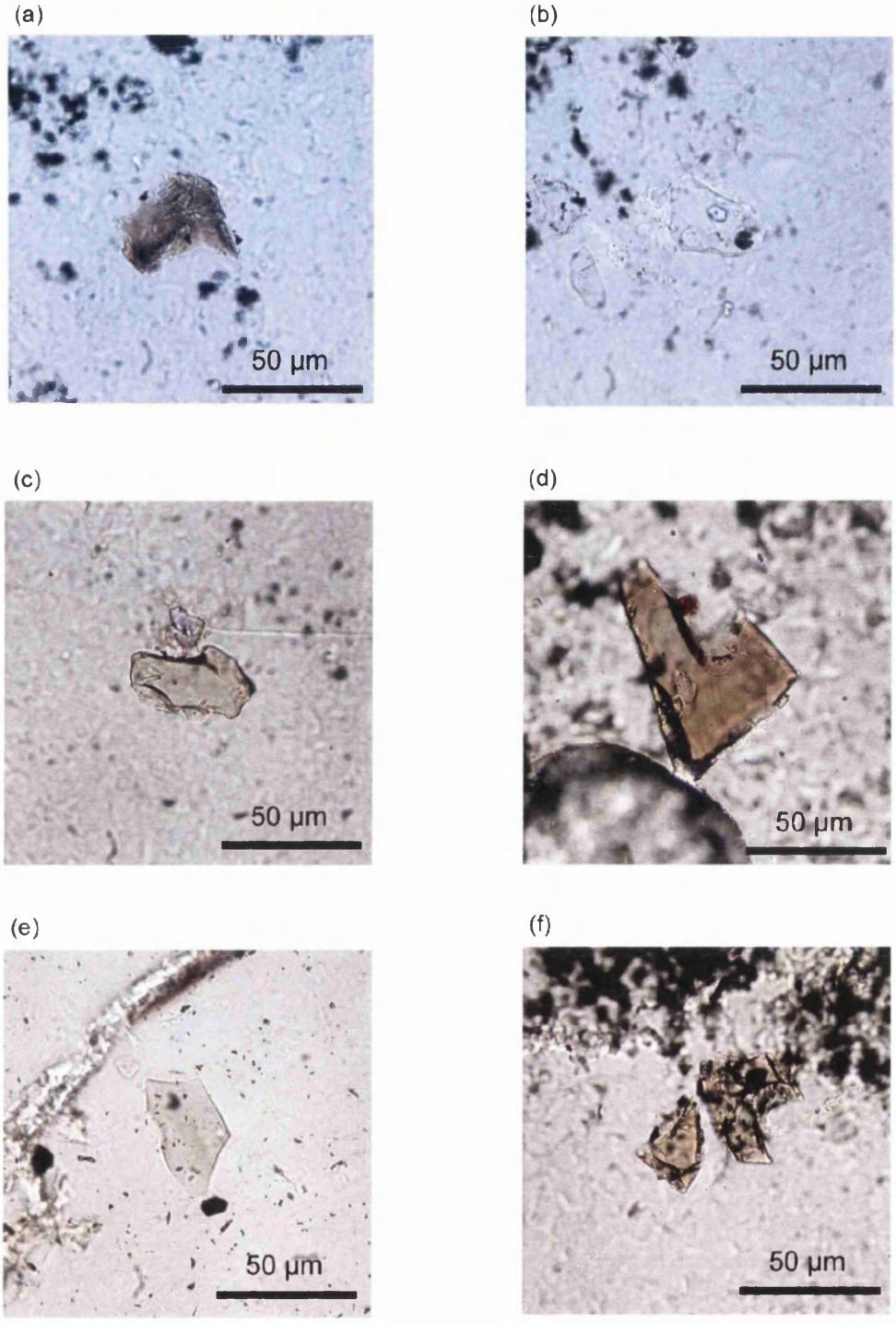


**Figure 5.4:** Images of tephra shards from NGRIP MIS 4 tephra horizons. (a) NGRIP 2441.14 m (b) NGRIP 2441.28 m (c) NGRIP 2454.95 m (d) NGRIP 2500.9 m (e) NGRIP 2548.35 m and (f) NGRIP 2574.55 m.

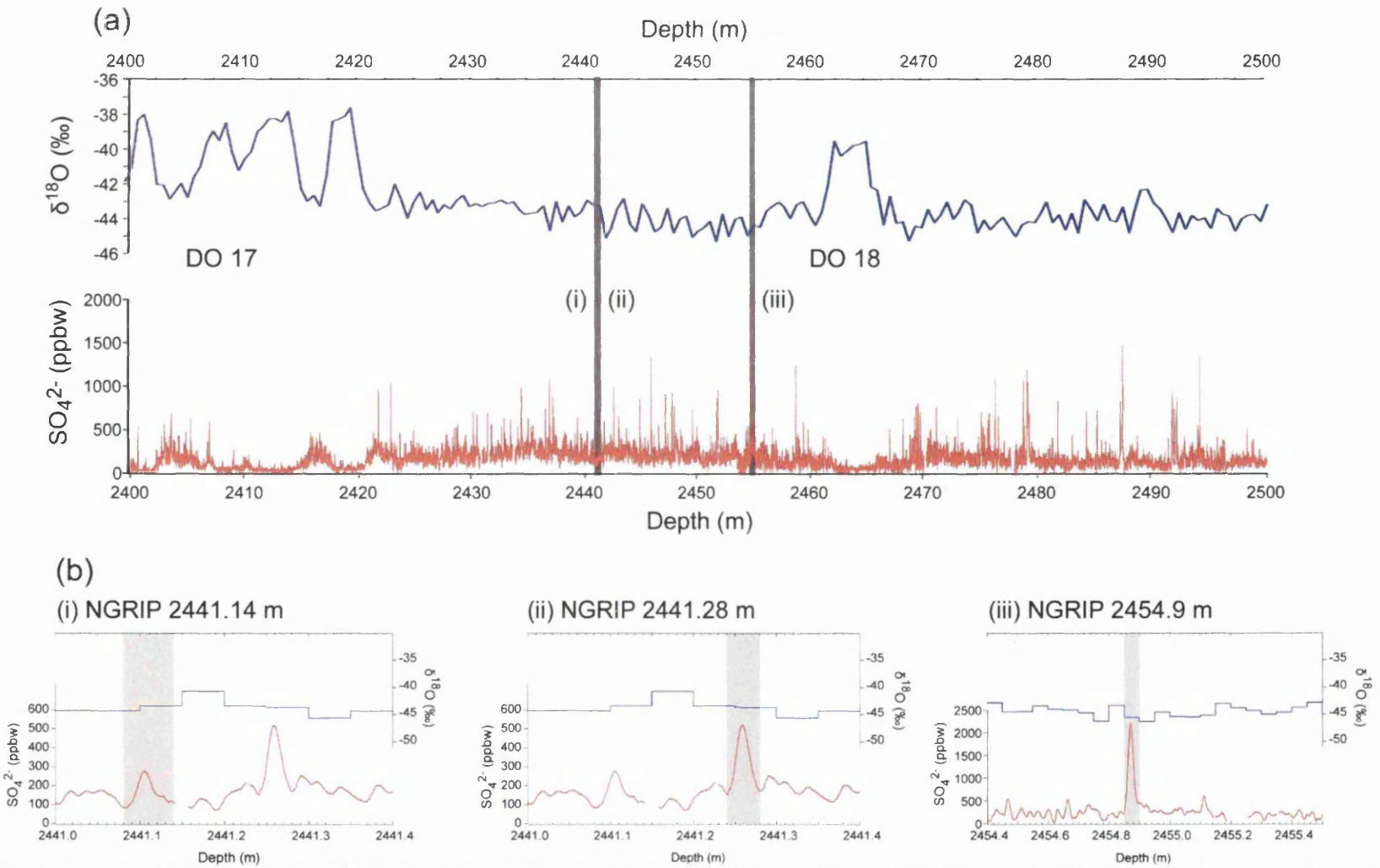


**Figure 5.5:** (a) Stratigraphic position of the six cryptotephra horizons identified within the NGRIP ice-core with respect to the oxygen isotope ratio and continuous sulphate concentration record for the core. (b) (i-vi) insets from (a) illustrating the detailed chemical records around the cryptotephra horizons. Isotopic values are expressed in ‰ with respect to V-SMOW. Continued overleaf.

(a) cont.

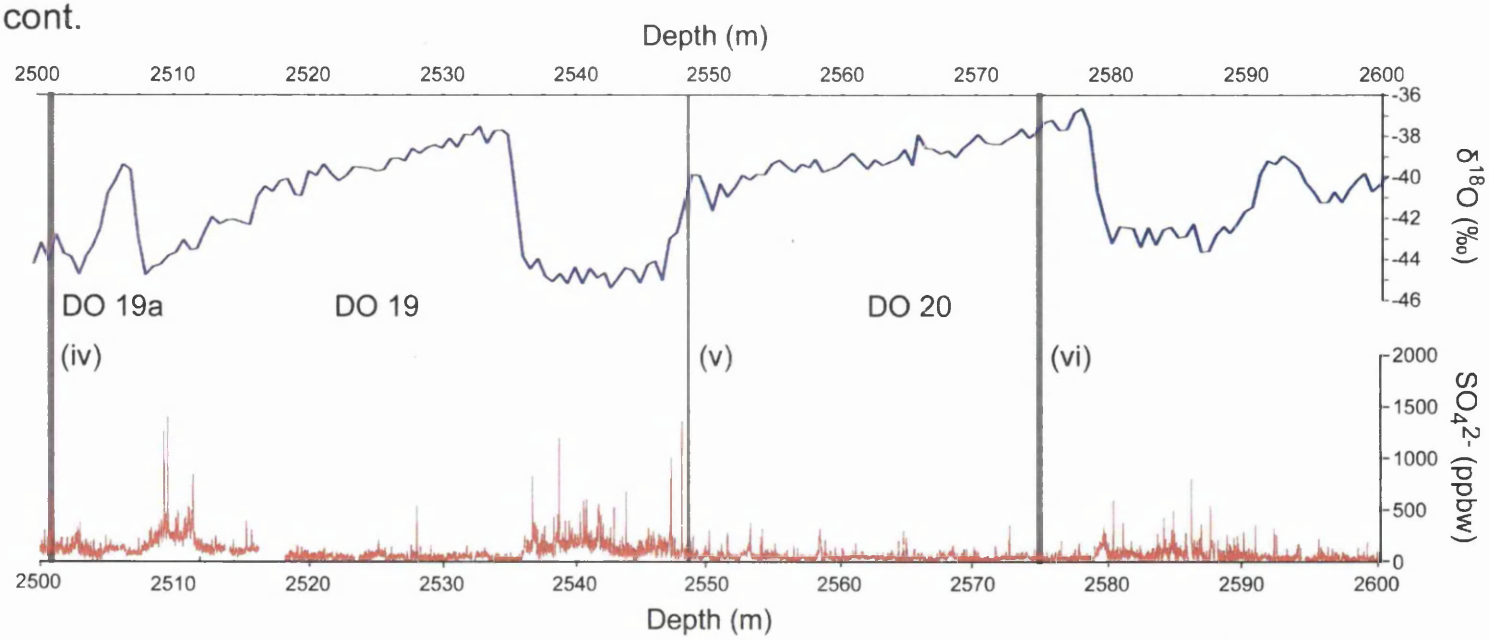


(b) cont.

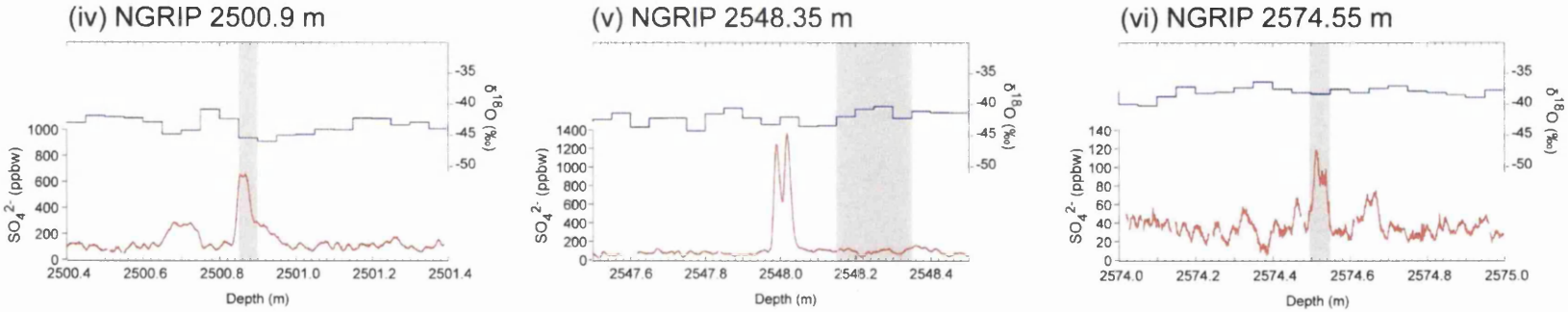


**Figure 5.5:** continued

**Table 5.2:** Summary of normalised major oxide and trace element data for glass shards from tephra horizons identified within the MIS 4 section of the NGRIP ice-core. Mean and 1 standard deviations are shown. Total oxides are raw values prior to normalisation. All major elements expressed as percentage weight. All trace element concentrations expressed as ppm. Total iron is expressed as FeO. n = number of shards analysed. The complete dataset of unnormalised data is provided in appendix 3.

| | NGRIP 2441.14 m | NGRIP 2441.28 m | NGRIP 2454.9 m | NGRIP 2500.9 m | NGRIP 2548.35 m | NGRIP 2574.55 m |
|---|---|---|---|---|---|---|
| n | 9 | 16 | 26 | 19 | 22 | 10 |
| $SiO_2$ | 55.49 (0.26) | 77.07 (0.24) | 48.03 (0.37) | 49.55 (0.31) | 49.75 (0.27) | 47.77 (0.35) |
| $TiO_2$ | 1.29 (0.17) | 0.36 (0.04) | 2.91 (0.13) | 3.22 (0.12) | 2.18 (0.07) | 4.89 (0.25) |
| $Al_2O_3$ | 15.88 (0.62) | 12.41 (0.10) | 13.78 (0.61) | 12.84 (0.42) | 13.57 (0.13) | 12.55 (0.11) |
| FeO | 10.31 (1.18) | 1.72 (0.13) | 9.80 (0.54) | 15.54 (0.46) | 12.96 (0.54) | 14.82 (0.40) |
| MnO | 0.22 (0.05) | 0.09 (0.06) | 0.17 (0.06) | 0.34 (0.08) | 0.21 (0.08) | 0.26 (0.04) |
| MgO | 4.18 (0.27) | 0.35 (0.03) | 7.10 (0.67) | 3.78 (0.12) | 6.78 (0.31) | 4.99 (0.08) |
| CaO | 8.36 (0.70) | 1.78 (0.12) | 13.40 (0.74) | 8.66 (0.19) | 11.55 (0.13) | 9.84 (0.10) |
| $Na_2O$ | 3.06 (0.79) | 4.08 (0.11) | 2.37 (0.32) | 3.44 (0.24) | 2.50 (0.18) | 3.17 (0.12) |
| $K_2O$ | 0.91 (0.20) | 2.13 (0.06) | 1.93 (0.15) | 0.98 (0.06) | 0.27 (0.02) | 0.78 (0.02) |
| $P_2O_5$ | 0.21 (0.04) | 0.02 (0.02) | 0.50 (0.03) | 1.65 (0.08) | 0.24 (0.02) | 0.86 (0.31) |
| Cl | 0.09 (0.02) | n/a | n/a | n/a | n/a | 0.06 (0.02) |
| Total Oxides | 98.43 (0.32) | 98.99 (0.92) | 98.46 (0.42) | 98.10 (0.66) | 98.00 (0.97) | 97.03 (0.61) |
| n | 6 | 8 | 8 | 10 | 7 | 6 |
| Sc | 12.0 (10.9) | 6.66 (9.25) | 23.0 (6.92) | 10.7 (8.90) | 18.3 (8.14) | 9.75 (5.85) |
| Rb | 28.4 (4.35) | 36.5 (6.55) | 30.0 (5.28) | 29.3 (4.25) | 15.4 (4.17) | 6.95 (1.84) |
| Sr | 201 (74.0) | 82.1 (16.6) | 222 (58.2) | 386 (199) | 75.9 (20.9) | 198 (51.4) |
| Y | 13.0 (4.66) | 11.0 (5.98) | 10.2 (2.57) | 40.4 (21.4) | 9.99 (5.07) | 17.7 (4.26) |
| Zr | 93.7 (6.74) | 145 (27.3) | 108 (13.8) | 278 (121) | 98.7 (9.01) | 94.0 (21.8) |
| Nb | 2.35 (1.03) | 0.99 (1.06) | 23.6 (7.86) | 32.5 (17.2) | 2.26 (1.62) | 13.8 (4.47) |
| Ba | 455 (84.5) | 788 (51.6) | 504 (15.3) | 210 (55.0) | 175 (44.8) | 89.6 (15.2) |
| La | 5.48 (0.99) | 7.35 (1.65) | 15.5 (4.08) | 24.1 (11.4) | 3.63 (0.92) | 10.8 (3.12) |
| Ce | 10.1 (1.72) | 13.5 (4.30) | 29.4 (8.01) | 52.4 (24.9) | 7.47 (1.46) | 22.3 (6.10) |
| Pr | 1.48 (0.35) | 1.68 (0.62) | 3.66 (1.07) | 7.33 (3.71) | 1.02 (0.35) | 2.75 (0.86) |
| Nd | 7.35 (3.16) | 7.86 (2.25) | 13.9 (3.75) | 34.4 (18.6) | 4.09 (2.56) | 13.6 (4.02) |
| Sm | 2.02 (0.63) | 1.71 (0.90) | 2.46 (0.60) | 9.41 (5.89) | 1.25 (0.93) | 2.70 (1.14) |
| Eu | 1.45 (0.40) | 1.17 (0.69) | 0.84 (0.39) | 3.46 (1.77) | 0.88 (0.71) | 0.93 (0.75) |
| Gd | 1.11 (0.83) | 1.77 (1.50) | 2.14 (0.77) | 7.34 (4.21) | 0.96 (0.81) | 3.21 (1.94) |
| Tb | 0.13 (0.15) | 0.14 (0.11) | 0.37 (0.15) | 1.18 (0.66) | 0.26 (0.13) | 0.37 (0.10) |
| Dy | 2.06 (1.27) | 1.03 (0.76) | 1.78 (0.41) | 6.32 (3.34) | 1.57 (0.95) | 2.70 (1.47) |
| Ho | 0.37 (0.09) | 0.43 (0.24) | 0.32 (0.11) | 1.04 (0.59) | 0.24 (0.13) | 0.56 (0.17) |
| Er | 0.99 (0.39) | 1.22 (0.85) | 0.89 (0.29) | 2.55 (1.53) | 0.65 (0.38) | 1.40 (0.51) |
| Tm | 0.19 (0.03) | 0.19 (0.11) | 0.20 (0.09) | 0.33 (0.15) | 0.07 (0.04) | 0.18 (0.08) |
| Yb | 0.88 (0.57) | 1.20 (0.78) | 0.93 (0.33) | 2.11 (1.11) | 0.79 (0.43) | 1.21 (0.62) |
| Lu | 0.24 (0.10) | 0.22 (0.12) | 0.12 (0.07) | 0.41 (0.24) | 0.12 (0.05) | 0.18 (0.06) |
| Hf | 2.01 (0.54) | 3.63 (0.86) | 2.38 (0.60) | 4.25 (1.57) | 1.98 (0.47) | 1.89 (0.57) |
| Ta | 0.20 (0.06) | 0.36 (0.11) | 1.27 (0.43) | 1.28 (0.89) | 0.22 (0.23) | 0.80 (0.24) |
| Th | 1.52 (0.27) | 2.52 (0.38) | 2.35 (0.39) | 2.24 (0.63) | 1.01 (0.26) | 1.14 (0.21) |
| U | 0.66 (0.38) | 0.74 (0.22) | 0.62 (0.15) | 0.55 (0.19) | 0.39 (0.05) | 0.50 (0.07) |

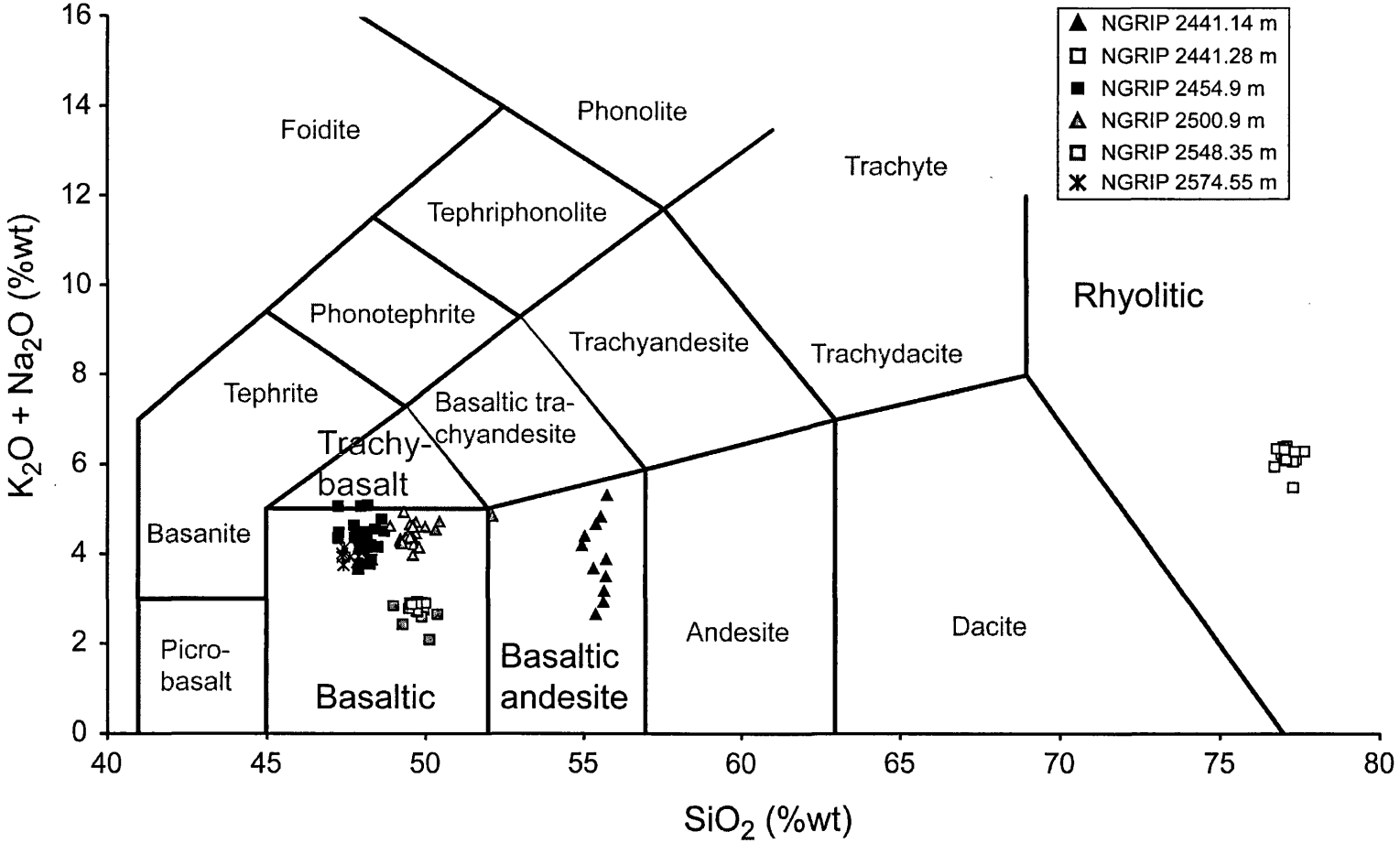


**Figure 5.6:** Total alkalis versus silica plot for geochemical analyses from six NGRIP tephra horizons. Chemical classification and nomenclature after Le Maitre et al. (1989).

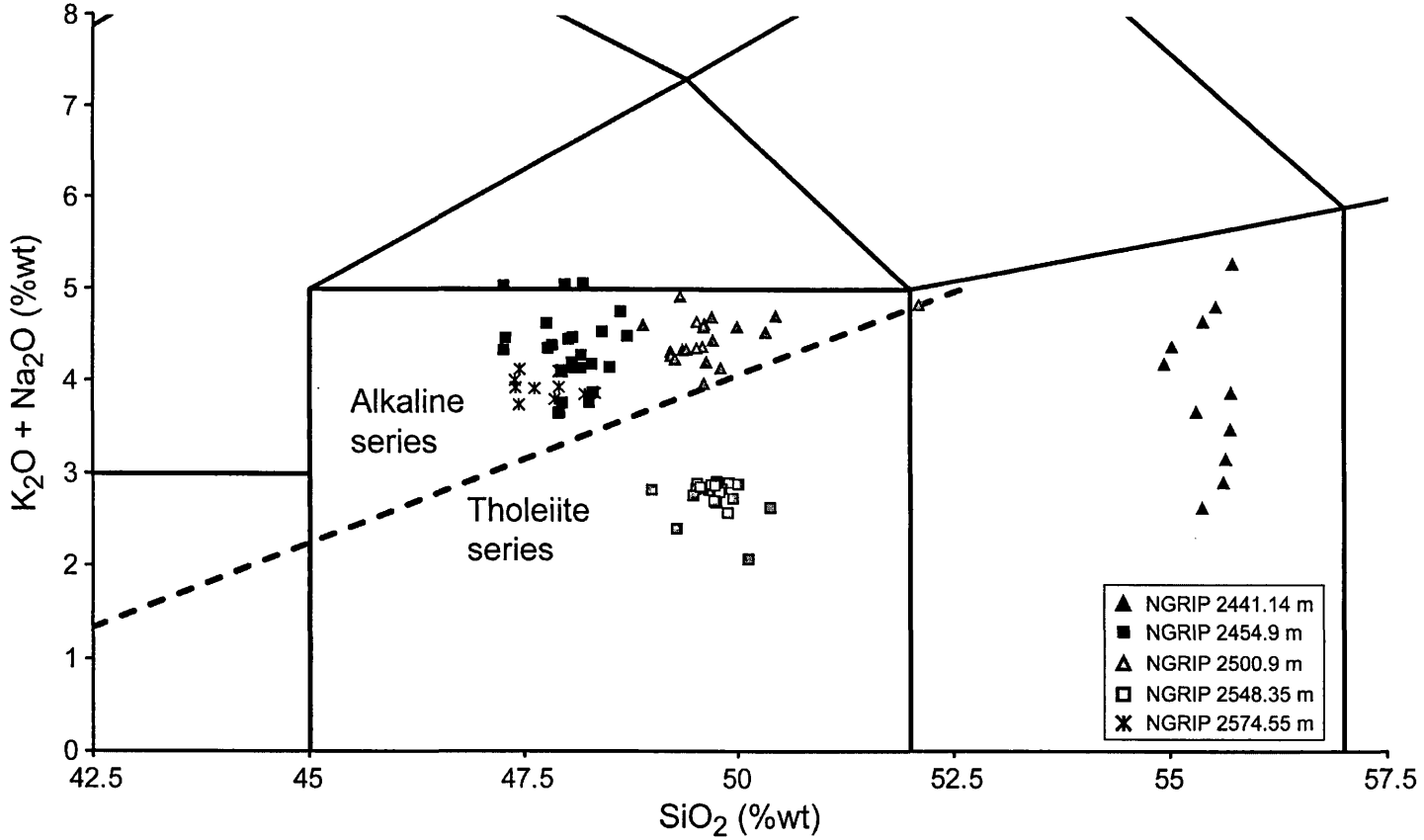


**Figure 5.7:** Inset of the total alkalis versus silica plot from figure 5.6 focusing on the basaltic and basaltic andesitic horizons from the NGRIP ice-core. The dashed line represents the subdivision of volcanic rocks into alkaline and subalkaline (tholeiitic) series. The boundary utilised was defined by MacDonald and Katsura (1964).

The trace element composition of six or more individual shards from each horizon was characterised using LA-ICP-MS (table 5.2) and figure 5.8 illustrates the chondrite-normalised REE profiles from each of the horizons with the individual and average profiles shown.

## 5.4 Geochemistry of the NGRIP Tephra Horizons and Source Identification

### 5.4.1 NGRIP 2441.14 m

The tephra horizon at 2441.14 m depth is composed of dark brown, blocky glass shards with a diameter of ~25 µm. This horizon was deposited during the stadial period following the DO 18 climatic event (figure 5.5a). The high resolution sulphate chemostratigraphy for the core shows that this horizon is directly related to a minor peak in sulphate concentration of 300 ppbw (figure 5.5b (i)).

Eleven shards from this horizon were analysed by EPMA and all exhibit a basaltic-andesitic composition (figure 5.6). Two outliers from the main population with anomalous $Al_2O_3$ and MgO concentrations were identified and removed from further analysis.

The geochemistry of this horizon is characterised by $SiO_2$ concentrations of approximately 55.5 %wt, MgO concentrations of ~3.9-4.5 %wt and low FeO concentrations between 9-11.5 %wt. Some elements such as FeO and CaO have large compositional ranges; however such heterogeneity is characteristic of volcanic glass with a basaltic andesitic affinity and analyses all fall on the same geochemical trends (figure 5.9b; Lacasse et al., 1996). Low total alkali values for this horizon (3-5 %wt) suggest that these shards are related to the tholeiitic rock series of Iceland. This is supported by the low $TiO_2$ and FeO concentrations of the shards, which are also characteristic geochemical features of the tholeiitic rock suite (Jakobsson et al., 2008). As a consequence this horizon can be regarded as having a source from a volcanic system within the Icelandic rift zone.

Material of a basaltic-andesitic composition is rarely produced by Icelandic volcanic centres and only the Hekla volcanic system has regularly erupted material of this composition (Jakobsson, 1979). Recent examples include the Hekla eruptions of 2000

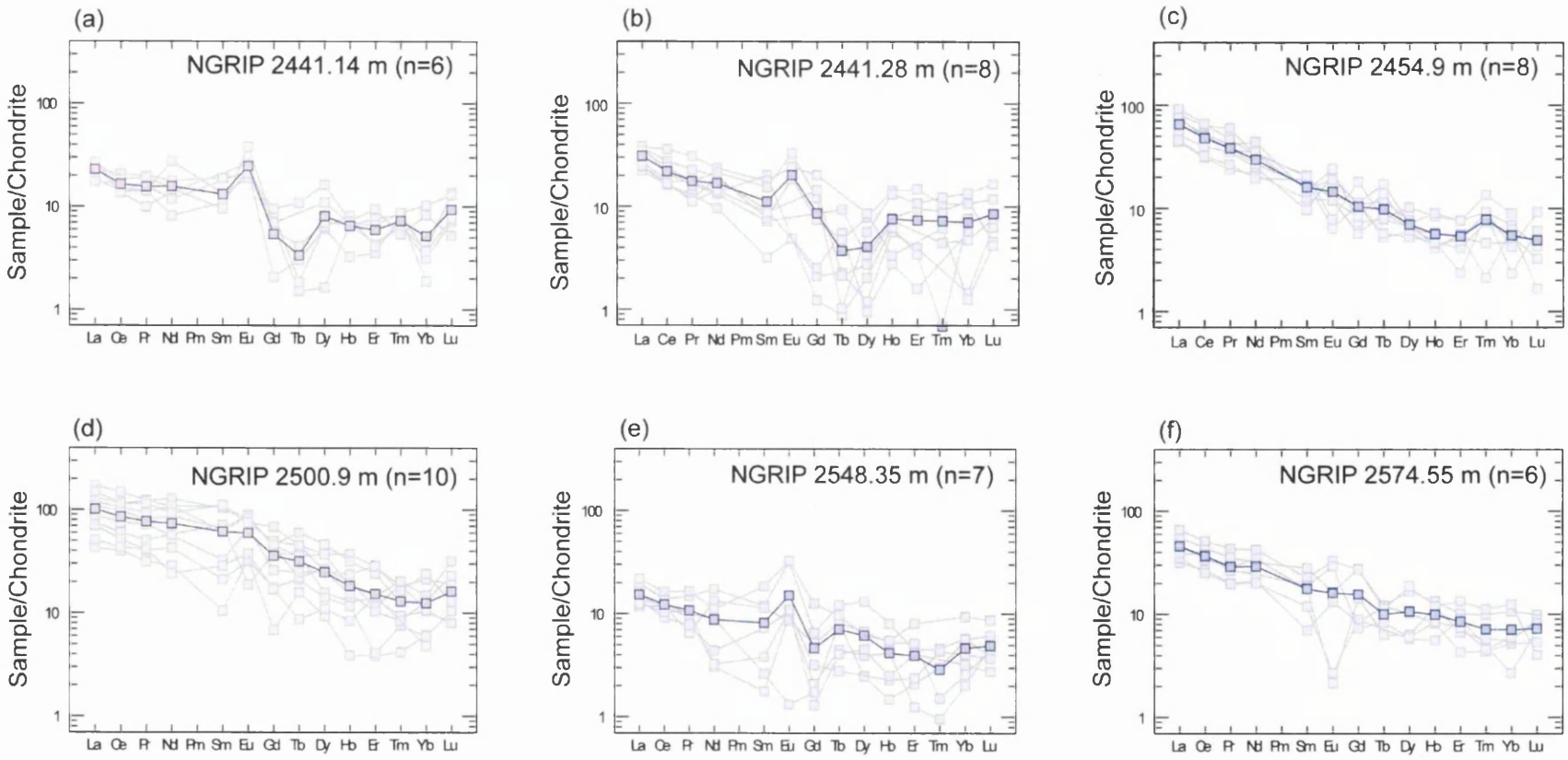


**Figure 5.8:** Chondrite-normalised REE profiles for individual tephra shards from (a) NGRIP 2441.14 m (b) NGRIP 2441.28 m (c) NGRIP 2454.9 m (d) NGRIP 2500.9 m (e) NGRIP 2548.35 m and (f) NGRIP 2574.55 m. The average REE profile for each horizon is highlighted. Chondrite values from Sun and McDonough (1989).

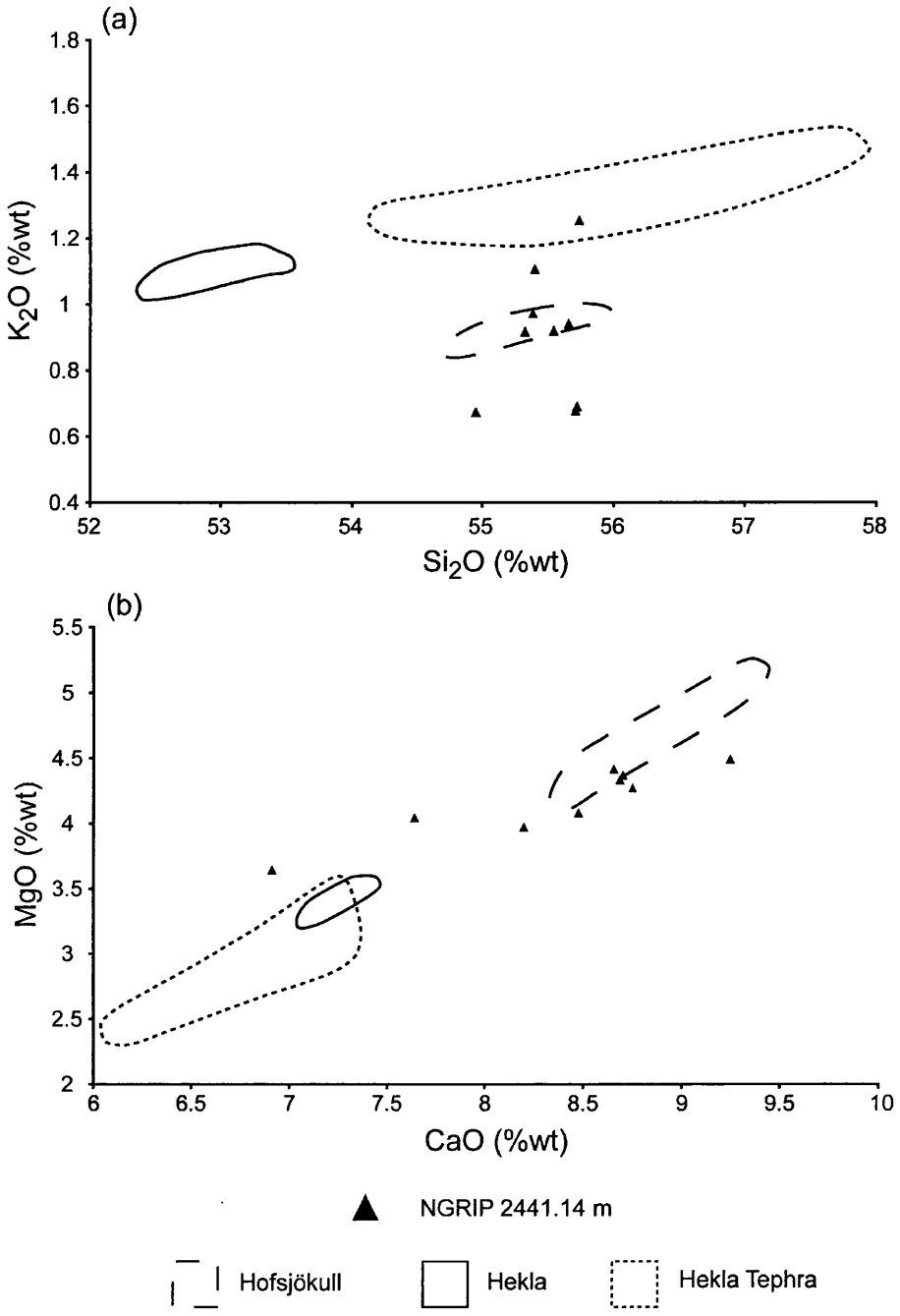


**Figure 5.9:** Geochemical data from NGRIP 2441.14 m compared to geochemical fields for basaltic andesitic products of the Hofsjökull and Hekla volcanic systems on (a) $SiO_2$ vs. $K_2O$ and (b) CaO vs. MgO compositional variation diagrams. Geochemical fields for Hofsjökull and Hekla whole rock analyses defined using data from Jakobsson et al. (2008) and Jakobsson (1979) respectively. Geochemical field for Hekla tephra products defined using analyses from Haflidason et al. (2000), Höskuldsson et al. (2007) and Wastegård et al. (2008).

AD and 1970 AD (Hökuldsson et al., 2007). In addition, basaltic andesitic material is occasionally identified within distal deposits attributed to the Hekla volcanic centre, typically in association with more evolved material (e.g. Boygle, 1994; Wastegård et al., 2008). However, the Hekla volcanic system is located in the southern flank zone of Iceland and thus produces material with an affinity to the transitional alkali rock suite.

Figure 5.9 compares the geochemical composition of NGRIP 2441.14 m to the basaltic andesitic products of the Hekla volcanic system. In addition, a geochemical field for basaltic andesitic material from the Hofsjökull system, based on four analyses reported in Jakobsson et al. (2008), is included because these analyses have a tholeiitic composition and the volcanic system is located within the Icelandic rift zone.

As expected the plots show that the geochemistry of the NGRIP 2441.14 m tephra horizon displays little affinity to both the whole rock and tephra analyses attributed to the Hekla system. Greater affinity is observable between the horizon and the basaltic andesitic products of the Hofsjökull system. Similarity coefficients comparisons between the average composition of NGRIP 2441.14 m and the analyses used to construct the geochemical fields in figure 5.9 support this observation, with the highest values observed for the comparison to the Hofsjökull products (table 5.3).

**Table 5.3:** Range of similarity coefficients calculated for comparisons between the average geochemical composition of NGRIP 2441.14 m and analyses used to construct the geochemical fields displayed in figure 5.9.

| | Hofsjökull Whole Rock | Hekla Whole Rock | Hekla Tephra Horizons |
|---|---|---|---|
| n | 4 | 4 | 12 |
| NGRIP 2441.14 m | 0.90-0.91 | 0.76-0.84 | 0.80-0.82 |

Overall, these comparisons support the proposition of an Icelandic rift zone source for this horizon and the Hofsjökull volcanic system may be the source. However, due to the limited amount of data from Icelandic basaltic andesitic material for comparative purposes, other systems within the rift zone cannot be ruled out as potential sources.

Figure 5.8a illustrates the REE profiles for the six shards from this basaltic andesitic horizon. The average REE profile shows a relatively flat pattern for both the HREEs and the LREEs, a distinct positive Eu anomaly and depletion in Gd and Tb. This pattern is generally observed for all of the individual shards analyses with more coherency between the profiles for the LREEs than the HREEs and the positive Eu anomaly is a distinct feature of all of the profiles.

An end member REE characterisation of Icelandic basaltic andesitic material has not been defined for comparative purposes, however REE concentrations are expected to be enriched relative to basaltic material due to the greater geochemical evolution of basaltic-andesitic. This is not the case for the NGRIP 2441.14 m horizon with the LREEs having concentrations similar to evolved tholeiitic basalt and the concentrations for the HREEs are lower than the proximal material (figure 5.10). In addition, the overall shape of the NGRIP 2441.14 m profile is uncharacteristic of Icelandic products, with the most distinct feature of the profile, the strong positive Eu anomaly, not being observed within any published proximal characterisations. Therefore, this characterisation may represent a previously unrecognised REE profile for Iceland, however, other factors may have contributed to this distinct REE profile. The strong positive Eu anomaly may be due to either polyatomic interference or the contamination of the juvenile glass by micro-inclusions within the tephra shards.

The potential for $^{137}Ba^{16}O$ to interfere with measurements of $^{153}Eu$ concentrations within the LA-ICP-MS system was highlighted in section 4.3.2. However, it is unlikely that polyatomic interference is the solitary factor causing the positive Eu anomaly within NGRIP 2441.14 m because it should not influence the remaining REEs.

It is more likely that the presence of micro-inclusions has influenced the REE profile. Tephra shards can contain micro-inclusions of various minerals that are present within lavas, such as augite, plagioclase, olivine and Fe-Ti oxides (Shane, 2000; Sigurdsson et al., 1978). Plagioclase, is a prominent phenocryst phase within most Icelandic basalts and has been identified as a micro-inclusion within Icelandic basaltic tephra deposits (Meyer et al., 1985; Larsen et al., 2001). This micro-inclusion tends to be severely depleted in all of the REE, apart from Eu (figure 5.10). Therefore, the incorporation of plagioclase in an analysis of juvenile glass would cause an overall depletion in the measured concentrations of the REEs relative to the actual composition of the glass. However, the depletion in Eu concentrations would be less pronounced due to the relative enrichment of this element within plagioclase.

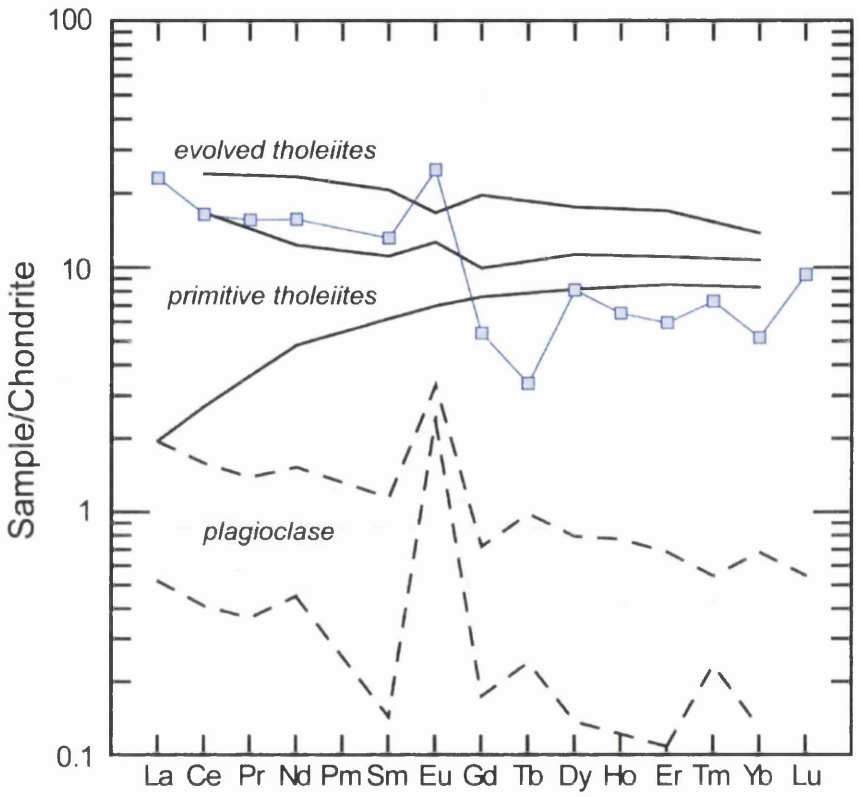


**Figure 5.10:** Comparison of the average REE pattern for the NGRIP 2441.14 m tephra horizon to the end-member characterisation of Icelandic tholeiitic material (Óskarsson et al., 1982) and a geochemical field for plagioclase identified within Icelandic tholeiitic basalts by Hansen and Grönvold (2000).

### 5.4.2 NGRIP 2441.28 m

The clear platy glass shards that characterise the tephra horizon at 2441.28 m depth range in diameter between 30 and 50 μm and in total 24 shards were identified and 16 were analysed geochemically. This horizon was deposited during the stadial period following DO 18, shortly before NGRIP 2441.14 m. The deposition of this horizon can also be directly related to the deposition of atmospheric sulphates on the ice sheet as figure 5.5b (ii) demonstrates that a peak in sulphate concentrations of 500 ppbw coincides with this horizon.

NGRIP 2441.28 m has a relatively homogenous composition with $SiO_2$ concentrations of ~77 %wt, FeO concentrations between 1.5 and 1.9 %wt and $K_2O$ concentrations of approximately 2.13 %wt. Figure 5.6 illustrates that this is the only horizon composed of rhyolitic material identified within the MIS 4 section of the NGRIP ice-core. It was highlighted in section 2.4.4 that the most likely source of tephra horizons deposited within the Greenland ice-cores is Iceland due to its relative proximity and high explosivity. Figure 5.11 compares the FeO and CaO concentrations for the NGRIP horizon with analyses of both whole rock samples, representing all of the central volcanoes in Iceland reported by Jónasson (2007), and tephra horizons sourced from Icelandic volcanic systems. This comparison demonstrates that the combination of FeO and CaO concentrations for the shards within NGRIP 2441.28 m are significantly different from those recorded for both the whole rock and tephra material. Furthermore, the Icelandic material is classified as having a higher-Fe composition, according to the boundary line defined by Warshaw and Smith (1988), whereas the NGRIP 2441.28 m horizon exhibits a lower-Fe composition. Therefore, it is highly unlikely that this horizon was derived from an Icelandic volcanic system.

Based on proximity to the depositional site the next most likely source for this horizon is the Jan Mayen volcanic region, however Jan Mayen products are potassic with high $K_2O$ concentrations in excess of those measured for this horizon.

Other potential sources of rhyolitic horizons were highlighted in section 2.4.4 and include the Alaskan and Aleutian Peninsula, Kamchatka-Kurlie Islands and Japanese volcanic regions. The biplots in figure 5.12 highlight geochemical similarities between the products of these three volcanic regions and the geochemistry of NGRIP 2441.28 m. In particular, this horizon shows a close affinity to the products of the Japanese volcanic regions as it consistently falls within the compositional field for this region.

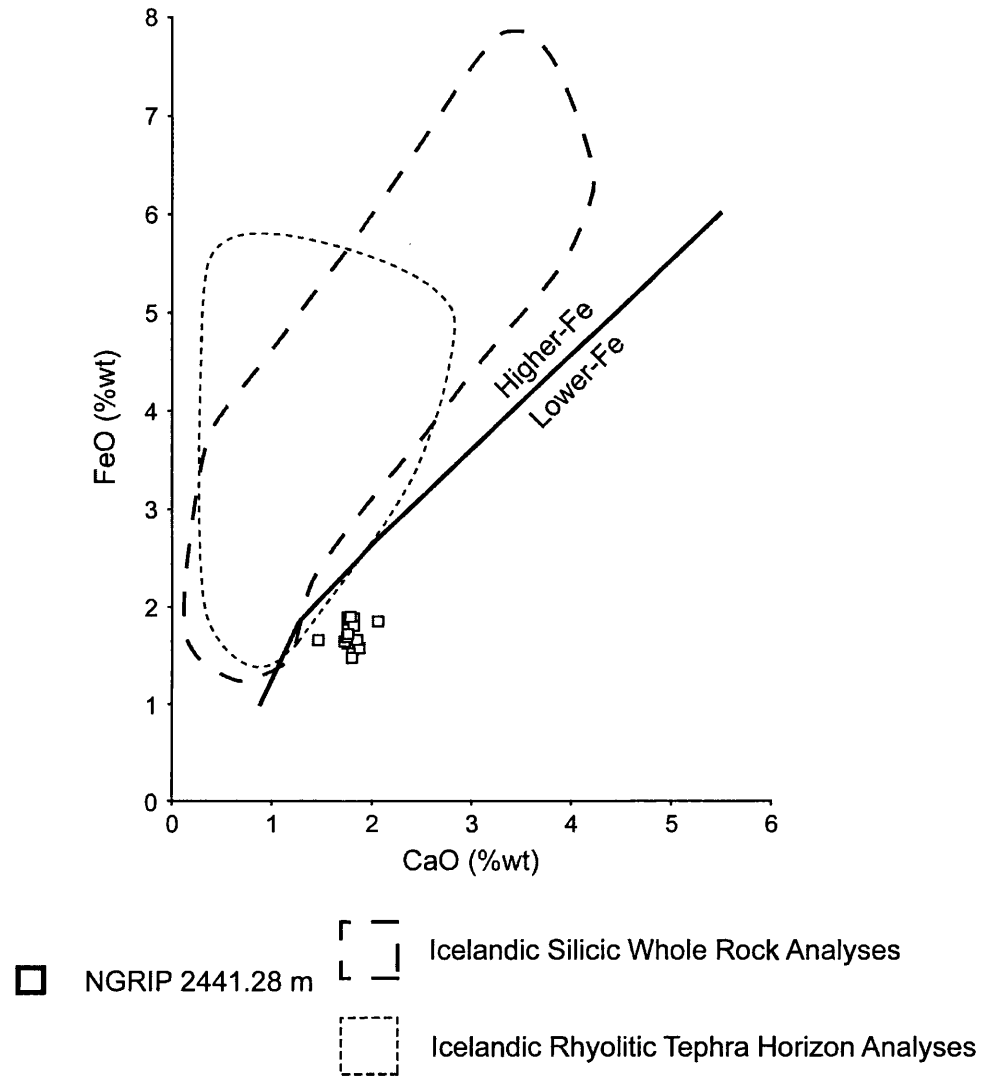


**Figure 5.11:** Comparison of geochemical data for the NGRIP 2441.28 m tephra horizon to geochemical fields for Icelandic whole rock and tephra material on a CaO vs. FeO compositional variation diagram. Geochemical field for Icelandic whole rock products from figure 4 of Jónasson (2007). Geochemical field for Icelandic rhyolitic tephra horizons based on data reported in Haflidason et al. (2000), Larsen et al. (1999) and Wallrabe-Adams and Lackschewitz (2003). Division line between higher-Fe and lower-Fe types from Warshaw and Smith (1988).

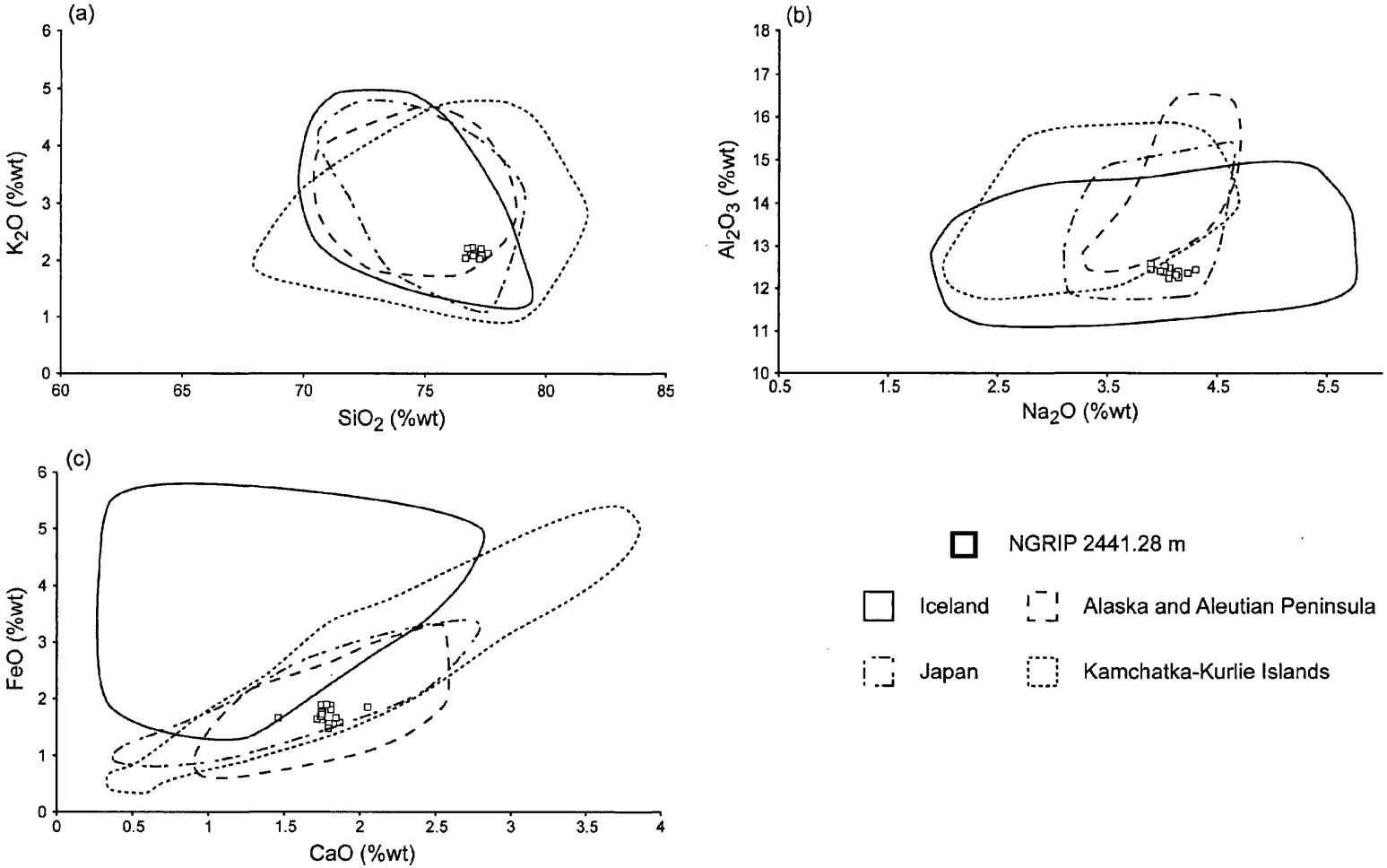


**Figure 5.12:** (a) $SiO_2$ vs. $K_2O$ (b) $Na_2O$ vs. $Al_2O_3$ and (c) CaO vs. FeO compositional variation diagrams comparing geochemical data from NGRIP 2441.28 m to the typical ranges of rhyolitic material from four volcanic systems identified as potential sources for tephra deposited in the Greenland ice-cores. Data used for the definition of the geochemical fields from Haflidason et al. (2000), Larsen et al. (1999) and Wallrabe-Adams and Lackschewitz (2003) (Iceland), Kaufman et al. (2001) and Preece et al. (1999, 2000) (Alaska and Aleutian Peninsula), Machida (1999) and Aoki and Machida (2006) (Japan) and Cao et al. (1995) (Kamchatka-Kurlie Islands).

An inspection of the tephrochronological frameworks for the Alaskan and Aleutian Peninsula, Kamchatka-Kurlie Islands and Japanese volcanic regions has identified horizons from all of these regions erupted during the MIS 4-6 period. Geochemical similarities between any of these deposits and NGRIP 2441.28 m may provide evidence for the source of this eruption or potentially correlative horizons.

The K3 tephra horizon was identified within the MIS 4 section of a marine core from the Sea of Okhotsk by Gorbarenko et al. (2002) and is believed to have been sourced from the Nemo Volcano, Onekotan Island, Kurile Islands. A direct correlation between this horizon and NGRIP 2441.28 m is unlikely as the similarity coefficient value for the comparison of the records is 0.908, and below the threshold for identical eruptions of 0.95.

Within the tephrochronological record for Alaskan eruptions no MIS 4 horizons have been identified, however Kaufman et al. (2001) described and geochemically characterised three rhyolitic tephra horizons from a MIS 5 sequence from south-western Alaska. Two of these horizons, the Togiak and Kulukak Bay tephras, were deposited during the MIS 5a substage and the Aeolis Mountain tephra was deposited during MIS 5d. Similarity coefficient comparisons to NGRIP 2441.28 m show that both the Togiak and Aeolis Mountain horizons are unrelated with values of 0.88 and 0.77 respectively. However, the Kulukak Bay tephra does display some compositional similarities to NGRIP 2441.28 m with similarity coefficient values of 0.944 and 0.932 for two different occurrences of this tephra (figure 5.13; Kaufman et al., 2001).

Japanese volcanic regions were particularly active between the last interglacial and the beginning of the last glacial period with approximately 33 tephra horizons identified (Aoki and Machida, 2006). Some of these horizons are widespread, for example, five of these horizons have been identified within the MD01-2412 core extracted from the Sea of Okhotsk (Sakamoto et al., 2006). Similarity coefficient comparisons between the geochemistry of these horizons and NGRIP 2441.28 m have a very wide range between 0.715 and 0.964. Similarity coefficients in excess of 0.95 were calculated for the comparisons between NGRIP 2441.28 m and three tephra horizons (Kc-2/3, Kc-4 and Kc-6) that were all erupted from the Kutcharo caldera on the island of Hokkaido, Japan during MIS 5b, 5d and 6 respectively. These similarities are illustrated by the strong overlaps between NGRIP 2441.28 m and the geochemistry of the Japanese horizons in figure 5.13. A broad similarity to the Kulukak Bay tephra can be observed, however there is a significant offset for the $Al_2O_3$ and CaO concentrations.

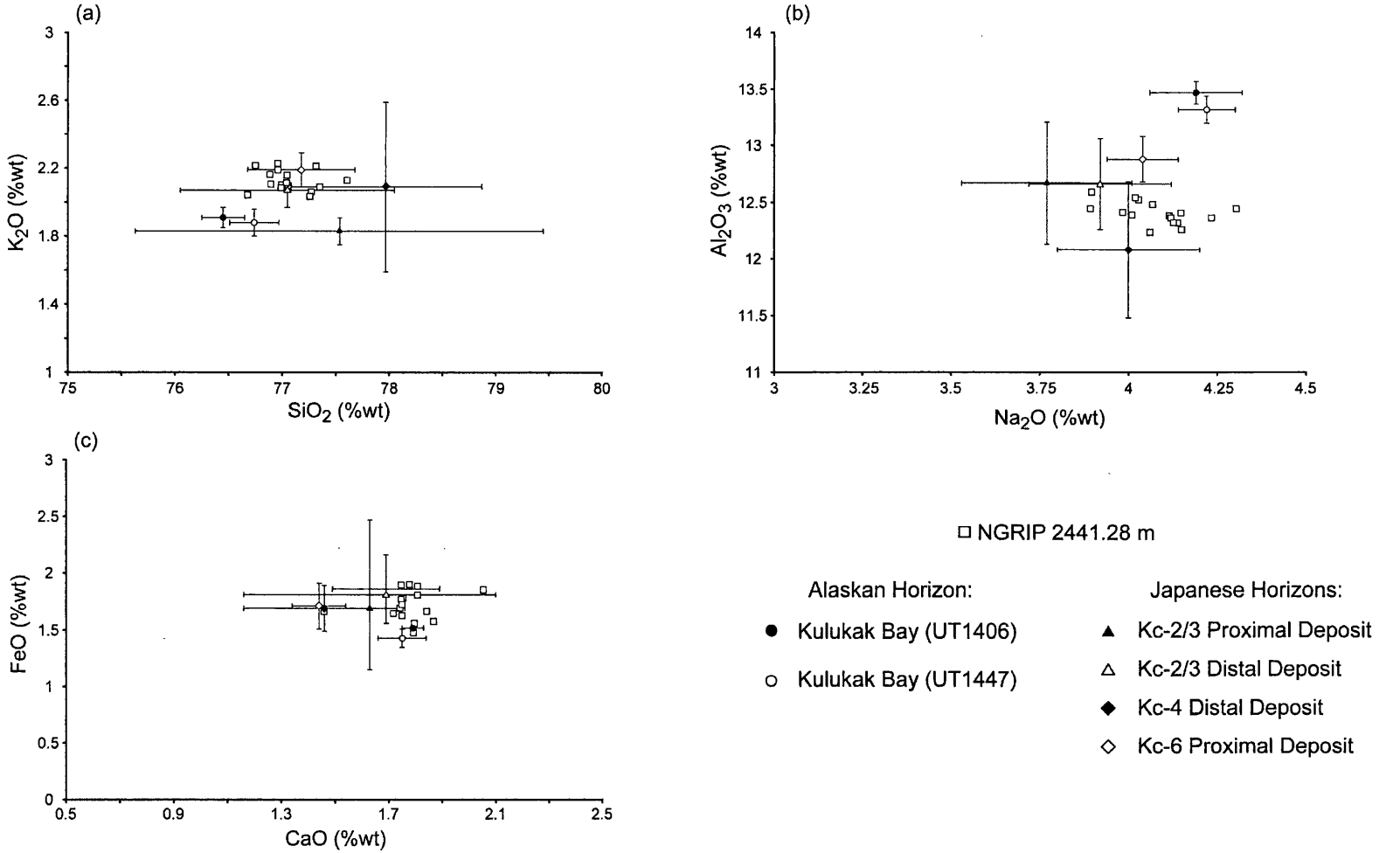


**Figure 5.13:** Geochemical comparison of analyses of individual shards from the NGRIP 2441.28 m tephra horizon to mean and standard deviation values for the Alaskan Kulukak Bay tephra horizon and three tephra horizons erupted from the Kutcharo Caldera, Hokkaido, Japan on (a) $SiO_2$ vs. $K_2O$ (b) $Na_2O$ vs. $Al_2O_3$ and (c) CaO vs. FeO compositional variation diagrams. Data for Kulukak Bay horizon from Kaufman et al. (2001). Analyses of proximal and distal deposits of the Japanese horizons from Aoki and Machida (2006) and Sakamoto et al. (2006) respectively.

Overall, a direct correlation between NGRIP 2441.28 m and a horizon previously recognised within geological archives cannot be determined. However, the major element geochemical similarities to Japanese proximal deposits and individual tephra horizons erupted from the Kutcharo caldera strongly indicate that this region was the source of NGRIP 2441.28 m.

The REE profiles of individual shards within this rhyolitic tephra horizon demonstrate a strong coherency for the LREEs from La to Nd, however strong heterogeneity can be observed for all of the remaining elements (figure 5.8b). This may be a consequence of greater analytical noise for the analysis of the HREEs due to their lower abundance and thus lower count rates during analysis (Pearce et al., 2007). The average profile gained from these individual analyses shows a gentle curve between La and Sm, a distinct positive Eu anomaly, depletion in Tb and Dy and a flat profile for the HREEs between Ho and Lu.

A comparison to the end-member REE and trace element characterisation for Icelandic silicic material appears to support the major element evidence that this horizon did not derive from an Icelandic source. Because, large differences can be observed in both the shape of the REE profiles and the absolute concentrations of the elements (figure 5.14a). The potential for this horizon to be sourced from Japan was determined using major element evidence and some similarities to the products of Japanese volcanic regions can be observed for the LREEs and HREEs, however there is significant deviation for the MREEs (figure 5.14b (i)). In addition, similarities in REE profile cannot be observed between NGRIP 2441.28 m and previously suggested sources in the North Pacific region (figure 5.14b (ii-iv)). Similarities to these proximal characterisations may have indicated that a miscorrelation to a Japanese source had been made.

The profile shape for NGRIP 2441.28 m displays strong similarities to the REE profile for NGRIP 2441.14 m (figure 5.10). Therefore, it appears that as with the trace element characterisations of NGRIP 2441.14 m the analyses of shards within NGRIP 2441.28 m represent either a previously unrecognised REE profile or they have been affected by the presence of micro-inclusions within the shards or polyatomic interference. Consequentially, the trace element characterisation of this horizon does not provide evidence that aids the identification of a volcanic source.

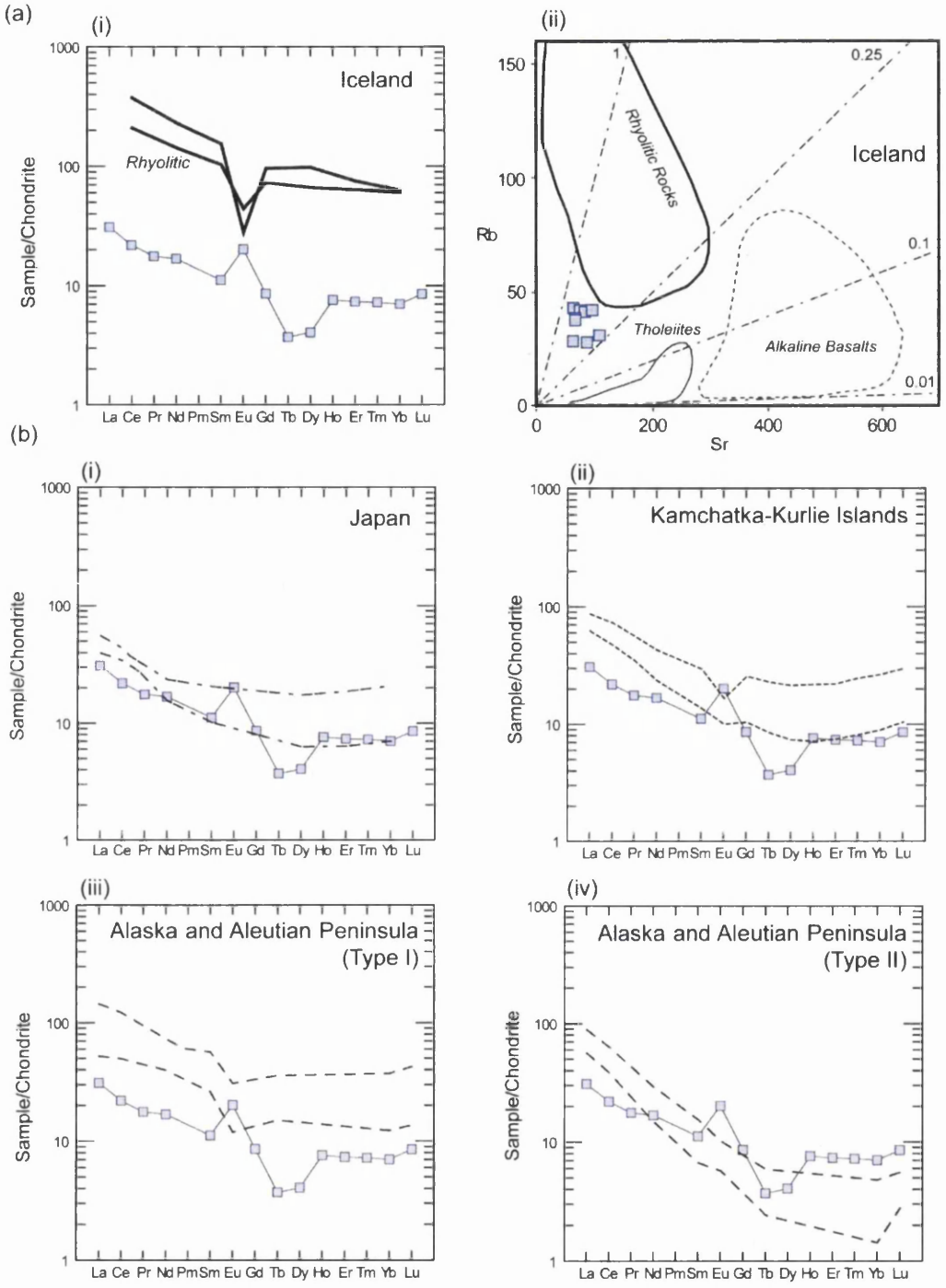


**Figure 5.14:** (a) (i) Average REE profile for NGRIP 2441.28 m compared to the end-member characterisation for Icelandic rhyolitic material defined by Óskarsson et al. (1982). (ii) Sr vs. Rb diagram comparing analyses from NGRIP 2441.28 m to geochemical fields defined by Óskarsson et al. (1982). (b) Average REE profile for NGRIP 2441.28 m compared to geochemical fields for the rhyolitic products of (i) Japan (Clift et al., 2003), (ii) Kamchatka and Kurlie Islands (Cao et al., 1995) and (iii and iv) Alaska and Aleutian Peninsula (Preece et al., 1999).

### 5.4.3 NGRIP 2454.9 m

45 glass shards were identified between 2454.85-2454.9 m depth in the NGRIP core. These shards are light greeny-brown in colour with a blocky morphology and contain occasional vesicles. Shard diameters range between 40 and 75 μm. This horizon was deposited during the stadial period shortly after the end of DO 18. Figures 5.5a and 5.5b (iii) show that this tephra horizon is associated with a large peak in sulphate concentrations of ~2250 ppbw; the highest levels of sulphate concentration within the study period.

Geochemical analyses show these shards have a basaltic to trachybasaltic composition with $SiO_2$ concentrations of ~48 %wt and high CaO concentrations of between 12.4 and 14.3 %wt (figure 5.6). The most distinguishing characteristic of their composition is high $K_2O$ values between 1.7-2.1 %wt. With the exception of one population of GRIP 2499.75 m these are the highest $K_2O$ values observed for all basaltic horizons identified within this study. $K_2O$ values of this magnitude are atypical for basalts from Icelandic volcanic systems, which range between 0.1 and 1 %wt (O'Nions and Grönvold, 1973; Haflidason et al., 2000). Based on a comparison to whole rock data from Jan Mayen products (Imsland, 1984) and a collation of analyses from Icelandic material the high $K_2O$ values imply that this horizon originated from the Jan Mayen volcanic region (figure 5.15). This suggestion is supported by further geochemical comparisons in figure 5.16.

The individual REE profiles measured from shards within NGRIP 2454.9 m, illustrated on figure 5.8c, demonstrate a relatively homogenous trace element composition, with a slight increase in variability for the less abundant HREEs. The average REE profile for this horizon is a steep curve between La and Ho and a relatively flat profile for the HREEs between Er and Lu.

The REE profile exhibits a very similar shape to proximal Jan Mayen deposits (figure 5.17a; Maaløe et al., 1986) although, the concentrations of trace elements are lower within the NGRIP material. The biplots in figure 5.17b (i) and (ii) support this observation with lower absolute concentrations shown for all of the elements. However, as shown on figure 5.17b (i), the ratio between Ce and La is the same for the NGRIP 2454.9 m analyses and the proximal deposits as they all fall on the same ratio trend line. These figures also highlight the greater variability within the concentrations of the less abundant elements of Lu and Yb.

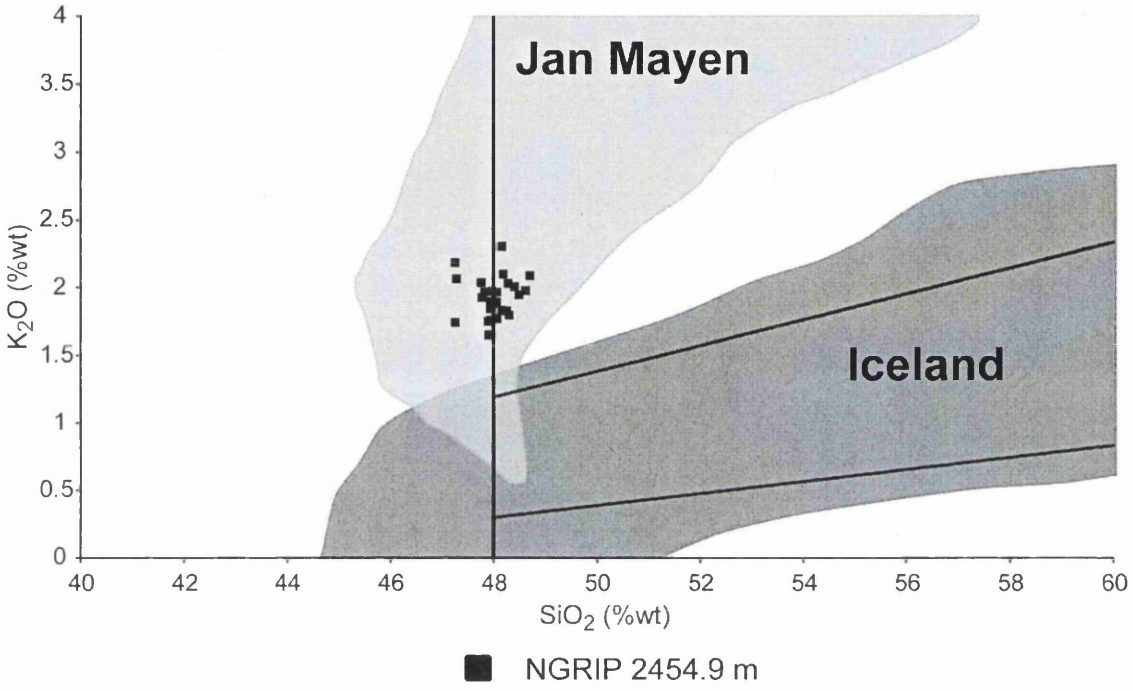


**Figure 5.15:** Geochemical data for the NGRIP 2454.9 m tephra horizon compared to geochemical fields for Icelandic and Jan Mayen proximal volcanic material on a $Si_2O$ vs. $K_2O$ variation diagram. Composition field for the typical composition of Jan Mayen volcanic products based on data from Imsland (1984). Composition field for the typical composition of Icelandic volcanic products based on data from Jakobsson (1979), Haflidason et al. (2000), Larsen et al., (2002) and Höskuldsson et al. (2006).

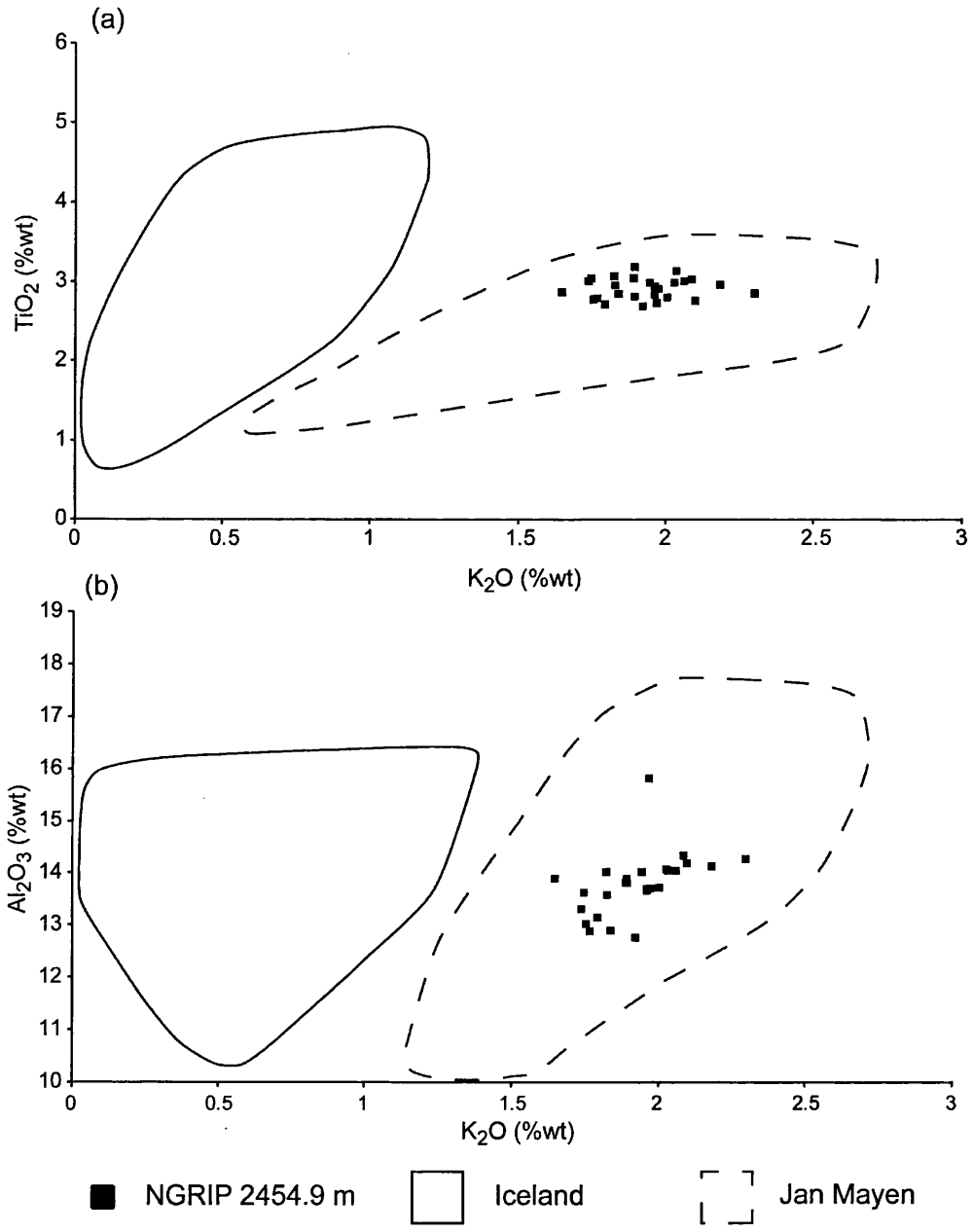


**Figure 5.16:** Geochemical data from the NGRIP 2454.9 m tephra horizon compared to geochemical fields for Icelandic and Jan Mayen proximal basaltic volcanic material on (a) $K_2O$ vs. $TiO_2$ and (b) $K_2O$ vs. $Al_2O_3$ compositional variation diagrams. Compositional field for Jan Mayen products based on data from Imsland (1984). Compositional field for Icelandic products based on data from tephra horizons with <50%wt $SiO_2$ summarised in Haflidason et al. (2000).

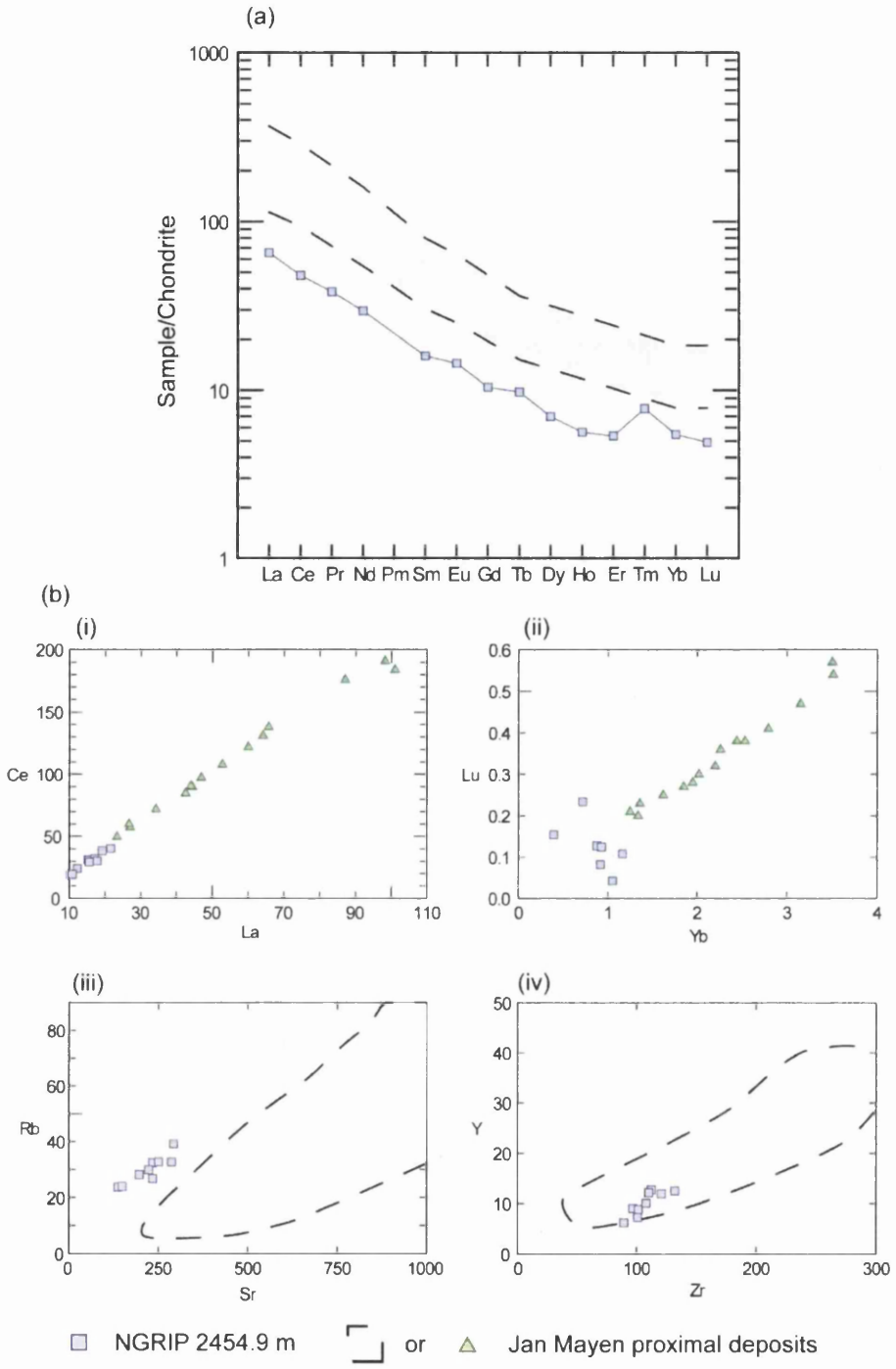


**Figure 5.17:** (a) Chondrite-normalised REE profile for NGRIP 2454.9 m compared to the typical REE profile of volcanic material proximal to the Jan Mayen volcanic region. (b) (i) La vs. Ce (ii) Yb vs. Lu (iii) Sr vs. Rb and (iv) Zr vs. Y compositional variation diagrams comparing individual shard analyses from NGRIP 2454.9 m to analyses of proximal Jan Mayen products. Analyses of proximal Jan Mayen material used in figures a and b(i) and (ii) from Maaløe et al. (1986). Data used to define geochemical fields in figures b(iii) and (iv) from Imsland (1984).

Imsland (1984) reported the concentration of the light trace elements Rb, Sr, Y and Zr within bulk analyses of basaltic and trachybasaltic material from the Jan Mayen volcanic region. These analyses were used to define the geochemical fields shown in figure 5.17b (iii) and (iv), and these biplots demonstrate that strong similarities exist between the Rb, Y and Zr concentrations from the NGRIP 2454.9 m analyses and the proximal deposits.

The overall similarities in the shape of the REE profile and the concentration of selected lighter trace elements suggests that the Jan Mayen volcanic region was the source of this tephra horizon. A possible explanation for the offset in the REE profiles is that gas blank misestimation occurred during the LA-ICP-MS analysis of shards from NGRIP 2454.9 m. Misestimation can cause offsets in absolute concentrations while the shape of profiles and ratios between trace elements are preserved (see section 4.4.3). However, it is also possible that the analyses reported by Maaløe et al. (1986) did not fully capture the compositional range of REEs within Jan Mayen products as only 15 analyses were reported. The greater similarities to the analyses of Rb, Sr, Y and Zr reported by Imsland (1984) may be due to the more comprehensive nature of this study with 68 proximal samples analysed.

### 5.4.4 NGRIP 2500.9 m

The shards identified between 2500.85-2500.9 m were greenish-brown in colour, blocky in morphology, contained occasional vesicles and range in diameter between 50 and 80 μm. This horizon was deposited shortly after the cooling transition at the end of DO 19a and can be directly related to a peak in sulphate concentrations (700 ppbw) measured through CFA (figure 5.5b (iv)).

Of 21 single-grain analyses gained from this horizon 2 were found to be consistent outliers from a main population (figure 5.18). Figure 5.7 demonstrates that all of the tephra shards from the main population of NGRIP 2500.9 m have a basaltic composition and their compositions fall above, but close to, the TAS division line defined by MacDonald and Katsura (1964). Implying that the material has an affinity to either the Icelandic alkaline or the transitional alkaline rock suite. A distinctive geochemical characteristic of this horizon is the high FeO values (average, 15.54 ± 0.46 %wt), the highest values for any of the horizons identified within this study. FeO concentrations of this magnitude are not observed within analyses of

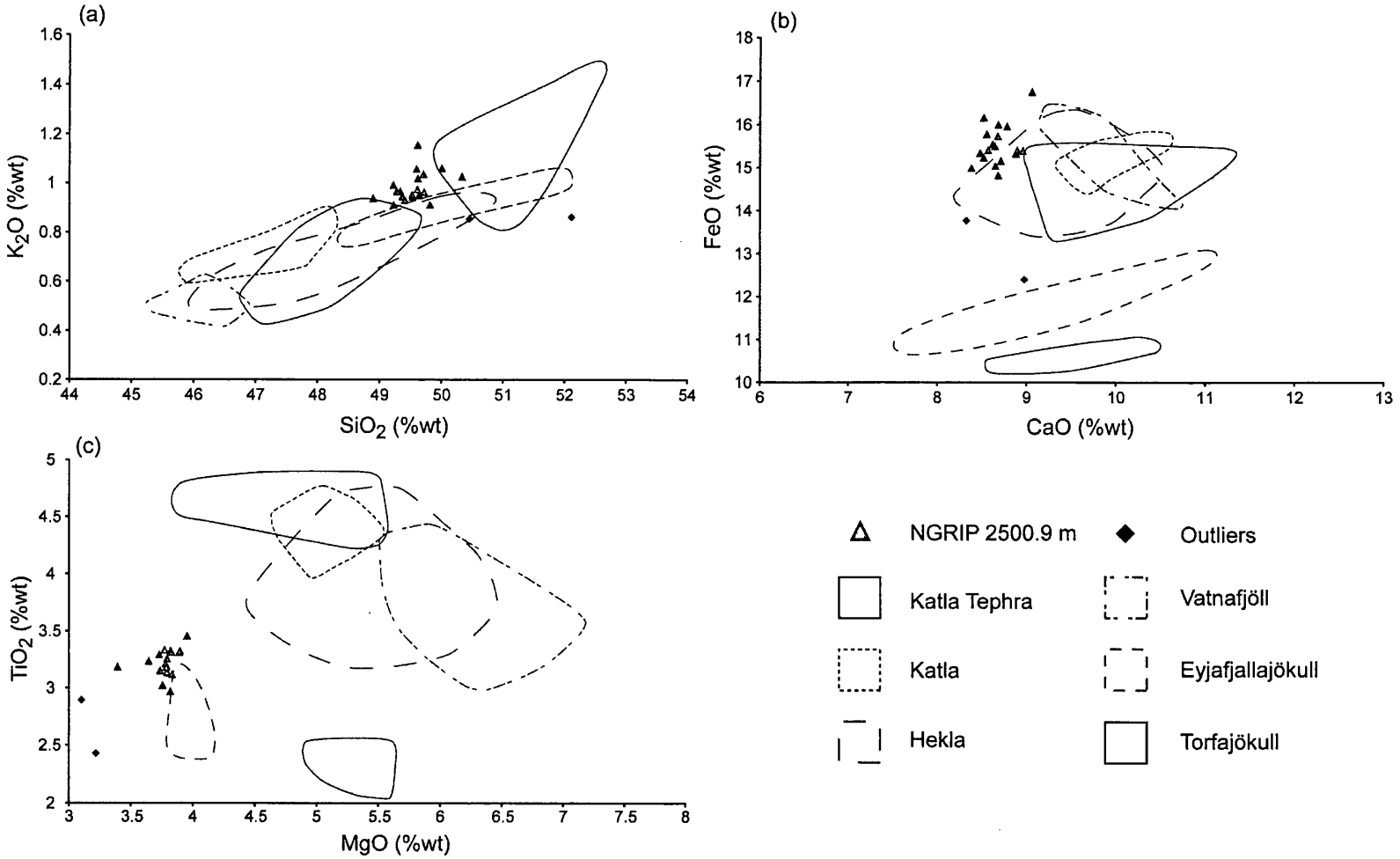


**Figure 5.18:** Geochemical data from the NGRIP 2500.9 m tephra horizon compared to geochemical fields for Icelandic transitional alkali volcanic systems plotted on (a) $SiO_2$ vs. $K_2O$ (b) CaO vs. FeO and (c) MgO vs. $TiO_2$ compositional variation diagrams. Geochemical field for tephra horizons from Katla based on average analyses in Haflidason et al. (2000). Geochemical fields for the five Icelandic volcanic systems defined using individual whole rock analyses presented in Jakobsson (1979) and Jakobsson et al. (2008).

alkaline basalts and coupled with low CaO concentrations of between 8.3 and 9.0 %wt this horizon is classified as having a transitional alkaline composition (Jakobsson et al., 2008). Material of this composition is produced by Icelandic volcanic systems within either the southern or eastern flank zones.

The biplots in figure 5.18 compare the geochemistry of NGRIP 2500.9 m to major element analyses of transitional alkaline basaltic lavas from the Katla, Hekla, Vatnafjöll, Torfajökull, and Eyjafjallajökull volcanic systems which are all located in either the southern or eastern flank zones (Jakobsson, 1979; Jakobsson et al., 2008). In addition, analyses from tephra horizons attributed to the Katla volcanic system that were compiled in Haflidason et al. (2000) are included.

The geochemical analyses from NGRIP 2500.9 m plot close to or within some of the geochemical fields defined for these volcanic systems, however they do not show a consistent affinity to one particular volcanic system. For example, on figures 5.18a and 5.18c the analyses plot close to the field defined for the Eyjafjallajökull system, however, the high FeO values for NGRIP 2500.9 m far exceed those measured for the Eyjafjallajökull basalts. Therefore at present the source volcanic system of this horizon remains unknown.

Figure 5.8d demonstrates that this horizon has the most heterogonous trace element composition relative to the other NGRIP horizons. In addition, the average REE concentrations and the elements lighter and heavier than the REEs are the highest measured from the NGRIP tephra horizons (table 5.2). The average REE profile for this horizon has a gentle slope for the LREEs that steepens for the MREEs and the HREEs and a slight positive Eu anomaly can be observed.

The major element composition of these shards indicates that this horizon has a transitional alkali basaltic composition. Although an end member composition has not been defined for Icelandic transitional alkali material, it is expected that the characteristic profile would lie between those for the tholeiitic and alkalic products (Óskarsson et al., 1982). The REE profile for NGRIP 2500.9 m overlaps with the end member characterisation of alkaline material; however the shape of the profile shows affinities to both characterisations (figure 5.19a). The relatively flat LREE profile is more similar to tholeiitic material and the steeper MREE and HREE profiles are more akin to alkali material. A comparison of Rb and Sr concentrations to typical Icelandic material (figure 5.19b) emphasises the heterogeneity observed within the REE concentrations

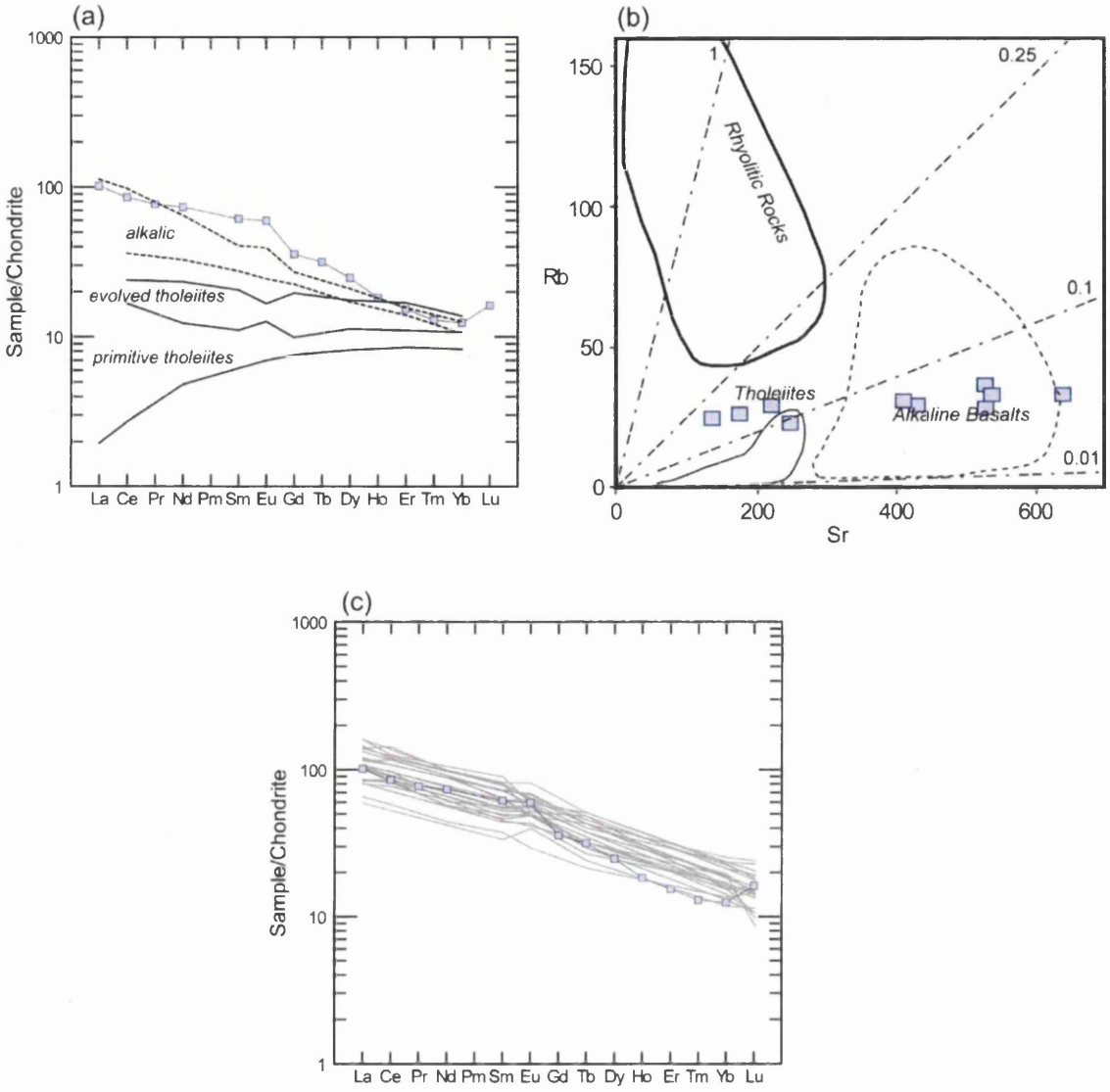


**Figure 5.19:** (a) Comparison between the chondrite-normalised average REE profile for NGRIP 2500.9 m and end-member characterisations of Icelandic tholeiitic and alkalic proximal deposits (Óskarsson et al., 1982). (b) Sr vs. Rb compositional variation diagram for NGRIP 2500.9 m and end-member characterisations of Icelandic material (Óskarsson et al., 1982). (c) Comparison between the chondrite-normalised average REE profile for NGRIP 2500.9 m and REE profiles for material produced by the Hekla and Katla volcanic systems reported in Meyer et al. (1985).

with a large spread in Sr values apparent. This heterogeneity appears to indicate that the Sr concentrations are not characteristic of one rock type and similarities to those measured within both tholeiitic and alkaline material can be observed, however, the average Sr concentration will fall within the field for alkalic basalts.

When the REE profile for NGRIP 2500.9 m is compared to profiles for transitional alkali material from the Hekla and Katla volcanic systems strong similarities in the absolute REE concentrations and the shape of the profiles can be observed, including the occurrence of slight positive Eu anomalies within the Icelandic proximal material (figure 5.19c). Despite these similarities one cannot ascribe a source from either of these volcanic systems to this horizon. Because, both were ruled out as potential sources based on major element compositional comparisons and REE profiles from other volcanic systems producing transitional alkali material have not been considered. However, the similarities do support the proposition that this horizon has a transitional alkali composition and was sourced from either the SFZ or EFZ of Iceland.

### 5.4.5 NGRIP 2548.35 m

Tephra shards were found in a 20 cm sample with a basal depth of 2548.35 m in the NGRIP ice-core. These shards are light green-brown in colour and range in size from 25 to 50 μm in diameter. This tephra horizon was deposited during the rapid cooling transition between DO 20 and the subsequent stadial period (figure 5.5a). This horizon occurs stratigraphically below a double peak in sulphate concentrations and the separation between the top depth of the horizon and the sulphate peak is 15 cm (figure 5.5b (v)).

Geochemical analyses from NGRIP 2548.35 m demonstrate that the shards have a basaltic composition and that it is the only NGRIP horizon of a basaltic tholeiitic nature (figure 5.7). This implies that the eruption producing this material occurred within the Icelandic rift zone. The geochemical characteristics of this horizon are $SiO_2$ values between 49 and 50 %wt, low $TiO_2$ concentrations of ~2.2 %wt and relatively high CaO concentrations of 11.1-11.7 %wt. Overall the composition of the horizon is homogenous with limited variation between individual shards and only one outlier was identified (figure 5.20).

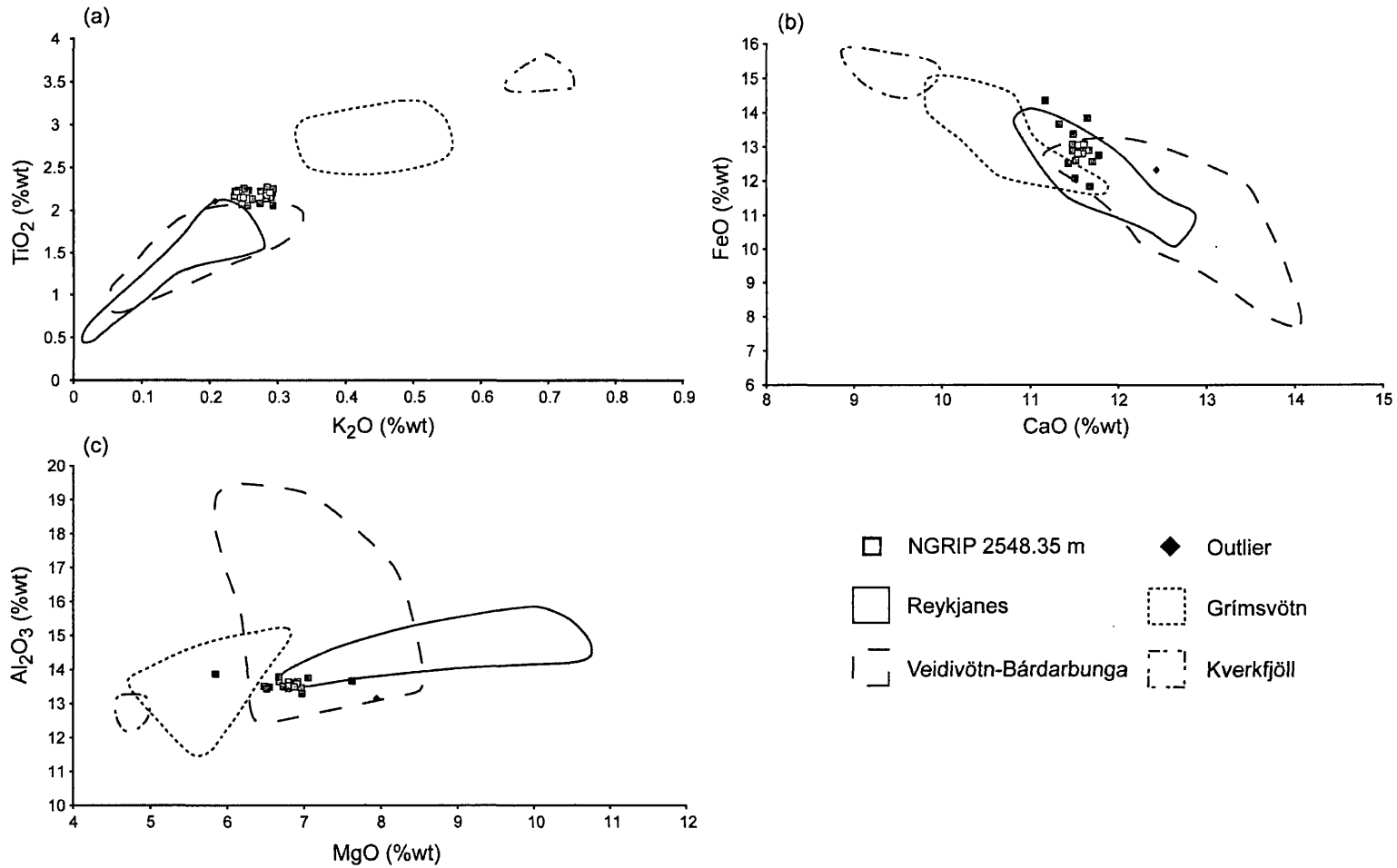


**Figure 5.20:** Geochemical data for NGRIP 2548.35 m compared to geochemical fields for four Icelandic tholeiitic volcanic systems on (a) $K_2O$ vs. $TiO_2$ (b) CaO vs. FeO and (c) MgO vs. $Al_2O_3$ compositional variation diagrams. Geochemical fields for the Grímsvötn and Veidivötn-Bárdarbunga volcanic systems defined using whole rock analyses from Jakobsson (1979) and analyses of tephra horizons complied by Haflidason et al. (2000). Geochemical field for the Reykjanes system defined using whole rock analyses from Jakobsson et al. (2008) and the Kverkfjöll system using whole rock data from Höskuldsson et al. (2006).

Deducing a source for tephra horizons originating from a rift zone source is complicated by the large amount of volcanic systems located in this zone, however not all are capable of producing widespread horizons (Jakobsson et al., 2008). Therefore, geochemical comparisons were made to the volcanic systems of Veidivötn-Bárdarbunga, Grímsvötn, Kverkfjöll and Reykjanes because of their high tephra production rates and explosivity during the postglacial period (Larsen and Eiríksson, 2008). In addition, three of the systems are located under the present ice cap and it has been suggested that the presence of water increases the explosivity of basaltic eruptions (Thordarson and Höskuldsson, 2008). It is assumed that ice extent during MIS 4 was greater than at present.

The biplots in figure 5.20 demonstrate that the NGRIP 2548.35 m horizon falls within or very close to the geochemical fields for the Reykjanes and Veidivötn-Bárdarbunga volcanic systems and both can be regarded as likely sources for this horizon. Major element similarities between these two volcanic systems constrains further source correlation.

This horizon displays strong geochemical similarities to a basaltic horizon deposited during MIS 5a; with a similarity coefficient of 0.956 when compared to the 5a-Low/BAS-I horizon described by Wastegård and Rasmussen (2001). Individual analyses from these horizons highlights the compositional similarities and suggests that these horizons have a common source from either the Reykjanes or Veidivötn-Bárdarbunga volcanic systems (figure 5.21). The relative stratigraphic position of the horizons demonstrates that despite the high geochemical similarities they do not represent the products of the same eruption; as NGRIP 2548.35 m was deposited at the end of DO 20 relative to the oxygen isotope ratio stratigraphy for the NGRIP core (figure 5.5). Whilst, based on the magnetic susceptibility curve for the MD95-2009 marine core 5a-Low/BAS-I lies stratigraphically at the beginning of DO 21 (Rasmussen et al., 2003).

Trace element analyses were gained from 7 individual shards within the NGRIP 2548.35 m tephra horizon and the REE profiles of these shards are illustrated on figure 5.8e. With the exception of the lightest REE, La, Ce and Pr, there is a large variation in the concentration of elements between the individual analyses. This can be attributed to the low concentration of the elements within these shards, which will produce lower counts and greater analytical noise during LA-ICP-MS analysis. Overall, the average REE profile for this horizon has a gentle slope with a distinct positive Eu anomaly, recorded in all but one of the individual analyses, and depletions in Gd, Ho, Er and Tm.

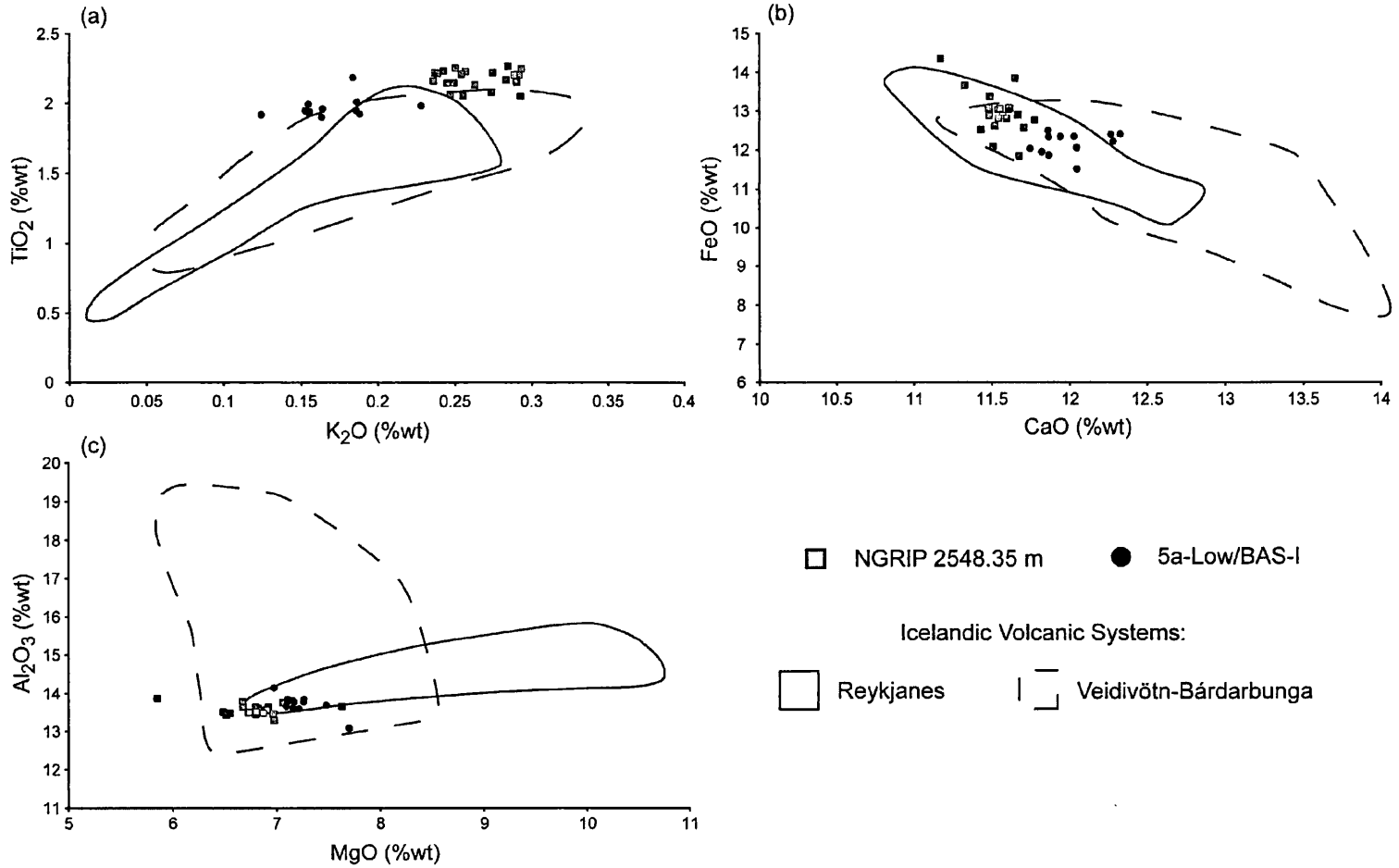


**Figure 5.21:** Comparison of individual shard analyses from the NGRIP 2548.35 m and 5a-Low/BAS-I tephra horizons and geochemical fields for the Veidivötn-Bárdarbunga and Reykjanes volcanic systems on (a) $K_2O$ vs. $TiO_2$ (b) CaO vs. FeO and (c) MgO vs. $Al_2O_3$ compositional variation diagrams. Geochemical data for 5a-Low/BAS-I provided by Stefan Wastegård (pers. comm., 2009). Geochemical field for the Veidivötn-Bárdarbunga volcanic system defined using whole rock analyses from Jakobsson (1979) and analyses of tephra horizons complied by Haflidason et al. (2000). Geochemical field for the Reykjanes volcanic system defined using whole rock analyses from Jakobsson et al. (2008).

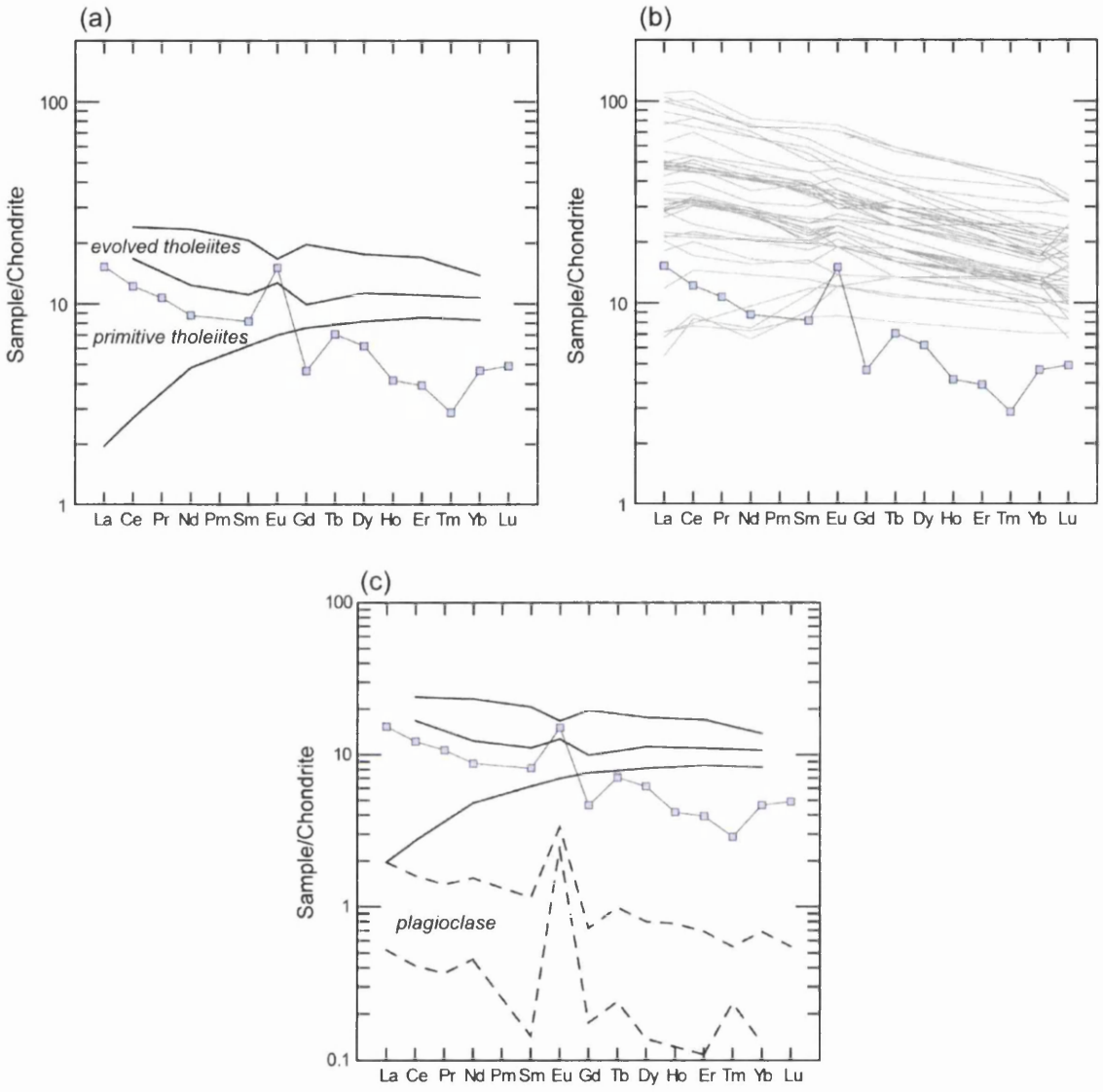


**Figure 5.22:** (a) Comparisons between the average chondrite-normalised REE profile for NGRIP 2548.35 m and (a) the tholeiitic end member characterisation of Óskarsson et al. (1982), (b) analyses of proximal Icelandic tholeiitic basalts reported in Meyer et al. (1985) and (c) the end member characterisation of Icelandic tholeiitic material and a geochemical field for plagioclase identified within Icelandic tholeiitic basalts by Hansen and Grönvold (2000).

The tholeiitic nature of this horizon was ascertained in the preceding section, and it can be seen that the REE profile for NGRIP 2548.35 m does not show a close correspondence to proximal tholeiitic material (figures 5.22a and b). Firstly, the shape of the profile differs due to the strong positive Eu anomaly and the depletion for certain elements and secondly, particularly for the HREEs, the concentrations of the REEs are depleted relative to the proximal material. Relative REE depletion has been identified in other comparisons between MIS 4 distal tephra horizons and proximal material, such as for NGRIP 2454.9 m and NGRIP 2574.55 m. However, in those cases profile shapes akin to Jan Mayen and Icelandic material, respectively, have been preserved.

As for the REE profile for NGRIP 2441.14 m, the characterisation of NGRIP 2548.35 m may represent a previously unrecognised characterisation however it is likely that it is due to contamination from micro-inclusions, e.g. plagioclase, in the tephra shards. The analysis of small amounts of this mineral in association with juvenile glass could have resulted in the distinctive shape of the REE profile for this horizon (figure 5.22c).

### 5.4.6 NGRIP 2574.55 m

The tephra horizon at a depth of 2574.55 m in the NGRIP ice-core is composed of glass shards with a greeny-brown blocky appearance with typical diameters of approximately 40 μm. This horizon was deposited following the thermal optimum of DO 20 and is coincident with a peak in the deposition of atmospheric sulphate (figure 5.5b (vi)). The magnitude of this sulphate peak is lower than the other peaks described previously because it occurred within an interstadial period.

The shards are basaltic in composition (figure 5.6) with high FeO concentrations of between 14.5-15.5 %wt, relatively low CaO concentrations of ~9.8 %wt and high values for $TiO_2$, ranging between 4.3 and 5 %wt. This geochemical composition is characteristic of the Icelandic transitional alkali rock suite and the high $TiO_2$ values are characteristic of the Katla volcanic region. Overall, the geochemistry of this horizon closely matches analyses from tephra horizons attributed to the Katla system (Figure 5.23 and 5.24; Larsen and Eiríksson, 2008; Haflidason et al., 2000). The $TiO_2$ concentrations in particular are far in excess of those for other NGRIP horizons (figure 5.23). Therefore, based on the geochemical evidence, this tephra horizon can be correlated to a source from the Katla volcanic region of Iceland.

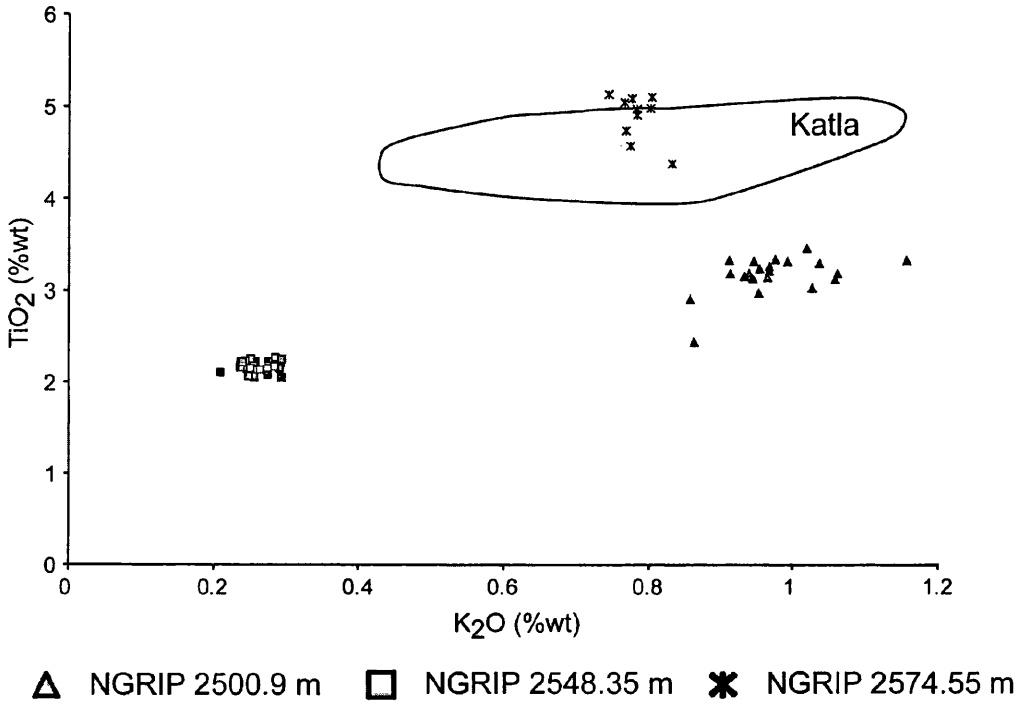


**Figure 5.23:** Geochemical data for the NGRIP 2500.9 m, NGRIP 2548.35 m and NGRIP 2574.55 m tephra horizons compared to a geochemical field for Katla material on a $TiO_2$ vs. $K_2O$ compositional variation diagram. The compositional field for the products of the Katla volcanic region is based on lava compositional data from Jakobsson (1979) and the geochemical composition of tephra horizons from the centre described in Haflidason et al. (2000).

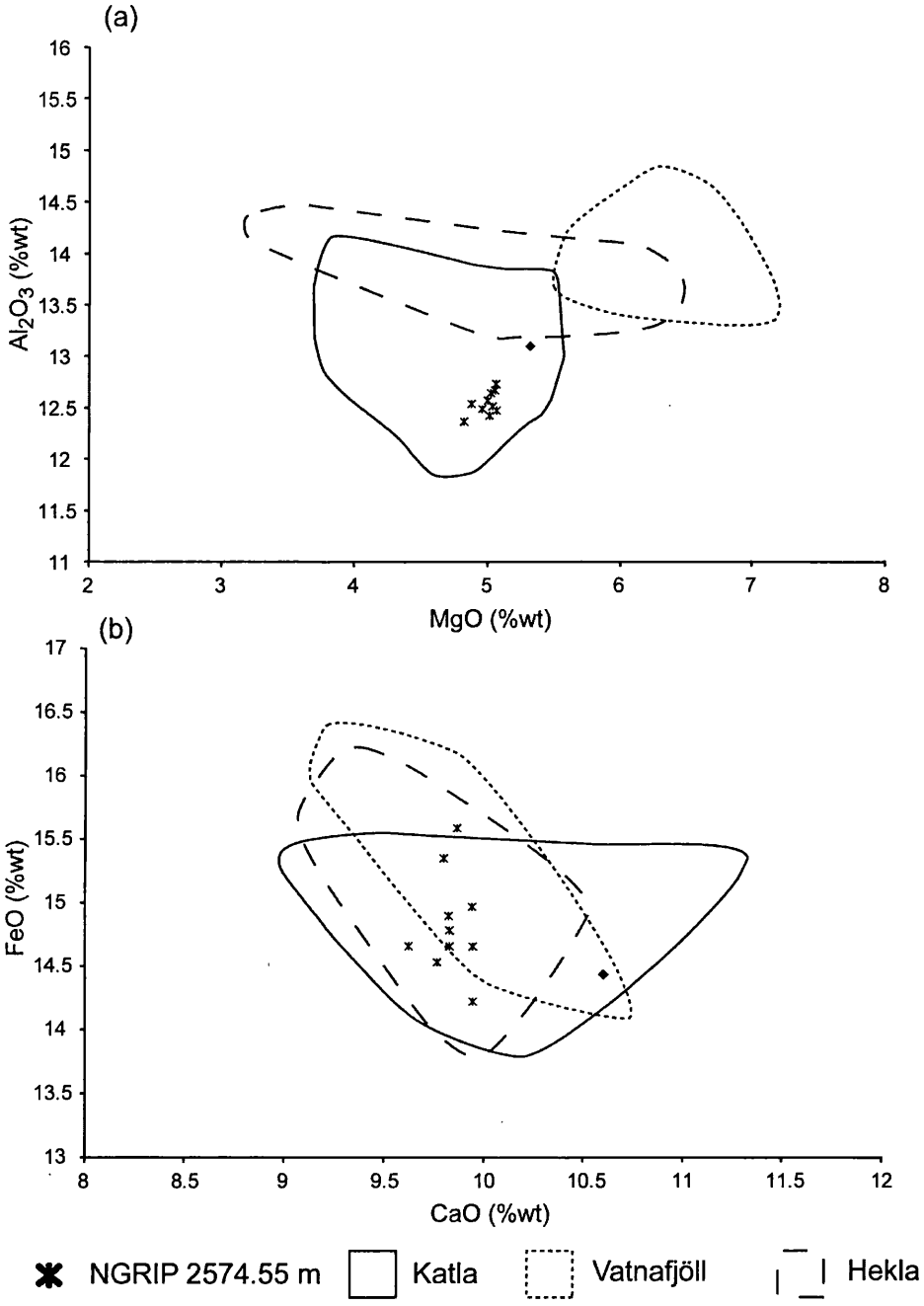


**Figure 5.24:** Geochemical data from the NGRIP 2574.55 m tephra horizon and three Icelandic transitional alkali volcanic systems plotted on (a) MgO vs. $Al_2O_3$ and (b) CaO vs. FeO composition variation diagrams. Compositional fields for the Icelandic volcanic centres are based on data from Jakobsson (1979) and Haflidason et al. (2000). The compositional field for the Hekla volcanic region was defined based on geochemical analyses with <50%wt $SiO_2$.

Geochemical comparisons to horizons within the MIS 2-5e tephrostratigraphy show that NGRIP 2574.55 m has composition similarities to four horizons. With high similarity coefficient values in excess of 0.95 for the comparisons with the 5a (~83 ka) and 5a (~84 ka) horizons identified by Lacasse et al. (1998) and the NGRIP 1895.3 m and NGRIP 2631.9 m horizons identified by Davies (unpublished) (appendix 6). The Katla volcanic system has been identified as the source for all of these previously identified horizons; thus the compositional similarities provide further evidence that this is the source of NGRIP 2574.55 m. In addition, the identification of these five horizons suggests that Katla was an important source of widespread basaltic tephra horizons throughout the last glacial period.

The REE composition of NGRIP 2574.55 m is relatively homogenous with a low level of variability shown in figure 5.8f and only a slight decrease in precision between the light and heavy REEs. The average REE profile for this horizon has a low gradient of slope that shows a slight flattening for the HREEs. The gradient of the average REE profile is not as smooth as those gained for other horizons, however this may be due to the lower number of analyses gained from shards within this horizon.

The affinity of this horizon to the Icelandic transitional alkaline rock suite produced by the Katla volcanic system was established based on major element evidence. The gradient of the REE profile for NGRIP 2574.55 m displays greater affinity to the end-member characterisation of alkaline material than tholeiitic material (figure 5.25a). However, the concentrations of REEs are distinctly lower within the NGRIP 2574.55 m tephra horizon than the end member characterisation of the alkaline material. The relationship of a similar gradient with a relative depletion in REE concentrations is also apparent when the characterisation is compared to REE profiles for transitional alkali deposits proximal to the Katla and Hekla systems reported in Meyer et al. (1985) and Lacasse et al. (2007). As was shown in section 4.6.3 this is not an uncommon feature of the REE profiles for distal tephra horizons sourced from the Katla volcanic system. This depletion may indicate that distal Katla tephra horizons are less enriched in REEs compared to proximal whole-rock deposits or that the present REE characterisations do not capture the full geochemical variability between proximal transitional alkali deposits.

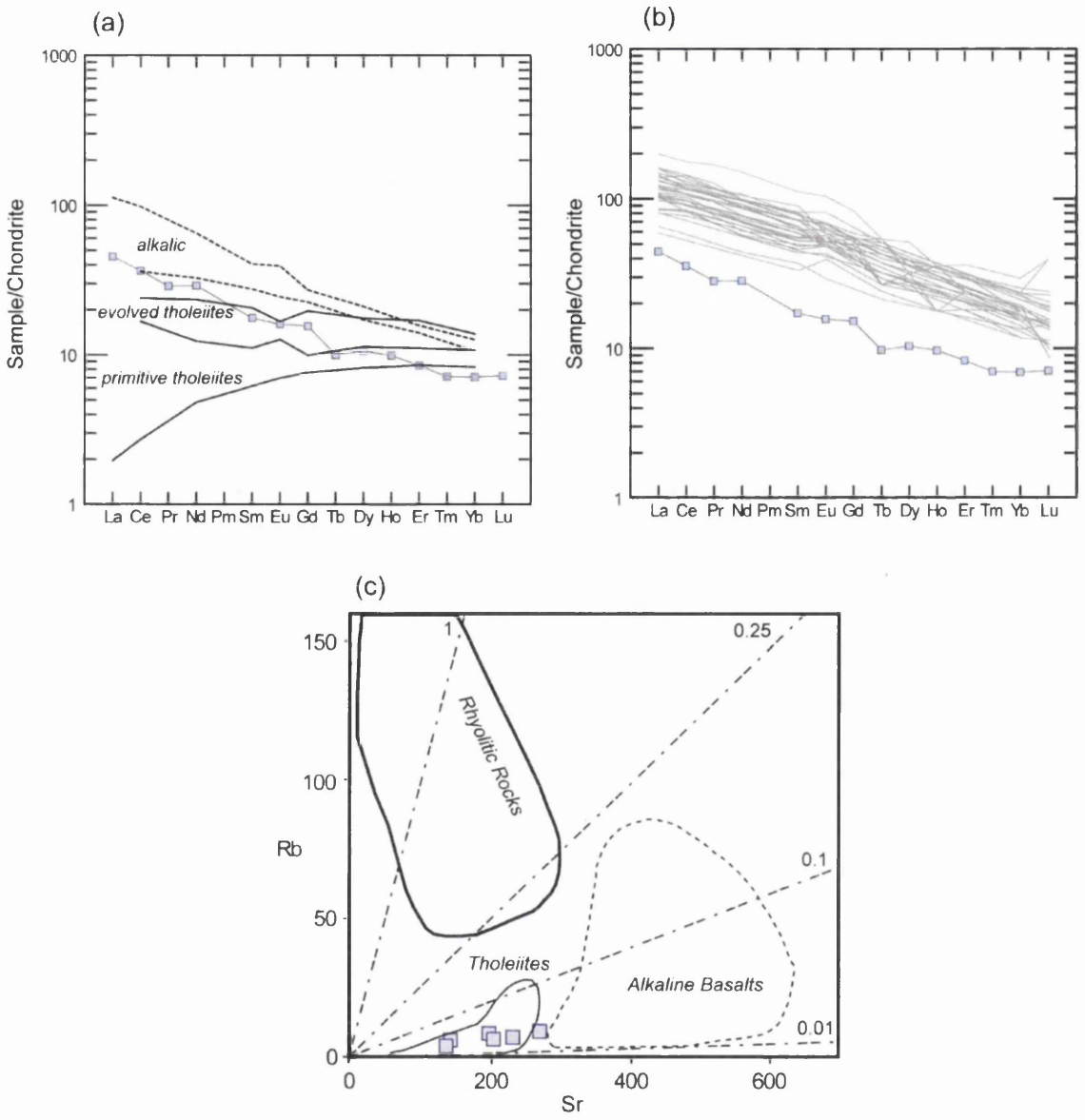


**Figure 5.25:** (a) Comparison between the average chondrite-normalised REE profile for NGRIP 2574.55 m and end-member characterisations of Icelandic tholeiitic and alkaline basaltic proximal deposits (Óskarsson et al., 1982). (b) Comparison between the average REE profile for NGRIP 2574.55 m and REE profiles for material produced by the Hekla and Katla volcanic systems reported in Meyer et al. (1985) and Lacasse et al. (2007). (c) Sr vs. Rb compositional variation diagram for NGRIP 2574.55 m and end-member characterisations of Icelandic material (Óskarsson et al., 1982).

However, it is not possible to determine if either of these scenarios is correct because analytical issues relating to gas blank misestimation may have had an impact on the characterisations. If proximal and distal deposits have the same absolute REE concentrations then gas blank misestimation could have caused the offset in absolute concentrations but retention of the REE profile observed for NGRIP 2574.55 m. Trace element ratios are unaffected by misestimation and figure 5.25c demonstrates that the Rb/Sr ratios for NGRIP 2574.55 m are not atypical for transitional alkali material, but the offset in absolute concentrations means they fall within the geochemical field for tholeiitic material.

## 5.5 Chapter Summary

The principal findings of this chapter are:

- The identification of six tephra horizons within the MIS 4 section of the NGRIP ice-core that can be dated based on their stratigraphic position within the core and the current GICC05 timescale (table 5.4).

- Major element characterisations of these horizons have been used to determine their geochemical composition and suggest potential source volcanic regions or volcanic systems (table 5.4).

- Trace element characterisations, gained through the analysis of individual shards, have been shown to provide characterisations consistent with the major element composition of the horizons. However, it has also been demonstrated that some characterisations have been affected by micro-inclusions within the shards.

- The absolute trace element concentrations of these characterisations may have been affected by the misestimation of gas blanks.

- Five of the six horizons can be directly related to sulphate peaks within the high-resolution chemostratigraphy for the core and the implications of this will be discussed further in section 8.2.3.1.

**Table 5.4:** Summary of the approximate age, geochemistry and potential sources of tephra horizons identified within the MIS 4 section of the NGRIP ice-core. Approximate ages for the horizons were derived from a composite timescale of the counted GICC05 timescale back to 60 kyr b2k and the modelled ss09sea timescale for the remainder of the core (A. Svensson, *pers. comm.*, 2009). The b2k timescale is referenced to 2000 AD and the uncertainly on these age estimates is ~±1300 years.

| Tephra Horizon | Approximate Age (yr b2k) | Geochemistry | Potential Source |
|---|---|---|---|
| NGRIP 2441.14 m | 61410 | Basaltic andesitic (tholeiitic) | Icelandic Rift Zone |
| NGRIP 2441.28 m | 61425 | Rhyolitic | Kutcharo, Hokkaido, Japan |
| NGRIP 2454.9 m | 63090 | Basaltic-Trachybasaltic | Jan Mayen |
| NGRIP 2500.9 m | 68900 | Basaltic (transitional alkali) | Iceland (SFZ or EFZ) |
| NGRIP 2548.35 m | 74200 | Basaltic (tholeiitic) | Reykjanes or Veidivötn-Bárdarbunga |
| NGRIP 2574.55 m | 76160 | Basaltic (transitional alkali) | Katla |

# 6. Tephrochronology of Marine Isotope Stage 4 within the GRIP ice-core

## 6.1 Introduction

This chapter describes tephra horizons identified within the GRIP ice-core following attempts to trace the horizons described in chapter 5 into this record. Identified horizons have been characterised for both their major element and trace element compositions and comparisons to proximal deposits have been made in an attempt to identify source volcanic regions. Geochemical comparisons have also been made to horizons forming the present MIS 2-5e tephrochronological framework (appendix 6).

## 6.2 Sub-sampling of the GRIP ice-core

Following the identification of tephra horizons in the NGRIP core four sections of the GRIP ice-core were sampled in an attempt to trace the horizons between the two records. Using the synchronisation method detailed in section 3.2.3.2 ice between 2488.2-2492.05 m, 2498.1-2501.95 m, 2530-2534.3 m and 2564.1-2566.3 m depth within the GRIP core was sampled (figure 6.1). The length of these sections was related to the density of tie points around those depths in the cores (figure 6.2).

For example, only a short section of ice was sampled in an attempt to trace NGRIP 2548.35 m between the cores as a large sulphate peak at 2548 m depth in the NGRIP ice-core has been synchronised to a sulphate peak at 2565.17 m depth in the GRIP core and the horizon falls near a rapid climate transition. Longer sections were sampled for the tracing of the other horizons due to the low density of tie-points around their stratigraphic positions. This was a consequence of the horizons being deposited within stadial periods when increased dust deposition neutralises the ECM signal, the principal chemical record used in the synchronisation as a continuous ECM record is available from each core. No attempt was made to trace NGRIP 2574.55 m in the GRIP core as this tephra was identified after the sampling had been completed.

In total 26 ice-core bags were sampled with 94 individual samples taken from the bags and all were inspected for their tephra content (appendix 4).

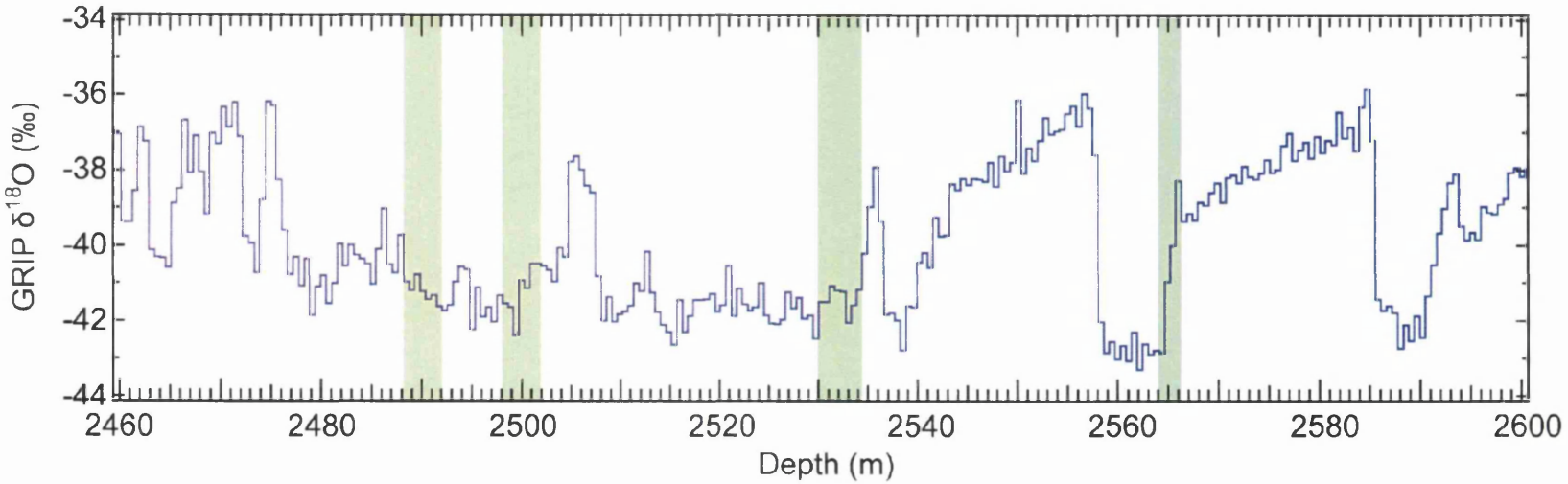


**Figure 6.1:** Stratigraphic position of ice-core bags from the GRIP ice-core sampled during this study with reference to the oxygen isotope record for the core. Isotopic values are expressed in ‰ with respect to V-SMOW.

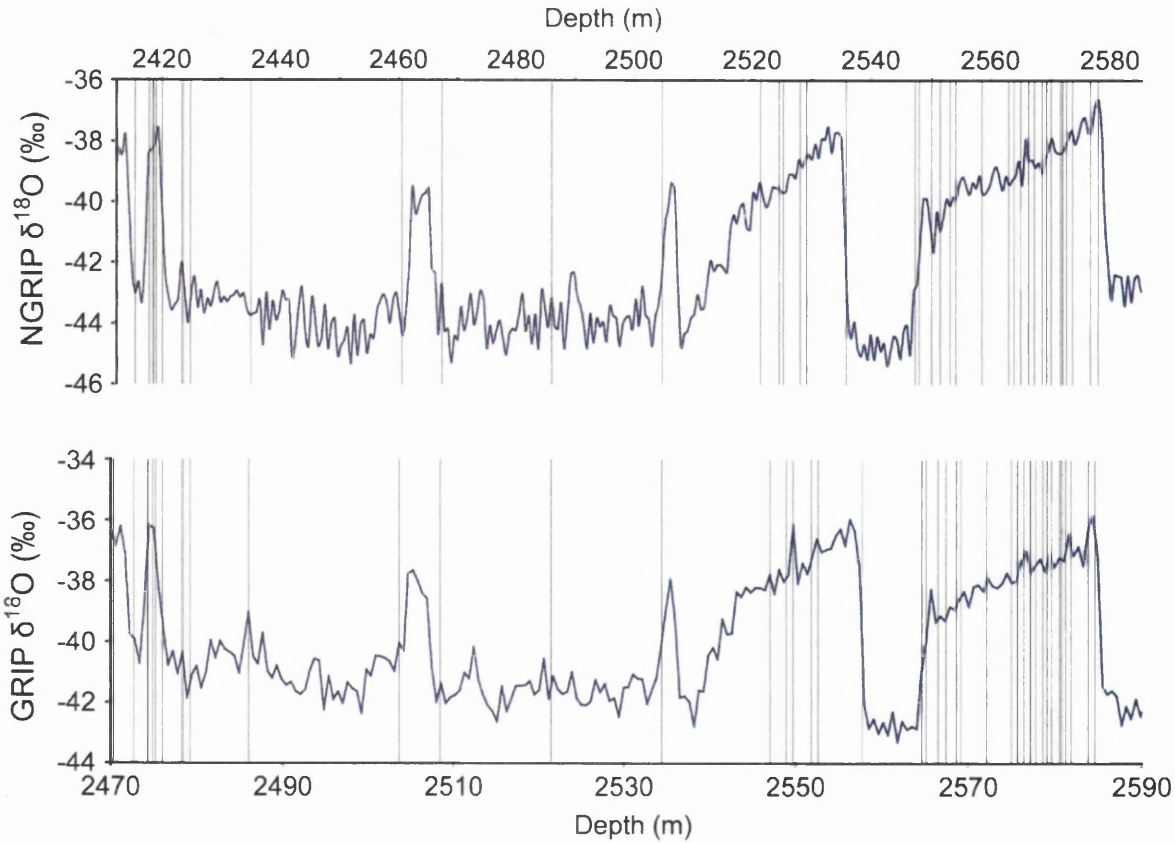


**Figure 6.2:** Stratigraphic position of tie-points between the NGRIP and GRIP ice-cores for the MIS 4 period defined by the synchronisation of chemical records from the cores (Seierstad and Rasmussen, unpublished). Isotopic values are expressed in ‰ with respect to V-SMOW.

## 6.3 Cryptotephra Horizons within the GRIP ice-core

Six samples were found to contain a concentration of volcanic glass shards significant enough to be considered as a horizon (>20) and these were processed for geochemical analysis (figure 6.3). The horizons outlined here were defined based on the high concentration of shards relative to background levels and a homogenous geochemical signal from the shards.

The stratigraphic position of these horizons with respect to the oxygen isotope ratio and detailed ECM records for the GRIP core are shown in figure 6.4. These horizons will also be referred to by the depth of the base of the sample containing the material (table 6.1). Table 6.2 presents the average major element compositions for the horizons and all of the data from the major element analysis of the GRIP horizons are shown on a TAS plot (figure 6.5), with an inset focusing on analyses from basaltic and basaltic andesitic material provided in figure 6.6.

The trace element composition of individual shards within five of the horizons was determined using the LA-ICP-MS system (table 6.2). Analyses were not obtained from shards within GRIP 2564.3 m due to the small size of many of the particles and misfiring of the laser system during analyses. Ten or more individual shards from each horizon were characterised and figure 6.7 illustrates the chondrite-normalised REE profiles from each of the horizons with the individual and average profiles illustrated.

**Table 6.1:** Summary of the ice samples from the MIS 4 period of the GRIP ice-core containing a significant number of tephra shards.

| Bag Number | Depth Interval (cm) | Depth of Sample Top (m) | Depth of Sample Base (m) |
|---|---|---|---|
| 4543 | 20-40 | 2498.3 | 2498.5 |
| 4545 | 40-55 | 2499.6 | 2499.75 |
| 4548 | 0-20 | 2500.85 | 2501.05 |
| 4604 | 10-15 | 2531.75 | 2531.8 |
| 4606 | 0-20 | 2532.75 | 2532.95 |
| 4663 | 0-20 | 2564.1 | 2564.3 |

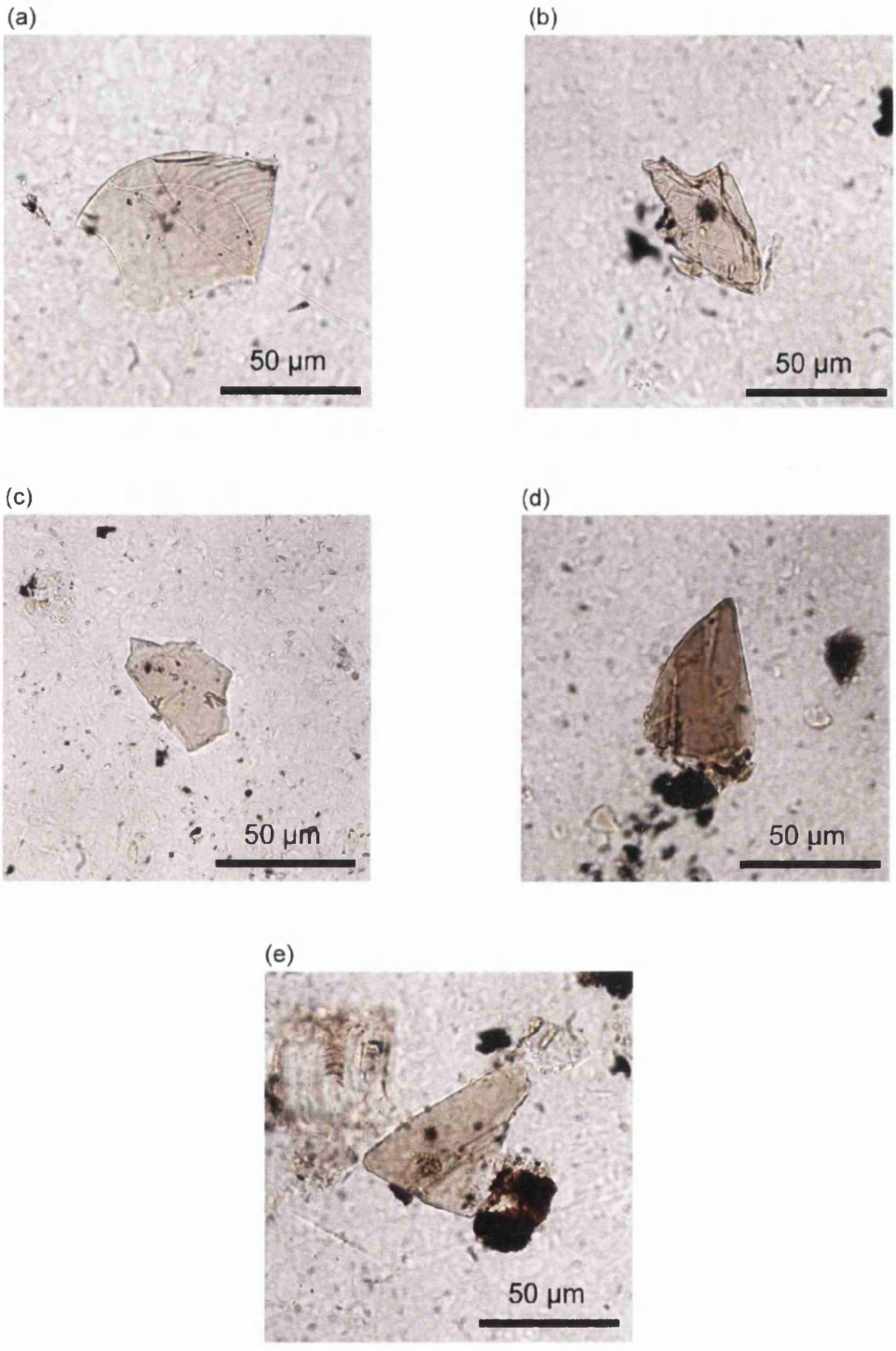


**Figure 6.3:** Images of tephra shards from GRIP MIS 4 tephra horizons. (a) GRIP 2498.5 m (b) GRIP 2499.75 m (c) GRIP 2501.05 m (d) GRIP 2531.8 m and (e) GRIP 2532.95 m.

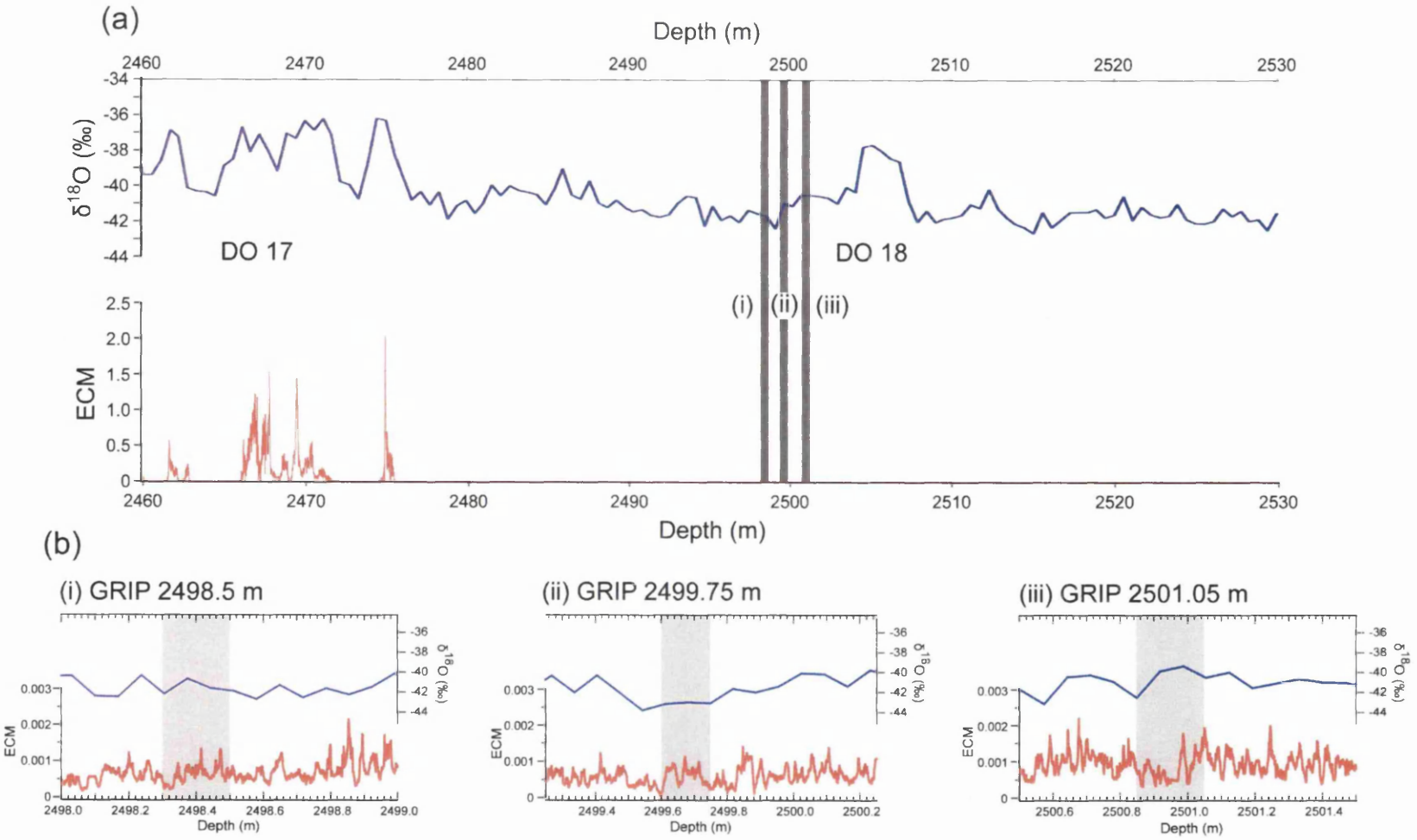


**Figure 6.4:** (a) Stratigraphic position of the six cryptotephra horizons identified within the GRIP ice-core with respect to the oxygen isotope ratio and continuous ECM record for the core. (b) (i-vi) insets from (a) illustrating the detailed chemical records around the cryptotephra horizons. Isotopic values are expressed in ‰ with respect to V-SMOW. Continued overleaf.

(a) cont.

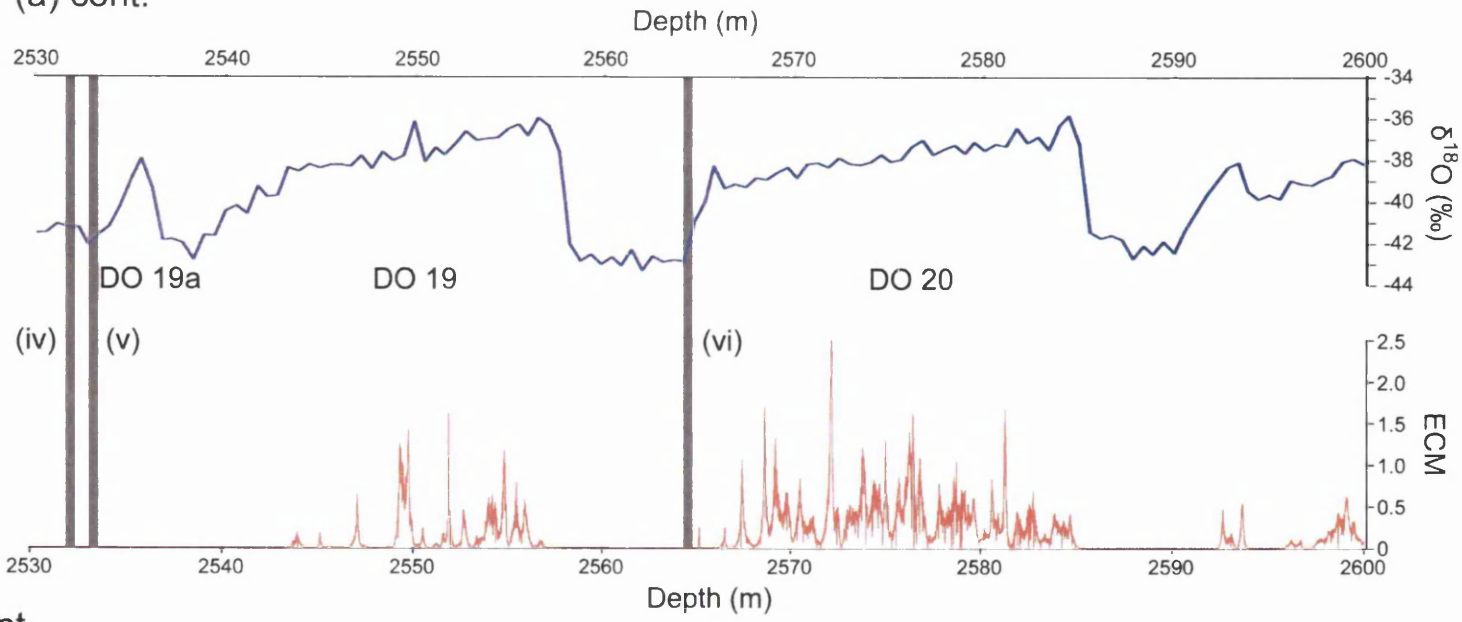


(b) cont.

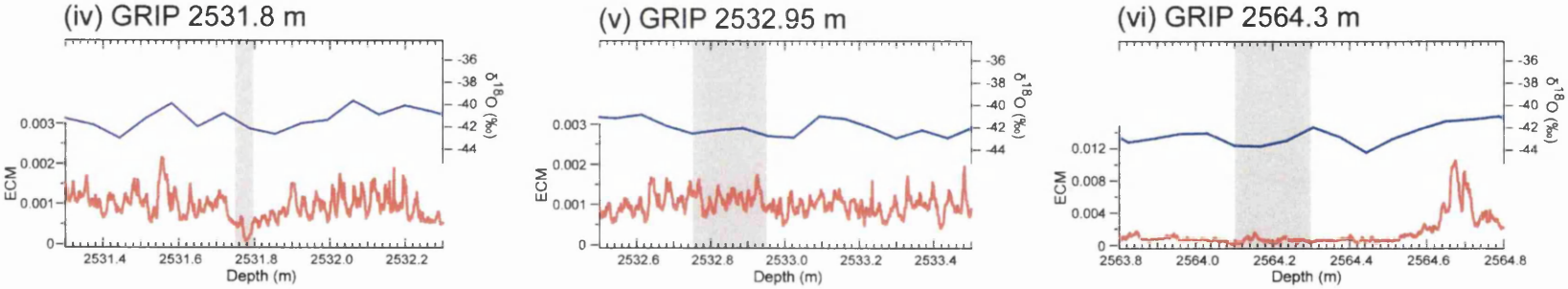


**Figure 6.4:** continued

**Table 6.2:** Summary of normalised major oxide and trace element data for glass shards from tephra horizons identified within the MIS 4 section of the GRIP ice-core. Mean and 1 standard deviations are shown. Total oxides are raw values prior to normalisation. All major elements expressed as percentage weight. All trace element concentrations expressed as ppm. Total iron is expressed as FeO. n = number of shards analysed. The complete dataset of unnormalised data is provided in appendix 4.

| | GRIP 2498.5 m | GRIP 2499.75 m-1 | GRIP 2499.75 m-2 | GRIP 2501.05 m |
|---|---|---|---|---|
| n | 24 | 20 | 9 | 23 |
| $SiO_2$ | 48.78 (0.70) | 48.62 (0.75) | 50.28 (0.28) | 47.54 (0.39) |
| $TiO_2$ | 2.78 (0.14) | 2.79 (0.18) | 2.89 (0.15) | 3.01 (0.13) |
| $Al_2O_3$ | 13.94 (0.39) | 13.97 (0.73) | 12.93 (0.20) | 14.55 (0.41) |
| FeO | 11.66 (0.58) | 9.62 (0.73) | 13.53 (0.41) | 11.93 (0.84) |
| MnO | 0.21 (0.06) | 0.20 (0.07) | 0.25 (0.03) | 0.18 (0.05) |
| MgO | 6.94 (0.42) | 6.70 (0.92) | 5.91 (0.27) | 6.94 (0.51) |
| CaO | 12.25 (0.46) | 13.05 (1.07) | 10.93 (0.32) | 12.57 (0.48) |
| $Na_2O$ | 2.49 (0.18) | 2.43 (0.35) | 2.51 (0.43) | 2.50 (0.19) |
| $K_2O$ | 0.44 (0.09) | 2.00 (0.21) | 0.37 (0.05) | 0.37 (0.06) |
| $P_2O_5$ | 0.47 (0.27) | 0.53 (0.02) | 0.37 (0.02) | 0.37 (0.02) |
| Cl | 0.03 (0.01) | 0.08 (0.03) | 0.03 (0.01) | 0.04 (0.02) |
| Total Oxides | 96.12 (0.63) | 97.64 (0.68) | 97.43 (0.71) | 97.25 (0.84) |
| | | | | |
| n | 16 | 10 | n/a | 14 |
| Sc | 16.7 (5.81) | 2.47 (5.18) | n/a | 21.9 (11.2) |
| Rb | 8.32 (4.72) | 16.5 (7.04) | n/a | 8.48 (3.53) |
| Sr | 235 (96.1) | 194 (93.6) | n/a | 352 (139) |
| Y | 18.7 (5.63) | 11.9 (3.13) | n/a | 21.7 (7.38) |
| Zr | 98.3 (28.7) | 81.8 (26.2) | n/a | 110 (34.9) |
| Nb | 11.0 (4.54) | 15.2 (9.59) | n/a | 15.8 (6.92) |
| Ba | 114 (28.0) | 257 (116) | n/a | 118 (35.3) |
| La | 12.3 (3.22) | 16.3 (6.59) | n/a | 13.6 (3.31) |
| Ce | 26.7 (7.75) | 31.0 (13.3) | n/a | 31.1 (7.99) |
| Pr | 3.29 (1.14) | 3.29 (1.46) | n/a | 4.28 (1.17) |
| Nd | 14.4 (4.14) | 12.3 (6.23) | n/a | 20.8 (7.26) |
| Sm | 4.00 (2.11) | 3.01 (1.39) | n/a | 4.44 (2.09) |
| Eu | 1.02 (0.74) | 0.65 (0.43) | n/a | 1.82 (0.72) |
| Gd | 3.55 (1.60) | 2.38 (1.24) | n/a | 4.87 (1.80) |
| Tb | 0.58 (0.21) | 0.29 (0.17) | n/a | 0.68 (0.28) |
| Dy | 3.48 (1.27) | 2.08 (0.81) | n/a | 4.58 (1.44) |
| Ho | 0.66 (0.21) | 0.38 (0.12) | n/a | 0.80 (0.37) |
| Er | 1.62 (0.58) | 1.04 (0.41) | n/a | 2.33 (0.72) |
| Tm | 0.22 (0.11) | 0.14 (0.05) | n/a | 0.34 (0.15) |
| Yb | 1.60 (0.58) | 1.13 (0.57) | n/a | 1.74 (0.88) |
| Lu | 0.23 (0.09) | 0.16 (0.09) | n/a | 0.28 (0.13) |
| Hf | 2.96 (1.21) | 2.39 (0.84) | n/a | 3.04 (1.13) |
| Ta | 0.72 (0.31) | 1.00 (0.70) | n/a | 0.93 (0.42) |
| Th | 1.64 (0.36) | 2.31 (0.73) | n/a | 1.26 (0.20) |
| U | 0.74 (0.31) | 0.95 (0.24) | n/a | 0.43 (0.14) |

**Table 6.2:** continued.

| | GRIP 2531.8 m | GRIP 2532.95 m | GRIP 2564.3 m-1 | GRIP 2564.3 m-2 |
|---|---|---|---|---|
| n | 22 | 23 | 6 | 6 |
| $SiO_2$ | 50.65 (0.42) | 50.94 (0.47) | 52.96 (0.23) | 51.39 (0.35) |
| $TiO_2$ | 3.11 (0.18) | 3.22 (0.27) | 3.24 (0.10) | 3.69 (0.17) |
| $Al_2O_3$ | 12.72 (0.40) | 12.70 (0.33) | 12.88 (0.23) | 12.59 (0.27) |
| FeO | 14.83 (0.33) | 13.99 (0.60) | 12.53 (0.26) | 13.27 (0.27) |
| MnO | 0.33 (0.06) | 0.24 (0.05) | 0.29 (0.04) | 0.28 (0.02) |
| MgO | 3.73 (0.15) | 5.11 (0.53) | 3.75 (0.08) | 4.22 (0.16) |
| CaO | 8.63 (0.19) | 9.72 (0.58) | 8.15 (0.16) | 8.67 (0.19) |
| $Na_2O$ | 3.35 (0.33) | 2.83 (0.19) | 3.38 (0.16) | 3.47 (0.23) |
| $K_2O$ | 0.96 (0.12) | 0.67 (0.12) | 1.12 (0.02) | 1.01 (0.05) |
| $P_2O_5$ | 1.62 (0.14) | 0.45 (0.07) | 1.64 (0.15) | 1.34 (0.06) |
| Cl | 0.07 (0.01) | 0.04 (0.01) | 0.06 (0.01) | 0.06 (0.01) |
| Total Oxides | 96.81 (0.80) | 96.73 (0.93) | 96.15 (0.57) | 95.81 (0.63) |
| | | | | |
| n | 14 | 14 | n/a | n/a |
| Sc | 18.5 (9.80) | 18.9 (16.6) | n/a | n/a |
| Rb | 25.1 (5.88) | 21.7 (6.10) | n/a | n/a |
| Sr | 663 (113) | 301 (107) | n/a | n/a |
| Y | 64.7 (10.4) | 40.1 (15.8) | n/a | n/a |
| Zr | 416 (72.2) | 217 (86.1) | n/a | n/a |
| Nb | 51.2 (10.2) | 22.8 (10.9) | n/a | n/a |
| Ba | 344 (57.2) | 194 (53.0) | n/a | n/a |
| La | 50.3 (10.9) | 21.1 (8.47) | n/a | n/a |
| Ce | 122 (23.3) | 50.0 (21.6) | n/a | n/a |
| Pr | 17.2 (3.90) | 6.46 (1.99) | n/a | n/a |
| Nd | 81.8 (19.7) | 32.1 (12.4) | n/a | n/a |
| Sm | 18.4 (4.79) | 8.72 (4.93) | n/a | n/a |
| Eu | 7.29 (2.13) | 3.57 (1.72) | n/a | n/a |
| Gd | 17.6 (3.55) | 8.80 (4.46) | n/a | n/a |
| Tb | 2.56 (0.47) | 1.43 (0.67) | n/a | n/a |
| Dy | 13.8 (3.48) | 8.78 (4.05) | n/a | n/a |
| Ho | 2.65 (0.92) | 1.44 (0.51) | n/a | n/a |
| Er | 6.17 (1.30) | 4.15 (2.17) | n/a | n/a |
| Tm | 0.76 (0.25) | 0.71 (0.38) | n/a | n/a |
| Yb | 5.10 (1.44) | 3.94 (1.45) | n/a | n/a |
| Lu | 0.74 (0.24) | 0.63 (0.36) | n/a | n/a |
| Hf | 9.76 (2.54) | 5.08 (1.94) | n/a | n/a |
| Ta | 3.09 (0.77) | 1.75 (0.69) | n/a | n/a |
| Th | 3.77 (0.68) | 2.41 (0.58) | n/a | n/a |
| U | 1.23 (0.28) | 0.87 (0.31) | n/a | n/a |

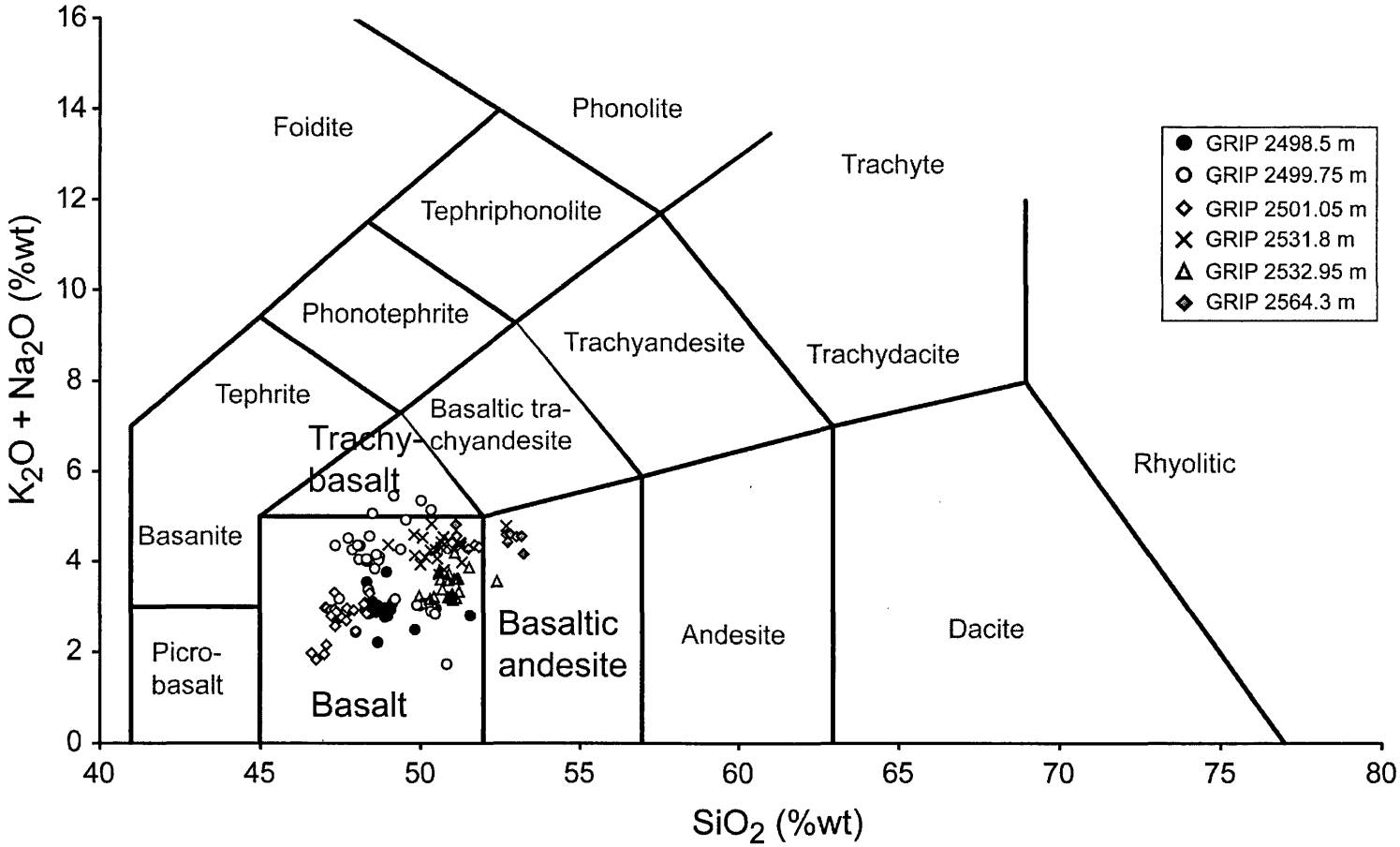


**Figure 6.5:** Total alkalis versus silica plot for six GRIP tephra horizons. Chemical classification and nomenclature after Le Maitre et al. (1989).

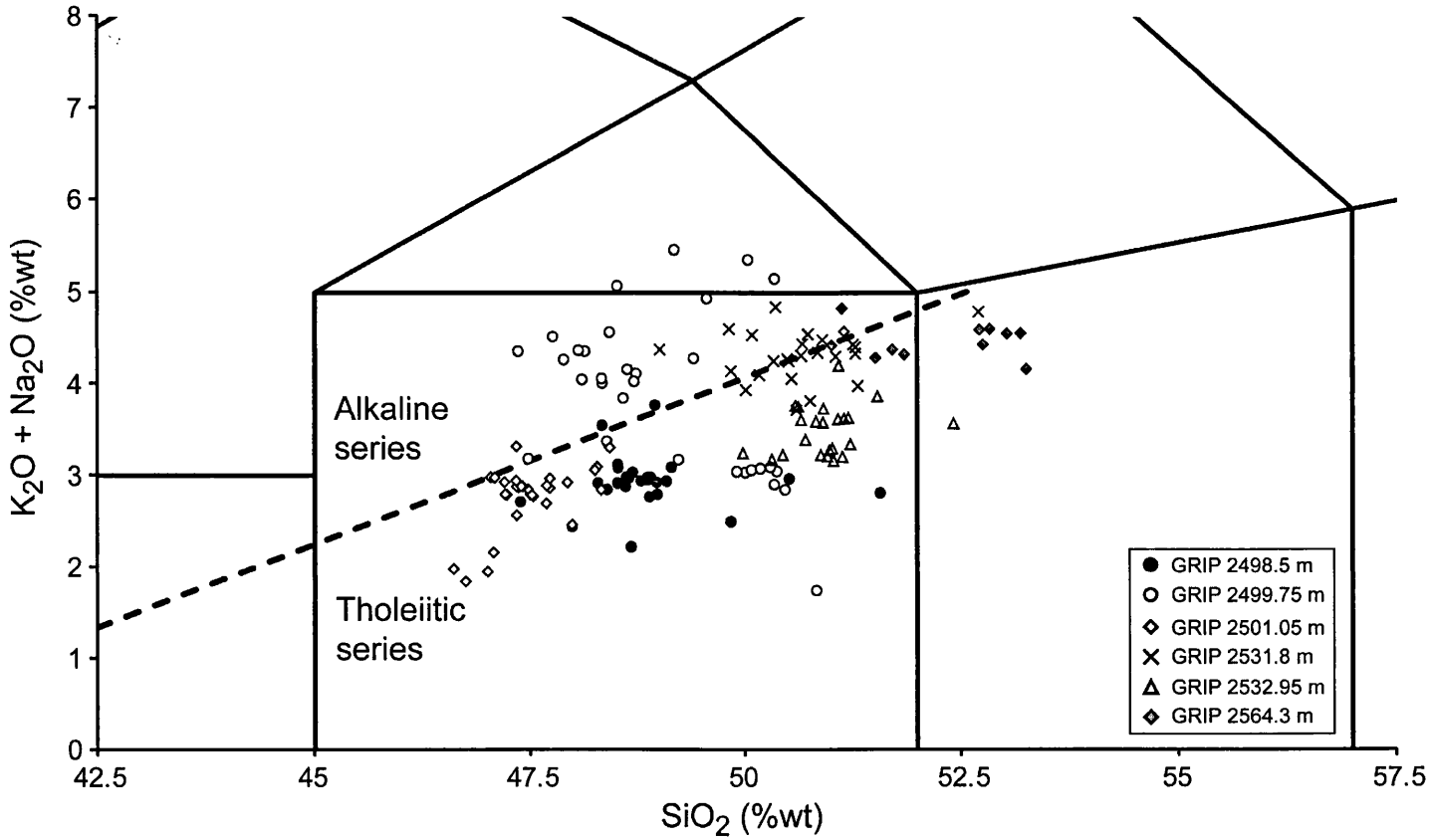


**Figure 6.6:** Inset of the total alkalis versus silica plot from figure 6.5 focusing on the basaltic and basaltic andesitic horizons from the GRIP ice-core. The dashed line represents the subdivision of volcanic rocks into alkaline and subalkaline (tholeiitic) series. The boundary utilised was defined by MacDonald and Katsura (1964).

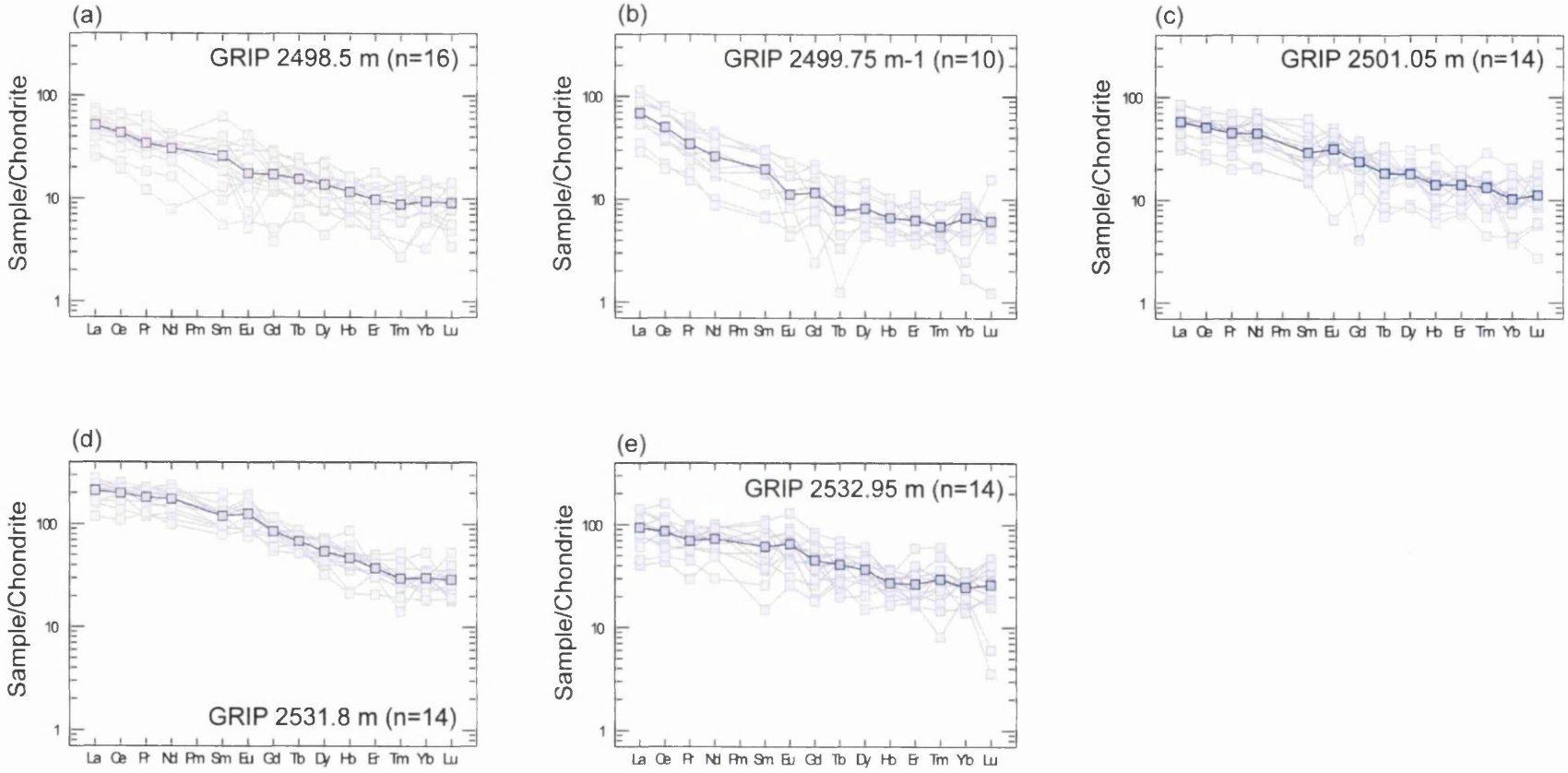


**Figure 6.7:** Chondrite-normalised REE profiles for individual tephra shards from (a) GRIP 2498.5 m (b) GRIP 2499.75 m-1 (c) GRIP 2501.05 m (d) GRIP 2531.8 m and (e) GRIP 2532.95 m. The average REE profile for each horizon is highlighted. Chondrite values from Sun and McDonough (1989).

## 6.4 Geochemistry of the GRIP Tephra Horizons and Source Identification

### 6.4.1 GRIP 2498.5 m

This tephra horizon is composed of light green shards with a platy morphology ranging between 50 and 60 μm in size. It was deposited during the stadial climatic period following DO 18 (figure 6.4). No distinct signals in the ECM record can be related to this tephra, probably due to its deposition during a stadial period when a high dust load within the cores can neutralise the ECM acidity signal.

Twenty-seven shards from this horizon were analysed by EPMA and demonstrated that this horizon has a basaltic composition (figure 6.5). The geochemical characteristics of these analyses are $SiO_2$ values between 48 and 49 %wt, $K_2O$ values between ~0.4 and 0.5 %wt, high MgO values between approximately 6 and 7.5 %wt and high CaO concentrations of ~12.2 %wt. These analyses plot just below the dividing line defined by MacDonald and Katsura (1964), which indicates that they could have either a tholeiitic or transitional alkali composition (figure 6.6). The high CaO and MgO concentrations are more characteristic of tholeiitic material; therefore it is likely that this horizon was sourced from a volcanic system in the Icelandic rift zone (Jakobsson et al., 2008). This is supported by the biplots shown in figure 6.8 with the shards displaying similar $TiO_2$ and $K_2O$ values to the products of the Grímsvötn volcanic system and similar CaO and MgO concentrations to the Reykjanes and Veidivötn-Bárdarbunga systems. However, a consistent affinity to one particular rift zone volcanic system is not observed as a consequence the volcanic source of this horizon remains unknown.

Figure 6.7a illustrates the 16 individual trace element analyses that were gained from shards within the GRIP 2498.5 m tephra horizon. These individual profiles show that this horizon has a relatively heterogeneous REE geochemistry. The average REE profile of these analyses has a consistently low gradient for the LREEs and MREEs and a flat profile for the HREEs between Er and Lu.

A comparison to the end-member characterisations for tholeiitic and alkaline basaltic material shows that GRIP 2498.5 m displays greater geochemical similarities to the profile of alkaline material (figure 6.9a) as it is relatively enriched in both the LREEs and MREEs compared to the tholeiitic characterisation. The similarity in profile gradient

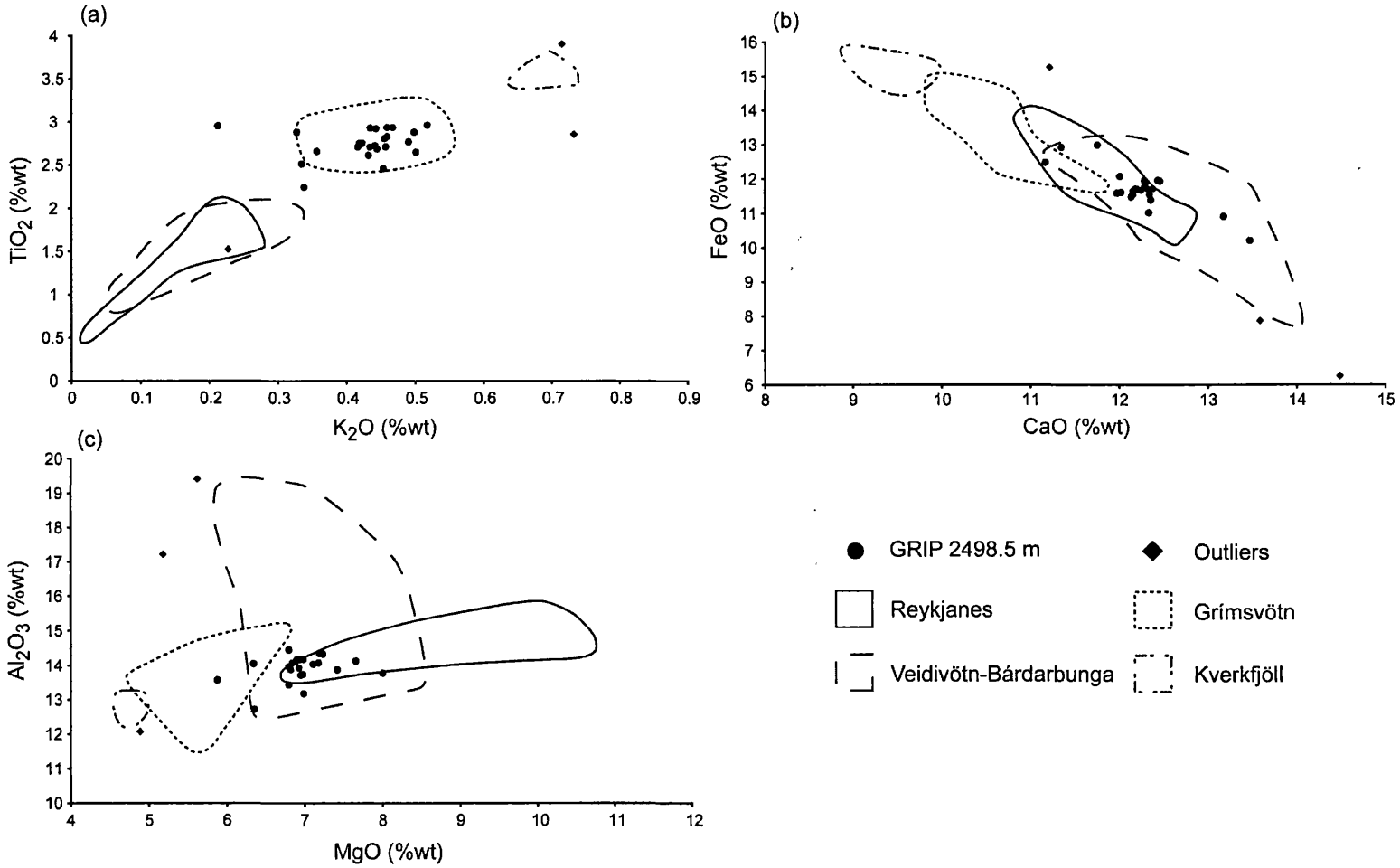


**Figure 6.8:** Geochemical data for GRIP 2498.5 m compared to geochemical fields for four Icelandic tholeiitic volcanic systems on (a) $K_2O$ vs. $TiO_2$ (b) CaO vs. FeO and (c) MgO vs. $Al_2O_3$ compositional variation diagrams. Geochemical fields for the Grímsvötn and Veidivötn-Bárdarbunga volcanic systems defined using whole rock analyses from Jakobsson (1979) and analyses of tephra horizons complied by Haflidason et al. (2000). Geochemical field for the Reykjanes system defined using whole rock analyses from Jakobsson et al. (2008) and the Kverkfjöll system using whole rock data from Höskuldsson et al. (2006).

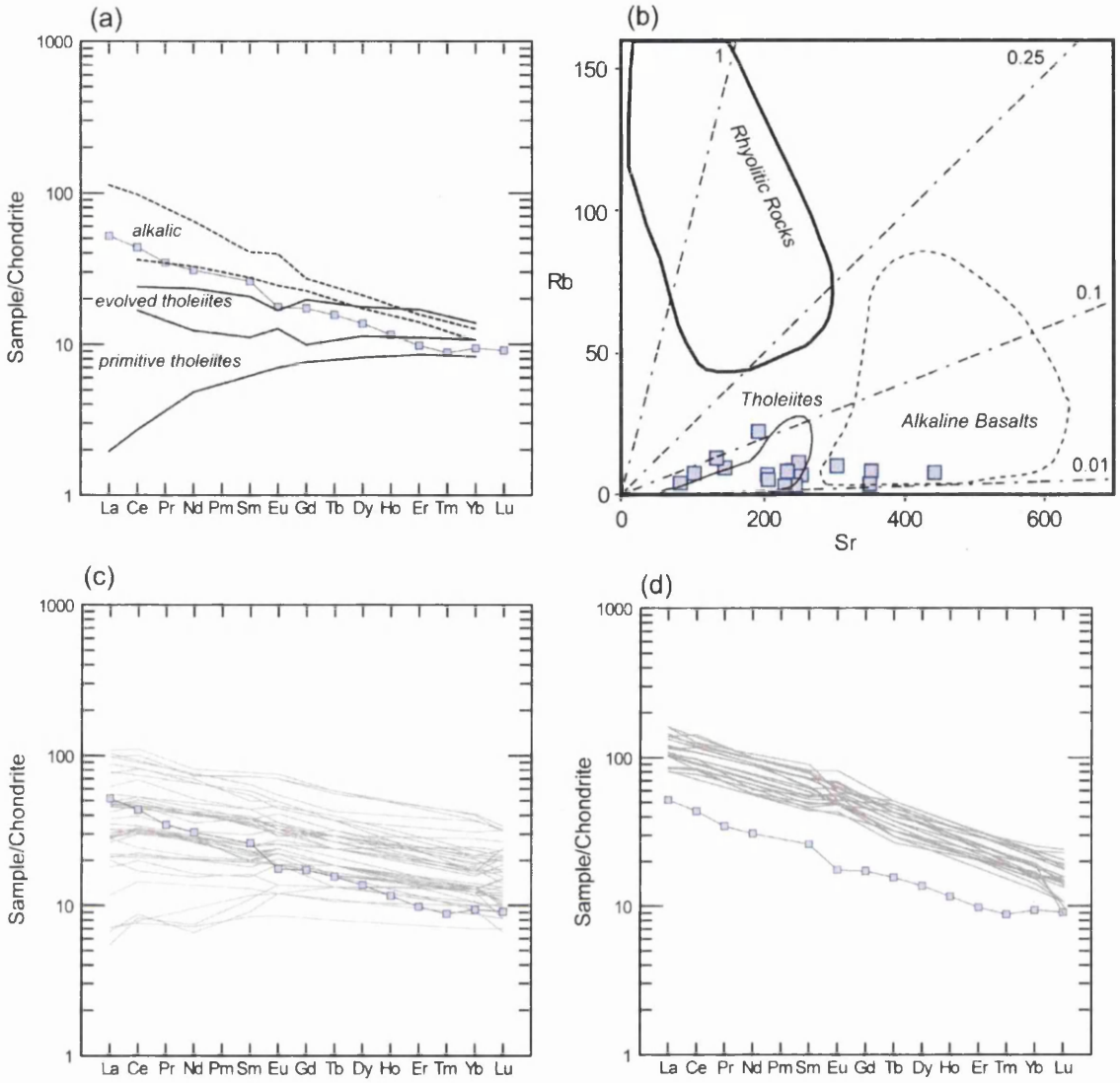


**Figure 6.9:** (a) Average chondrite-normalised REE profile for GRIP 2498.5 m compared to end-member characterisations of Icelandic tholeiitic and alkaline basaltic material. (b) Sr v Rb compositional variation diagram comparing individual analyses from tephra shards within GRIP 2498.5 m to end-member characterisations defined by Óskarsson et al. (1982). (c and d) Average chondrite-normalised REE profile for GRIP 2498.5 m compared to REE profiles reported in Meyer et al. (1985) for tholeiitic and transitional alkaline proximal material respectively.

to more alkaline material is also observed when the profile for GRIP 2498.5 m is compared to REE profiles of tholeiitic and transitional alkaline basaltic material, reported in Meyer et al. (1985), in figures 6.9c and 6.9d respectively. The Rb and Sr concentrations for most shards closely match the geochemical field for tholeiitic material defined by Óskarsson et al. (1982). However, the absolute concentrations for this horizon may have been affected by gas blank misestimation and therefore the Rb/Sr ratio does not provide supporting evidence for the characterisation of this horizon being more akin to tholeiitic or alkali material (figure 6.9b).

The greater similarity of the trace element composition of this horizon to proximal alkaline material could be due to GRIP 2498.5 m being misclassified as tholeiitic based on the major element geochemistry. However, this is unlikely due to the characteristic CaO and MgO concentrations of the shards and the similarities to the products of rift zone volcanic systems, shown in figure 6.8, which both strongly indicate that this horizon has an affinity to the Icelandic tholeiitic rock suite.

Potential explanations for the mismatch between the major and trace element characterisations will be discussed in section 8.3.1.1.

### 6.4.2 GRIP 2499.75 m

GRIP 2499.75 m is composed of light greeny-brown blocky and platy glass shards with a typical diameter of 50 μm. This horizon was deposited in the stadial period following DO 18, shortly before GRIP 2498.5 m (figure 6.4). Geochemical analyses of the shards from this horizon are basaltic to trachybasaltic in composition and can be split into two distinct populations. The bimodal nature of this tephra is most distinct when the %wt values for $K_2O$ and FeO are compared (figure 6.10). The dominant population (GRIP 2499.75 m-1) consists of 20 EPMA analyses, while 9 analyses are grouped as the secondary population (GRIP 2499.75 m-2). Two clear outliers were identified and were disregarded in further analysis.

#### 6.4.2.1 Population 1

The geochemical composition of GRIP 2499.75 m-1 is relatively heterogeneous with a wide range of concentrations for elements such as $SiO_2$ (47.3-50.3 %wt) and CaO (9-15 %wt). However, as the analyses appear to fall on the same geochemical trends

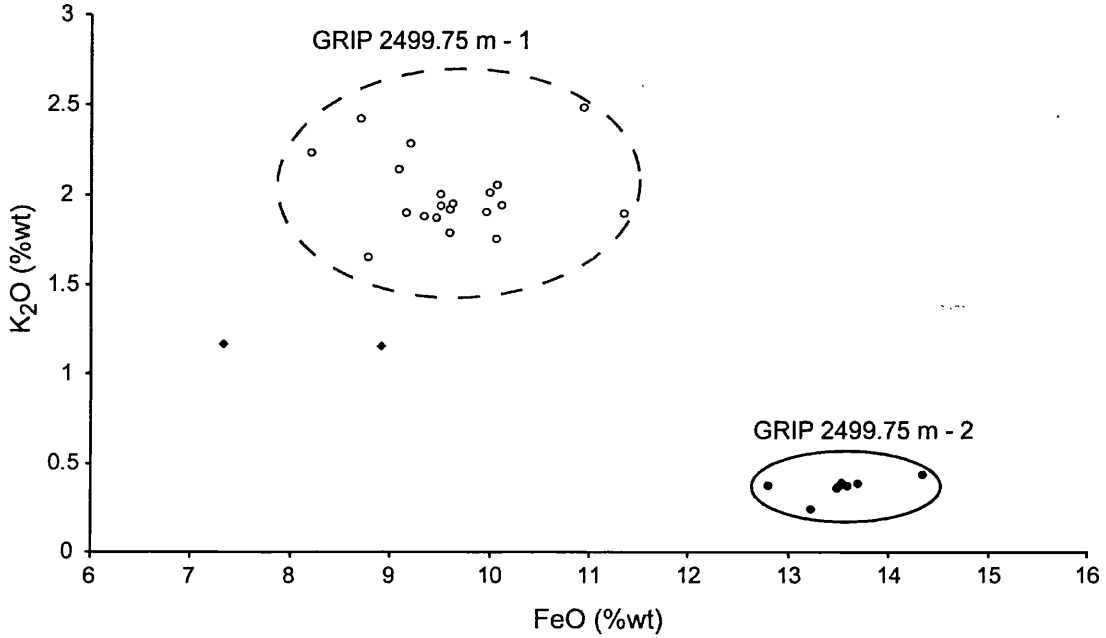


**Figure 6.10:** Geochemical data from the GRIP 2499.75 m tephra horizon plotted on a FeO vs. $K_2O$ compositional variation diagram demonstrating the bimodality of the geochemical data from the glass shards within this horizon.

(figure 6.12) they will be considered as one population. The $K_2O$ values for GRIP 2499.75 m-1 shards range between 1.6 and 2.5 %wt, which is greater than typical values for Icelandic basaltic shards, and all of the analyses fall outside the geochemical field for Icelandic material and within the field for Jan Mayen material (figure 6.11). Biplots of additional major oxides also display this relationship, figure 6.12, therefore the Jan Mayen volcanic region can be considered as the source for population 1 of the GRIP 2499.75 m tephra horizon.

The REE profiles for 10 individual analyses gained from shards within GRIP 2499.75 m-1 are illustrated in figure 6.7b. This shows that this horizon has a relatively heterogeneous trace element composition with a similar level of variability shown for all of the REEs. The average REE profile for this horizon has a steep curve between La and Tb and a relatively flat profile for the HREEs between Dy and Lu.

The shape of this profile shows a strong similarity to proximal Jan Mayen deposits, with the distinctive steeper curve for the LREEs than for Icelandic characterisations (figure 6.13a). However, as with NGRIP 2454.9 m the average concentrations of the REEs are generally lower within GRIP 2499.75 m-1 than the proximal material (figure 6.13a and b (i) and (ii)). Figures 6.13b (iii) and (iv) compare the concentrations of Rb, Sr, Zr and Y within the GRIP 2499.75m-1 shards to geochemical fields defined by analyses reported in Imsland (1984). These plots demonstrate reasonable similarities between the absolute values for GRIP 2499.75 m-1 tephra shards and the proximal Jan Mayen deposits.

Overall, the trace element characterisation of this horizon provides further evidence that this horizon was sourced from the Jan Mayen volcanic region. Potential explanations for the offset in the REE profiles and absolute trace element concentrations between GRIP 2499.75 m-1 and the Jan Mayen proximal deposits are that they were caused by gas blank misestimation or the proximal characterisations do not capture the full compositional range of Jan Mayen products (see section 5.4.3).

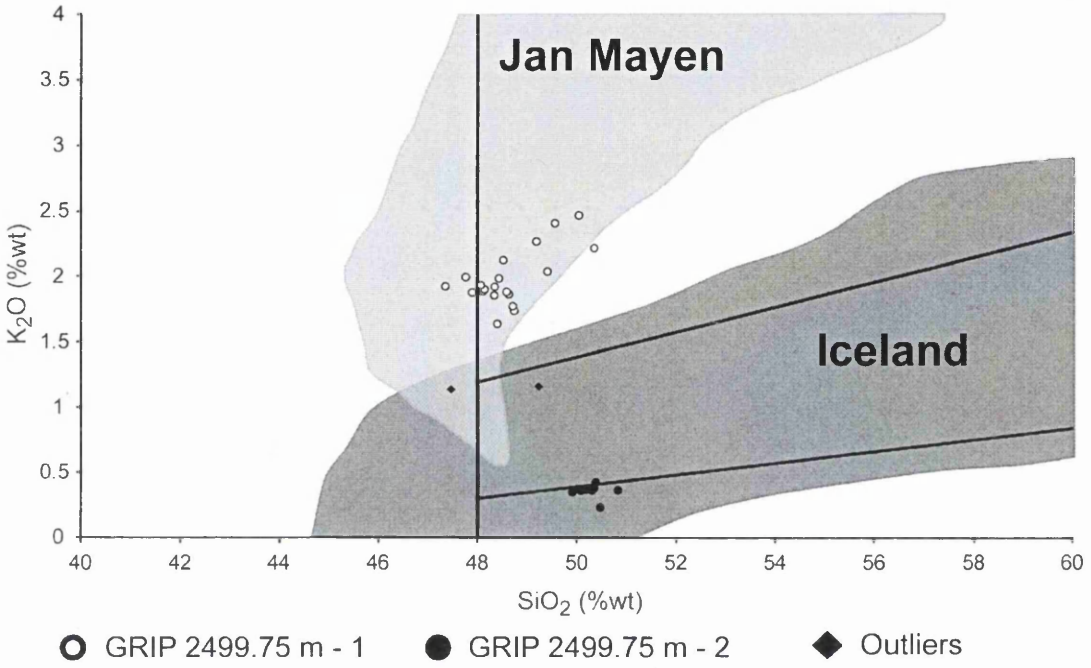


**Figure 6.11:** Geochemical data for the GRIP 2499.75 m tephra horizon compared to geochemical fields for Icelandic and Jan Mayen proximal volcanic material on a $SiO_2$ vs. $K_2O$ variation diagram. Composition field for the typical composition of Jan Mayen volcanic products based on data from Imsland (1984). Composition field for the typical composition of Icelandic volcanic products based on data from Jakobsson (1979), Haflidason et al. (2000), Larsen et al., (2002) and Höskuldsson et al. (2006).

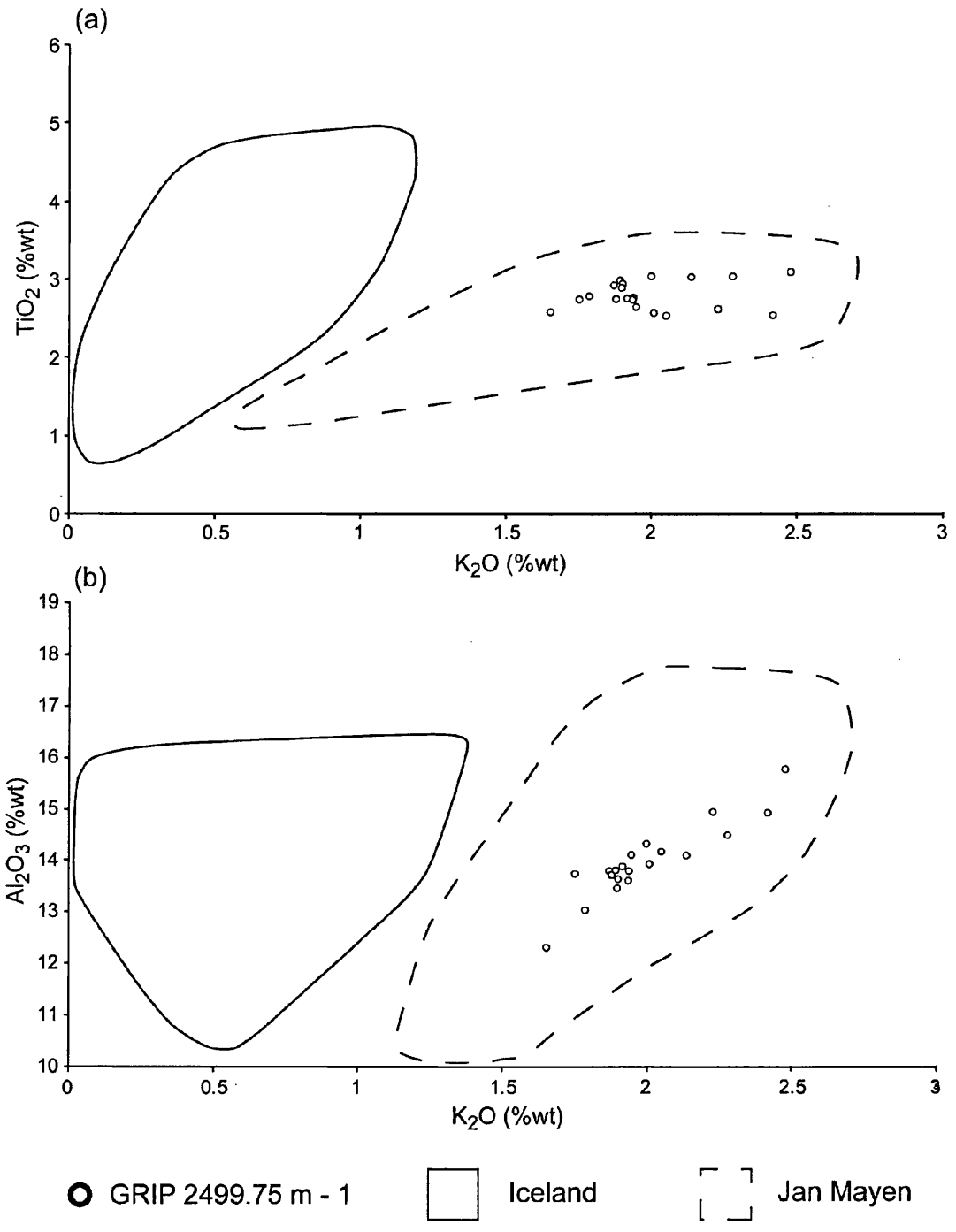


**Figure 6.12:** Geochemical data from population 1 of the GRIP 2499.75 m tephra horizon compared to geochemical fields for Icelandic and Jan Mayen proximal volcanic material on (a) $K_2O$ vs. $TiO_2$ and (b) $K_2O$ vs. $Al_2O_3$ compositional variation diagrams. Compositional field for Jan Mayen products based on data from Imsland (1984). Compositional field for Icelandic products based on data from tephra horizons with <51%wt $SiO_2$ summarised in Haflidason et al. (2000).

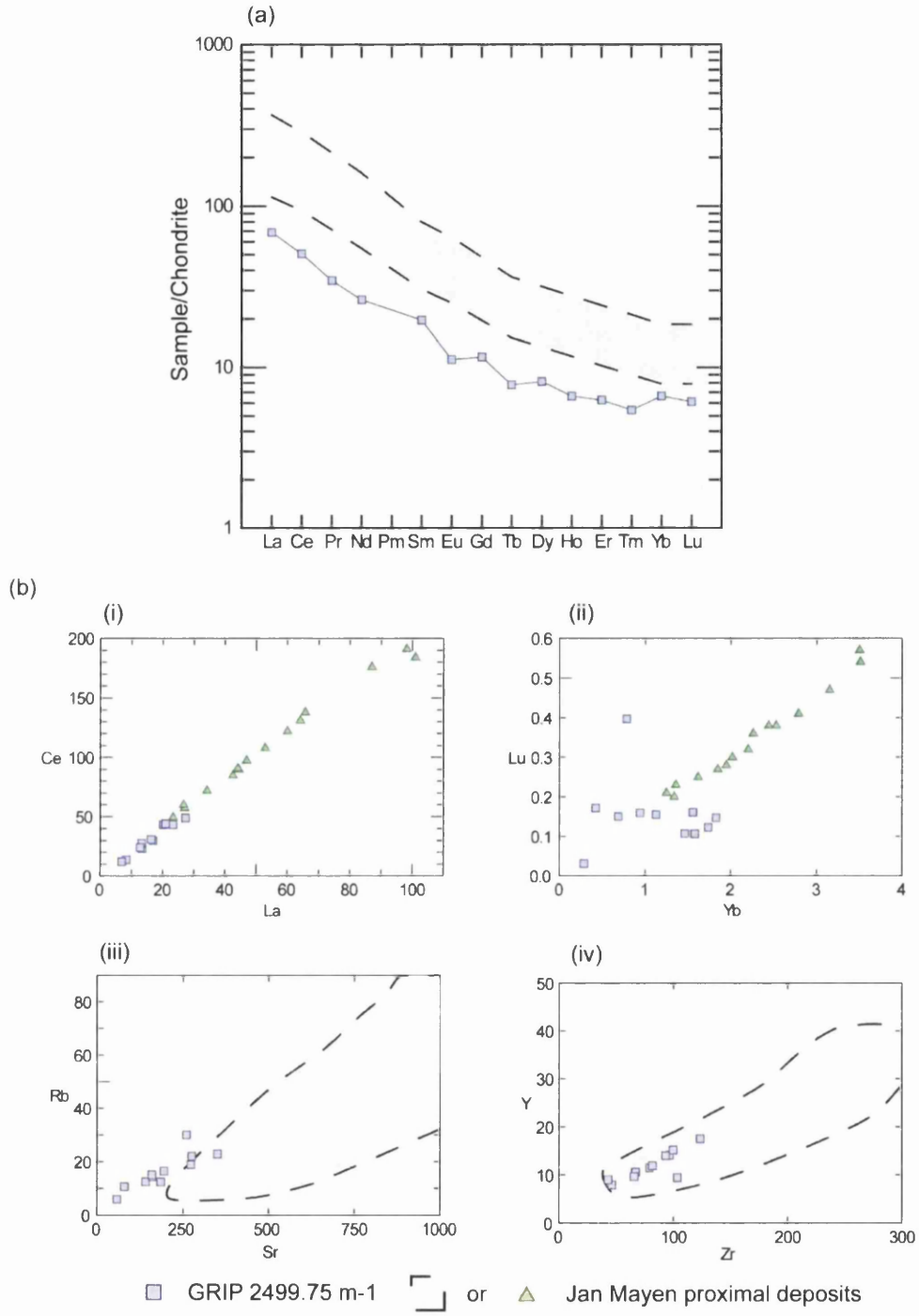


**Figure 6.13:** (a) Chondrite-normalised REE profile for GRIP 2499.75 m-1 compared to the typical REE profile of volcanic material proximal to the Jan Mayen volcanic region. (b) (i) La vs. Ce (ii) Yb vs. Lu (iii) Sr vs. Rb and (iv) Zr vs. Y compositional variation diagrams comparing individual shard analyses from GRIP 2499.75 m-1 to analyses of proximal Jan Mayen products. Analyses of proximal Jan Mayen material used in figures a and b(i) and (ii) from Maaløe et al. (1986). Data used to define geochemical fields in figures b(iii) and (iv) from Imsland (1984).

### 6.4.2.2 Population 2

The $K_2O$ values for the GRIP 2499.75 m-2 analyses fall within the typical range of Icelandic basalts (figure 6.11) and as they all plot well below the division line defined by MacDonald and Katsura (1964) (figure 6.6) they can be considered as having an affinity to the Icelandic tholeiitic rock suite. A comparison to Icelandic volcanic systems producing tholeiitic material demonstrates that the material has a clear affinity to products of the Grímsvötn volcanic system (figure 6.14). Therefore, the Grímsvötn volcanic system can be considered to be the source of GRIP 2499.75 m-2. Trace element characterisations were not gained from any of the shards related to the GRIP 2499.75 m-2 population.

Similarity coefficient comparisons to previously identified MIS 2-5e eruptions show that out of the 9 MIS 4 ice-core horizons within the comparison GRIP 2499.75 m-2 has a geochemical affinity to the highest number of eruptions (appendix 6). 7 horizons have a similarity coefficient exceeding 0.95 when their composition is compared to GRIP 2499.75 m-2 and these geochemical similarities can be observed in figure 6.15. Out of the previously identified horizons within this comparison only FMAZ III has been directly ascribed to a Grímsvötn source by Rasmussen et al. (2003). In addition, Wastegård and Rasmussen (2001) suggested that the 5a-Top/BAS-I, 5c-Midt/BAS-I and 5e-Low/BAS-IV horizons were sourced from the Eastern Volcanic Zone; a complex of volcanic systems including Grímsvötn. Source volcanic systems for the remaining horizons were not determined by the authors, however, the geochemical similarities between these horizons and the strong affinities to the products of the Grímsvötn volcanic system (figure 6.15) suggests that this was the source for all of the horizons.

Overall this comparison suggests that the Grímsvötn volcanic system was consistently erupting material with a similar composition throughout the MIS 2-5e period. In addition, the identification of the horizons within distal sequences indicates that the volcanic eruptions were of a sufficient explosivity to produce widespread horizons.

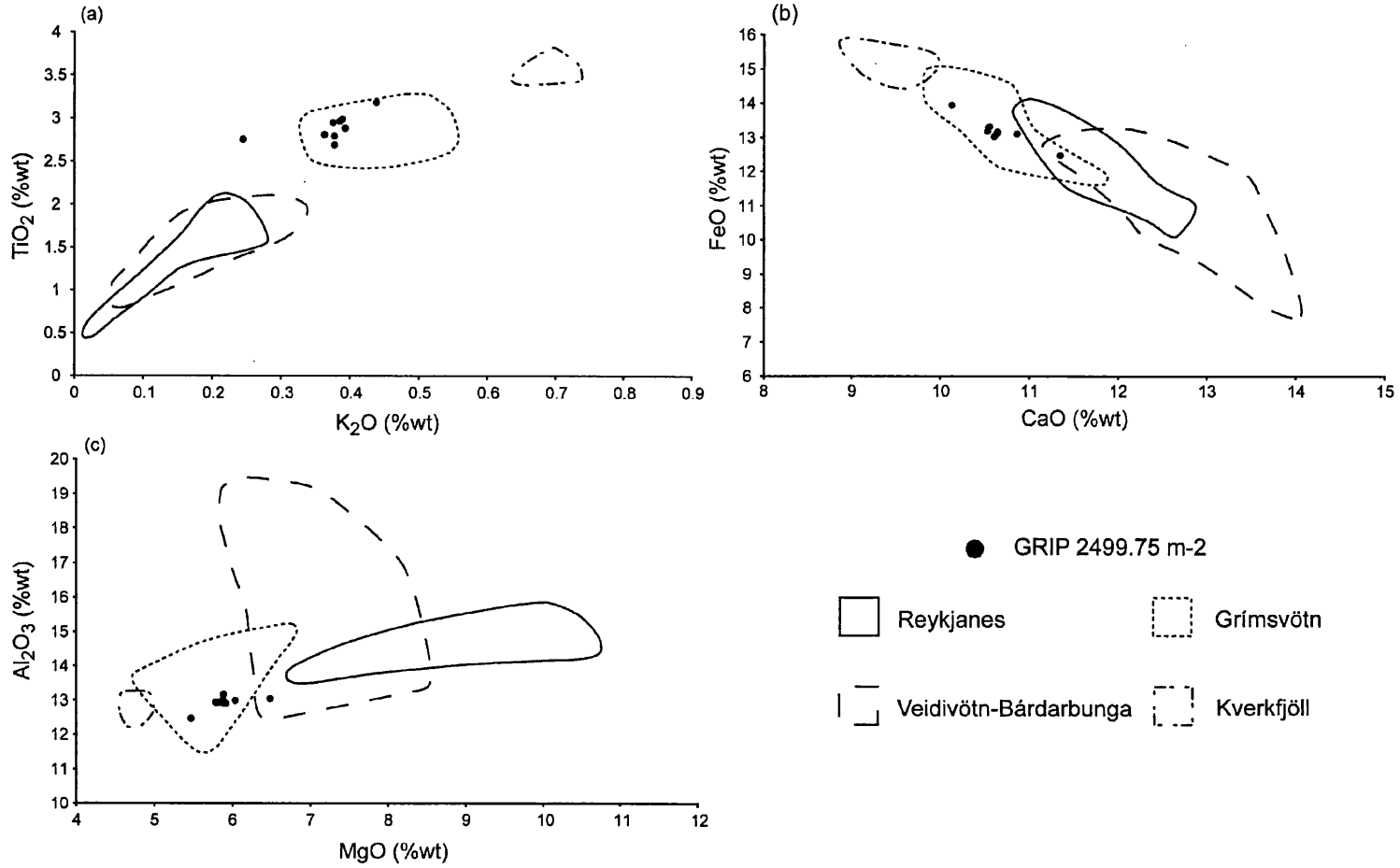


**Figure 6.14:** Geochemical data for GRIP 2499.75 m-2 compared to geochemical fields for four Icelandic tholeiitic volcanic systems on (a) $K_2O$ vs. $TiO_2$ (b) CaO vs. FeO and (c) MgO vs. $Al_2O_3$ compositional variation diagrams. Geochemical fields for the Grímsvötn and Veidivötn-Bárdarbunga volcanic systems defined using whole rock analyses from Jakobsson (1979) and analyses of tephra horizons complied by Haflidason et al. (2000). Geochemical field for the Reykjanes system defined using whole rock analyses from Jakobsson et al. (2008) and the Kverkfjöll system using whole rock data from Höskuldsson et al. (2006).

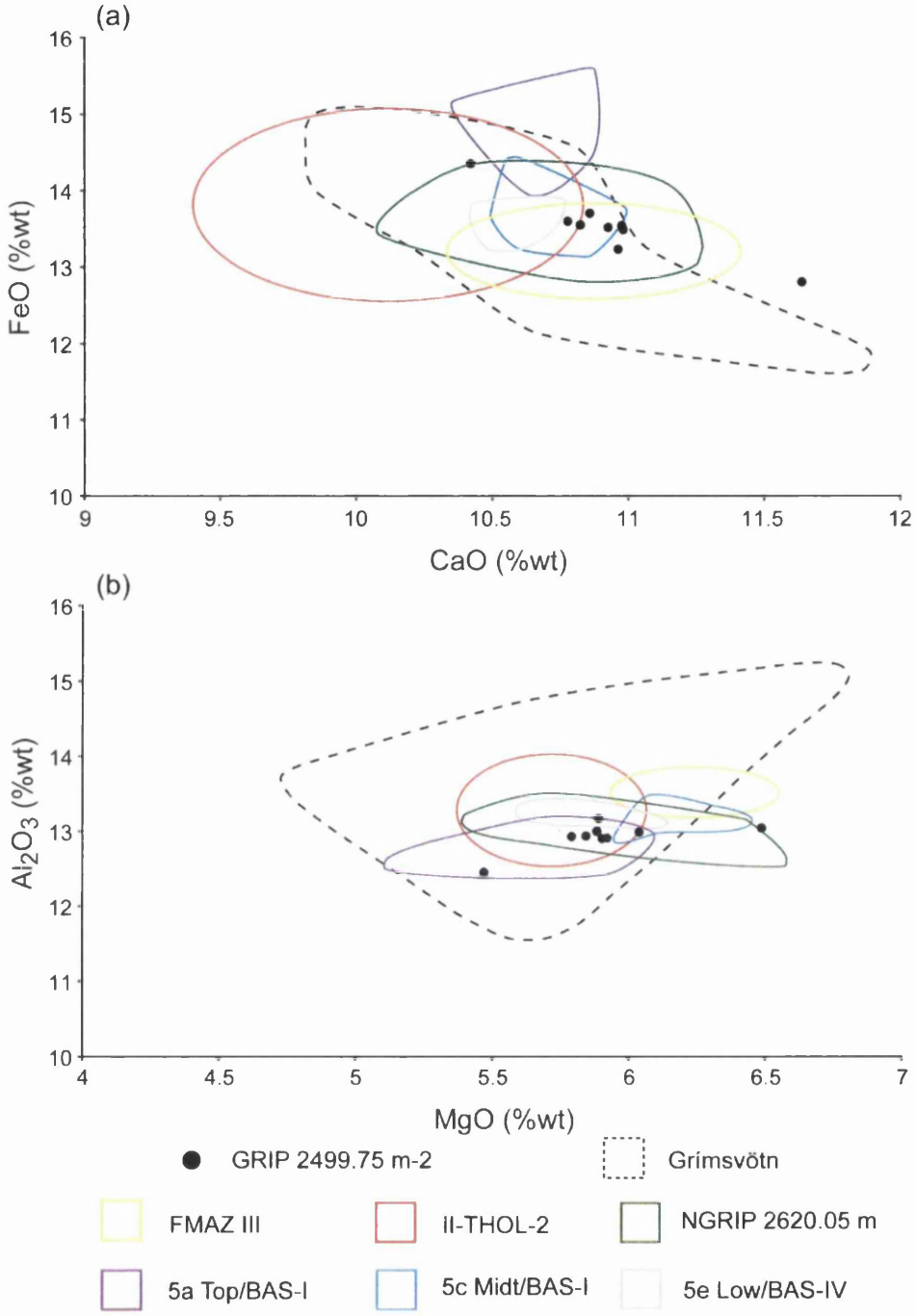


**Figure 6.15:** (a) CaO vs. FeO and (b) MgO vs. $Al_2O_3$ compositional variation diagrams comparing geochemical data from the GRIP 2499.75 m-2 tephra horizon to MIS 2-5e tephra horizons with similar major element compositions and the geochemical field for products of the Grímsvötn volcanic system. Geochemical data used for the definition of the fields for the MIS 2-5e tephra horizons from Rasmussen et al. (2003) (FMAZ III, II-THOL-2), Davies (unpublished) (NGRIP 2620.05 m) and Wastegård and Rasmussen (2001) (5a Top/BAS-I, 5c Midt/BAS-I, 5e Low/BAS-IV). Geochemical field for the Grímsvötn volcanic system defined using whole rock analyses from Jakobsson (1979) and analyses of tephra horizons complied by Haflidason et al. (2000).

### 6.4.3 GRIP 2501.05 m

The tephra horizon at 2501.05 m within the GRIP core is composed of light greeny-brown, blocky glass shards which range between 40 and 60 μm in diameter. This horizon was deposited shortly after the DO 18 climatic event, and shortly before GRIP 2499.75 m (figure 6.4).

Single shard analyses within this horizon display a heterogeneous composition (figure 6.16) with high variability observed within the concentrations of MgO, FeO and $K_2O$. The analyses plot below and close to the MacDonald and Katsura (1964) division line on figure 6.6 implying that they have either a transitional alkaline or tholeiitic composition. However, as with material from GRIP 2498.5 m, these analyses have an affinity to the tholeiitic rock suite due to their high CaO concentrations ranging between ~12 and 13 %wt and high MgO concentrations of 6-7 %wt, both more characteristic of tholeiitic material. However, as a consistent affinity to one particular volcanic system producing tholeiitic material is not observed (figure 6.16) a rift zone source for this horizon cannot be identified.

In total 14 LA-ICP-MS analyses were made of individual shards from GRIP 2501.05 m and their REE profiles are shown in figure 6.7c. The REE composition of the horizon is slightly heterogeneous, with more variation in absolute concentrations and less coherency between the individual REE profiles for the less abundant HREEs. The average REE profile for the horizon has a reasonably low gradient that is consistent for the whole profile.

Figure 6.17a shows that both the gradient of the REE profile and concentrations for GRIP 2501.05 m display a close relationship to the end member characterisation of the alkaline basalts. Due to the heterogeneity in the Sr concentrations, however, the analyses plotted on figure 6.17b do not display a consistent affinity to either the tholeiitic or alkaline basaltic characterisations of Óskarsson et al. (1982). Comparisons to proximal tholeiitic and transitional alkaline basaltic material reported in Meyer et al. (1985), figures 6.17c and 6.17d respectively, also demonstrates that based on the REE profile gradient this horizon has a closer REE affinity to the more alkaline material. These relationships are similar to those observed for GRIP 2498.5 m and will be discussed further in section 6.4.1.

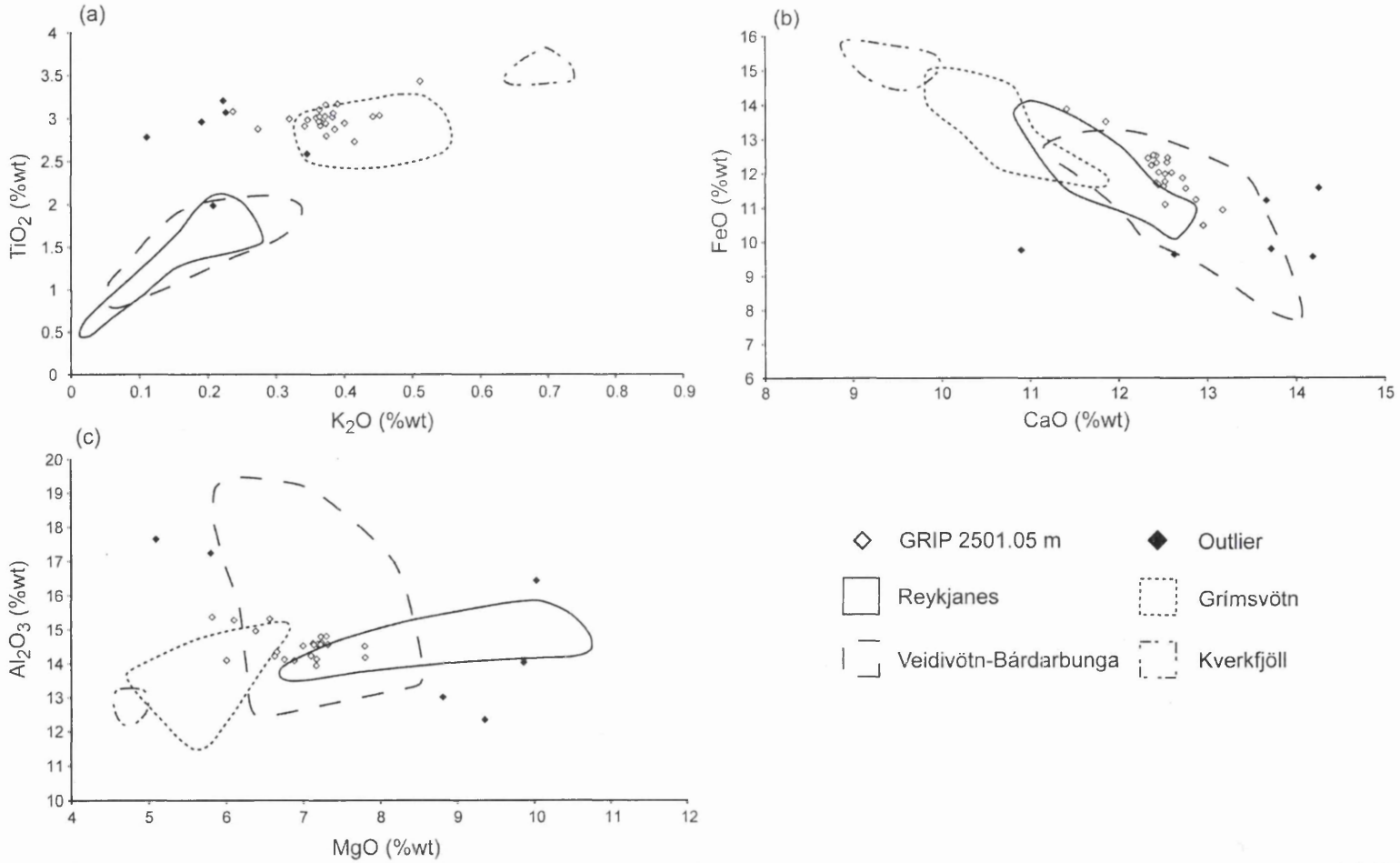


**Figure 6.16:** Geochemical data for GRIP 2501.05 m compared to geochemical fields for four Icelandic tholeiitic volcanic systems on (a) $K_2O$ vs. $TiO_2$ (b) CaO vs. FeO and (c) MgO vs. $Al_2O_3$ compositional variation diagrams. Geochemical fields for the Grímsvötn and Veidivötn-Bárdarbunga volcanic systems defined using whole rock analyses from Jakobsson (1979) and analyses of tephra horizons complied by Haflidason et al. (2000). Geochemical field for the Reykjanes system defined using whole rock analyses from Jakobsson et al. (2008) and the Kverkfjöll system using whole rock data from Höskuldsson et al. (2006).

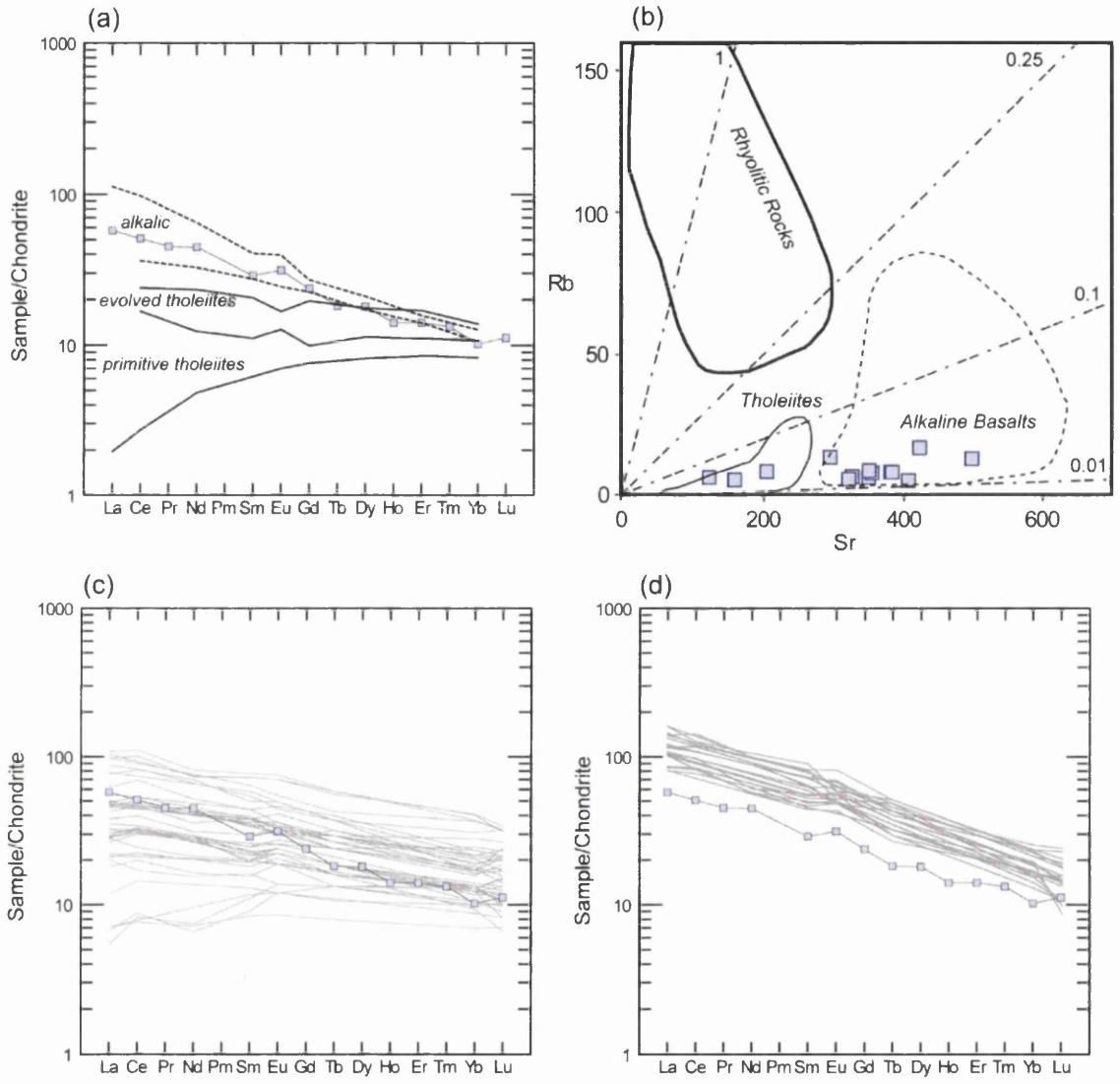


**Figure 6.17:** (a) Average chondrite-normalised REE profile for GRIP 2501.05 m compared to end-member characterisations of Icelandic tholeiitic and alkaline basaltic material (Óskarsson et al., 1982). (b) Sr v Rb compositional variation diagram comparing individual analyses from tephra shards within GRIP 2501.05 m to end-member characterisations defined by Óskarsson et al. (1982). (c and d) Average chondrite-normalised REE profile for GRIP 2501.05 m compared to REE profiles reported in Meyer et al. (1985) for tholeiitic and transitional alkaline proximal material respectively.

### 6.4.4 GRIP 2531.8 m

This tephra horizon is composed of small light brown, platy glass shards, with some larger dark brown and blocky shards. All of the shards range in size between 50 and 80 μm. This horizon was deposited shortly after the DO 19a climatic event (figure 6.4), and no distinct signal in the ECM record from the GRIP core is related to this volcanic material.

An inspection of the major element data for this horizon highlights 3 outlier shards based on their FeO concentrations (figure 6.18b). With these analyses excluded, one relatively homogenous geochemical population is observed with only the concentrations of $K_2O$ displaying a high degree of heterogeneity. This basaltic tephra is characterised by relatively low CaO values (8.3-9.0 %wt) and by high FeO values (14.83 ± 0.33 %wt), which are only exceeded by NGRIP 2500.9 m in this study. Analyses from this population plot above and below the dividing line of MacDonald and Katsura (1964) (figure 6.6) which, combined with the distinct FeO and CaO concentrations for this horizon, implies that this horizon can be classified as a transitional alkali basalt.

Compared to geochemical fields for the Icelandic volcanic systems producing transitional alkali material the analyses from GRIP 2531.8 m fall within the field defined for the Hekla volcanic system on figure 6.18a and b. However, the lower MgO concentrations within GRIP 2531.8 m prevent the pinpointing of Hekla as the source for this eruption.

The individual shard analyses from this horizon display a coherent pattern showing the least variability and the highest concentrations of LREEs for any of the GRIP horizons (figure 6.7d). The average REE profile for GRIP 2531.8 m slopes gently for the LREEs, steepens from Eu to Tm for the MREEs and HREEs and is relatively flat for the heaviest REEs of Tm, Yb and Lu.

This tephra horizon is enriched in all of the REEs, displaying concentrations up to an order of magnitude higher than tholeiitic and alkalic material (figure 6.19a). This relative enrichment is emphasised in the Sr concentrations with a large number of the shards exceeding those recorded for proximal Icelandic basalts (figure 6.19b). These high

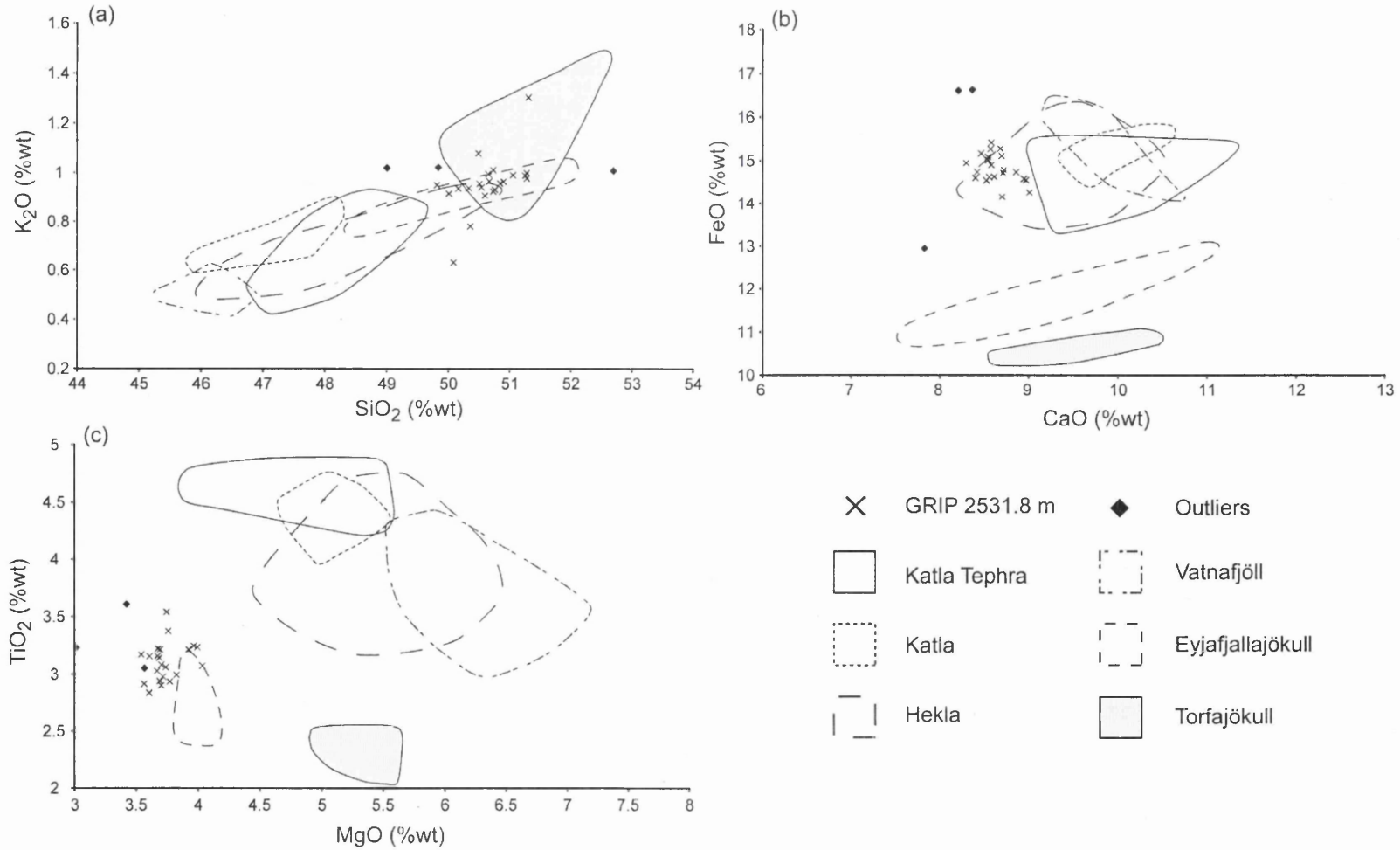


**Figure 6.18:** Geochemical data from the GRIP 2531.8 m tephra horizon compared to geochemical fields for Icelandic transitional alkali volcanic systems on (a) $SiO_2$ vs. $K_2O$ (b) CaO vs. FeO and (c) MgO vs. $TiO_2$ compositional variation diagrams. Geochemical field for tephra horizons from Katla based on average analyses in Haflidason et al. (2000). Geochemical fields for the five Icelandic volcanic systems defined using individual whole rock analyses presented in Jakobsson (1979) and Jakobsson et al. (2008).

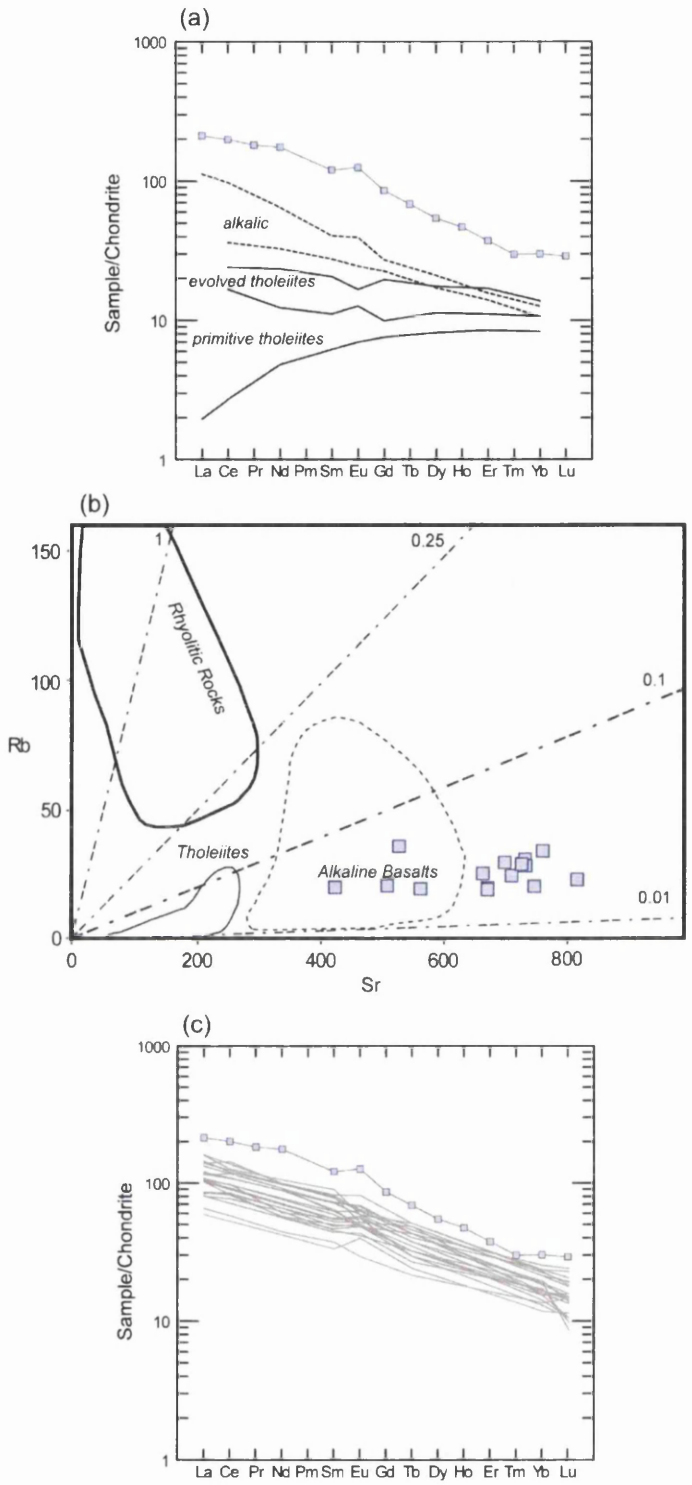


**Figure 6.19:** (a) Comparison between the average chondrite-normalised REE profile for GRIP 2531.8 m and end-member characterisations of Icelandic tholeiitic and alkalic proximal deposits (Óskarsson et al., 1982). (b) Sr vs. Rb compositional variation diagram for GRIP 2531.8 m analyses and end-member characterisations of Icelandic material (Óskarsson et al., 1982). (c) Comparison between the average REE profile for GRIP 2531.8 m and REE profiles for material produced by the Hekla and Katla volcanic systems reported in Meyer et al. (1985).

absolute trace element concentrations are likely to be due to the misestimation of the gas blank during the LA-ICP-MS analysis of shards from GRIP 2531.8 m.

The shape of the REE profile shows similarities to the transitional alkali products of the Hekla and Katla volcanic systems (figure 6.19c), supporting the major element characterisation of this horizon. The relative offset towards higher trace element concentrations could also be due to the impact of gas blank misestimation.

### 6.4.5 GRIP 2532.95 m

The glass shards identified between 2532.75 and 2532.95 m depth in the GRIP ice-core are light green in colour, and display a platy morphology. Shard size ranges between 40 and 60 μm. This horizon was deposited shortly after the DO 19a climatic event and shortly before the GRIP 2531.8 m tephra horizon.

EPMA analyses from 23 individual shards within this horizon are classified as basaltic and overall the deposit has a relatively heterogonous geochemical composition (figure 6.20). This variability is most apparent within the CaO concentrations that vary between 8.5 and 10.5 %wt and MgO concentrations which range between 4.5 and 6 %wt. The high $SiO_2$ concentration (~50-51 %wt) and total alkali values between 3.2 and 4.2 %wt demonstrates that the shards have a tholeiitic composition (figure 6.5).

GRIP 2532.95 m displays strong affinities to both the Grímsvötn and Kverkfjöll volcanic systems (figure 6.20). It has previously been suggested that these systems belong to one volcanic system (Grönvold and Jóhannesson, 1984), therefore the combined Grímsvötn-Kverkfjöll volcanic system can be regarded as the source of the GRIP 2532.95 m tephra horizon.

Within the similarity coefficient comparison between this horizon and previously identified MIS 2-5e horizons five comparisons produced a coefficient exceeding 0.95 (appendix 6). Figure 6.21 illustrates the compositional similarities between GRIP 2532.95 m and the II-THOL-2 component of NAAZ II and the 5d (~113 ka) horizon characterised by Rasmussen et al. (2003) and Lacasse et al. (1998) respectively. There are also significant overlaps with the geochemical fields for the Pop. 5d-1, Pop. 5d-2 and Pop. 5ebase-1 ash zone components described within Fronval et al. (1998). These zones have a heterogeneous composition and may contain material produced

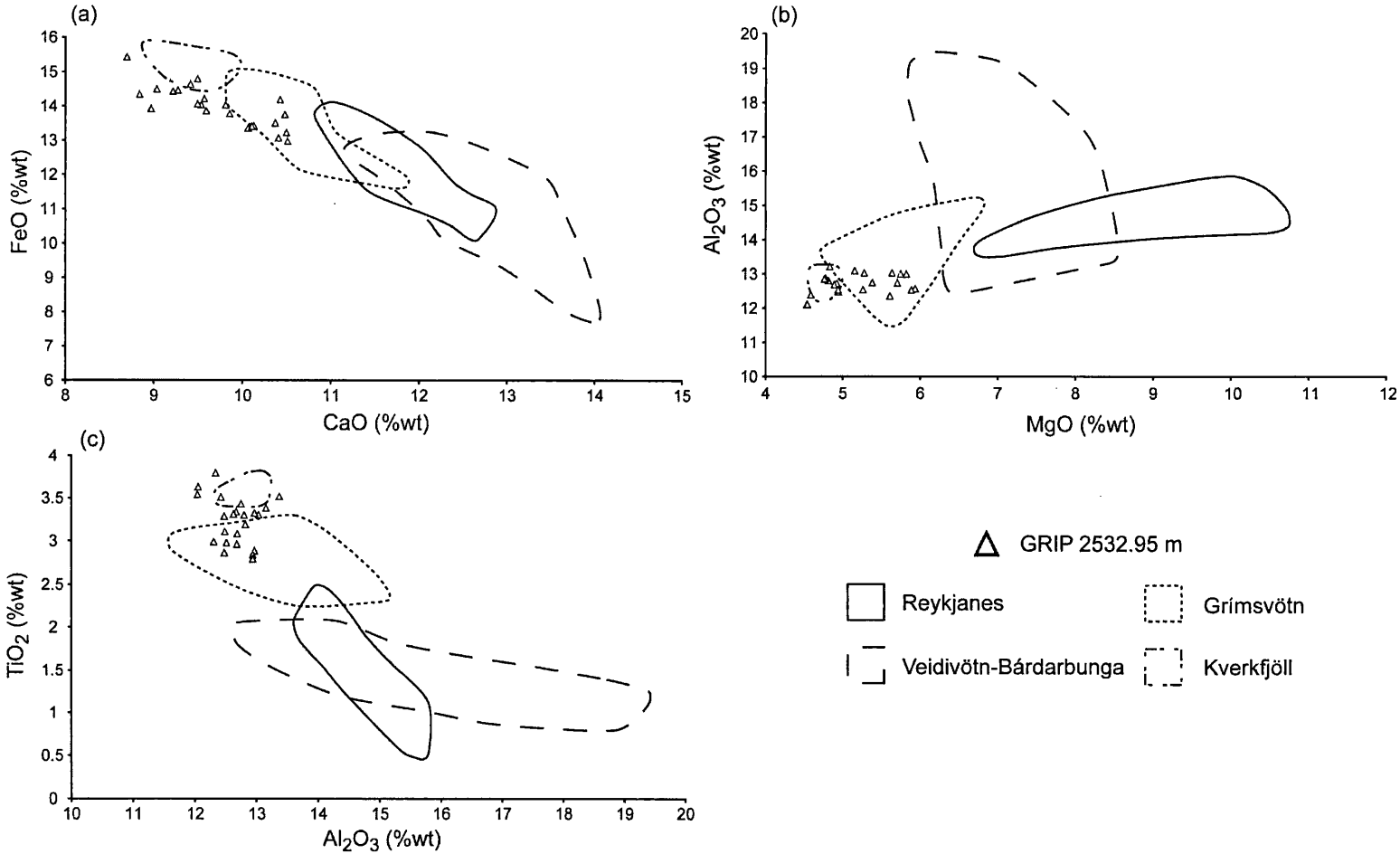


**Figure 6.20:** Geochemical data for GRIP 2532.95 m compared to geochemical fields for four Icelandic tholeiitic volcanic systems on (a) CaO vs. FeO (b) MgO vs. $Al_2O_3$ and (c) $Al_2O_3$ vs. $TiO_2$ compositional variation diagrams. Geochemical fields for the Grímsvötn and Veidivötn-Bárdarbunga volcanic systems defined using whole rock analyses from Jakobsson (1979) and analyses of tephra horizons complied by Haflidason et al. (2000). Geochemical field for the Reykjanes system defined using whole rock analyses from Jakobsson et al. (2008) and the Kverkfjöll system using whole rock data from Höskuldsson et al. (2006).

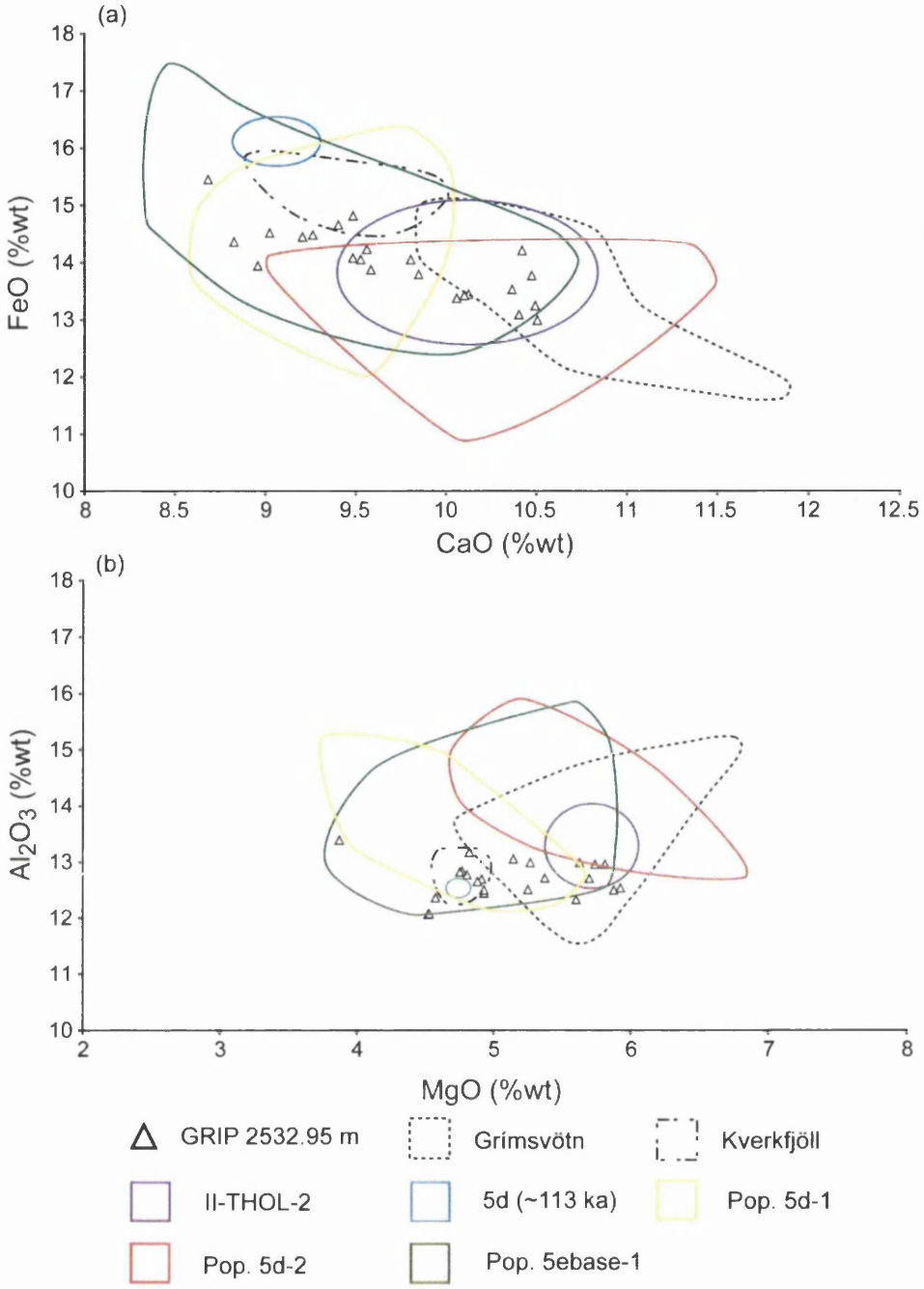


**Figure 6.21:** (a) CaO vs. FeO and (b) MgO vs. $Al_2O_3$ compositional variation diagrams comparing geochemical data from the GRIP 2532.95 m tephra horizon to MIS 2-5e tephra horizons with similar major element compositions and the geochemical fields for products of the Grímsvötn and Kverkfjöll volcanic systems. Geochemical data used for the definition of the fields for the MIS 2-5e tephra horizons from Rasmussen et al. (2003) (II-THOL-2), Lacasse et al. (1998) (5d (~113 ka)) and Fronval et al. (1998) (Pop. 5d-1, Pop. 5d-2 and Pop 5ebase-1). Geochemical field for the Grímsvötn volcanic system defined using whole rock analyses from Jakobsson (1979) and analyses of tephra horizons complied by Haflidason et al. (2000). Geochemical field for the Kverkfjöll system defined using whole rock data from Höskuldsson et al. (2006).

by a range of volcanic systems, however the overlaps with the Grímsvötn and Kverkfjöll geochemical fields suggests that some of the material was derived from these systems.

Overall, the biplots indicate that it is highly likely all of these horizons were either derived from the Grímsvötn-Kverkfjöll volcanic system or contain some material derived from this system. These similarities demonstrate that the Grímsvötn-Kverkfjöll volcanic system was active throughout MIS stages 3, 4 and 5 producing a series of tephra horizons with similar major element compositions. The relevance of this finding to the volcanic history of Iceland will be discussed in section 8.2.2.

The REE composition of GRIP 2532.95 m displays a moderate level of heterogeneity compared to the other GRIP tephra horizons (figure 6.7). The average profile for the REEs has a slight negative gradient for the LREEs, that steepens for the MREEs between Gd and Ho and a flat profile for the HREEs between Ho and Lu (figure 6.7e). A slight positive Eu anomaly can be observed.

The REE profile displays a slightly steeper profile relative to tholeiitic material (figure 6.22a), however, the REE profile is not as steep as the typical profile for alkaline material. In addition, this horizon is enriched in REEs relative to the tholeiitic characterisation. This enrichment may be due to greater geochemical evolution of GRIP 2532.95 m, evident in the high $SiO_2$ values of ~51%wt. A comparison of the concentrations of the light elements of Rb and Sr to the geochemical fields defined for the Icelandic rock suites also shows that trace elements are generally more enriched within GRIP 2532.95 m than the proximal tholeiitic material end-member characterisation (figure 6.22b). However, it should be acknowledged that this relative enrichment could have resulted from an offset in absolute trace element concentrations caused by gas blank misestimation.

The concentrations of the REEs and the profile shape for GRIP 2532.95 m are comparable to those measured within proximal deposits from Grimsvötn reported by Meyer et al. (1985) (figure 6.22c). In addition, some of the proximal characterisations display a positive Eu anomaly, which can be observed in the REE profile for GRIP 2532.95 m. These similarities provide evidence in support of Grimsvötn-Kverfjöll being the source of this horizon.

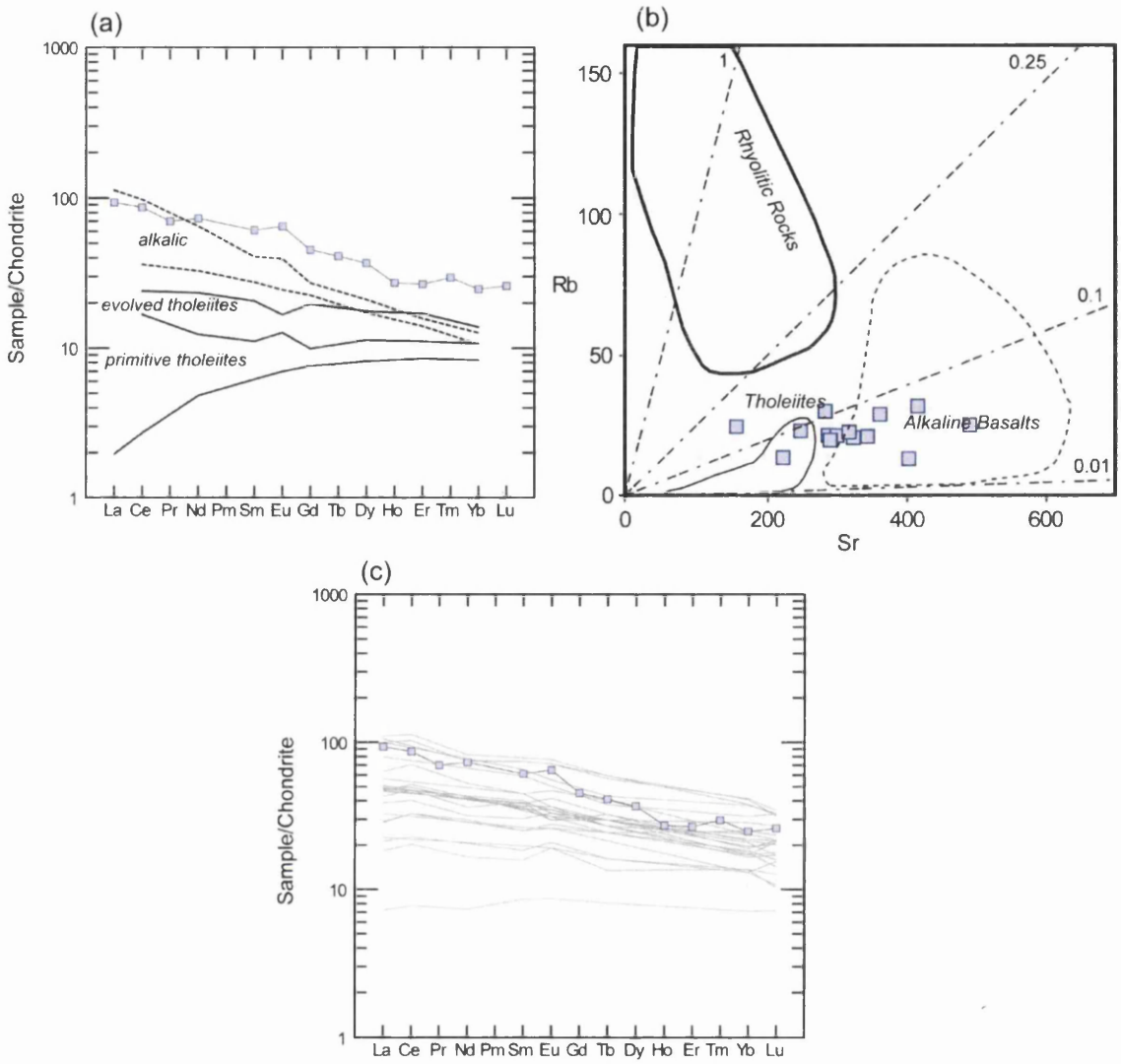


**Figure 6.22:** (a) Comparison between the average chondrite-normalised REE profile for GRIP 2532.95 m and end-member characterisations of Icelandic tholeiitic and alkalic proximal deposits (Óskarsson et al., 1982). (b) Sr vs. Rb compositional variation diagram for GRIP 2532.95 m and end-member characterisations of Icelandic material (Óskarsson et al., 1982). (c) Comparison between the average chondrite-normalised REE profile for GRIP 2532.95 m and REE profiles for material produced by the Grímsvötn volcanic system reported in Meyer et al. (1985).

### 6.4.6 GRIP 2564.3 m

The tephra horizon deposited at 2564.3 m depth within the GRIP ice-core is composed of glass shards with a light greeny-brown colour, platy and blocky morphologies and they range in size between 20 and 40 μm in diameter. The shards were deposited during the rapid cooling event at the end of the DO 20 interstadial event.

Twelve shards were analysed by EPMA and the results demonstrate that this horizon has a bimodal geochemical composition with a basaltic andesitic and a basaltic component (figure 6.5). This bimodality is clear and can be observed in the concentrations of CaO, FeO, $SiO_2$, $K_2O$ and MgO (figure 6.23).

Population 1 is characterised by $SiO_2$ concentrations of ~53 %wt, FeO concentrations between 12.25-12.75 %wt and CaO concentrations around 8.15 %wt, whereas population 2 is characterised by lower $SiO_2$ concentrations around 51.4 %wt, and higher FeO and CaO concentrations of ~13-13.5 %wt and 8.4-9 %wt respectively (table 6.2). A common feature of both populations is an affinity with the transitional alkali rock suite of Iceland as they plot on the division line of MacDonald and Katsura (1964) (figure 6.6). This implies that they were sourced from a volcanic system within either the southern or eastern flank zone of Iceland. The potential source for each horizon will be explored separately.

#### 6.4.6.1 Population 1

It was stated in section 5.4.1 that the volcanic system within Iceland producing the most basaltic andesitic material is Hekla, which is located in the southern flank zone of Iceland. The analyses from GRIP 2564.3 m show a strong affinity to the $SiO_2$, $K_2O$ and FeO concentrations of whole rock analyses from basaltic andesitic material produced by the Hekla system (figure 6.2.4). Some differences are apparent, however, with the MgO concentrations in the GRIP tephra exceeding those from type-site material (figure 6.2.4b). Nevertheless there is a high similarity coefficient for the average composition of GRIP 2564.3 m and the analyses of Hekla whole rock products (table 6.3). The low correspondence to Hekla tephra deposits appears to be due to a more evolved composition relative to these distal deposits. Despite this, some similarities can be

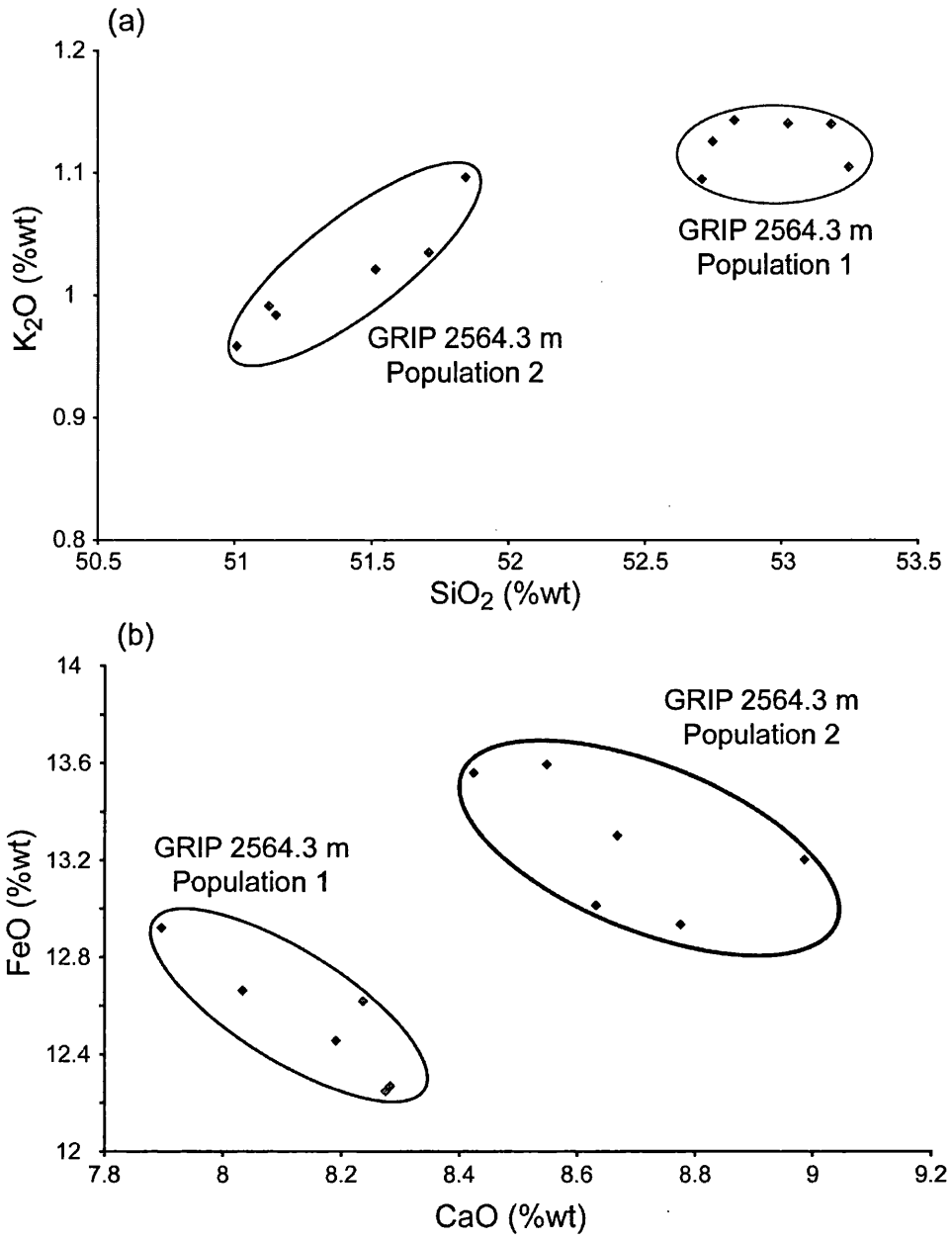


**Figure 6.23:** (a) $SiO_2$ vs. $TiO_2$ and (b) CaO vs. FeO compositional variation diagrams for geochemical analyses from the GRIP 2564.3 m tephra horizon demonstrating the bimodal geochemistry of the analyses.

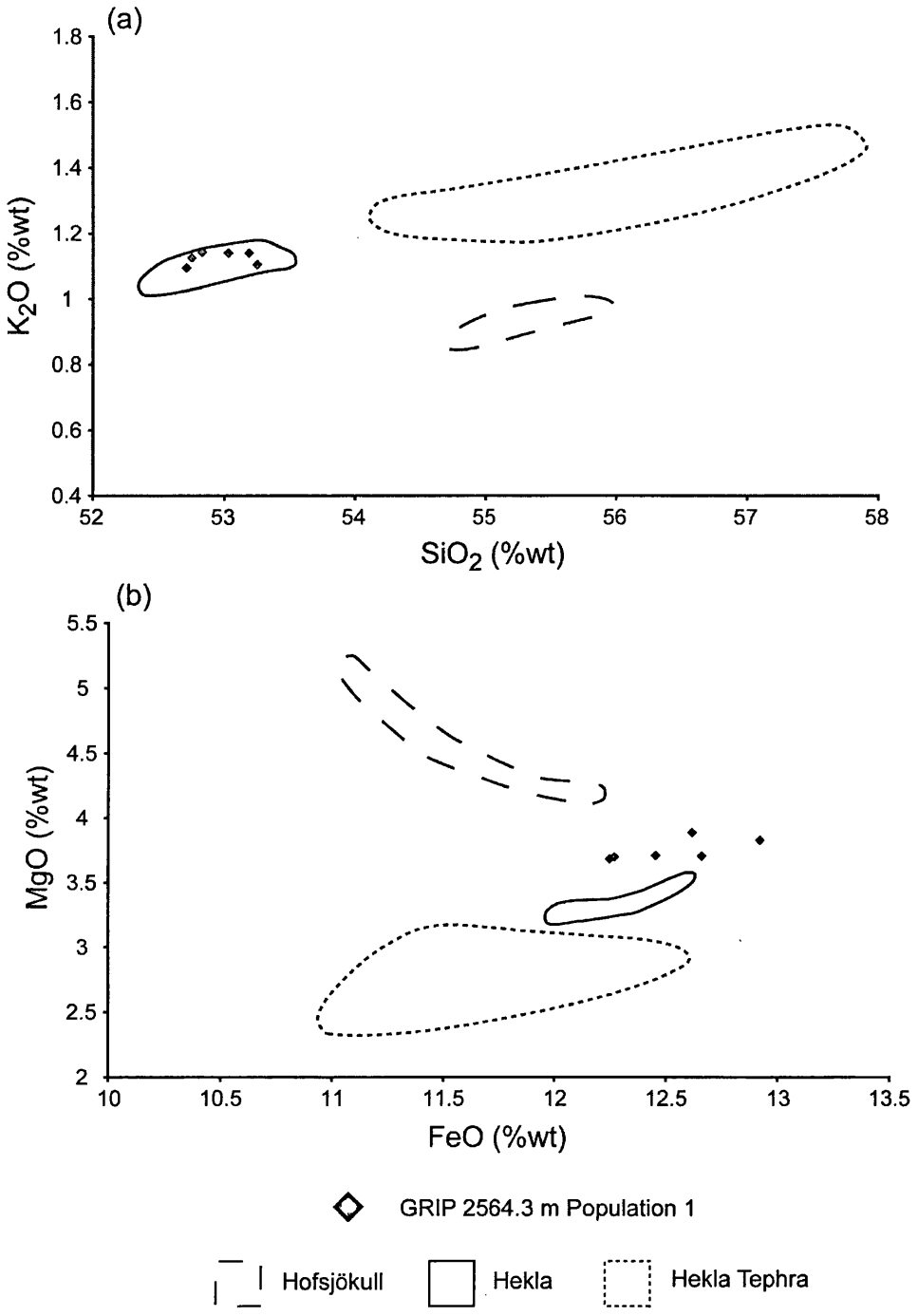


**Figure 6.24:** Geochemical data from GRIP 2564.3 m population 1 compared to geochemical fields for basaltic andesitic products of the Hofsjökull and Hekla volcanic systems on (a) $SiO_2$ v $K_2O$ and (b) FeO and MgO compositional variation diagrams. Geochemical fields for Hofsjökull and Hekla whole rock analyses defined using data from Jakobsson et al. (2008) and Jakobsson (1979) respectively. Geochemical field for Hekla tephra products defined using analyses from Haflidason et al. (2000), Höskuldsson et al. (2007) and Wastegård et al. (2008).

identified, for instance on figure 6.24a the linear covariance between $K_2O$ and $SiO_2$ is the same for GRIP 2564.3 m-1 and the analyses from the tephra horizons.

The relatively high levels of production of basaltic andesitic material within the Hekla system leads one to assume that population 1 of GRIP 2564.3 m was sourced from this volcanic system.

**Table 6.3:** Range of similarity coefficients calculated for comparisons between the average geochemical composition of GRIP 2564.3 m-1 and analyses used to construct the geochemical fields displayed in figure 6.24.

| | Hofsjökull Whole Rock | Hekla Whole Rock | Hekla Tephra Horizons |
|---|---|---|---|
| n | 4 | 4 | 12 |
| GRIP 2564.3 m-1 | 0.81-0.89 | 0.90-0.93 | 0.80-0.86 |

### 6.4.6.2 Population 2

This component also plots close to the geochemical field for the Hekla system and does not show a consistent affinity to any of the other systems producing transitional alkali material (figure 6.25). The analyses do not always plot within the field defined for the Hekla system, however, as it has been deposited in association with transitional alkali basaltic andesitic material it can be assumed that both populations represent the products of a Hekla eruption.

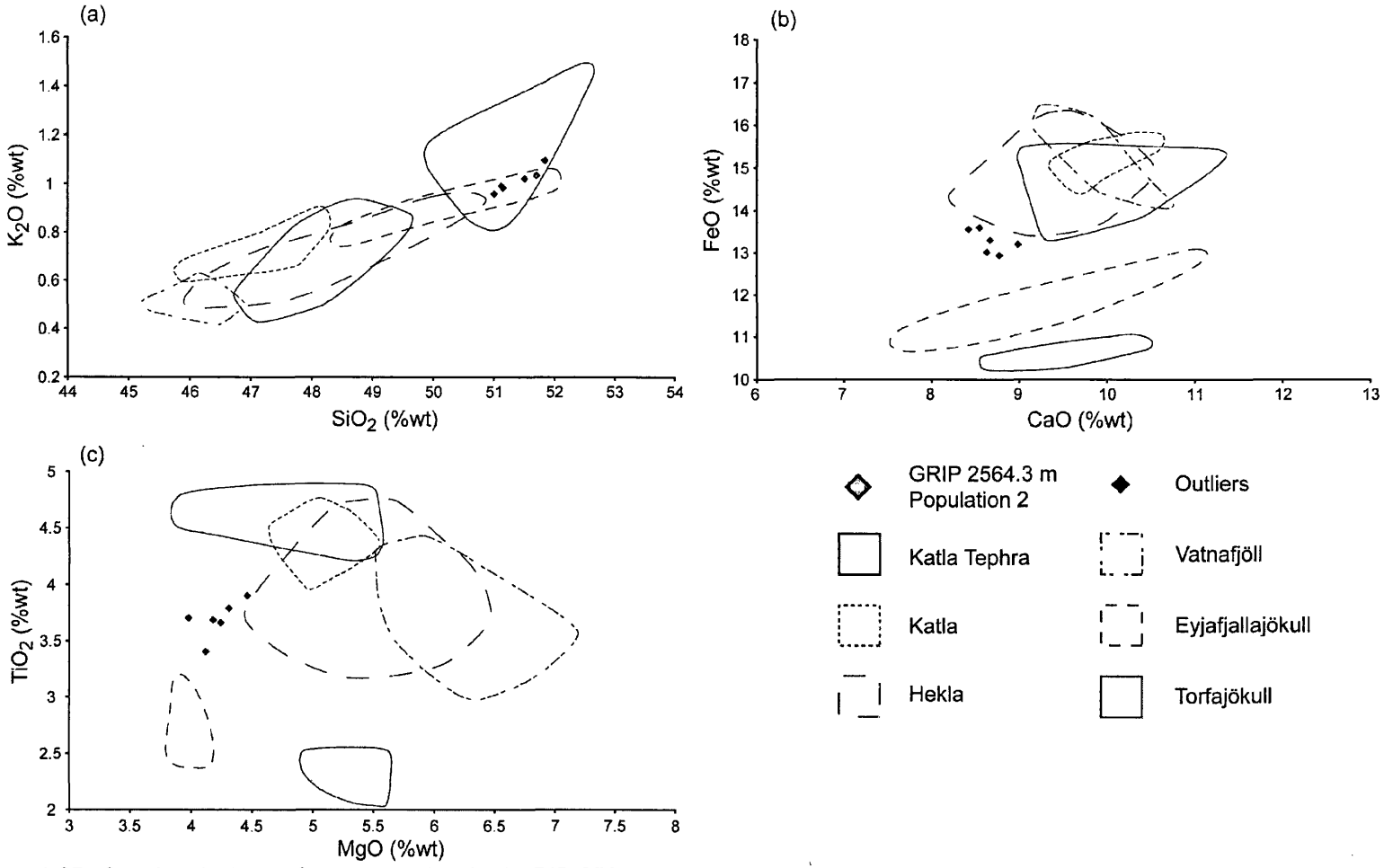


**Figure 6.25:** Geochemical data from population 2 of GRIP 2564.3 m tephra horizon compared to geochemical fields for Icelandic transitional alkali volcanic systems on (a) $SiO_2$ vs. $K_2O$ (b) FeO vs. CaO and (c) MgO vs. $TiO_2$ compositional variation diagrams. Geochemical field for tephra horizons from Katla based on average analyses in Haflidason et al. (2000). Geochemical fields for the five Icelandic volcanic systems defined using individual whole rock analyses presented in Jakobsson (1979) and Jakobsson et al. (2008).

## 6.5 Chapter Summary

The principal findings of this chapter are:

•The identification of six tephra horizons within the MIS 4 section of the GRIP ice-core that can be dated based on their stratigraphic position within the core and the current GICC05 timescale (table 6.4).

•Major element characterisations of these horizons have been used to determine their geochemical composition and suggest potential source volcanic regions or volcanic systems (table 6.4).

•Two horizons of bimodal composition have been identified. The bimodalism within the GRIP 2499.75 m horizon was caused by the deposition of material from two approximately coeval volcanic eruptions from different source regions. Whereas, the geochemical bimodalism within GRIP 2564.3 m resulted from either one eruption of bimodal composition or two closely spaced eruptions from the same volcanic source.

•For the majority of horizons trace element characterisations, gained through the analysis of individual shards, have been shown to provide characterisations consistent with the major element composition of the horizons. However, for two horizons the major element and trace element characterisations are inconsistent which will be discussed further in section 8.3.1.1.

•The absolute trace element concentrations of these characterisations may have been affected by the misestimation of gas blanks during the calculation of concentrations.

**Table 6.4:** Summary of the approximate age, geochemistry and potential sources of tephra horizons identified within the MIS 4 section of the GRIP ice-core. Approximate ages for the horizons were derived from the synchronisation of the NGRIP GICC05 timescale to the GRIP ice-core using common reference horizons (A. Svensson, *pers. comm.*, 2009). The b2k timescale is referenced to 2000 AD and the uncertainly on these age estimates is ~±1300 years.

| Tephra Horizon | Approximate Age (yr b2k) | Geochemistry | Potential Source |
|---|---|---|---|
| GRIP 2498.5 m | 62860 | Basaltic (tholeiitic) | Icelandic Rift Zone |
| GRIP 2499.75 m-1 | 63090 | Basaltic-Trachybasaltic | Jan Mayen |
| GRIP 2499.75 m-2 | 63090 | Basaltic (tholeiitic) | Grímsvötn |
| GRIP 2501.05 m | 63315 | Basaltic (tholeiitic) | Icelandic Rift Zone |
| GRIP 2531.8 m | 68900 | Basaltic (transitional alkali) | Iceland (SFZ or EFZ) |
| GRIP 2532.95 m | 69095 | Basaltic (tholeiitic) | Grímsvötn-Kverkfjöll |
| GRIP 2564.3 m | 73955 | P1 - Basaltic andesitic (transitional alkali)<br>P2 - Basaltic (transitional alkali) | Hekla<br>Hekla |

# 7. Tephrochronology of Marine Isotope Stage 4 within the North Atlantic Marine Core MD04-2822

## 7.1 Introduction

The overall goal of this research is to use volcanic horizons to define tie-points between different depositional environments to explore the relative timing of environmental responses to the Dansgaard-Oeschger events. The MIS 4 section of a North Atlantic marine core, which preserves a record of the Dansgaard-Oeschger events observed within the ice-core records, has been investigated to determine if horizons can be traced between the marine and ice-core depositional environments. This chapter reports the discovery and characterisation of horizons within this marine sequence, exploring potential volcanic sources and the transport processes responsible for their deposition.

## 7.2 MD04-2822

MD04-2822 was collected in June 2004 by the *RV Marion Dufresne* , from the deep-water margins of the Barra Fan in the Rockall Trough (approx. 56° 50'N, 11° 20'W; water depth 2344 m; figure 3.1). Based on nanofossil stratigraphy, the 37.7 m long core is believed to extend into MIS 6 with no breaks in sedimentation. The core was collected to investigate the dynamics of the British Ice Sheet over the last 130 ka and to decipher the impact of millennial-scale climatic fluctuations observed in other marine records from the North Atlantic region (e.g. Bond et al., 1993, 1997).

A tentative tuned correlation was made between MD04-2822 and the NGRIP ice-core oxygen isotope record using ITRAX core scan XRF calcium count data and percentage counts for the planktonic foraminifera *Neogloboquadrina pachyderma (sinistral)* (figure 7.1; Hibbert and Austin, unpublished). This correlation highlights similar variations in the proxy records, which are thought to relate to the Dansgaard-Oeschger events. The North Atlantic Ash Zone II, which is present in both cores provides an independent fix-point for this correlation (W. Austin, *pers. comm.*, 2008). This tephra falls during DO 15 within both cores and provides a fix-point for this event, strengthening the correlation of the DO events around this depth (figure 7.1).

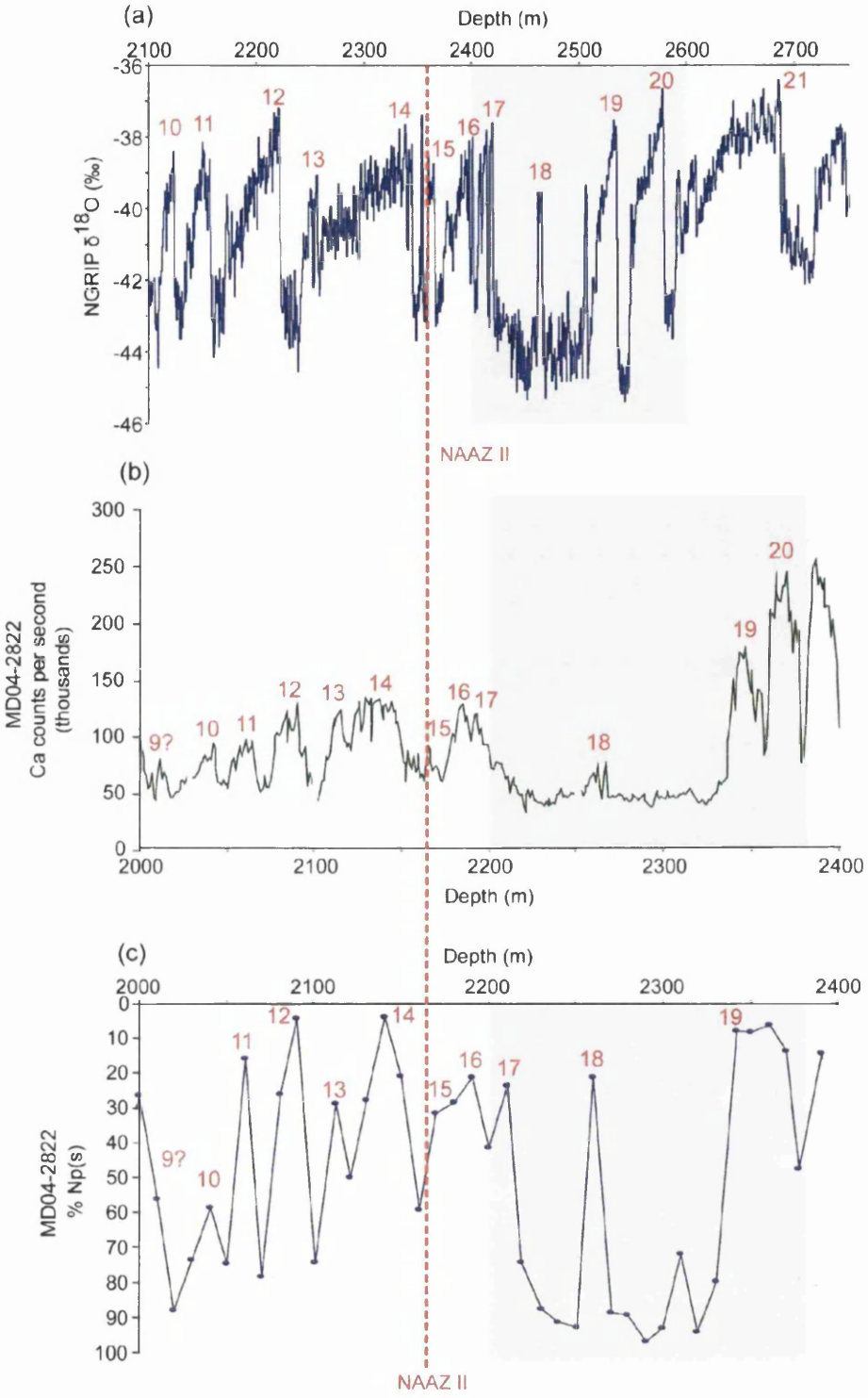


**Figure 7.1:** Correlation of Dansgaard-Oeschger events between (a) the NGRIP oxygen isotope record (b) XRF Ca count rates from MD04-2822 and (c) 10 cm resolution percentage abundance of *Neogloboquadrina pachyderma (sinistral)* within MD04-2822. Data within (a) from NGRIP members (2004) and (b and c) unpublished data provided by Fiona Hibbert and Dr Bill Austin. D-O events for NGRIP defined by Dansgaard (1993) and D-O events for MD04-2822 defined by (Hibbert and Austin, unpublished). Red dotted line represents North Atlantic Ash Zone II (NAAZ II). The grey boxes highlight the sections of core investigated within this study.

Based on this correlation MD04-2822 was sampled between 2200 and 2380 cm (figure 7.1), as this period relates to the MIS 4 climatic period and contains the marine events that have been correlated to DO events 18, 19 and 20, coeval with the period studied within the ice-core records.

### 7.2.1 Sampling Strategy

The core was sampled at a 1 cm resolution between 2200 and 2380 cm depth. The 25-80 μm grain size fraction from 0.5 g of dry weight sediment from a sample every 2 cm, starting from the 2201-2202 cm depth sample, was processed using the heavy liquid separation technique outlined in section 3.3.1. The material present within the 2.3-2.5 and >2.5 g/cm$^3$ density fractions was mounted on microscope slides for optical inspection of tephra shard concentrations.

In addition, material from the 80-125 μm and >125 μm grain size fractions of selected core sections, potentially containing horizons identified within the ice-cores, were investigated. The NGRIP and GRIP oxygen isotope profiles were correlated to the Ca count record from MD04-2822 using common climatic events as tie points (figure 7.2). To account for possible asynchronicity in the environmental response to the climatic events broad sampling periods were selected. Thus, in total the >80 μm grain size fraction was investigated for 40 samples from the following depth intervals: 2225-2260 cm, 2315-2336 cm, 2355-2366 cm and 2371-2380 cm. Due to the small amount of material remaining in the larger size fractions, it was not necessary to isolate any tephra shards from the host sediment using density separation.

## 7.3 Tephra Shard Concentrations between 2200 and 2380 cm depth in MD04-2822

Shard concentrations for the different density and size fractions of the samples are shown in figure 7.3. This figure shows that the highest concentration of tephra shards was identified below 2316 cm depth within the 2.3-2.5 g/cm$^3$ density fraction of the 25-80 μm size fraction. Two major peaks in the concentration of colourless glass shards (figure 7.4), that are considered to represent tephra horizons, were identified between 2316 and 2380 cm depth. One discrete peak is located at 2327-2328 cm depth and a broader peak is observed between 2359 and 2368 cm depth.

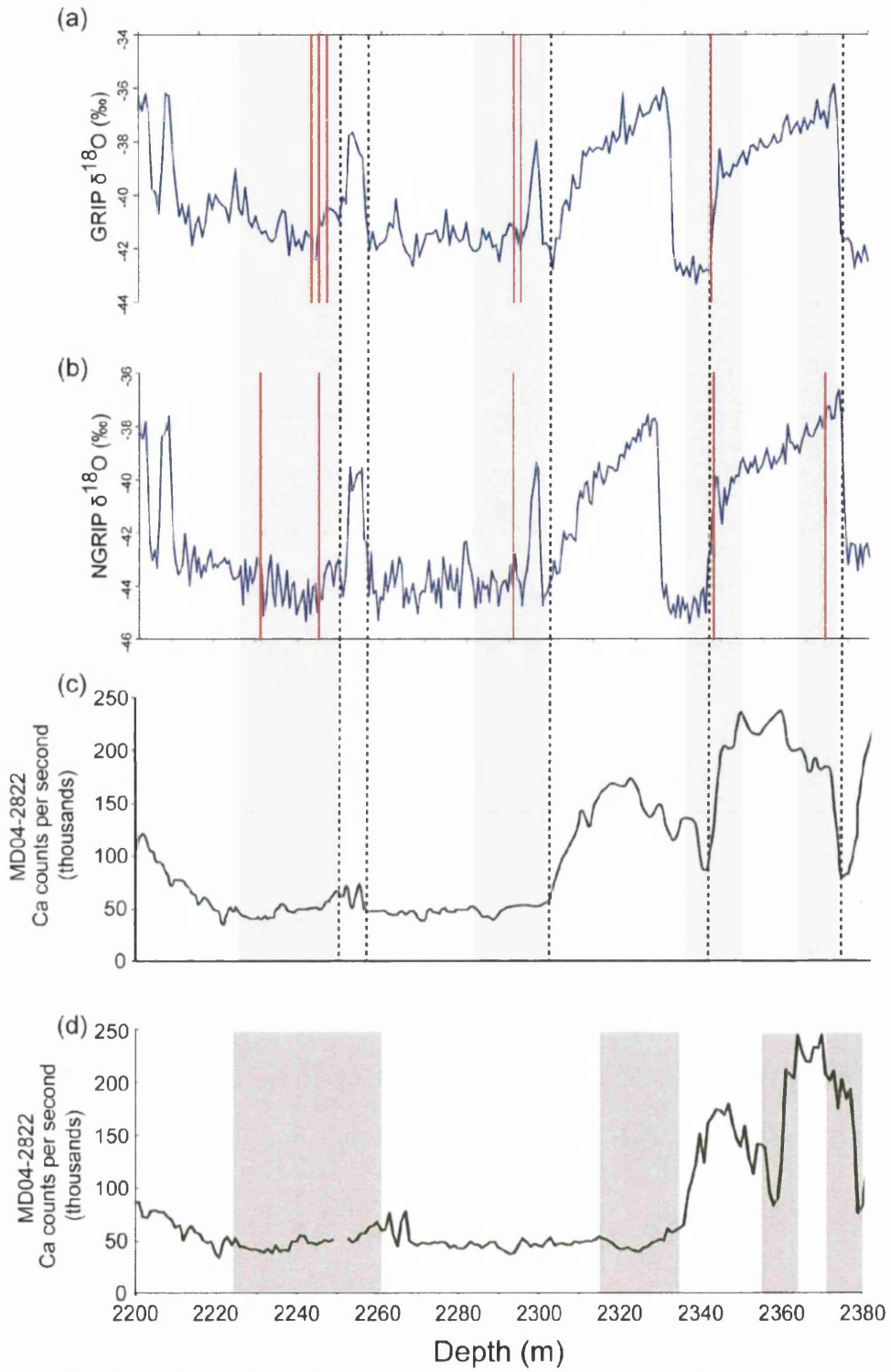


**Figure 7.2:** Marine isotope stage 4 oxygen isotope records from (a) the GRIP ice-core and (b) the NGRIP ice-core. Ca XRF count rates from MD04-2822 (c) tuned to the ice-core records and (d) plotted versus depth in the core. The red lines on figures (a) and (b) represent the depths at which the tephra horizons described in chapters 4 and 5 were identified. The black dotted lines connecting figures (a), (b) and (c) are the tie-lines between common climatic events used to tune the Ca count record of MD04-2822 to the ice-core records. The grey shaded segments represent the periods from which material >80 μm in diameter was inspected.

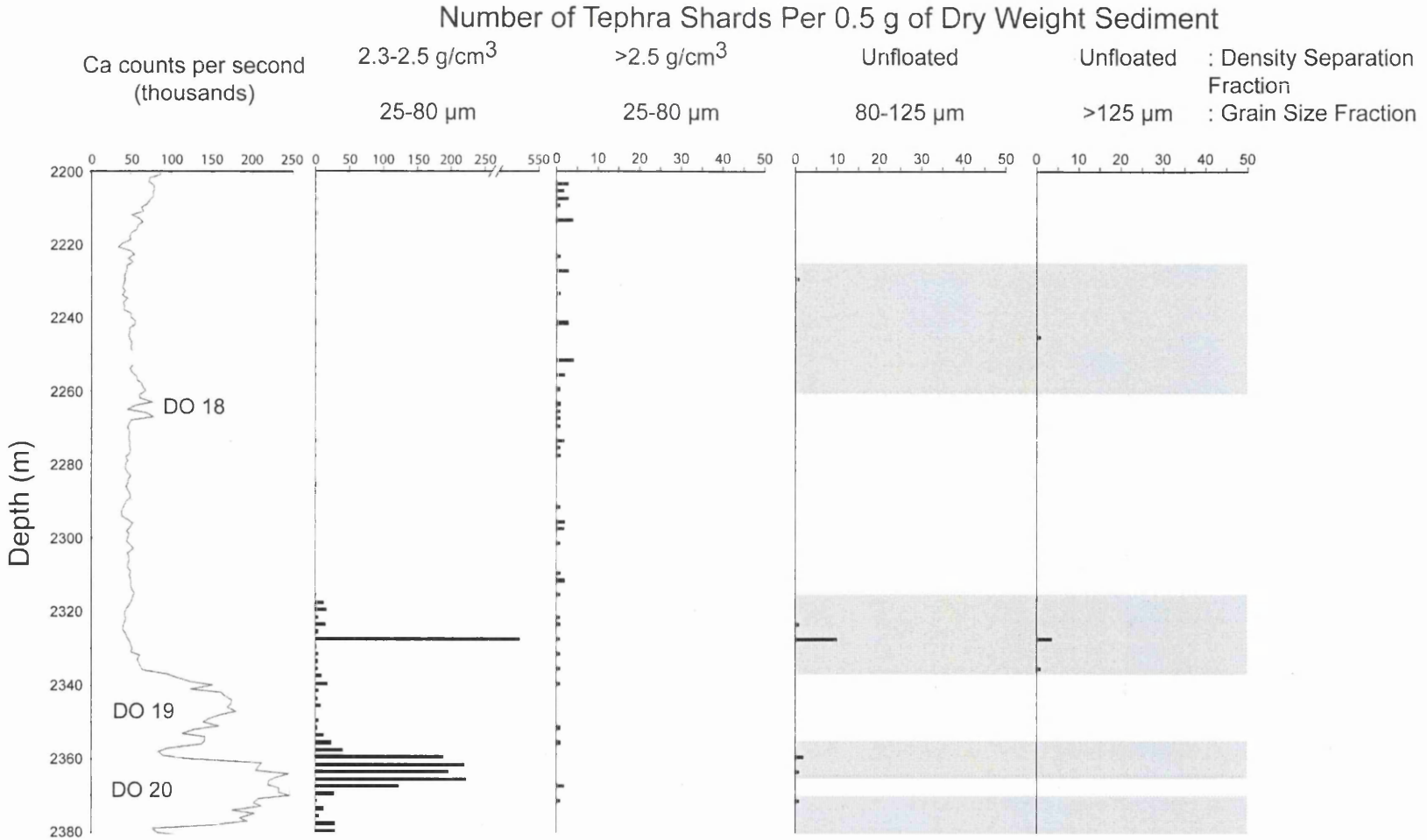


**Figure 7.3:** Tephra shard concentrations between 2200-2380 cm depth within MD04-2822 plotted alongside the Ca counts per second record from the core. The grey boxes denote the sections of the core from which samples from the larger grain sizes were inspected for their tephra content.

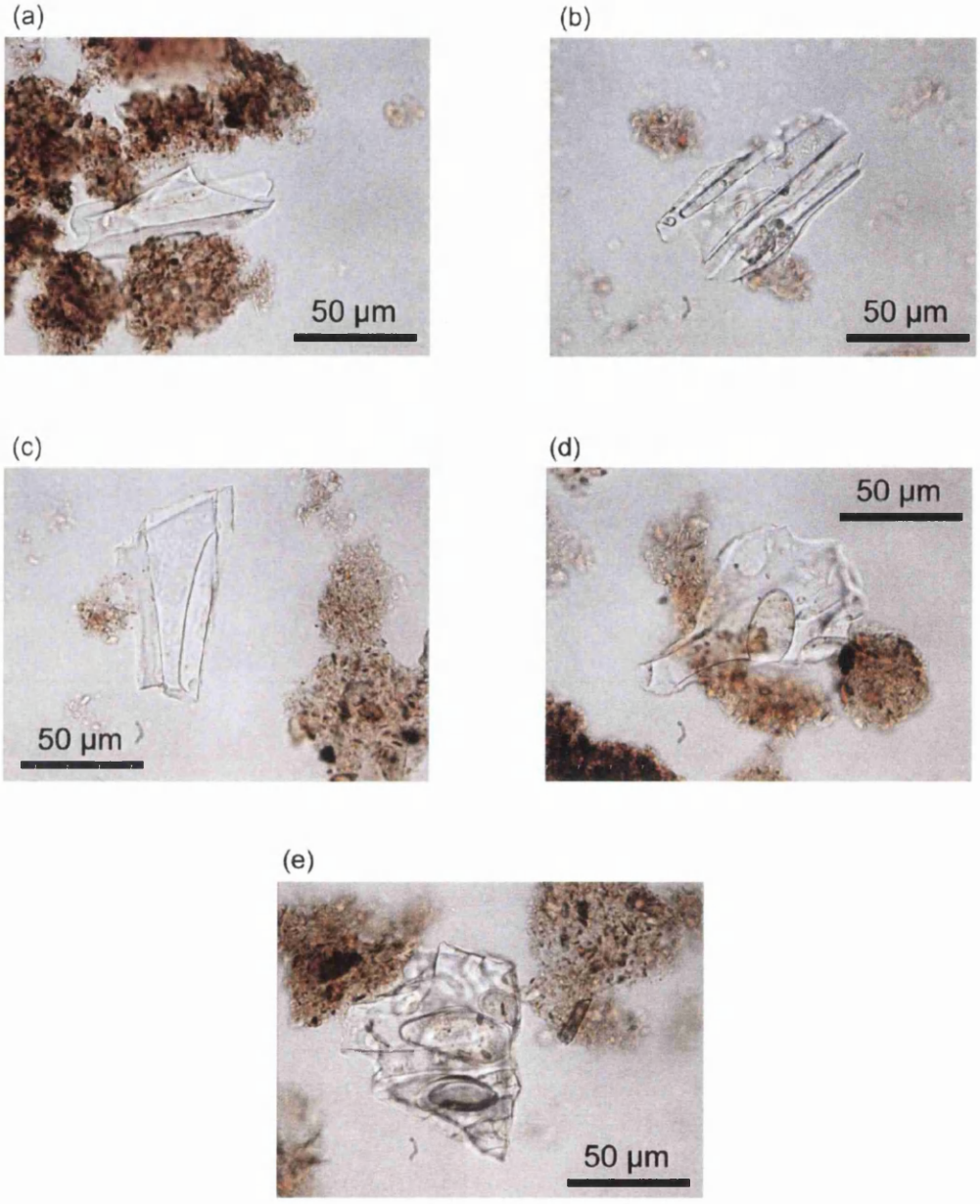


**Figure 7.4:** Images of colourless shards from samples of the MD04-2822 marine core. (a) 2327-2328 cm (b) 2359-2360 cm (c and d) 2361-2362 cm and (e) 2363-2364 cm.

The peak at 2327-2328 cm records the highest concentration of shards, 531 per 0.5 g of dry weight sediment (gdw), observed within this investigation. This peak in material is highly resolved with the shard concentration greatly exceeding that of any other investigated samples (figure 7.3). Colourless glass shards were also identified within the 80-125 μm and >125 μm grain size fractions of this sample with concentrations of 10 and 4 shards per 0.5 g dry weight sediment respectively. These both represent the maximum shard concentrations observed within the larger grain size fractions.

Between 2359 and 2368 cm depth five consecutive samples have shard concentrations exceeding 120 shards per 0.5 gdw and concentrations exceed 200 shards at 2 depths, 2361-2362 cm and 2365-2366 cm. The overall symmetrical bell-shaped distribution in the concentration of shards between these depths suggests that tephra shards have been mixed up and down within the sedimentary column, potentially by bioturbation within the sediment surface mixing zone (Kristjánsdóttir et al., 2007).

Within the 25-80 μm size fraction very few tephra shards with a density greater than 2.5 g/cm$^3$ were identified. No distinct peaks in concentration are apparent with the highest concentration being 4 shards per 0.5 gdw sediment at 2251-2252 cm depth. This was deemed insufficient to constitute a tephra horizon and, therefore, no further analysis was conducted on material from the >2.5 g/cm$^3$ density fraction. Similarly low concentrations of tephra shards were identified between 2200 and 2316 cm depth within the 2.3-2.5 g/cm$^3$ density fraction.

### 7.3.1 Selection of Samples for Geochemical Analysis

Based on the tephra shard counts thirteen samples from the 25-80 μm and 2.3-2.5 g/cm$^3$ fractions were selected for geochemical analysis. These samples were prepared according to the methodology outlined in section 3.5.1. Figure 7.5 indicates the stratigraphic position of these samples. Samples were selected according to the highest shard concentrations and the possibility that the samples may provide an insight into mixing and secondary reworking processes. Major element analyses were obtained from 10 of the samples (figure 7.5). Insufficient material was present on the slides prepared from the 2323-2324 cm, 2345-2346 cm and 2379-2380 cm samples. Tephra shards from the five samples with the highest shard concentrations were additionally analysed using the LA-ICP-MS system to gain trace element characterisations for the two tephra horizons identified within the record.

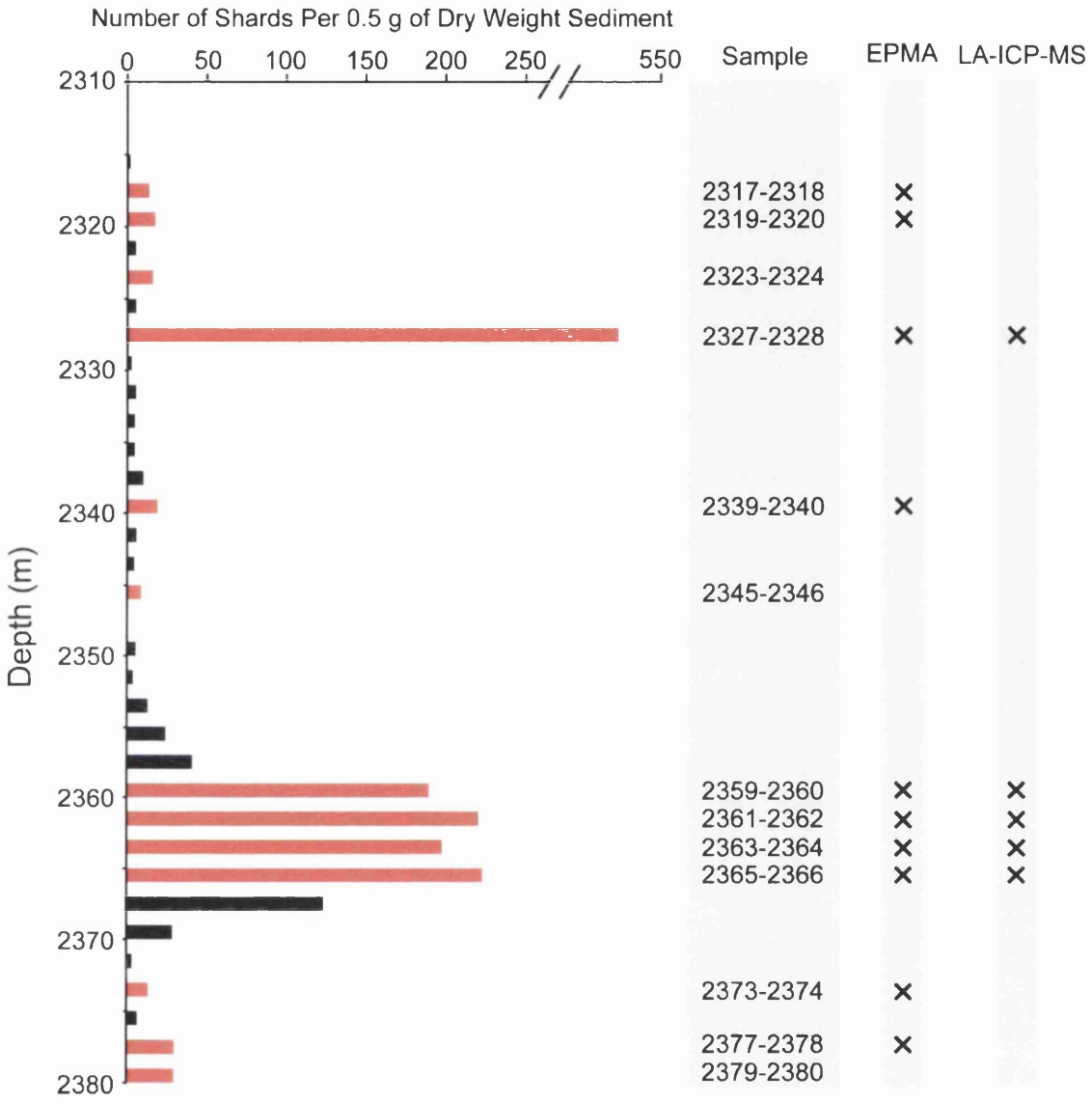


**Figure 7.5:** Tephra shard concentrations within the 25-80 µm grain size and 2.3-2.5 g/cm$^3$ density fraction of samples between 2310 and 2380 cm depth within MD04-2822. Red bars denote samples selected for geochemical analysis.

## 7.4 Major Element Analyses and Data Normalisation

141 individual tephra shards from the 10 samples were analysed for their major element composition. All of the shards were found to have a rhyolitic composition and one of the most noticeable characteristics of the analyses was the low total oxide values with an average of 94.06 % (s.d. 1.02 %). There is no significant variation in total oxides between the different samples, with the mean total oxide value for the individual samples always falling within one standard deviation of the overall mean. Analyses of the secondary standard Lipari conducted during the analysis of the shards from MD04-2822 did not display low total oxide values in comparison to the reference values for this glass (appendix 1). Therefore, it can be inferred that the low total oxide values are a characteristic of the tephra shards from MD04-2822 and are not caused by an analytical error. Similar low total oxides have also been measured in rhyolitic material of a similar age found within other North Atlantic marine cores (e.g. Fronval et al., 1998; Wallrabe-Adams and Lackschewitz, 2003; Austin et al. 2004).

This is most likely due to increased water content in the shards as a result of post-depositional hydration, a common feature of tephra particles extracted from marine cores, that does not have an affect on their geochemistry. To remove the variability in water content as an influence on major oxide concentrations the data was normalised to a water-free basis, i.e. to have 100% total oxide values (see section 3.5.2.1). This allows the data to be compared to geochemical analyses of material from other depositional environments that have not experienced a comparable level of hydration. Therefore, within this chapter all the data from MD04-2822 presented on plots and any datasets used for comparison are normalised. All of the raw unnormalised data are presented in appendix 5.

Figure 7.6 illustrates the geochemical data gained from all of the MD04-2822 shards on total-alkalis versus silica plots and demonstrates that all shards have a rhyolitic composition. The data generally fall within two geochemical groups that may be related to the composition of the two major tephra horizons (figure 7.6b). The following sections will present the major and trace element geochemical data from the two tephra horizons and discuss the nature of the horizons and their potential volcanic source.

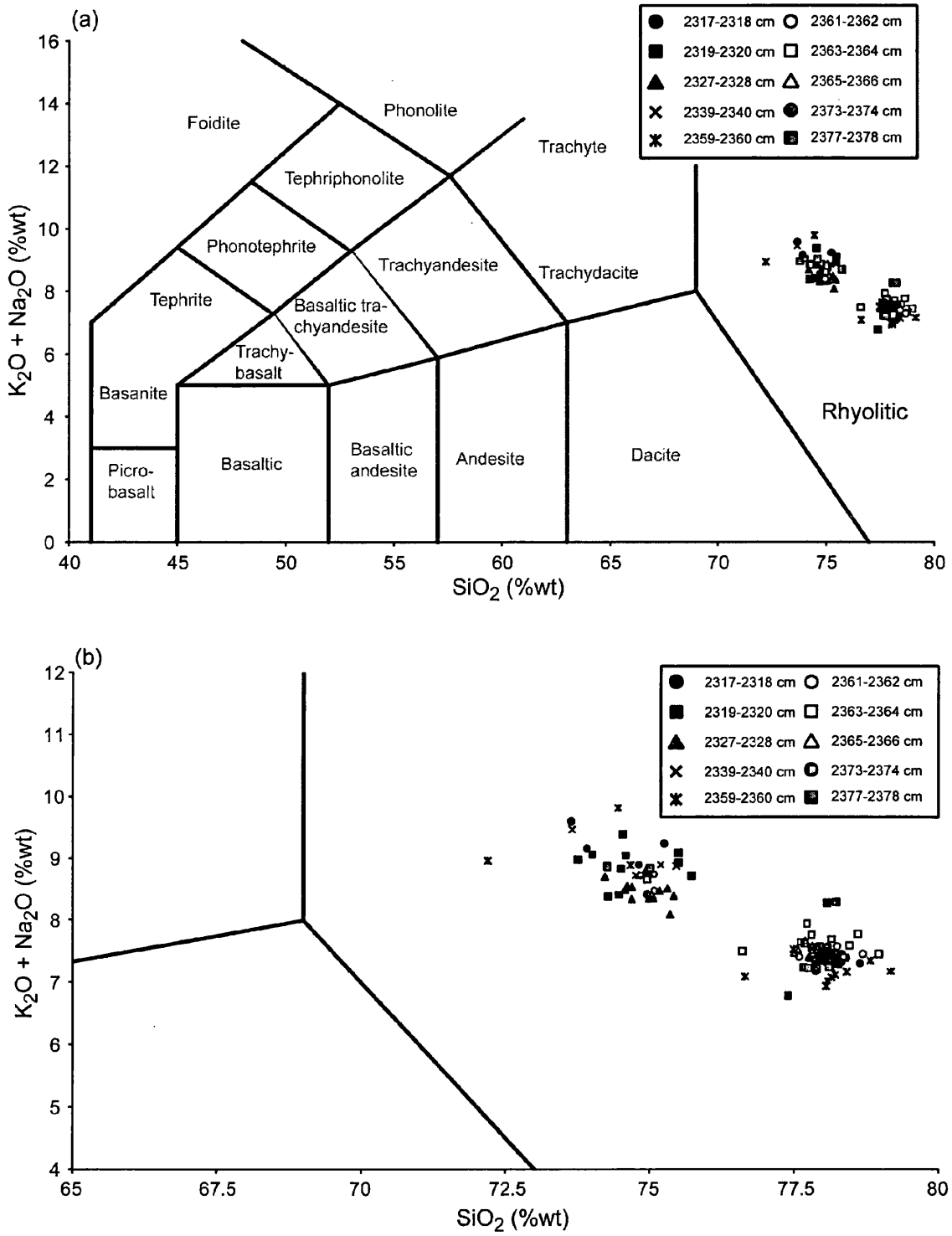


**Figure 7.6:** (a) Total alkalis versus silica plot for analyses from ten samples from MD04-2822. (b) Inset of TAS plot focusing on the rhyolitic analyses. Chemical classification and nomenclature after Le Maitre et al. (1989).

## 7.5 Marine Isotope Stage 4 Cryptotephra Horizons within MD04-2822

### 7.5.1 Horizon 1 – 2327-2328 cm

The shards from 2327-2328 cm are colourless with a platy and fluted morphology, and range in size between 50 and 125 μm in diameter. This horizon was deposited during the stadial period following a climatic oscillation recorded in the Ca count record and correlated to DO event 19 (figure 7.3). The horizon forms a distinct and discrete peak in the shard concentration profile far exceeding the counts for adjacent samples (figure 7.5). This horizon will be referred to as the MD04-2822 2327-2328 cm tephra horizon.

#### 7.5.1.1 Major Element Characterisation

Geochemical analyses of 17 individual shards from this sample can be grouped into two populations of rhyolitic material (figure 7.7; table 7.1). Figures 7.7a and 7.7b clearly illustrate the existence of these two populations, despite the appearance of one population on the $SiO_2$ v $K_2O$ plot (figure 7.7c). Bimodality is most distinct within the concentrations of FeO, CaO and $Al_2O_3$ with population 1 exhibiting higher FeO concentrations and lower $Al_2O_3$ and CaO concentrations relative to population 2. Population 1 is characterised by FeO concentrations between 2.6 and 3.0 %wt, $Al_2O_3$ concentrations of ~12.4 %wt and CaO concentrations of 0.54-0.63 %wt. In contrast, population 2 has FeO concentrations of ~2.3 %wt, $Al_2O_3$ concentrations between 12.9 and 13.3 %wt and CaO concentrations between 0.73 and 0.85 %wt. Concentrations of $TiO_2$, MnO and MgO are minor in both populations. The recognition of two geochemical populations within this horizon could indicate that these are deposits from one eruption with a bimodal composition or two approximately coeval eruptions.

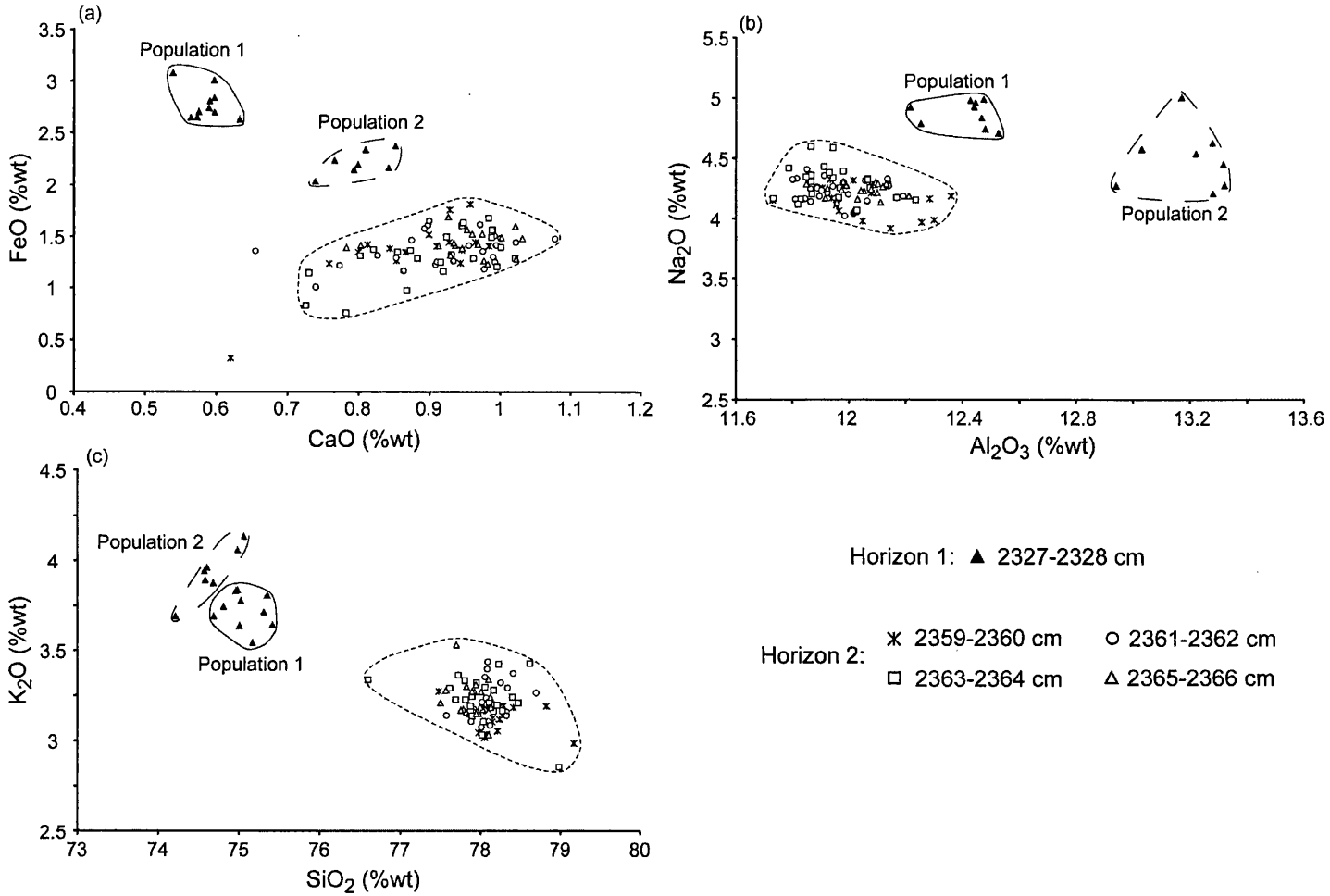


**Figure 7.7:** Geochemical data from tephra shards within five samples from the two tephra horizons identified within MD04-2822 plotted on (a) CaO vs. FeO (b) $Al_2O_3$ vs. $Na_2O$ and (c) $SiO_2$ vs. $K_2O$ compositional variation diagrams. The geochemical fields for the horizons marked on these biplots will be utilised in subsequent figures.

**Table 7.1:** Summary of normalised major oxide and trace element data for glass shards from the MD04-2822 2327-2328 cm sample. Mean and 1 standard deviations are shown. Total oxides are raw values prior to normalisation. All major elements expressed as percentage weight. All trace element concentrations expressed as ppm. Total iron is expressed as FeO. n = number of shards analysed. The complete dataset of unnormalised data is provided in appendix 5.

| | 2327-2328cm Population 1 | 2327-2328cm Population 2 |
|---|---|---|
| n | 10 | 7 |
| $SiO_2$ | 74.96 (0.34) | 74.83 (0.30) |
| $TiO_2$ | 0.24 (0.09) | 0.12 (0.13) |
| $Al_2O_3$ | 12.49 (0.26) | 13.20 (0.15) |
| FeO | 2.78 (0.16) | 2.21 (0.12) |
| MnO | 0.15 (0.10) | 0.07 (0.07) |
| MgO | 0.04 (0.01) | 0.12 (0.02) |
| CaO | 0.59 (0.02) | 0.80 (0.04) |
| $Na_2O$ | 4.88 (0.11) | 4.42 (0.17) |
| $K_2O$ | 3.71 (0.09) | 3.95 (0.11) |
| $P_2O_5$ | 0.00 (0.02) | 0.02 (0.03) |
| Cl | 0.15 (0.01) | 0.22 (0.03) |
| Total Oxides | 93.60 (1.03) | 93.54 (0.96) |
| | | |
| n | 3 | 2 |
| Sc | 15.9 (8.21) | 16.8 (9.46) |
| Rb | 155 (22.0) | 161 (8.32) |
| Sr | 57.3 (4.09) | 69.8 (11.0) |
| Y | 157 (13.0) | 122 (9.03) |
| Zr | 1073 (114) | 553 (30.0) |
| Nb | 212 (23.5) | 94.2 (2.55) |
| Cs | 2.80 (0.66) | 1.22 (0.34) |
| Ba | 1051 (108) | 1487 (89.4) |
| La | 170 (18.0) | 111 (7.20) |
| Ce | 321 (30.1) | 219 (10.7) |
| Pr | 39.3 (3.13) | 25.2 (2.00) |
| Nd | 161 (17.4) | 104 (12.0) |
| Sm | 31.2 (4.87) | 24.9 (0.32) |
| Eu | 4.67 (1.41) | 4.89 (0.62) |
| Gd | 27.0 (3.32) | 19.6 (2.59) |
| Tb | 4.31 (0.80) | 3.06 (0.12) |
| Dy | 26.6 (4.01) | 21.4 (3.81) |
| Ho | 6.09 (0.19) | 4.01 (0.10) |
| Er | 16.4 (3.13) | 12.7 (1.44) |
| Tm | 2.30 (0.29) | 1.67 (0.01) |
| Yb | 16.0 (2.56) | 13.1 (1.46) |
| Lu | 2.19 (0.37) | 1.66 (0.12) |
| Hf | 30.5 (4.94) | 16.4 (0.73) |
| Ta | 13.8 (1.58) | 6.54 (0.21) |
| Th | 21.4 (2.42) | 17.5 (1.14) |
| U | 6.14 (1.79) | 4.15 (0.42) |

### 7.5.1.2 Volcanic Source Identification

The most likely source of rhyolitic tephra horizons within North Atlantic marine sediments is the Icelandic volcanic region. Figure 7.8a compares the geochemical composition of MD04-2822 2327-2328 cm to geochemical fields defined by Jakobsson et al. (2008) for the three Icelandic rock suites, shown earlier in figure 2.1. On this TAS plot all of the analyses plot in an area of overlap between the transitional alkali and tholeiitic rock suites. Figure 7.8b illustrates the potassium enrichment ($K_2O/Si_2O$) values for the individual shards from MD04-2822 2327-2328 cm and shows that they vary between 0.046 and 0.056. These all exceed the threshold of 0.045 defined by Lacasse and Garbe-Schönberg (2001), indicating that this material is the product of a volcanic system within an off-rift (flank) zone which only produce transitional alkali or alkali material. Therefore, this evidence coupled with the TAS plot indicates that the two components of this horizon have an affinity to the transitional alkali rock suite of Iceland and a source within either the SFZ or EFZ. A proposition supported by the relatively high FeO and low CaO concentrations for the populations; which are characteristic of flank zone rhyolitic products (Jakobsson et al., 2008).

The attribution of rhyolitic horizons to a particular volcanic source within Iceland is hampered by a lack of comparative data sources as the geochemistry of only a few Icelandic central volcanoes producing silicic material has been well-documented (Jónasson, 2007). In addition limited silicic material is available for characterisation relative to basaltic material as the production of the latter is more prevalent. For example, during the postglacial period 91% of the erupted magma was basaltic whereas only 3% was silicic (Thordarson and Höskuldsson, 2008).

Nevertheless, two silicic data-sets are used here in an attempt to pinpoint a source volcanic system within either the SFZ or EFZ. Firstly, whole rock data from Jónasson (2007), which presented major element analyses of material from all central volcanoes erupting silicic rocks during the past 800 ka. Secondly, Larsen and Eiríksson (2007) compiled a data-set of proximal silicic tephra erupted from major producers during the Lateglacial and Holocene period from Larsen et al. (1999, 2001, 2002).

A comparison of the geochemical composition of 2327-2328 cm to whole rock data from five volcanic systems located within either the SFZ or EFZ and producing transitional alkali material is shown in figure 7.9. The geochemical fields for some of

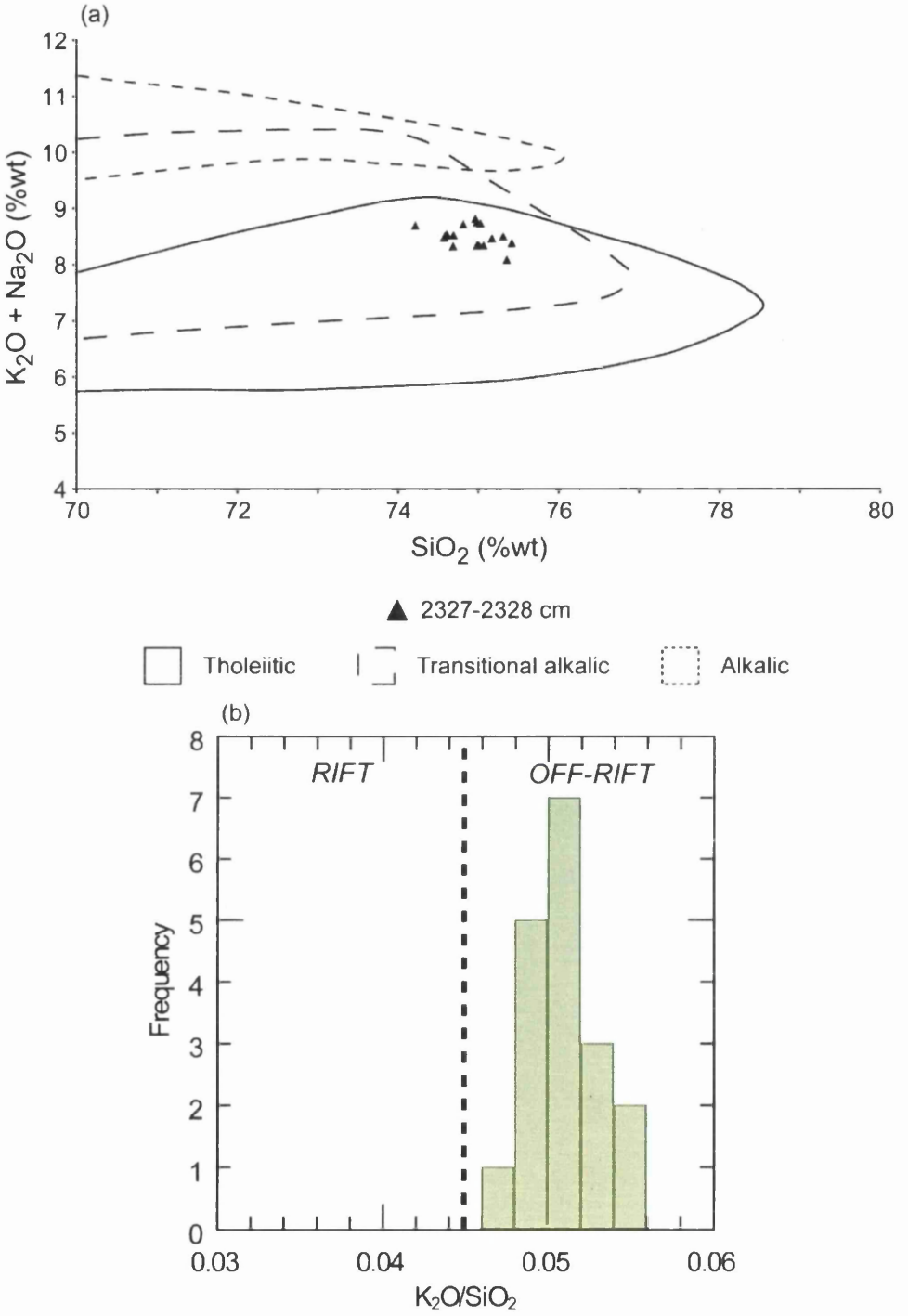


**Figure 7.8:** (a) TAS plot comparison between geochemical data from the MD04-2822 2327-2328 cm tephra horizon and geochemical fields for the Icelandic rock suites defined by Jakobsson et al. (2008). (b) Histogram of the K enrichment ($K_2O/SiO_2$ ratio) from individual shards. Division line between rhyolitic material produced within the Icelandic rift and off-rift zones defined as 0.045 by Lacasse and Garbe-Schönberg (2001)

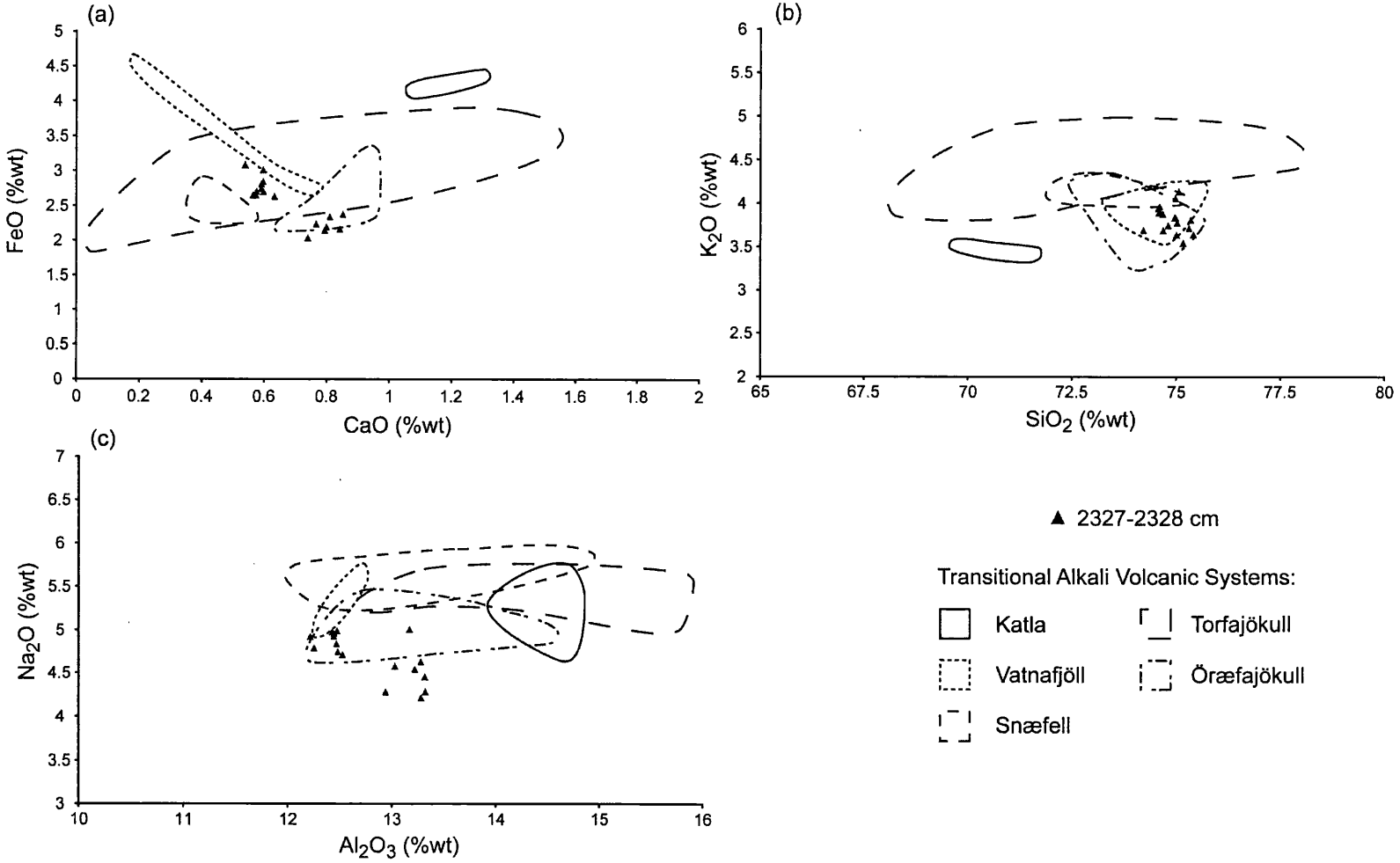


**Figure 7.9:** Major element analyses of shards within the MD04-2822 2327-2328 cm tephra horizon compared to geochemical fields for transitional alkali material from five Icelandic volcanic systems on (a) CaO vs. FeO (b) $SiO_2$ vs. $K_2O$ and (c) $Al_2O_3$ vs. $Na_2O$ compositional variation diagrams. Geochemical fields defined using individual silicic rock analyses reported by Jónasson (2007).

the volcanic systems are quite restricted, which may be due to limited analyses or a consequence of geochemical homogeneity of the system products. The geochemical fields for the two populations of MD04-2822 2327-2328 cm overlap and show the most consistent similarity to the products of the Öræfajökull and Vatnafjöll central volcanoes. For example, on figure 7.9b both populations fall within the fields of these volcanic systems and broad similarities can be observed on the other biplots. However the similarities are not strong enough to indicate that either system is the definite source for the populations of this horizon. The comparison to the geochemical envelopes for proximal transitional alkali silicic tephra deposits does not provide any evidence for the source of this horizon as no consistent relationships can be observed (figure 7.10).

As with the basaltic horizons with an Icelandic source identified within the NGRIP and GRIP records similarity coefficient comparisons were made between horizons identified within MD04-2822 and other eruptions that occurred during the MIS 2-5e time period. High similarity coefficients in excess of 0.96 were calculated for the comparisons between population 2 of MD04 2327-2328 cm, one component of 5d-Low/RHY and the 5e-Top/RHY horizon described by Wastegård and Rasmussen (2001) (appendix 6). Broad similarities are also apparent when these horizons are compared to population 1 of MD04-2822 2327-2328 cm as the similarity coefficients exceed 0.90. The geochemical similarities between the horizons can be observed in figure 7.11. Wastegård and Rasmussen (2001) did not determine a potential source for the 5d-Low/RHY and 5e-Top/RHY horizons, therefore the similarities do not provide evidence for a source for MD04-2822 2327-2328 cm. However, they strongly suggest that all these horizons were the products of the same volcanic system active during MIS 4 and MIS 5.

Overall, the comparison to whole rock data suggests that either the Öræfajökull or Vatnafjöll volcanic systems could be the source of this horizon, however, at present the evidence is not convincing enough to definitively ascribe a source region to this horizon.

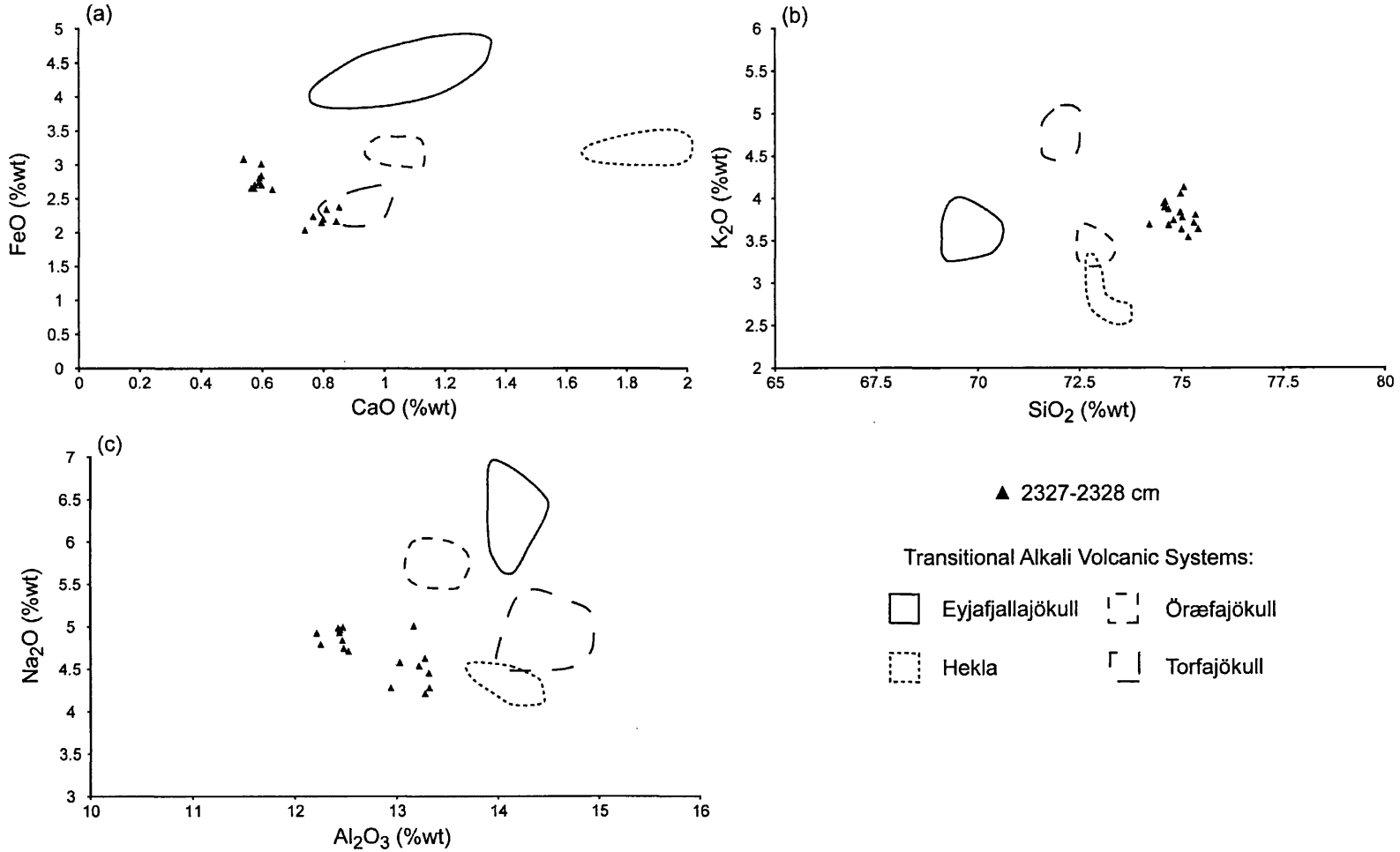


**Figure 7.10:** Major element analyses of shards within the MD04-2822 2327-2328 cm tephra horizon compared to geochemical fields for transitional alkali tephra deposits from four Icelandic volcanic systems (a) CaO vs. FeO (b) $SiO_2$ vs. $K_2O$ and (c) $Al_2O_3$ vs. $Na_2O$ compositional variation diagrams. Geochemical fields defined individual tephra shard analyses reported in Larsen et al. (1999, 2001, 2002).

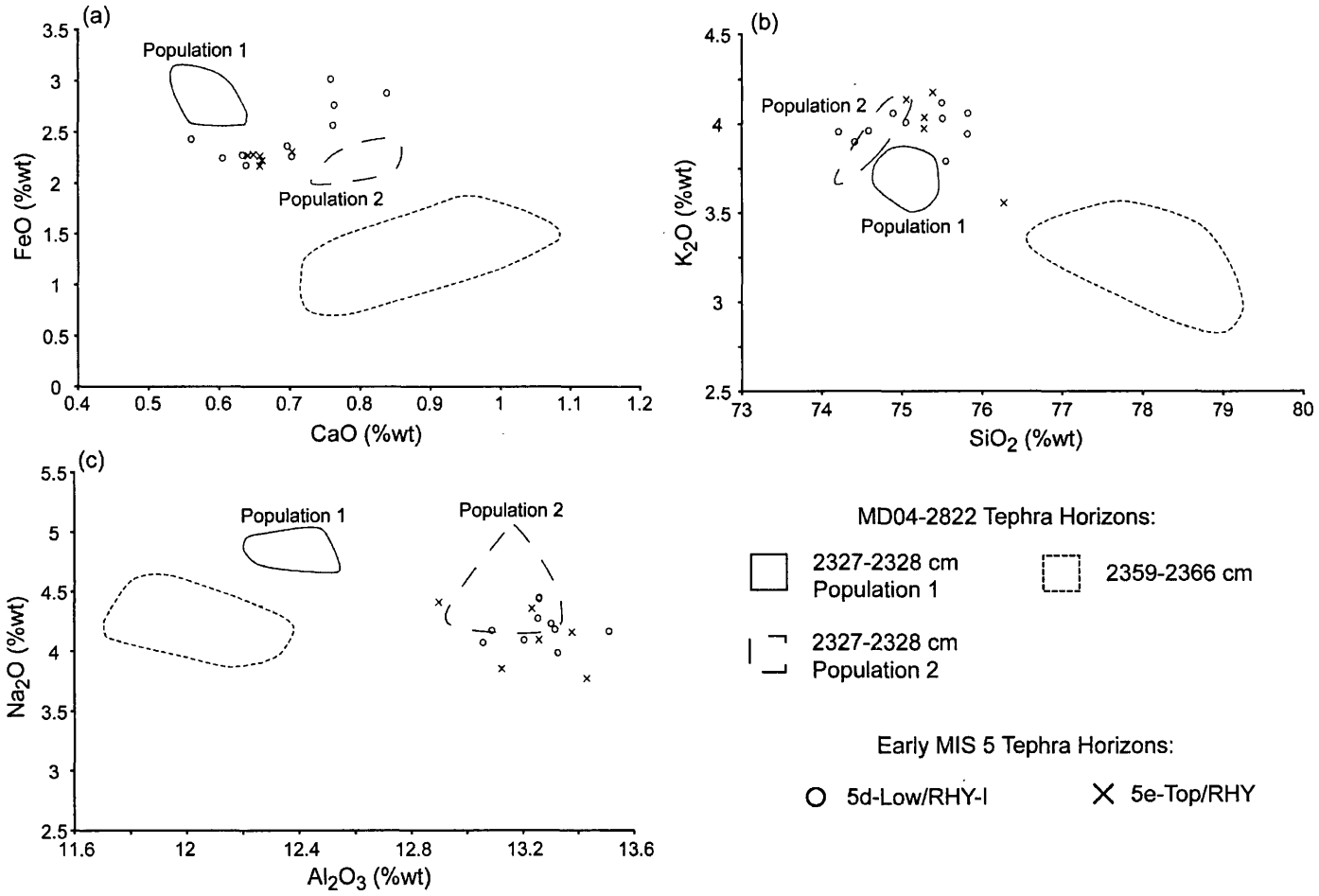


**Figure 7.11:** Comparison between geochemical fields for tephra horizons within MD04-2822 and the composition of the 5d-Low/RHY-I and 5e-Top/RHY tephra horizons on (a) CaO vs. FeO (b) $SiO_2$ vs. $K_2O$ and (c) $Na_2O$ vs. $Al_2O_3$ compositional variation diagrams. Individual shard analyses for the 5d-Low/RHY-I and 5e-Top/RHY tephra horizons from Wastegård (*pers. comm.*, 2009).

#### 7.5.1.3 Trace Element Characterisation

Five shards from MD04-2822 2327-2328 cm were analysed for their trace element composition; three with an affinity to the major element population 1 and two with an affinity to population 2. Figure 7.12a illustrates the individual REE profiles for each of these analyses and combined with the biplots in figure 7.12b and c demonstrates that bimodalism is also apparent within the trace element data for some of the elements. For example the shards within population 1 are more enriched in the LREEs between La and Nd than those from population 2. Despite the differences in the concentration of these elements, the shape of the REE profiles are comparable, with a steep profile for the LREEs, a distinct negative Eu anomaly and a relatively flat profile for the HREEs.

Figure 7.13a shows that the shape of the REE profiles for both of the populations closely match the end-member characterisation of Icelandic silicic products defined by Óskarsson et al. (1982), with the exception that the negative Eu anomaly is of a greater magnitude within the latter. Strong similarities are also seen with proximal Icelandic silicic material analyses reported in Jónasson (2007). The only deviations in the profiles are apparent in the MREEs, where the analyses from Jónasson (2007) display a more pronounced Eu anomaly and enrichment in Gd than the two populations of MD04-2822 2327-2328 cm (figure 7.13b). Figure 7.13c also demonstrates the similarities between the trace element characterisations of MD04-2822 2327-2328 cm shards and Icelandic proximal deposits as the concentrations of Rb and Sr for the material fall within the geochemical field defined for rhyolitic material by Óskarsson et al. (1982).

### 7.5.2 Horizon 2 – 2359-2360 cm, 2361-2362 cm, 2363-2364 cm and 2365-2366 cm

A distributed peak in tephra shards was identified between 2359 and 2368 cm depth within MD04-2822. This peak in material is composed of colourless tephra shards with blocky morphologies. The shards contain occasional open vesicles and range in size between 60 and 100 μm in diameter. This horizon was deposited around the climatic cooling at the end of the interstadial period of DO event 20 (figure 7.3). Four samples containing the highest shard concentrations were selected for geochemical analysis, and will be collectively referred to as the MD04-2822 2359-2366 cm tephra horizon.

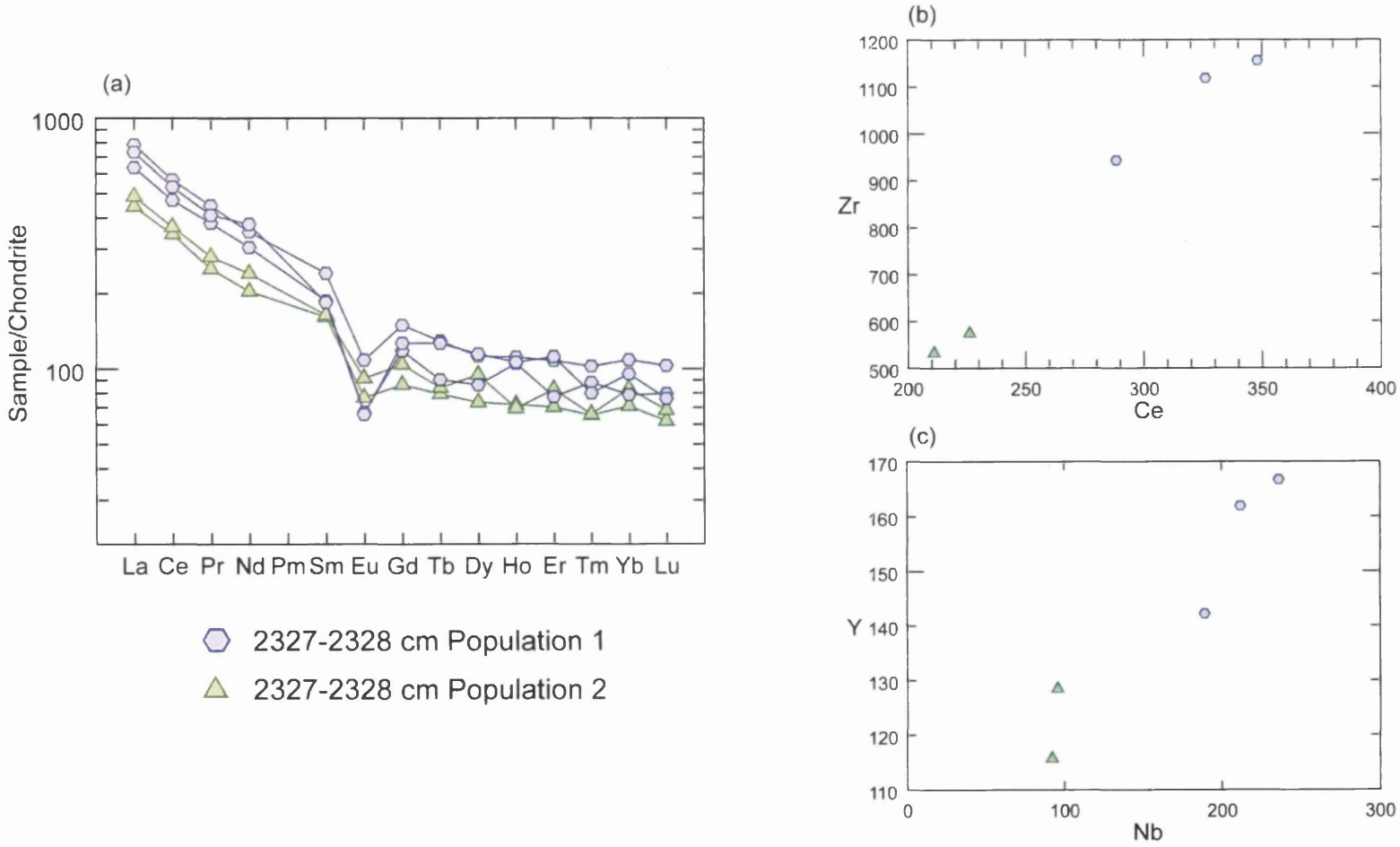


**Figure 7.12:** (a) Chondrite-normalised REE profiles for individual LA-ICP-MS analyses from both populations of MD04-2822 2327-2328 cm. Chondrite compositions from Sun and McDonough (1989). (b) Ce vs. Zr and (c) Nb vs. Y compositional variation diagrams for trace element analyses from 2327-2328 cm.

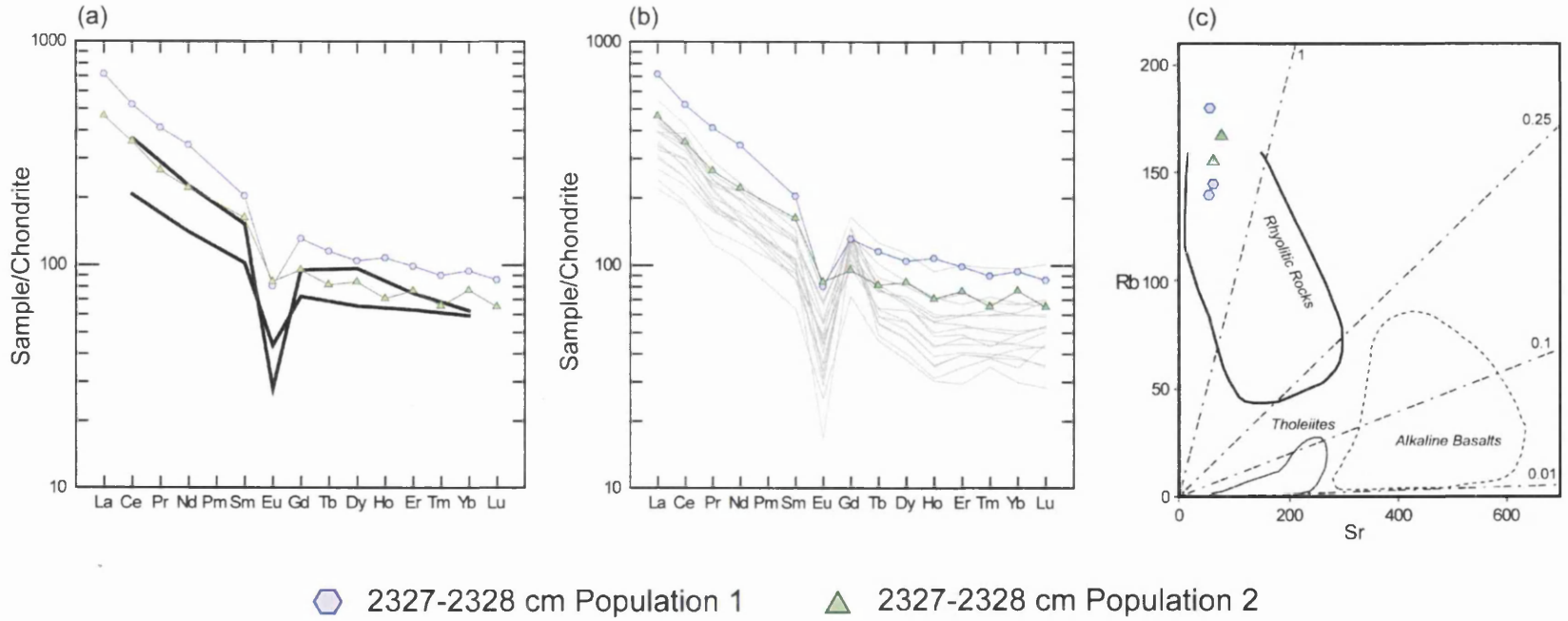


**Figure 7.13:** (a) Comparison between the average chondrite-normalised REE profiles for the two populations within MD04-2822 2327-2328 cm and the end-member characterisation of Icelandic rhyolitic material described by Óskarsson et al. (1982). (b) Comparison between MD04-2822 2327-2328 cm REE profiles and REE profiles for silicic rocks from Iceland reported in Jónasson (2007). (c) Sr vs. Rb compositional variation diagram comparing individual analyses from tephra shards within MD04-2822 2327-2328 cm to end-member characterisations defined by Óskarsson et al. (1982).

**Table 7.2:** Summary of normalised major oxide and trace element data for glass shards from the MD04-2822 2359-2360 cm, 2361-2362 cm, 2363-2364 cm and 2365-2366 cm samples. Mean and 1 standard deviations are shown. Total oxides are raw values prior to normalisation. All major elements expressed as percentage weight. All trace element concentrations expressed as ppm. Total iron is expressed as FeO. n = number of shards analysed. The complete dataset of unnormalised data is provided in appendix 5. Horizon dataset excludes the trace element analyses from the 2361-2362 cm sample.

| | 2359-2360 cm | 2361-2362 cm | 2363-2364 cm | 2365-2366 cm | 2359-2366 cm Average |
|---|---|---|---|---|---|
| n | 16 | 25 | 24 | 18 | 83 |
| $SiO_2$ | 78.20 (0.38) | 78.10 (0.22) | 78.02 (0.44) | 77.90 (0.18) | 78.06 (0.33) |
| $TiO_2$ | 0.09 (0.08) | 0.10 (0.06) | 0.09 (0.05) | 0.09 (0.07) | 0.09 (0.07) |
| $Al_2O_3$ | 12.06 (0.17) | 11.95 (0.11) | 11.95 (0.12) | 12.04 (0.09) | 11.99 (0.13) |
| FeO | 1.36 (0.32) | 1.36 (0.17) | 1.36 (0.30) | 1.44 (0.12) | 1.37 (0.24) |
| MnO | 0.07 (0.10) | 0.07 (0.10) | 0.04 (0.09) | 0.03 (0.07) | 0.04 (0.09) |
| MgO | 0.00 (0.01) | 0.00 (0.01) | 0.00 (0.01) | 0.00 (0.01) | 0.00 (0.01) |
| CaO | 0.88 (0.09) | 0.92 (0.10) | 0.93 (0.14) | 0.95 (0.07) | 0.92 (0.11) |
| $Na_2O$ | 4.14 (0.13) | 4.23 (0.09) | 4.29 (0.14) | 4.23 (0.06) | 4.23 (0.12) |
| $K_2O$ | 3.12 (0.08) | 3.21 (0.10) | 3.23 (0.12) | 3.24 (0.10) | 3.20 (0.10) |
| $P_2O_5$ | 0.00 (0.01) | -0.01 (0.02) | -0.01 (0.02) | -0.01 (0.02) | -0.01 (0.02) |
| Cl | 0.06 (0.01) | 0.06 (0.01) | 0.07 (0.01) | 0.06 (0.01) | 0.06 (0.01) |
| Total Oxides | 94.42 (0.53) | 94.22 (0.55) | 94.11 (0.64) | 94.46 (0.67) | 94.28 (0.61) |
| n | 10 | 13 | 14 | 11 | 35 |
| Rb | 141 (37.9) | 118 (23.4) | 125 (10.7) | 122 (10.5) | 122 (43.5) |
| Sr | 112 (4.14) | 120 (16.2) | 113 (17.3) | 118 (6.49) | 114 (11.9) |
| Y | 149 (14.6) | 124 (22.4) | 152 (19.7) | 155 (18.9) | 152 (17.8) |
| Zr | 289 (23.3) | 243 (37.9) | 296 (40.3) | 295 (30.0) | 294 (32.1) |
| Nb | 92.7 (9.23) | 75.6 (13.6) | 96.0 (11.8) | 97.1 (13.2) | 95.4 (11.4) |
| Cs | 3.63 (4.16) | 1.86 (0.99) | 1.62 (0.59) | 1.78 (0.61) | 2.24 (2.37) |
| Ba | 1141 (109) | 917 (132) | 1064 (113) | 921 (448) | 1035 (280) |
| La | 75.7 (7.35) | 61.4 (9.99) | 74.2 (9.40) | 73.2 (8.39) | 74.3 (8.35) |
| Ce | 157 (17.4) | 127 (22.6) | 154 (19.7) | 153 (14.7) | 155 (17.2) |
| Pr | 19.3 (1.76) | 15.9 (3.39) | 18.3 (2.62) | 19.7 (2.05) | 19.0 (2.26) |
| Nd | 82.3 (11.8) | 65.7 (12.1) | 81.1 (9.62) | 85.2 (9.40) | 82.7 (10.1) |
| Sm | 19.9 (3.01) | 15.4 (3.65) | 20.1 (3.60) | 20.0 (3.88) | 20.0 (3.43) |
| Eu | 4.81 (0.62) | 4.56 (1.33) | 4.51 (1.08) | 4.79 (0.64) | 4.68 (0.83) |
| Gd | 22.7 (2.86) | 19.1 (4.48) | 22.9 (2.76) | 22.2 (2.61) | 22.6 (2.68) |
| Tb | 3.62 (0.59) | 2.81 (0.63) | 3.55 (0.49) | 3.80 (0.63) | 3.65 (0.56) |
| Dy | 24.7 (3.36) | 19.0 (3.66) | 24.3 (4.06) | 26.8 (4.26) | 25.2 (3.99) |
| Ho | 5.10 (0.77) | 4.09 (0.83) | 5.09 (0.86) | 5.74 (0.86) | 5.30 (0.86) |
| Er | 14.7 (1.95) | 11.1 (2.51) | 14.4 (2.13) | 16.0 (1.90) | 15.0 (2.21) |
| Tm | 2.19 (0.24) | 1.74 (0.44) | 2.05 (0.46) | 2.34 (0.38) | 2.18 (0.39) |
| Yb | 14.9 (2.28) | 11.8 (2.58) | 15.8 (1.89) | 16.1 (1.90) | 15.6 (2.01) |
| Lu | 2.28 (0.42) | 1.88 (0.31) | 2.16 (0.27) | 2.23 (0.36) | 2.21 (0.34) |
| Hf | 12.3 (2.45) | 9.02 (1.82) | 11.6 (1.31) | 12.5 (2.12) | 12.1 (1.94) |
| Ta | 6.83 (0.68) | 5.26 (0.90) | 6.63 (0.91) | 6.61 (1.12) | 6.68 (0.91) |
| Th | 18.0 (5.19) | 12.9 (2.49) | 16.1 (1.79) | 16.6 (1.94) | 16.8 (3.17) |
| U | 4.38 (1.25) | 4.73 (0.88) | 4.34 (0.34) | 4.21 (0.88) | 4.31 (0.83) |

### 7.5.2.1 Major Element Characterisation

Between sixteen and twenty five shards were analysed from each of the four samples (table 7.2). An initial inspection of the data highlighted some consistent major element outliers; two within the 2359-2360 cm sample and one from the 2365-2366 cm sample. These analyses differ greatly from the main geochemical populations observed within the samples and will be discussed separately within section 7.6.

Biplots of the analyses from each sample show there is a high degree of consistency in the geochemical composition of the tephra shards from all four samples (figure 7.7). Figure 7.14 illustrates the concentration of six major elements within individual shards against the core depth and suggests that no significant or systematic shifts in composition have occurred during the deposition of the broad peak in shard concentrations. This plot additionally emphasises the geochemical similarities between the samples. Occasional outliers can be observed in figure 7.7 however an inspection of these analyses shows that they only display slightly anomalous values for one or two major oxides therefore are not excluded from the dataset.

This qualitative assessment of geochemical similarity between the samples is supported by similarity coefficient comparisons between the four samples. These range between 0.977 and 0.996 and thus all greatly exceed 0.95, the value Beget et al. (1992) determined as the threshold above which samples can be deemed to be identical (table 7.3).

**Table 7.3:** Similarity coefficient analysis of the average major element concentrations of shards within the 2359-2360 cm, 2361-2362 cm, 2363-2364 cm and 2365-2366 cm samples from MD04-2822.

| | 2359-2360 cm | 2361-2362 cm | 2363-2364 cm | 2365-2366 cm |
|---|---|---|---|---|
| 2359-2360 cm | 1.000 | | | |
| 2361-2362 cm | 0.988 | 1.000 | | |
| 2363-2364 cm | 0.984 | 0.996 | 1.000 | |
| 2365-2366 cm | 0.977 | 0.986 | 0.984 | 1.000 |

Therefore, the 83 single-shard analyses from the four samples are combined as one geochemical dataset for this tephra horizon, MD04-2822 2359-2366 cm (table 7.2). The main geochemical characteristics of this horizon are $SiO_2$ values ranging between 77.5 and 79 %wt, $Al_2O_3$ concentrations of 11.7-12.4 %wt, CaO concentrations of approximately 0.90 %wt and FeO values varying between 0.8 and 1.8 %wt (figure 7.7).

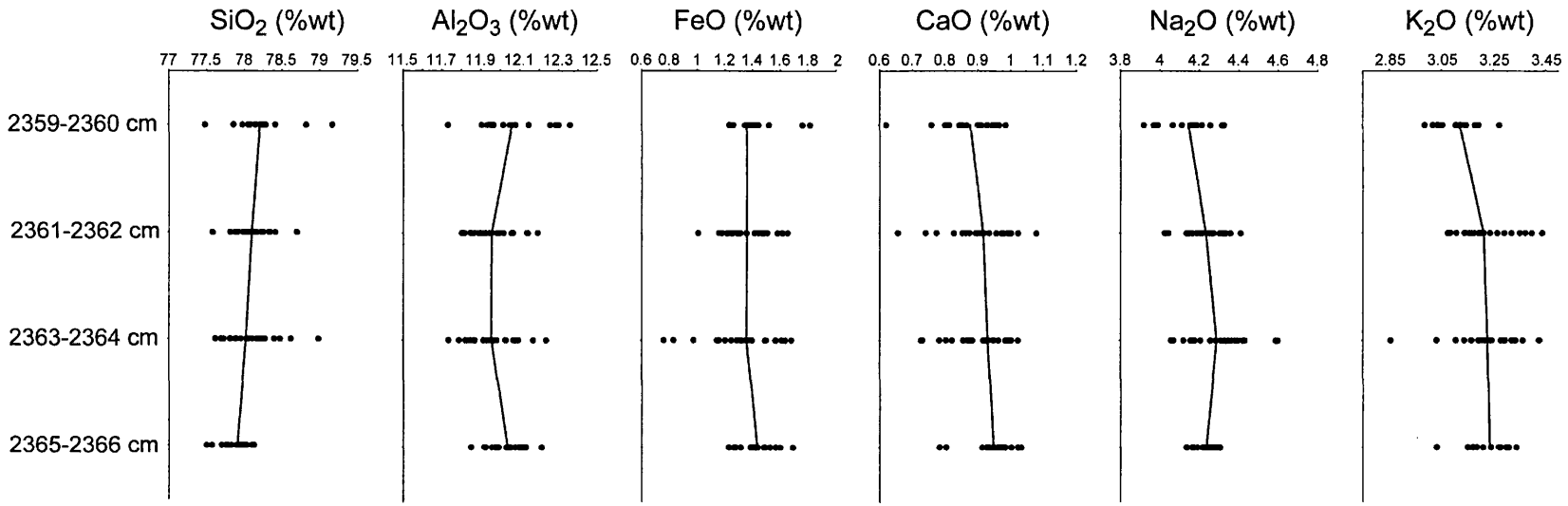


**Figure 7.14:** Major element concentrations for four samples from MD04-2822 plotted against depth within the core.

There are minor concentrations of $TiO_2$, MgO and MnO within shards from this horizon (table 7.2).

### 7.5.2.2 Volcanic Source Identification

The Toba eruption in Sumatra was one of the most significant volcanic eruptions during the Quaternary period (section 2.4.5.2). Evidence suggests that the timing of this eruption coincided with the rapid cooling transition between DO event 20 and the subsequent stadial period; similar to the timing of the eruption which deposited MD04-2822 2359-2366 cm. Both of these eruptions produced rhyolitic material and the geochemistry of the horizons are compared in figure 7.15. Some similarities can be observed in the concentrations of FeO, CaO and $SiO_2$, however large differences are observed between other oxide concentrations such as $K_2O$ and $Na_2O$. These differences are emphasised by low similarity coefficient values (<0.8) and statistically significant differences between the average compositions of the horizons (table 7.4). Therefore, a correlation between these horizons can be ruled out and it is most likely that the MD04-2822 2359-2366 cm horizon was sourced from an Icelandic volcanic system.

**Table 7.4:** Similarity coefficient and statistical distance comparison between the major element geochemical composition of the MD04-2822 2359-2366 cm tephra horizon and proximal and distal deposits of the Youngest Toba Tuff from Chesner (1998), Westgate et al. (1998) and Schulz et al. (2002). Critical value for $D^2$ of 16.8 at the 99 % confidence level.

| | | Chesner (1998) | Westgate et al. (1998) | Schulz et al. (2002) |
|---|---|---|---|---|
| MD04-2822 | SC | 0.799 | 0.790 | 0.779 |
| 2359-2366 cm | $D^2$ | **130** | **214** | **113** |

Compared to the geochemistry of Icelandic material almost all the analyses from this horizon fall within the field for the tholeiitic rock suite on the TAS plot in figure 7.16a; indicating that this horizon was probably sourced from a volcanic system within the Icelandic rift zone. A rift zone source is also suggested by the $K_2O/SiO_2$ ratios, which vary between 0.036-0.044 and thus do not exceed the ratio threshold of 0.045 between Icelandic rift and off-rift products defined by Lacasse and Garbe-Schönberg (2001) (figure 7.16b). An affinity to the Icelandic tholeiitic rock suite and a rift zone source for MD04-2822 2359-2366 cm is also indicated by the relatively low FeO and high CaO concentrations for the horizon compared to the other rock suites and the products of flank zone volcanic systems (Jakobsson et al., 2008).

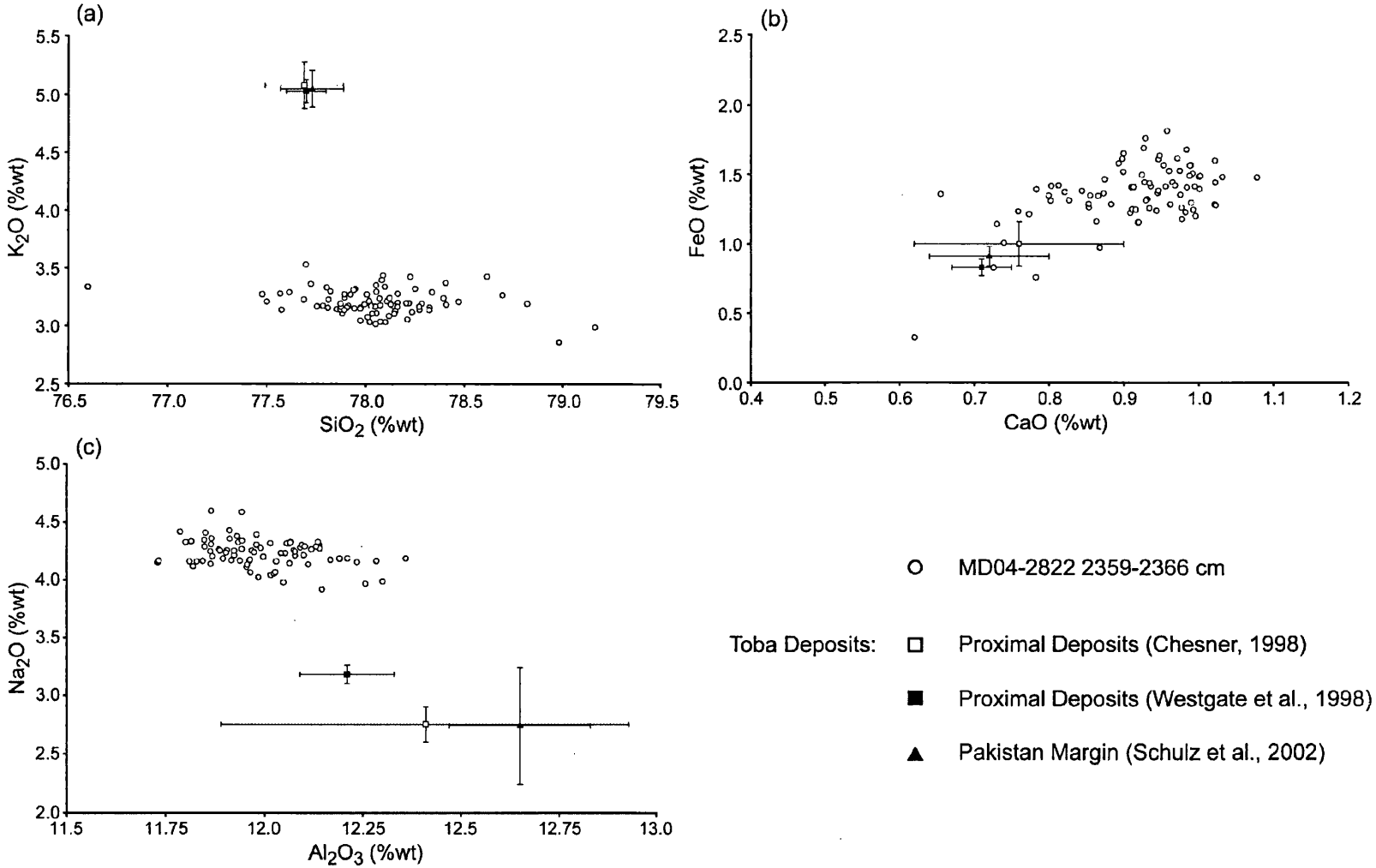


**Figure 7.15:** Comparison of individual analyses from shards within the MD04-2822 2359-2366 cm tephra horizon and published mean and standard deviation values for deposits from the Toba eruption on (a) $SiO_2$ vs. $K_2O$ (b) CaO vs. FeO and (c) $Al_2O_3$ vs. $Na_2O$ compositional variation diagrams.

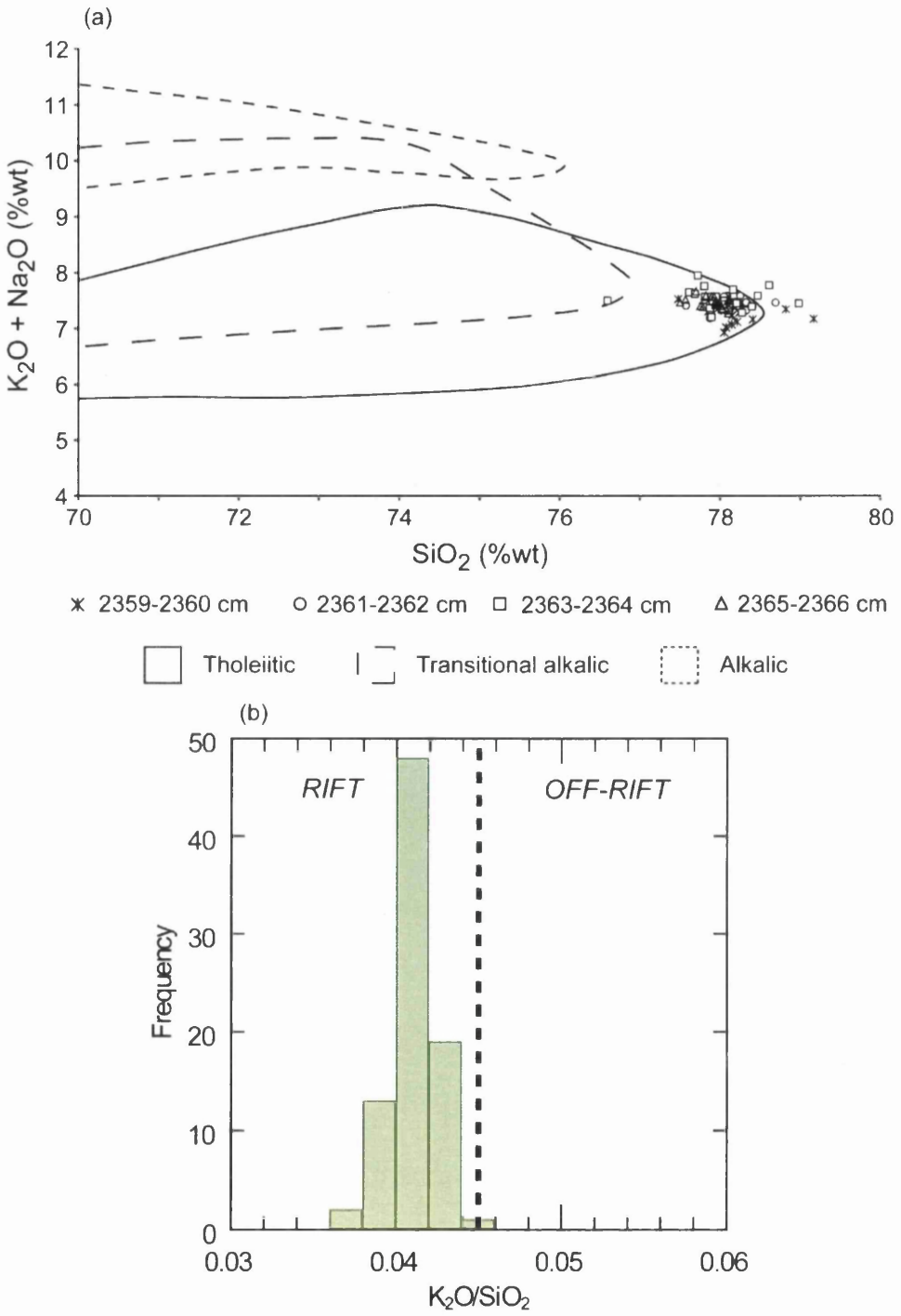


**Figure 7.16:** (a) TAS plot comparison between geochemical data from the MD04-2822 2359-2366 cm tephra horizon and geochemical fields for the Icelandic rock suites defined by Jakobsson et al. (2008). (b) Histogram of the K enrichment ($K_2O/SiO_2$ ratio) from individual shards. Division line between rhyolitic material produced within the Icelandic rift and off-rift zones defined as 0.045 by Lacasse and Garbe-Schönberg (2001).

Attempts to match this horizon to a source from a particular volcanic system within the rift zone have been unsuccessful (figure 7.17). Overall, no consistent geochemical relationship to any of the volcanic systems can be identified. Strong similarities in $Na_2O$ and $Al_2O_3$ concentrations between MD04-2822 2359-2366 cm and the products of the Krafla system can be observed on figure 7.17, however, similar overlaps are not observed on the other biplots. Comparisons to tephra deposits were not possible as Larsen and Eiríksson (2008) only reported the typical composition of tholeiitic material produced by one volcanic region, Askja, and an inspection of the data shows that it is not geochemically related to MD04-2822 2359-2366 cm. In addition, this horizon did not display any geochemical similarities to other Icelandic rhyolitic horizons within the MIS 2-5e tephrochronological framework for the North Atlantic region (appendix 6).

Therefore, at present it is not possible to identify the volcanic system within the Icelandic rift zone from which this horizon was sourced. The identification of an explosive Icelandic eruption on the rapid cooling transition at the end of DO event 20 could account for the large sulphate peaks recorded in the Greenland ice-cores around this period that have been previously attributed to the Toba eruption (see section 2.4.5.2).

#### 7.5.2.3 Potential Correlative Tephra Horizon

The lack of previously identified and geochemically characterised Icelandic horizons during MIS 4 was emphasised in section 2.4.5.1. However, a distinct peak in rhyolitic material at approximately 440 cm depth deposited during early MIS 4 was identified within ENAM33, a marine core from the Faeroe Islands region. Compared to a high-resolution grain size record from ENAM33 in Rasmussen et al. (2003) this rhyolitic peak was deposited during a period correlated to DO events 19 and 20. Therefore based on their relative stratigraphic positions this horizon is a potential correlative for the MD04-2822 2359-2366 cm tephra horizon, however no geochemical data is available from the shards at 440 cm depth within ENAM33 (S. Wastegård, *pers. comm.*, 2009).

#### 7.5.2.4 Trace Element Characterisation

The trace element composition of ten or more shards within each of the samples from MD04-2822 2359-2366 cm was determined using the LA-ICP-MS system (table 7.2)

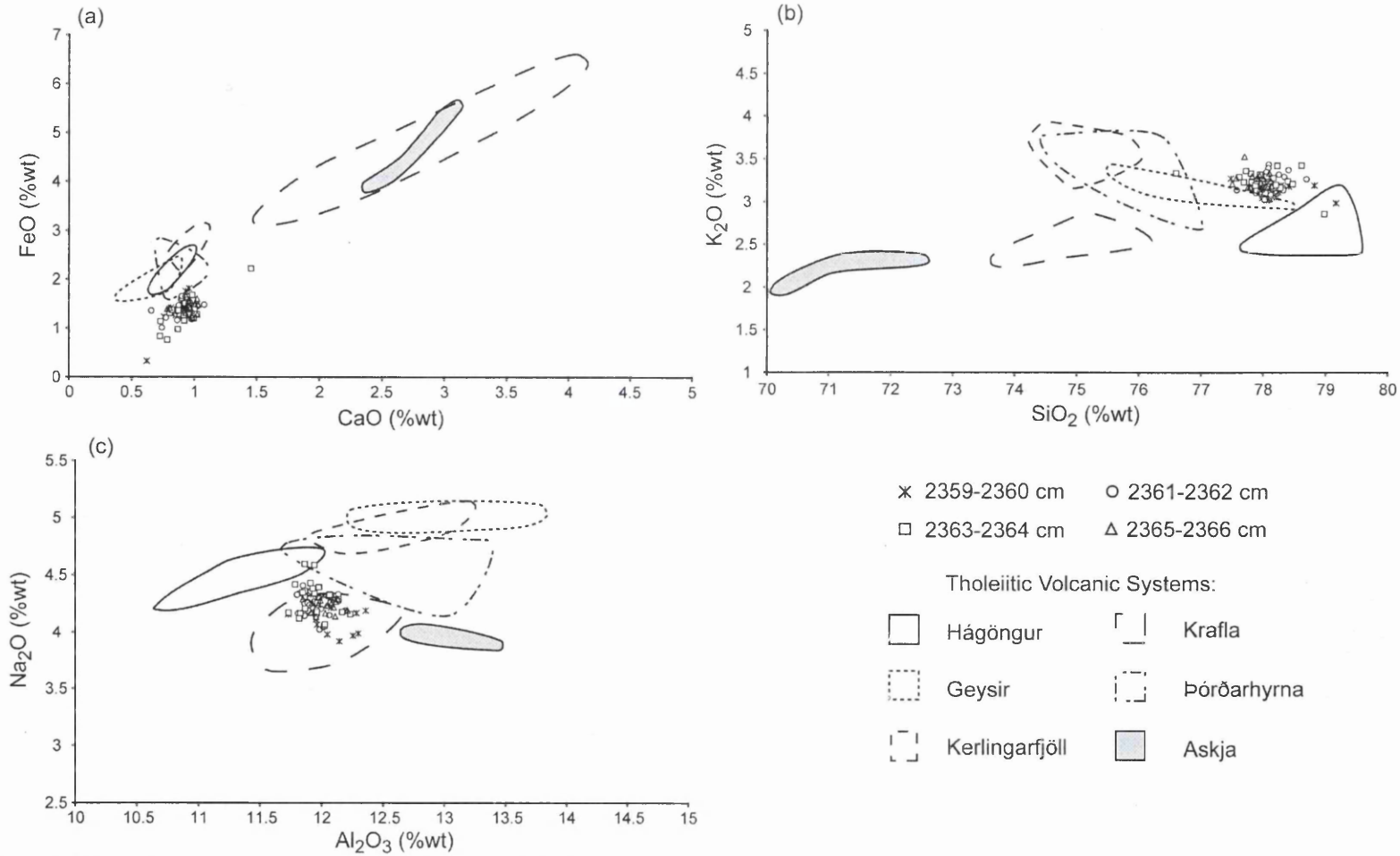


**Figure 7.17:** Major element analyses of shards within the MD04-2822 2359-2366 cm tephra horizon compared to geochemical fields for rhyolitic tholeiitic material from six Icelandic volcanic systems on (a) CaO vs. FeO (b) $SiO_2$ vs. $K_2O$ and (c) $Al_2O_3$ vs. $Na_2O$ compositional variation diagrams. Geochemical fields defined using individual silicic rock analyses reported by Jónasson (2007).

and the individual REE element profiles for the characterisations are shown in figure 7.18. For all of the samples there is a high coherency between the shapes of the individual shard profiles and each sample has a relatively homogeneous composition with more variability displayed for the HREEs due to their lower abundance. The trace element composition of 2361-2362 cm is slightly more heterogeneous than the other three samples.

The average REE profiles for each of the samples show strong similarities, with a steep profile and enrichment for the LREEs, a negative Eu anomaly, a slight enrichment in Gd and a relatively flat profile for the HREEs (figure 7.19a). The average REE concentrations of three of the samples display a close correspondence that is more distinct for the LREEs than the HREEs, due to the lower analytical precision for the less abundant, heavier elements. The profile for the remaining sample, 2361-2362 cm, is offset from the other three profiles displaying lower average concentration values for all of the REEs apart from Eu. This offset is also apparent in the concentration of trace elements within individual shards (figure 7.19b). The geochemical field for the shards within 2361-2362 cm is generally offset towards lower values but still falls along the same ratio trend lines as the other samples. The major element data do not indicate that the shards from 2361-2362 cm are geochemically different from the shards within the other horizons. It is possible that geochemical differences are only apparent within the trace elements, however, it is most likely that the offset has been caused by the misestimation of gas blank values during the analytical period when shards from the 2361-2362 cm sample were analysed. This issue can cause the offsets in calculated absolute concentrations observed on figure 7.19. This misestimation can also decrease the precision of analyses; providing an explanation for the higher variability between individual analyses from the 2361-2362 cm sample compared to the other three samples (figure 7.18). As a consequence of these observations the average absolute trace element concentrations for the MD04-2822 2359-2366 cm horizon do not include the analyses from shard within the 2361-2362 cm sample (table 7.2).

There are strong similarities between the average REE profiles for this horizon and the end-member characterisation of Icelandic rhyolitic material (Óskarsson et al., 1982; figure 7.20a). In addition, a high degree of coherency can be seen between this tephra and proximal Icelandic deposits (Jónasson, 2007; figure 7.20b). The only slight deviation is seen within the MREEs where the negative Eu anomaly and enrichment in Gd are more pronounced within the proximal material. This was also observed for the REE profile from MD04-2822 2327-2328 cm. The concentrations of Rb and Sr within the individual shards also fall within the geochemical field defined for Icelandic proximal material by Óskarsson et al. (1982) (figure 7.20c).

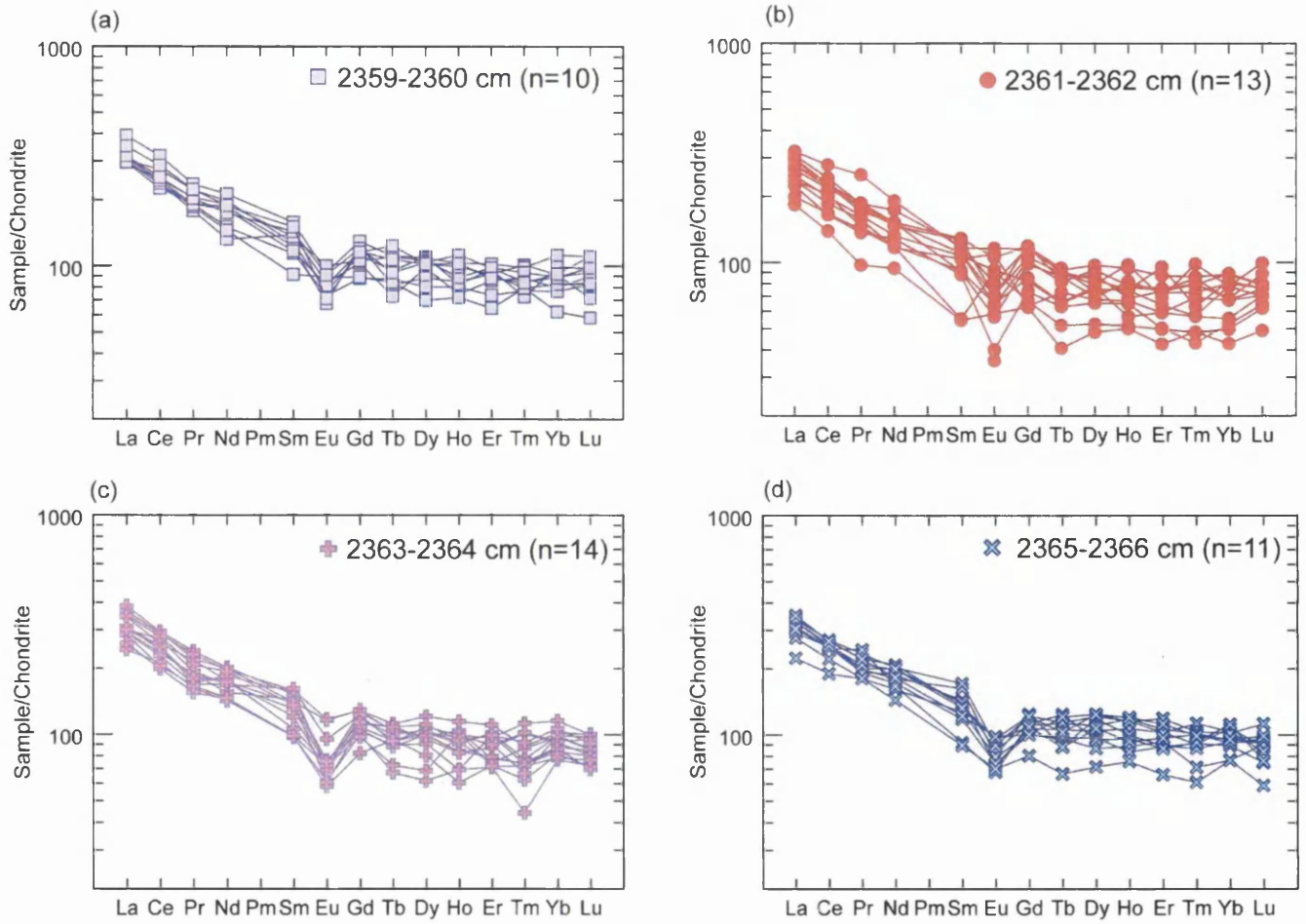


**Figure 7.18:** Chondrite-normalised REE analyses for tephra shards from the (a) 2359-2360 cm (b) 2361-2362 cm (c) 2363-2364 cm and (d) 2365-2366 cm depth samples from MD04-2822. Chondrite compositions from Sun and McDonough (1989).

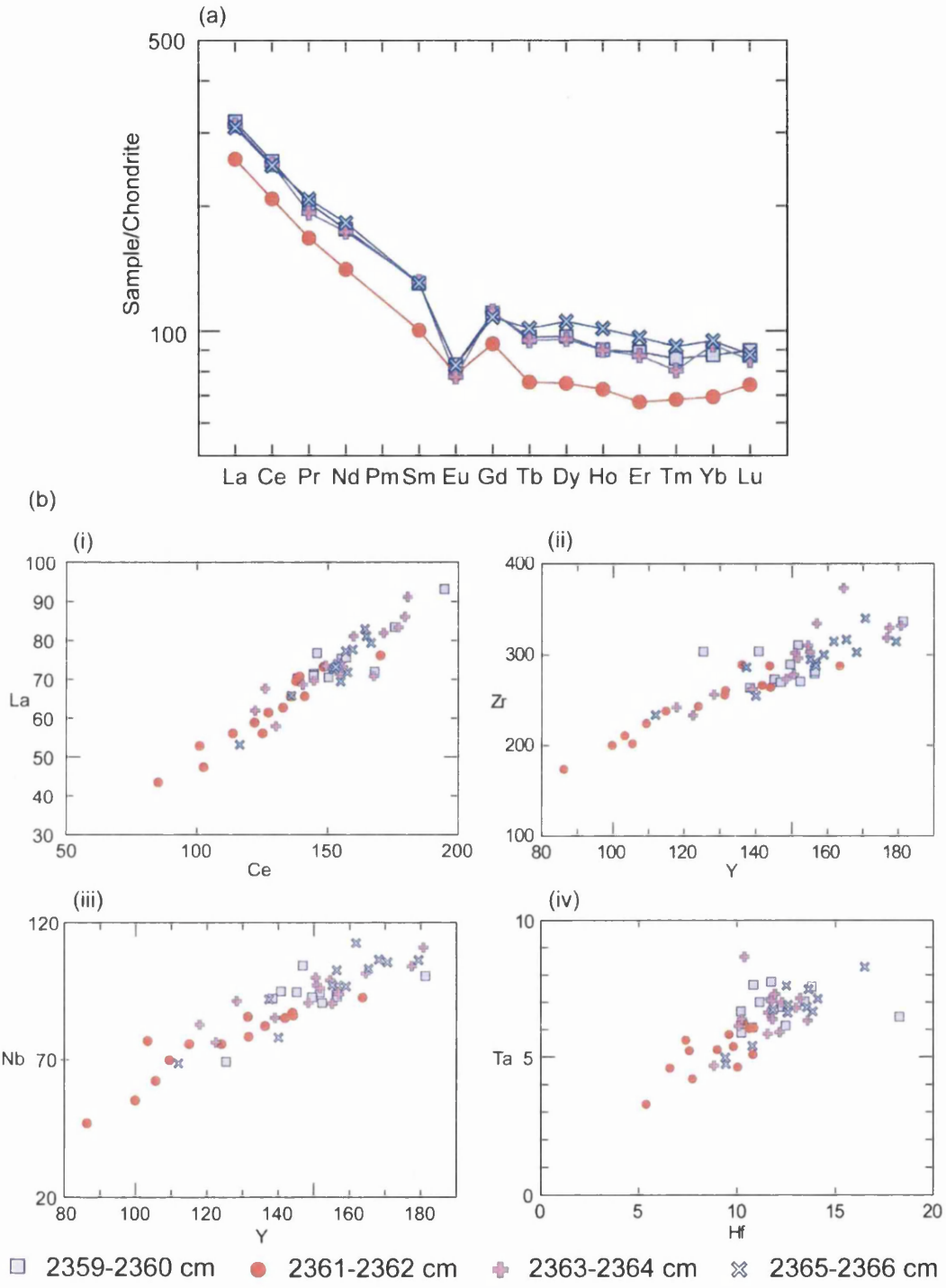


**Figure 7.19:** Trace element geochemical data from shards within the 2359-2360 cm, 2361-2362 cm, 2363-2364 cm and 2365-2366 cm samples. (a) Average chondrite-normalised REE profiles using chondrite compositions from Sun and McDonough (1989) (b) (i) Ce vs. La (ii) Y vs. Zr (iii) Y vs. Nb and (iv) Hf vs. Ta compositional variation diagram.

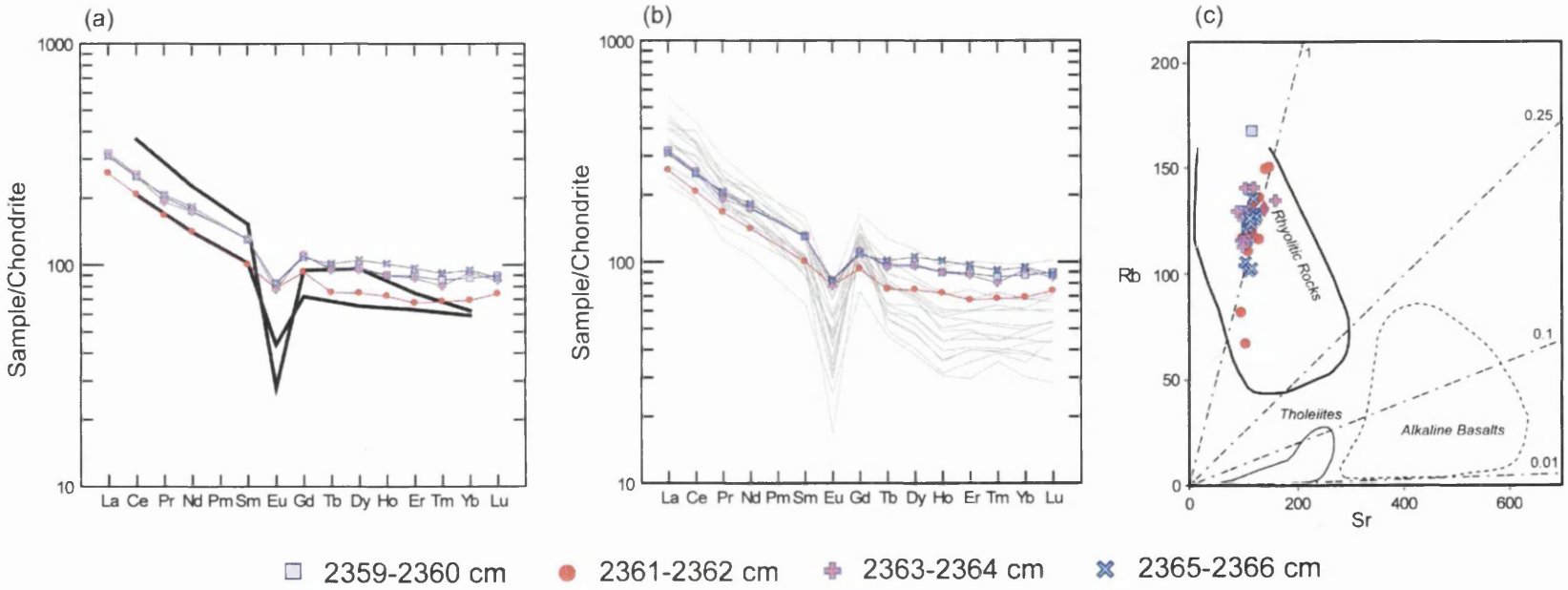


**Figure 7.20:** (a) Comparison between the chondrite-normalised average REE profiles for samples from the MD04-2822 2359-2366 cm tephra horizon and the end-member characterisation of Icelandic rhyolitic material described by Óskarsson et al. (1982). (b) Comparison between MD04-2822 2359-2366 cm REE profiles and characterisations of silicic rocks from Iceland reported in Jónasson (2007). (c) Sr vs. Rb compositional variation diagram comparing individual analyses from tephra shards within the four samples to end-member characterisations defined by Óskarsson et al. (1982).

## 7.6 Major Element Compositions of Tephra Shards within Other MD04-2822 Samples

In addition to the analysis of tephra shards from the two main tephra horizons major element analyses were gained from shards within five additional samples. The analyses from the five samples are described in the following sections, along with previously identified outliers from the MD04-2822 2359-2366 cm horizon, with respect to their stratigraphic position.

### 7.6.1 Samples above MD04-2822 2327-2328 cm

Material from two samples above 2327-2328 cm was geochemically analysed (table 7.5). The analyses from 2319-2320 cm can be grouped into two geochemical populations based on differences in the CaO, $Al_2O_3$ and $SiO_2$ concentrations measured from the shards (figure 7.21; table 7.5). These biplots show that the single analysis gained from the 2317-2318 cm sample has a geochemical affinity to the second population observed within the 2319-2320 cm samples. These populations, particularly the second population from MD04-2822 2319-2320 cm, have broad composition similarities to the geochemical fields defined for the MD04-2822 2327-2328 cm tephra horizon.

**Table 7.5:** Summary of normalised major oxide data for glass shards from the MD04-2822 2317-2318 cm and 2319-2320 cm samples. Mean and 1 standard deviations are shown. Total oxides are raw values prior to normalisation. All major elements expressed as percentage weight. Total iron is expressed as FeO. n = number of shards analysed. The complete dataset of unnormalised data is provided in appendix 5.

| | $SiO_2$ | $TiO_2$ | $Al_2O_3$ | FeO | MnO | MgO | CaO | $Na_2O$ | $K_2O$ | $P_2O_5$ | Cl | Total Oxides |
|---|---|---|---|---|---|---|---|---|---|---|---|---|
| **MD04-2822 2317-2318 cm** | | | | | | | | | | | | |
| Shard 1 | 75.26 | 0.22 | 11.93 | 2.58 | 0.15 | 0.02 | 0.44 | 5.10 | 4.13 | 0.01 | 0.17 | 95.60 |
| **MD04-2822 2319-2320 cm** | | | | | | | | | | | | |
| Population 1 (n=2) | 75.50 | 0.18 | 12.21 | 2.45 | 0.01 | 0.04 | 0.41 | 4.93 | 4.08 | 0.00 | 0.17 | 92.43 |
| S.D. | 0.00 | 0.06 | 0.15 | 0.03 | 0.06 | 0.01 | 0.04 | 0.00 | 0.11 | 0.01 | 0.04 | 3.17 |
| Population 2 (n=4) | 74.38 | 0.09 | 13.30 | 2.19 | 0.10 | 0.13 | 0.92 | 4.68 | 3.95 | 0.01 | 0.25 | 92.85 |
| S.D. | 0.13 | 0.07 | 0.10 | 0.28 | 0.02 | 0.01 | 0.03 | 0.11 | 0.17 | 0.02 | 0.02 | 0.85 |

### 7.6.2 Samples between MD04-2822 2327-2328 cm and 2359-2366 cm

Four shards from the minor peak in shard concentration within sample 2339-2340 cm were analysed. Of these analyses only one demonstrates a consistent geochemical

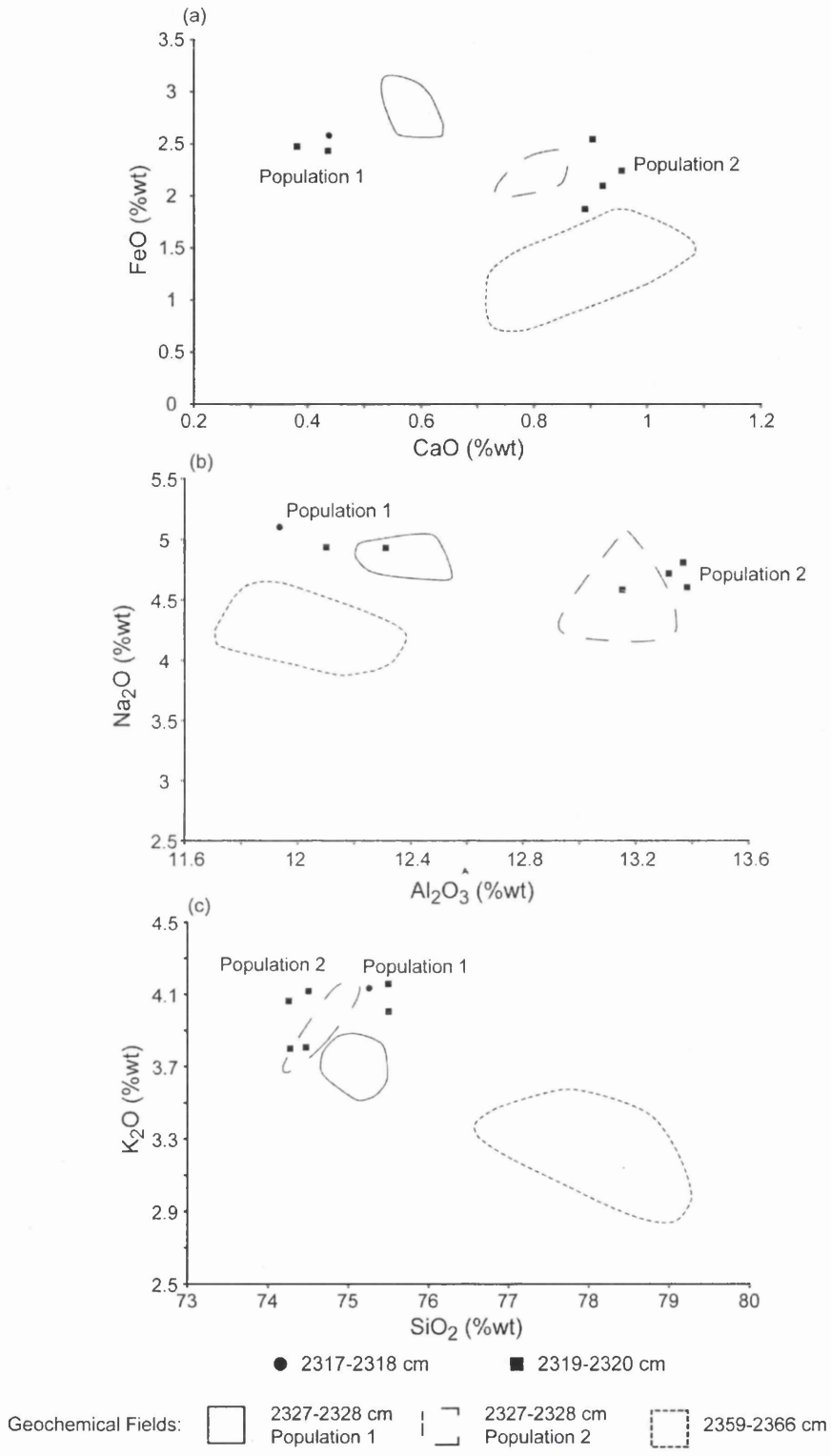


**Figure 7.21:** Geochemical data from shards extracted from the 2317-2318 cm and 2319-2320 cm depth samples plotted on (a) CaO vs. FeO (b) $Al_2O_3$ vs. $Na_2O$ and (c) $SiO_2$ vs. $K_2O$ compositional variation diagrams.

relationship to either tephra horizon, with analysis 1 in table 7.6 having a composition very similar to shards from MD04-2822 2359-2366 cm and falling consistently within the geochemical field for this horizon (figure 7.22). The remaining analyses and the outliers from 2359-2360 cm are more closely related to the geochemistry of MD04-2822 2327-2328 cm, however, none of the analyses consistently fall within the geochemical fields defined for either population (figure 7.22).

**Table 7.6:** Summary of normalised major oxide data for glass shards from the MD04-2822 2339-2340 cm sample and geochemical outliers from the 2359-2360 cm sample. Mean and 1 standard deviations are shown. Total oxides are raw values prior to normalisation. All major elements expressed as percentage weight. Total iron is expressed as FeO. n = number of shards analysed. The complete dataset of unnormalised data is provided in appendix 5.

| | $SiO_2$ | $TiO_2$ | $Al_2O_3$ | FeO | MnO | MgO | CaO | $Na_2O$ | $K_2O$ | $P_2O_5$ | Cl | Total Oxides |
|---|---|---|---|---|---|---|---|---|---|---|---|---|
| **MD04-2822 2339-2340 cm** | | | | | | | | | | | | |
| Shard 1 | 78.08 | 0.09 | 12.16 | 1.12 | 0.01 | 0.01 | 0.93 | 4.37 | 3.13 | -0.00 | 0.10 | 94.00 |
| Shard 2 | 75.46 | 0.15 | 12.01 | 2.28 | 0.23 | 0.05 | 0.58 | 4.76 | 4.11 | 0.03 | 0.33 | 93.26 |
| Shard 3 | 75.20 | 0.17 | 12.16 | 2.60 | 0.08 | 0.02 | 0.54 | 4.82 | 4.07 | -0.03 | 0.33 | 93.67 |
| Shard 4 | 74.76 | 0.41 | 12.78 | 2.30 | 0.11 | 0.16 | 0.62 | 4.83 | 3.89 | 0.01 | 0.12 | 93.35 |
| **MD04-2822 2359-2360 cm** | | | | | | | | | | | | |
| Outlier 1 | 74.89 | 0.12 | 13.20 | 2.11 | 0.00 | 0.05 | 0.67 | 4.75 | 3.97 | 0.02 | 0.22 | 94.62 |
| Outlier 2 | 74.66 | 0.49 | 12.75 | 2.25 | 0.08 | 0.18 | 0.57 | 4.60 | 4.28 | 0.02 | 0.11 | 94.30 |

### 7.6.3 Samples Below MD04-2822 2359-2366 cm

8 and 14 tephra shards were analysed from the 2373-2374 cm and 2377-2378 cm samples respectively. Two shards from each sample have a consistent affinity to the geochemistry of the 2359-2366 cm horizon (figure 7.23; table 7.7). The remaining six analyses from 2373-2374 cm and five analyses from shards within 2377-2378 cm display some affinities to the geochemistry of the 2327-2328 cm horizon (figure 7.23). In addition an outlier from the main population of 2365-2366 cm has an affinity to this population.

An inspection of the seven remaining shards from 2377-2378 cm indicates that they do not show a consistent affinity to either the geochemical composition of the two tephra horizons or the population described above (table 7.7).

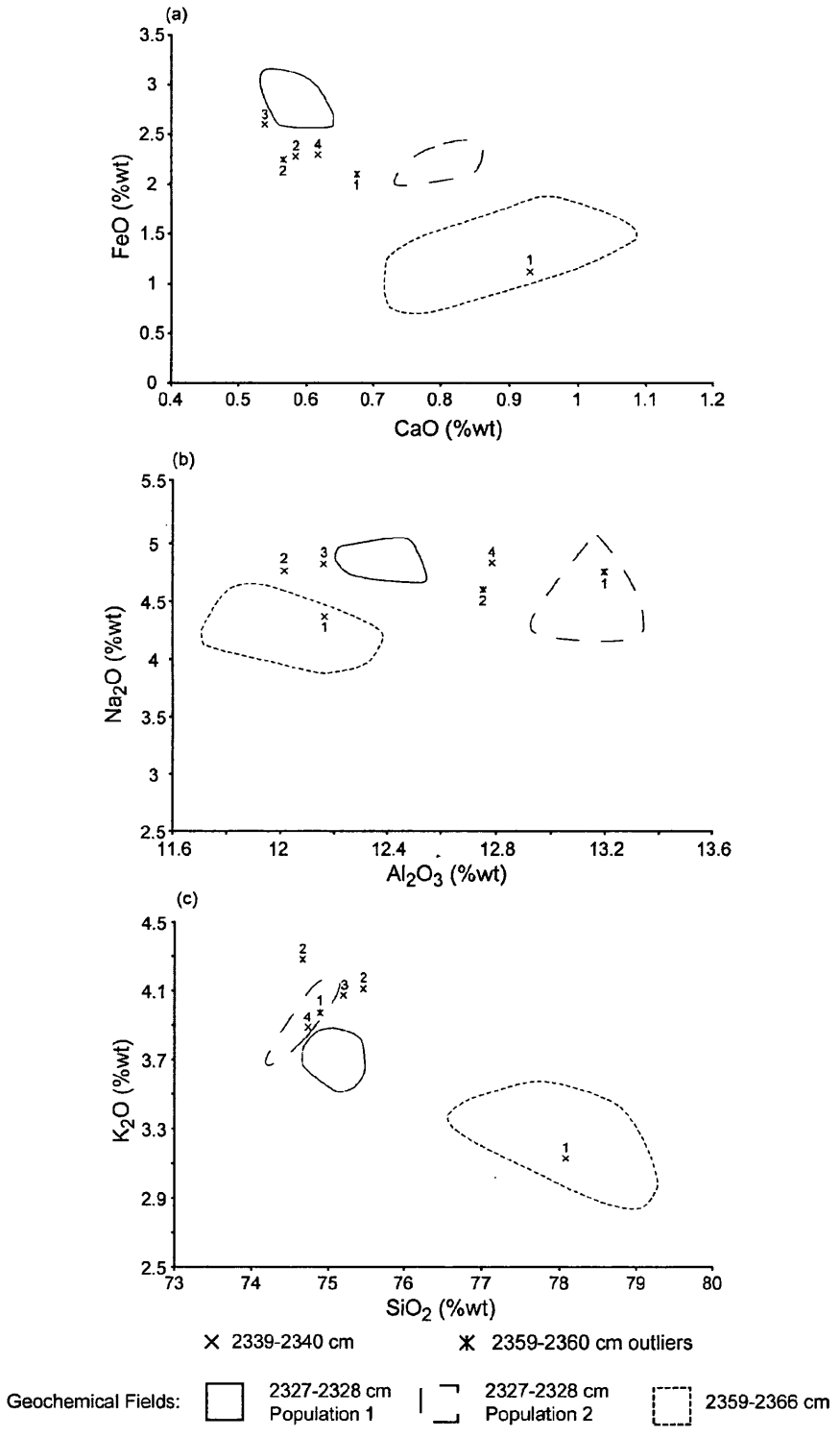


**Figure 7.22:** Geochemical data from shards extracted from the 2339-2340 cm sample and analyses outlying from the main geochemical population of shards from the 2359-2360 cm sample plotted on (a) CaO vs. FeO (b) $Al_2O_3$ vs. $Na_2O$ and (c) $SiO_2$ vs. $K_2O$ compositional variation diagrams.

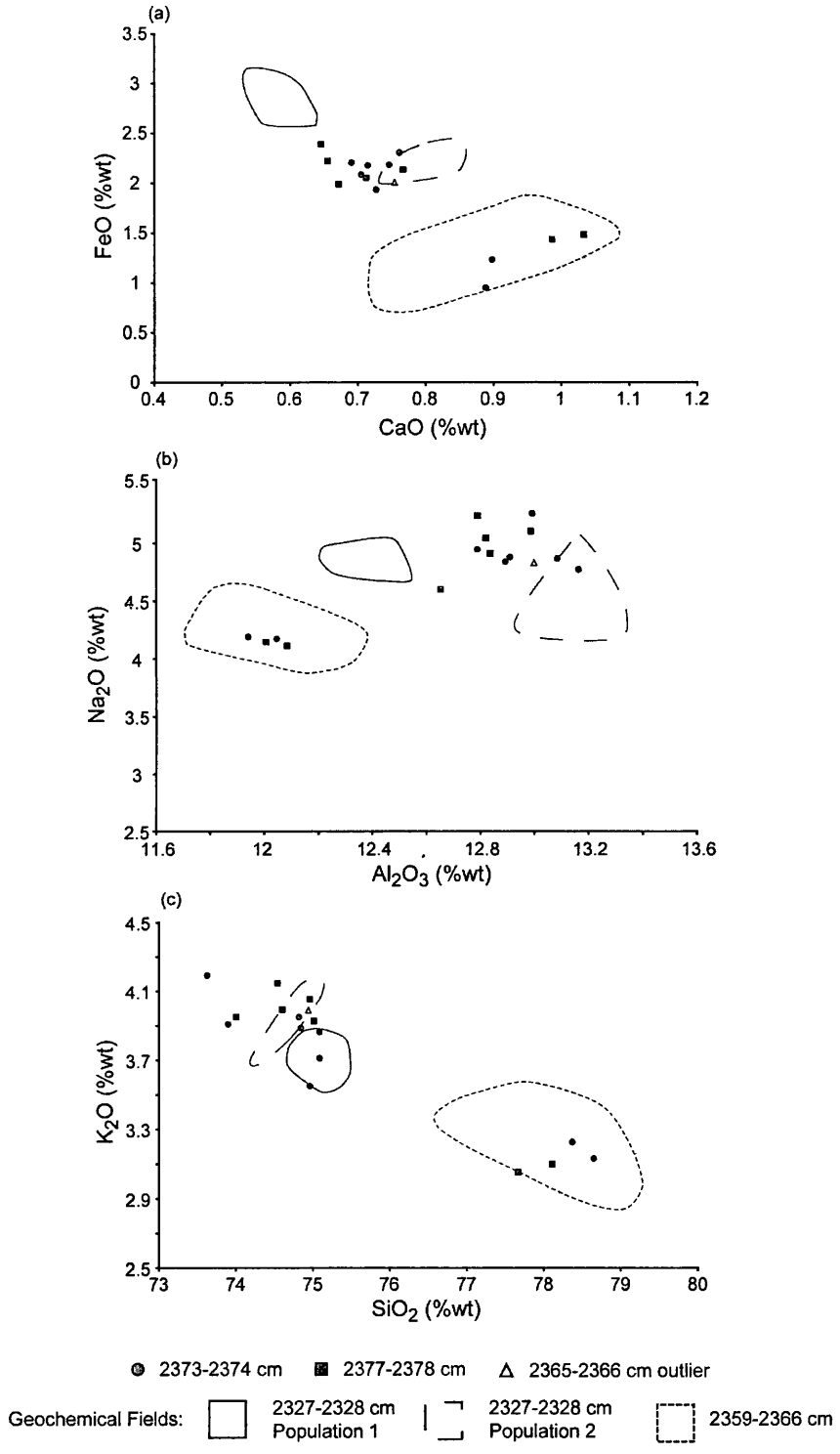


**Figure 7.23:** Geochemical data from shards extracted from the 2373-2374 cm and 2377-2378 cm samples and an analysis outlying from the main geochemical population of shards from the 2365-2366 cm sample plotted on (a) CaO vs. FeO (b) $Al_2O_3$ vs. $Na_2O$ and (c) $SiO_2$ vs. $K_2O$ compositional variation diagrams.

**Table 7.7:** Summary of normalised major oxide data for glass shards from the MD04-2822 2373-2374 cm and 2377-2378 cm samples and geochemical outliers from the 2365-2366 cm sample. Mean and 1 standard deviations are shown. Total oxides are raw values prior to normalisation. All major elements expressed as percentage weight. Total iron is expressed as FeO. n = number of shards analysed. The complete dataset of unnormalised data is provided in appendix 5.

| | $SiO_2$ | $TiO_2$ | $Al_2O_3$ | FeO | MnO | MgO | CaO | $Na_2O$ | $K_2O$ | $P_2O_5$ | Cl | Total Oxides |
|---|---|---|---|---|---|---|---|---|---|---|---|---|
| **MD04-2822 2365-2366 cm** | | | | | | | | | | | | |
| Outlier | 74.94 | 0.13 | 13.00 | 2.01 | 0.07 | 0.05 | 0.76 | 4.82 | 3.99 | 0.00 | 0.23 | 93.99 |
| **MD04-2822 2373-2374 cm** | | | | | | | | | | | | |
| Main Population (n=6) | 74.78 | 0.19 | 12.97 | 2.15 | 0.09 | 0.10 | 0.72 | 4.92 | 3.81 | 0.00 | 0.23 | 93.52 |
| S.D. | 0.45 | 0.13 | 0.14 | 0.13 | 0.12 | 0.08 | 0.03 | 0.17 | 0.15 | 0.03 | 0.05 | 0.88 |
| Correlatives to MD04-2822 2359-2366 cm | | | | | | | | | | | | |
| | 78.65 | 0.09 | 12.05 | 0.95 | -0.11 | 0.00 | 0.89 | 4.17 | 3.13 | -0.02 | 0.06 | 93.25 |
| | 78.37 | 0.03 | 11.94 | 1.23 | 0.05 | 0.01 | 0.90 | 4.19 | 3.23 | -0.04 | 0.05 | 94.33 |
| **MD04-2822 2377-2378 cm** | | | | | | | | | | | | |
| Main Population (n=5) | 74.62 | 0.28 | 12.82 | 2.16 | 0.12 | 0.13 | 0.69 | 4.98 | 4.01 | 0.01 | 0.16 | 94.18 |
| S.D. | 0.40 | 0.13 | 0.12 | 0.16 | 0.12 | 0.09 | 0.05 | 0.24 | 0.09 | 0.03 | 0.08 | 0.81 |
| Correlatives to MD04-2822 2359-2366 cm | | | | | | | | | | | | |
| | 78.11 | 0.09 | 12.01 | 1.43 | 0.04 | -0.01 | 0.99 | 4.15 | 3.10 | 0.02 | 0.06 | 92.88 |
| | 77.66 | 0.21 | 12.06 | 1.48 | 0.20 | 0.01 | 1.03 | 4.19 | 3.05 | -0.00 | 0.08 | 92.98 |
| Outlier 1 | 78.24 | 0.02 | 11.76 | 0.97 | 0.04 | 0.03 | 0.50 | 3.99 | 4.29 | 0.02 | 0.13 | 95.36 |
| Outlier 2 | 78.07 | 0.04 | 12.08 | 0.87 | -0.02 | 0.04 | 0.50 | 4.11 | 4.16 | 0.00 | 0.12 | 94.43 |
| Outlier 3 | 77.75 | -0.01 | 11.72 | 2.26 | 0.12 | 0.05 | 0.82 | 3.47 | 3.75 | -0.01 | 0.05 | 90.22 |
| Outlier 4 | 77.40 | 0.22 | 11.87 | 2.35 | 0.25 | 0.02 | 1.03 | 3.05 | 3.73 | 0.01 | 0.07 | 92.60 |
| Outlier 5 | 75.73 | 0.17 | 12.02 | 2.50 | -0.03 | 0.01 | 0.54 | 4.66 | 4.05 | 0.03 | 0.29 | 93.22 |
| Outlier 6 | 74.27 | 0.12 | 13.13 | 2.44 | 0.02 | 0.06 | 0.92 | 5.02 | 3.82 | -0.01 | 0.19 | 93.09 |
| Outlier 7 | 73.75 | 0.13 | 13.04 | 2.80 | 0.11 | 0.08 | 0.92 | 5.10 | 3.87 | 0.00 | 0.20 | 94.69 |

### 7.6.4 Implications

Overall these results suggest that material with a similar composition to the two main tephra horizons can be identified at different depths within the core. This may be indicative of secondary reworking processes such as bottom currents or gravity flows, however the low shard concentrations suggests that these processes are insignificant and have not affected the integrity of the two tephra horizons. The homogenous geochemical nature, relatively high shard counts and discreetness of the two tephra horizons demonstrates that they represent primary deposits unaffected by sedimentary processes. Background shards with differing compositions may be present within the horizons, as shown by the outlying analyses from the 2359-2360 cm and 2365-2366 cm samples, however, this background signal is diluted by the high influx of shards during the deposition of the tephra horizons.

The identification of a distinct geochemical population within the 2373-2374 cm and 2377-2378 cm samples may indicate that a significant horizon lies below 2380 cm depth and the geochemical similarities to the MD04-2822 2327-2328 cm tephra horizon suggests they might have the same source. This provides an explanation for the higher concentration of shards within the samples at the base of the core.

## 7.7 Primary Airfall or Ice Rafted Deposits?

Icelandic tephra horizons deposited within North Atlantic marine sediments during the last glacial period have been transported to distal depositional sites via two main processes, ice rafting or direct atmospheric transportation (primary airfall). Volcanic material can be ice-rafted within the northeast Atlantic gyre prior to deposition via melting of either sea-ice, from areas surrounding Iceland, or tephra rich icebergs calved from Icelandic ice-sheets (Austin et al., 2004). Icebergs calved from terrestrial sources are very likely to contain material from a number of eruptions; therefore material rafted from icebergs would yield volcanic horizons with heterogeneous compositions (Lacasse et al., 1998). The relative homogeneity of the two MD04-2822 tephra horizons identified within this study implies that iceberg calving can be ruled out as the transport process responsible for their deposition.

The size of shards within distal horizons is a principal line of evidence for ascertaining whether shards have been deposited from primary airfall or rafting of sea-ice. In general, there is an exponential decay in the size of shards deposited directly from the atmosphere with increasing distance from the volcanic source of an eruption (Lacasse, 2001). The deposition of large ash shards onto sea-ice proximal to Iceland and subsequent transportation of this material can result in material larger than could be transported in the atmosphere being deposited at distal locations. For example, the recognition of shards up to 1 mm in diameter, 1800 km south of Iceland, indicated that the dispersal of North Atlantic Ash Zone II to locations as far south as 45°N was caused by sea-ice rafting processes (Ruddiman and Glover, 1972; Lacasse et al., 1996).

The maximum size of particles that can be atmospherically transported to a depositional site can be constrained using the exponential relationships between the size of shards and distance from source observed for large explosive eruptions, such as Toba and the Campanian Ignimbrite eruptions (Lacasse et al., 1996). These empirical relationships are used as there are limitations associated with determining

the atmospheric shard dispersal patterns from past eruptions, which would have been affected by unknown parameters such as the height of the eruptive column and the prevailing wind conditions during the eruption (Lacasse, 2001). For example, simulations of shard dispersal using present day atmospheric circulation models are inappropriate for comparison because enhanced atmospheric circulation during glacial climates would have a significant effect on dispersal patterns (Lacasse, 2001).

The maximum diameter of shards within the MD04-2822 tephra horizons 2327-2328 cm and 2359-2366 cm are 150 μm and 100 μm respectively and the depositional site lies approximately 900 km southeast of Icelandic volcanic sources. Exponential relationships for shard dispersal from the Toba and Campanian Ignimbrite eruptions indicate that shards with a diameter of ~370 and ~225 μm respectively can be transported 900 km from the eruptive source (Lacasse et al., 1996). As the size of particles within the two MD04-2822 horizons fall far below these thresholds it is highly likely they were atmospherically transported.

In addition, the size of the shards within the two horizons is notably smaller than has been observed for material transported to the depositional site via sea-ice rafting. North Atlantic Ash Zone II was transported via this process and the maximum shard diameter for material within this horizon in MD04-2822 is 890 μm (F. Hibbert, *pers. comm.*, 2009).

## 7.8 Chapter Summary

The principal findings of this chapter are:

- Two tephra horizons of MIS 4 age have been identified within the MD04-2822 core.

- The major element and trace element characterisations of these horizons demonstrate that the MD04-2822 2327-2328 cm and 2359-2366 cm tephra horizons have affinities to the rhyolitic products of the Icelandic transitional alkaline and tholeiitic rock suites respectively.

- These affinities indicate that MD04-2822 2327-2328 cm was sourced from an Icelandic flank zone and the MD04-2822 2359-2366 cm horizon from the

Icelandic rift zone. However, individual source volcanic systems within these regions could not be ascertained through comparisons to major element analyses of proximal Icelandic deposits.

•The integrity of the horizons has not been adversely affected by secondary reworking.

•The horizons were most likely deposited via direct atmospheric transportation and represent primary air-fall deposits. Ice rafting from calved icebergs can be ruled out as a transportation process due to the geochemical homogeneity of the horizons and sea-ice rafting because of the relatively small maximum shard sizes within the horizons.

# 8. Synthesis and Discussion

## 8.1 Synthesis of the MIS 4 Tephrochronological Records from NGRIP, GRIP and MD04-2822

### 8.1.1 Introduction

14 cryptotephra horizons have been identified within core sections spanning the MIS 4 period of the three geological archives (NGRIP, GRIP and MD04-2822) investigated within this study. This section explores whether any of these horizons represent coeval events and thus act as time-synchronous tie-lines between the marine and ice-core records. The stratigraphic position of the horizons relative to the three Dansgaard-Oeschger events (18, 19 and 20) and their geochemical composition are used to determine whether any of these horizons can be traced between the sequences and if any compositional similarities are apparent between closely spaced eruptions.

The stratigraphic positions of the tephra horizons described within chapters 5, 6 and 7 are illustrated in figure 8.1. The positions of the horizons within MD04-2822 have been related to those within the ice-core records using the approximate tuning between the records described in section 7.2.1. Three stratigraphic periods can be identified where tephra horizons can be identified in multiple cores (figure 8.1) and potential correlations between the horizons will be explored with reference to these three stratigraphic periods. These periods fall towards the end of each Dansgaard-Oeschger event (figure 8.1).

### 8.1.2 Period 1

During the period following the DO 18 climatic event four tephra horizons have been identified within the Greenland ice-cores: NGRIP 2454.9 m, GRIP 2498.5 m, GRIP 2499.75 m and GRIP 2501.05 m. Major element characterisations demonstrate that two horizons have an affinity to the Icelandic tholeiitic rock suite (GRIP 2498.5 m and GRIP 2499.75 m), one was sourced from the Jan Mayen volcanic region (NGRIP 2454.9 m) and the remaining horizon is bimodal with populations related to both the tholeiitic and Jan Mayen rock suites (GRIP 2499.75 m).

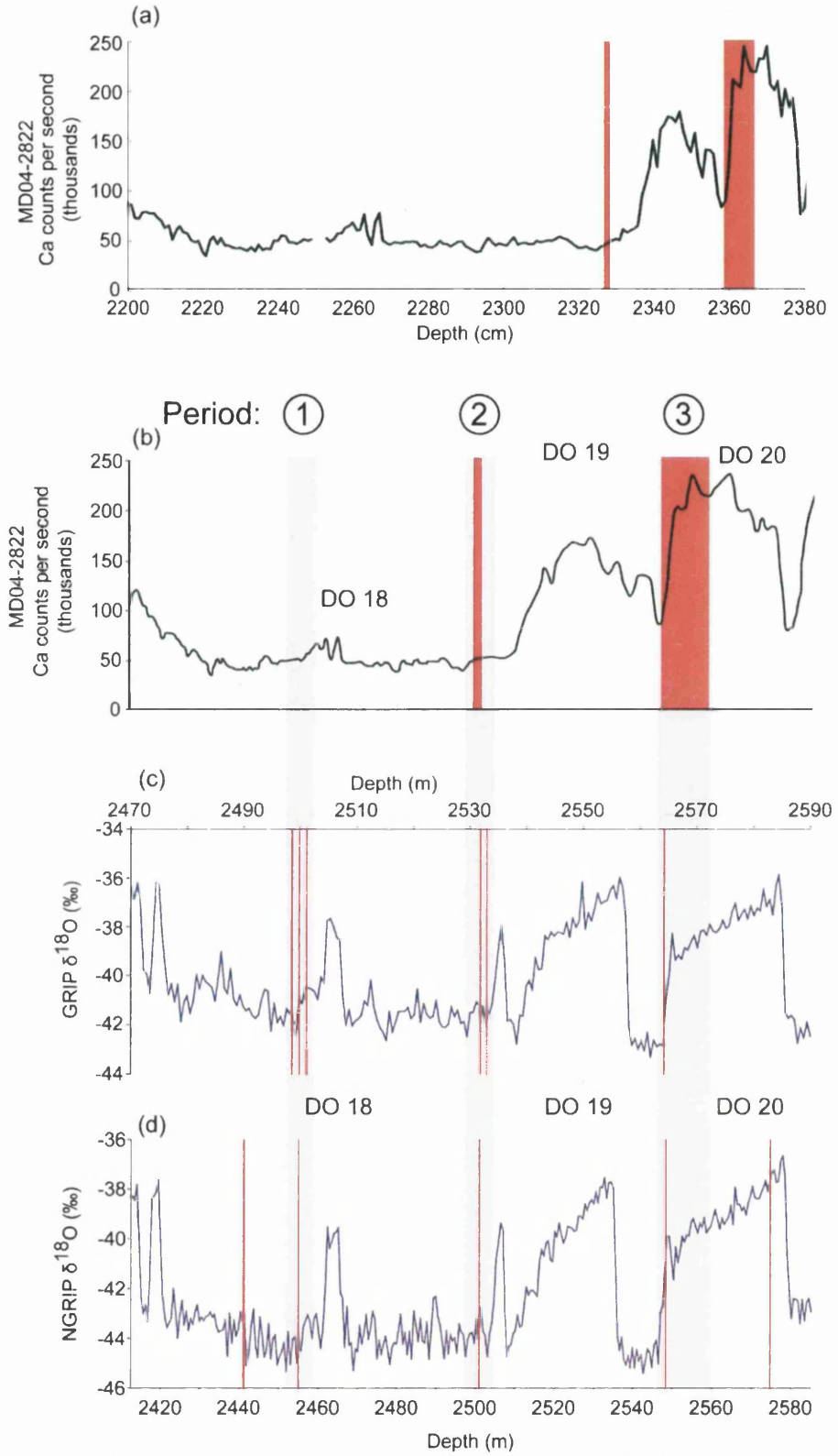


**Figure 8.1:** (a) Stratigraphic position of tephra horizons within MD04-2822 relative to the Ca count rate record for the core. (b) Position of tephra horizons within MD04-2822 relative to the ice-core tuned Ca count record for the core used in figure 7.2. (c) Stratigraphic position of tephra horizons within the GRIP ice-core. (d) Stratigraphic position of tephra horizons within the NGRIP ice-core.

### 8.1.2.1 Jan Mayen Horizons: NGRIP 2454.9 m and GRIP 2499.75 m-1

Both the NGRIP 2454.9 m and GRIP 2499.75 m-1 tephra horizons were identified as originating from the Jan Mayen volcanic region and these horizons show distinct major element similarities (figure 8.2), with clear overlaps between their geochemical fields. The only observable difference is that GRIP 2499.75 m-1 contains five shards with a more evolved composition, indicated by the higher $SiO_2$ and $K_2O$ concentrations (figure 8.3a). Statistical comparison of the two complete data-sets emphasises the strong geochemical similarities between the horizons as a high similarity coefficient of 0.972 is calculated and a low $D^2$ value of 1.2 strongly suggests a correlation between these horizons (tables 8.1 and 8.2). If the more evolved shards within GRIP 2499.75 m-1 are removed from the averages these statistical parameters are strengthened with a similarity coefficient of 0.976 and a $D^2$ value of 0.79. Therefore, the major element compositional data supports the proposition that these horizons are the products of the same volcanic eruption.

**Table 8.1:** Similarity coefficients values for comparisons between the average major element compositions of the tephra horizons deposited during period 1. Bold values exceed 0.90.

| | NGRIP 2454.9 m | GRIP 2498.5 m | GRIP 2499.75 m-1 | GRIP 2499.75 m-2 | GRIP 2501.05 m |
|---|---|---|---|---|---|
| NGRIP 2454.9 m | 1.000 | | | | |
| GRIP 2498.5 m | 0.855 | 1.000 | | | |
| GRIP 2499.75 m-1 | **0.972** | 0.865 | 1.000 | | |
| GRIP 2499.75 m-2 | 0.799 | **0.912** | 0.805 | 1.000 | |
| GRIP 2501.05 m | 0.848 | **0.956** | 0.845 | **0.924** | 1.000 |

**Table 8.2:** $D^2$ values for statistical distance comparisons between the average major element compositions of tephra horizons deposited during period 1. Critical $D^2$ value of 20.1 at the 99% confidence level as 8 oxide values were utilised. Bold values are comparisons where a statistical difference can not be identified.

| | NGRIP 2454.9 m | GRIP 2498.5 m | GRIP 2499.75 m-1 | GRIP 2499.75 m-2 | GRIP 2501.05 m |
|---|---|---|---|---|---|
| NGRIP 2454.9 m | 0.0 | | | | |
| GRIP 2498.5 m | 81.4 | 0.0 | | | |
| GRIP 2499.75 m-1 | **1.2** | 52.0 | 0.0 | | |
| GRIP 2499.75 m-2 | 165 | 26.8 | 89.5 | 0.0 | |
| GRIP 2501.05 m | 114 | **5.9** | 67.4 | 59.7 | 0.0 |

The trace element compositions of NGRIP 2454.9 m and GRIP 2499.75 m-1 were shown to provide further evidence of a Jan Mayen source for these horizons. The REE profiles show strong similarities, which are most distinct for the more abundant LREEs between La and Nd (figure 8.3a). For the MREEs and HREEs there is less consistency between the average profiles potentially due to increased noise induced by the lower

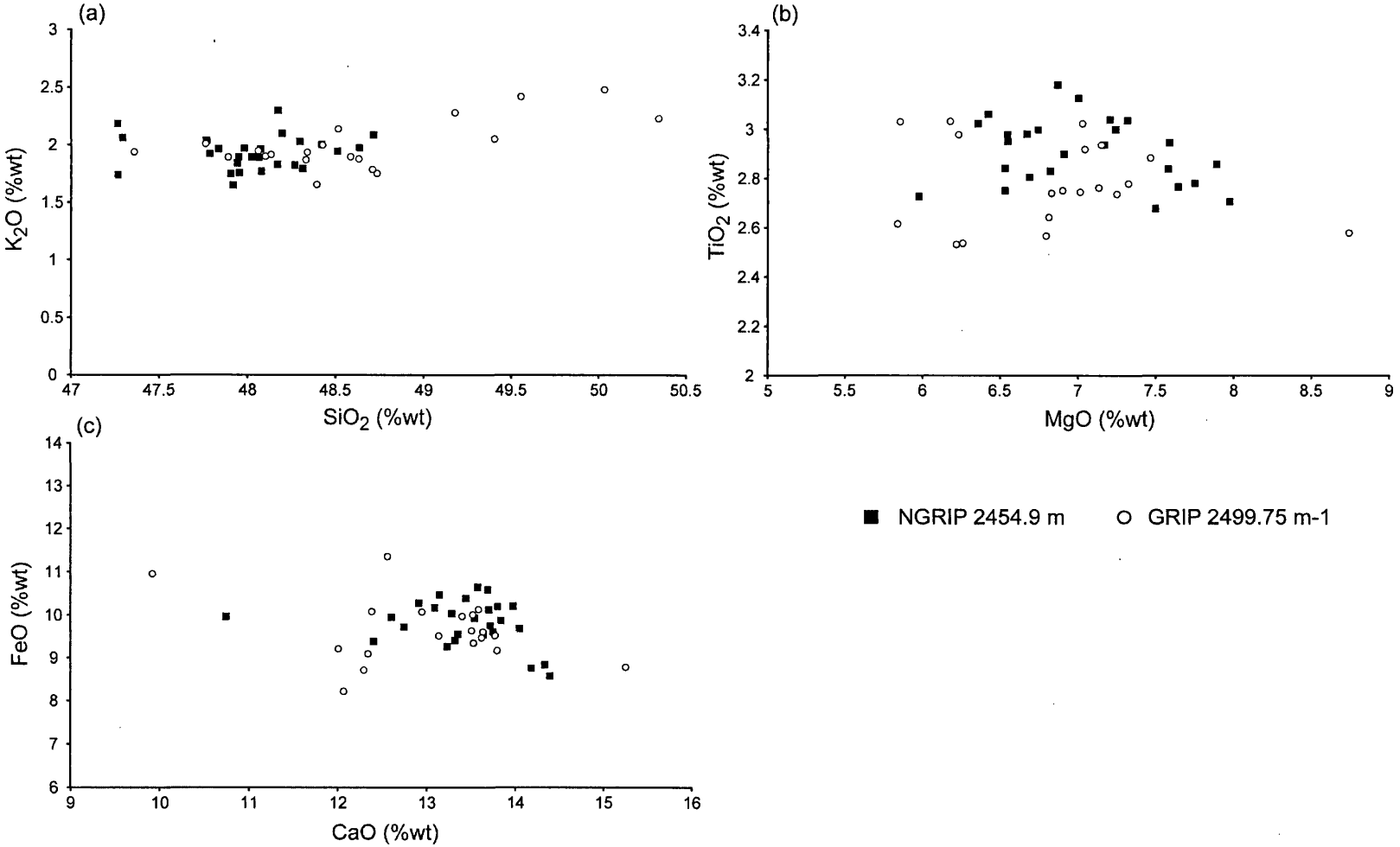


**Figure 8.2:** (a) $SiO_2$ vs. $K_2O$ (b) MgO vs. $TiO_2$ and (c) CaO vs. FeO compositional variation diagrams comparing the major element geochemistry of the NGRIP 2454.9 m and GRIP 2499.75 m-1 tephra horizons.

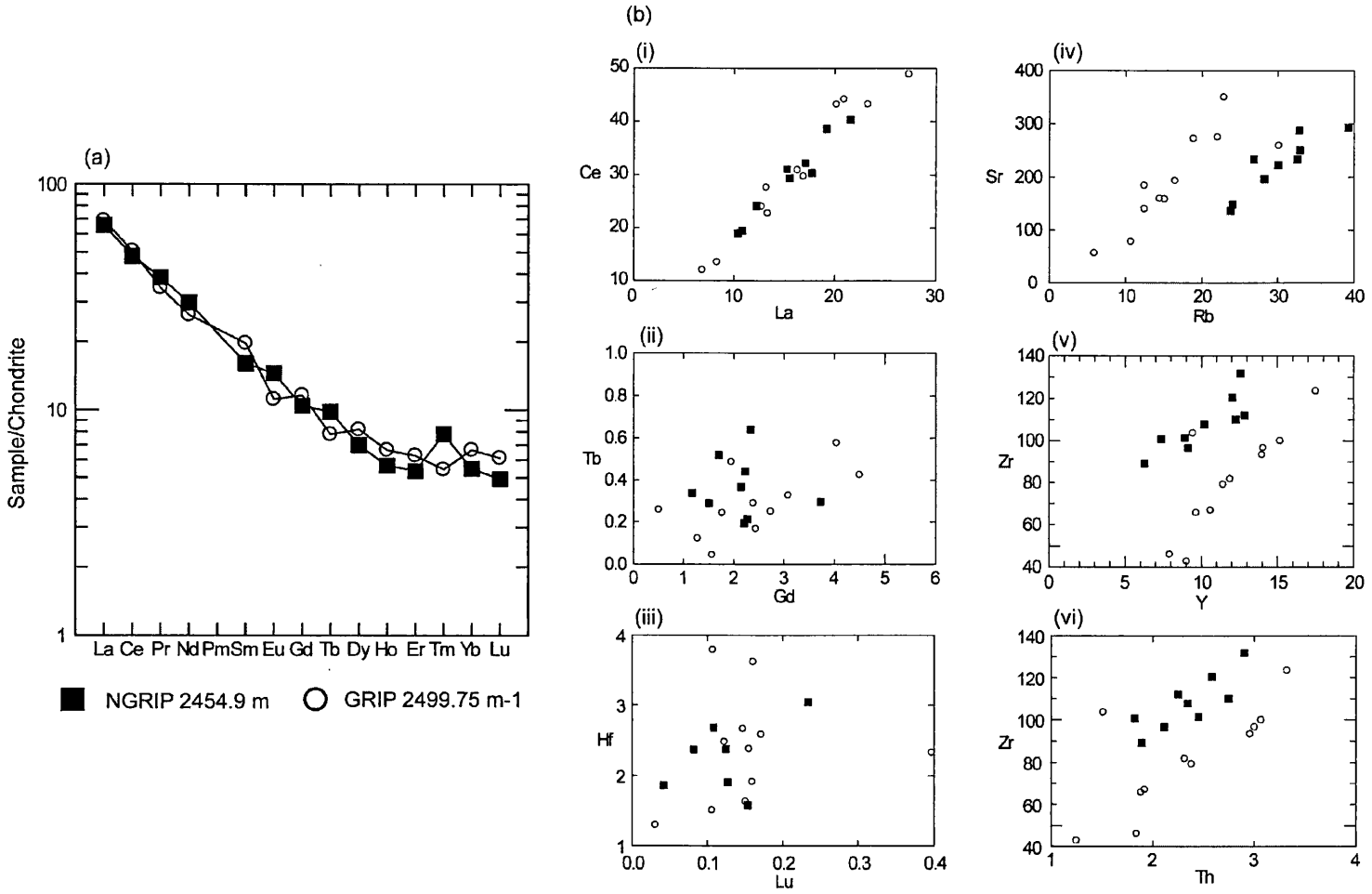


**Figure 8.3:** (a) Average chondrite-normalised REE profiles for the NGRIP 2454.9 m and GRIP 2499.75 m-1 tephra horizons. (b) (i) La vs. Ce (ii) Gd vs. Tb (iii) Lu vs. Hf (iv) Rb vs. Sr (v) Y vs. Zr and (vi) Th vs. Zr compositional variation diagrams of individual shards from the NGRIP 2454.9 m and GRIP 2499.75 m-1 tephra horizons.

analytical precision for these less abundant elements. However, the overall shape of the profiles are similar, no distinct divergences can be identified and comparisons of REE concentrations from individual shards within the horizons show there are strong overlaps in the geochemical fields for each horizon (figure 8.3b (i-iii)). Similarities are also observed in REE ratios (figure 8.4 (i) and (ii)).

Despite these similarities, correlations are not evident when lighter elements are compared (figure 8.3b (iv-vi)). On these plots different geochemical fields are defined for each horizon. Linear covariance between the element pairs can be observed, however, the variance for each horizon does not follow the same ratio trend lines. Trace element ratio-ratio comparisons emphasise the different element ratios between the two data-sets, with discriminatory ratios including Y/Zr and Rb/Sr (figure 8.4 (iii-vi)). The difference in incompatible element ratios between the horizons could be due to mantle melting in the magma chamber adding primitive material between eruptive events or these horizons originating from two different magma chambers containing material of a similar major element composition, but differing trace element concentrations (Rollinson, 1993).

A statistical distance comparison between the two data-sets using the concentration of 14 trace elements produces a $D^2$ value of 5.68, less than the critical value at the 99% confidence level of 29.14, which does not provide quantitative evidence to support the difference observed on the biplots. However, this may be the result of trace element concentration differences only being observed for a couple of elements such as Rb and Zr.

The differences in both trace element concentration and ratios between the two data-sets demonstrates that the two deposits are not identical, therefore, a correlation cannot be confirmed as these deposits represent the products of two separate Jan Mayen eruptions.

### 8.1.2.2 Tholeiitic Horizons: GRIP 2498.5 m, GRIP 2499.75 m-2 and GRIP 2501.05 m

Three tephra horizons with an affinity to the tholeiitic rock suite of Iceland, GRIP 2498.5 m, GRIP 2499.75 m-2 and GRIP 2501.05 m were identified within a 2.7 m long section of the GRIP ice-core. The current timescale for the GRIP core indicates that the

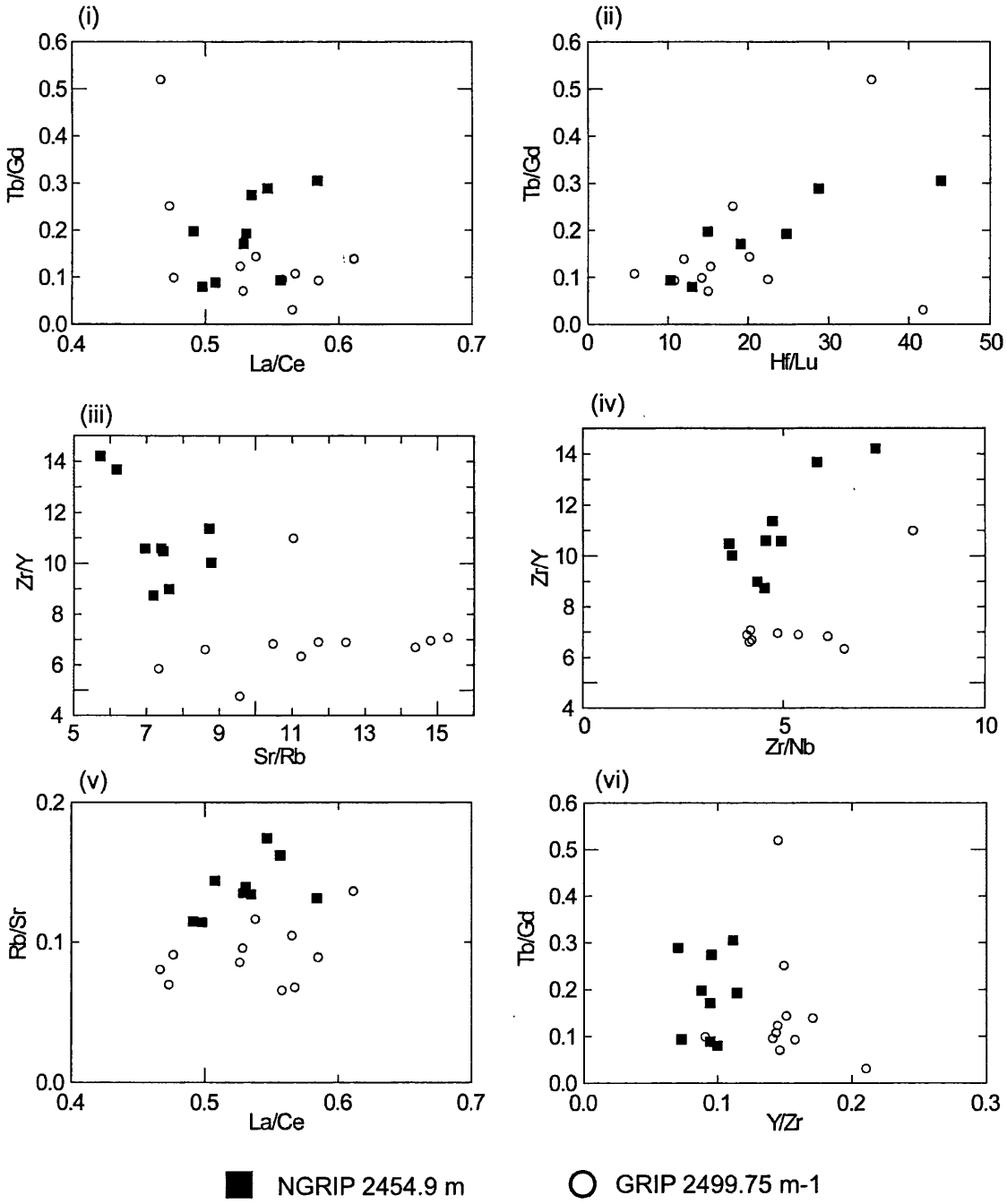


**Figure 8.4:** Trace element ratio-ratio diagrams for analyses of individual shards from the NGRIP 2454.9 m and GRIP 2499.75 m-1 tephra horizons.

temporal separation between the deposition of the GRIP 2501.05 m and GRIP 2498.5 m horizons was approximately 450 years. Statistical comparisons between the average major element compositions of all these horizons display high similarity coefficients between 0.912 and 0.956, supporting an affinity to the same rock suite (table 8.1).

The $D^2$ values presented in table 8.2, however, show that the major element geochemistry of GRIP 2499.75 m-2 is statistically different from the other two horizons and these differences are apparent on figure 8.5. With GRIP 2499.75 m-2 displaying higher FeO and $SiO_2$ concentrations and lower CaO concentrations relative to the other two horizons. This implies that the GRIP 2499.75 m-2 horizon originates from a different volcanic system within the Icelandic rift zone.

Figure 8.5 also highlights the general geochemical similarities between the compositions of GRIP 2498.5 m and GRIP 2501.05 m, mentioned in section 6.4.3. The only observable difference is on the $SiO_2$ vs. $K_2O$ plot in figure 8.5c which indicates that the GRIP 2498.5 m tephra horizon has a slightly more evolved composition than GRIP 2501.05 m. These horizons have a relatively high similarity coefficient value of 0.956 and are not statistically different (table 8.1). Overall, these observations strongly suggest that both the GRIP 2498.5 m and GRIP 2501.05 m tephra horizons were produced by the same volcanic system within the Icelandic rift zone.

The close temporal separation between the deposition of the GRIP 2498.5 m and GRIP 2501.05 m horizons and their broad major element compositional similarities may hinder direct correlation between sequences if only one of these horizons can be identified. Trace element characterisations could be used to discriminate between these horizons as the average REE patterns display some slight differences with the elemental concentrations generally higher within the GRIP 2501.05 m horizon (figure 8.6a). However, when analyses from individual shards are compared strong similarities in composition between the horizons can be observed; with high overlaps in the geochemical fields and similar linear covariance relationships between element pairs for both horizons (figure 8.6b). Therefore, it is not possible to discriminate between these horizons based on their trace element compositions.

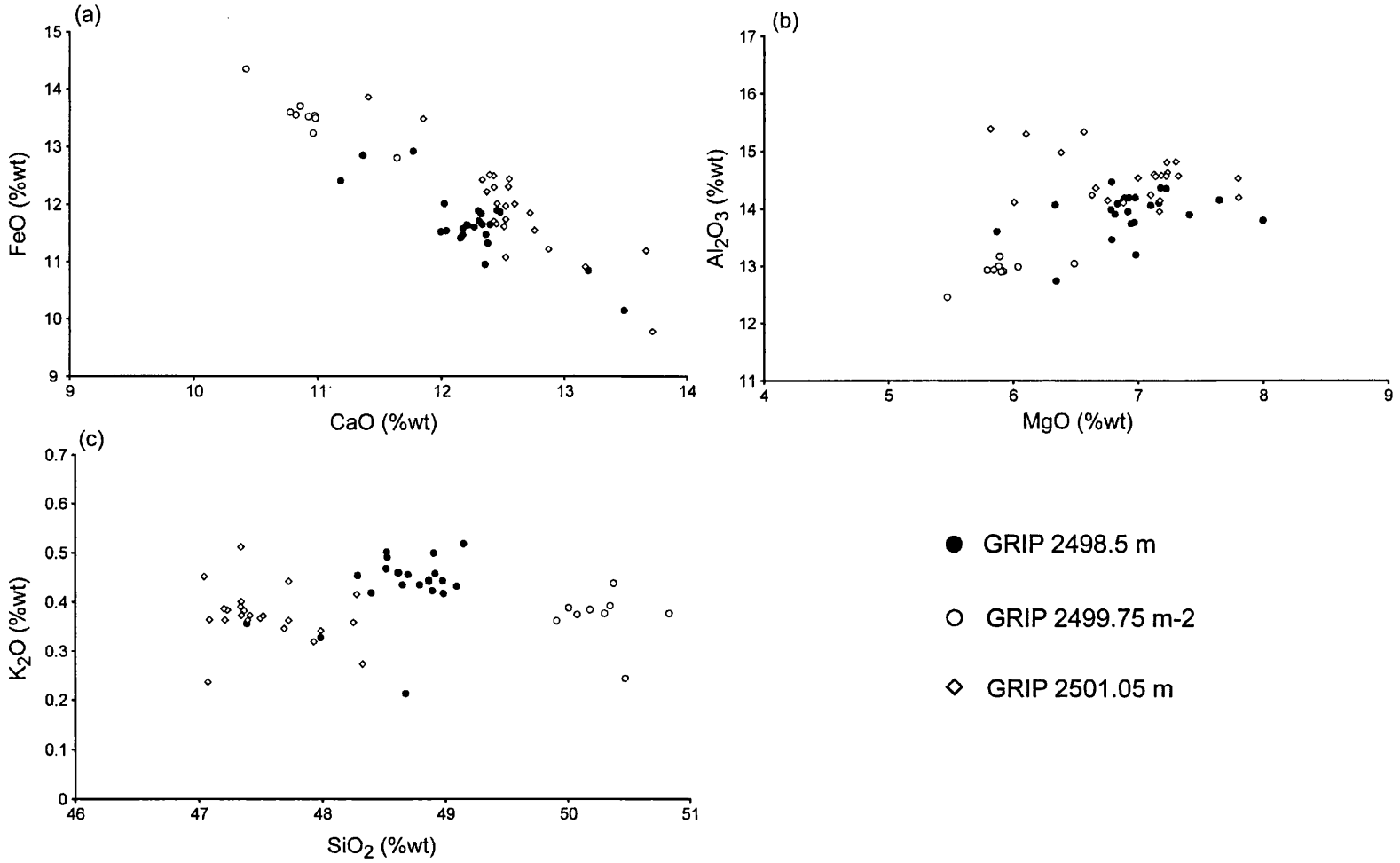


**Figure 8.5:** (a) CaO vs. FeO (b) MgO vs. $Al_2O_3$ and (c) $SiO_2$ vs. $K_2O$ compositional variation diagrams comparing the major element geochemistry of the GRIP 2498.5 m, GRIP 2499.75 m-2 and GRIP 2501.05 m tephra horizons.

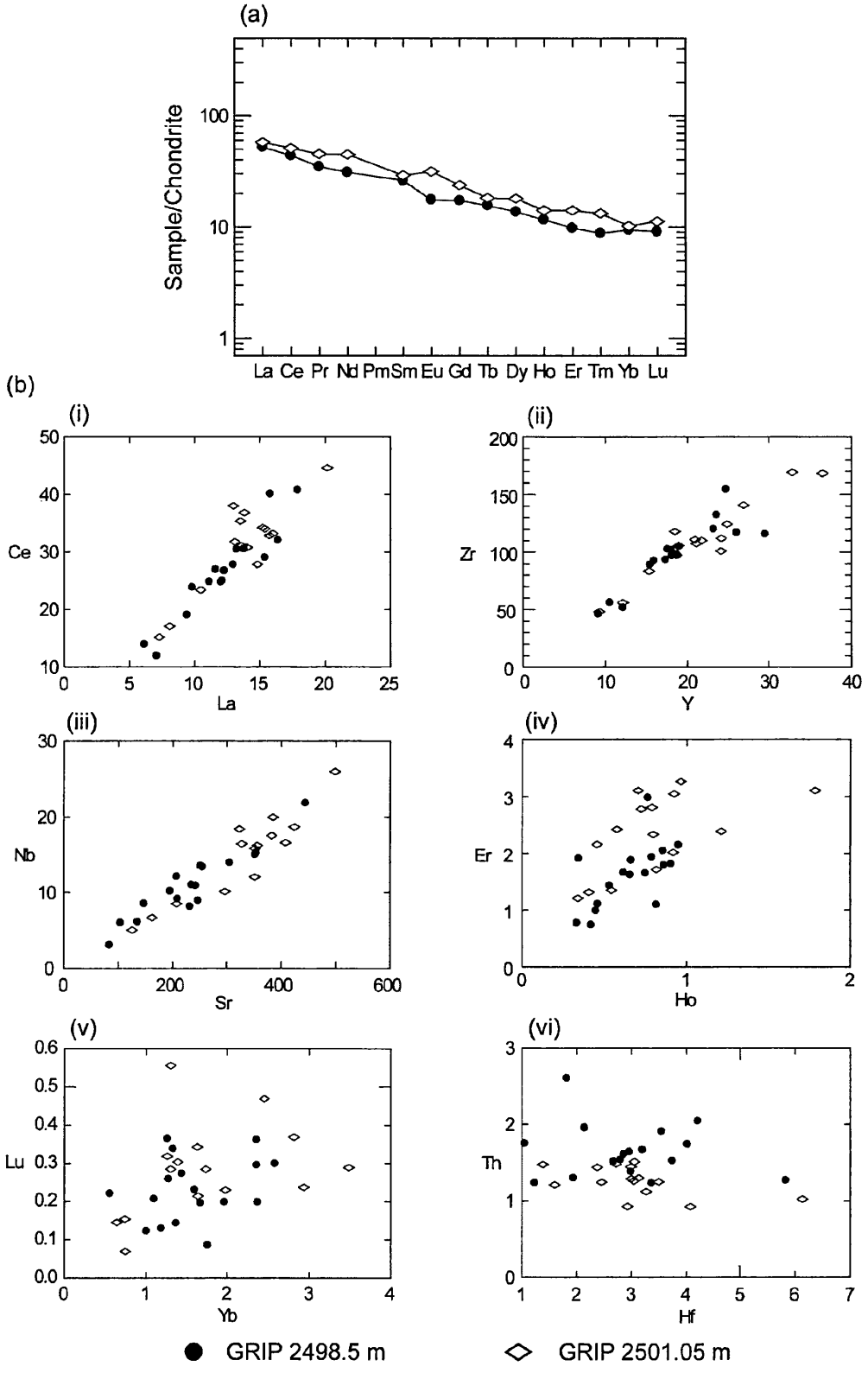


**Figure 8.6:** (a) Average chondrite-normalised REE profiles for the GRIP 2498.5 m and GRIP 2501.05 m tephra horizons. (b) (i) La vs. Ce (ii) Y vs. Zr (iii) Sr vs. Nb (iv) Ho vs. Er (v) Yb vs. Lu and (vi) Hf vs. Th compositional variation diagrams of individual shards from the NGRIP 2454.9 m and GRIP 2499.75 m-1 tephra horizons.

### 8.1.3 Period 2

Four tephra horizons, NGRIP 2500.9 m, GRIP 2531.8 m, GRIP 2532.95 m and MD04-2822 2327-2328 cm, were deposited within the MIS 4 sequences during a period following the DO 19a climatic event. The approximate ages for the GRIP horizons indicate that 200 years separated the deposition of these tephras (table 6.4).

The three ice-core horizons all have basaltic compositions, whereas MD04-2822 2327-2328 cm has a rhyolitic composition, which precludes an ice-marine correlation (figure 8.7).

The major element characterisations for the three basaltic ice-core horizons are compared on figure 8.8, which shows that the composition of GRIP 2532.95 m appears unrelated to the other horizons. The geochemical field for this horizon rarely overlaps with the fields for NGRIP 2500.9 m and GRIP 2531.8 m. This is supported by the low similarity coefficients of 0.875 and 0.883 between the horizons (table 8.3). The geochemical differences between the GRIP 2532.95 m and NGRIP 2500.9 m tephra horizons are also statistically significant with the $D^2$ value exceeding the critical value (table 8.4). However, the biplots in figure 8.8 suggest that NGRIP 2500.9 m and GRIP 2531.8 m may be related.

**Table 8.3:** Similarity coefficients values for comparisons between the average major element compositions of the tephra horizons deposited during period 2. Bold values exceed 0.90.

| | NGRIP 2500.9 m | GRIP 2531.8 m | GRIP 2532.95 m |
|---|---|---|---|
| NGRIP 2500.9 m | 1.000 | | |
| GRIP 2531.8 m | **0.978** | 1.000 | |
| GRIP 2532.95 m | 0.875 | 0.883 | 1.000 |

**Table 8.4:** $D^2$ values for statistical distance comparisons between the average major element compositions the tephra horizons deposited during period 2. Critical $D^2$ value of 20.1 at the 99% confidence level as 8 oxide values were utilised. Bold values are comparisons where a statistical difference can not be identified.

| | NGRIP 2500.9 m | GRIP 2531.8 m | GRIP 2532.95 m |
|---|---|---|---|
| NGRIP 2500.9 m | 0.0 | | |
| GRIP 2531.8 m | **6.5** | 0.0 | |
| GRIP 2532.95 m | 28.7 | **16.1** | 0.0 |

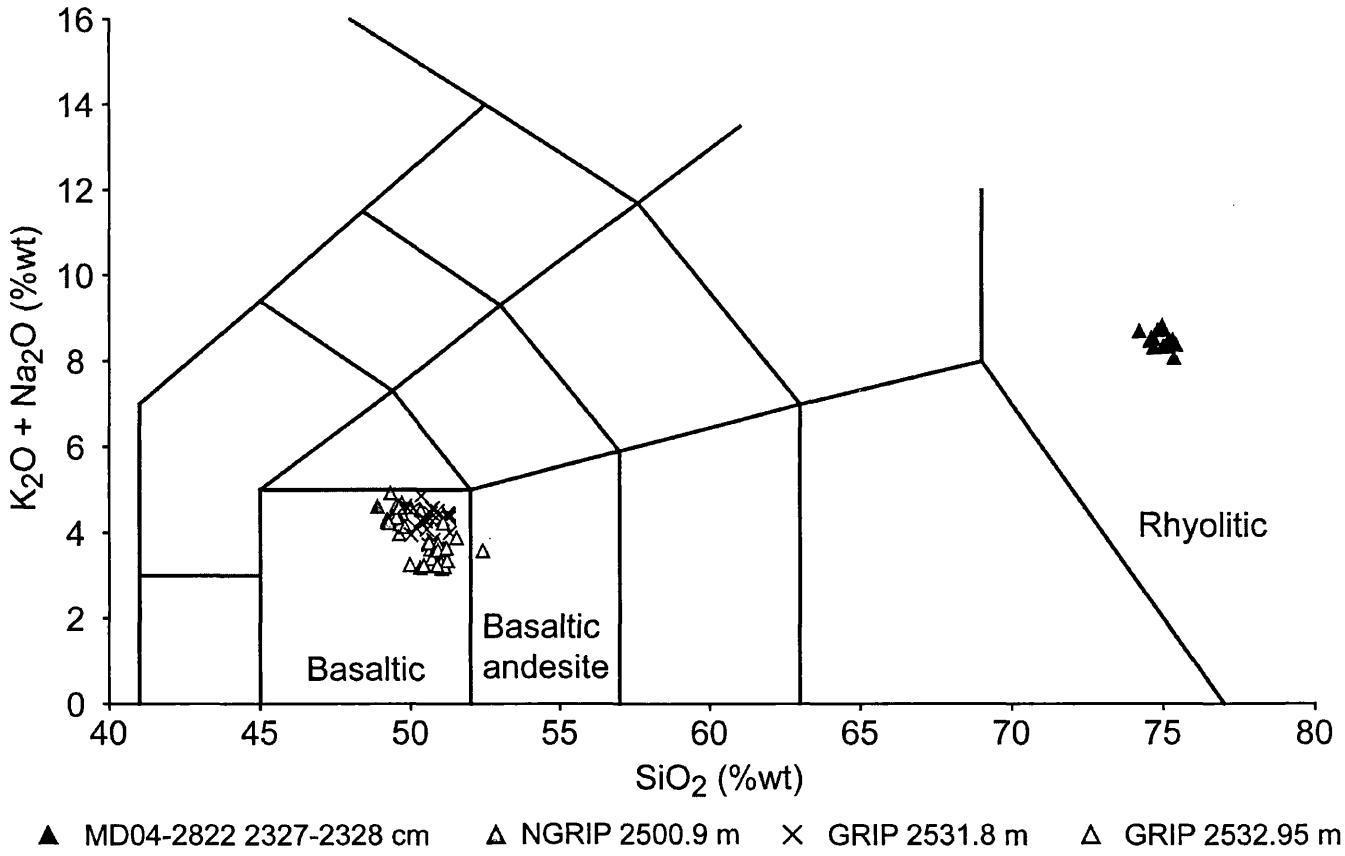


**Figure 8.7:** Total alkali versus silica plot comparing the geochemical composition of the MD04-2822 2327-2328 cm, NGRIP 2500.9 m, GRIP 2531.8 m and GRIP 2532.95 m tephra horizons that were all deposited during period 2 (see text). Chemical classification and nomenclature after Le Maitre et al. (1989).

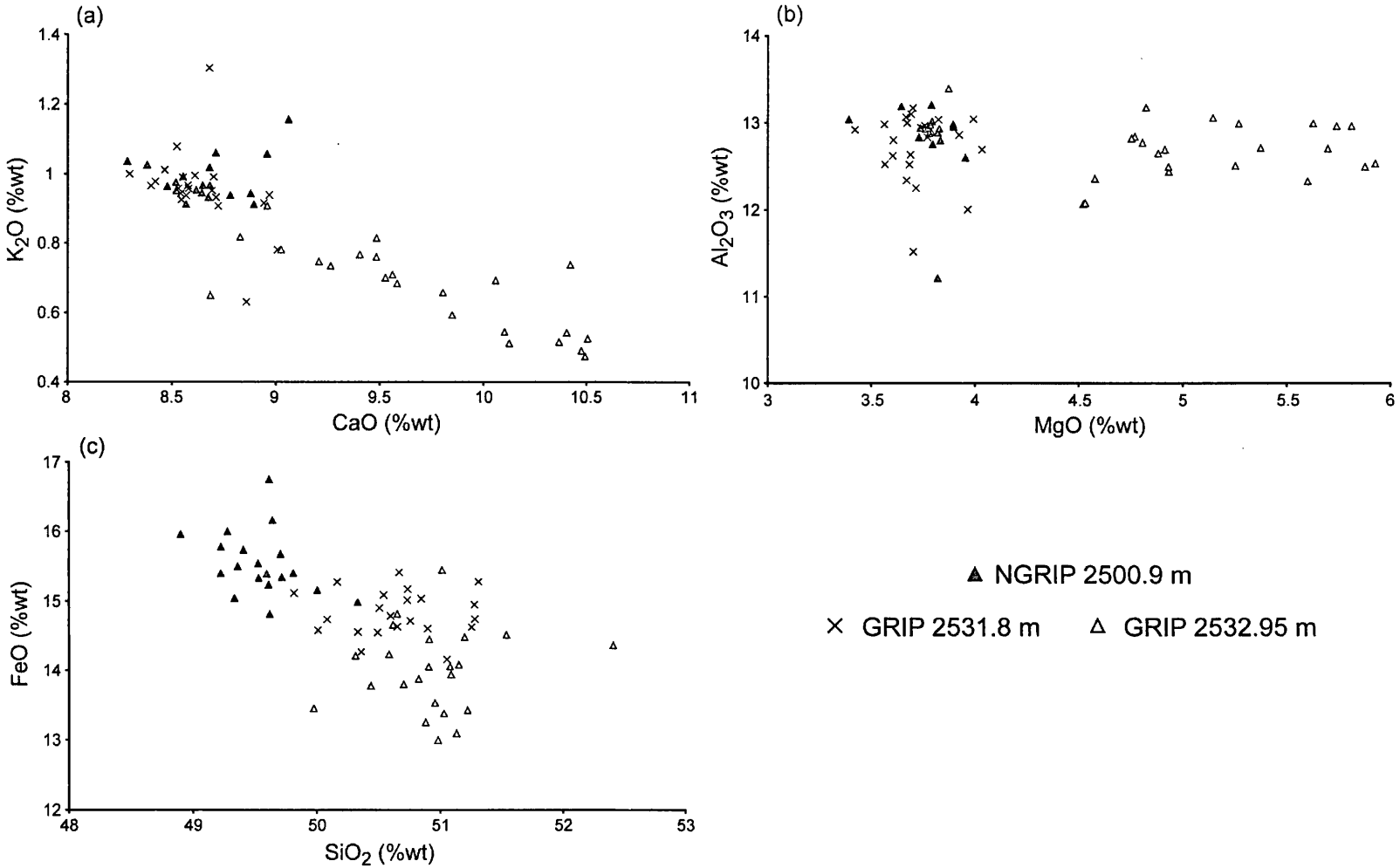


**Figure 8.8:** (a) CaO vs. $K_2O$ (b) MgO vs. $Al_2O_3$ and (c) $SiO_2$ vs. FeO compositional variation diagrams comparing the major element geochemistry of the NGRIP 2500.9 m, GRIP 2531.8 m and GRIP 2532.95 m tephra horizons.

### 8.1.3.1 Transitional Alkali Horizons: NGRIP 2500.9 m and GRIP 2531.8 m

NGRIP 2500.9 m and GRIP 2531.8 m, both display affinities to the Icelandic transitional alkali rock suite. These similarities are illustrated in the distinct overlaps in the compositional fields on the biplots in figures 8.8a and 8.8b, and the high similarity coefficient of 0.978 and relatively low $D^2$ value of 6.5 for the statistical comparisons between the horizons. However some geochemical differences can be observed, most notably in the $SiO_2$ values and slight differences are evident in FeO concentrations (figure 8.8c).

The major element compositions of these two horizons were measured during different EPMA analytical periods. The secondary standard analyses of BCR2g conducted during these periods provide a potential explanation for the offsets, if it is assumed that the horizons are the products of the same eruption. In general analyses of the BCR2g standard displayed lower $SiO_2$ and higher FeO concentrations when NGRIP 2500.9 m was analysed compared to when the analysis of GRIP 2531.8 m was conducted. These relative differences are consistent with the offsets between the $SiO_2$ and FeO concentrations of NGRIP 2500.9 m and GRIP 2531.8 m shards shown on figure 8.8c. No significant offsets in the concentrations of other major oxides measured during the different analytical periods were observed.

Therefore, the major element characterisations of NGRIP 2500.9 m and GRIP 2531.8 m indicate that these horizons can be correlated, with the slight compositional offsets being attributed to minor differences in EPMA operating conditions during the analytical periods.

The trace element characterisations of these two horizons were described in sections 5.4.4 and 6.4.4, and figure 8.9a compares the average REE profiles for the two horizons. From this figure it can be observed that the horizons share similar gently sloping REE profiles for the LREEs between La and Sm but steepen for the MREEs and HREEs. Small positive Eu anomalies can be observed in both of the profiles. Despite the similarities in the profiles a distinct difference in the absolute REE concentrations can be observed, with the average concentration of elements within the GRIP 2531.8 m horizon being approximately double those from NGRIP 2500.9 m.

These differences are also observed on the trace element concentrations plots using individual shard analyses (figure 8.9b). Slight overlaps in the geochemical fields for the

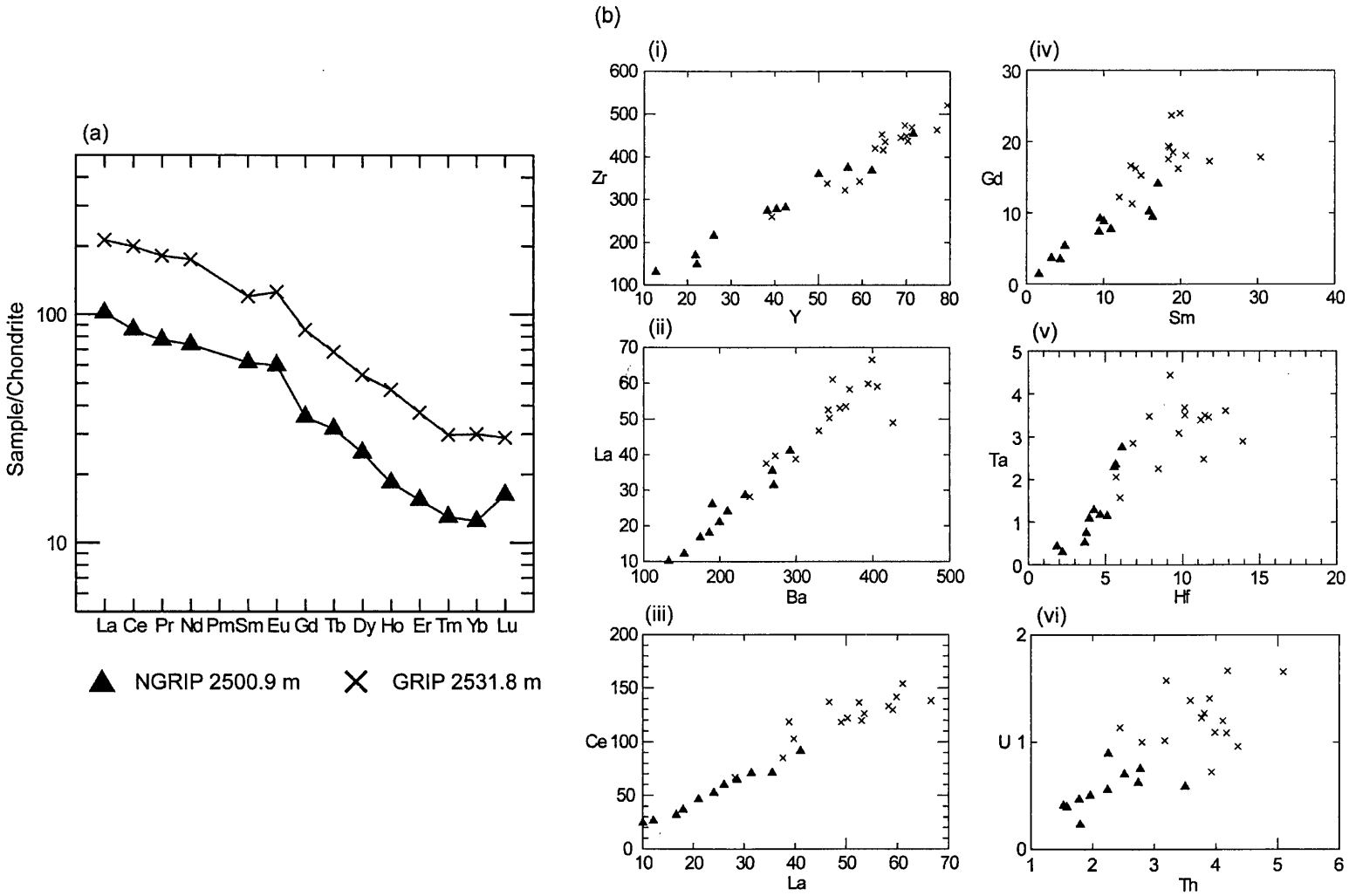


**Figure 8.9:** (a) Average chondrite-normalised REE profiles for the NGRIP 2500.9 m and GRIP 2531.8 m tephra horizons. (b) (i) Y vs. Zr (ii) Ba vs. La (iii) La vs. Ce (iv) Sm vs. Gd (v) Hf vs. Ta and (vi) Th vs. U compositional variation diagrams of individual shards from the NGRIP 2500.9 m and GRIP 2531.8 m tephra horizons.

two horizons can be identified, however higher concentrations are consistently observed within GRIP 2531.8 m shards. These differences are statistically significant as the $D^2$ value for the comparison of 14 element concentrations is 30.72, which exceeds the critical value of 29.14 at the 99% confidence level. Linear covariance along the same ratio trend lines can be observed between all of the trace elements pairs, but it is most distinct on figure 8.9b (i-iii). As these are more abundant elements they are consequentially less affected by the reduction in analytical precision caused by lower count rates for less abundant elements (Pearce et al., 2007).

To remove the potential influence of misestimation of background levels of elements in the LA-ICP-MS system trace element ratios were compared as they are unaffected by any offset. The biplots in figure 8.10 demonstrate that, with the exception of one outlying shard from NGRIP 2500.9 m, the trace element ratios are consistent between the two data-sets. This suggests that either one or both of the characterisations were affected by unexpected gas blank variability.

Therefore, based on the stratigraphic evidence and both the major and trace element characterisations NGRIP 2500.9 m and GRIP 2531.8 m are regarded as the products of the same volcanic eruption and thus, represent a time-synchronous tie-line between the two cores.

### 8.1.4 Period 3

Three tephra horizons, the basaltic NGRIP 2548.35 m, the basaltic/basaltic andesitic GRIP 2564.3 m and the rhyolitic MD04-2822 2359-2366 m, were deposited during a period encompassing the end of the DO 20 interstadial event and the rapid climate cooling following this event. The distinct geochemical differences between the ice and marine horizons prevents a correlation between the records (figure 8.11).

The ice-core horizons have affinities to different Icelandic rock suites, which strongly suggests that these horizons do not represent the products of the same volcanic eruption. This is supported by the biplots shown in figure 8.11 and 8.12, which illustrate large differences in the concentrations of $SiO_2$, $TiO_2$ and CaO. In addition, similarity coefficient and statistical distance comparisons emphasise the differences in composition between the horizons (tables 8.5 and 8.6). Low similarity coefficient values of 0.790 and 0.794 were calculated when the average composition of NGRIP

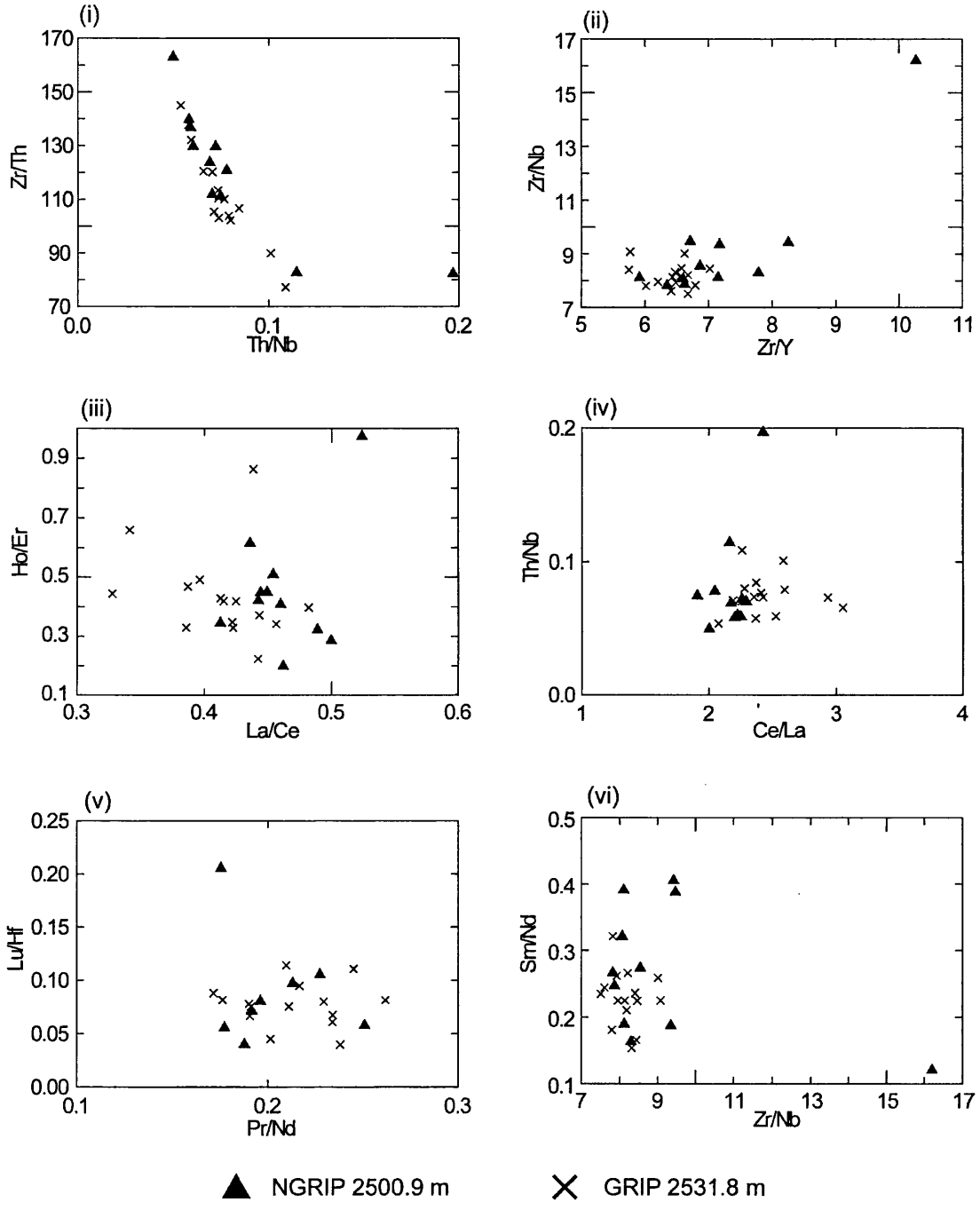


**Figure 8.10:** Trace element ratio-ratio diagrams for analyses of individual shards from the NGRIP 2500.9 m and GRIP 2531.8 m tephra horizons.

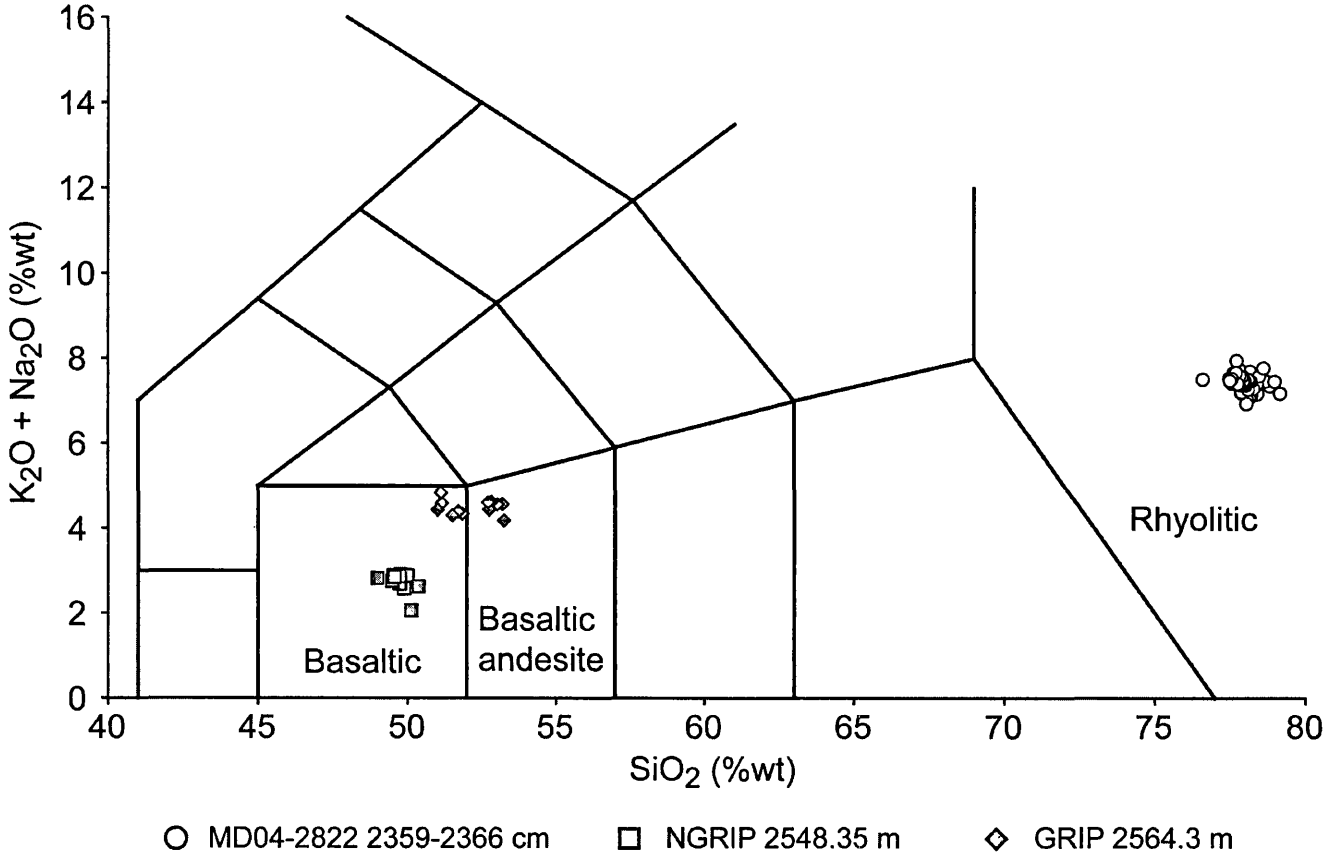


**Figure 8.11:** Total alkali versus silica plot comparing the geochemical composition of the MD04-2822 2359-2366 cm, NGRIP 2548.35 m and GRIP 2564.3 m tephra horizons that were all deposited during period 3 (see text). Chemical classification and nomenclature after Le Maitre et al. (1989).

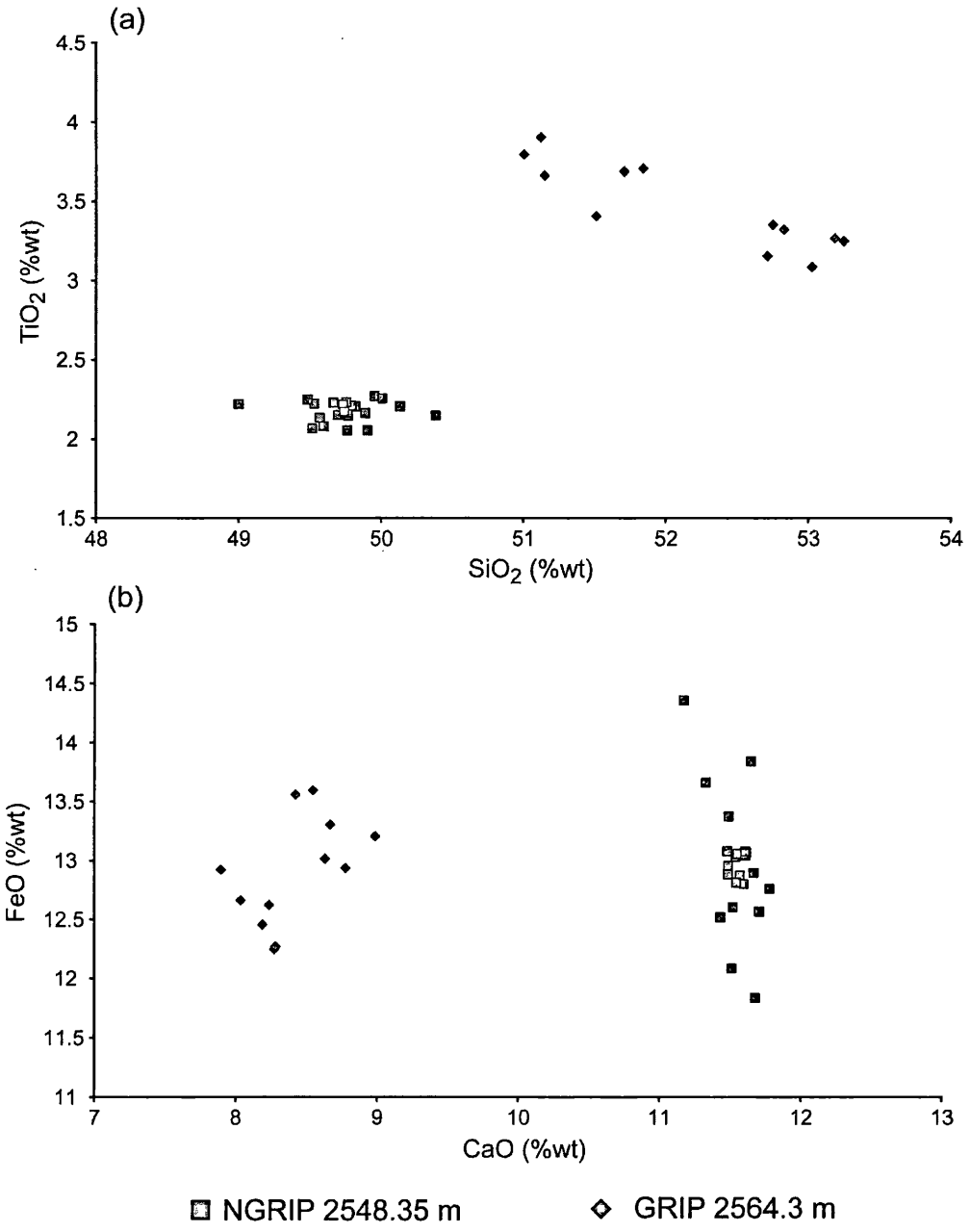


**Figure 8.12:** (a) $SiO_2$ vs. $K_2O$ and (b) CaO vs. FeO compositional variation diagrams comparing the major element geochemistry of the NGRIP 2548.35 m and 2564.3 m tephra horizons.

2548.35 m was compared to the two geochemical populations of GRIP 2564.3 m and the differences were found to be statistically significant with $D^2$ values of 540 and 314 (table 8.6). These observations demonstrate that the two tephra horizons are the products of different volcanic eruptions.

**Table 8.5:** Similarity coefficients values for comparisons between the average major element compositions of the tephra horizons deposited during period 3. Bold values exceed 0.90.

| | NGRIP 2548.35 m | GRIP 2564.3 m-1 | GRIP 2564.3 m-2 |
|---|---|---|---|
| NGRIP 2548.35 m | 1.000 | | |
| GRIP 2564.3 m-1 | 0.790 | 1.000 | |
| GRIP 2564.3 m-2 | 0.794 | **0.939** | 1.000 |

**Table 8.6:** $D^2$ values for statistical distance comparisons between the average major element compositions of the tephra horizons deposited during period 3. Critical $D^2$ value of 20.1 at the 99% confidence level as 8 oxide values were utilised.

| | NGRIP 2548.35 m | GRIP 2564.3 m-1 | GRIP 2564.3 m-2 |
|---|---|---|---|
| NGRIP 2548.35 m | 0.0 | | |
| GRIP 2564.3 m-1 | 540 | 0.0 | |
| GRIP 2564.3 m-2 | 314 | 35.2 | 0.0 |

### 8.1.5 Summary of the Tephrochronological Framework

14 separate horizons were identified within the three investigated sequences. However, evidence presented in chapter 6 and section 8.1.3.1 demonstrates that each horizon does not represent the products of single volcanic eruptions.

Two of these horizons represent products from the same eruption (NGRIP 2500.9 m and GRIP 2531.8 m). Another horizon, GRIP 2499.75 m, has a bimodal composition as a consequence of the deposition of material produced from two different volcanic systems as one component was attributed to the Jan Mayen volcanic system and one to the Grímsvötn volcanic system. Based on the age-depth model for the core and the length of sample containing the products of the two eruptions the maximum temporal separation between the events is 30 years. The bimodality observed within the GRIP 2564.3 m and MD04-2822 2327-2328 cm horizons can be attributed to bimodality of the material produced during a single eruption, because the separate components within these horizons have broad major element similarities and affinities to the same Icelandic rock suites.

Therefore, the framework that has been created provides evidence for 14 separate volcanic eruptions during the MIS 4 period. Of these horizons 11 have been linked to an Icelandic source. Relating the geochemistry of these horizons to characterisations of the three rock suites produced by Icelandic volcanic systems showed that 7 have a tholeiitic composition, 4 have a transitional alkaline composition and none of the horizons are related to the alkalic rock suite. 2 horizons have a Jan Mayen source and a horizon sourced from a more distal volcanic region, potentially from the Kutcharo volcanic system, Hokkaido, Japan has been identified. The relative stratigraphic positions of the horizons with reference to the NGRIP oxygen isotope stratigraphy are illustrated in figure 8.13 and table 8.7 provides the average major and trace element geochemical characterisations of the horizons.

The potential for the identification of horizons within ice-cores to provide independent ages to the eruptions was emphasised in section 2.4.6, and ages gained from the GICC05 timescale for the 12 horizons within NGRIP and GRIP are provided in table 8.7.

(a)

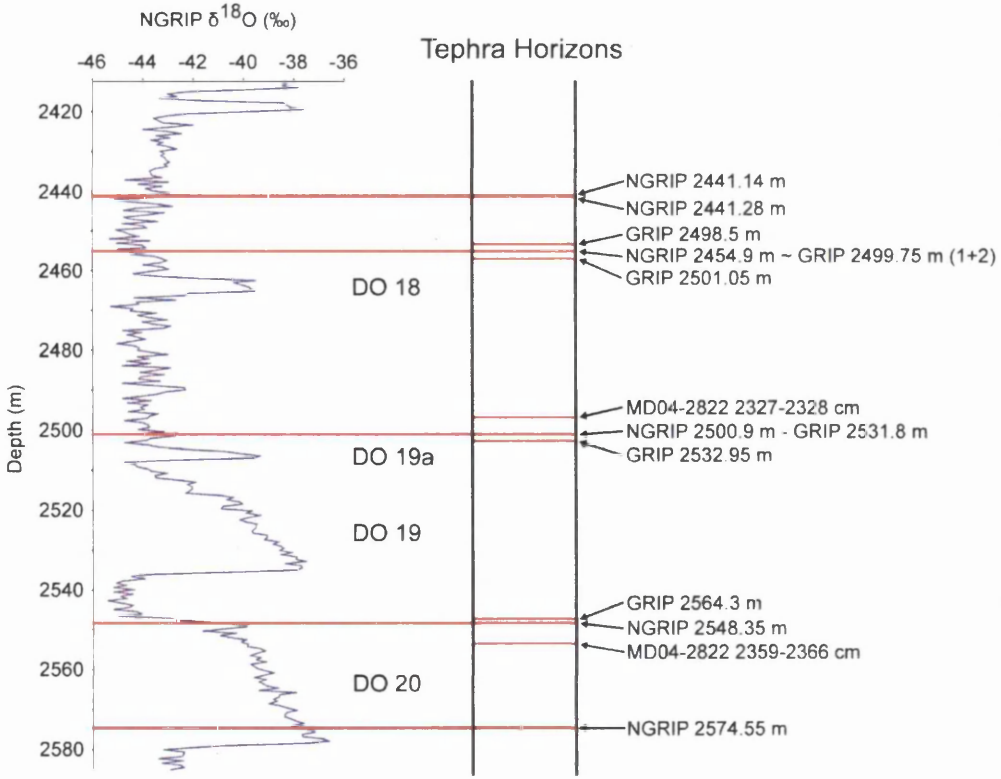


(b)

| Tephra Horizon | Approximate Age (yr b2k) | Potential Source |
|---|---|---|
| NGRIP 2441.14 m | 61410 | Icelandic Rift Zone |
| NGRIP 2441.28 m | 61425 | Hokkaido, Japan (?) |
| GRIP 2498.5 m | 62860 | Icelandic Rift Zone |
| NGRIP 2454.9 m | 63090 | Jan Mayen |
| GRIP 2499.75 m -1 | 63090 | Jan Mayen |
| GRIP 2499.75 m -2 | 63090 | Grímsvötn |
| GRIP 2501.05 m | 63315 | Icelandic Rift Zone |
| MD04-2822 2327-2328 cm -1 | ~68000 | Iceland (SFZ or EFZ) |
| MD04-2822 2327-2328 cm -2 | ~68000 | Iceland (SFZ or EFZ) |
| NGRIP 2500.9 m | 68900 | Iceland (SFZ or EFZ) |
| GRIP 2531.8 m | 68900 | Iceland (SFZ or EFZ) |
| GRIP 2532.95 m | 69095 | Grimsvötn-Kverfjöll |
| GRIP 2564.3 m -1 | 73955 | Hekla |
| GRIP 2564.3 m -2 | 73955 | Hekla |
| NGRIP 2548.35 m | 74200 | Reykjanes or Veidivötn-Bárdarbunga |
| MD04-2822 2359-2366 cm | ~74500 | Icelandic Rift Zone |
| NGRIP 2574.55 m | 76160 | Katla |

**Figure 8.13:** (a) Approximate stratigraphic position of the MIS 4 tephra horizons identified within this study with reference to the oxygen isotope ratio record from the NGRIP ice core. Horizons identified within the NGRIP record are traced across to the isotope record. Isotopic values are expressed in ‰ with respect to V-SMOW. (b) Approximate age and potential sources for the tephra horizons in the framework. The b2k timescale is referenced to 2000 AD and the uncertainly on the ice-core age estimates is ~1300 years. Ages for marine horizons are tentative and based on their stratigraphic position relative to the ice-core horizons.

**Table 8.7:** Summary of normalised major oxide and trace element data for glass shards from horizons within the MIS 4 tephrochronological framework. Mean and 1 standard deviations are shown. Total oxides are raw values prior to normalisation. All major elements expressed as percentage weight. All trace element concentrations expressed as ppm. Total iron is expressed as FeO. n = number of shards analysed. The complete dataset of unnormalised data is provided in the appendices. The b2k timescale is referenced to 2000 AD and the uncertainly on the ice-core age estimates is ~1300 years.

| Tephra Horizon | n | $SiO_2$ | $TiO_2$ | $Al_2O_3$ | FeO | MnO | MgO | CaO | $Na_2O$ | $K_2O$ | $P_2O_5$ | Cl | Total Oxides | Geochemistry |
|---|---|---|---|---|---|---|---|---|---|---|---|---|---|---|
| NGRIP 2441.14 m | 9 | 55.49 (0.26) | 1.29 (0.17) | 15.88 (0.62) | 10.31 (1.18) | 0.22 (0.05) | 4.18 (0.27) | 8.36 (0.70) | 3.06 (0.79) | 0.91 (0.20) | 0.21 (0.04) | 0.09 (0.02) | 98.43 (0.32) | Basaltic andesitic (tholeiitic) |
| NGRIP 2441.28 m | 16 | 77.07 (0.24) | 0.36 (0.04) | 12.41 (0.10) | 1.72 (0.13) | 0.09 (0.06) | 0.35 (0.03) | 1.78 (0.12) | 4.08 (0.11) | 2.13 (0.06) | 0.02 (0.02) | n/a | 98.99 (0.92) | Rhyolitic |
| GRIP 2498.5 m | 24 | 48.78 (0.70) | 2.78 (0.14) | 13.94 (0.39) | 11.66 (0.58) | 0.21 (0.06) | 6.94 (0.42) | 12.25 (0.46) | 2.49 (0.18) | 0.44 (0.09) | 0.47 (0.27) | 0.03 (0.01) | 96.12 (0.63) | Basaltic (tholeiitic) |
| NGRIP 2454.9 m | 26 | 48.03 (0.37) | 2.91 (0.13) | 13.78 (0.61) | 9.80 (0.54) | 0.17 (0.06) | 7.10 (0.67) | 13.40 (0.74) | 2.37 (0.32) | 1.93 (0.15) | 0.50 (0.03) | n/a | 98.46 (0.42) | Basaltic-Trachybasaltic |
| GRIP 2499.75 m -1 | 20 | 48.62 (0.75) | 2.79 (0.18) | 13.97 (0.73) | 9.62 (0.73) | 0.20 (0.07) | 6.70 (0.92) | 13.05 (1.07) | 2.43 (0.35) | 2.00 (0.21) | 0.53 (0.02) | 0.08 (0.03) | 97.64 (0.68) | Basaltic-Trachybasaltic |
| GRIP 2499.75 m -2 | 9 | 50.28 (0.28) | 2.89 (0.15) | 12.93 (0.20) | 13.53 (0.41) | 0.25 (0.03) | 5.91 (0.27) | 10.93 (0.32) | 2.51 (0.43) | 0.37 (0.05) | 0.37 (0.02) | 0.03 (0.01) | 97.43 (0.71) | Basaltic (tholeiitic) |
| GRIP 2501.05 m | 23 | 47.54 (0.39) | 3.01 (0.13) | 14.55 (0.41) | 11.93 (0.84) | 0.18 (0.05) | 6.94 (0.51) | 12.57 (0.48) | 2.50 (0.19) | 0.37 (0.06) | 0.37 (0.02) | 0.04 (0.02) | 97.25 (0.84) | Basaltic (tholeiitic) |
| MD04-2822 2327-2328 cm -1 | 10 | 74.96 (0.34) | 0.24 (0.09) | 12.49 (0.26) | 2.78 (0.16) | 0.15 (0.10) | 0.04 (0.01) | 0.59 (0.02) | 4.88 (0.11) | 3.71 (0.09) | 0.00 (0.02) | 0.15 (0.01) | 93.60 (1.03) | Rhyolitic (transitional alkali) |
| MD04-2822 2327-2328 cm -2 | 7 | 74.83 (0.30) | 0.12 (0.13) | 13.20 (0.15) | 2.21 (0.12) | 0.07 (0.07) | 0.12 (0.02) | 0.80 (0.04) | 4.42 (0.17) | 3.95 (0.11) | 0.02 (0.03) | 0.22 (0.03) | 93.54 (0.96) | Rhyolitic (transitional alkali) |
| NGRIP 2500.9 m | 19 | 49.55 (0.31) | 3.22 (0.12) | 12.84 (0.42) | 15.54 (0.46) | 0.34 (0.08) | 3.78 (0.12) | 8.66 (0.19) | 3.44 (0.24) | 0.98 (0.06) | 1.65 (0.08) | n/a | 98.10 (0.66) | Basaltic (transitional alkali) |
| GRIP 2531.8 m | 22 | 50.65 (0.42) | 3.11 (0.18) | 12.72 (0.40) | 14.83 (0.33) | 0.33 (0.06) | 3.73 (0.15) | 8.63 (0.19) | 3.35 (0.33) | 0.96 (0.12) | 1.62 (0.14) | 0.07 (0.01) | 96.81 (0.80) | Basaltic (transitional alkali) |
| GRIP 2532.95 m | 23 | 50.94 (0.47) | 3.22 (0.27) | 12.70 (0.33) | 13.99 (0.60) | 0.24 (0.05) | 5.11 (0.53) | 9.72 (0.58) | 2.83 (0.19) | 0.67 (0.12) | 0.45 (0.07) | 0.04 (0.01) | 96.73 (0.93) | Basaltic (tholeiitic) |
| GRIP 2564.3 m -1 | 6 | 52.96 (0.23) | 3.24 (0.10) | 12.88 (0.23) | 12.53 (0.26) | 0.29 (0.04) | 3.75 (0.08) | 8.15 (0.16) | 3.38 (0.16) | 1.12 (0.02) | 1.64 (0.15) | 0.06 (0.01) | 96.15 (0.57) | Basaltic andesitic (transitional alkali) |
| GRIP 2564.3 m -2 | 6 | 51.39 (0.35) | 3.69 (0.17) | 12.59 (0.27) | 13.27 (0.27) | 0.28 (0.02) | 4.22 (0.16) | 8.67 (0.19) | 3.47 (0.23) | 1.01 (0.05) | 1.34 (0.06) | 0.06 (0.01) | 95.81 (0.63) | Basaltic (transitional alkali) |
| NGRIP 2548.35 m | 22 | 49.75 (0.27) | 2.18 (0.07) | 13.57 (0.13) | 12.96 (0.54) | 0.21 (0.08) | 6.78 (0.31) | 11.55 (0.13) | 2.50 (0.18) | 0.27 (0.02) | 0.24 (0.02) | n/a | 98.00 (0.97) | Basaltic (tholeiitic) |
| MD04-2822 2359-2366 cm | 83 | 78.06 (0.33) | 0.09 (0.07) | 11.99 (0.13) | 1.37 (0.24) | 0.04 (0.09) | 0.00 (0.01) | 0.92 (0.11) | 4.23 (0.12) | 3.20 (0.10) | -0.01 (0.02) | 0.06 (0.01) | 94.28 (0.61) | Rhyolitic (tholeiitic) |
| NGRIP 2574.55 m | 10 | 47.77 (0.35) | 4.89 (0.25) | 12.55 (0.11) | 14.82 (0.40) | 0.26 (0.04) | 4.99 (0.08) | 9.84 (0.10) | 3.17 (0.12) | 0.78 (0.02) | 0.86 (0.31) | 0.06 (0.02) | 97.03 (0.61) | Basaltic (transitional alkali) |

**Table 8.7:** continued.

| Tephra Horizon | n | Sc | Rb | Sr | Y | Zr | Nb | Ba | La | Ce | Pr | Nd | Sm |
|---|---|---|---|---|---|---|---|---|---|---|---|---|---|
| NGRIP 2441.14 m | 6 | 12.0 (10.9) | 28.4 (4.35) | 201 (74.0) | 13.0 (4.66) | 93.7 (6.74) | 2.35 (1.03) | 455 (84.5) | 5.48 (0.99) | 10.1 (1.72) | 1.48 (0.35) | 7.35 (3.16) | 2.02 (0.63) |
| NGRIP 2441.28 m | 8 | 6.66 (9.25) | 36.5 (6.55) | 82.1 (16.6) | 11.0 (5.98) | 145 (27.3) | 0.99 (1.06) | 788 (51.6) | 7.35 (1.65) | 13.5 (4.30) | 1.68 (0.62) | 7.86 (2.25) | 1.71 (0.90) |
| GRIP 2498.5 m | 16 | 16.7 (5.81) | 8.32 (4.72) | 235 (96.1) | 18.7 (5.63) | 98.3 (28.7) | 11.0 (4.54) | 114 (28.0) | 12.3 (3.22) | 26.7 (7.75) | 3.29 (1.14) | 14.4 (4.14) | 4.00 (2.11) |
| NGRIP 2454.9 m | 8 | 23.0 (6.92) | 30.0 (5.28) | 222 (58.2) | 10.2 (2.57) | 108 (13.8) | 23.6 (7.86) | 504 (15.3) | 15.5 (4.08) | 29.4 (8.01) | 3.66 (1.07) | 13.9 (3.75) | 2.46 (0.60) |
| GRIP 2499.75 m -1 | 10 | 2.47 (5.18) | 16.5 (7.04) | 194 (93.6) | 11.9 (3.13) | 81.8 (26.2) | 15.2 (9.59) | 257 (116) | 16.3 (6.59) | 31.0 (13.3) | 3.29 (1.46) | 12.3 (6.23) | 3.01 (1.39) |
| GRIP 2499.75 m -2 | | n/a | n/a | n/a | n/a | n/a | n/a | n/a | n/a | n/a | n/a | n/a | n/a |
| GRIP 2501.05 m | 14 | 21.9 (11.2) | 8.48 (3.53) | 352 (139) | 21.7 (7.38) | 110 (34.9) | 15.8 (6.92) | 118 (35.3) | 13.6 (3.31) | 31.1 (7.99) | 4.28 (1.17) | 20.8 (7.26) | 4.44 (2.09) |
| MD04-2822 2327-2328 cm -1 | 3 | 15.9 (8.21) | 155 (22.0) | 57.3 (4.09) | 157 (13.0) | 1073 (114) | 212 (23.5) | 1051 (108) | 170 (18.0) | 321 (30.1) | 39.3 (3.13) | 161 (17.4) | 31.2 (4.87) |
| MD04-2822 2327-2328 cm -2 | 2 | 16.8 (9.46) | 161 (8.32) | 69.8 (11.0) | 122 (9.03) | 553 (30.0) | 94.2 (2.55) | 1487 (89.4) | 111 (7.20) | 219 (10.7) | 25.2 (2.00) | 104 (12.0) | 24.9 (0.32) |
| NGRIP 2500.9 m | 10 | 10.7 (8.90) | 29.3 (4.25) | 386 (199) | 40.4 (21.4) | 278 (121) | 32.5 (17.2) | 210 (55.0) | 24.1 (11.4) | 52.4 (24.9) | 7.33 (3.71) | 34.4 (18.6) | 9.41 (5.89) |
| GRIP 2531.8 m | 14 | 18.5 (9.80) | 25.1 (5.88) | 663 (113) | 64.7 (10.4) | 416 (72.2) | 51.2 (10.2) | 344 (57.2) | 50.3 (10.9) | 122 (23.3) | 17.2 (3.90) | 81.8 (19.7) | 18.4 (4.79) |
| GRIP 2532.95 m | 14 | 18.9 (16.6) | 21.7 (6.10) | 301 (107) | 40.1 (15.8) | 217 (86.1) | 22.8 (10.9) | 194 (53.0) | 21.1 (8.47) | 50.0 (21.6) | 6.46 (1.99) | 32.1 (12.4) | 8.72 (4.93) |
| GRIP 2564.3 m -1 | | n/a | n/a | n/a | n/a | n/a | n/a | n/a | n/a | n/a | n/a | n/a | n/a |
| GRIP 2564.3 m -2 | | n/a | n/a | n/a | n/a | n/a | n/a | n/a | n/a | n/a | n/a | n/a | n/a |
| NGRIP 2548.35 m | 7 | 18.3 (8.14) | 15.4 (4.17) | 75.9 (20.9) | 9.99 (5.07) | 98.7 (9.01) | 2.26 (1.62) | 175 (44.8) | 3.63 (0.92) | 7.47 (1.46) | 1.02 (0.35) | 4.09 (2.56) | 1.25 (0.93) |
| MD04-2822 2359-2366 cm | 35 | 122 (43.5) | 114 (11.9) | 152 (17.8) | 294 (32.1) | 95.4 (11.4) | 2.24 (2.37) | 1035 (280) | 74.3 (8.35) | 155 (17.2) | 19.0 (2.26) | 82.7 (10.1) | 20.0 (3.43) |
| NGRIP 2574.55 m | 6 | 9.75 (5.85) | 6.95 (1.84) | 198 (51.4) | 17.7 (4.26) | 94.0 (21.8) | 13.8 (4.47) | 89.6 (15.2) | 10.8 (3.12) | 22.3 (6.10) | 2.75 (0.86) | 13.6 (4.02) | 2.70 (1.14) |

**Table 8.7:** continued.

| Eu | Gd | Tb | Dy | Ho | Er | Tm | Yb | Lu | Hf | Ta | Th | U | Tephra Horizon |
|---|---|---|---|---|---|---|---|---|---|---|---|---|---|
| 1.45 | 1.11 | 0.13 | 2.06 | 0.37 | 0.99 | 0.19 | 0.88 | 0.24 | 2.01 | 0.20 | 1.52 | 0.66 | NGRIP 2441.14 m |
| (0.40) | (0.83) | (0.15) | (1.27) | (0.09) | (0.39) | (0.03) | (0.57) | (0.10) | (0.54) | (0.06) | (0.27) | (0.38) | |
| 1.17 | 1.77 | 0.14 | 1.03 | 0.43 | 1.22 | 0.19 | 1.20 | 0.22 | 3.63 | 0.36 | 2.52 | 0.74 | NGRIP 2441.28 m |
| (0.69) | (1.50) | (0.11) | (0.76) | (0.24) | (0.85) | (0.11) | (0.78) | (0.12) | (0.86) | (0.11) | (0.38) | (0.22) | |
| 1.02 | 3.55 | 0.58 | 3.48 | 0.66 | 1.62 | 0.22 | 1.60 | 0.23 | 2.96 | 0.72 | 1.64 | 0.74 | GRIP 2498.5 m |
| (0.74) | (1.60) | (0.21) | (1.27) | (0.21) | (0.58) | (0.11) | (0.58) | (0.09) | (1.21) | (0.31) | (0.36) | (0.31) | |
| 0.84 | 2.14 | 0.37 | 1.78 | 0.32 | 0.89 | 0.20 | 0.93 | 0.12 | 2.38 | 1.27 | 2.35 | 0.62 | NGRIP 2454.9 m |
| (0.39) | (0.77) | (0.15) | (0.41) | (0.11) | (0.29) | (0.09) | (0.33) | (0.07) | (0.60) | (0.43) | (0.39) | (0.15) | |
| 0.65 | 2.38 | 0.29 | 2.08 | 0.38 | 1.04 | 0.14 | 1.13 | 0.16 | 2.39 | 1.00 | 2.31 | 0.95 | GRIP 2499.75 m -1 |
| (0.43) | (1.24) | (0.17) | (0.81) | (0.12) | (0.41) | (0.05) | (0.57) | (0.09) | (0.84) | (0.70) | (0.73) | (0.24) | |
| n/a | n/a | n/a | n/a | n/a | n/a | n/a | n/a | n/a | n/a | n/a | n/a | n/a | GRIP 2499.75 m -2 |
| 1.82 | 4.87 | 0.68 | 4.58 | 0.80 | 2.33 | 0.34 | 1.74 | 0.28 | 3.04 | 0.93 | 1.26 | 0.43 | GRIP 2501.05 m |
| (0.72) | (1.80) | (0.28) | (1.44) | (0.37) | (0.72) | (0.15) | (0.88) | (0.13) | (1.13) | (0.42) | (0.20) | (0.14) | |
| 4.67 | 27.0 | 4.31 | 26.6 | 6.09 | 16.4 | 2.30 | 16.0 | 2.19 | 30.5 | 13.8 | 21.4 | 6.14 | MD04-2822 2327-2328 cm -1 |
| (1.41) | (3.32) | (0.80) | (4.01) | (0.19) | (3.13) | (0.29) | (2.56) | (0.37) | (4.94) | (1.58) | (2.42) | (1.79) | |
| 4.89 | 19.6 | 3.06 | 21.4 | 4.01 | 12.7 | 1.67 | 13.1 | 1.66 | 16.4 | 6.54 | 17.5 | 4.15 | MD04-2822 2327-2328 cm -2 |
| (0.62) | (2.59) | (0.12) | (3.81) | (0.10) | (1.44) | (0.01) | (1.46) | (0.12) | (0.73) | (0.21) | (1.14) | (0.42) | |
| 3.46 | 7.34 | 1.18 | 6.32 | 1.04 | 2.55 | 0.33 | 2.11 | 0.41 | 4.25 | 1.28 | 2.24 | 0.55 | NGRIP 2500.9 m |
| (1.77) | (4.21) | (0.66) | (3.34) | (0.59) | (1.53) | (0.15) | (1.11) | (0.24) | (1.57) | (0.89) | (0.63) | (0.19) | |
| 7.29 | 17.6 | 2.56 | 13.8 | 2.65 | 6.17 | 0.76 | 5.10 | 0.74 | 9.76 | 3.09 | 3.77 | 1.23 | GRIP 2531.8 m |
| (2.13) | (3.55) | (0.47) | (3.48) | (0.92) | (1.30) | (0.25) | (1.44) | (0.24) | (2.54) | (0.77) | (0.68) | (0.28) | |
| 3.57 | 8.80 | 1.43 | 8.78 | 1.44 | 4.15 | 0.71 | 3.94 | 0.63 | 5.08 | 1.75 | 2.41 | 0.87 | GRIP 2532.95 m |
| (1.72) | (4.46) | (0.67) | (4.05) | (0.51) | (2.17) | (0.38) | (1.45) | (0.36) | (1.94) | (0.69) | (0.58) | (0.31) | |
| n/a | n/a | n/a | n/a | n/a | n/a | n/a | n/a | n/a | n/a | n/a | n/a | n/a | GRIP 2564.3 m -1 |
| n/a | n/a | n/a | n/a | n/a | n/a | n/a | n/a | n/a | n/a | n/a | n/a | n/a | GRIP 2564.3 m -2 |
| 0.88 | 0.96 | 0.26 | 1.57 | 0.24 | 0.65 | 0.07 | 0.79 | 0.12 | 1.98 | 0.22 | 1.01 | 0.39 | NGRIP 2548.35 m |
| (0.71) | (0.81) | (0.13) | (0.95) | (0.13) | (0.38) | (0.04) | (0.43) | (0.05) | (0.47) | (0.23) | (0.26) | (0.05) | |
| 4.68 | 22.6 | 3.65 | 25.2 | 5.30 | 15.0 | 2.18 | 15.6 | 2.21 | 12.1 | 6.68 | 16.8 | 4.31 | MD04-2822 2359-2366 cm |
| (0.83) | (2.68) | (0.56) | (3.99) | (0.86) | (2.21) | (0.39) | (2.01) | (0.34) | (1.94) | (0.91) | (3.17) | (0.83) | |
| 0.93 | 3.21 | 0.37 | 2.70 | 0.56 | 1.40 | 0.18 | 1.21 | 0.18 | 1.89 | 0.80 | 1.14 | 0.50 | NGRIP 2574.55 m |
| (0.75) | (1.94) | (0.10) | (1.47) | (0.17) | (0.51) | (0.08) | (0.62) | (0.06) | (0.57) | (0.24) | (0.21) | (0.07) | |

## 8.2 Significance of the Tephrochronological Framework

The identification of 14 tephra horizons deposited during the MIS 4 climatic period makes a significant contribution to the overall tephrochronological framework for the last 130,000 years within the North Atlantic region (figure 8.14). Up until now, no other tephra horizons of MIS 4 age had been recognised in Greenland ice-core or North Atlantic marine sequences and this study demonstrates the high degree of volcanic activity in relation to other climatic periods (figure 8.14). Not only does the creation of this framework significantly increase the number of horizons identified within the NGRIP ice-core record it also demonstrates that volcanic sources other than Iceland have contributed to the tephrochronology of the North Atlantic region during the last glacial period. Furthermore, a comprehensive geochemical dataset of the major and trace element composition of these horizons is of great importance for tracing these tephras into other sequences. As well as the geochemical information, independent ages are presented for the horizons identified in the ice-core records, which will be of great value for the construction of age-depth models in marine and terrestrial sequences when these tephras can be traced.

Although attempts to trace coeval horizons within the NGRIP and GRIP ice-cores to the MD04-2822 marine core were unsuccessful, the creation of this framework is an important first step towards establishing ice-marine tie-lines for the MIS 4 climatic period. The identification of a significant number of volcanic horizons highlights the potential for the synchronisation of MIS 4 climatic records for the investigation of the relative timing of environmental responses to the DO events. In particular, a number of key horizons in this framework fall on or close to rapid climate transitions and as such have a high potential to assess the relative timing of these short events. For instance, NGRIP 2574.55 m falls shortly after the start of DO 20, both NGRIP 2548.35 m and GRIP 2564.3 m horizons fall on the cooling transition at the end of DO 20 and the NGRIP 2500.9 m – GRIP 2531.8 m horizon falls shortly after the end of DO 19 (figure 8.13).

The scope for identifying MIS 4 horizons within marine cores from the North Atlantic region is considerable due to the large amount of records available and the geographical distribution of cores on different dispersal pathways from Iceland and Jan Mayen. It is likely that investigation of additional marine cores, utilising the methods employed within this project and incorporating suggested modifications, will

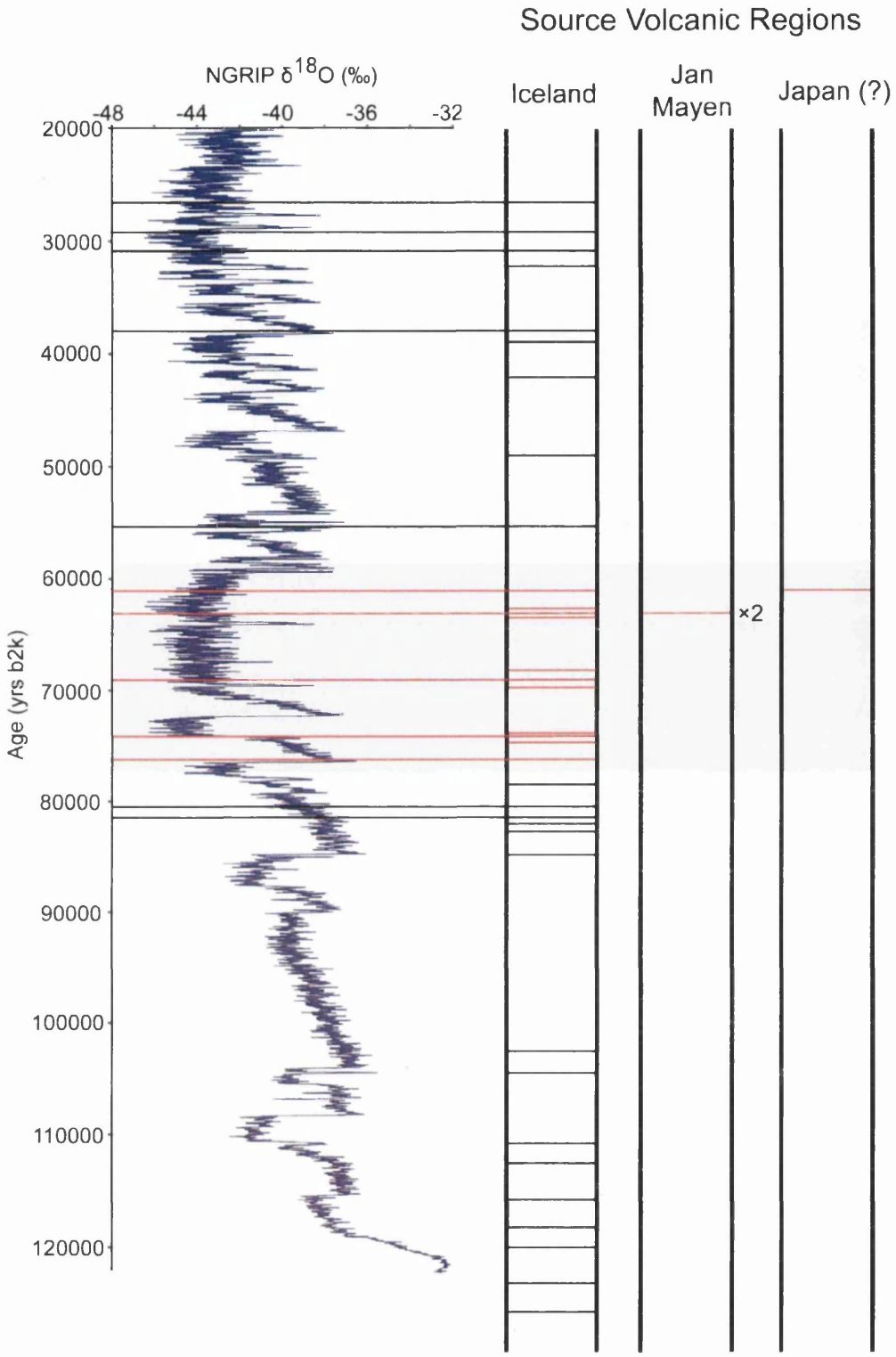


**Figure 8.14:** Revised tephrochronological framework for the MIS 2-5e periods of the Greenland ice-cores and North Atlantic marine cores, including the addition of new source regions, following the identification of 14 new volcanic horizons during this study. Red lines = tephra horizons added to the tephrochronological framework. Black lines = previously identified horizons (see figure 1.2). Grey shaded area represents the study period. Horizons traced across to the isotope record were identified in the NGRIP record. Isotopic values are expressed in ‰ with respect to V-SMOW.

lead to the definition of tie-lines between MIS 4 sequences and move towards the exploration of the relative timing of DO events 18, 19 and 20. Target areas for such studies include areas with high sedimentation rates, as this will increase the resolution of the tephrochronological record as well as the proxy climatic evidence.

### 8.2.1 Identification of Tephras from New Volcanic Regions

Previous studies have demonstrated that the North Atlantic tephrochronological framework for the last glacial is made up solely of material with an Icelandic origin. This study, however, has demonstrated that other volcanic regions have contributed widespread tephra horizons. The NGRIP 2454.9 m and GRIP 2499.75 m-1 horizons have been attributed to a Jan Mayen source and the NGRIP 2441.28 m horizon is tentatively ascribed a Japanese source (figure 8.14).

The Jan Mayen horizons have a distinctive $K_2O$-rich geochemistry and as such are valuable marker horizons that are easily distinguished from the products of Icelandic volcanic systems. Other studies have identified Jan Mayen tephras in distal settings (Lacasse and Garbe-Schönberg, 2001; Hunt, 2004). For instance, eight silicic (trachyte and rhyolite) horizons of Jan Mayen origin within North Atlantic ODP core 907 from the Iceland Plateau spanning the period from 0.6-6 Ma. In addition, five trachyte horizons with a Jan Mayen source have been identified within Holocene terrestrial sequences from Ireland. Chambers et al. (2004) reported the discovery of four of these horizons within a Holocene lake sequence from An Loch Mór and Hall and Pilcher (2002) described the ca. 1600 PMG-5 horizon identified within a peat sequence from Portmagee. Up until now, however, no tephras of Jan Mayen origin have been identified in North Atlantic records spanning the last glacial period. In addition, none of the previously identified horizons from Jan Mayen have a basaltic-trachybasaltic composition like the NGRIP 2454.9 m and GRIP 2499.75 m-1 horizons. Thus, for the first time it is demonstrated that Jan Mayen was active during the last glacial period and that the products of basaltic-trachybasaltic eruptions had a widespread dispersal. This makes a significant contribution to our understanding of the volcanic history of Jan Mayen during this period.

A Japanese source has been proposed for NGRIP 2441.28 m based on the major element characterisation presented in section 5.4.2. The westerly jet stream, which transports East Asian dust to the Greenland Ice Sheet, provides a plausible

stratospheric pathway for the shards to be transported along from Japan prior to deposition. The potential for tephra shards to be transported along this pathway is higher during MIS 4 and the last glacial as evidence suggests that this period saw intensified circulation of air masses to Greenland, which, is likely to enhance tephra dispersal (Lacasse, 2001; Mayewski et al., 1994). This strongly supports the proposition that Japan is the source, however, the correlation remains tentative until a more precise correlation can be made to a proximal tephrostratigraphy.

If Japan is the source then this provides new possibilities for the correlation of records on a hemispheric scale. In particular, there would be the potential for correlating North Pacific marine sediments and high-resolution terrestrial sequences (e.g. Lake Suigetsu) that preserve evidence for rapid climatic changes within the last glacial period (e.g. Kotilainen and Shackleton, 1995; Hewitt et al., 1997; Kiefer et al., 2001; Nakagawa, 2008). This would represent the first direct tie-point between such archives and has significant implications for testing the impact of DO events between the North Atlantic and Pacific regions.

### 8.2.2 Understanding the Volcanic History of Iceland

This framework provides vital information on the volcanic history of Iceland during MIS 4, which up until now was a period frequently overlooked in tephra studies. As yet no other studies have provided evidence of Icelandic volcanism during this period. In the framework presented here, 11 horizons of Icelandic origin have been identified and 64 % of the horizons are attributed to the tholeiitic rock suite, 36 % to the transitional alkali rock suite and none to the alkali suite. The predominance of tholeiitic horizons is consistent with the abundances of igneous rocks produced in Iceland during the Late Pleistocene and Holocene period. Jakobsson et al. (2008) ascertained that during this period tholeiitic volcanic systems produced 80 % of the igneous rocks, transitional alkali systems 12 % and alkali systems 8 %. The identification of Icelandic tephras of basaltic composition in the ice-core records is likely to be a consequence of ice cover over the source volcanic systems. Basaltic eruptions are typically effusive with limited accompanied dispersal of tephra, however, ice cover and the interaction of water and magma can increase the explosivity of basaltic eruptions promoting widespread tephra fall (Oladottir et al., 2008).

Katla, Hekla, Grimsvötn-Kverfjöll and either the Reykjanes or Veidvötn-Bárdarbunga volcanic systems have been pinpointed as the sources for five of the horizons in this framework (table 8.7). An assessment of the overall framework for the last glacial period provides some indication of the relative activity of the Icelandic volcanic systems throughout this period. In particular, it has been demonstrated that the combined Grimsvötn-Kverfjöll volcanic system was highly active during the MIS 2-5e period as 12 volcanic horizons with affinities to the products of this system have been identified (see sections 6.4.2.2 and 6.4.5). In addition, the Katla volcanic system was relatively active with 6 horizons from this source within the overall framework (section 5.4.6). Geochemical similarities between NGRIP 2548.35 m and the 5a-Low/BAS-I tephra horizon identified by Wastegård and Rasmussen (2001) suggest that these two horizons had a source from either the Veidivötn-Bárdarbunga or Reykjanes volcanic systems. An unknown volcanic system within the SFZ or EFZ produced the MD04-2822 2327-2328 cm horizon as well as the 5d-Low/RHY and the 5e-Top/RHY horizons described by Wastegård and Rasmussen (2001).

For six of the horizons in this framework a source from either the Icelandic rift zone or an Icelandic flank zone is suggested based on rock suite affinities, however, it was not possible to pinpoint specific source volcanic systems. This implies that they were produced by volcanic systems with a low eruptive frequency or limited widespread dispersal of eruptive products during the Holocene. These volcanic systems will not be well represented within the geochemical datasets used for comparisons as they are biased towards more productive centres due to the amount of material available for characterisation (Hunt, 2004). In addition, these systems may have been active during MIS 4 but not during the Holocene period. Geochemical datasets are typically biased towards Holocene deposits as they rely on the characterisation of tephra material within terrestrial archives such as peat, soil and lacustrine sequences that would have been ice-covered during the glacial period (Larsen and Eiríksson, 2007). Another possible factor is that analyses of proximal deposits are from bulk rock samples which do not capture the geochemical heterogeneity of the material that can be determined through single-shard EPMA of distal deposits. The homogeneity of proximal analyses will restrict the extent of the geochemical fields for different volcanic systems on elemental biplots. Despite these limitations the inability to correlate some horizons to a source does not affect the usefulness of this framework for correlation purposes. Correlation between horizons relies predominantly on the robust geochemical characterisation of horizons as presented in the MIS 4 framework.

A noticeable feature of the Icelandic tephrochronological framework is that only basaltic horizons have been identified within the ice-core record whereas rhyolitic horizons are solely identified within MD04-2822. This could reflect different dispersal pathways or may be due to the methods employed to isolate tephra shards.

It is possible that material of differing composition is dispersed along different atmospheric pathways during MIS 4; with basaltic material preferentially transported to the NW of Iceland and rhyolitic material to the SE of Iceland. This could be related to interplay between the eruptive dynamics of rhyolitic and basaltic eruptions and atmospheric circulation. Plinian rhyolitic eruptions are more explosive and the material erupted is injected higher up into the atmosphere than material produced during the less explosive basaltic hydromagmatic eruptions (Larsen and Eiríksson, 2007). Observations of present-day atmospheric conditions over Iceland demonstrate that wind direction varies with altitude, with southerly winds dominating at low altitudes and westerly winds at higher altitudes (Lacasse, 2001). Interaction of these volcanic and atmospheric processes could result in the preferential transportation of the products of rhyolitic eruptions to sites east of Iceland, with basaltic material transported at a lower level in the atmosphere to sites north of Iceland. This provides a potential explanation for the differing dispersal of material if present-day atmospheric conditions provide an appropriate analogy for MIS 4 conditions. Further investigation is required to assess the geochemical composition of tephra horizons deposited within marine sediments on different dispersive pathways from Iceland during the MIS 4 period. Particularly as basaltic material deposited on a SE dispersal pathway during prior and subsequent time periods has been identified in past studies (e.g. Rasmussen et al., 2003; Wastegård et al., 2006). If it is demonstrated that differences occur in the dispersal of material with rhyolitic and basaltic compositions during MIS 4 the synchronisation of records lying on different dispersive pathways could be limited.

Another potential explanation is that the different methods used to extract material from ice-cores and marine cores may have a significant role in the composition of tephras identified, through bias towards the detection of basaltic and rhyolitic tephra shards respectively. Bias is highly unlikely to be a factor for the ice-core preparation methods as centrifuging is the only extraction method utilised as removal of any host sediment is not required. However, methodological issues may have resulted in the lack of identification of basaltic material within the marine core, which will be discussed in section 8.2.3.2.

Within section 8.1 three temporal periods were identified during which multiple volcanic horizons were produced by Icelandic volcanic systems. These three periods all fall on or shortly after cooling transitions at the ends of DO events 18, 19 and 20 (figure 8.13). This observation may be related to climatically-driven fluctuations in ice-sheet extent increasing volcanic activity due to changing crustal stresses; a theory introduced in section 2.4.3.

Records of ice rafted debris from North Atlantic marine sediments demonstrate that the Icelandic Ice Sheet underwent changes in its dynamics and extent during the last glacial period with iceberg discharge events occurring on millennial timescales (e.g. Elliot et al., 1998, 2001; Lackschewitz et al., 1998). These discharge events are believed to be related to the atmospheric DO events recorded in the ice-cores (Rasmussen et al., 1996). However, without precise synchronisation of the records it is not possible to determine the relative timing of these discharges and whether they occur during stadial or interstadial periods (McCabe and Clark, 1998). In addition, the destruction of ice-marginal features during the ice advance related to the Last Glacial Maximum, when the Icelandic Ice Sheet was at its maximum extent, prevents the reconstruction of ice volume changes. However, model simulations of ice sheet response to the temperature changes which occurred during the DO events suggests that the Icelandic Ice Sheet did undergo related volume changes, with the margin advancing during the cold stadials and retreating during the warm interstadials (Marshall and Koutnik, 2006). In addition, according to the model, peak levels of iceberg discharge, indicative of high ice-sheet flux, can be related to these ice advances and occurred ~300 years into the stadial periods (Marshall and Koutnik, 2006).

If these simulations are correct, then the temporal relationship between the occurrence of volcanic eruptions and the DO events observed within the ice-core records may be the result of ice advances, which are more pronounced at the start of stadial periods, causing increased isostatic crustal stresses below Iceland. Thus, it is recommended that other tephra studies focus on the cooling transition and stadial periods to test this observation. Not only does this framework pinpoint potential tie-points to other records it also has the potential to provide vital clues into the magmatic and volcanic processes in Iceland during this period of constant and rapid change.

### 8.2.3 How Complete is the Tephrochronological Framework?

Although this framework provides a significant contribution to our knowledge of volcanism during the last glacial period, an assessment of the methods employed for the detection of horizons within the NGRIP record suggests that some horizons may have been missed. In addition, the absence of basaltic material within MD04-2822 may be a result of the extraction techniques utilised.

#### 8.2.3.1 Using Sulphate as an Indicator of Cryptotephra Horizons in Ice-cores

The high-resolution record of sulphate in the NGRIP ice-core was used as the main criteria for the sampling of the core, with ice sections relating to distinct peaks in concentration being sampled. This strategy was employed due to the close relationship between sulphate levels in the atmosphere and volcanism (Zielinski et al., 1997; Bigler et al., 2007). Indeed, five out of the six horizons identified within the NGRIP record are directly associated with distinct peaks in the sulphate chemostratigraphy (figure 8.15). However, of these five horizons only the NGRIP 2454.9 m tephra horizon is associated with a sulphate peak that exceeds the set threshold (figure 8.15(iii)). This indicates that the magnitude of a sulphate peak is not related to the likelihood of associated tephra shards being present. Three of the horizons, NGRIP 2441.14 m, NGRIP 2441.28 m and NGRIP 2500.9 m were only identified because the ice-core bags containing these horizons were stratigraphically related to bags containing distinct sulphate peaks and were sampled to conform to the guidelines described in section 3.2.4.1. The bag containing NGRIP 2574.55 m was sampled during continuous sampling of the rapid warming transition into DO 20. Therefore, tephra horizons may have been missed due to the reliance on sampling distinct, high-magnitude peaks in sulphate.

Most notable however is NGRIP 2548.35 m, which shows no associated sulphate peak and lies stratigraphically below a distinct double peak in sulphate around 2548 m depth (figure 8.15(v)). The offset between the top depth of the horizon and the sulphate peak is ~15 cm, which equates to a minimum temporal separation of ~19 years. Offsets of this nature, with tephra shards being deposited prior to distinct chemical signals, have previously been suggested to result from highly explosive low latitude eruptions (Vinther et al., 2006). With differential transportation of the tephra shards and sulphate aerosols through the troposphere and stratosphere respectively resulting in a delay of

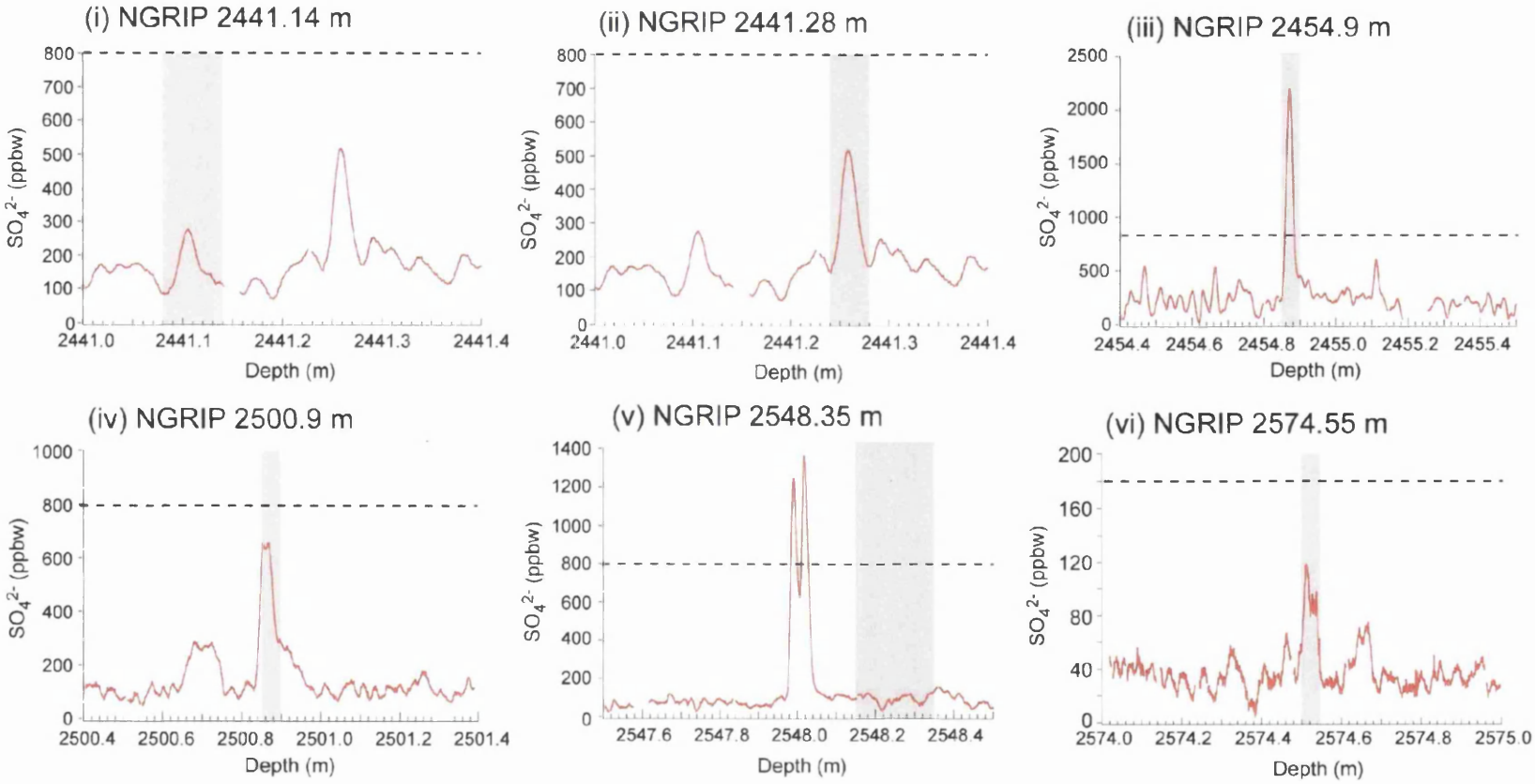


**Figure 8.15:** Comparisons between the positions of cryptotephra horizons identified within the NGRIP ice-core record and the high-resolution sulphate record for the core. Grey shaded areas represent depth intervals containing high concentrations of tephra shards. Black dashed lines represent the sample selection thresholds.

the order of months between the deposition of tephra shards and sulphate aerosols. However, for NGRIP 2548.35 m, the temporal offset between tephra and sulphate deposition is too great and this horizon is known to have an Icelandic source. Therefore, the offset can be regarded as real and volcanic aerosols were not deposited in conjunction with the tephra. The identification of Icelandic horizons without an associated chemical signal is not unprecedented, as the identification of the Fugloyarbanki Tephra in the NGRIP record demonstrates (Davies et al., 2008). These situations may arise due to differential dispersal pathways for the aerosols and tephra following an eruption resulting in the aerosol signal not being recorded in Greenland. Alternatively, the aerosols may be dissolved in the meltwater created during subglacial eruptions (Mortensen et al., 2005). The identification of tephra horizons within the ice-cores without a coeval chemical signal has significant implications for future tephrochronological work on ice-core records.

Overall, these results indicate that the sulphate record can be used as a guide to the location of cryptotephra horizons within the NGRIP ice-core, however, a sole focus on high magnitude peaks is not recommended. The sulphate record acts as a proxy for volcanic eruptions but not a proxy for the deposition of tephra shards. As yet a proxy for the tephra content of ice has not been identified.

A potential solution for future studies is to adopt a continuous screening procedure. A low-resolution continuous record of particulate material from individual ice-core bags could provide a guide for subsequent high-resolution direct-ice sampling, as utilised within this study. This procedure would identify horizons, such as NGRIP 2548.35 m, which do not have a direct association to a sulphate peak. Attempts were made to create a low-resolution continuous record of tephra concentration for the NGRIP ice-core, through the filtering of particulate material from the wastewater produced when the ice-core bags were melted for CFA analysis (Davies, 2002). However, investigations of filters from the last glacial-interglacial transition by Davies (2002) suggested that contamination within the filtration system meant that the tephra shards retained on the filters did not provide an accurate record of shards within the ice segments. A continuous record of particulate material will be obtained from the new NEEM ice-core. Improved methods for the collection of clean water from the CFA system will circumvent contamination issues and facilitate the creation of a low-resolution continuous tephra record for the core (S. Davies, *pers. comm.*, 2009).

An additional factor that may have precluded the identification of tephra horizons is the small surface area of the ice-core sampled, ~ 2 $cm^2$. This represents only 2.66 % of the total surface area of the core. If tephra shards are unevenly distributed over the surface of the ice sheet following deposition, the sampling of only a small area of ice may lead to horizons not being identified. Local depositional variations could be induced by variations in surface topography such as sastrugi, centimetre to metre scale dune-like surface features that are common on the ice sheet (Bory et al., 2002). This is particularly relevant within the distal location of Greenland where high levels of shard concentration are not expected. This issue is unavoidable due to the high demand for ice for other techniques as well as for archiving.

#### 8.2.3.2 Use of Density Separation for Cryptotephra Horizon Identification in Marine Sequences

Identification of tephra horizons within the MD04-2822 marine sequence employed isolation methods that are not widely applied to marine records. The method of density separation of core material from the 25-80 μm grain size fraction is more akin to investigations of terrestrial sequences (e.g. Turney, 1998; Zillén et al., 2002; Davies et al., 2005; Koren et al., 2008) than previous investigations of North Atlantic marine sequences which were generally concerned with the >150 μm grain size fraction (e.g. Wastegård and Rasmussen, 2001; Rasmussen et al., 2003; Wastegård et al., 2006; Kristjánsdóttir et al., 2007). However, the use of this method led to the identification of two fine-grained and relatively discrete rhyolitic cryptotephra horizons, within which the vast majority of the shards were less than 80 μm in diameter. The detection of similar horizons within other North Atlantic marine sequences has been reported, however, the full details of these horizons have not been published (Lowe et al., 2008). Density separation has also been successfully utilised to identify fine-grained deposits within marine cores from the Southern Adriatic (Lowe et al., 2007).

The focus on the 25-80 μm grain size fraction instead of larger material increased the potential for the identification of primary airfall deposits and the relative stratigraphic integrity of these horizons compared to ice-rafted deposits improves their effectiveness as chronostratigraphic marker horizons. Inspection of the >80 μm fraction focused on selected samples, guided by the ice-core tephrochronological framework, however, other horizons may have been identified if the >80 μm fraction was investigated for the entire core section.

Although rhyolitic material was the dominant component found in the marine samples limited amounts of basaltic material was also identified within the >2.5 g/cm$^3$ density fraction from all samples. However, no distinct horizons were identified. This is of particular interest as the horizons identified within the ice-core records provide firm evidence for the occurrence of volcanic eruptions during the study period capable of transporting basaltic material to distal locations. The limited identification of basaltic material may have been due to the focus on finer grained material and the potential that basaltic material within the core is generally greater than 80 μm in diameter due to transportation by sea-ice rafting. However, this appears unlikely as the >80 μm grain size fraction from four core sections did not yield any basaltic glass shards (see appendix 5).

The limited identification of basaltic material within the >2.5 g/cm$^3$ density fraction may have been hampered by the high quartz content of the core material. Quartz has a similar density to basaltic material which meant that a relatively large volume of material with a density >2.5 g/cm$^3$ had to be inspected using optical microscopy. Alterations to the methodology used such as the use of magnetic separation (Mackie et al., 2002) or the separation of the material with a density >2.5 g/cm$^3$ into a greater number of density fractions may reduce the volume of material to be inspected. The application of these techniques may lead to the identification of more basaltic material within the MD04-2822 core, and could be focused on sections of the core most likely to contain the basaltic horizons identified in the ice-core records.

Alternatively other methods for the detection of cryptotephra horizons could be employed. An increasing number of rapid-assay, non-destructive techniques are being suggested for the detection of cryptotephra horizons as they may circumvent the need to employ the relatively time-consuming method of density separation (Gehrels et al., 2008). Methods for tephra analysis of marine sediments previously suggested include X-ray diffraction to identify grain size variations (Andrews et al., 2006), INAA on bulk sediments to detect trace element variations (Lim et al., 2008) and magnetic susceptibility measurements to identify Fe-rich particles (Lowe et al., 2007). In addition, a non-destructive method that could be used to trace cryptotephra horizons in marine sequences is X-ray fluorescence (XRF). Improvements in XRF analytical techniques and the development of XRF core scanners mean that it is possible to rapidly obtain high resolution, 1 mm records of the chemical composition of split sediment cores (Jansen et al., 1998; Kido et al., 2006; Richter et al., 2006). The application of this

technique for the tracing of cryptotephra horizons within distal terrestrial sequences has demonstrated high potential (e.g. Kylander et al., 2008; Schupack et al., 2008) and it may be possible to use XRF chemical records to identify cryptotephra horizons within marine cores. The XRF scanning of marine cores is becoming more routine as the chemical records have many palaeoceanographic applications including tracking climatic changes and recognising sedimentological events (Richter et al., 2006). Therefore, when future marine sequences are investigated the record of cryptotephra content obtained through density separation, could be compared to determine if any elements indicate the presence of horizons. Experimentation of this nature is required before XRF records alone could be used to pinpoint the location of cryptotephra horizons.

## 8.3 Use of LA-ICP-MS for the Trace Element Characterisation of Distal Tephra Horizons in the North Atlantic Region

Trace element characterisations of distal tephra horizons were obtained through the analysis of individual glass shards using a new LA-ICP-MS system with a 14 μm laser beam diameter. An assessment of the extent to which this geochemical technique can be applied within distal tephrochronological studies has been undertaken with mixed results.

On the one hand, it is demonstrated that REE profiles for some horizons analysed in this study show strong similarities in shape and gradient to the geochemical envelopes published for proximal deposits. Discrepancies, however, are apparent in absolute concentrations which can be attributed to the misestimation of gas blank levels during LA-ICP-MS analysis. Trace element characterisations also reinforce correlations between tephra horizons initially established by major element analysis, however, in some cases correlations can be refuted based on trace element differences. Moreover, it is shown that trace element analysis can in some instances be used to discriminate between tephras with an identical major element composition.

However, a number of limitations were also encountered during this study. These include (1) issues relating to the misestimation of the gas blanks during analysis; (2) the analysis and influence of micro-inclusions; (3) the geochemical heterogeneity of distal tephra horizons; (4) the distinct lack of comprehensive data-sets for comparison

purposes and; (5) the application of statistical techniques in the assessment of trace element differences.

### 8.3.1 Comparisons of Distal and Proximal Deposits

Comparisons of the trace element characterisations for the distal horizons to published characterisations of proximal deposits provide encouraging results for the future use of this technique. With a focus on the REE profiles, as they were the main concern of studies in proximal settings, strong similarities can be observed in the profile shapes and gradients for the majority of distal horizons (figure 8.16). Some of the profiles are not as smooth as those for the proximal deposits, however, this is probably due to the low number of shards analysed from some horizons. Figure 8.16 provides examples of distal to proximal REE similarities for Icelandic rhyolitic, tholeiitic and transitional alkali material. In addition, the distinctive trace element signature of proximal material from the Jan Mayen volcanic region compared to Icelandic deposits can be observed within the characterisations of the distal NGRIP 2454.9 m and GRIP 2499.75 m-1 horizons (figure 8.16d). Overall, the similarities in profile shape support the correlations based on major elements and demonstrate the reliability and robustness of the trace element data. In addition, trace element ratios are consistent between the proximal and distal deposits.

One potential limitation on these characterisations is that the absolute concentrations have been affected by gas blank misestimation. The impact of this limitation was highlighted in section 4.4.3, through the analysis of datasets created using different elements as internal standards. Although this issue creates offsets in absolute concentration, the REE profile shape is maintained as trace element ratios are unaffected. The potential influence of gas blank misestimation on the distal characterisations is well illustrated by the characterisations of three basaltic transitional alkali horizons shown in figure 8.16c. Whilst, the shapes of the REE profiles are similar only the trace element concentrations calculated for NGRIP 2500.9 m fall within the REE envelope for the proximal deposits. The characterisation of GRIP 2531.8 m appears offset towards higher concentrations and for NGRIP 2574.55 m offset towards lower concentrations. Lower absolute trace element concentrations than proximal characterisations were also calculated for the two horizons sourced from the Jan Mayen volcanic system (e.g. figure 8.16d).

Another possible explanation for the apparent offsets is that the current proximal characterisations do not capture the full trace element compositional range of Icelandic

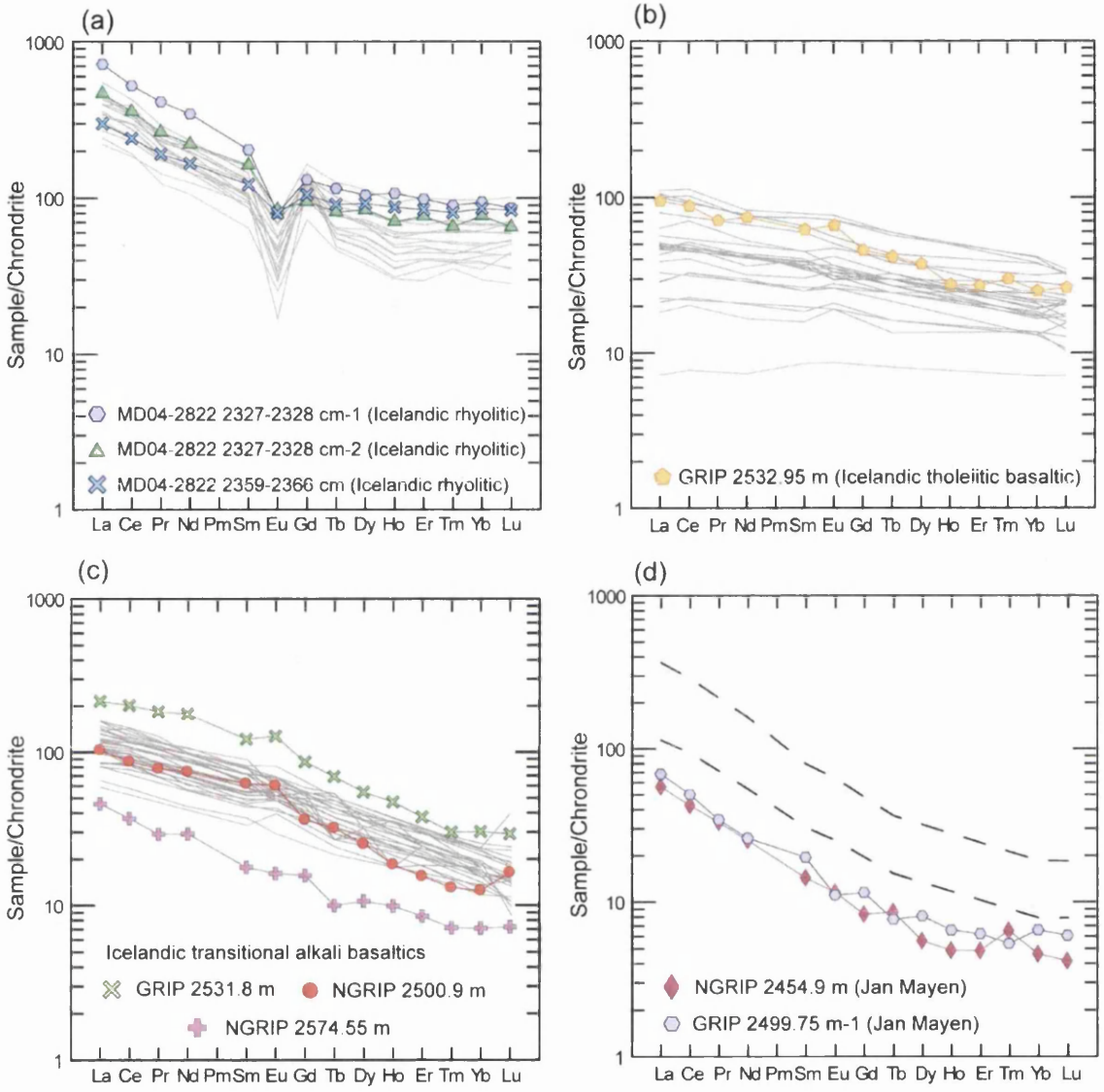


**Figure 8.16:** Comparisons of REE characterisations of MIS 4 tephra horizons to characterisations of proximal deposits within the source regions of the horizons. The REE concentrations for the MD04-2822 2359-2366 cm are based on the average trace element characterisations of shards from the 2359-2360 cm, 2363-2364 cm and 2365-2366 cm samples. Geochemical data for the proximal characterisations from (a) Jónasson (2007) (b and c) Meyer et al. (1995) and (d) Maaløe et al. (1986).

and Jan Mayen products. However, until reliable absolute trace element concentrations are gained following the resolution of the gas blank misestimation issue, through the application of the procedural recommendations outlined in section 8.3.5, it is not possible to ascertain the extent to which this could account for any observed offsets.

Gas blank misestimation does provide some limitations on the use of the absolute trace element concentrations in this study, however, it does not prevent the use of the trace element ratios.

#### 8.3.1.1 Inconsistency between Major and Trace Element Characterisations

The previous section highlighted that in most cases trace element characterisations matched the major element characterisations for the distal deposits. However, for two of the horizons within the MIS 4 framework the comparisons of the trace element characterisations to proximal deposits were incompatible with sources identified based on major element characterisations.

Within section 8.1.2.2 it was determined that the GRIP 2498.5 m and GRIP 2501.05 m horizons have the same but unidentified source, with the tholeiitic composition of the horizons suggesting that they originated from a volcanic system within the Icelandic rift zone. However, the trace element characterisations of these horizons do not support this proposition as their steeper than anticipated REE profiles are more akin, despite an offset in concentration, to those for transitional alkali material from the southern flank zone analysed by Meyer et al. (1985) (figure 8.17). This inconsistency in profile gradient cannot be attributed to gas blank misestimation because any offsets created by this effect are of the same magnitude for all elements and do impact on the gradient of REE profiles.

The steeper REE profiles for GRIP 2498.5 m and GRIP 2501.05 m compared to the characterisations of proximal tholeiitic material indicate that they are relatively enriched in LREEs and MREEs suggesting that they are more geochemically evolved. The observation of greater geochemical evolution of distal deposits compared to proximal deposits was attributed by Smith et al. (2005) to the use of bulk techniques to characterise proximal deposits. Because, if less evolved crystals and phenocrysts are incorporated in whole-rock analyses they will appear less evolved relative to analyses of distal glass deposits (Smith et al., 2005). However, as geochemical evolutionary differences have not been observed for the majority of the horizons characterised

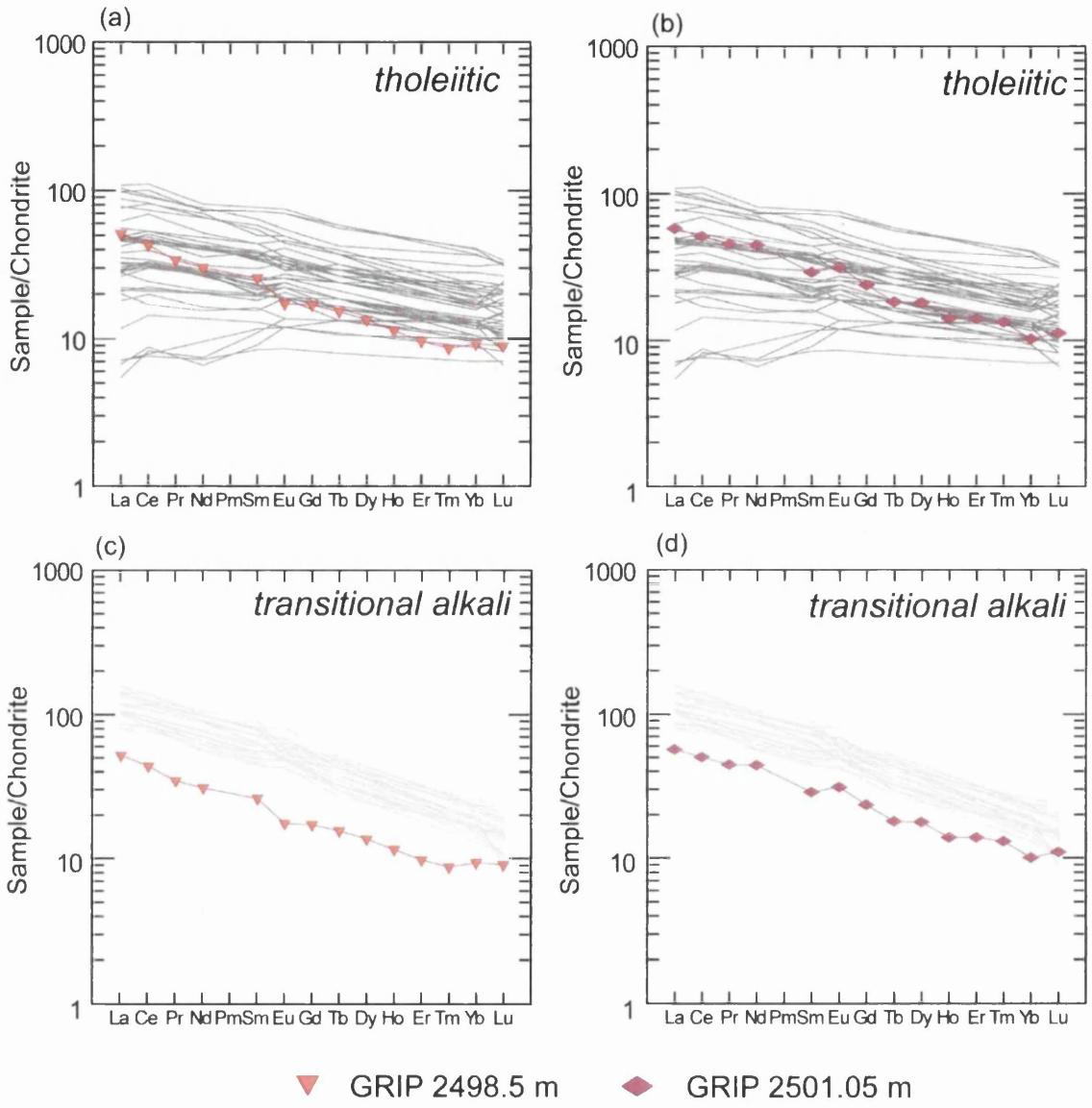


**Figure 8.17:** Comparisons of REE characterisations of the tholeiitic GRIP 2498.5 m and GRIP 2501.05 m tephra horizons to characterisations of proximal Icelandic material with a (a and b) tholeiitic composition (dark grey lines) and (c and d) transitional alkali composition (light grey lines). Geochemical data for the proximal characterisations from Meyer et al. (1985).

within this study it appears to be an unlikely cause for the inconsistencies for GRIP 2498.5 m and GRIP 2501.05 m.

A potential explanation is that the dataset of trace element characterisations of proximal deposits does not cover the full compositional range of tholeiitic material, due to rocks from all of the volcanic systems within the Icelandic rift zone not being included in the dataset. Characterisation of material from more volcanic systems may reveal proximal tholeiitic deposits with REE profiles of the same gradient as GRIP 2498.5 m and GRIP 2501.05 m. Therefore, further investigation of the composition of proximal deposits is required before the cause of the steeper REE profiles for GRIP 2498.5 m and GRIP 2501.05 m can be determined.

Overall, these observations suggest that despite the similarities presented in section 8.3.1 the relationship between the trace element composition of distal and proximal deposits warrants further investigation through the acquisition of further trace element characterisations of both distal and proximal Icelandic deposits. These observations do not provide a limitation on the use of the characterisations for GRIP 2498.5 m and GRIP 2501.05 m within comparisons to potentially correlative horizons. However, as they may have been affected by gas blank misestimation trace element ratios should be considered within any comparisons if offsets are apparent.

### 8.3.2 Testing Major Element Correlations

Mixed results were observed when testing the correlation of different tephra horizons previously based solely on major element compositions. Firstly, trace element similarities between two occurrences of the Fugloyarbanki Tephra (figure 4.18) and between the NGRIP 2500.9 m and GRIP 2531.8 m tephra horizons (figure 8.10) demonstrated that the characterisations increase the robustness of these correlations. Whilst, trace element differences between two deposits attributed to the Saksunarvatn Ash and between the Jan Mayen NGRIP 2454.9 m and GRIP 2499.75 m-1 tephra horizons, figures 8.18 and 8.19 respectively, demonstrate that for some horizons with major element similarities, differences in trace element composition can be observed. Trace element differences were subtle as contrasts could not be observed for the REEs and were only apparent for lighter elements such as Y, Zr, Rb and Sr (figures 818b(ii) and 8.19b(ii)).

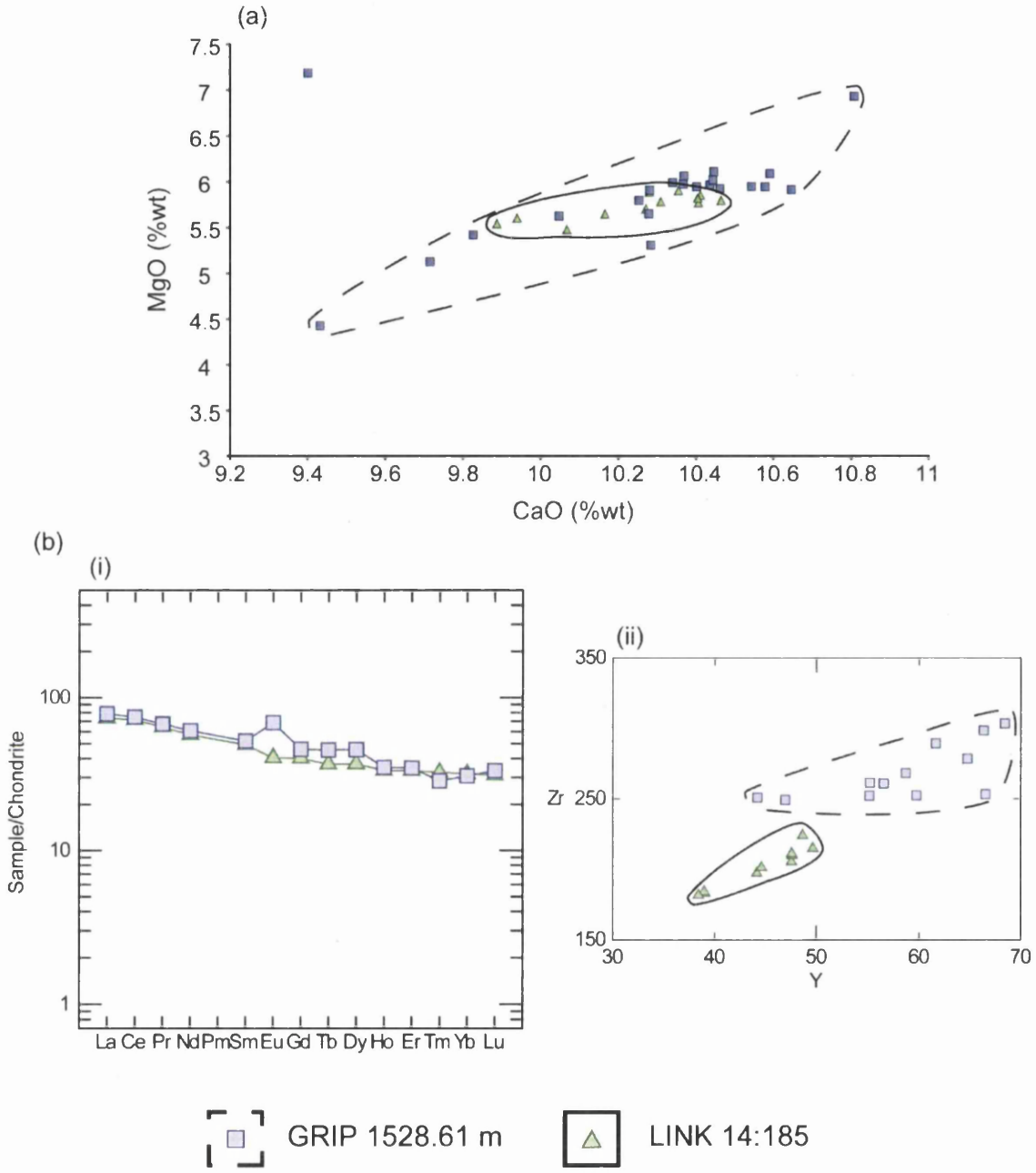


**Figure 8.18:** Geochemical comparisons of two Saksunarvatn Ash deposits previously correlated based on major element compositions. (a) CaO vs. MgO compositional variation diagram. (b) (i) Chondrite-normalised REE plot and (ii) Y vs. Zr compositional variation diagram for LINK 14:185 and GRIP 1528.61 m. Chondrite compositions from Sun and McDonough (1989).

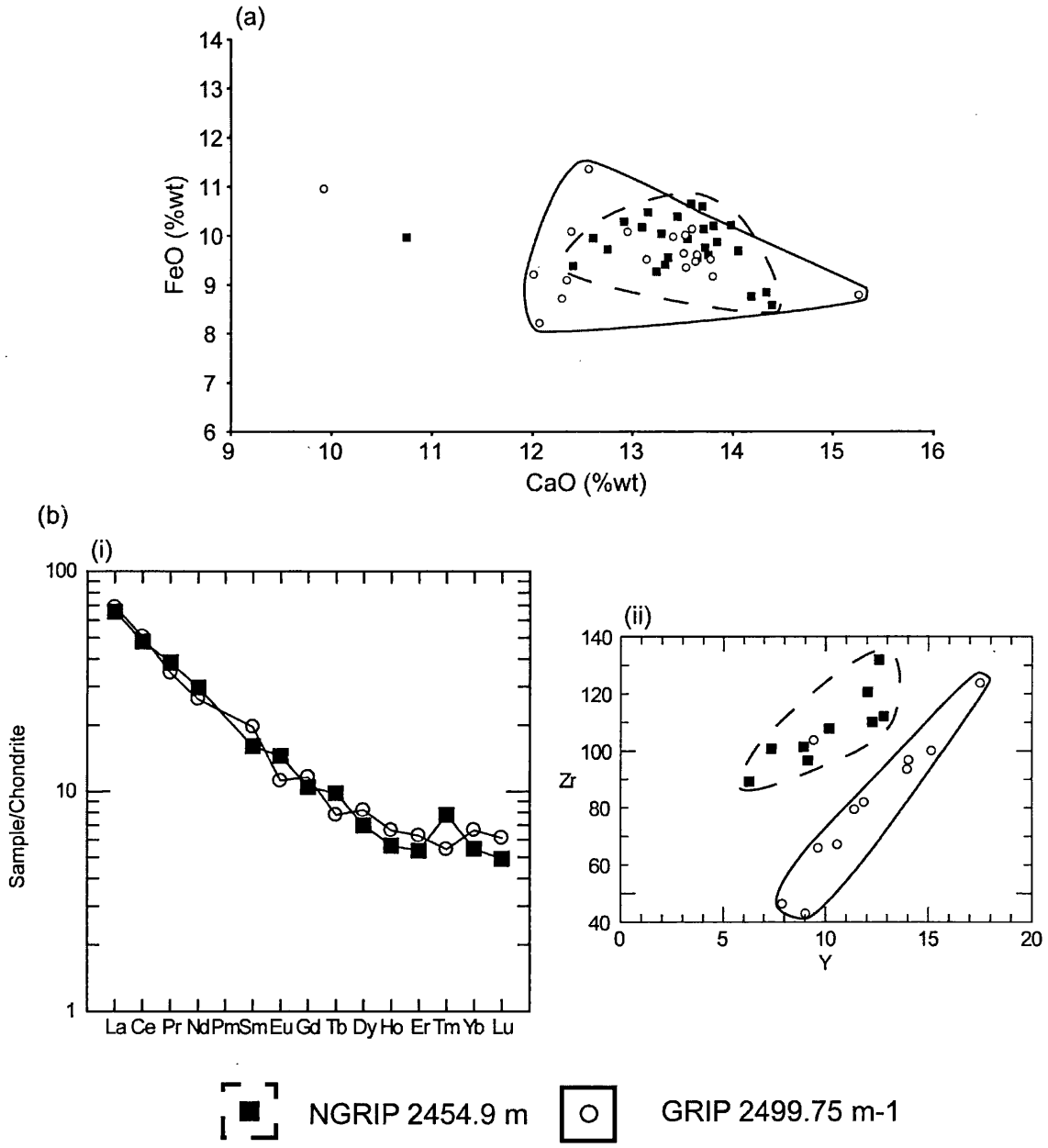


**Figure 8.19:** Geochemical comparisons of two Jan Mayen tephra horizons previously correlated based on major element compositions. (a) CaO vs. FeO compositional variation diagram. (b) (i) Chondrite-normalised REE plot and (ii) Y vs. Zr compositional variation diagram for LINK 14:185 and GRIP 1528.61 m. Chondrite compositions from Sun and McDonough (1989).

The difference in the concentration of these incompatible elements for the Saksunarvatn Ash horizons was attributed to fractional crystallisation between eruptive events, while the difference in incompatible element ratios for the two Jan Mayen horizons was attributed to mantle melting between events. The identification of trace element differences between these two pairs of horizons indicates that they cannot be used as chronostratigraphic markers as they do not represent the products of the same volcanic eruptions.

These observations demonstrate the importance of analysing the trace element composition of tephra horizons and not having a sole reliance on major element characterisation for the correlation of horizons. Further exploration of this issue within this study was constrained by the lack of major element correlative horizons identified within the three investigated MIS 4 sequences. However, there is a very broad scope for the future investigation of this issue if LA-ICP-MS is employed as a standard characterisation technique in support of EPMA within future tephrochronological studies. This will present more opportunities to test if trace element characterisations strengthen or call into question major element correlations.

### 8.3.3 Testing the Use of Trace Element Analysis for Discrimination Purposes

The third key issue to be explored was if horizons with a mutual source, and consequentially similar major element geochemistry, could be distinguished based on trace element characterisations. This may aid the discrimination of horizons erupted within a short time period that would be hard to resolve within low-resolution sequences with poor chronostratigraphic control.

Five horizons with similar major element geochemical compositions were selected to test whether trace element analysis can be successfully used for discrimination purposes. These horizons originate from the Icelandic Katla volcanic system and were found within either the NGRIP or GRIP ice-cores. Two horizons deposited within ~5000 years showed distinct Y/Zr ratios, which permitted the geochemical discrimination of these deposits (figure 8.20a). However, no differences were observed in the trace element composition of two other horizons deposited within a period of ~1425 years (figure 8.20b). Such tephra pairs can prove problematic for tephra studies, particularly if only one horizon can be identified in other sequences.

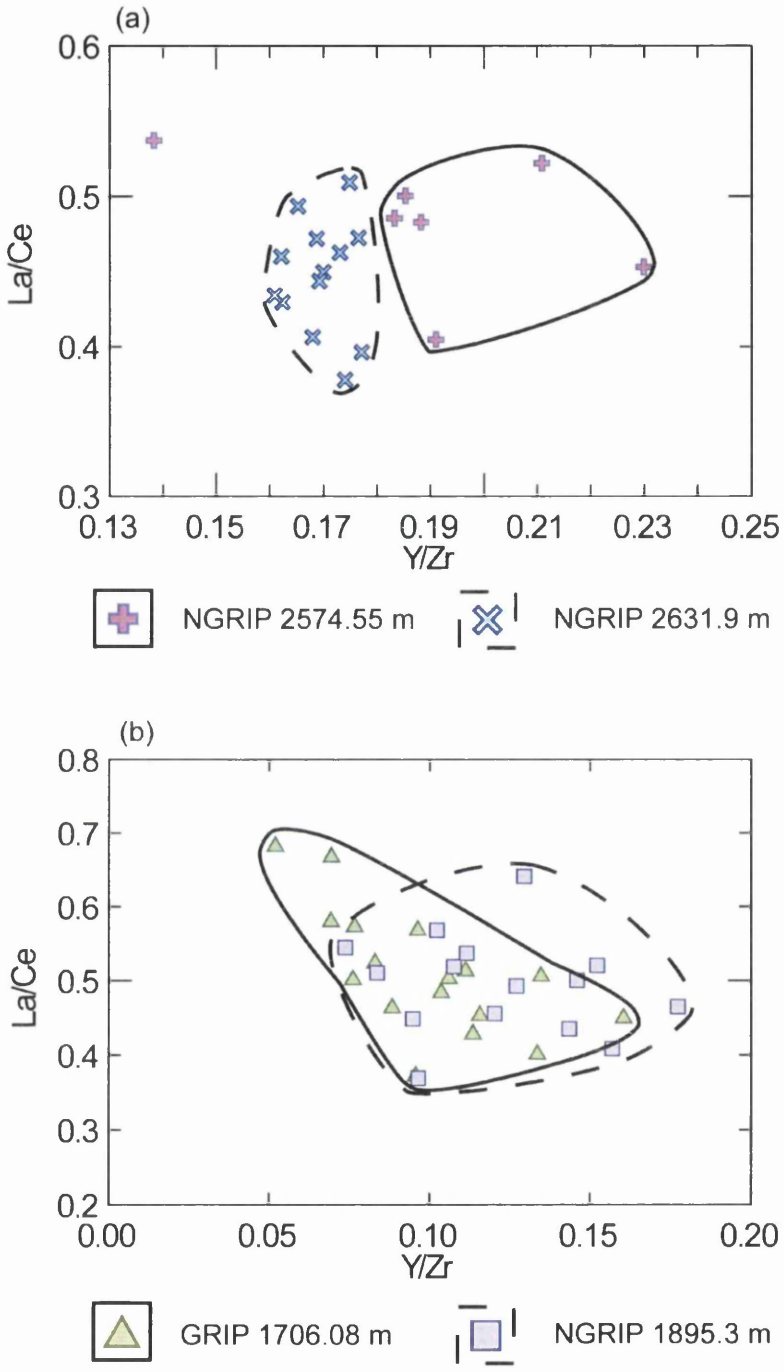


**Figure 8.20:** Trace element ratio-ratio plots demonstrating (a) the trace element discrimination of the NGRIP 2574.55 m and NGRIP 2631.9 m horizons and (b) the trace element similarities between the GRIP 1706.08 m and NGRIP 1895.3 m.

In addition, the trace element discrimination of the Saksunarvatn and Jan Mayen horizons previously correlated based on major element evidence, see section 8.3.2, demonstrates that horizons from a mutual source and with a close temporal separation can have contrasting trace element compositions. While, the trace element similarities between GRIP 2498.5 m and GRIP 2501.05 m (section 8.1.2.2; figure 8.6), which were erupted with an approximately 450 year separation, demonstrates that a mutual source can produce horizons with similar trace element geochemistries with a short temporal separation.

Overall, these observations imply that in some cases trace element geochemistry can be used to discriminate between horizons with similar major element compositions and deposited with a short temporal separation. This ability may be controlled by the timing of changes in magmatic conditions at the volcanic source. Evidence for closely spaced eruptions having almost identical trace element compositions suggests that trace element similarities between horizons can increase the robustness of correlations, but, they cannot be regarded as conclusive proof and any other available evidence should be used to support correlations.

Further work is required to fully establish the trace element characterisations of tephras within the North Atlantic region. A potential focus includes the products of the combined Grímsvötn-Kverkfjöll volcanic system, which has been highly active during the MIS 2-5e period producing material with similar major element chemistry.

In addition, the collation of trace element characterisations of horizons within dated sequences will not only aid tephrochronological studies but may also allow the magmatic evolution of individual volcanic systems to be investigated. An example of this was provided by the identification of a magma chamber replenishment event of the Katla volcanic system during the last glacial period (section 4.6.2). To gain a true insight into these processes reliable, absolute trace element concentrations need to be obtained, for this to be achieved a number of procedural issues outlined in section 8.3.5 need to be addressed.

### 8.3.4 Further Limitations

#### 8.3.4.1 Incorporation of Micro-inclusions during Shard Analyses

The characterisations of the NGRIP 2441.14 m, NGRIP 2441.28 m and NGRIP 2548.35 m horizons have limited use in future investigations due to one limitation that has been identified within these LA-ICP-MS analyses; the potential incorporation of micro-inclusions during the analysis of individual shards. These tephras have similar REE profile shapes (figure 8.21), despite having very different major element compositions ranging from basaltic to rhyolitic. It was demonstrated within chapter 5 that these profile shapes do not strongly relate to any characterisations of proximal deposits and it was suggested that the REE profiles for these three horizons can be attributed to the incorporation of plagioclase during glass shard analyses. The occurrence of plagioclase inclusions was not detected during microprobe analysis, however this is not unexpected as a much larger volume of the shard is analysed during LA-ICP-MS. The penetration of the laser beam into shards during LA-ICP-MS could result in phenocrysts below the surface being incorporated into analyses. These micro-inclusions would not be detected during EPMA as this technique only characterises material at the surface of the shard (Pearce et al., 2002). Polyatomic interference of BaO with Eu concentrations may account for the most prominent feature of the characterisations, the large positive Eu anomalies, however, it would not account for the other differences between the distal and proximal characterisations.

#### 8.3.4.2 Heterogeneity within Distal Tephra Horizons

Another limitation of the comparisons made within this study was the inability to assess the cause of variable trace element heterogeneity within the distal deposits. It was possible to determine geochemical heterogeneity within the distal horizons because a number of individual glass shards were analysed from each sample and distinct differences in heterogeneity can be observed between the horizons, e.g. figure 8.22. However, the extent to which this heterogeneity resulted from two factors, the analytical precision of the LA-ICP-MS system and the actual variability in composition between shards, could not be determined.

Firstly, the small size of the shards within the distal horizons meant that the precision of the analyses made using a 14 μm beam diameter could not be compared to more

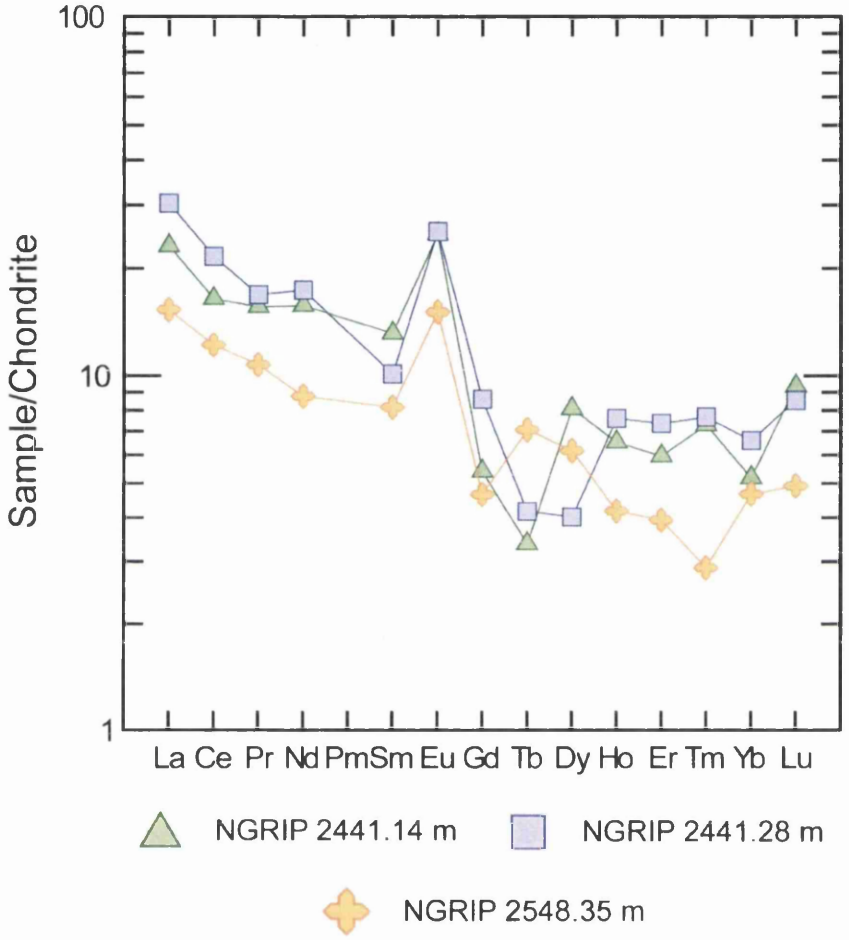


**Figure 8.21:** Average chondrite-normalised REE profiles for the NGRIP 2441.14 m, NGRIP 2441.28 m and NGRIP 2548.35 m tephra horizons.

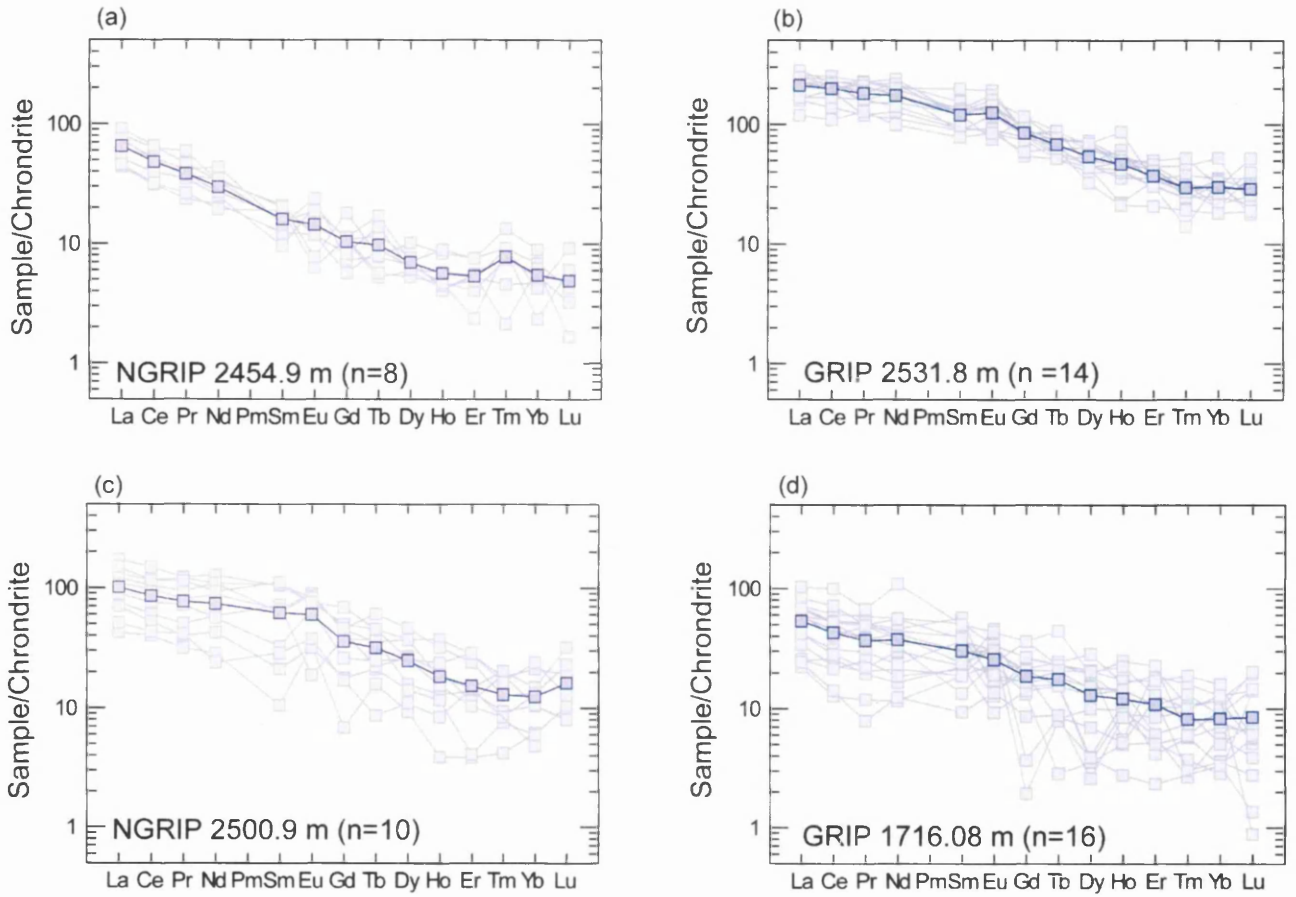


**Figure 8.22:** Chondrite-normalised average REE profiles for individual shards from the (a) NGRIP 2454.9 m (b) GRIP 2531.8 m (c) NGRIP 2500.9 m and (d) GRIP 1716.08 m tephra horizons displaying the differing levels of heterogeneity between the characterisations. Average profiles for the characterisations are highlighted. All samples analysed during the either the first or second LA-ICP-MS analytical periods between which no variations in analytical precision occurred; determined based on the analysis of the NIST 612 references standard (see section 4.2.2).

precise characterisations acquired using a larger beam diameter. Secondly, the heterogeneity of proximal deposits is not reported in literature sources and this may have provided a measure of expected heterogeneity within the distal horizons. The published characterisations utilised for comparisons are made using bulk analysis methods that homogenise whole rocks and only provide a single measure of the concentration of trace elements. Multiple whole-rock analyses have been reported, however, the variability in composition between individual deposits does not provide a suitable estimate of the heterogeneity within a deposit.

The extent to which the heterogeneity of the distal characterisations is due to instrumental issues could be assessed if improvements are made to the analytical precision of the LA-ICP-MS system. This may be achieved through procedural recommendations related to the treatment of gas blanks (see section 8.3.5.1). In addition, more comprehensive data-sets of proximal characterisations that assess the heterogeneity of these deposits are required to properly investigate the nature of heterogeneity within the characterisations of distal deposits.

### 8.3.4.3 Use of the Statistical Distance Function for the Comparison of Trace Element Datasets

The statistical distance function was employed to determine if any observed trace element differences between horizons were statistically significant and provide statistical evidence to support qualitative observations. However, throughout the study it was found that in many cases qualitative differences were not shown to be statistically significant.

This finding highlights two serious limitations to the use of the statistical distance function for the comparison of the trace element datasets produced in this study. Firstly, the heterogeneity of the characterisations meant that the average trace element concentrations had high standard deviations and anomalously low $D^2$ values were calculated. This will always be an issue if Euclidian methods are used to compare heterogeneous datasets. Secondly, it has been demonstrated that geochemical differences between horizons are often subtle and only apparent for a couple of elements. These subtleties are often masked through the comparison of a representative number of elements.

Other multi-variate statistical methods such as cluster analysis (e.g. Baron et al., 2008), discriminate function analysis (e.g. Charman and Grattan, 1999; Pollard et al., 2006) could have been utilised for the comparison of the datasets. However, all of these techniques would be ineffective for the analysis of the highly variable trace element datasets with subtle differences between them compared in this study (Pearce et al., 2008b). Therefore, caution should be given to statistical distance values calculated using datasets of this nature and it is strongly recommended that qualitative comparisons of geochemical datasets are made on multiple bivariate plots to determine if horizons are correlatives.

### 8.3.5 Procedural Recommendations for Future Investigations

Based on these findings and the experimental work outlined in sections 4.3 and 4.4 a series of procedural recommendations are made for the future use the LA-ICP-MS system for the characterisation of small glass tephra shards.

#### 8.3.5.1 Gas Blank Acquisition

The main recommendation for the analysis of small shards is related to the methods used to estimate background signals within the LA-ICP-MS system. It was demonstrated that linear interpolation between sets of gas blanks measured prior and subsequent to the acquisition of a series of sample analyses provides an inappropriate method for gas blank estimation and can introduce offsets in trace element concentrations. Such issues have not been encountered in past studies because the laser beam diameters were larger and produced far greater counts for elements during sample analyses. As a consequence, it is recommended that a gas blank analysis is made prior to each individual sample analysis and that sufficient time (~45 seconds) is left between sample analyses and gas blank analyses to allow any remaining sample material to leave the system. The elemental counts from the gas blank taken prior to a sample analysis will then be subtracted from the sample counts during the calculation of absolute trace element concentrations.

This will increase the time it takes to make analyses and reduce the number of analyses that can be made each day. However, it should permit the acquisition of more accurate absolute trace element concentrations with improved precision, compared to the characterisations presented within this study. The effectiveness of this procedure

has been demonstrated by experimentation conducted following data acquisition in this study (Pearce, *pers. comm.*, 2009). The potential misestimation of gas blanks was raised as an issue by the identification of differences in trace element concentrations calculated using different internal standards. Therefore, it is recommended that during any subsequent investigations the standardisation of datasets using both Si and Ca internal standards should be conducted and the calculated concentrations compared. The comparison of these datasets will provide a measure of the effectiveness of the new procedures, because if the issues regarding gas blank estimation of both Si and Ca counts are resolved the calculated concentrations should consistently be equal.

#### 8.3.5.2 Laser Beam Diameter and Internal Standard

Within sections 4.3 and 4.4 two methodological issues relating to potential alterations in the procedures used for the acquisition and calculation of trace element data from the LA-ICP-MS system were explored. Firstly, it was ascertained that using the current instrumental set-up there is the potential to produce reliable characterisations of individual shards using a 6 µm laser diameter comparable to those produced using a 14 µm diameter. However, this only occurs if the ratio between sample counts and background counts exceeds a threshold beyond which Si count rates do not influence calculated concentrations. The inconsistency in the reliability of characterisations produced using a 6 µm laser beam diameter prevents the recommendation of this as the standard beam diameter to utilise within the analysis of small tephra shards.

To consistently produce these reliable characterisations the sensitivity of the ICP-MS system could be increased to improve the ratio of sample counts to background counts. However, a limiting factor for this is that improving overall ICP-MS sensitivity will also improve sensitivity to background signals and thus sufficient increases in the sample to background count ratios may not be achieved. Therefore, it is advised that experimentation with the characterisation of small tephra shards with a 10 µm laser beam diameter is conducted as this will increase the volume of sample material being ablated, increasing sample to background ratios. This study focused on the use of a 6 µm beam diameter in an attempt to test the full spatial resolution capabilities of the new LA-ICP-MS system, however, in light of the findings presented in section 4.3 it may have been more appropriate to experiment with a 10 µm beam diameter.

The second issue to be explored was the use of Ca as an internal standard within the calculation of absolute trace element concentrations. It was found that the

concentration data produced when Ca was used as the internal standard was variably offset from concentrations calculated using Si as an internal standard. This was attributed to the lower sample count rates for Ca and the higher susceptibility to misestimation of background counts. To increase the counts rates for Ca and reduce the variability in the calculated trace element concentrations relative to Si standardised data it is recommended that a different Ca isotope is measured. The isotope $^{43}Ca$ measured within this study has a relative abundance of 0.14 %, whilst the $^{44}Ca$ isotope has a higher abundance of 2.09 %. The measurement of the abundance of the $^{44}Ca$ isotope will increase the number of counts per second recorded per ppm of Ca during sample analyses, thus improving the ratio between sample and background counts for Ca. This should decrease the offsets within the concentration data calculated using Ca as an internal standard relative to the Si standardised data and also reduce the susceptibility to the effects of gas blank misestimation. However, prior to the sole use of $^{44}Ca$ as an internal standard comparisons to $^{29}Si$ standardised data, such as those made within this study, should be conducted.

#### 8.3.5.3 Relocation of Tephra Shards during LA-ICP-MS Analysis

The relocation of shards previously analysed using EPMA when LA-ICP-MS analyses are being made is vital for the calibration of concentrations through internal standardisation. To achieve this careful records have to be kept of the nature of shards and shard sections when viewed under both transmitted and reflected light. For the LA-ICP-MS system utilised within this study it was found that the relocation of shards using reflected light was most appropriate due to the optical capabilities of the associated microscope system. As a consequence the acquisition of back-scatter electron images of shards during EPMA may provide the most reliable means to relocate shards, especially if different operators are conducting the EPMA and LA-ICP-MS analyses. In addition, the use of backscatter electron imagery may permit the identification of micro-inclusions within the shards that can not be identified optically and these shards can be avoided during LA-ICP-MS analysis.

### 8.3.5.4 Summary of Procedural Recommendations

To summarise the key procedural recommendations for the future characterisation of individual shards within distal tephra horizons are:

- The acquisition of gas blank analyses prior to the analysis of each individual shard.

- Measurement of the $^{44}Ca$ isotope instead of the $^{43}Ca$ isotope and an assessment of its use for internal standardisation.

- Continued use of a 14 μm laser beam diameter for characterisation and an investigation of the potential use of a 10 μm beam diameter.

- Careful documentation of the shards analysed during EPMA through the acquisition of backscattered electron images of shard sections.

# 9. Conclusions

## 9.1 Summary of Main Findings

•For the first time, a detailed North Atlantic tephrochronological framework for the MIS 4 climatic period is presented. This framework has been constructed entirely through the identification of cryptotephra horizons. Fourteen previously unknown volcanic eruptions form the backbone of this framework with six cryptotephra horizons identified in the NGRIP ice-core, six in the GRIP ice-core and two within the MD04-2822 marine core.

•Comprehensive major and trace element geochemical compositional data for these horizons and high-precision, independent age estimates for each eruption identified within the ice-cores significantly enhances this framework as a tool for the synchronisation of MIS 4 records. In addition, this template identifies key intervals that can be targeted during the future tracing of these horizons in other records.

•Geochemical characterisations demonstrate that 11 of these horizons originate from Icelandic volcanic systems, two from the Jan Mayen volcanic region and one has been tentatively linked to a source from a Japanese volcanic system.

-This makes a significant contribution to the volcanic history of Iceland during the MIS 4 period particularly as no other eruptions during this period have been identified. The timing of these eruptions relative to climatic records suggests that rapid climatic changes may have triggered volcanism in Iceland during the MIS 4 period.

-Identification of Jan Mayen products provides the first evidence that this volcanic region was active, producing widespread horizons of basaltic-trachybasaltic composition material during the last glacial period.

-The possibility that the products of a Japanese eruption have been recognised within the NGRIP ice-core significantly increases the scope of synchronising records from a regional to a hemispheric scale.

•Despite the successful development of this framework an assessment of the high-resolution sulphate records for the NGRIP ice-core suggests that some MIS 4 horizons may have been overlooked. The use of continuous screening procedures within future studies of ice-cores may avert this situation.

•Analysis of the MD04-2822 marine sequence using the density separation technique permitted one of the first identifications of fine ash primary-airfall tephra horizons within North Atlantic marine sequences. The relative integrity of these horizons compared to ice-rafted horizons increases their robustness as chronostratigraphic markers. Modifications to the density separation techniques utilised within future studies will help to determine if the lack of basaltic material identified within MD04-2822 is a consequence of the methodologies employed or the preferential dispersal of basaltic material on specific pathways from Iceland.

•Using a new LA-ICP-MS system, which couples a lower wavelength laser with a more sensitive mass spectrometer, it has been possible to obtain trace element characterisations from individual tephra shards as small as ~20 μm in diameter from distal, cryptotephra horizons. Trace element ratios for the distal horizons compare well to the proximal deposits from both the Icelandic volcanic systems and the Jan Mayen volcanic region. This dataset represents one of the most comprehensive sets of trace element characterisations for tephra horizons in distal locations within the North Atlantic region.

•The potential of this new LA-ICP-MS system to analyse single shards ~20 μm in diameter is a significant improvement on the past spatial resolution of this technique. These advancements have important implications for tephra studies in settings distal from any volcanic region as well as being particularly relevant for deciphering magmatic evolution processes.

•This work demonstrates the value of undertaking trace element analysis within tephra studies, particularly in light of two key discoveries.

-Firstly, it has been shown that correlations based solely on major elements are in some instances insufficient for correlation purposes. Notably, two deposits previously related to the Saksunarvatn Ash were shown to have contrasting trace element compositions, which calls into question the use of this horizon as a chronostratigraphic tie-line.

-Secondly, trace element differences between horizons from the same volcanic source, which can be attributed to magmatic processes at the source, can in some cases be successfully used to discriminate between horizons. Such differences may permit the discrimination of closely spaced horizons from the same source and with similar major element geochemistries.

•Although the LA-ICP-MS technique has been employed successfully in this investigation, one key limitation still remains. It became apparent that gas blank levels may have been misestimated and therefore had a significant effect on the calculated trace element concentrations. This issue arose due to the improvement in spatial resolution. This misestimation of gas blanks can be resolved through the incorporation of procedural recommendations outlined in section 8.3.5 within future studies. This issue, however, does not affect the use of trace element ratios from the characterisations made within this study for future comparative purposes.

## 9.2 Recommendations for Future Work

•The framework presented here has significant potential for the application of tephrochronology to test the synchronicity of DO events during the MIS 4 climatic period. Key target-intervals in other MIS 4 records potentially containing tephra horizons within this framework can now be pinpointed. Some of the horizons within this framework are particularly important for investigating the timing of rapid climate events because they fall close to or on these transitions (section 8.2). In order to further explore the potential of tephrochronology additional work is required to pinpoint horizons in other sequences.

•North Atlantic Ocean records are ideal as a primary focus of future studies, with a particular emphasis on high-resolution records from areas with high sedimentation rates and sequences retaining a clear DO event signal. These investigations should be extensive and conducted on sequences from a range of geographical locations on different dispersal pathways from the volcanic source regions of Iceland and Jan Mayen, particularly those between Iceland and Jan Mayen and the Greenland ice-core sites. Use of density separation techniques will help to isolate primary airfall deposits and modifications to extraction procedures such as stepped flotation or magnetic separation may aid in the isolation of basaltic material. Investigations could also be

extended to long North Atlantic region terrestrial sequences preserving a record of the last glacial period such as the Les Echets, France lacustrine sequence (Veres et al., 2007).

•Investigations can also focus on the MIS 4 section of a new deep ice-core presently being extracted from the Greenland Ice Sheet, NEEM. The identification of horizons isolated in this study would aid in the synchronisation of the deep ice-cores and enable the transferral of the GICC05 high-precision chronology. A continuous screening procedure has the potential of creating a more comprehensive tephrochronological record for the MIS 4 period. In addition, the location of the drill site in the far NW of Greenland may increase the number of horizons from north Pacific Rim volcanic regions, thus increasing the number of potential hemispheric tie-lines.

•The MIS 4 period within key North Pacific Ocean and Japanese terrestrial palaeoclimatic sequences (e.g. Lake Suigetsu) warrant investigation in an attempt to locate NGRIP 2441.28 m. The identification of NGRIP 2441.28 m within any of these sequences would provide corroborating evidence for this horizon being sourced from an eruption of a Japanese volcano and would help to determine if it can act as a hemispheric tie-line between palaeoclimatic sequences.

•There is considerable scope associated with the use of LA-ICP-MS for the improvement of tephra horizons characterisations both in proximal and distal settings. A number of key procedural recommendations are outlined and will allow the robust characterisation of absolute trace element concentrations. It is recommended that this technique be incorporated as a routine procedure in tephra studies. Not only will this enable large comprehensive geochemical datasets to be obtained but also will test correlations based solely on major elements. In particular, further work is required to provide a full characterisation of the Saksunarvatn Ash in the North Atlantic region. Other key chronostratigraphic marker horizons such as the Vedde Ash, Borrobol Tephra, FMAZ III and NAAZ II should also be characterised.

•Other priorities also include characterisation of proximal deposits, particularly from Iceland, as well as rhyolitic type-material from different regions. Pinpointing a source for rhyolitic horizons is particularly difficult with so many overlapping major element envelopes, trace element characterisations are required to further address this issue.

•Attempts should also be made to determine the trace element concentration of key horizons using different methods to LA-ICP-MS, such as the ion-microprobe and if enough material is available, solution ICP-MS to test the accuracy of the characterisations made using LA-ICP-MS.

# References


Alley, R.B. and Clark, P.U. (1999) "The glaciation of the northern hemisphere: a global perspective", *Annual Review of Earth and Planetary Sciences*, **27**, 149-182

Alley, R.B., Gow, A.J., Johnsen, S.J., Kipfstuhl., J., Meese, D.A. and Thorsteinsson, Th. (1995) "Comparison of deep ice cores", *Nature*, **373**, 393-394

Altabet, M.A., Higginson, M.J. and Murray, D.M. (2002) "The effect of millennial-scale changes in Arabian Sea denitrification on atmospheric $CO_2$", *Nature*, **415**, 159-162

Andersen, K.K., Svensson, A., Johnsen, S.J., Rasmussen, S.O., Bigler, M., Röthlisberger, R., Ruth, U., Siggaard-Andersen, M-L., Steffensen, J.P., Dahl-Jensen, D., Vinther, B.M. and Clausen, H.B. (2006) "The Greenland Ice Core Chronology 2005, 15-42ka. Part 1: constructing the time scale", *Quaternary Science Reviews*, **23-24**, 3246-3257

Andrews, J.T., Eberl, D.D. and Kristjansdottir, G.B. (2006) "An exploratory method to detect tephras from quantitative XRD scans: examples from Iceland and east Greenland marine sediments", *The Holocene*, **16**, 1035-1042

Andrews, J.T., Geirsdóttir, A., Hardardóttir, J., Principato, S., Grönvold, K., Kristjansdóttir, G.B., Helgadóttir, G., Drexler, J. and Sveinbjörnsdóttir, A. (2002) "Distribution, sediment magnetism and geochemistry of the Saksunarvatn (10,180 +/- 60 cal. yr BP) tephra in marine, lake, and terrestrial sediments, northwest Iceland", *Journal of Quaternary Science,* **17,** 731-745

Antoine, P., Rousseau, D.-D., Lautridou, J.-P. and Hatté, C. (1999) "Last interglacial-glacial climatic cycle in loess-palaeosol successions of north-western France", *Boreas*, **28**, 551-563

Aoki, K. and Machida, H. (2006) "Major element composition of volcanic glass shards in the late Quaternary widespread tephras in Japan – Distinction of tephras using $K_2O$-$TiO_2$ diagrams", *Bulletin of the Geological Survey of Japan*, **57**, 239-258

Arrhenius, G. (1952) "Sediment cores from the east Pacific. Properties of the sediment", *Swedish Deep-Sea Expedition 1947-1948 Reports*, **5**, 1-228

Arrowsmith, P. (1987) "Laser ablation of solids for elemental analysis by inductively coupled plasma mass spectrometry", *Analytical Chemistry*, **59**, 1437-1444

Austin, W.E.N., Bard, E., Hunt, J.B., Kroon, D. and Peacock, J.D. (1995) "The $^{14}C$ age of the Icelandic Vedde Ash: implications for Younger Dryas marine reservoir age corrections", *Radiocarbon*, **37**, 53-62

Austin, W.E.N., Wilson, L.J. and Hunt, J.B. (2004) "The age and chronostratigraphical significance of North Atlantic Ash Zone II", *Journal of Quaternary Science*, **19**, 137-146

Bäckström, D.L. (1998) *Late Quaternary paleoceanographic and palaeoclimatic records from the south-west of the Faeroe Islands, northeastern Atlantic Ocean*, Unpublished Diploma Thesis, Göteborg University

Baillie, M.G.L. and Munro, M.A.R. (1988) "Irish tree rings, Santorini and volcanic dust veils", *Nature*, **332**, 344-346

Bard, E. (2002) "Climate shock: abrupt changes over millennial time scales", *Physics Today*, **December 2002**, 32-38

Barker, D.S. (1983) *Igneous Rocks*, Englewood Cliffs, Prentice Hall

Baron, D., Negrini, R.M., Golob, E.M., Miller, D., Sarna-Wojcicki, A., Fleck, R.J., Hacker, B. and Erendi, A. (2008) "Geochemical characterisation and $^{40}Ar/^{39}Ar$ dating of the Kern River ash bed and related tephra layers: implications for the stratigraphy of petroleum-bearing formations in the San Joaquin Valley, California", *Quaternary International*, **178**, 246-260

Basile, I., Petit, J.R., Touron, S., Grousset, F.E. and Barkov, N. (2001) "Volcanic layers in Antarctic (Vostok) ice cores: Source identification and atmospheric implications", *Journal of Geophysical Research*, **106**, 31915-31932

Bay, R.C., Bramall, N. and Buford Price, P. (2004) "Bipolar correlation of volcanism with millennial climate change", *Proceedings of the National Academy of Sciences*, **101**, 6341-6345

Begét, J., Mason, O. and Anderson, P. (1992) "Age, extent and climatic significance of the c. 3400 BP Aniakchak tephra, western Alaska, USA", *The Holocene*, **2**, 51-56

Behl, R.J. and Kennett, J.P. (1996) "Brief interstadial events in the Santa Barbara basin, NE Pacific, during the past 60kyr", *Nature*, **379**, 243-246

Benson, L., Lund, S., Negrini, R., Linsley, B. and Zic, M. (2003) "Response of North American Great Basin Lakes to Dansgaard-Oeschger oscillations", *Quaternary Science Reviews*, **22**, 2239-2251

Bigazzi, G., Hadler Neto, J.C., Iunes, P.J. and Osório Araya, A.M. (2005) "Fisson-track dating of South American natural glasses: an overview", *Radiation Measurements*, **39**, 585-594

Bigler, M. (2004) *Hochauflösende Spurenstoffmessungen an polaren Eisbohrkernen: Glazio-chemische und klimatische Prozessstudien*, Unpublished PhD Thesis, University of Bern, Switzerland

Bigler, M., Svensson, A., Steffensen, J.P. and Kaufmann, P. (2007) "A new continuous high-resolution detection system for sulphate in ice cores", *Annals of Glaciology*, **45**, 178-182

Bird, M.I., Ayliffe, L.K., Fifield, L.K., Turney, C.S.M., Cresswell, R.G., Barrows, T.T. and David, B. (1999) "Radiocarbon dating of "old" charcoal using a wet oxidation, stepped-combustion procedure", *Radiocarbon*, **41**, 127-140

Birks, H.H., Gulliksen, S., Haflidason, H., Mangerud, J. and Possnert, G. (1996) "New radiocarbon dates for the Vedde Ash and the Saksunarvatn Ash from Western Norway", *Quaternary Research*, **45**, 119-127

Björck, S., Muscheler, R., Kromer, B., Andresen, C.S., Heinemeier, J., Johnsen, S.J., Conley, D., Koç, N., Spurk, M. and Veski, S. (2001) "High-resolution analyses of

an early Holocene climate event may imply decreased solar forcing as an important climate trigger", *Geology*, **29**, 1107-1110

Blockley, S.P.E., Lane, C.S., Lotter, A.F. and Pollard, A.M. (2007) "Evidence for the presence of the Vedde Ash in Central Europe", *Quaternary Science Reviews*, **26**, 3030-3036

Blockley, S.P.E., Pyne-O'Donnell, S.D.F., Lowe, J.J., Matthews, I.P., Stone, A., Pollard, A.M., Turney, C.S.M. and Molyneux, E.G. (2005) "A new and less destructive laboratory procedure for the physical separation of distal glass tephra shards from sediments", *Quaternary Science Reviews*, **16-17**, 1952-1960

Bond, G., Broecker, W., Johnsen, S., McManus, J., Labeyrie, L., Jouzel, J. and Bonani, G. (1993) "Correlations between climate records from North Atlantic sediments and Greenland ice", *Nature*, **365**, 143-147

Bond, G., Showers, W., Cheseby, M., Lotti, R., Almasi, P., deMenocal, P., Priore, P., Cullen, H., Hajdas, I., and Bonani, G. (1997) "A Pervasive Millennial-Scale Cycle in North Atlantic Holocene and Glacial Climates", *Science*, **278**, 1257-1266

Borchardt, G.A., Aruscavage, P.J. and Millard, H. Jr (1972) "Correlation of the Bishop ash, a Pleistocene marker bed, using instrumental neutron activation analysis", *Journal of Sedimentary Petrology*, **42**, 201-206

Bory, A.J.-M., Biscaye, P.E., Svensson, A. and Grousset, F.E. (2002) "Seasonal variability in the origin of recent atmospheric mineral dust at NorthGRIP, Greenland", *Earth and Planetary Science Letters*, **196**, 123-134

Boygle, J.E. (1994), *Tephra in lake sediments: An unambiguous geochronological marker?*, Ph.D. Thesis, University of Edinburgh

Bramlette, M.N. and Bradley, W.H. (1941) "Geology and biology of North Atlantic deep-sea cores between Newfoundland and Ireland: I. Lithology and geologic interpretation", *U.S. Geological Survey Professional Paper*, **196-A**, 1-34

Braun, H., Christl, M., Rahmstorf, S., Ganopolski, A., Mangini, A., Kubatzki, C., Roth, K. and Kromer, B. (2005) "Possible solar origin of the 1,470-year glacial climate cycle demonstrated in a coupled model", *Nature*, **438**, 208-211

Braun, H., Ditlevsen, P. and Chialvo, D.R. (2008) "Solar forced Dansgaard-Oeschger events and their phase relation with solar proxies", *Geophysical Research Letters*, **35**, L06703, doi: 10.1029/2008GL033414

Broecker, W.S. (2000) "Abrupt climate change: causal constraints provided by the paleoclimate record", *Earth Science Reviews*, **51**, 137-154

Broecker, W.S., Peteet, D.M. and Rind, D. (1985) "Does the ocean-atmosphere system have more than one stable mode of operation?", *Nature*, **315**, 21-25

Brown, F.H., Sarna-Wojcicki, A.M., Meyer, C.E. and Haileab, B. (1992) "Correlation of Pliocene and Pleistocene tephra layers between the Turkana Basin of East Africa and the Gulf of Aden", *Quaternary International*, **13/14**, 55-67

Bryant, C.J., Arculus, R.J. and Eggins, S.M. (1999) "Laser ablation inductively couple mass spectrometry and tephras; a new approach to understanding arc magmatism", *Geology*, **27**, 1119-1122

Buckland, P.C., Dugmore, A.J. and Edwards, K.J. (1997) "Bronze age myths? Volcanic activity and human response in the Mediterranean and North Atlantic regions", *Antiquity*, **71**, 581-593

Carr, M.J. (2008) *IGPET Software*, Rockware Inc.

Cao, L.-Q., Arculus, R.J. and McKelvey, B.C. (1995) "Geochemistry and Petrology of Volcanic Ashes Recovered From Sites 881 Through 884: A Temporal Record of Kamchatka and Kurile Volcanism". In Rea, D.K., Basov, I.A., Scholl, D.W. and Allan, J.F. (eds) *Proceedings of the Ocean Drilling Program, Scientific Results*, **145**, 345-381

Chalmas, R. (2004) *Analysis of the volcanic signal in the NGRIP ice core during the ice age*, Unpublished Master Thesis, University of Copenhagen

Chambers, F.M., Daniell, J.R.G., Hunt, J.B., Molloy, K. and O'Connell, M. (2004) "Tephrostratigraphy of An Loch Mór, Inis Oírr, western Ireland: implications for Holocene tephrochronology in the northeastern Atlantic region", *The Holocene*, **14**, 703-720

Chappellaz, J., Floch, G., Landais, A., Barnola, J.M., Flückiger, J., Blunier, T. and Johnsen, S. (2003), *Rapid $CH_4$ Changes During Marine Isotope Stage 4 and their Climatic and Glaciological Consequences*, Geophysical Research Abstracts Vol. 5, 05575

Charles, C.D., Lynch-Steiglitz, J., Ninnemann, U.S. and Fairbanks, R.G. (1996) "Climate connections between the hemisphere revealed by deep sea sediment core/ice core correlations", *Earth and Planetary Science Letters*, **142**, 19-27

Charman, D.J. and Grattan, J. (1999) "An assessment of discriminant function analysis in the identification and correlation of distal Icelandic tephras in the British Isles", *Geological Society (London) Special Publication*, **161**, 147-160

Chen, F.H., Bloemendal, J., Wang, J.M., Li, J.J. and Oldfield, F. (1997) "High-resolution multi-proxy climate records from Chinese loess: evidence for rapid climate changes over the past 75kyr", *Palaeogeography, Palaeoclimatology, Palaeoecology*, **130**, 323-335

Chesner, C.A. (1998) "Petrogenesis of the Toba Tuffs, Sumatra, Indonesia", *Journal of Petrology*, **39**, 397-438

Clark, P.U., Pisias, N.G., Stocker, T.F. and Weaver, A.J. (2002) "The role of the thermohaline circulation in abrupt climate change", *Nature*, **415**, 863-869

Clausen, H.B., Hammer, C.U., Hvidberg, C.S., Dahl-Jensen, D., Steffensen, J.P., Kipfstuhl, J. and Legrand, M. (1997) "A comparison of the volcanic records over the past 4000 years from the Greenland Ice Core Project and Dye 3 Greenland ice cores", *Journal of Geophysical Research*, **102**, 26707-26723

Clement, A.C. and Peterson, L.C. (2008) "Mechanisms of Abrupt Climate Change of the Last Glacial Period", *Reviews of Geophysics*, **46**, RG4002, doi:10.1029/2006RG000204

Clift, P.D., Layne, G.D., Najman, Y.M.R., Kopf, A., Shimizu, N. and Hunt, J. (2003) "Temporal Evolution of Boron Flux in the NE Japan and Izu Arcs Measured by Ion Microprobe from the Forearc Tephra Record", *Journal of Petrology*, **44**, 1211-1236

Croll, J. (1875) *Climate and Time in Their Geological Relations. A Theory of Secular Changes of the Earth's Climate*, Appleton, New York

Dahl-Jensen, D., Gundestrup, N.S., Keller, K.R., Johnsen, S.J., Gogineni, S.P., Allen, C.T., Chuah, T.S., Miller, H., Kipstuhl, S. and Waddington, E.D. (1997) "A search in north Greenland for a new ice-core drill site", *Journal of Glaciology*, **43**, 300-306

Dahl-Jensen, D., Gundestrup, N.S., Miller, H., Watanabe, O., Johnsen, S.J., Steffensen, J.P., Clausen, H.B., Svensson, A. and Larsen, L.B. (2002) "The NorthGRIP deep drilling programme", *Annals of Glaciology*, **35**, 1-4

Dansgaard, W. (2004) *Frozen Annals-Greenland Ice Sheet Research*, The Niels Bohr Institute, University of Copenhagen

Dansgaard, W., Johnsen, S.J., Clausen, H.B., Dahl-Jensen, D., Gundestrup, N.S., Hammer, C.U., Hvidberg, C.S., Steffensen, J.P., Sveinbjörnsdottir, A.E., Jouzel, J. and Bond, G. (1993) "Evidence for general instability of past climate from a 250-kyr ice-core record", *Nature,* 364, pp.218-220

Davies, S.M. (2002) *Extending the known distributions of micro-tephra layers of last glacial-interglacial transition age in Europe,* Unpublished PhD Thesis, Royal Holloway, University of London

Davies, S.M., Branch, N.P., Lowe, J.J. and Turney, C.S.M. (2002) "Towards a European tephrochronological framework for Termination 1 and the Early Holocene", *Philosophical Transactions of the Royal Society of London,* **A360**, 767-802

Davies, S.M., Hoek, W.Z., Bohncke, J.P., Lowe, J.J., Pyne-O'Donnell, S. and Turney, C.S.M. (2005a) "Detection of Lateglacial distal tephra layers in the Netherlands", *Boreas*, **34**, 123-135

Davies, S.M., Pearce, N.J.G., Wastegård, S., Johnsen, S.J. and Steffensen, J.P. (2005b) "Trace element analysis of basaltic tephras from the Greenland ice-cores". In Alloway, B.V., Froese, D.G and Westgate, J.A. (eds) *Proceedings of the International Field Conference and Workshop on Tephrochronology and Volcanism, Dawson City, Yukon Territory, Canada, July 31-August 8, 2005*, Institute of Geological and Nuclear Sciences, New Zealand

Davies, S.M., Wastegård, S., Rasmussen, T.L., Svensson, A., Johnsen, S.J., Steffensen, J.P. and Andersen, K.K. (2008) "Identification of the Fugloyarbanki tephra in the NGRIP ice core: a key tie-point for marine and ice-core sequences during the last glacial period", *Journal of Quaternary Science*, **23**, 409-414

Davies, S.M., Wastegård, S. and Wohlfarth, B. (2003) "Extending the limits of the Borrobol Tephra to Scandinavia and detection of the new early Holocene tephras", *Quaternary Research*, **59**, 345-352

Davies, S.M., Wohlfarth, B., Wastegård, S., Andersson, M., Blockley, S. and Possnert, G. (2004) "Were there two Borrobol Tephras during the early Lateglacial period: implications for tephrochronology?", *Quaternary Science Reviews*, **23**, 581-589

De Angelis, M., Fehrenbach, L., Jéhanno, C. and Maurette, M. (1985) "Micrometre-sized volcanic glasses in polar ices and snows", *Nature*, **317**, 52-54

Denton, J.S. and Pearce, N.J.G. (2008) "Comment on "A synchronized dating of three Greenland ice cores throughout the Holocene" by B.M. Vinther et al.: No Minoan tephra in the 1642 B.C. layer of the GRIP ice core", *Journal of Geophysical Research*, **113**, D04303, doi: 10.1029/2007JD008970

De Silva, S.L. and Zielinski, G.A. (1998) "Global influence of the AD1600 eruption of Huaynaputina, Peru", *Nature*, **393**, 455-458

Di Vito, M.A., Isaia, R., Orsi, G., Southon, J., de Vita, S., D'Antonio, M., Pappalardo, L. and Piochi, M. (1999) "Volcanism and deformation since 12000 years at the

Campi Flegrei caldera (Italy)", *Journal of Volcanology and Geothermal Research*, **91,** 221-246

Dugmore, A.J. (1989) "Icelandic volcanic ash in Scotland", *Scottish Geographical Magazine*, **105**, 168-172

Dugmore, A.J. and Newton, A.J. (1997) "Holocene tephra layers in the Faroe Islands", *Frodskaparrit,* **45,** 141-154

Eastwood, W.J., Pearce, N.J.G., Westgate, J.A. Perkins, W.T., Lamb, H.F. and Roberts, N. (1999) "Geochemistry of Santorini tephra in lake sediments from southwest Turkey", *Global and Planetary Change*, **21**, 17-29

Eastwood, W.J., Pearce, N.J.G., Westgate, J.A., Preece, S.J. and Perkins, W.T. (2004) "Tephra Geochemistry Confirms the Caldera-forming Eruption of Aniachak, not Santorini, at 1645BC", *PAGES News*, **12**, 12-15

Eiríksson, J., Knudsen, K.-L., Haflidason, H. and Henriksen, P. (2000) "Late-glacial and Holocene palaeoceanography of the North Icelandic shelf", *Journal of Quaternary Science*, **15**, 23-42

Elliot, M., Labeyrie, L., Bond, G., Cortijo, E., Turon, J.-L., Tisnerat, N. and Duplessy, J.-C. (1998) "Millennial-scale iceberg discharges in the Irminger Basin during the last glacial period: Relationship with the Heinrich events and environmental settings", *Paleoceanography*, **13**, 433-446

Elliot, M., Labeyrie, L., Dokken, T. and Manthé, S. (2001) "Coherent patterns of ice-rafted debris deposits in the Nordic regions during the last glacial (10-60 ka)", *Earth and Planetary Science Letters*, **194**, 151-163

Elliot, M., Labeyrie, L. and Duplessy, C.J. (2002) "Changes in North Atlantic deep-water formation associated with the Dansgaard-Oeschger temperature oscillations (60-10 ka)", *Quaternary Science Reviews,* **21**, 1153-1165

Emiliani, C. (1955) "Pleistocene Paleotemperatures", *Journal of Geology,* **63**, 539-578

Enache, M.D. and Cumming, B.F. (2006) "The morphological and optical properties of volcanic glass; a tool to assess density-induced vertical migration of tephra in sediment cores", *Journal of Paleolimnology*, **35**, 661-667

EPICA Community Members (2006) "One-to-one coupling of glacial climate variability in Greenland and Antarctica", *Nature*, **444**, 195-198

Fairbanks, R.G., Mortlock, R.A., Chiu, T.-C., Cao, L., Kaplan, A., Guilderson, T.P., Fairbanks, T.W., Bloom, A., Grootes, P.M. and Nadeau, M.-J. (2005) "Radiocarbon calibration curve spanning 0 to 50,000 years BP based on paired $^{230}Th/^{234}U/^{238}U$ and $^{14}C$ dates on pristine corals", *Quaternary Science Reviews*, **24**, 1781-1796

Fiacco, R.J., Palais, J.M., Germani, M.S., Zielinski, G.A. and Mayewski, P.A. (1993) "Characteristics and Possible Source of a 1479 A.D. Volcanic Ash Layer in a Greenland Ice Core", *Quaternary Research*, **39**, 267-273

Fiacco, R.J., Thordarson, T., Germani, M.S., Self, S., Palais, J.M., Whitlow, S. and Grootes, P.M. (1994) "Atmospheric Aerosol Loading and Transport Due to the 1783-84 Laki Eruption in Iceland, Interpreted from Ash Particles and Acidity in the GISP2 Ice Core", *Quaternary Research*, **42**, 231-240

Fisher, R.V. (1961) "Proposed classification of volcanoclastic sediments and rocks", *Geological Society of America Bulletin*, **72**, 1409-1414

Fisher, D.A. and Koerner, R.M. (1988) "The effects of wind on $\delta^{18}O$ and accumulation give an inferred record of seasonal $\delta$ amplitude from the Agassiz Ice Cap, Ellesmere Island, Canada", *Annals of Glaciology*, **10**, 34-37

Fraser, D.G. (1995) "The nuclear microprobe- PIXE, PIGE, RBS, NRA and ERDA". In Potts, P.J., Bowles, F.W., Reed, S.J.B. and Cave, M.R. (eds) *Microprobe Techniques in the Earth Sciences*, The Mineralogical Society, London

Froggatt, P.C. (1983) "Toward a comprehensive Upper Quaternary tephra and ignimbrite stratigraphy in New Zealand using electron microprobe analysis of glass shards", *Quaternary Research*, **19**, 188-200

Froggatt, P.C. (1992) "Standardization of the chemical analysis of tephra deposits. Report of the ICCT Working Group", *Quaternary International*, **13/14**, 93-96

Fronval, T., Jansen, E., Haflidason, H. and Sejrup, H.P. (1998) "Variability in Surface and Deep Water Conditions in the Nordic Seas during the Last Interglacial Period", *Quaternary Science Reviews*, **17**, 963-985

Gehrels, M.J., Newnham, R.M., Lowe, D.J., Wynne, S., Hazell, Z. and Caseldine, C. (2008) "Towards rapid assay of cryptotephra in peat cores: Review and evaluation of various methods", *Quaternary International*, **178**, 68-84

Genty, D., Blamart, D., Ouahdi, R., Gilmour, M., Baker, A., Jouzel, J. and Van-Exter, S. (2003) "Precise timing of Dansgaard-Oeschger climate oscillations in western Europe from stalagmite data", *Nature*, **421**, 833-837

Gibbard, P. and Van Kolfschoten, T. (2004) "The Pleistocene and Holocene Epochs". In Gradstein, F.M., Ogg, J.G. and Smith, A.G. (eds) *A Geologic Timescale 2004*, Cambridge University Press, Cambridge, pp. 441-452

Gonzalez, J., Mao, X.L., Roy, J., Mao, S.S. and Russo, R.E. (2002) "Comparison of 193, 213 and 266 nm laser ablation ICP-MS", *Journal of Analytical Atomic Spectrometry*, **17**, 1108-1113

Gorbarenko, S.A., Nürnberg, D., Derkachev, A.N., Astakhov, A.S., Southon, J.R. and Kaiser, A. (2002) "Magnetostratigraphy and tephrochronology of the Upper Quaternary sediments in the Okhotsk Sea: implication of terrigenous, volcanogenic and biogenic matter supply", *Marine Geology*, **183**, 107-129

Goujon, C., Barnola, J.-M. and Ritz, C. (2003) "Modeling the densification of polar firn including heat diffusion: Application to close-off characteristics and gas isotopic fractionation for Antarctica and Greenland sites", *Journal of Geophysical Research*, **108**, 4792, doi:10.1029/2002JD003319

Gray, A.L. (1985) "Solid sample introduction by laser ablation inductively coupled plasma mass spectrometry", *Analyst*, **61**, 551-556

Greenland Ice-core Project (GRIP) Members (1993) "Climate instability during the last interglacial period recorded in the GRIP ice core", *Nature*, **364**, 203-207

Grönvold, K. and Jóhannesson, H. (1984) "Eruption in Grímsvötn 1983; course of events and chemical studies of the tephra", *Jökull,* 34, 1-10

Grönvold, K., Óskarsson, N., Johnsen, S.J., Clausen, H.B., Hammer, C.U., Bond, G. and Bard, E. (1995) "Ash layers from Iceland in the Greenland GRIP ice core correlated with oceanic and land sediments", *Earth and Planetary Science Letters*, **135**, 149-155

Grootes, P.M. and Stuvier, M. (1997) "$^{18}O/^{16}O$ variability in Greenland snow and ice with $10^{-3}$ to $10^{5}$ year time resolution", *Journal of Geophysical Research*, **102**, 26455-26470

Grootes, P.M., Stuiver, M., White, J.W.C., Johnsen, S.J. and Jouzel, J. (1993) "Comparison of oxygen isotope records from GISP2 and GRIP Greenland ice cores", *Nature*, **366**, 552-554

Gudmundsson, A. (2000) "Dynamics of volcanic systems in Iceland: example of tectonism and volcanism at juxtaposed hotspots and mid-ocean ridge systems", *Annual Review of Earth and Planetary Sciences*, **28**, 107-140

Haflidason, H., Eiriksson, J. and Van Kreveld, S. (2000) "The tephrochronology of Iceland and the North Atlantic region during the Middle and Late Quaternary: a review", *Journal of Quaternary Science*, **15**, 3-22

Hall, V.A. and Pilcher, J.R. (2002) "Late-Quaternary Icelandic tephras in Ireland and Great Britain: detection, characterization and usefulness", *The Holocene*, **12**, 223-230

Hammer, C.U. (1980) "Acidity of Polar Ice Cores In Relation To Absolute Dating, Past Volcanism, and Radio-echoes", *Journal of Glaciology*, **25**, 359-372

Hammer, C.U., Clausen, H.B. and Dansgaard, W. (1980) "Greenland ice sheet evidence of post-glacial volcanism and its climatic impact", *Nature*, **288**, 230-235

Hammer, C.U., Kurat, G., Hoppe, P., Grum, W. and Clausen, H.B. (2003) "Thera Eruption Date 1645BC confirmed by new ice core data?". In Bietak, M. (ed) *The Synchronisation of Civilisations in the Eastern Mediterranean*, Austrian Academy of Science, Vienna, 87-94

Hansen, H. and Grönvold, K. (2000) "Plagioclase ultraphyric basalts in Iceland: the mush of the rift", *Journal of Volcanology and Geothermal Research*, **98**, 1-32

Hays, J.D., Imbrie, J. and Shackleton, N.J. (1976) "Variations in the earth's orbit: Pacemaker of the ice ages", *Science,* **194**, pp.1121-1132

Hemming, S.R. (2004) "Heinrich Events: massive late Pleistocene detritus layers of the North Atlantic and their global impact", *Review of Geophysics*, **42**, RG1005, doi:10.1029/2003RG000128

Hemond, C., Arndt, N.T., Lichtenstein, U. and Hofman, A.W. (1993) "The Heterogeneous Iceland Plume: Nd-Sr-O Isotopes and Trace Element Constraints", *Journal of Geophysical Research*, **98**, 15,833-15,850

Hendy, I.L. and Kennett, J.P. (2000) "Dansgaard/Oeschger cycles and the California current system: planktonic foraminiferal response to rapid climate change in Santa Barbara Basin, ODP hole 893A", *Paleoceanography*, **15**, 30-42

Herron, M.M. (1982) "Impurity sources of $F^-$, $Cl^-$, $NO_3^-$ and $SO_4^{2-}$ in Greenland and Antarctic precipitation", *Journal of Geophysical Research*, **87**, 3052-3060

Hewitt, A.T., McDonald, D. and Bornhold, B.D. (1997) "Ice-rafted debris in the North Pacific and correlation to North Atlantic climatic events", *Geophysical Research Letters*, **24**, 3261-3264

Hillenbrand, C.-D., Moreton, S.G., Caburlotto, A., Pudsey, C.J., Lucchi, R.G., Smellie, J.L., Benetti, S., Grobe, H., Hunt, J.B. and Larter, R.D. (2008) "Volcanic time-markers for Marine Isotope Stages 6 and 5 in Southern Ocean sediments and Antarctic ice cores: implications for tephra correlations between palaeoclimatic records", *Quaternary Science Reviews*, **27**, 518-540

Hinton, R.W. (1995) "Ion microprobe analysis in geology". In Potts, P.J., Bowles, F.W., Reed, S.J.B. and Cave, M.R. (eds) *Microprobe Techniques in the Earth Sciences*, The Mineralogical Society, London

Hodder, A.P.W., de Lange, P.J. and Lowe, D.J. (1991) "Dissolution and depletion of ferromagnesian minerals from Holocene tephra layers in an acid bog, New Zealand, and implications for tephra correlation", *Journal of Quaternary Science*, **6**, 195-208

Höskuldsson, Á., Óskarsson, N., Pedersen, R., Grönvold, K., Vogfjörð, K. and Ólafsdóttir, R. (2007) "The millennium eruption of Hekla in February 2000", *Bulletin of Volcanology,* **70**, 169-182

Höskuldsson, Á., Sparks, R.S.J. and Carroll, M.R. (2006) "Constraints on the dynamics of subglacial basalt eruptions from geological and geochemical observations at Kverkfjöll, NE-Iceland", *Bulletin of Volcanology*, **68**, 689-701

Hughen, K.A., Eglinton, T.I., Xu, L. and Makou, M. (2004) "Abrupt tropical vegetation response to rapid climate changes", *Science*, **304**, 1955-1959

Hughen, K., Southon, J., Lehman, S., Bertrand, C. and Turnbull, J. (2006) "Marine-derived $^{14}C$ calibration and activity record for the past 50,000 years updated from the Cariaco Basin", *Quaternary Science Reviews*, **25**, 3216-3227

Hunt, J.B. (2004) "Tephrostratigraphical evidence for the timing of Pleistocene explosive volcanism at Jan Mayen", *Journal of Quaternary Science*, **19**, 121-136

Hunt, J.B., Fannin, G.T., Hill P.G. and Peacock, J.D. (1995) "The tephrochronology and radiocarbon dating of North Atlantic, Late-Quaternary sediments: an example from the St. Kilda Basin". In Scrutton, R.A., Stoker, M.S., Shimmield, G.B. and Tudhope, A.W. (eds) *The Tectonics, Sedimentation and Palaeoceanography of the North Atlantic Region*, **90**, 227-240, Geological Society Special Publication, London

Hunt, J.B. and Hill, P.G. (1993) "Tephra geochemistry: a discussion of some persistent analytical problems", *The Holocene*, **3**, 271-278

Hunt, J.B. and Hill, P.G. (1996) "An inter-laboratory comparison of the electron probe microanalysis of glass geochemistry", *Quaternary International*, **34-36**, 229-241

Hunt, J.B. and Najman, Y.M.R. (2003) "Tephrochronological and tephrostratigraphical potential of Pliocene-Pleistocene volcaniclastic deposits in the Japan forearc, ODP Leg 186". In Suyehiro, K., Sachs, I.S., Acton, G.D. and Oda, M. (eds) *Proceedings of the Ocean Drilling Program, Scientific Results*, **186**, 1-29

Imbrie, J., Shackleton, N.J., Pisias, N.G., Morley, J.J., Prell, W.L., Martinson, D.G.,

Hayes, J.D., McIntyre, A. and Mix, A.C. (1984) "The orbital theory of Pleistocene climate: support from a revised chronology of the marine $\delta^{18}O$ record". In Berger, A. (ed) *Milankovitch and Climate, Part 1*, Reidel, Hingham, Massachusetts, pp.269-305

Imsland, P. (1978) *The geology of the volcanic island, Jan Mayen, Arctic Ocean*, Nordic Volcanological Institute Research Report 7813, University of Iceland, Reykjavik

Imsland, P. (1984) *Petrology and evolution of the Jan Mayen magma system*, Visindafelag Islendinga, **43**, 1-332

Jakobsson, S.P. (1972) "Chemistry and distribution pattern of recent basaltic rocks in Iceland", *Lithos*, **5**, 365-386

Jakobsson, S.P. (1979) "Petrology of recent basalts of the Eastern Volcanic Zone, Iceland", *Acta Naturalia Islandia*, **26**, 1-103

Jakobsson, S.P., Jónasson, K. and Sigurdsson, I.A. (2008) "The three igneous rock suites of Iceland", *Jökull*, **58**, 117-138

Jansen, J.H.F., Van der Gaast, S.J., Koster, B. and Vaars, A.J. (1998) "CORTEX, a shipboard XRF-scanner for element analyses in split sediment cores", *Marine Geology*, **151**, 143-153

Johannsdottir, G.E., Thordarson, T., and Geirsdottir, A. (2006) "The Widespread 10ka Saksunarvatn Tephra: A Product of Three Separate Eruptions?", *EOS Trans. AGU*, **87(52)**, Fall Meeting Supplement, Abstract V33B-0666

Johannsdottir, G.E., Thordarson, T., Geirsdottir, A. and Larsen, G. (2005), *The widespread ~10ka Saksunarvatn Tephra: A Product of three large Basaltic Phreatoplinian Eruptions*, Geophysical Research Abstracts Vol. 7, 05991. SRef-ID: 1607-7962/gra/EGU05-A-05991

Johnsen, S.J., Clausen, H.B., Dansgaard, W., Fuhrer, K., Gundestrup, N., Hammer, C.U., Iversen, P., Steffensen, J.P., Jouzel, J. and Stayffer, B. (1992) "Irregular glacial interstadials recorded in a new Greenland ice core", *Nature*, **359**, 311-313

Johnsen, S.J., Dahl-Jensen, D., Gundestrup, N., Steffensen, J.P., Clausen, H.B., Miller, H., Masson-Delmotte, V., Sveinbjörnsdottir, A.E. and White, J. (2001) "Oxygen isotope and palaeotemperature records from six Greenland ice-core stations: Camp Century, Dye-3, GRIP, GISP2, Renland and NorthGRIP", *Journal of Quaternary Science*, **16**, 299-307

Jónasson, K. (2007) "Silicic volcanism in Iceland: Composition and distribution within the active volcanic zones", *Journal of Geodynamics*, **43**, 101-117

Jull, M. and McKenzie, D. (1996) "The effect of deglaciation on mantle melting beneath Iceland", *Journal of Geophysical Research*, **101**, 21,815-21,828

Kaufman, D.S., Manley, W.F., Wolfe, A.P., Hu, F.S., Preece, S.J., Westgate, J.A. and Forman, S.L. (2001) "The Last Interglacial to Glacial Transition, Togiak Bay, Southwestern Alaska", *Quaternary Research*, **55**, 190-202

Keenan, D.J. (2003) "Volcanic ash retrieved from the GRIP ice core is not from Thera", *Geochemistry, Geophysics, Geosystems*, **4**, (www.agu.org/journals/gc/)

Kido, Y., Koshikawa, T. and Tada, R. (2006) "Rapid and quantitative major element analysis method for wet fine-grained sediments using an XRF microscanner", *Marine Geology*, **229**, 209-225

Kiefer, T., Sarnthein, M., Erlenkeuser, H., Grootes, P.M. and Roberts, A.P. (2001) "North Pacific response to millennial-scale changes in ocean circulation over the last 60 kyr", *Paleoceanography*, **16**, 179-189

Kitagawa, H. and van der Plicht, J. (2000) "Atmospheric radiocarbon calibration beyond 11,900 cal BP from Lake Suigetsu", *Radiocarbon,* **42**, 369-380

Knutti, R., Fluckiger, J., Stocker, T.F. and Timmerman, A. (2004) "Strong hemispheric coupling of glacial climate through freshwater discharge and ocean circulation", *Nature*, **430**, 851-856

Koren, J.H., Svendsen, J.I., Mangerud, J. and Furnes, H. (2008) "The Dimna Ash – a 12.8 $^{14}$C ka-old volcanic ash in Western Norway", *Quaternary Science Reviews*, **27**, 85-94

Kotilainen, A.T. and Shackleton, N.J. (1995) "Rapid climate variability in the North Pacific Ocean during the past 95,000 years", *Nature*, **377**, 323-326

Kristjánsdóttir, G.B., Stoner, J.S., Jennings, A.E., Andrews, J.T. and Grönvold, K. (2007) "Geochemistry of Holocene cryptotephras from the North Iceland Shelf (MD99-2269): intercalibration with radiocarbon and palaeomagnetic chronostratigraphies", *The Holocene*, **17**, 155-176

Kvamme, T., Mangerud, J., Furnes, H. and Ruddiman, W. (1989) "Geochemistry of Pleistocene ash zones in cores from the North Atlantic", *Norsk Geologisk Tidskrift*, **69**, 251-272

Kylander, M.E., Coulter, S., Klimaschewski, A. and Wohlfarth, B. (2008) "A New Analytical Technique for the Identification of Tephra Layers in Sediments", *Eos Trans. AGU,* **89(53),** Fall Meeting Supplement, Abstract PP11B-1394

Kyle, P.R., Jezek, P.A., Mosley-Thompson, E. and Thompson, L.G. (1981) "Tephra layers in the Byrd Station ice core and the Dome C ice core, Antarctica, and their climatic implications", *Journal of Volcanology and Geothermal Research*, **11**, 29-39

Lacasse, C. (2001) "Influence of climate variability on the atmospheric transport of Icelandic tephra in the subpolar North Atlantic", *Global and Planetary Change*, **29**, 31-55

Lacasse, C. and Garbe-Schönberg, C.-D. (2001) "Explosive volcanism on Iceland and the Jan Mayen area during the last 6Ma: sources and timing of major eruptions", *Journal of Volcanology and Geothermal Research*, **107**, 113-147

Lacasse, C., Paterne, M., Werner, R., Wallrabe-Adams, H.-J., Sigurdsson, H., Carey, S. and Pinte, G. (1996a) "Geochemistry and Origin of Pliocene and Pleistocene Ash Layers from the Iceland Plateau, Site 907". In Thiede, J., Myhre, A.M., Firth, J.V., Johnson, G.L. and Ruddiman, W.F. (eds) *Proceedings of the Ocean Drilling Program, Scientific Results*, **151**, 309-331

Lacasse, C., Sigurdsson, H., Carey, S.N., Jóhannesson, H., Thomas, L.E. and Rodgers, N.W. (2007) "Bimodal volcanism at the Katla subglacial caldera, Iceland: insight into the geochemistry and petrogenesis of rhyolitic magmas", *Bulletin of Volcanology*, **69**, 373-399

Lacasse, C., Sigurdsson, H., Carey, S. Paterne, M. and Guichard, F. (1996b) "North Atlantic deep-sea sedimentation of Late Quaternary tephra from the Iceland hotspot", *Marine Geology*, **129**, 207-235

Lacasse, C., Sigurdsson, H., Jóhannesson, H., Paterne, M. and Carey, S. (1995) "Source of Ash Zone 1 in the North Atlantic", *Bulletin of Volcanology*, **57**, 18-32

Lackschewitz, K.S., Baumann, K.-H., Gehrke, B., Wallrabe-Adams, H.-J., Thiede, J., Bonani, G., Endler, R., Erlenkeuser, H. and Heinemeier, J. (1998) "North Atlantic Ice Sheet Fluctuations 10,000-70,000 Yr Ago as Inferred from Deposits on the Reykjanes Ridge, Southeast of Greenland", *Quaternary Research*, **49**, 171-182

Lackschewitz, K.S. and Wallrabe-Adams, H.J. (1997) "Composition and origin of volcanic ash zones in Late Quaternary sediments from the Reykjanes Ridge: evidence for ash fallout and ice-rafting", *Marine Geology*, **136**, 209-224

Lamb, H.H. (1972) *Climate: Present, Past and Future. Fundamentals and Climate Now*, Methuen, London

Landais, A., Barnola, J.M., Masson-Delmotte, V., Jouzel, J., Chappellaz, J., Caillon, N., Huber, C., Leuenberger, M and Johnsen, S.J. (2004a) "A continuous record of temperature evolution over a sequence of Dansgaard-Oeschger events during Marine Isotopic Stage 4 (76-62 kyr BP)", *Geophysical Research Letters*, **31**, 10.1029/2003GB002122c

Landais, A., Caillon, N., Goujon, C., Grachev, A.M., Barnola, J.M., Chappellaz, J., Jouzel, J., Masson-Delmotte, V. and Leuenberger, M. (2004b) "Quantification of rapid temperature changes during DO event 12 and phasing with methane inferred from air isotopic measurements", *Earth and Planetary Science Letters*, **225**, 221-232

Landais, A. Jouzel, J., Masson-Delmotte, V. and Caillon, N. (2005) "Large temperature variations over rapid climatic events in Greenland: a method based on air isotopic measurements", *Comptes Rendus Geoscience*, **337**, 947-956

Lang, C., Leuenberger, M., Schwander, J. and Johnsen, S. (1999) "16°C rapid temperature variation in central Greenland 70,000 years ago", *Science*, **286**, 934-937

Langway, C.C., Osada, K., Clausen, H.B., Hammer, C.U. and Shoji, H. (1988) "An inter-hemispheric volcanic time-marker in ice cores from Greenland and Antarctica", *Annals of Glaciology*, **10**, 102-108

Larsen, G., Dugmore, A. and Newton, A. (1999) "Geochemistry of historical-age silicic tephras in Iceland", *The Holocene*, **9**, 463-471

Larsen, G. and Eiríksson, J. (2008) "Late Quaternary terrestrial tephrochronology of Iceland- frequency of explosive eruptions, type and volume of tephra deposits", *Journal of Quaternary Science*, **23**, 109-120

Larsen, G. Eiríksson, J., Knudsen, K.L. and Heinemeier, J. (2002) "Correlation of late Holocene terrestrial and marine tephra markers, north Iceland: implications for reservoir age changes", *Polar Research*, **21**, 283-290

Larsen, G., Newton, A.J., Dugmore, A.J. and Vilmundardóttir, E.G. (2001) "Geochemistry, dispersal, volumes and chronology of Holocene silicic tephra layers from the Katla volcanic system, Iceland", *Journal of Quaternary Science*, **16**, 119-132

Le Maitre, R.W., Bateman, P., Dudek, A., Keller, J., Lameyre, Le Bas, M.J., Sabine, P.A., Schmid, R., Sorensen, H., Streckeisen, A., Woolley, A.R. and Zanettin, B. (1989) *A Classification of Igneous Rocks and Glossary of Terms*, Blackwell, Oxford

Lim, C., Ikehara, K. and Toyoda, K. (2008) "Cryptotephra detection using high-resolution trace-element analysis of Holocene marine sediments, southwest Japan", *Geochimica et Cosmochimica Acta*, **72**, 5022-5036

Lowe, D.J. and Higham, T.F.G. (1998) "Hit-or-myth? Linking a 1259AD acid spike with an Okataina eruption", *Antiquity*, **72**, 427-431

Lowe, D.J. and Hunt, J.B. (2001) "A summary of terminology used in tephra-related studies". In Juvigné, E.T. and Raynal, J.-P. (eds) *Tephras: Chronology, Archaeology,* CDERAD editeur, Goudet (France). *Les Dossiers de l'Archeo-Logis,* **1**, 17-22

Lowe, J.J. (2001) "Abrupt climate changes in Europe during the last glacial-interglacial transition: the potential for testing hypotheses on the synchroneity of climate events using tephrochronology", *Global and Planetary Change*, **30**, 73-84

Lowe, J.J., Blockley, S., Trincardi, F., Asioli, A., Cattaneo, A., Matthews, I.P., Pollard, M. and Wulf, S. (2007) "Age modelling of late Quaternary marine sequences in the Adriatic: Towards improved precision and accuracy using volcanic event stratigraphy", *Continental Shelf Research*, **27**, 560-582

Lowe, J.J., Hoek, W., INTIMATE Group (2001) "Inter-regional correlation of palaeoclimate records for the Last Glacial-Interglacial Transition: a protocol for improved precision recommended by the INTIMATE project group", *Quaternary Science Reviews*, **20**, 1175-1187

Lowe, J.J., Rasmussen, S.O., Björck, S., Hoek, W., Steffensen, J.P., Walker, M.J.C., Yu, Z.C., INTIMATE group (2008) "Synchronisation of palaeoenvironmental events in the North Atlantic region during the Last Termination: a revised protocol recommended by the INTIMATE group", *Quaternary Science Reviews*, **27**, 6-17

Lowe, J.J. and Turney, C.S.M. (1997) "Vedde Ash layer discovered in small lake basin on Scottish mainland", *Journal of the Geological Society*, **154**, 605-612

Lowe, J.J. and Walker, M.J.C. (1997) *Reconstructing Quaternary Environments*, Prentice Hall, Harlow

Maaløe, S., Sørensen, I., and Hertogen, J. (1986) "The Trachybasaltic Suite of Jan Mayen", *Journal of Petrology*, **27**, 439-466

MacAyel, D.R. (1993) "Binge/purge oscillations of the Laurentide Ice Sheet as a cause of the North Atlantic's Heinrich events", *Palaeoceanography*, **8**, 775-784

MacDonald, G.A. and Katsura, T. (1964) "Chemical composition of Hawaiian lavas", *Journal of Petrology*, **5**, 83-133

Machida, H. (1999) "The stratigraphy, chronology and distribution of distal marker-tephras in and around Japan", *Global and Planetary Change*, **21**, 71-94

Mackie, E., Davies, S.M., Turney, C.S.M., Dobbyn, K., Lowe, J.J. and Hill, P. (2002) "The use of magnetic separation techniques to detect basaltic microtephra in last glacial-interglacial transition (LGIT: 15-10 ka cal. BP) sediment sequences in Scotland", *Scottish Journal of Geology*, **38 (1)**, 21-30

Mangerud, J., Furnes, H. and Jóhansen, J. (1986) "A 9000-year-old ash bed on the Faroe Islands", *Quaternary Research*, **26**, 262-265

Manning, S.W. (1998) "Correction. New GISP2 Ice-Core Evidence Supports 17$^{th}$ Century BC Date for the Santorini (Minoan) Eruption: Response to Zielinski and Germani (1998)", *Journal of Archaeological Science*, **25**, 1039-1042

Marshall, S.J. and Koutnik, M.R. (2006) "Ice sheet action versus reaction: Distinguishing between Heinrich events and Dansgaard-Oeschger cycles in the North Atlantic", *Paleoceanography*, **21**, PA2021, doi:10.1029/2005PA001247

Martrat, B., Grimalt, J.O., Shackleton, N.J., de Abreu, L., Hutterli, M.A. and Stocker, T.F. (2007) "Four climate cycles of recurring deep and surface water destabilizations on the Iberian Margin", *Science*, **317**, 502-507

Martinson, D.G., Pisias, N.G., Hays, J.D., Imbrie, J., Moore, T.C. and Shackleton, N.J. (1987) "Age dating and the orbital theory of the ice ages: development of a high resolution 0-300,000 year Chronostratigraphy", *Quaternary Research*, **27**, pp.1-29

Maslin, M., Seidov, D. and Lowe, J.J. (2001) "Synthesis of the Nature and Causes of Rapid Climate Transitions During the Quaternary". In Seidov, D., Maslin, M. and Haupt, B.J. (eds), *The Oceans and Rapid Climate Change: Past, Present and Future*, American Geophysical Monograph 126, pp.9-52

Matthews, R.K. (1969) "Tectonic implications of glacio-eustatic sea level fluctuations", *Earth and Planetary Science Letters*, **5**, 459-462

Mayewski, P.A., Holdsworth, G., Spencer, M.J., Whitlow, S., Twickler, M., Morrison, M.C., Ferland, K.K. and Meeker, L.D. (1993) "Ice core sulfate from three northern hemisphere sites: Source and temperature forcing implications", *Atmospheric Environment Part A*, **27**, 2915-2919

Mayewski, P.A., Meeker, L.D., Twickler, M.S., Whitlow, S., Yang, Q., Berry Lyons, W. and Prentice, M. (1997) "Major features and forcing of high-latitude northern hemisphere atmospheric circulation using a 110,000-year-long glaciochemical series", *Journal of Geophysical Research*, **102**, 26345-26366

Mayewski, P.A., Meeker, L.D., Whitlow, S., Twickler, M.S., Morrison, M.C., Bloomfield, P., Bond, G.C., Alley, R.B., Gow, A.J., Grootes, P.M., Meese, D.A., Ram, M., Taylor, K.C. and Wumkes, W. (1994) "Change in atmospheric circulation and ocean ice cover over the North Atlantic during the last 41,000 years", *Science*, **263**, 1747-1751

McCabe, A.M. and Clark, P.U. (1998) "Ice sheet variability around the North Atlantic Ocean during the last deglaciation", *Nature*, **392**, 373-377

McGarvie, D. (2009) "Rhyolitic volcano-ice interactions in Iceland", *Journal of Volcanology and Geothermal Research,* **185,** 367-389

Meyer, P.S., Sigurdsson, H. and Schilling, J.-G. (1985) "Petrological and Geochemical Variations Along Iceland's Neovolcanic Zones", *Journal of Geophysical Research*, **90**, 10,043-10,072

Milankovitch, M. (1941) *Canon of Insolation and the Ice Age Problem,* Koniglich Serbische Akademie, Belgrade

Mortensen, A.K., Bigler, M., Grönvold, K., Steffensen, J.P., and Johnsen, S.J. (2005) "Volcanic ash layers from the Last Glacial Termination in the NGRIP ice core", *Journal of Quaternary Science*, **20**, 209-219

Murphy, J.J. (1876) "The Glacial Climate and the Polar Ice-Cap", *Quarterly Journal of the Geological Society of London*, **32**, 400-406

Nakada, M. and Yokose, H. (1992) "Ice age as a trigger of active Quaternary volcanism and tectonism", *Tectonophysics*, **212**, 321-329

Nakagawa, T. (2008) *Lake Suigetsu SG06 sediment core: Project outline, some early (but significant) results and near future perspectives*, 10th INTIMATE Conference, Oxford, England

Nielsen, T., Rasmussen, T.L., Ceramicola, S. and Kuijpers, A. (2007) "Quaternary sedimentation, margin architecture and ocean circulation variability around the Faroe Islands, North Atlantic", *Quaternary Science Reviews*, **26**, 1016-1036

Norddahl, H. and Haflidason, H. (1992) "The Skogar Tephra, a Younger Dryas marker in North Iceland", *Boreas*, **21**, 23-41

North Greenland Ice Core Project Members (2004) "High-resolution record of Northern Hemisphere climate extending into the last interglacial period", *Nature,* 431, pp. 147-151

Óladóttir, B. A., Sigmarsson, O., Larsen, G. and Thordarson, T. (2008) "Katla volcano, Iceland: magma composition, dynamics and eruption frequency as recorded by Holocene tephra layers", *Bulletin of Volcanology*, **70**, 475-493

O'Nions, R.K. and Grönvold, K. (1973) "Petrogenetic Relationships of Acid and Basic Rocks in Iceland: Sr-Isotopes and Rare-Earth Elements in Late and Postglacial Volcanics", *Earth and Planetary Science Letters*, **19**, 397-409

O'Nions, R.K., Pankhurst, R.J., Fridleifsson, I.B. and Jakobsson, S.P. (1973) "Strontium Isotopes and Rare Earth Elements in Basalts from the Heimaey and Surtsey Volcanic Eruptions", *Nature*, **243**, 213-214

O'Nions, R.K., Pankhurst, R.J. and Grönvold, K. (1976) "Nature and Development of Basalt Magma Sources Beneath Iceland and the Reykjanes Ridge", *Journal of Petrology*, **17**, 315-338

Oppenheimer, C. (2002) "Limited global change due to the largest known Quaternary eruption, ~74kyr BP?", *Quaternary Science Reviews*, **21**, 1593-1609

Oppenheimer, C. (2003) "Ice Core and Palaeoclimatic Evidence for the Timing and Nature of the Great Mid-13$^{th}$ Century Volcanic Eruption", *International Journal of Climatology,* **23**, 417-426

Ortega-Guerreo, B. and Newton, A.J. (1998) "Geochemical Characterization of Late Pleistocene and Holocene Tephra Layers from the Basin of Mexico, Central Mexico", *Quaternary Research*, **50**, 90-106

Ortiz, J.D., O'Connell, S.B., DelViscio, J., Dean, W., Carriquiry, J.D., Marchitto, T., Zheng, Y. and van Geen, A. (2004) "Enhanced marine productivity off western North America during warm climate intervals of the past 52ky", *Geology*, **32**, 521-524

Óskarsson, N., Sigvaldason, G.E. and Steinthórsson, S. (1982) "A Dynamic Model of Rift Zone Petrogenesis and the Regional Petrology of Iceland", *Journal of Petrology*, **23**, 28-74

Palais, J.M., Germani, M.S. and Zielinski, G.A. (1992) "Inter-hemispheric transport of volcanic ash from a 1259A.D. volcanic eruption to the Greenland and Antarctic ice sheets", *Geophysical Research Letters*, **19**, 801-804

Palais, J.M., Kirchner, S. and Delmas, R.J. (1990) "Identification of some global volcanic horizons by major element analysis of fine ash in Antarctic ice", *Annals of Glaciology*, **14**, 216-220

Palais, J.M., Taylor, K., Mayewski, P.A. and Grootes, P. (1991) "Volcanic ash from the 1362AD Oraefajokull eruption (Iceland) in the Greenland Ice Sheet", *Geophysical Research Letters*, **18**, 1241-1244

Paterne, M., Guichard, F., Labeyrie, J., Gillot, P.Y. and Duplessy, J.C. (1986) "Tyrrhenian Sea tephrochronology of the oxygen isotope record for the past 60,000 years", *Marine Geology*, **72**, 259-285

Patience, A.J. and Kroon, D. (1991) "Oxygen Isotope Chronostratigraphy". In Smart, P.L. and Frances, P.D. (eds) *Quaternary Dating Methods-A User's Guide*, Technical Guide 4, Quaternary Research Association, pp.119-228

Pearce, N.J.G., Alloway, B.V. and Westgate, J.A. (2008a) "Mid-Pleistocene silicic tephra beds in the Auckland region, New Zealand: Their correlation and origins based on the trace element analyses of single glass shards", *Quaternary International,* **178**, 16-43

Pearce, N.J.G., Bendall, C.A. and Westgate, J.A. (2008b) "Comment on "Some numerical considerations in the geochemical analysis of distal microtephra" by A.M. Pollard, S.P.E. Blockley and C.S. Lane", *Applied Geochemistry*, **23**, 1353-1364

Pearce, N.J.G., Denton, J.S., Perkins, W.T., Westgate, J.A., and Alloway, B.V. (2007) "Correlation and characterisation of individual glass shards from tephra deposits using trace element laser ablation ICP-MS analyses: current status and future potential", *Journal of Quaternary Science*, **22**, 721-736

Pearce, N.J.G., Eastwood, W.J., Westgate, J.A. and Perkins, W.T. (2002) "Trace-element composition of single glass shards in distal Minoan tephra from SW Turkey", *Journal of the Geological Society, London*, **159**, 545-556

Pearce, N.J.G., Perkins, W.T., Westgate, J.A., Gorton, M.P., Jackson, S.E., Neal, C.R. and Chenery, S.P. (1997) "A compilation of new and published major and trace element data for NIST SRM 610 and NIST SRM 612 glass reference materials", *Geostandards Newsletter*, **21**, 151-171

Pearce, N.J.G., Westgate, J.A. and Perkins. W.T. (1996) "Developments in the analysis of volcanic glass shards by laser ablation ICP-MS: quantitative and single internal standard-multi-element methods", *Quaternary International*, **34-36**, 213-227

Pearce, N.J.G., Westgate, J.A., Perkins, W.T., Eastwood, W.J. and Shane, P. (1999) "The application of laser ablation ICP-MS to the analysis of volcanic glass shards from tephra deposits: bulk glass and single shard analysis", *Global and Planetary Change*, **21**, 151-171

Pearce, N.J.G., Westgate, J.A., Perkins, W.T. and Preece, S.J. (2004a) "The application of ICP-MS methods to tephrochronological problems", *Applied Geochemistry*, **19**, 289-322

Pearce, N.J.G., Westgate, J.A., Preece, S.J., Eastwood, W.J. and Perkins, W.T. (2004b) "Identification of Aniakchak (Alaska) tephra in Greenland ice core challenges the 1645BC date for Minoan eruption of Santorini", *Geochemistry, Geophysics, Geosystems*, **5** (www.agu.org/journals/gc/)

Perkins, M.E., Brown, F.H., Nash, W.P., McIntosh, W. and Williams, S.K. (1998) "Sequence, age, and source of silicic fallout tuffs in middle to late Miocene basins of the northern Basin and Range province", *Bulletin of the Geological Society of America*, **110**, 344-360

Perkins, M.E., Nash, W.P., Brown, F.H. and Fleck, R.J. (1995) "Fallout tuffs of Trapper Creek, Idaho – a record of Miocene explosive volcanism in the Snake River Plain volcanic province", *Bulletin of the Geological Society of America*, **107**, 1484-1506

Perkins, W.T. and Pearce, N.J.G. (1995) "Mineral microanalysis by laserprobe inductively coupled plasma mass spectrometry". In Potts, P.J., Bowles, J.F.W., Reed, S.J.B. and Cave, M.R. (eds) *Microprobe techniques in the Earth Sciences*, The Mineralogical Society, London

Perkins, W.T., Pearce, N.J.G. and Westgate, J.A. (1997) "Calibration strategies for laser ablation ICP-MS: examples from the analysis of trace elements in volcanic glass shards and sulphide minerals", *Geostandards Newsletter*, **21**, 175-190

Peterson, L.C. and Huag, G.H. (2006) "Variability in the mean latitude of the Atlantic Intertropical Convergence Zone as recorded by riverine input of sediments to the Cariaco Basin (Venezuela)", *Palaeogeography, Palaeoclimatology, Palaeoecology*, **234**, 97-113

Peterson, L.C., Haug, G.H., Hughen, K.A. and Röhl, U. (2000) "Rapid changes in the hydrological cycle of the tropical Atlantic during the last glacial", *Science*, **290**, 1947-1951

Pisias, N.G., Martinson, D.G., Moore Jr, T.C., Shackleton, N.J., Prell, W., Hays, J. and Boden, G. (1984) "High Resolution Stratigraphic Correlation of Benthic Oxygen Isotopic Records Spanning the Last 300,000 years", *Marine Geology*, **56**, 119-136

Pollard, A.M., Blockley, S.P.E. and Lane, C.S. (2006) "Some numerical considerations in the geochemical analysis of distal microtephra", *Applied Geochemistry*, **21**, 1692-1714

Potts, P.J., Thompson, M. and Wilson, S. (2002) "G-Probe-1- An international proficiency test for microprobe laboratories-Report on Round 1: February 2002 (TB1 basaltic glass)", *Geostandards Newsletter: the Journal of Geostandrards and Geoanalysis*, **26**, 197-235

Preece, S.J., Westgate, J.A., Alloway, B.V. and Milner, M.W. (2000) "Characterization, identity, distribution and source of late Cenozoic tephra beds in the Klondike district of the Yukon, Canada", *Canadian Journal of Earth Sciences*, **37**, 983-996

Preece, S.J., Westgate, J.A., Stemper, B.A. and Péwé, T.L. (1999) "Tephrochronology of late Cenozoic loess at Fairbanks, central Alaska", *GSA Bulletin*, **111**, 71-90

Pyne-O'Donnell, S.D.F., Blockley, S.P.E., Turney, C.S.M. and Lowe, J.J. (2007) "Distal volcanic ash layers in the Lateglacial Interstadial (GI-1): problems of stratigraphic discrimination", *Quaternary Science Reviews*, **27**, 72-84

Rahmstorf, S. (2003) "Timing of abrupt climate change: A precise clock", *Geophysical Research Letters*, **30**, 1510, doi:10.1029/2003GL017115

Ram, M., Donarummo Jr., J. and Sheridan, M. (1996) "Volcanic ash from Icelandic ~57, 300 yr BP eruption found in GISP 2 (Greenland) ice core", *Geophysical Research Letters*, **23**, 3167-3169

Rampino, M.R. and Self, S. (1993) "Climate-volcanism feedback and the Toba eruption of ~74,000 years ago", *Quaternary Research*, **40**, 269-280

Rampino, M.R., Self, S. and Fairbridge, R.W. (1979) "Can rapid climatic change cause volcanic eruptions?", *Science*, **206**, 826-829

Ranner, P.H., Allen, J.R.M. and Huntley, B. (2005) "A new early Holocene cryptotephra from northwest Scotland", *Journal of Quaternary Science*, **20**, 201-208

Rasmussen, S.O., Andersen, K.K., Svensson, A.M., Steffensen, J.P., Vinther, B.M., Clausen, H.B., Siggaard-Andersen, M.-L., Johnsen, S.J., Larsen, L.B., Dahl-Jensen, D., Bigler, M., Röthlisberger, R., Fischer, H., Goto-Azuma, K., Hansson, M.E. and Ruth, U. (2006) "A new Greenland ice core chronology for the last glacial termination", *Journal of Geophysical Research*, **111**, D06102, doi:10.1029/2005JD006079

Rasmussen, S.O., Seierstad, I.K., Andersen, K.K., Bigler, M., Dahl-Jensen, D. and Johnsen, S.J. (2008) "Synchronisation of the NGRIP, GRIP and GISP2 ice cores across MIS 2 and palaeoclimatic implications", *Quaternary Science Reviews*, **27**, 18-28

Rasmussen, T.L., Thomsen, E., Nielsen, T. and Wastegård, S. (submitted) "Continuous flow of Atlantic surface water into the Nordic Seas 12,600-10,000 cal. years BP", *Quaternary Science Reviews*

Rasmussen, T.L., Thomsen, E., Tjeerd, C.E., van Veering, T.C.E. and Labeyrie, L.D. (1996) "Rapid changes in the surface and deep water conditions at the Faeroe Margin during the last 58, 000 years", *Paleoceanography*, **11**, 757-771

Rasmussen, T.L., Van Weering, T.C.E. and Labeyrie, L. (1997) "Climatic Instability, Ice Sheets and Ocean Dynamics at High Northern Latitudes During the Last Glacial Period (58-10 ka BP)", *Quaternary Science Reviews*, **16**, 71-80

Rasmussen, T.L., Wastegård, S., Kuijpers, A., Van Weering, T.C.E., Heinemeier, J. and Thomsen, E. (2003) "Stratigraphy and distribution of tephra layers in marine sediment cores from the Faeroe Islands, North Atlantic", *Marine Geology*, **199**, 263-277

Reed, S.J.B. (1993) *Electron microprobe analysis. Cambridge Monographs on Physics*, second edition, Cambridge University Press, Cambridge

Reed, S.J.B. (2005) *Electron Microprobe Analysis and Scanning Electron Microscopy in Geology*, second edition, Cambridge University Press, Cambridge

Richter, T.O., Van der Gaast, S.J., Koster, B., Vaare, A., Gieles, R., de Stiger, H.C., de Haas, H. and van Weering, T.C.E. (2006) "The Avaatech XRF core scanner: technical description and application to NE Atlantic sediments". In Rothwell, G. (ed.) *New Techniques in Sediment Core Analysis*, Geological Society Special Publication, London, **267**, 39-50

Rohling, E.J., Mayewski, P.A. and Challenor, P. (2003) "On the timing and mechanism of millennial-scale climate variability during the last glacial cycle", *Climate Dynamics*, **20**, 257-267

Rollinson, H. (1993) *Using Geochemical Data: Evaluation, Presentation, Interpretation*, Longman, Harlow

Rooth, C. (1982) "Hydrology and ocean circulation", *Progress in Oceanography*, **11**, 131-149

Rose, W.I. Jr. (1977) "Scavenging of volcanic aerosol by ash: Atmospheric and volcanologic implications", *Geology*, **5**, 621-624

Rose, N.L., Golding, P.N.E. and Batterbee, R.W. (1996) "Selective concentration and enumeration of tephra shards from lake sediment cores", *Holocene*, **6**, 243-246

Röthlisberger, R., Bigler, M., Hutterli, M., Sommer, S., Stauffer, B., Junghans, H.G. and Wagenbach, D. (2000) "Technique for Continuous High-Resolution Analysis of Trace Substances in Firn and Ice Cores", *Environmental Science and Technology*, **34**, 338-342

Ruddiman, W. and Glover, R. (1972) "Vertical mixing of ice-rafted volcanic ash in North Atlantic sediments", *Geological Society Bulletin*, **83**, 2817-2836

Ruth, U., Wagenbach, D., Bigler, M., Steffensen, J.P., Röthlisberger, R. and Miller, H. (2002) "High-resolution microparticle profiles at NorthGRIP, Greenland: case studies of the calcium-dust relationship", *Annals of Glaciology*, **35**, 237-242

Ruth, U., Wagenbach, D., Steffensen, J.P. and Bigler, M. (2003) "Continuous record of microparticle concentration and size distribution in the central Greenland NGRIP ice core during the last glacial period", *Journal of Geophysical Research*, **108(D3)**, 4098, doi: 10.1029/2002JD002376

Sakamoto, T., Ikehara, M., Uchida, M., Aoki, K., Shibata, Y., Kanamatsu, T., Harada, N., Iijima, K., Katsuki, K., Asahi, H., Takahashi, K., Sakai, H. and Kawahata, H. (2006) "Millennial-scale variations of sea-ice expansion in the southwestern part of the Okhotsk Sea during the past 120kyr: Age model and ice-rafted debris in IMAGES Core MD01-2412", *Global and Planetary Change*, **53**, 58-77

Schmid, P., Peltz, C., Hammer, V.M.F., Halwax, E., Ntaflos, T., Nagl, P. and Bichler, M. (2000) "Separation and Analysis of Theran Volcanic Glass by INAA, XRF and EPMA", *Microchimica Acta*, **133**, 143-149

Schupack, B.B., Miller, G.H. and Larsen, D.J. (2008) *Detecting the Unseen: A New Analytical Approach Towards the Identification of Cryptotephras in Distal Lacustrine Archives,* 38th International Arctic Workshop, Boulder, Colorado

Schulz, H., Emeis, K.-C., Erlenkeuser, H., von Rad, U. and Rolf, C. (2002) "The Toba Volcanic Event and Interstadial/Stadial Climates at the Marine Isotopic Stage 5 to 4 Transition in the Northern Indian Ocean", *Quaternary Research*, **57**, 22-31

Schulz, H., von Rad, U. and Erlenkeuser, H. (1998) "Correlation between Arabian Sea and Greenland climate oscillations of the past 110,00 years", *Nature*, **393**, 54-57

Severinghaus J.P. and Brook, J. (1999) "Abrupt climate change at the end of the last glacial period inferred from trapped air in polar ice", *Science*, **286**, 930-934

Shackleton, N.J. (1967) "Oxygen isotope analyses and Pleistocene temperatures re-assessed", *Nature*, **215**, 15-17

Shackleton, N.J. (1987) "Oxygen Isotopes, Ice Volume and Sea Level", *Quaternary Science Reviews*, **6**, 183-190

Shackleton, N.J. and Opdyke, N.D. (1973) "Oxygen isotope and paleomagnetic stratigraphy of equatorial Pacific core V28-238: oxygen isotope temperatures and ice volume on a $10^5$ and $10^6$ year scale", *Quaternary Research*, **3**, 39-55

Shane, P. (2000) "Tephrochronology: a New Zealand case study", *Earth-Science Reviews*, **49**, 223-259

Shane, P.A., Black, T.M., Eggins, S.M. and Westgate, J.A. (1998) "Late Miocene marine tephra beds: recorders of rhyolitic volcanism in North Island, New Zealand", *New Zealand Journal of Geology and Geophysics*, **41**, 165-178

Sigmarsson, O., Óladóttir, B., Larsen, G. and Thordarson, T. (2005) *Temporal variations of trace element ratios in basaltic tephra from Katla volcano, Iceland: a reconnaissance study*, Geophysical Research Abstracts Vol. 7, 10182, SRef-ID: 1607-7962/gra/EGU05-A-10182

Sigmarsson, O., Óladóttir, B., Mason, P., Larsen, G. and Thordarson, T. (2008) *Can changes in mantle melting affect magma chambers? Clues from trace elements in tephra from Katla volcano and Eldgjá basalts, Iceland*, IAVCEI 2008 General Assembly, Reykjavik, Iceland, Abstracts: Oral Presentations: Thursday, p. 20

Sigurdsson, H., Schilling, J.-G. and Meyer, P.S. (1978) "Skagi and Langjökull Volcanic Zones in Iceland: 1. Petrology and Structure", *Journal of Geophysical Research*, **83**, 3971-3982

Sjøholm, J., Sejrup, H.P. and Furnes, H. (1991) "Quaternary volcanic ash zones on the Iceland Plateau, southern Norwegian Sea", *Journal of Quaternary Science*, **6**, 159-173

Smith, V.C., Shane, P. and Nairn, I.A. (2005) "Trends in rhyolite geochemistry, mineralogy and magma storage during the last 50 kyr at Okataina and Taupo volcanic centres, Taupo Volcanic Zone, New Zealand", *Journal of Volcanology and Geothermal Research*, **148**, 372-406

Smith, D.G.W. and Westgate, J.A. (1969) "Electron probe technique for characterising pyroclastic deposits", *Earth and Planetary Science Letters*, **5**, 313-319

Song, S.-R., Chen, C.-H., Lee., M.-Y., Yang, T.F., Iizuka, Y. and Wei, K.-Y. (2000) "Newly discovered eastern dispersal of the youngest Toba Tuff", *Marine Geology*, **167**, 303-312

Sparks, R.S.J., Bursik, M.I., Carey, S.N., Gilbert, J.S., Glaze, L.S., Sigurdsson, H. and Woods, A.W. (1997) *Volcanic Plumes*, Wiley, Chichester

Stocker, T.F. (2000) "Past and future reorganisation in the climate system", *Quaternary Science Reviews*, **19**, 301-319

Sun, S.S. and McDonough, W.F. (1989) "Chemical and isotopic systems of oceanic basalts: implications for mantle composition and processes". In Saunders, A.D. and Norry, M.J. (eds) *Magmatism in ocean basins*, Geol. Soc. London Spec. Pub., **42,** 313-345

Svensson, A., Andersen, K.K., Bigler, M., Clausen, H.B., Dahl-Jensen, D., Davies, S.M., Johnsen, S.J., Muscheler, R., Parrenin, F., Rasmussen, S.O., Röthlisberger, R., Seierstad, I., Steffensen, J.P. and Vinther, B.M. (2008) "A 60 000 year Greenland stratigraphic ice core chronology", *Climate of the Past*, **4**, 47-57

Svensson, A., Andersen, K.K., Bigler, M., Clausen, H.B., Dahl-Jensen, D., Davies, S.M., Johnsen, S.J., Muscheler, R., Rasmussen, S.O., Röthlisberger, R., Steffensen, J.P. and Vinther, B.M. (2006) "The Greenland Ice Core Chronology 2005, 15-42ka. Part 2: comparison to other records", *Quaternary Science Reviews*, **25**, 3258-3267

Svensson, A., Biscaye, P.E. and Grousset, F.E. (2000) "Characterisation of late glacial continental dust in the Greenland Ice Core Project ice core", *Journal of Geophysical Research*, **105**, 4637-4656

Svensson, A., Nielsen, S.W., Kipfstuhl, S., Johnsen, S.J., Steffensen, J.P., Bigler, M., Ruth, U. and Röthlisberger, R. (2005) "Visual stratigraphy of the North Greenland Ice Core Project (NorthGRIP) ice core during the last glacial period", *Journal of Geophysical Research*, **110**, D02108, doi:10.1029/2004JD005134

Taylor, K., Alley, R., Fiaccio, J., Grootes, P., Lamorey, G., Mayewski, P. and Spencer, M.J. (1992) "Ice-core dating and chemistry by direct-current electric conductivity", *Journal of Glaciology*, **38**, 325-332

Textor, C., Graf, H.-F., Timmreck, C. and Robock, A. (2004) "Emissions from volcanoes". In Granier, C., Artaxo, P. and Reeves, C. (eds) *Emissions of Atmospheric Trace Compounds*, Kluwer, Dordrecht, 269-303

Thorarinsson, S. (1944) "Tefrokronologiska studier på Island", *Geografiska Annaler,* **26**, 1-217

Thorarinsson, S. (1974) *The Swift Flowing Rivers- The History of Grimsvötn Eruptions and Jökulhlaups in Skeidara*, Menningarsjodur Publishing, Reykjavik

Thordarson, T. and Hoskuldsson, Á. (2008) "Postglacial volcanism in Iceland", *Jökull,* **58**, 197-228

Thordarson, T. and Larsen, G. (2007) "Volcanism in Iceland in historical time: volcano types, eruption styles and eruptive history", *Journal of Geodynamics*, **43**, 118-152

Timmerman, A. and Menviel, L. (2009) "What Drives Climate Flip-Flops?", *Science*, **325**, 273-274

Toms, P.S., King, M., Zárate, M.A., Kemp, R.A. and Foit Jr., F.F. (2004) "Geochemical characterization, correlation, and optical dating of tephra in alluvial sequences of central western Argentina", *Quaternary Research*, **62**, 60-75

Ton-That, T., Singer, B. and Paterne, M. (2001) "$^{40}Ar/^{39}Ar$ dating of latest Pleistocene (41ka) marine tephra in the Mediterranean Sea: implications for global climate records", *Earth and Planetary Science Letters*, **184**, 645-658

Turney, C.S.M. (1998) "Extraction of rhyolitic ash from minerogenic lake sediments", *Journal of Paleolimnology*, **19**, 199-206

Turney, C.S.M., Harkness, D.D. and Lowe, J.J. (1997) "The use of microtephra horizons to correlate Late-glacial lake sediment successions in Scotland", *Journal of Quaternary Science*, **12**, 525-531

Turney, C.S.M., Lowe, J.J., Davies, S.M., Hall, V., Lowe, D.J., Wastegård, S., Hoek, W.Z., Alloway, B. and SCOTAV and INTIMATE Members (2004) "Tephrochronology of Last Termination Sequences in Europe: a protocol for improved analytical precision and robust correlation procedures (a joint SCOTAV-INTIMATE proposal)", *Journal of Quaternary Science*, **19**, 111-120

Urey, H.C. (1948) "Oxygen isotopes in nature and the laboratory", *Science*, **108**, 489-496

Van Den Bogaard, C. and Schmincke, H.-U. (2002) "Linking the North Atlantic to central Europe: a high-resolution Holocene tephrochronological record from northern Germany", *Journal of Quaternary Science*, **17**, 3-20

Van der Plicht, J., Beck, J.W., Bard, E., Baillie, M.G.L., Blackwell, P.G., Buck, C., Freidrich, M., Guilderson, T.P., Hughen, K.A., Kromer, B., McCormac, F.G.,

Bronk Ramsey, C., Reimer, P.J., Reimer, R.W., Remmele, S., Richards, D.A., Southon, J.R., Stuvier, M. and Weyhenmeyer, C.E. (2004) "Notcal04 – comparison/calibration $^{14}C$ records 26-50 cal kyr BP", *Radiocarbon*, **46**, 1225-1238

Van Geel, B., Raspopov, O.M., Renssen, H., van der Plicht, J., Dergachev, V.A. and Meijer, H.A.J. (1999) "The role of solar forcing upon climate change", *Quaternary Science Reviews*, **18**, 331-338

Van Kreveld, S., Sarnthein, M., Erlenkeuser, H., Grootes, P., Jung, S., Nadeau, M.J., Pflaumann, U. and Voelker, A. (2000) "Potential links between surging ice sheets, circulation changes, and the Dansgaard-Oeschger cycles in the Irminger Sea, 60-18 kyr", *Paleoceanography*, **15**, 425-442

Veres, D., Wohlfarth, B., Andrieu-Ponel, V., Björck, S., de Beaulieu, J.-L., Digerfeldt, G., Ponel, P., Ampel, L., Davies, S., Gandouin, E. and Belmecheri, S. (2007) "The lithostratigraphy of the Les Echets basin, France: tentative correlation between cores", *Boreas,* **36**, 326-340

Vinther, B.M., Clausen, H.B., Johnsen, S.J., Rasmussen, S.O., Andersen, K.K., Buchardt, S.L., Dahl-Jensen, D, Seierstad, I.K., Siggaard-Andersen, M.-L., Steffensen, J.P., Svensson, A., Olsen, J. and Heinemeier, J. (2006) "A synchronised dating of three Greenland ice cores throughout the Holocene", *Journal of Geophysical Research*, **111**, doi: 10.1029/2005JD006921

Vinther, B.M., Clausen, H.B., Johnsen, S.J., Rasmussen, S.O., Steffensen, J.P., Andersen, K.K., Buchardt, S.L., Dahl-Jensen, D, Seierstad, I.K., Svensson, A., Siggaard-Andersen, M.-L., Olsen, J. and Heinemeier, J. (2008) "Reply to comment by J.S. Denton and N.J.G. Pearce on "A synchronised dating of three Greenland ice cores throughout the Holocene"", *Journal of Geophysical Research*, **113**, D12306, doi:10.1029/2007JD009083

Voelker, A.H.L. (2002) "Global distribution of centennial-scale records for marine isotope stage (MIS) 3: A database", *Quaternary Science Reviews*, **21**, 1185-1212

Vogel, J.S., Cornell, W., Nelson, D.E. and Southon, J.R. (1990) "Vesuvius/Avellino, one possible source of seventeenth century BC climatic disturbances", *Nature*, **344**, 534-537

Wallrabe-Adams, H-J. and Lackschewitz, K.S. (2003) "Chemical composition, distribution, and origin of silicic volcanic ashes in the Greenland-Iceland-Norwegian Sea: explosive volcanism from 10 to 300 ka as recorded in deep-sea sediments", *Marine Geology*, **193**, 273-293

Walker, M.J.C. (2005) *Quaternary Dating Methods*, John Wiley and Sons, Chichester

Walker, M., Johnsen, S., Rasmussen, S.O., Popp, T., Steffensen, J.-P., Gibbard, P., Hoek, W., Lowe, J., Andrews, J., Björck, S., Cwynar, L.C., Hughen, K., Kershaw, P., Kromer, B., Litt, T., Lowe, D.J., Nakagawa, T., Newnham, R. and Schwander, J. (2009) "Formal definition and dating of the GSSP (Global Stratotype Section and Point) for the base of the Holocene using the Greenland NGRIP ice core and selected auxiliary records", *Journal of Quaternary Science*, **24**, 3-17

Wang, X., Auler, A.S., Edwards, R.L., Cheng, H., Ito, E. and Solheid, M. (2006) "Interhemispheric anti-phasing of rainfall during the last glacial period", *Quaternary Science Reviews*, **25**, 3391-3403

Wang, Y.J., Cheng, H., Edwards, R.L., An, Z.S., Wu, J.Y., Shen, C.-C. and Dorale, J.A. (2001) "A high-resolution absolute-dated late Pleistocene monsoon record from Hulu Cave, China" *Science*, **294**, 2345-2348

Warren, P. (1984) "Absolute dating of the Bronze Age eruption of Thera (Santorini)", *Nature*, **308**, 492-493

Warshaw, C.M. and Smith, R.L. (1988) "Pyroxenes and fayalites in the Bandelier Tuff, New Mexico: Temperatures and comparison with other rhyolites", *American Mineralogist*, **73**, 1025-1037

Wastegård, S., Björck, S., Grauert, M. and Hannon, G.E. (2001) "The Mjauvotn tephra and other Holocene tephra horizons from the Faroe Islands: a link between the

Icelandic source region, the Nordic Seas, and the European continent", *The Holocene,* **11,** 101-109

Wastegård, S., Björck, S., Greve, C. and Rasmussen, T.L. (2005) "A tephra-based correlation between the Faroe Islands and the Norwegian Sea raises questions about chronological relationships during the last interglacial", *Terra Nova*, **17**, 7-12

Wastegård, S., Björck, S., Possnert, G. and Wohlfarth, B. (1998) "Evidence for the occurrence of Vedde Ash in Sweden: radiocarbon and calendar age estimates", *Journal of Quaternary Science,* **13**, 271-274

Wastegård, S. and Rasmussen, T.L. (2001) "New tephra horizons from Oxygen Isotope 5 in the North Atlantic: correlation potential for terrestrial, marine and ice-core archives", *Quaternary Science Reviews*, **20**, 1587-1593

Wastegård, S., Rasmussen, T.L., Kuijpers, A., Nielsen, T. and van Weering, T.C.E. (2006) "Composition and origin of ash zones from Marine Isotope Stages 3 and 2 in the North Atlantic", *Quaternary Science Reviews,* **25**, 2409-2419

Wastegård, S., Rundgren, M., Schoning, K., Andersson, S., Björck, S., Borgmark, A. and Possnert, G. (2008) "Age, geochemistry and distribution of the mid-Holocene Hekla-S/Kebister tephra", *The Holocene*, **18**, 539-549

Wastegård, S., Wohlfarth, B., Subetto, D.A. and Sapelko, T.V. (2000) "Extending the known distribution of the Younger Dryas Vedde Ash into northwestern Russia", *Journal of Quaternary Science*, **15**, 581-586

Westgate, J.A., Perkins, W.T., Fuge, R., Pearce, N.J.G. and Wintle, A.G. (1994) "Trace element analysis of volcanic glass shards by laser ablation inductively coupled plasma mass spectrometry: application to tephrochronological studies", *Applied Geochemistry*, **9**, 323-335

Westgate, J.A., Preece, S.J., Froese, D.G., Pearce, N.J.G., Roberts, R.G., Demuro, M., Hart, W.K. and Perkins, W. (2008) "Changing ideas on the identity and stratigraphic significance of the Sheep Creek tephra beds in Alaska and the

Yukon Territory, northwestern North America", *Quaternary International,* **178**, 183-209

Westgate, J.A., Shane, P.A.R., Pearce, N.J.G., Perkins, W.T., Korisettar, R., Chesner, C.A., Williams, M.A.J. and Acharyya, S.K. (1998) "All Toba Occurrences across Peninsular India Belong to the 75,000 yr BP eruption", *Quaternary Research*, **50**, 107-112

Wilson, M. (1989) *Igneous Petrogenesis: a global tectonic approach*, Unwin, Hyman, London

WoldeGabriel, G., Hart, W.K. and Heiken, G. (2005) "Innovative Tephra Studies in the East African Rift System", *EOS, Transactions American Geophysical Union,* **86**, doi: 10.1029/2005EO270003

Wulf, S., Kraml, M., Brauer, A., Keller, J. and Negendank, J.F.W. (2004) "Tephrochronology of the 100ka lacustrine sediment record of Lago Grande Monticchio", *Quaternary International*, **122**, 7-30

Yang, Q., Mayewski, P.A., Whitlow, S.I. and Twickler, M.S. (1997) "Major features of glaciochemistry over the last 110,000 years in the GISP2 ice core", *Journal of Geophysical Research*, **102**, 23289-23299

Yuan, D., Cheng, H., Edwards, R.L., Dykoski, C.A., Kelly, M.J., Zhang, M., Qing, J., Lin, Y., Wang, Y., Wu, J., Dorale, J.A., An, Z. and Cai, Y. (2004) "Timing, duration and transitions of the last interglacial Asian monsoon", *Science*, **304**, 575-578

Zdanowicz, C.M., Zielinski, G.A. and Germani, M.S. (1999) "Mount Mazama eruption: Calendrical age verified and atmospheric impact assessed", *Geology*, **27**, 621-624

Zielinski, G.A. (1995) "Stratospheric loading and optical depth estimates of explosive volcanism over the last 2100 years derived from the Greenland Ice Sheet Project 2 ice core", *Journal of Geophysical Research*, **100**, 20937-20955

Zielinski, G.A. (2000) "Use of paleo-records in determining variability within the volcanism-climate system", *Quaternary Science Reviews*, **19**, 417-438

Zielinski, G.A. and Germani, M.S. (1998a) "New Ice-Core evidence Challenges the 1620s BC age for the Santorini (Minoan) Eruption", *Journal of Archaeological Science*, **25**, 279-289

Zielinski, G.A. and Germani, M.S. (1998b) "Reply to: Correction. New GISP2 Ice-Core Evidence Supports 17$^{th}$ Century BC Date for the Santorini (Minoan) Eruption", *Journal of Archaeological Science*, **25**, 1043-1045

Zielinski, G.A., Germani, M.S., Larsen, G., Baillie, M.G.L., Whitlow, S., Twickler, M.S. and Taylor, K. (1995) "Evidence of the Eldgjá eruption in the GISP2 Greenland ice core: relationship to eruption processes and climatic conditions in the tenth century", *The Holocene*, **5**, 129-140

Zielinski, G.A., Mayewski, P.A., Meeker, L.D., Grönvold, K., Germani, M.S., Whitlow, S., Twickler, M.S. and Taylor, K. (1997) "Volcanic aerosol records and tephrochronology of the Summit, Greenland, ice cores", *Journal of Geophysical Research*, **102,** 26,625-26,640

Zielinski, G.A., Mayewski, P.A., Meeker, L.D., Whitlow, S. and Twickler, M.S. (1996a) "A 110,000-Yr Record of Explosive Volcanism from the GISP2 (Greenland) Ice Core", *Quaternary Research*, **45**, 109-118

Zielinski, G.A., Mayewski, P.A., Meeker, L.D., Whitlow, S., Twickler, M.S. and Taylor, K. (1996b) "Potential atmospheric impact of the Toba mega-eruption ~71,000 years ago", *Geophysical Research Letters*, **23**, 837-840

Zillén, L.M., Wastegård, S. and Snowball, I.F. (2002) "Calendar year ages of three mid-Holocene tephra layers identified in varved lake sediments in west central Sweden", *Quaternary Science Reviews*, **21**, 1583-1591

# Appendix 1 – EPMA Standard Analyses

The following tables present analyses of references standards (TB1G, BCR2g and Lipari) conducted during the EPMA analysis of tephra shards within this study during three analytical periods.

During the first analytical period horizons NGRIP 2441.28 m, NGRIP 2454.9 m, NGRIP 2500.9 m, NGRIP 2548.35 m, GRIP 1528.61 m, LINK 14:185, NGRIP 1848 m, LINK 17:634, GRIP 1716.08 m, NGRIP 1915.5 m and NGRIP 2631.9 m were analysed.

During the second analytical period horizons NGRIP 2441.14 m, NGRIP 2574.55 m, GRIP 2498.5 m, GRIP 2499.75 m, GRIP 2501.05 m, GRIP 2531.8 m, GRIP 2532.95 m and GRIP 2564.3 m were analysed. Only the TB1G and BCR2g standards were analysed as all material was basaltic.

During the third analytical period horizons shards from MD04-2822 samples 2317-2318 cm, 2319-2320 cm, 2327-2328 cm, 2339-2340 cm, 2359-2360 cm, 2361-2362 cm, 2363-2364 cm, 2365-2366 cm, 2373-2374 cm and 2377-2378 cm were analysed. Only the Cannetto Lami Lava, Lipari standards was analysed as all material was rhyolitic.

**References Values**

•TB1G: Potts et al. (2002)

•BCG2g: USGS Website (http://minerals.cr.usgs.gov/geo_chem_stand/basaltbcr2.html) Date Accessed: 14th May 2007

•Cannetto Lami Lava, Lipari:
a: Sparks, R.S.J. (1990)- written communication to University of Edinburgh
b: Hunt and Hill (1996)

| n | $SiO_2$ | $TiO_2$ | $Al_2O_3$ | FeO | MnO | MgO | CaO | $Na_2O$ | $K_2O$ | $P_2O_5$ | Total |
|---|---|---|---|---|---|---|---|---|---|---|---|
| **Analytical Period 1: TB1G** | | | | | | | | | | | |
| 1 | 53.85 | 0.83 | 16.46 | 8.73 | 0.28 | 3.66 | 6.85 | 3.33 | 4.42 | 0.67 | 99.07 |
| 2 | 53.78 | 0.85 | 16.21 | 8.67 | 0.25 | 3.61 | 6.88 | 3.20 | 4.40 | 0.61 | 98.45 |
| 3 | 53.78 | 0.94 | 16.21 | 8.76 | 0.28 | 3.62 | 6.76 | 3.19 | 4.32 | 0.62 | 98.48 |
| 4 | 53.68 | 0.84 | 16.47 | 8.37 | 0.07 | 3.62 | 6.82 | 3.19 | 4.39 | 0.68 | 98.12 |
| 5 | 53.95 | 0.90 | 16.45 | 8.90 | 0.20 | 3.57 | 6.83 | 3.24 | 4.41 | 0.59 | 99.03 |
| 6 | 53.73 | 0.94 | 16.44 | 9.05 | 0.16 | 3.64 | 6.85 | 3.11 | 4.45 | 0.59 | 98.97 |
| 7 | 53.68 | 0.97 | 16.13 | 8.87 | 0.13 | 3.63 | 6.94 | 3.30 | 4.50 | 0.61 | 98.76 |
| 8 | 53.62 | 0.91 | 16.41 | 8.89 | 0.34 | 3.64 | 6.85 | 3.32 | 4.46 | 0.62 | 99.06 |
| 9 | 53.95 | 0.92 | 16.48 | 8.90 | 0.19 | 3.65 | 6.87 | 3.19 | 4.59 | 0.61 | 99.33 |
| 10 | 54.04 | 0.97 | 16.41 | 8.30 | 0.16 | 3.67 | 6.78 | 3.12 | 4.48 | 0.58 | 98.51 |
| 11 | 53.70 | 0.89 | 16.33 | 9.13 | 0.14 | 3.65 | 6.77 | 3.17 | 4.35 | 0.63 | 98.76 |
| 12 | 53.58 | 0.89 | 16.34 | 8.53 | 0.28 | 3.62 | 6.83 | 3.20 | 4.42 | 0.59 | 98.27 |
| 13 | 54.33 | 0.96 | 16.51 | 8.73 | 0.16 | 3.59 | 6.90 | 3.24 | 4.54 | 0.61 | 99.56 |
| 14 | 54.04 | 0.75 | 16.30 | 8.77 | 0.21 | 3.67 | 6.92 | 3.17 | 4.40 | 0.60 | 98.82 |
| 15 | 54.07 | 0.94 | 16.28 | 8.41 | 0.18 | 3.59 | 6.88 | 3.16 | 4.39 | 0.62 | 98.51 |
| 16 | 53.71 | 0.85 | 16.29 | 8.61 | 0.28 | 3.66 | 7.04 | 3.22 | 4.52 | 0.68 | 98.85 |
| 17 | 54.19 | 0.92 | 16.30 | 8.48 | 0.16 | 3.62 | 6.77 | 3.14 | 4.56 | 0.60 | 98.73 |
| 18 | 53.91 | 0.88 | 16.35 | 9.14 | 0.12 | 3.64 | 6.85 | 3.20 | 4.39 | 0.61 | 99.09 |
| 19 | 54.15 | 0.91 | 16.26 | 8.21 | 0.28 | 3.64 | 6.97 | 3.15 | 4.37 | 0.60 | 98.55 |
| 20 | 53.86 | 0.94 | 16.40 | 8.43 | 0.23 | 3.58 | 6.84 | 3.18 | 4.42 | 0.64 | 98.52 |
| 21 | 53.91 | 0.92 | 16.40 | 8.72 | 0.06 | 3.64 | 6.84 | 3.25 | 4.33 | 0.60 | 98.68 |
| 22 | 53.70 | 0.92 | 16.25 | 8.02 | 0.15 | 3.64 | 7.03 | 3.29 | 4.56 | 0.62 | 98.20 |
| 23 | 53.69 | 0.85 | 16.24 | 8.81 | 0.29 | 3.63 | 6.98 | 3.21 | 4.40 | 0.54 | 98.64 |
| 24 | 53.72 | 0.99 | 16.33 | 8.13 | 0.18 | 3.59 | 6.83 | 3.12 | 4.44 | 0.57 | 97.92 |
| 25 | 54.06 | 0.92 | 16.52 | 8.55 | 0.16 | 3.64 | 7.04 | 3.19 | 4.57 | 0.59 | 99.26 |
| 26 | 54.09 | 0.92 | 16.29 | 8.63 | 0.23 | 3.66 | 6.80 | 3.24 | 4.53 | 0.62 | 99.01 |
| 27 | 53.73 | 0.92 | 16.23 | 8.26 | 0.16 | 3.65 | 7.05 | 3.10 | 4.46 | 0.63 | 98.19 |
| 28 | 54.11 | 0.93 | 16.45 | 8.58 | 0.13 | 3.67 | 6.96 | 3.06 | 4.55 | 0.63 | 99.07 |
| 29 | 54.02 | 0.89 | 16.42 | 8.63 | 0.23 | 3.62 | 7.08 | 3.21 | 4.51 | 0.64 | 99.25 |
| 30 | 53.93 | 0.87 | 16.29 | 8.31 | 0.10 | 3.67 | 6.91 | 3.24 | 4.45 | 0.55 | 98.32 |
| 31 | 53.91 | 0.80 | 16.40 | 8.34 | 0.23 | 3.59 | 7.00 | 3.15 | 4.48 | 0.55 | 98.46 |
| 32 | 53.90 | 0.88 | 16.31 | 8.57 | 0.22 | 3.62 | 6.59 | 3.22 | 4.44 | 0.61 | 98.36 |
| 33 | 53.98 | 0.84 | 16.36 | 8.87 | 0.28 | 3.64 | 6.76 | 3.24 | 4.42 | 0.54 | 98.94 |
| 34 | 53.97 | 0.88 | 16.40 | 8.60 | 0.18 | 3.61 | 6.80 | 3.22 | 4.59 | 0.56 | 98.80 |
| 35 | 53.49 | 0.86 | 16.24 | 8.67 | 0.21 | 3.63 | 6.99 | 3.23 | 4.59 | 0.58 | 98.49 |
| 36 | 53.57 | 0.83 | 15.92 | 8.90 | 0.16 | 3.60 | 6.77 | 3.22 | 4.38 | 0.57 | 97.91 |
| 37 | 53.33 | 0.87 | 15.94 | 8.21 | 0.14 | 3.66 | 6.95 | 3.28 | 4.48 | 0.60 | 97.48 |
| 38 | 53.25 | 0.92 | 16.23 | 8.24 | 0.13 | 3.61 | 7.02 | 3.20 | 4.48 | 0.59 | 97.66 |
| 39 | 53.48 | 0.87 | 16.40 | 8.59 | 0.16 | 3.64 | 6.80 | 3.12 | 4.38 | 0.56 | 98.01 |
| 40 | 53.64 | 0.88 | 16.24 | 9.16 | 0.13 | 3.66 | 6.85 | 3.19 | 4.51 | 0.55 | 98.80 |
| 41 | 53.76 | 0.93 | 16.45 | 8.51 | 0.13 | 3.62 | 6.91 | 3.26 | 4.35 | 0.58 | 98.51 |
| 42 | 53.87 | 0.89 | 16.54 | 8.95 | 0.18 | 3.65 | 6.76 | 3.16 | 4.30 | 0.60 | 98.89 |
| 43 | 53.80 | 0.96 | 16.24 | 8.27 | 0.24 | 3.70 | 6.92 | 3.13 | 4.50 | 0.51 | 98.28 |
| 44 | 53.64 | 0.80 | 16.44 | 8.87 | 0.16 | 3.58 | 6.84 | 3.08 | 4.32 | 0.59 | 98.31 |
| 45 | 53.58 | 0.99 | 16.28 | 8.50 | 0.12 | 3.65 | 6.86 | 3.12 | 4.60 | 0.60 | 98.30 |
| 46 | 53.58 | 0.92 | 16.16 | 8.37 | 0.20 | 3.61 | 6.79 | 3.22 | 4.40 | 0.63 | 97.89 |
| 47 | 53.53 | 0.90 | 16.39 | 8.53 | 0.26 | 3.66 | 7.09 | 3.28 | 4.48 | 0.54 | 98.66 |
| 48 | 53.66 | 0.80 | 16.38 | 8.64 | 0.23 | 3.62 | 7.10 | 3.19 | 4.53 | 0.58 | 98.72 |
| 49 | 53.85 | 0.85 | 16.26 | 8.38 | 0.17 | 3.63 | 6.88 | 3.24 | 4.50 | 0.59 | 98.34 |
| 50 | 53.95 | 0.89 | 16.31 | 8.45 | 0.12 | 3.60 | 6.92 | 3.25 | 4.32 | 0.58 | 98.41 |
| 51 | 53.86 | 0.96 | 16.50 | 8.67 | 0.28 | 3.65 | 7.03 | 3.21 | 4.41 | 0.64 | 99.21 |
| 52 | 53.48 | 0.84 | 16.35 | 8.47 | 0.15 | 3.62 | 6.83 | 3.23 | 4.43 | 0.66 | 98.06 |
| 53 | 53.88 | 0.95 | 16.40 | 8.39 | 0.16 | 3.66 | 6.97 | 3.27 | 4.55 | 0.59 | 98.81 |
| 54 | 53.46 | 0.82 | 16.23 | 8.93 | 0.12 | 3.71 | 6.72 | 3.27 | 4.40 | 0.72 | 98.38 |
| 55 | 53.53 | 0.96 | 16.12 | 7.96 | 0.25 | 3.65 | 6.95 | 3.15 | 4.37 | 0.61 | 97.55 |
| 56 | 53.52 | 0.86 | 16.21 | 9.06 | 0.18 | 3.69 | 6.81 | 3.24 | 4.59 | 0.60 | 98.76 |
| 57 | 53.36 | 0.89 | 16.44 | 8.40 | 0.22 | 3.67 | 6.92 | 3.16 | 4.52 | 0.60 | 98.18 |
| 58 | 53.47 | 0.88 | 16.33 | 8.89 | 0.14 | 3.62 | 6.81 | 3.15 | 4.35 | 0.61 | 98.25 |
| 59 | 53.48 | 0.86 | 16.24 | 8.53 | 0.21 | 3.64 | 6.73 | 3.14 | 4.57 | 0.56 | 97.97 |
| 60 | 53.63 | 0.94 | 16.34 | 8.90 | 0.18 | 3.68 | 6.83 | 3.26 | 4.46 | 0.62 | 98.84 |
| **Mean** | **53.77** | **0.89** | **16.33** | **8.61** | **0.19** | **3.64** | **6.88** | **3.20** | **4.45** | **0.60** | **98.55** |
| St. Dev. | 0.23 | 0.05 | 0.12 | 0.28 | 0.06 | 0.03 | 0.10 | 0.06 | 0.08 | 0.04 | 0.45 |
| **Reference Values** | **54.22** | **0.85** | **16.68** | **8.14** | **0.18** | **3.64** | **6.87** | **3.20** | **4.37** | **0.59** | **98.74** |

| n | $SiO_2$ | $TiO_2$ | $Al_2O_3$ | FeO | MnO | MgO | CaO | $Na_2O$ | $K_2O$ | $P_2O_5$ | Total |
|---|---|---|---|---|---|---|---|---|---|---|---|
| **Analytical Period 1: BCR2g** | | | | | | | | | | | |
| 1 | 53.76 | 2.41 | 13.25 | 12.24 | 0.18 | 3.63 | 7.28 | 3.03 | 1.78 | 0.37 | 97.93 |
| 2 | 53.95 | 2.38 | 13.18 | 13.05 | 0.24 | 3.64 | 7.41 | 3.11 | 1.73 | 0.41 | 99.10 |
| 3 | 53.51 | 2.42 | 13.34 | 13.29 | 0.20 | 3.65 | 7.28 | 2.95 | 1.79 | 0.39 | 98.79 |
| 4 | 53.45 | 2.40 | 13.04 | 13.15 | 0.19 | 3.70 | 7.48 | 3.02 | 1.75 | 0.41 | 98.58 |
| 5 | 53.58 | 2.26 | 13.05 | 13.51 | 0.21 | 3.71 | 7.25 | 3.22 | 1.76 | 0.34 | 98.90 |
| 6 | 53.73 | 2.36 | 13.24 | 13.16 | 0.27 | 3.69 | 7.21 | 3.13 | 1.79 | 0.34 | 98.93 |
| 7 | 53.86 | 2.31 | 12.97 | 13.51 | 0.08 | 3.67 | 7.24 | 3.03 | 1.82 | 0.38 | 98.87 |
| 8 | 53.36 | 2.45 | 13.24 | 13.45 | 0.28 | 3.72 | 7.35 | 3.12 | 1.81 | 0.39 | 99.17 |
| 9 | 53.60 | 2.32 | 13.21 | 13.32 | 0.17 | 3.68 | 7.47 | 3.09 | 1.77 | 0.40 | 99.03 |
| 10 | 53.83 | 2.39 | 13.25 | 13.50 | 0.25 | 3.73 | 7.20 | 3.14 | 1.70 | 0.37 | 99.34 |
| 11 | 53.93 | 2.24 | 13.01 | 13.31 | 0.27 | 3.78 | 7.18 | 3.12 | 1.72 | 0.39 | 98.96 |
| 12 | 53.83 | 2.35 | 13.17 | 13.09 | 0.35 | 3.68 | 7.49 | 3.09 | 1.73 | 0.34 | 99.12 |
| 13 | 53.37 | 2.37 | 13.35 | 13.07 | 0.22 | 3.77 | 7.23 | 3.03 | 1.76 | 0.36 | 98.52 |
| 14 | 53.52 | 2.46 | 13.17 | 13.53 | 0.23 | 3.72 | 7.17 | 3.06 | 1.76 | 0.37 | 98.98 |
| 15 | 53.70 | 2.44 | 13.19 | 13.39 | 0.21 | 3.77 | 7.36 | 3.00 | 1.70 | 0.42 | 99.18 |
| 16 | 53.77 | 2.25 | 13.30 | 12.63 | 0.26 | 3.73 | 7.17 | 3.12 | 1.77 | 0.40 | 98.42 |
| 17 | 53.32 | 2.40 | 13.34 | 13.03 | 0.18 | 3.62 | 7.31 | 3.12 | 1.90 | 0.37 | 98.58 |
| 18 | 53.94 | 2.39 | 13.31 | 12.90 | 0.15 | 3.64 | 7.18 | 3.09 | 1.77 | 0.32 | 98.70 |
| 19 | 54.13 | 2.37 | 13.40 | 13.01 | 0.22 | 3.66 | 7.30 | 3.00 | 1.83 | 0.37 | 99.29 |
| 20 | 54.03 | 2.35 | 13.25 | 13.38 | 0.21 | 3.68 | 7.10 | 3.14 | 1.77 | 0.39 | 99.30 |
| 21 | 53.45 | 2.38 | 13.33 | 13.28 | 0.26 | 3.71 | 7.39 | 3.23 | 1.83 | 0.40 | 99.26 |
| 22 | 53.65 | 2.39 | 13.26 | 13.04 | 0.11 | 3.70 | 7.42 | 3.00 | 1.79 | 0.38 | 98.74 |
| 23 | 53.41 | 2.48 | 13.23 | 12.61 | 0.25 | 3.67 | 7.17 | 3.08 | 1.84 | 0.37 | 98.11 |
| 24 | 53.99 | 2.36 | 13.20 | 12.52 | 0.10 | 3.72 | 7.29 | 3.11 | 1.75 | 0.36 | 98.40 |
| 25 | 53.88 | 2.27 | 13.29 | 12.79 | 0.35 | 3.63 | 7.48 | 3.07 | 1.88 | 0.40 | 99.03 |
| 26 | 53.36 | 2.28 | 13.10 | 13.11 | 0.07 | 3.72 | 7.48 | 3.05 | 1.86 | 0.31 | 98.35 |
| 27 | 53.14 | 2.46 | 13.19 | 12.98 | 0.32 | 3.72 | 7.29 | 3.09 | 1.69 | 0.30 | 98.19 |
| 28 | 53.60 | 2.32 | 13.01 | 12.95 | 0.32 | 3.75 | 7.29 | 3.08 | 1.78 | 0.35 | 98.44 |
| 29 | 53.62 | 2.40 | 13.27 | 13.39 | 0.34 | 3.68 | 7.12 | 3.14 | 1.73 | 0.37 | 99.07 |
| 30 | 53.23 | 2.27 | 13.25 | 13.09 | 0.32 | 3.72 | 7.37 | 3.03 | 1.73 | 0.40 | 98.42 |
| 31 | 53.26 | 2.19 | 13.21 | 12.51 | 0.18 | 3.73 | 7.29 | 3.09 | 1.84 | 0.37 | 97.68 |
| 32 | 53.27 | 2.36 | 12.99 | 13.32 | 0.19 | 3.72 | 7.27 | 3.02 | 1.73 | 0.37 | 98.23 |
| 33 | 53.53 | 2.35 | 12.90 | 12.98 | 0.15 | 3.68 | 7.32 | 3.07 | 1.86 | 0.34 | 98.19 |
| 34 | 53.75 | 2.33 | 13.09 | 13.26 | 0.18 | 3.72 | 7.24 | 3.12 | 1.77 | 0.41 | 98.89 |
| 35 | 53.95 | 2.36 | 13.02 | 13.22 | 0.20 | 3.67 | 7.21 | 3.09 | 1.85 | 0.35 | 98.91 |
| 36 | 53.61 | 2.52 | 13.27 | 12.87 | 0.18 | 3.64 | 7.34 | 3.16 | 1.72 | 0.33 | 98.64 |
| 37 | 53.81 | 2.42 | 13.38 | 12.97 | 0.19 | 3.68 | 7.28 | 3.04 | 1.79 | 0.37 | 98.93 |
| 38 | 53.93 | 2.24 | 13.16 | 12.23 | 0.22 | 3.65 | 7.20 | 3.16 | 1.79 | 0.38 | 97.96 |
| 39 | 53.88 | 2.43 | 13.12 | 12.99 | 0.18 | 3.72 | 7.28 | 3.12 | 1.72 | 0.44 | 98.89 |
| 40 | 54.35 | 2.28 | 13.17 | 12.82 | 0.18 | 3.66 | 7.17 | 3.00 | 1.84 | 0.33 | 98.82 |
| 41 | 53.16 | 2.34 | 13.12 | 13.30 | 0.25 | 3.73 | 7.22 | 2.97 | 1.76 | 0.43 | 98.28 |
| 42 | 53.63 | 2.31 | 13.07 | 13.07 | 0.09 | 3.80 | 7.20 | 3.05 | 1.76 | 0.40 | 98.39 |
| 43 | 53.67 | 2.45 | 13.25 | 13.34 | 0.21 | 3.71 | 7.25 | 3.11 | 1.71 | 0.38 | 99.09 |
| 44 | 53.99 | 2.38 | 13.11 | 13.16 | 0.31 | 3.71 | 7.26 | 3.09 | 1.76 | 0.41 | 99.18 |
| 45 | 53.49 | 2.33 | 13.28 | 12.87 | 0.30 | 3.70 | 7.34 | 3.17 | 1.73 | 0.40 | 98.60 |
| 46 | 53.62 | 2.50 | 13.18 | 12.78 | 0.16 | 3.77 | 7.28 | 3.12 | 1.77 | 0.36 | 98.54 |
| 47 | 53.44 | 2.38 | 13.15 | 12.89 | 0.20 | 3.69 | 7.35 | 3.14 | 1.74 | 0.38 | 98.36 |
| 48 | 53.41 | 2.52 | 13.13 | 13.31 | 0.29 | 3.71 | 7.29 | 3.15 | 1.80 | 0.31 | 98.92 |
| 49 | 53.43 | 2.34 | 13.14 | 13.11 | 0.18 | 3.75 | 7.08 | 3.13 | 1.79 | 0.40 | 98.36 |
| 50 | 53.40 | 2.28 | 13.25 | 12.69 | 0.26 | 3.71 | 7.33 | 3.00 | 1.76 | 0.38 | 98.06 |
| 51 | 53.29 | 2.39 | 13.01 | 13.31 | 0.05 | 3.77 | 7.22 | 3.04 | 1.90 | 0.33 | 98.30 |
| 52 | 53.25 | 2.37 | 13.22 | 13.17 | 0.15 | 3.70 | 7.18 | 3.06 | 1.77 | 0.34 | 98.22 |
| 53 | 53.00 | 2.34 | 13.02 | 13.29 | 0.24 | 3.71 | 7.33 | 3.12 | 1.74 | 0.32 | 98.11 |
| 54 | 53.29 | 2.43 | 13.19 | 13.04 | 0.32 | 3.67 | 7.37 | 3.08 | 1.78 | 0.34 | 98.51 |
| 55 | 53.15 | 2.33 | 13.18 | 12.91 | 0.28 | 3.73 | 7.39 | 3.03 | 1.82 | 0.30 | 98.11 |
| 56 | 54.63 | 2.45 | 13.41 | 11.77 | 0.16 | 3.62 | 7.20 | 3.11 | 1.83 | 0.38 | 98.56 |
| 57 | 54.73 | 2.34 | 13.40 | 12.14 | 0.27 | 3.56 | 6.93 | 3.17 | 1.88 | 0.39 | 98.81 |
| 58 | 54.52 | 2.31 | 13.24 | 11.96 | 0.16 | 3.63 | 6.98 | 3.18 | 1.76 | 0.38 | 98.10 |
| 59 | 54.29 | 2.49 | 13.26 | 11.99 | 0.20 | 3.56 | 7.12 | 3.26 | 1.88 | 0.41 | 98.46 |
| 60 | 54.42 | 2.36 | 13.27 | 12.51 | 0.13 | 3.60 | 7.16 | 3.25 | 1.91 | 0.36 | 98.97 |
| **Mean** | **53.68** | **2.37** | **13.19** | **12.98** | **0.21** | **3.69** | **7.27** | **3.09** | **1.78** | **0.37** | **98.65** |
| St. Dev. | 0.38 | 0.07 | 0.12 | 0.41 | 0.07 | 0.05 | 0.12 | 0.07 | 0.05 | 0.03 | 0.40 |
| **Reference Values** | **54.1** | **2.26** | **13.5** | **12.42** | **0.20** | **3.59** | **7.12** | **3.16** | **1.79** | **0.35** | **98.49** |

| n | | $SiO_2$ | $TiO_2$ | $Al_2O_3$ | FeO | MnO | MgO | CaO | $Na_2O$ | $K_2O$ | $P_2O_5$ | Total |
|---|---|---|---|---|---|---|---|---|---|---|---|---|
| **Analytical Period 1: Cannetto Lami Lava, Lipari** | | | | | | | | | | | | |
| 1 | | 74.55 | 0.04 | 12.88 | 1.54 | 0.11 | 0.05 | 0.80 | 4.00 | 5.21 | 0.06 | 99.23 |
| 2 | | 74.52 | 0.05 | 12.77 | 1.58 | 0.11 | 0.06 | 0.73 | 3.82 | 5.27 | -0.03 | 98.91 |
| 3 | | 74.46 | 0.03 | 13.07 | 1.64 | 0.03 | 0.05 | 0.80 | 3.98 | 5.28 | -0.04 | 99.36 |
| 4 | | 74.72 | 0.12 | 12.84 | 1.89 | -0.03 | 0.03 | 0.74 | 4.09 | 5.01 | -0.02 | 99.44 |
| 5 | | 73.96 | 0.09 | 12.90 | 1.78 | 0.09 | 0.04 | 0.74 | 3.99 | 5.14 | -0.04 | 98.74 |
| 6 | | 74.54 | -0.01 | 13.09 | 1.43 | 0.13 | 0.03 | 0.76 | 3.86 | 5.18 | -0.01 | 99.03 |
| 7 | | 74.11 | 0.11 | 13.02 | 1.60 | 0.04 | 0.05 | 0.73 | 4.04 | 5.05 | 0.02 | 98.76 |
| 8 | | 73.79 | 0.12 | 12.89 | 1.52 | 0.07 | 0.05 | 0.73 | 3.95 | 5.14 | -0.02 | 98.26 |
| 9 | | 74.41 | 0.09 | 13.06 | 1.46 | 0.03 | 0.04 | 0.73 | 4.08 | 5.11 | 0.00 | 99.01 |
| 10 | | 74.41 | 0.10 | 13.10 | 1.59 | 0.14 | 0.05 | 0.74 | 3.90 | 5.21 | 0.00 | 99.24 |
| 11 | | 74.38 | 0.11 | 12.97 | 1.65 | 0.11 | 0.06 | 0.72 | 4.04 | 5.13 | -0.01 | 99.16 |
| 12 | | 74.52 | 0.09 | 13.07 | 1.65 | 0.07 | 0.05 | 0.75 | 4.05 | 5.23 | 0.00 | 99.47 |
| 13 | | 74.73 | 0.08 | 12.89 | 1.66 | 0.00 | 0.04 | 0.74 | 4.06 | 5.23 | 0.01 | 99.42 |
| 14 | | 74.83 | 0.05 | 13.13 | 1.55 | 0.07 | 0.03 | 0.73 | 4.11 | 5.13 | -0.02 | 99.62 |
| 15 | | 74.31 | 0.05 | 13.04 | 1.33 | 0.16 | 0.04 | 0.73 | 4.04 | 5.11 | 0.03 | 98.83 |
| 16 | | 74.45 | 0.04 | 12.90 | 1.62 | 0.01 | 0.05 | 0.74 | 4.06 | 5.16 | -0.03 | 99.02 |
| 17 | | 74.41 | 0.07 | 13.03 | 1.56 | 0.05 | 0.04 | 0.76 | 4.22 | 5.17 | 0.01 | 99.32 |
| 18 | | 74.66 | 0.11 | 12.90 | 1.44 | 0.02 | 0.05 | 0.76 | 3.86 | 5.20 | -0.02 | 98.99 |
| 19 | | 74.33 | 0.05 | 13.11 | 1.94 | 0.08 | 0.05 | 0.76 | 4.01 | 5.33 | -0.03 | 99.66 |
| 20 | | 74.29 | 0.10 | 12.84 | 1.49 | -0.04 | 0.05 | 0.79 | 4.01 | 5.09 | -0.06 | 98.65 |
| 21 | | 73.99 | 0.05 | 13.04 | 1.48 | 0.02 | 0.04 | 0.72 | 4.02 | 5.19 | -0.02 | 98.56 |
| 22 | | 73.87 | 0.02 | 12.87 | 1.54 | 0.06 | 0.03 | 0.74 | 4.15 | 5.03 | 0.00 | 98.31 |
| 23 | | 73.89 | 0.07 | 12.85 | 1.32 | 0.17 | 0.04 | 0.77 | 4.09 | 5.15 | 0.01 | 98.36 |
| 24 | | 73.72 | 0.07 | 12.85 | 1.40 | 0.09 | 0.03 | 0.75 | 3.99 | 5.05 | -0.01 | 97.95 |
| 25 | | 73.97 | 0.14 | 12.91 | 1.70 | 0.03 | 0.05 | 0.73 | 4.03 | 5.29 | -0.03 | 98.85 |
| 26 | | 73.76 | 0.04 | 12.66 | 1.52 | 0.07 | 0.05 | 0.71 | 3.92 | 5.37 | 0.03 | 98.13 |
| 27 | | 74.28 | 0.08 | 13.08 | 1.49 | 0.10 | 0.05 | 0.69 | 4.06 | 5.18 | 0.02 | 99.02 |
| 28 | | 73.65 | 0.01 | 12.72 | 1.57 | 0.16 | 0.03 | 0.77 | 4.04 | 5.11 | 0.00 | 98.07 |
| 29 | | 74.62 | 0.09 | 13.17 | 1.78 | 0.07 | 0.04 | 0.73 | 3.96 | 5.11 | -0.05 | 99.55 |
| 30 | | 74.41 | 0.03 | 12.89 | 1.63 | -0.01 | 0.04 | 0.81 | 3.98 | 5.09 | -0.03 | 98.88 |
| 31 | | 74.15 | 0.05 | 12.97 | 1.33 | 0.01 | 0.05 | 0.65 | 4.07 | 5.18 | -0.04 | 98.46 |
| 32 | | 74.23 | 0.06 | 12.82 | 1.82 | 0.03 | 0.04 | 0.74 | 4.10 | 5.21 | -0.01 | 99.06 |
| 33 | | 74.36 | 0.06 | 12.95 | 1.38 | 0.12 | 0.03 | 0.79 | 4.00 | 5.15 | -0.02 | 98.84 |
| 34 | | 74.45 | 0.08 | 12.95 | 1.46 | 0.08 | 0.04 | 0.72 | 3.97 | 5.14 | -0.06 | 98.89 |
| 35 | | 73.73 | 0.04 | 12.82 | 1.78 | 0.12 | 0.05 | 0.71 | 4.01 | 5.10 | -0.04 | 98.37 |
| 36 | | 74.11 | 0.03 | 12.97 | 1.49 | 0.13 | 0.03 | 0.81 | 4.00 | 5.19 | -0.02 | 98.75 |
| 37 | | 74.40 | 0.09 | 12.83 | 1.49 | 0.17 | 0.05 | 0.78 | 3.98 | 5.09 | 0.04 | 98.92 |
| 38 | | 74.46 | 0.07 | 13.05 | 1.60 | 0.09 | 0.05 | 0.74 | 3.91 | 5.13 | -0.01 | 99.09 |
| 39 | | 74.15 | 0.08 | 12.96 | 1.65 | 0.01 | 0.04 | 0.77 | 4.15 | 5.24 | -0.08 | 99.06 |
| 40 | | 74.26 | 0.09 | 12.89 | 1.77 | 0.14 | 0.04 | 0.78 | 4.06 | 5.11 | -0.02 | 99.12 |
| 41 | | 74.85 | 0.04 | 12.78 | 1.51 | 0.05 | 0.03 | 0.75 | 4.11 | 5.24 | 0.03 | 99.39 |
| 42 | | 74.35 | 0.06 | 12.93 | 1.40 | 0.15 | 0.04 | 0.75 | 4.03 | 5.15 | -0.03 | 98.86 |
| 43 | | 73.91 | 0.11 | 13.08 | 1.62 | 0.10 | 0.04 | 0.73 | 4.12 | 5.32 | 0.00 | 99.03 |
| 44 | | 74.19 | 0.10 | 12.91 | 1.83 | 0.06 | 0.05 | 0.67 | 3.91 | 4.93 | -0.02 | 98.66 |
| 45 | | 74.03 | 0.13 | 12.84 | 1.51 | 0.09 | 0.06 | 0.78 | 4.14 | 5.19 | -0.02 | 98.78 |
| 46 | | 74.50 | 0.13 | 12.92 | 1.54 | 0.10 | 0.04 | 0.78 | 4.10 | 5.18 | 0.03 | 99.34 |
| 47 | | 74.40 | 0.07 | 12.87 | 1.44 | 0.08 | 0.05 | 0.70 | 4.06 | 5.22 | -0.06 | 98.88 |
| 48 | | 74.30 | -0.01 | 12.98 | 1.46 | 0.03 | 0.04 | 0.76 | 3.97 | 5.23 | -0.05 | 98.77 |
| 49 | | 74.36 | 0.08 | 12.94 | 1.51 | 0.13 | 0.02 | 0.75 | 3.97 | 5.21 | -0.03 | 98.97 |
| 50 | | 74.24 | 0.11 | 12.93 | 1.46 | 0.10 | 0.03 | 0.82 | 4.09 | 5.21 | 0.06 | 99.03 |
| 51 | | 74.65 | 0.09 | 12.99 | 1.31 | 0.04 | 0.04 | 0.75 | 3.94 | 5.16 | 0.00 | 98.99 |
| 52 | | 73.94 | 0.06 | 12.83 | 1.75 | 0.11 | 0.04 | 0.78 | 3.99 | 4.99 | -0.01 | 98.49 |
| 53 | | 73.66 | 0.09 | 12.80 | 1.65 | 0.01 | 0.05 | 0.75 | 3.99 | 5.24 | 0.03 | 98.27 |
| 54 | | 74.20 | 0.08 | 12.87 | 1.49 | 0.10 | 0.05 | 0.74 | 3.98 | 5.29 | 0.01 | 98.81 |
| 55 | | 73.97 | 0.07 | 12.72 | 1.54 | -0.06 | 0.05 | 0.77 | 3.92 | 5.32 | -0.01 | 98.36 |
| 56 | | 73.75 | 0.02 | 13.03 | 1.56 | 0.07 | 0.04 | 0.78 | 4.10 | 5.27 | 0.02 | 98.66 |
| **Mean** | | **74.25** | **0.07** | **12.93** | **1.57** | **0.07** | **0.04** | **0.75** | **4.02** | **5.17** | **-0.01** | **98.89** |
| St. Dev. | | 0.31 | 0.03 | 0.11 | 0.14 | 0.05 | 0.01 | 0.03 | 0.08 | 0.09 | 0.03 | 0.40 |
| **Reference Values** | a | **74.03** | **0.08** | **12.72** | ***1.75*** | **0.08** | **0.00** | **0.72** | **4.06** | **5.18** | **0** | **98.62** |
| | b | **73.72** | **nr** | **13.04** | ***1.76*** | **nr** | **0.03** | **0.76** | **4.06** | **5.06** | **nr** | **98.43** |

| n | $SiO_2$ | $TiO_2$ | $Al_2O_3$ | FeO | MnO | MgO | CaO | $Na_2O$ | $K_2O$ | $P_2O_5$ | Cl | Total |
|---|---|---|---|---|---|---|---|---|---|---|---|---|
| **Analytical Period 2: TB1G** | | | | | | | | | | | | |
| 1 | 54.32 | 0.83 | 16.27 | 8.87 | 0.27 | 3.71 | 7.16 | 2.79 | 3.72 | 0.59 | 0.01 | 98.55 |
| 2 | 54.63 | 0.79 | 16.32 | 8.89 | 0.17 | 3.63 | 7.13 | 2.85 | 4.19 | 0.62 | 0.00 | 99.23 |
| 3 | 54.59 | 0.78 | 16.11 | 9.12 | 0.18 | 3.65 | 7.04 | 2.75 | 3.73 | 0.62 | 0.02 | 98.58 |
| 4 | 54.08 | 0.83 | 16.39 | 9.04 | 0.21 | 3.66 | 7.02 | 2.84 | 3.66 | 0.59 | 0.00 | 98.31 |
| 5 | 54.11 | 0.87 | 16.29 | 8.93 | 0.26 | 3.61 | 7.20 | 3.11 | 4.16 | 0.60 | 0.01 | 99.15 |
| 6 | 54.44 | 0.93 | 16.34 | 8.86 | 0.20 | 3.61 | 7.05 | 3.15 | 4.15 | 0.63 | 0.00 | 99.36 |
| 7 | 54.77 | 0.83 | 16.38 | 8.90 | 0.22 | 3.62 | 7.07 | 3.14 | 4.19 | 0.59 | 0.00 | 99.71 |
| 8 | 54.15 | 0.95 | 16.51 | 8.70 | 0.20 | 3.57 | 7.19 | 3.16 | 4.19 | 0.61 | 0.01 | 99.25 |
| 9 | 54.16 | 0.76 | 16.28 | 8.59 | 0.08 | 3.59 | 7.03 | 3.18 | 4.22 | 0.63 | 0.00 | 98.52 |
| 10 | 54.38 | 0.89 | 16.15 | 8.62 | 0.16 | 3.64 | 7.20 | 3.21 | 4.16 | 0.59 | 0.01 | 99.01 |
| 11 | 54.49 | 0.87 | 16.37 | 8.60 | 0.27 | 3.63 | 7.05 | 3.24 | 4.17 | 0.61 | 0.00 | 99.32 |
| 12 | 54.27 | 0.80 | 16.36 | 8.70 | 0.21 | 3.57 | 7.14 | 3.18 | 4.16 | 0.60 | 0.00 | 98.99 |
| 13 | 54.19 | 0.90 | 16.34 | 8.50 | 0.18 | 3.56 | 7.10 | 3.15 | 4.23 | 0.62 | 0.00 | 98.76 |
| 14 | 54.51 | 0.79 | 16.41 | 8.69 | 0.19 | 3.58 | 7.12 | 3.13 | 4.33 | 0.61 | 0.01 | 99.37 |
| 15 | 54.40 | 0.71 | 16.34 | 8.43 | 0.19 | 3.59 | 7.18 | 3.18 | 4.10 | 0.12 | 0.00 | 98.24 |
| 16 | 54.36 | 0.86 | 16.37 | 8.97 | 0.18 | 3.57 | 7.08 | 3.25 | 4.19 | 0.58 | 0.01 | 99.42 |
| 17 | 54.47 | 0.81 | 16.45 | 8.55 | 0.18 | 3.60 | 7.03 | 3.13 | 4.21 | 0.60 | 0.01 | 99.02 |
| 18 | 53.92 | 0.84 | 14.46 | 8.89 | 0.19 | 3.59 | 6.33 | 3.17 | 4.31 | 0.52 | 0.01 | 96.22 |
| 19 | 54.29 | 0.80 | 16.07 | 8.58 | 0.21 | 3.49 | 7.02 | 3.21 | 4.44 | 0.57 | 0.00 | 98.68 |
| 20 | 54.38 | 0.80 | 16.15 | 8.64 | 0.22 | 3.54 | 6.92 | 3.13 | 4.50 | 0.62 | 0.00 | 98.90 |
| 21 | 54.19 | 0.83 | 16.16 | 8.55 | 0.16 | 3.54 | 7.02 | 3.12 | 4.47 | 0.58 | -0.01 | 98.63 |
| 22 | 54.60 | 0.92 | 16.13 | 8.49 | 0.20 | 3.45 | 6.91 | 3.21 | 4.47 | 0.59 | 0.01 | 98.99 |
| 23 | 54.36 | 0.88 | 16.24 | 9.00 | 0.12 | 3.47 | 6.96 | 3.03 | 4.44 | 0.63 | 0.00 | 99.13 |
| 24 | 53.95 | 0.92 | 15.77 | 8.76 | 0.21 | 3.52 | 7.04 | 3.20 | 4.41 | 0.60 | 0.01 | 98.40 |
| 25 | 53.92 | 0.82 | 15.85 | 8.94 | 0.19 | 3.59 | 7.03 | 3.21 | 4.44 | 0.54 | 0.00 | 98.53 |
| 26 | 53.93 | 0.82 | 15.88 | 9.03 | 0.23 | 3.59 | 7.01 | 3.23 | 4.42 | 0.60 | 0.00 | 98.76 |
| **Mean** | **54.30** | **0.84** | **16.17** | **8.76** | **0.20** | **3.58** | **7.04** | **3.11** | **4.22** | **0.58** | **0.01** | **98.81** |
| St. Dev. | 0.23 | 0.06 | 0.40 | 0.20 | 0.04 | 0.06 | 0.17 | 0.14 | 0.23 | 0.10 | 0.01 | 0.65 |
| **Reference Values** | **54.22** | **0.85** | **16.68** | **8.14** | **0.18** | **3.64** | **6.87** | **3.20** | **4.37** | **0.59** | **n/a** | **98.74** |

| n | $SiO_2$ | $TiO_2$ | $Al_2O_3$ | FeO | MnO | MgO | CaO | $Na_2O$ | $K_2O$ | $P_2O_5$ | Cl | Total |
|---|---|---|---|---|---|---|---|---|---|---|---|---|
| **Analytical Period 2: BCR2g** | | | | | | | | | | | | |
| 1 | 54.90 | 2.28 | 13.32 | 11.99 | 0.09 | 3.57 | 7.00 | 2.29 | 1.80 | 0.39 | 0.00 | 97.62 |
| 2 | 55.23 | 2.21 | 13.26 | 11.79 | 0.17 | 3.58 | 7.17 | 2.29 | 1.81 | 0.42 | 0.00 | 97.92 |
| 3 | 55.07 | 2.49 | 13.57 | 11.67 | 0.25 | 3.60 | 7.22 | 2.32 | 1.81 | 0.39 | 0.00 | 98.38 |
| 4 | 55.18 | 2.19 | 13.36 | 11.87 | 0.30 | 3.56 | 7.31 | 2.36 | 1.87 | 0.41 | 0.01 | 98.42 |
| 5 | 54.64 | 2.27 | 13.31 | 12.04 | 0.21 | 3.59 | 7.39 | 2.36 | 1.77 | 0.42 | 0.01 | 98.00 |
| 6 | 55.03 | 2.40 | 13.43 | 11.94 | 0.23 | 3.53 | 7.15 | 2.95 | 1.84 | 0.37 | 0.02 | 98.89 |
| 7 | 55.19 | 2.12 | 13.23 | 11.66 | 0.23 | 3.56 | 7.24 | 2.92 | 1.83 | 0.39 | 0.00 | 98.37 |
| 8 | 55.04 | 2.31 | 13.24 | 11.84 | 0.19 | 3.58 | 7.12 | 2.87 | 1.88 | 0.41 | 0.00 | 98.48 |
| 9 | 55.21 | 2.41 | 13.42 | 12.25 | 0.28 | 3.59 | 7.13 | 2.95 | 1.86 | 0.39 | 0.00 | 99.48 |
| 10 | 55.20 | 2.29 | 13.38 | 12.08 | 0.30 | 3.57 | 7.17 | 3.01 | 1.83 | 0.39 | 0.00 | 99.21 |
| 11 | 53.52 | 2.21 | 13.18 | 12.78 | 0.24 | 3.66 | 7.58 | 2.85 | 1.73 | 0.34 | 0.01 | 98.09 |
| 12 | 54.13 | 2.37 | 13.21 | 13.30 | 0.12 | 3.65 | 7.39 | 3.00 | 1.76 | 0.38 | 0.01 | 99.31 |
| 13 | 53.80 | 2.33 | 13.14 | 13.05 | 0.13 | 3.61 | 7.36 | 2.98 | 1.75 | 0.36 | 0.01 | 98.52 |
| 14 | 54.07 | 2.28 | 13.05 | 12.61 | 0.21 | 3.64 | 7.51 | 3.02 | 1.76 | 0.37 | 0.03 | 98.55 |
| 15 | 54.27 | 2.43 | 13.19 | 13.17 | 0.20 | 3.59 | 7.52 | 3.11 | 1.77 | 0.38 | 0.01 | 99.64 |
| 16 | 55.36 | 2.37 | 13.47 | 11.85 | 0.20 | 3.51 | 7.15 | 3.11 | 1.85 | 0.32 | 0.00 | 99.18 |
| 17 | 55.45 | 2.42 | 13.42 | 11.64 | 0.16 | 3.51 | 7.13 | 3.02 | 1.84 | 0.38 | 0.00 | 98.96 |
| 18 | 54.92 | 2.18 | 13.40 | 12.21 | 0.26 | 3.48 | 7.14 | 3.20 | 1.85 | 0.19 | -0.01 | 98.83 |
| 19 | 53.85 | 2.01 | 12.26 | 13.08 | 0.16 | 3.61 | 7.21 | 2.98 | 1.74 | 0.33 | 0.01 | 97.23 |
| 20 | 54.34 | 2.18 | 12.07 | 13.25 | 0.12 | 3.56 | 7.07 | 2.97 | 1.75 | 0.32 | 0.01 | 97.63 |
| 21 | 54.32 | 2.32 | 12.26 | 13.08 | 0.28 | 3.55 | 7.11 | 2.98 | 1.77 | 0.34 | 0.02 | 98.01 |
| 22 | 53.58 | 2.47 | 11.93 | 12.34 | 0.23 | 3.62 | 6.94 | 3.00 | 1.72 | 0.33 | 0.01 | 96.17 |
| 23 | 54.20 | 2.09 | 11.94 | 12.35 | 0.20 | 3.55 | 6.73 | 3.00 | 1.75 | 1.52 | 0.01 | 97.32 |
| 24 | 54.59 | 2.28 | 11.99 | 12.82 | 0.16 | 3.50 | 6.65 | 3.10 | 1.80 | 0.38 | -0.01 | 97.27 |
| 25 | 54.77 | 2.39 | 12.02 | 11.59 | 0.20 | 3.49 | 6.77 | 3.19 | 1.79 | 0.35 | 0.03 | 96.60 |
| 26 | 54.86 | 2.19 | 12.16 | 12.29 | 0.17 | 3.51 | 6.55 | 3.16 | 1.84 | 0.34 | 0.01 | 97.08 |
| 27 | 55.27 | 2.25 | 13.33 | 12.44 | 0.17 | 3.38 | 7.16 | 3.11 | 1.85 | 0.26 | 0.01 | 99.24 |
| 28 | 55.12 | 2.25 | 13.24 | 12.14 | 0.26 | 3.35 | 7.21 | 3.05 | 1.85 | 0.32 | 0.01 | 98.80 |
| 29 | 55.14 | 2.50 | 13.10 | 12.04 | 0.24 | 3.41 | 7.10 | 3.03 | 1.85 | 0.28 | 0.00 | 98.71 |
| 30 | 55.39 | 2.42 | 13.29 | 12.51 | 0.15 | 3.37 | 7.08 | 3.07 | 1.83 | 0.36 | 0.02 | 99.50 |
| 31 | 55.51 | 2.43 | 13.21 | 12.29 | 0.17 | 3.39 | 7.07 | 2.97 | 1.90 | 0.42 | 0.00 | 99.36 |
| 32 | 53.65 | 2.29 | 12.37 | 11.88 | 0.22 | 3.55 | 7.16 | 3.14 | 1.87 | 0.34 | 0.01 | 96.47 |
| 33 | 54.16 | 2.15 | 12.67 | 11.96 | 0.26 | 3.51 | 7.22 | 3.01 | 1.84 | 0.36 | 0.02 | 97.15 |
| 34 | 54.01 | 2.45 | 12.62 | 11.93 | 0.21 | 3.51 | 7.17 | 3.04 | 1.92 | 0.29 | 0.01 | 97.15 |
| **Mean** | **54.67** | **2.30** | **12.94** | **12.29** | **0.21** | **3.54** | **7.14** | **2.92** | **1.81** | **0.39** | **0.01** | **98.22** |
| St. Dev. | 0.60 | 0.12 | 0.54 | 0.51 | 0.05 | 0.08 | 0.22 | 0.27 | 0.05 | 0.21 | 0.01 | 0.95 |
| **Reference Values** | **54.1** | **2.26** | **13.5** | **12.42** | **0.20** | **3.59** | **7.12** | **3.16** | **1.79** | **0.35** | **n/a** | **98.49** |

| n | $SiO_2$ | $TiO_2$ | $Al_2O_3$ | FeO | MnO | MgO | CaO | $Na_2O$ | $K_2O$ | $P_2O_5$ | Cl | Total |
|---|---|---|---|---|---|---|---|---|---|---|---|---|
| **Analytical Period 3: Cannetto Lami Lava, Lipari** | | | | | | | | | | | | |
| 1 | 74.89 | 0.08 | 12.76 | 1.62 | 0.05 | 0.04 | 0.79 | 4.09 | 5.12 | -0.02 | 0.37 | 99.81 |
| 2 | 74.02 | -0.08 | 12.94 | 1.62 | 0.04 | 0.04 | 0.71 | 3.96 | 5.10 | 0.00 | 0.32 | 98.75 |
| 3 | 74.84 | 0.11 | 12.72 | 1.56 | 0.09 | 0.04 | 0.75 | 4.03 | 5.07 | 0.02 | 0.38 | 99.61 |
| 4 | 73.76 | 0.09 | 12.88 | 1.55 | 0.02 | 0.06 | 0.74 | 3.97 | 5.03 | -0.01 | 0.36 | 98.47 |
| 5 | 74.23 | 0.14 | 12.76 | 1.36 | 0.10 | 0.03 | 0.74 | 4.00 | 5.10 | -0.01 | 0.38 | 98.84 |
| 6 | 73.92 | 0.25 | 12.73 | 1.71 | 0.03 | 0.05 | 0.75 | 4.09 | 5.11 | -0.01 | 0.37 | 99.01 |
| 7 | 73.42 | -0.10 | 12.90 | 1.49 | 0.04 | 0.05 | 0.74 | 4.05 | 5.11 | -0.01 | 0.38 | 98.18 |
| 8 | 73.81 | 0.57 | 12.98 | 1.54 | 0.03 | 0.05 | 0.72 | 4.23 | 5.09 | -0.04 | 0.42 | 99.44 |
| 9 | 74.21 | -0.14 | 13.21 | 1.96 | -0.27 | 0.04 | 0.73 | 3.86 | 4.96 | 0.05 | 0.35 | 99.37 |
| 10 | 73.60 | 0.29 | 13.13 | 1.84 | -0.99 | 0.05 | 0.76 | 3.99 | 5.01 | -0.06 | 0.40 | 99.07 |
| 11 | 73.61 | 0.00 | 13.26 | 1.27 | 0.21 | 0.07 | 0.65 | 4.05 | 5.06 | -0.03 | 0.35 | 98.53 |
| 12 | 73.42 | 0.07 | 12.82 | 1.39 | 0.09 | 0.05 | 0.73 | 3.96 | 5.15 | 0.03 | 0.38 | 98.07 |
| 13 | 73.70 | 0.08 | 12.86 | 2.10 | 0.06 | 0.03 | 0.76 | 3.98 | 5.01 | -0.02 | 0.35 | 98.92 |
| 14 | 73.48 | 0.08 | 12.74 | 1.66 | 0.15 | 0.04 | 0.74 | 3.96 | 5.12 | 0.04 | 0.39 | 98.41 |
| 15 | 73.66 | 0.05 | 12.81 | 1.61 | 0.10 | 0.04 | 0.75 | 4.10 | 5.14 | 0.04 | 0.35 | 98.64 |
| 16 | 73.68 | 0.06 | 12.85 | 1.54 | 0.08 | 0.03 | 0.73 | 4.18 | 5.14 | 0.02 | 0.35 | 98.67 |
| 17 | 73.17 | 0.03 | 12.70 | 1.76 | 0.01 | 0.04 | 0.80 | 3.97 | 5.11 | 0.00 | 0.33 | 97.93 |
| 18 | 73.16 | 0.20 | 12.60 | 1.73 | 0.04 | 0.06 | 0.80 | 4.04 | 5.07 | -0.01 | 0.38 | 98.07 |
| 19 | 73.69 | 0.06 | 12.95 | 1.50 | 0.01 | 0.04 | 0.74 | 4.01 | 5.06 | -0.02 | 0.41 | 98.47 |
| 20 | 72.96 | 0.06 | 12.92 | 1.52 | 0.09 | 0.07 | 1.06 | 3.98 | 5.14 | 0.00 | 0.33 | 98.13 |
| 21 | 72.89 | -0.07 | 12.88 | 1.66 | 0.14 | 0.06 | 0.71 | 4.02 | 5.08 | 0.02 | 0.36 | 97.82 |
| 22 | 73.33 | -0.10 | 12.76 | 1.53 | 0.05 | 0.05 | 0.72 | 3.99 | 5.17 | 0.00 | 0.39 | 97.99 |
| 23 | 74.60 | 0.05 | 12.86 | 1.66 | 0.12 | 0.04 | 0.76 | 4.01 | 5.17 | -0.01 | 0.37 | 99.64 |
| 24 | 73.73 | 0.13 | 12.79 | 1.61 | 0.10 | 0.06 | 0.73 | 4.03 | 5.18 | -0.03 | 0.38 | 98.73 |
| 25 | 73.79 | 0.03 | 12.83 | 1.69 | 0.01 | 0.03 | 0.76 | 4.11 | 5.11 | -0.02 | 0.37 | 98.72 |
| 26 | 73.35 | 0.10 | 12.76 | 1.88 | 0.11 | 0.04 | 0.72 | 4.02 | 5.09 | -0.02 | 0.36 | 98.42 |
| 27 | 73.75 | 0.07 | 12.88 | 1.55 | 0.11 | 0.04 | 0.76 | 3.84 | 5.11 | 0.02 | 0.35 | 98.48 |
| 28 | 74.01 | 0.05 | 12.86 | 1.51 | 0.10 | 0.03 | 0.79 | 4.00 | 5.24 | -0.02 | 0.41 | 99.00 |
| 29 | 74.37 | 0.18 | 12.85 | 1.64 | 0.19 | 0.05 | 0.75 | 4.06 | 5.07 | -0.03 | 0.39 | 99.56 |
| 30 | 73.98 | 0.05 | 12.90 | 1.56 | 0.12 | 0.03 | 0.73 | 4.04 | 5.11 | -0.01 | 0.33 | 98.84 |
| 31 | 73.93 | -0.06 | 12.84 | 1.67 | 0.15 | 0.05 | 0.74 | 3.99 | 5.22 | 0.00 | 0.33 | 98.91 |
| 32 | 73.97 | 0.00 | 12.95 | 1.66 | -0.05 | 0.03 | 0.72 | 4.03 | 5.08 | 0.01 | 0.37 | 98.80 |
| 33 | 74.31 | 0.08 | 12.87 | 1.57 | 0.02 | 0.03 | 0.73 | 4.11 | 5.11 | 0.00 | 0.36 | 99.18 |
| 34 | 73.58 | 0.09 | 12.81 | 1.25 | 0.04 | 0.04 | 0.72 | 4.05 | 5.18 | 0.03 | 0.36 | 98.15 |
| 35 | 74.16 | 0.09 | 12.87 | 1.50 | 0.16 | 0.03 | 0.76 | 4.12 | 5.05 | -0.01 | 0.36 | 99.08 |
| 36 | 74.33 | 0.12 | 13.07 | 1.47 | -0.02 | 0.05 | 0.77 | 4.14 | 5.23 | 0.01 | 0.40 | 99.59 |
| 37 | 73.61 | 0.03 | 12.78 | 1.60 | 0.01 | 0.05 | 0.75 | 4.02 | 5.08 | 0.02 | 0.36 | 98.32 |
| 38 | 73.86 | 0.14 | 12.73 | 1.60 | 0.12 | 0.06 | 0.77 | 4.06 | 5.13 | 0.01 | 0.29 | 98.78 |
| 39 | 73.35 | 0.03 | 12.75 | 1.66 | 0.13 | 0.03 | 0.74 | 4.17 | 5.16 | 0.00 | 0.35 | 98.38 |
| 40 | 73.95 | 0.06 | 12.87 | 1.61 | 0.02 | 0.05 | 0.75 | 4.14 | 5.20 | 0.00 | 0.40 | 99.05 |
| 41 | 73.46 | 0.19 | 13.14 | 1.62 | 0.08 | 0.05 | 0.80 | 4.15 | 5.18 | -0.01 | 0.37 | 99.03 |
| 42 | 74.16 | 0.05 | 12.84 | 1.74 | 0.06 | 0.03 | 0.71 | 4.17 | 5.23 | 0.00 | 0.36 | 99.36 |
| 43 | 73.59 | 0.11 | 12.83 | 1.56 | 0.07 | 0.04 | 0.75 | 4.12 | 5.17 | 0.00 | 0.35 | 98.57 |
| 44 | 73.51 | -0.05 | 12.89 | 1.63 | 0.12 | 0.04 | 0.76 | 4.05 | 5.10 | 0.00 | 0.38 | 98.48 |
| 45 | 73.54 | 0.09 | 12.78 | 1.41 | 0.06 | 0.05 | 0.78 | 4.06 | 5.12 | 0.00 | 0.38 | 98.26 |
| 46 | 73.04 | 0.15 | 12.71 | 1.43 | 0.17 | 0.03 | 0.77 | 4.08 | 5.13 | 0.03 | 0.41 | 97.93 |
| 47 | 73.96 | 0.07 | 12.81 | 1.22 | 0.12 | 0.05 | 0.69 | 4.10 | 5.08 | -0.02 | 0.34 | 98.42 |
| 48 | 73.34 | -0.03 | 12.69 | 1.59 | 0.12 | 0.03 | 0.76 | 3.91 | 5.11 | 0.00 | 0.36 | 97.92 |
| 49 | 73.71 | 0.13 | 12.84 | 1.60 | 0.08 | 0.05 | 0.67 | 4.09 | 5.12 | 0.00 | 0.33 | 98.61 |
| 50 | 74.61 | -0.03 | 13.02 | 1.59 | 0.01 | 0.04 | 0.77 | 4.09 | 5.18 | 0.01 | 0.36 | 99.68 |
| 51 | 73.71 | 0.12 | 12.96 | 1.79 | 0.17 | 0.06 | 0.72 | 4.10 | 5.19 | -0.04 | 0.37 | 99.18 |
| 52 | 73.95 | 0.10 | 12.92 | 1.50 | 0.06 | 0.05 | 0.70 | 4.00 | 5.13 | -0.02 | 0.36 | 98.76 |
| 53 | 73.35 | 0.12 | 12.91 | 1.38 | 0.14 | 0.02 | 0.73 | 4.13 | 5.06 | -0.01 | 0.34 | 98.19 |
| 54 | 73.51 | 0.06 | 12.86 | 1.57 | 0.01 | 0.04 | 0.77 | 4.00 | 5.12 | 0.00 | 0.35 | 98.30 |
| 55 | 73.31 | 0.10 | 12.90 | 1.64 | 0.10 | 0.05 | 0.74 | 3.97 | 5.18 | 0.00 | 0.37 | 98.36 |
| 56 | 73.89 | 0.08 | 12.80 | 1.74 | 0.04 | 0.03 | 0.71 | 4.10 | 5.25 | -0.04 | 0.33 | 98.97 |
| 57 | 73.38 | 0.03 | 12.93 | 1.49 | 0.03 | 0.04 | 0.71 | 4.08 | 5.09 | -0.03 | 0.34 | 98.12 |
| 58 | 73.90 | -0.04 | 13.01 | 1.17 | 0.11 | 0.04 | 0.68 | 3.98 | 5.22 | 0.01 | 0.37 | 98.49 |
| 59 | 74.04 | 0.23 | 13.11 | 1.47 | -0.01 | 0.05 | 0.73 | 4.08 | 5.17 | 0.02 | 0.37 | 99.27 |
| 60 | 73.72 | 0.14 | 12.87 | 1.46 | 0.14 | 0.05 | 0.76 | 4.06 | 5.20 | 0.01 | 0.35 | 98.77 |
| **Mean** | **73.76** | **0.07** | **12.87** | **1.58** | **0.06** | **0.04** | **0.75** | **4.05** | **5.13** | **0.00** | **0.36** | **98.71** |
| St. Dev. | 0.43 | 0.11 | 0.13 | 0.16 | 0.15 | 0.01 | 0.05 | 0.08 | 0.06 | 0.02 | 0.02 | 0.51 |
| **Reference Values** a | **74.03** | **0.08** | **12.72** | ***1.75*** | **0.08** | **0.00** | **0.72** | **4.06** | **5.18** | **n/a** | **0** | **98.62** |
| **Reference Values** b | **73.72** | **nr** | **13.04** | ***1.76*** | **nr** | **0.03** | **0.76** | **4.06** | **5.06** | **n/a** | **nr** | **98.43** |

# Appendix 2 – LA-ICP-MS Data

| Tephra Horizon Labels used in chapter 4 | Actual Horizon |
|---|---|
| Horizon A | MD04-2822 2327-2328 cm |
| Horizon B | MD04-2822 2359-2360 cm |
| Horizon C | MD04-2822 2361-2362 cm |
| Horizon D | MD04-2822 2363-2364 cm |
| Horizon E | MD04-2822 2365-2366 cm |
| Horizon F | GRIP 1528.61 m |
| Horizon G | GRIP 1716.08 m |
| Horizon H | GRIP 2498.5 m |
| Horizon I | GRIP 2499.75 m-1 |
| Horizon J | GRIP 2501.05 m |
| Horizon K | GRIP 2531.8 m |
| Horizon L | GRIP 2532.95 m |
| Horizon M | NGRIP 1848 m |
| Horizon N | NGRIP 1895.3 m |
| Horizon O | NGRIP 1915.5 m |
| Horizon P | NGRIP 2441.14 m |
| Horizon Q | NGRIP 2441.28 m |
| Horizon R | NGRIP 2454.9 m |
| Horizon S | NGRIP 2500.9 m |
| Horizon T | NGRIP 2548.35 m |
| Horizon U | NGRIP 2574.55 m |
| Horizon V | NGRIP 2631.9 m |
| Horizon W | LINK 14:185 |
| Horizon X | LINK 17:634 |

The following tables provide the trace element data from shards within horizons analysed using a 6 μm laser beam diameter. The subsequent tables provide the full geochemical data sets for the Fugloyarbanki Tephra and Saksunarvatn Ash horizons described in section 4.5 and full geochemical datasets for the horizons sourced from the Katla volcanic system described in section 4.6.

**Trace element concentrations of shards from the MD04-2822 2361-2362 cm sample analysed using a 6 µm laser beam diameter. n = shard number and relates to the major oxide analyses from this horizon. All concentrations are presented as ppm. Mean and 1 standard deviations are shown.**

| Horizon C – MD04-2822 2361-2362 cm | | | | | | | | | | |
|---|---|---|---|---|---|---|---|---|---|---|
| n | 1 | 3 | 4 | 6 | 7 | 11 | 13 | 23 | **Average** | St. Dev. |
| Sc | 94.68 | 73.37 | 67.22 | 30.19 | 34.22 | 35.87 | 24.71 | 27.66 | **48.49** | 26.19 |
| Rb | 136.00 | 180.59 | 231.69 | 135.34 | 148.04 | 157.23 | 113.25 | 147.32 | **156.18** | 36.11 |
| Sr | 260.55 | 318.97 | 387.93 | 253.88 | 228.80 | 267.38 | 247.35 | 234.67 | **274.94** | 53.35 |
| Y | 78.72 | 144.78 | 93.80 | 112.40 | 140.56 | 173.78 | 186.72 | 145.21 | **134.50** | 37.39 |
| Zr | 164.36 | 255.42 | 226.15 | 222.09 | 302.58 | 293.06 | 329.78 | 294.19 | **260.95** | 54.36 |
| Nb | 61.01 | 87.75 | 65.70 | 70.20 | 95.33 | 127.08 | 108.46 | 100.06 | **89.45** | 22.90 |
| Cs | 6.70 | 4.35 | 12.55 | 2.74 | 3.86 | 5.04 | 3.99 | 0.95 | **5.02** | 3.47 |
| Ba | 462.37 | 628.84 | 749.33 | 510.58 | 560.77 | 698.22 | 549.25 | 596.98 | **594.54** | 95.32 |
| La | 39.92 | 76.00 | 50.43 | 56.54 | 67.09 | 75.37 | 109.76 | 71.86 | **68.37** | 21.06 |
| Ce | 79.79 | 165.53 | 120.45 | 118.40 | 144.32 | 179.83 | 175.26 | 174.37 | **144.74** | 35.81 |
| Pr | 8.64 | 23.54 | 13.86 | 14.18 | 14.83 | 21.73 | 17.23 | 20.36 | **16.80** | 4.91 |
| Nd | 47.37 | 115.00 | 40.20 | 101.74 | 90.83 | 67.40 | 99.82 | 95.77 | **82.27** | 27.31 |
| Sm | 23.59 | -8.86 | -2.68 | 22.15 | -1.25 | 13.72 | 31.27 | 58.60 | **17.07** | 22.05 |
| Eu | 17.21 | 22.79 | 29.24 | 25.49 | 9.81 | 16.99 | 15.57 | 10.40 | **18.44** | 6.93 |
| Gd | 4.95 | 20.78 | 39.75 | 18.10 | 19.36 | 37.66 | 44.55 | 16.90 | **25.26** | 13.76 |
| Tb | 1.19 | 2.60 | 3.80 | 1.07 | 3.35 | 6.07 | 2.50 | 2.70 | **2.91** | 1.59 |
| Dy | 7.85 | 20.01 | 11.57 | 15.98 | 33.36 | 25.33 | 34.34 | 19.58 | **21.00** | 9.56 |
| Ho | 3.22 | 4.28 | 1.01 | 3.19 | 7.44 | 6.14 | 6.24 | 7.47 | **4.87** | 2.32 |
| Er | 4.98 | 12.73 | 16.37 | 6.62 | 16.60 | 18.55 | 15.55 | 12.39 | **12.98** | 4.89 |
| Tm | 0.85 | -1.72 | 4.57 | 1.58 | 5.38 | 2.95 | -1.38 | 2.76 | **1.87** | 2.57 |
| Yb | 11.51 | 17.20 | 2.33 | 13.78 | 20.45 | 23.78 | 20.92 | 20.96 | **16.37** | 6.99 |
| Lu | 2.30 | 2.40 | 1.67 | 0.72 | 3.04 | 2.99 | 4.00 | 2.28 | **2.42** | 0.98 |
| Hf | 9.86 | 7.92 | 5.02 | 10.72 | 11.62 | 9.05 | 17.44 | 9.10 | **10.09** | 3.57 |
| Ta | 6.04 | 9.62 | 9.88 | 3.62 | 6.05 | 9.31 | 7.29 | 8.03 | **7.48** | 2.17 |
| Th | 8.01 | 15.05 | 11.32 | 10.03 | 15.51 | 16.91 | 16.47 | 20.17 | **14.18** | 4.05 |
| U | 2.51 | 4.35 | 3.94 | 3.13 | 5.17 | 4.82 | 6.99 | 6.05 | **4.62** | 1.47 |

**Trace element concentrations of shards from the MD04-2822 2363-2364 cm sample analysed using a 6 µm laser beam diameter. n = shard number and relates to the major oxide analyses from this horizon. All concentrations are presented as ppm. Mean and 1 standard deviations are shown.**

| Horizon D – MD04-2822 2363-2364 cm | | | | | | | | | | |
|---|---|---|---|---|---|---|---|---|---|---|
| n | 1 | 3 | 7 | 8 | 10 | 12 | 17 | 20 | **Average** | St. Dev. |
| Sc | -9.41 | -25.01 | -29.00 | -51.30 | -32.59 | -45.64 | -59.09 | -53.71 | **-38.22** | 17.00 |
| Rb | 104.23 | 112.01 | 72.91 | 106.14 | 115.74 | 129.83 | 98.43 | 87.11 | **103.30** | 17.54 |
| Sr | 222.22 | 214.02 | 172.78 | 214.83 | 243.98 | 226.11 | 218.10 | 185.78 | **212.23** | 22.68 |
| Y | 157.20 | 156.99 | 134.86 | 188.46 | 198.63 | 189.74 | 181.49 | 202.14 | **176.19** | 23.83 |
| Zr | 263.97 | 319.73 | 363.13 | 375.05 | 450.18 | 342.01 | 302.47 | 376.65 | **349.15** | 56.29 |
| Nb | 94.94 | 109.85 | 105.26 | 146.38 | 145.79 | 142.43 | 117.49 | 130.85 | **124.12** | 20.00 |
| Cs | 4.66 | 3.94 | 1.04 | -0.66 | 0.22 | 2.31 | 3.21 | 3.44 | **2.27** | 1.89 |
| Ba | 604.83 | 814.31 | 626.24 | 867.33 | 788.65 | 1066.74 | 985.86 | 1130.31 | **860.53** | 192.22 |
| La | 95.44 | 78.05 | 87.61 | 97.31 | 103.69 | 95.83 | 82.36 | 87.64 | **90.99** | 8.53 |
| Ce | 187.00 | 155.76 | 160.56 | 181.62 | 188.17 | 200.33 | 180.73 | 191.14 | **180.66** | 15.21 |
| Pr | 26.34 | 22.87 | 18.93 | 26.74 | 32.96 | 31.18 | 21.40 | 23.95 | **25.55** | 4.77 |
| Nd | 136.99 | 76.67 | 81.32 | 97.23 | 98.88 | 111.57 | 95.68 | 139.79 | **104.77** | 23.37 |
| Sm | 23.07 | 30.73 | 10.83 | 12.05 | 26.55 | 25.70 | 20.62 | 18.96 | **21.06** | 6.96 |
| Eu | 0.57 | 7.24 | 7.48 | 14.59 | 8.79 | 10.06 | 9.45 | 14.86 | **9.13** | 4.52 |
| Gd | 18.57 | 25.33 | 32.59 | 15.41 | 32.90 | 46.25 | 35.14 | 27.43 | **29.20** | 9.80 |
| Tb | 3.35 | 3.13 | 5.95 | 3.16 | 5.27 | 3.51 | 7.72 | 6.16 | **4.78** | 1.74 |
| Dy | 38.65 | 28.21 | 21.12 | 28.20 | 39.17 | 34.31 | 32.25 | 40.92 | **32.85** | 6.78 |
| Ho | 4.23 | 4.18 | 6.22 | 6.06 | 5.10 | 8.99 | 5.56 | 7.12 | **5.93** | 1.59 |
| Er | 15.08 | 17.31 | 14.28 | 24.01 | 27.10 | 28.43 | 26.02 | 19.06 | **21.41** | 5.64 |
| Tm | 1.67 | 1.58 | 2.39 | 5.39 | -0.56 | 3.91 | 2.74 | 1.07 | **2.27** | 1.81 |
| Yb | 18.61 | 26.57 | 13.54 | 20.13 | 22.48 | 16.00 | 23.87 | 13.40 | **19.32** | 4.84 |
| Lu | 4.02 | 2.58 | 2.09 | 2.49 | 3.60 | 3.79 | 3.75 | 2.88 | **3.15** | 0.72 |
| Hf | 14.85 | 11.70 | 15.23 | 11.79 | 9.83 | 16.66 | 13.11 | 11.95 | **13.14** | 2.26 |
| Ta | 6.63 | 6.87 | 6.61 | 10.96 | 7.35 | 7.61 | 12.07 | 11.09 | **8.65** | 2.30 |
| Th | 16.12 | 19.60 | 14.97 | 15.47 | 25.80 | 22.35 | 16.64 | 22.31 | **19.16** | 3.99 |
| U | 3.76 | 6.65 | 5.83 | 4.93 | 6.15 | 6.38 | 4.99 | 4.45 | **5.39** | 1.02 |

**Trace element concentrations of shards from the MD04-2822 2365-2366 cm sample analysed using a 6 µm laser beam diameter. n = shard number and relates to the major oxide analyses from this horizon. All concentrations are presented as ppm. Mean and 1 standard deviations are shown.**

| Horizon E – MD04-2822 2365-2366 cm | | | | | | | | | |
|---|---|---|---|---|---|---|---|---|---|
| n | 1 | 3 | 7 | 9 | 13 | 14 | 17 | **Average** | St. Dev. |
| Sc | -9.18 | 10.31 | -21.59 | -9.60 | -18.49 | -11.75 | -10.98 | **-10.18** | 10.19 |
| Rb | 151.87 | 109.33 | 85.04 | 104.16 | 134.12 | 111.23 | 102.86 | **114.09** | 22.09 |
| Sr | 195.20 | 212.91 | 207.11 | 165.81 | 175.68 | 193.09 | 140.73 | **184.36** | 25.33 |
| Y | 153.66 | 183.86 | 224.09 | 175.31 | 179.83 | 185.04 | 212.78 | **187.80** | 23.63 |
| Zr | 304.94 | 355.57 | 356.97 | 305.58 | 300.73 | 339.02 | 389.48 | **336.04** | 33.73 |
| Nb | 110.62 | 117.25 | 102.93 | 123.79 | 111.41 | 114.10 | 93.74 | **110.55** | 9.78 |
| Cs | 7.36 | 1.83 | 1.99 | 1.97 | 2.90 | 1.70 | 4.32 | **3.15** | 2.07 |
| Ba | 701.90 | 835.07 | 707.08 | 779.87 | 810.06 | 782.58 | 663.42 | **754.28** | 63.67 |
| La | 75.39 | 73.69 | 93.44 | 69.47 | 74.24 | 116.48 | 92.15 | **84.98** | 16.79 |
| Ce | 156.84 | 164.87 | 193.50 | 185.65 | 202.34 | 191.07 | 162.61 | **179.55** | 17.81 |
| Pr | 15.91 | 18.02 | 29.25 | 30.70 | 22.21 | 24.08 | 23.25 | **23.35** | 5.39 |
| Nd | 98.88 | 93.83 | 116.76 | 103.19 | 117.69 | 117.93 | 86.59 | **104.98** | 12.72 |
| Sm | 8.98 | 17.65 | 37.59 | 3.05 | 7.88 | 20.29 | 36.25 | **18.81** | 13.69 |
| Eu | 10.09 | 10.32 | 8.87 | 3.61 | 12.46 | 6.56 | 17.69 | **9.94** | 4.46 |
| Gd | 5.51 | 18.20 | 35.86 | 22.45 | 10.50 | 26.33 | 10.00 | **18.41** | 10.67 |
| Tb | 1.71 | 5.28 | 3.84 | 5.51 | 3.56 | 5.08 | 4.76 | **4.25** | 1.34 |
| Dy | 23.73 | 24.71 | 39.33 | 22.77 | 21.88 | 26.24 | 27.47 | **26.59** | 5.94 |
| Ho | 4.80 | 7.51 | 7.27 | 7.45 | 6.93 | 6.53 | 5.89 | **6.62** | 0.99 |
| Er | 24.12 | 22.62 | 27.05 | 15.15 | 17.74 | 24.93 | 25.27 | **22.41** | 4.35 |
| Tm | 1.37 | 2.02 | 2.78 | 3.76 | 2.68 | 1.25 | 1.02 | **2.13** | 1.00 |
| Yb | 23.57 | 21.65 | 33.71 | 25.31 | 21.55 | 19.75 | 13.60 | **22.73** | 6.09 |
| Lu | 1.45 | 2.49 | 3.13 | 2.51 | 4.72 | 2.04 | 3.95 | **2.90** | 1.13 |
| Hf | 18.64 | 12.78 | 14.53 | 14.03 | 17.96 | 13.88 | 13.77 | **15.09** | 2.27 |
| Ta | 10.90 | 8.53 | 9.61 | 8.45 | 8.25 | 4.69 | 9.12 | **8.51** | 1.91 |
| Th | 17.96 | 13.47 | 23.91 | 16.45 | 18.41 | 22.23 | 22.12 | **19.22** | 3.71 |
| U | 3.80 | 4.38 | 6.07 | 4.66 | 5.89 | 4.80 | 5.56 | **5.02** | 0.84 |

**Trace element concentrations of shards from the GRIP 1716.08 m tephra horizon analysed using a 6 µm laser beam diameter. n = shard number and relates to the major oxide analyses from this horizon. All concentrations are presented as ppm. Mean and 1 standard deviations are shown.**

| Horizon G – GRIP 1716.08 m | | | | | | | |
|---|---|---|---|---|---|---|---|
| n | 1 | 9 | 15 | 16 | 22 | **Average** | St. Dev. |
| Sc | 69.00 | -12.67 | 102.52 | 7.07 | 25.12 | **38.21** | 46.94 |
| Rb | 24.55 | 38.10 | 54.84 | 50.63 | 55.59 | **44.74** | 13.29 |
| Sr | 483.81 | 636.18 | 1023.64 | 870.46 | 670.10 | **736.84** | 211.37 |
| Y | 28.80 | 49.06 | 63.15 | 44.57 | 44.00 | **45.92** | 12.30 |
| Zr | 171.44 | 305.90 | 460.51 | 315.09 | 450.75 | **340.74** | 119.35 |
| Nb | 45.10 | 41.50 | 96.09 | 70.92 | 73.34 | **65.39** | 22.47 |
| Cs | 1.52 | 0.35 | -5.48 | -0.78 | -0.11 | **-0.90** | 2.69 |
| Ba | 776.05 | 645.42 | 1182.27 | 705.84 | 714.33 | **804.78** | 216.04 |
| La | 15.68 | 30.80 | 53.03 | 19.87 | 24.79 | **28.83** | 14.66 |
| Ce | 32.12 | 60.96 | 87.61 | 62.47 | 77.81 | **64.19** | 21.07 |
| Pr | 3.49 | 5.00 | 12.43 | 9.95 | 17.44 | **9.66** | 5.66 |
| Nd | 64.10 | 68.24 | 127.21 | 13.43 | 58.72 | **66.34** | 40.53 |
| Sm | 12.00 | 4.36 | -8.16 | -6.62 | 4.20 | **1.15** | 8.43 |
| Eu | 5.16 | -1.47 | -0.05 | -7.35 | 8.75 | **1.01** | 6.21 |
| Gd | 0.84 | 5.09 | 6.29 | -5.47 | 0.14 | **1.38** | 4.65 |
| Tb | 0.39 | 3.16 | 1.95 | 0.33 | 2.24 | **1.61** | 1.23 |
| Dy | 3.10 | 22.12 | 2.42 | 11.29 | 22.91 | **12.37** | 9.90 |
| Ho | -0.45 | 1.60 | 1.66 | 2.46 | 0.54 | **1.16** | 1.13 |
| Er | 1.06 | 1.15 | 11.82 | -0.05 | 0.74 | **2.94** | 4.98 |
| Tm | 0.60 | -0.67 | -1.26 | -0.98 | -0.21 | **-0.50** | 0.73 |
| Yb | -0.78 | 0.74 | 6.07 | 7.94 | 2.10 | **3.22** | 3.67 |
| Lu | 0.10 | -0.85 | -1.42 | -1.07 | 2.06 | **-0.23** | 1.40 |
| Hf | 5.62 | 6.19 | 6.10 | 1.62 | 1.68 | **4.24** | 2.38 |
| Ta | 4.20 | 3.39 | 5.67 | 5.58 | 3.11 | **4.39** | 1.20 |
| Pb | 26.75 | 8.79 | 27.82 | 48.04 | 12.43 | **24.77** | 15.51 |
| Th | 1.18 | 3.10 | 4.47 | 2.05 | 4.99 | **3.16** | 1.60 |
| U | 0.10 | 0.10 | 2.13 | 0.84 | 1.76 | **0.99** | 0.94 |

**Trace element concentrations of shards from the GRIP 2501.05 m tephra horizon analysed using a 6 µm laser beam diameter. n = shard number and relates to the major oxide analyses from this horizon. All concentrations are presented as ppm. Mean and 1 standard deviations are shown.**

| Horizon J – GRIP 2501.05 m | | | | | | | |
|---|---|---|---|---|---|---|---|
| n | 4 | 8 | 9 | 16 | 19 | **Average** | St. Dev. |
| Sc | 268.64 | -274.62 | 21.60 | 85.38 | 86.70 | **37.54** | 197.36 |
| Rb | 34.38 | 56.15 | 16.09 | 8.75 | 7.61 | **24.60** | 20.64 |
| Sr | 4309.84 | 5422.25 | 1978.84 | 3943.83 | 2084.14 | **3547.78** | 1487.87 |
| Y | 37.66 | 16.53 | 39.02 | 13.84 | 22.11 | **25.83** | 11.81 |
| Zr | 250.43 | 193.06 | 82.03 | 46.21 | 73.69 | **129.08** | 87.99 |
| Nb | 18.51 | 22.96 | 4.26 | 12.54 | 26.01 | **16.86** | 8.68 |
| Cs | -2.44 | -11.88 | 1.50 | 0.16 | -1.19 | **-2.77** | 5.30 |
| Ba | -39.90 | -139.91 | -140.72 | -27.78 | -23.49 | **-74.36** | 60.51 |
| La | 17.63 | 27.18 | 11.93 | 9.77 | 17.59 | **16.82** | 6.75 |
| Ce | 49.14 | 37.24 | 14.24 | 5.69 | 20.25 | **25.31** | 17.63 |
| Pr | 5.49 | 10.07 | 5.17 | 5.66 | 9.24 | **7.13** | 2.34 |
| Nd | 56.46 | 41.67 | 17.07 | 11.93 | 14.51 | **28.33** | 19.72 |
| Sm | 2.11 | 33.50 | -2.75 | 1.23 | 5.22 | **7.86** | 14.61 |
| Eu | 19.68 | -22.06 | 3.21 | -5.21 | -0.91 | **-1.06** | 15.05 |
| Gd | -19.26 | -12.90 | -15.10 | -13.69 | -6.98 | **-13.59** | 4.43 |
| Tb | 0.85 | -3.16 | 4.31 | 0.40 | 0.78 | **0.64** | 2.65 |
| Dy | 11.46 | 0.30 | 9.14 | 8.11 | 5.85 | **6.97** | 4.24 |
| Ho | 1.58 | 1.78 | 1.01 | 0.19 | 1.50 | **1.21** | 0.64 |
| Er | 0.99 | 4.87 | 1.35 | 0.18 | 3.61 | **2.20** | 1.96 |
| Tm | 1.94 | -1.22 | -0.09 | -0.13 | 0.72 | **0.24** | 1.17 |
| Yb | 2.83 | 4.30 | 3.20 | -0.63 | 1.86 | **2.31** | 1.86 |
| Lu | -1.53 | -0.44 | -1.11 | -0.98 | 0.31 | **-0.75** | 0.71 |
| Hf | 3.52 | 14.37 | 10.50 | 1.75 | 6.36 | **7.30** | 5.15 |
| Ta | 6.97 | 6.34 | -0.52 | -0.73 | 2.09 | **2.83** | 3.67 |
| Th | 1.56 | 3.81 | 0.96 | 2.33 | 1.66 | **2.06** | 1.09 |
| U | 7.76 | 2.36 | 1.53 | 0.22 | 0.14 | **2.40** | 3.14 |

**Trace element concentrations of shards from the GRIP 2531.8 m tephra horizon analysed using a 6 µm laser beam diameter. n = shard number and relates to the major oxide analyses from this horizon. All concentrations are presented as ppm. Mean and 1 standard deviations are shown.**

| Horizon K – GRIP 2531.8 m | | | | | | | |
|---|---|---|---|---|---|---|---|
| n | 5 | 6 | 9 | 12 | 15 | **Average** | St. Dev. |
| Sc | -80.24 | -143.06 | -27.71 | 19.81 | 51.15 | **-36.01** | 77.78 |
| Rb | 49.19 | 63.72 | 45.25 | 52.46 | 36.37 | **49.40** | 10.02 |
| Sr | 4738.98 | 4041.72 | 4630.65 | 3488.39 | 3394.77 | **4058.90** | 623.75 |
| Y | 123.29 | 194.84 | 179.84 | 200.94 | 168.90 | **173.56** | 30.78 |
| Zr | 838.66 | 801.62 | 922.49 | 721.27 | 667.79 | **790.36** | 99.64 |
| Nb | 170.28 | 150.35 | 145.24 | 137.08 | 154.21 | **151.43** | 12.33 |
| Cs | -0.06 | -1.22 | -0.68 | 2.83 | 1.97 | **0.57** | 1.75 |
| Ba | -622.42 | -1133.10 | -1229.52 | -788.94 | -682.45 | **-891.29** | 273.52 |
| La | 131.78 | 114.46 | 236.38 | 92.59 | 92.01 | **133.44** | 59.89 |
| Ce | 186.71 | 136.69 | 172.88 | 137.85 | 165.09 | **159.84** | 22.02 |
| Pr | 74.62 | 79.64 | 86.74 | 63.37 | 46.58 | **70.19** | 15.71 |
| Nd | 154.07 | 107.17 | 198.24 | 222.42 | 237.63 | **183.90** | 53.28 |
| Sm | 36.27 | 59.72 | 134.97 | 56.00 | 46.43 | **66.68** | 39.24 |
| Eu | 1.56 | 15.55 | 21.80 | 10.64 | 9.58 | **11.83** | 7.50 |
| Gd | 71.65 | 27.85 | 83.93 | 41.94 | 36.21 | **52.32** | 24.18 |
| Tb | 6.82 | 10.32 | 8.74 | 3.28 | 4.27 | **6.69** | 2.95 |
| Dy | 27.09 | 50.90 | 55.73 | 58.67 | 32.84 | **45.05** | 14.19 |
| Ho | 9.71 | 14.61 | 14.85 | 9.89 | 13.05 | **12.42** | 2.49 |
| Er | 17.42 | 19.45 | 26.26 | 12.38 | 21.54 | **19.41** | 5.12 |
| Tm | 4.75 | 7.95 | 2.34 | 1.55 | 5.37 | **4.39** | 2.55 |
| Yb | 26.41 | 13.00 | 20.19 | 9.03 | 16.54 | **17.04** | 6.68 |
| Lu | 1.29 | 1.28 | 2.05 | 0.31 | 5.67 | **2.12** | 2.08 |
| Hf | 48.59 | 36.07 | 29.25 | 30.10 | 11.00 | **31.00** | 13.59 |
| Ta | 10.38 | 14.62 | 11.01 | 10.58 | 6.38 | **10.59** | 2.92 |
| Th | 15.11 | 20.69 | 14.33 | 10.14 | 16.04 | **15.26** | 3.78 |
| U | 3.30 | 8.34 | 2.10 | 1.78 | 1.98 | **3.50** | 2.77 |

**Trace element concentrations of shards from the GRIP 2532.95 m tephra horizon analysed using a 6 µm laser beam diameter. n = shard number and relates to the major oxide analyses from this horizon. All concentrations are presented as ppm. Mean and 1 standard deviations are shown.**

| Horizon L – GRIP 2532.95 m | | | | | | | |
|---|---|---|---|---|---|---|---|
| n | 1 | 3 | 4 | 8 | 19 | **Average** | St. Dev. |
| Sc | 83.40 | -117.18 | -126.54 | 41.58 | -40.51 | **-31.85** | 93.54 |
| Rb | -2.54 | 60.72 | 41.39 | 82.51 | 87.75 | **53.96** | 36.58 |
| Sr | 513.92 | 1510.08 | 2013.06 | 1105.15 | 1790.01 | **1386.44** | 593.98 |
| Y | 37.03 | 187.02 | 198.26 | 153.24 | 204.02 | **155.91** | 69.31 |
| Zr | 212.36 | 811.39 | 1128.18 | 513.45 | 1514.46 | **835.97** | 509.72 |
| Nb | 39.30 | 83.00 | 138.93 | 117.13 | 199.63 | **115.60** | 60.19 |
| Cs | -2.18 | 11.33 | 3.68 | 12.82 | -5.00 | **4.13** | 7.92 |
| Ba | -42.23 | -1518.51 | -1232.95 | -1010.91 | -2033.90 | **-1167.70** | 736.36 |
| La | 31.85 | 62.88 | 129.72 | 55.79 | 215.82 | **99.21** | 74.62 |
| Ce | 31.72 | 101.71 | 178.84 | 102.93 | 246.80 | **132.40** | 82.45 |
| Pr | 5.79 | 28.07 | 20.34 | 7.57 | 21.13 | **16.58** | 9.54 |
| Nd | 88.07 | 186.41 | 99.56 | 81.75 | 96.60 | **110.48** | 43.02 |
| Sm | 10.07 | 51.41 | 81.23 | 53.11 | 35.48 | **46.26** | 26.09 |
| Eu | -4.62 | 14.94 | 19.01 | -3.66 | 84.41 | **22.02** | 36.47 |
| Gd | 8.24 | 78.93 | 103.32 | 30.90 | 26.57 | **49.59** | 39.80 |
| Tb | 1.23 | 7.89 | 19.89 | 6.14 | 13.26 | **9.68** | 7.14 |
| Dy | 6.79 | 28.61 | 27.58 | 24.57 | 24.69 | **22.45** | 8.93 |
| Ho | 0.92 | 2.40 | 4.91 | 0.98 | 9.58 | **3.76** | 3.64 |
| Er | 14.96 | 7.76 | 40.90 | 27.89 | 27.10 | **23.72** | 12.80 |
| Tm | 0.88 | 1.46 | 1.59 | -1.14 | -2.09 | **0.14** | 1.66 |
| Yb | 12.57 | 20.32 | 29.09 | 11.99 | 39.73 | **22.74** | 11.77 |
| Lu | 3.10 | 3.54 | 9.22 | 5.66 | 7.39 | **5.78** | 2.58 |
| Hf | 5.73 | 2.37 | 19.44 | 10.30 | 7.19 | **9.01** | 6.49 |
| Ta | -1.11 | 4.22 | 6.81 | 12.02 | -9.21 | **2.55** | 8.10 |
| Th | 2.58 | 7.55 | 10.50 | 3.70 | 10.65 | **6.99** | 3.75 |
| U | 0.00 | 1.77 | 4.51 | 11.53 | 4.15 | **4.39** | 4.40 |

**Trace element concentrations of shards from the NGRIP 1915.5 m tephra horizon analysed using a 6 µm laser beam diameter. n = shard number and relates to the major oxide analyses from this horizon. All concentrations are presented as ppm. Mean and 1 standard deviations are shown.**

| Horizon O - NGRIP 1915.5 m | | | | | | | | | | | |
|---|---|---|---|---|---|---|---|---|---|---|---|
| n | 3 | 4 | 6 | 8 | 9 | 10 | 14 | 15 | 16 | **Average** | St. Dev. |
| Sc | 167.17 | 105.72 | 31.32 | 46.02 | -5.34 | 145.41 | 126.06 | 78.30 | 80.45 | 86.12 | 56.05 |
| Rb | 89.52 | 54.57 | 50.42 | 51.01 | 35.53 | 28.07 | 29.77 | 25.48 | 51.09 | 46.16 | 19.85 |
| Sr | 658.44 | 566.80 | 381.99 | 218.79 | 243.71 | 299.40 | 312.13 | 476.91 | 459.02 | 401.91 | 149.75 |
| Y | 31.94 | 24.53 | 15.11 | 19.00 | 13.81 | 16.73 | 21.80 | 28.49 | 31.47 | 22.54 | 6.94 |
| Zr | 214.66 | 174.65 | 128.67 | 123.81 | 126.08 | 123.07 | 101.71 | 159.03 | 161.61 | 145.92 | 34.69 |
| Nb | 43.20 | 30.83 | 14.44 | 8.17 | 7.00 | 14.31 | 19.73 | 22.08 | 22.55 | 20.26 | 11.39 |
| Cs | 2.08 | 0.66 | -0.14 | 3.33 | -0.40 | 0.80 | -0.82 | 1.11 | 0.00 | 0.74 | 1.31 |
| Ba | 0.10 | -11.60 | -54.42 | 0.14 | -33.05 | -141.92 | -130.43 | -216.95 | -138.78 | -80.77 | 78.23 |
| La | 20.29 | 20.83 | 12.22 | 12.40 | 12.35 | 14.60 | 11.13 | 19.60 | 15.16 | 15.40 | 3.85 |
| Ce | 39.02 | 35.32 | 18.73 | 13.90 | 14.31 | 20.91 | 20.21 | 27.06 | 35.13 | 24.96 | 9.53 |
| Pr | 9.35 | 8.21 | 4.50 | 5.19 | 4.45 | 2.86 | 4.90 | 4.45 | 5.28 | 5.47 | 2.03 |
| Nd | 35.34 | 20.77 | 3.76 | 12.39 | 18.26 | 10.21 | 6.20 | 34.14 | 19.80 | 17.87 | 11.21 |
| Sm | 2.61 | -2.57 | 7.19 | 7.16 | 4.04 | 8.06 | -1.25 | -2.94 | -2.42 | 2.21 | 4.61 |
| Eu | 40.48 | 21.64 | 14.83 | -1.65 | 1.65 | 3.55 | 6.20 | 8.24 | 0.50 | 10.61 | 13.41 |
| Gd | -46.44 | -13.97 | 12.01 | -3.90 | -5.91 | 32.73 | 34.34 | 43.50 | 30.33 | 9.19 | 29.26 |
| Tb | 1.80 | 2.07 | 0.19 | 0.54 | 0.78 | 0.07 | 1.83 | 1.09 | 0.87 | 1.03 | 0.73 |
| Dy | 5.85 | 10.71 | 6.03 | 6.47 | 2.82 | 0.96 | 0.69 | 0.37 | 4.97 | 4.32 | 3.42 |
| Ho | 1.35 | 1.42 | 0.56 | -0.08 | -0.06 | 0.78 | 0.59 | 1.16 | 0.14 | 0.65 | 0.58 |
| Er | 5.33 | 6.97 | 1.62 | -0.39 | 0.33 | 3.27 | 0.50 | 2.36 | 1.49 | 2.39 | 2.43 |
| Tm | -0.13 | -0.27 | -0.31 | -0.50 | -0.25 | -0.49 | 1.28 | 1.49 | -0.08 | 0.08 | 0.75 |
| Yb | 5.22 | 2.97 | 0.42 | 1.75 | 3.83 | 2.30 | 0.06 | 3.77 | 1.23 | 2.39 | 1.71 |
| Lu | -0.86 | 1.95 | 1.53 | 0.21 | -0.41 | 0.00 | 0.40 | -0.44 | 0.31 | 0.30 | 0.92 |
| Hf | 2.61 | 5.71 | 2.13 | -1.24 | 5.90 | 3.81 | 0.91 | 4.35 | 2.25 | 2.94 | 2.29 |
| Ta | 10.66 | 0.97 | 2.19 | 0.97 | 0.46 | 0.52 | 1.46 | 3.64 | 1.23 | 2.46 | 3.23 |
| Th | 1.90 | 3.02 | 0.78 | 2.41 | 1.51 | 2.29 | 1.11 | 2.21 | 2.50 | 1.97 | 0.72 |
| U | 0.83 | 0.67 | 0.27 | 0.79 | 1.05 | 0.34 | 0.58 | 1.74 | 0.95 | 0.80 | 0.44 |

**Trace element concentrations of shards from the NGRIP 2441.28 m tephra horizon analysed using a 6 µm laser beam diameter. n = shard number and relates to the major oxide analyses from this horizon. All concentrations are presented as ppm. Mean and 1 standard deviations are shown.**

| Horizon Q - NGRIP 2441.28 m | | | | | | | |
|---|---|---|---|---|---|---|---|
| n | 1 | 3 | 4 | 5 | 6 | **Average** | St. Dev. |
| Sc | 15.28 | -13.28 | 7.60 | 65.18 | 63.21 | 27.60 | 35.01 |
| Rb | 32.17 | 8.52 | 82.31 | 50.22 | 36.01 | 41.84 | 27.14 |
| Sr | 279.08 | 170.65 | 224.05 | 158.44 | 277.41 | 221.93 | 57.03 |
| Y | 52.70 | 24.54 | 42.70 | 12.54 | 19.77 | 30.45 | 16.69 |
| Zr | 205.04 | 148.28 | 298.29 | 197.40 | 253.37 | 220.48 | 57.27 |
| Nb | 9.90 | -9.71 | -23.84 | -1.50 | -20.14 | -9.06 | 13.77 |
| Cs | -0.57 | 1.55 | 4.64 | 0.92 | 2.45 | 1.80 | 1.93 |
| Ba | -3064.94 | -2831.91 | -2570.18 | -2996.94 | -2428.70 | -2778.54 | 273.12 |
| La | 12.60 | 7.05 | 8.94 | 13.54 | 2.09 | 8.85 | 4.61 |
| Ce | 35.49 | 11.69 | 22.74 | 15.57 | 20.31 | 21.16 | 9.08 |
| Pr | 1.21 | 3.14 | 2.85 | 0.69 | 5.32 | 2.64 | 1.82 |
| Nd | 10.17 | 4.37 | 0.03 | -7.61 | 1.77 | 1.75 | 6.49 |
| Sm | 20.34 | 2.88 | 6.38 | 2.28 | 9.88 | 8.35 | 7.36 |
| Eu | 8.91 | 7.46 | 7.41 | 10.50 | 3.21 | 7.50 | 2.71 |
| Gd | -4.23 | 3.07 | 6.13 | 2.35 | -1.31 | 1.20 | 4.03 |
| Tb | 3.64 | 0.56 | 3.54 | -1.07 | 2.11 | 1.76 | 2.02 |
| Dy | -0.28 | 4.16 | -3.46 | -3.88 | 0.20 | -0.65 | 3.25 |
| Ho | 1.53 | 0.78 | -0.39 | 0.98 | -0.06 | 0.57 | 0.78 |
| Er | 6.00 | 1.99 | 1.46 | 1.28 | 1.23 | 2.39 | 2.04 |
| Tm | -0.02 | 0.07 | 2.07 | 0.99 | -0.25 | 0.57 | 0.96 |
| Yb | 7.54 | 2.04 | -0.34 | -0.58 | 5.89 | 2.91 | 3.67 |
| Lu | 1.17 | 0.55 | 3.75 | 0.49 | 0.67 | 1.33 | 1.38 |
| Hf | 10.75 | 2.12 | 4.47 | 4.70 | 9.50 | 6.31 | 3.65 |
| Ta | 1.47 | 2.46 | 1.91 | -1.38 | 1.43 | 1.18 | 1.49 |
| Th | 6.38 | 1.47 | 4.12 | 4.13 | 9.20 | 5.06 | 2.89 |
| U | 1.35 | 0.87 | 0.60 | 0.93 | 0.47 | 0.84 | 0.34 |

**Trace element concentrations of shards from the NGRIP 2500.9 m tephra horizon analysed using a 6 µm laser beam diameter. n = shard number and relates to the major oxide analyses from this horizon. All concentrations are presented as ppm. Mean and 1 standard deviations are shown.**

| Horizon S – NGRIP 2500.9 m | | | | | | | |
|---|---|---|---|---|---|---|---|
| n | 1 | 3 | 6 | 10 | 16 | **Average** | St. Dev. |
| Sc | 24.55 | 110.38 | 11.88 | 35.72 | 6.65 | **37.83** | 42.10 |
| Rb | 56.25 | 125.35 | 40.34 | 42.80 | 29.83 | **58.91** | 38.31 |
| Sr | 488.75 | 702.49 | 689.74 | 515.64 | 229.53 | **525.23** | 191.93 |
| Y | 64.25 | 94.22 | 110.95 | 88.42 | 29.98 | **77.57** | 31.43 |
| Zr | 564.19 | 848.07 | 741.64 | 529.71 | 344.63 | **605.65** | 195.50 |
| Nb | 50.42 | 59.99 | 46.64 | 51.65 | 32.31 | **48.20** | 10.14 |
| Cs | 8.71 | -8.32 | 6.65 | 4.27 | -2.02 | **1.86** | 6.97 |
| Ba | 674.09 | 734.88 | 932.16 | 538.13 | 345.43 | **644.94** | 219.40 |
| La | 62.54 | 58.93 | 52.73 | 59.41 | 26.71 | **52.06** | 14.61 |
| Ce | 125.83 | 145.98 | 127.04 | 124.21 | 52.32 | **115.07** | 36.18 |
| Pr | 9.41 | 8.84 | 25.17 | 16.49 | 6.96 | **13.38** | 7.52 |
| Nd | 44.63 | 57.28 | 126.88 | 88.01 | 27.18 | **68.80** | 39.34 |
| Sm | 23.37 | 10.75 | 32.53 | 40.19 | 19.38 | **25.24** | 11.45 |
| Eu | 20.96 | 15.87 | 36.54 | 11.64 | 7.01 | **18.40** | 11.37 |
| Gd | 23.21 | 43.17 | 46.57 | 6.32 | 27.67 | **29.39** | 16.27 |
| Tb | 6.20 | 8.90 | 0.48 | 5.51 | 0.67 | **4.35** | 3.67 |
| Dy | 18.41 | 19.46 | 68.21 | 14.00 | 10.99 | **26.21** | 23.72 |
| Ho | 4.72 | 4.44 | 2.77 | 1.86 | 2.15 | **3.19** | 1.32 |
| Er | 8.64 | 18.92 | 3.73 | 21.66 | 8.55 | **12.30** | 7.62 |
| Tm | 0.14 | 1.69 | -1.33 | 1.78 | 1.60 | **0.78** | 1.35 |
| Yb | 0.63 | -2.48 | 12.29 | 4.28 | 0.91 | **3.13** | 5.65 |
| Lu | -0.35 | 0.20 | -0.38 | 2.06 | 1.29 | **0.56** | 1.07 |
| Hf | 30.82 | 11.36 | 4.62 | 17.00 | 12.13 | **15.19** | 9.79 |
| Ta | -1.30 | 8.67 | 5.13 | -0.93 | 1.03 | **2.52** | 4.28 |
| Th | 2.00 | 11.03 | 5.07 | 4.20 | 0.91 | **4.64** | 3.94 |
| U | 1.81 | 0.48 | 6.35 | 2.13 | 0.62 | **2.28** | 2.39 |

**Trace element concentrations of shards from the NGRIP 2574.55 m tephra horizon analysed using a 6 µm laser beam diameter. n = shard number and relates to the major oxide analyses from this horizon. All concentrations are presented as ppm. Mean and 1 standard deviations are shown.**

| Horizon U – NGRIP 2574.55 m | | | | | | | |
|---|---|---|---|---|---|---|---|
| n | 2 | 4 | 5 | 9 | 10 | **Average** | St. Dev. |
| Sc | 428.74 | | -293.67 | -83.16 | 63.03 | **28.74** | 304.22 |
| Rb | 25.02 | 10.14 | 10.86 | 25.31 | 12.61 | **16.79** | 7.70 |
| Sr | 694.26 | 536.08 | 493.71 | 716.84 | 751.86 | **638.55** | 115.70 |
| Y | 45.93 | 16.07 | 25.64 | 79.77 | 62.71 | **46.02** | 26.13 |
| Zr | 264.64 | 235.90 | 169.76 | 265.12 | 349.87 | **257.06** | 64.82 |
| Nb | 45.01 | 57.12 | 41.02 | 22.49 | 51.78 | **43.48** | 13.27 |
| Cs | -2.10 | -0.02 | -2.04 | -2.57 | 0.17 | **-1.31** | 1.28 |
| Ba | -8185.84 | -6255.83 | -2690.99 | -2871.76 | -3004.70 | **-4601.83** | 2488.78 |
| La | 42.51 | 22.52 | 22.00 | 25.99 | 31.24 | **28.85** | 8.48 |
| Ce | 79.23 | 71.25 | 36.47 | 73.08 | 94.39 | **70.89** | 21.28 |
| Pr | 3.09 | 7.35 | 2.95 | 3.85 | 11.84 | **5.81** | 3.81 |
| Nd | 67.68 | 41.61 | 37.71 | 95.98 | 23.67 | **53.33** | 28.66 |
| Sm | 6.08 | 5.54 | 1.46 | 9.72 | 3.02 | **5.16** | 3.16 |
| Eu | 26.57 | 6.40 | -0.50 | 6.55 | 21.48 | **12.10** | 11.39 |
| Gd | -16.19 | 5.34 | 5.35 | 5.63 | 1.38 | **0.30** | 9.39 |
| Tb | 3.99 | 3.40 | 0.25 | 1.30 | 3.69 | **2.53** | 1.65 |
| Dy | 9.81 | 14.50 | 3.43 | -2.89 | 5.23 | **6.02** | 6.58 |
| Ho | 0.56 | 0.65 | -0.31 | 2.55 | 2.88 | **1.27** | 1.38 |
| Er | 0.58 | 1.26 | -0.42 | 4.43 | 0.92 | **1.35** | 1.83 |
| Tm | 1.23 | 0.22 | 2.38 | 0.88 | 0.89 | **1.12** | 0.80 |
| Yb | 8.78 | 1.76 | 3.16 | 3.53 | 0.97 | **3.64** | 3.05 |
| Lu | 0.32 | -0.21 | 0.33 | 0.03 | 3.24 | **0.74** | 1.41 |
| Hf | 7.87 | 4.10 | 2.19 | 5.63 | 5.56 | **5.07** | 2.10 |
| Ta | 1.68 | 3.66 | 2.79 | 4.21 | 8.21 | **4.11** | 2.49 |
| Th | 2.94 | 2.86 | 0.63 | 1.75 | 1.99 | **2.04** | 0.94 |
| U | 0.53 | 0.69 | 0.53 | 0.00 | 0.39 | **0.43** | 0.26 |

**Trace element concentrations of shards from the NGRIP 2631.9 m tephra horizon analysed using a 6 µm laser beam diameter. n = shard number and relates to the major oxide analyses from this horizon. All concentrations are presented as ppm. Mean and 1 standard deviations are shown.**

| Horizon V – NGRIP 2631.9 m | | | | | | | | | | |
|---|---|---|---|---|---|---|---|---|---|---|
| n | 6 | 9 | 10 | 13 | 16 | 18 | 22 | 23 | **Average** | St. Dev. |
| Sc | 2670.29 | 3395.60 | 2203.17 | -1047.27 | -884.38 | -570.97 | -573.88 | -437.65 | **594.36** | 1828.90 |
| Rb | 73.09 | 23.00 | 44.64 | -20.17 | -24.73 | -12.26 | -10.75 | 2.70 | **9.44** | 34.73 |
| Sr | 1015.87 | 1167.55 | 877.39 | 409.92 | 442.65 | 504.62 | 492.07 | 364.68 | **659.34** | 311.87 |
| Y | 84.68 | 103.57 | 81.79 | 37.60 | 46.18 | 58.04 | 70.89 | 39.64 | **65.30** | 23.87 |
| Zr | 613.17 | 690.51 | 441.81 | 269.65 | 263.72 | 343.25 | 316.19 | 242.41 | **397.59** | 169.95 |
| Nb | 71.66 | 78.90 | 68.87 | 49.86 | 39.71 | 49.81 | 47.84 | 43.50 | **56.27** | 14.63 |
| Cs | 2.10 | 2.11 | -3.03 | -1.77 | -1.10 | 1.74 | -0.96 | -1.62 | **-0.32** | 2.01 |
| Ba | 157.85 | 173.99 | 90.57 | 57.13 | 46.33 | 56.01 | 52.25 | 42.00 | **84.52** | 52.50 |
| La | 57.99 | 117.41 | 68.17 | 32.37 | 31.56 | 40.13 | 36.61 | 28.14 | **51.55** | 30.06 |
| Ce | 188.86 | 198.76 | 134.22 | 90.64 | 96.22 | 91.14 | 95.04 | 72.00 | **120.86** | 48.30 |
| Pr | 19.02 | 17.49 | 17.61 | 8.24 | 10.00 | 9.85 | 13.70 | 7.60 | **12.94** | 4.61 |
| Nd | 79.00 | 145.71 | 87.19 | 31.27 | 47.70 | 58.81 | 67.93 | 48.84 | **70.80** | 35.21 |
| Sm | 13.54 | 13.13 | 47.38 | 0.53 | 0.80 | 27.27 | 24.00 | 16.64 | **17.91** | 15.27 |
| Eu | 29.65 | 12.27 | 18.73 | 2.34 | 1.91 | 1.56 | 0.12 | 3.23 | **8.73** | 10.65 |
| Gd | 40.55 | 58.93 | 16.03 | 9.67 | 12.05 | 11.66 | 8.77 | 5.71 | **20.42** | 18.98 |
| Tb | 2.85 | 3.82 | 2.61 | 0.92 | 1.12 | 1.20 | 1.70 | 1.01 | **1.91** | 1.07 |
| Dy | 15.34 | 33.58 | 12.80 | 5.23 | 5.98 | 10.06 | 6.30 | 10.77 | **12.51** | 9.22 |
| Ho | 0.90 | 4.28 | 1.18 | 2.19 | 2.69 | 1.26 | 1.85 | 2.42 | **2.10** | 1.09 |
| Er | 18.88 | 9.49 | 9.59 | 1.62 | 2.92 | 4.64 | 4.47 | 2.78 | **6.80** | 5.72 |
| Tm | -2.59 | -1.26 | 2.81 | 1.37 | -0.17 | 1.47 | 1.55 | -0.75 | **0.30** | 1.79 |
| Yb | 10.66 | 6.74 | 4.75 | 3.88 | 1.30 | 3.87 | 8.76 | 2.07 | **5.25** | 3.24 |
| Lu | 3.60 | 2.16 | 1.15 | 0.92 | 0.71 | -0.19 | 0.81 | 0.39 | **1.19** | 1.18 |
| Hf | 20.92 | 7.08 | 7.47 | 7.08 | 2.16 | 7.52 | 8.13 | 4.46 | **8.10** | 5.55 |
| Ta | 8.62 | -1.20 | 3.36 | 3.02 | 3.23 | 2.36 | 3.05 | 1.72 | **3.02** | 2.71 |
| Th | 1.57 | 9.08 | 3.99 | 3.50 | 1.84 | 2.57 | 3.80 | 1.61 | **3.49** | 2.46 |
| U | 2.10 | 1.36 | 0.92 | 0.56 | 0.82 | 0.81 | 1.05 | 0.47 | **1.01** | 0.52 |

**Major oxide concentrations of shards from the GRIP 1528.61 m tephra horizon. n = number of shards analysed. Mean and 1 standard deviations are shown. All oxides are presented as weight %. Total iron is expressed as FeO.**

| n | $SiO_2$ | $TiO_2$ | $Al_2O_3$ | FeO | MnO | MgO | CaO | $Na_2O$ | $K_2O$ | $P_2O_5$ | Total |
|---|---|---|---|---|---|---|---|---|---|---|---|
| **GRIP 1528.61 m** | | | | | | | | | | | |
| 1 | 48.32 | 2.69 | 12.59 | 13.18 | 0.22 | 5.69 | 10.04 | 2.50 | 0.41 | 0.30 | 95.94 |
| 2 | 48.13 | 3.06 | 12.49 | 13.31 | 0.28 | 4.87 | 9.23 | 2.73 | 0.47 | 0.43 | 95.01 |
| 3 | 47.72 | 2.88 | 12.38 | 13.49 | 0.18 | 5.38 | 9.79 | 2.56 | 0.50 | 0.36 | 95.25 |
| 4 | 47.71 | 2.71 | 12.07 | 13.67 | 0.29 | 6.87 | 8.99 | 2.53 | 0.46 | 0.35 | 95.65 |
| 5 | 48.61 | 2.63 | 12.93 | 13.61 | 0.22 | 5.10 | 9.89 | 2.35 | 0.44 | 0.36 | 96.14 |
| 6 | 48.18 | 2.72 | 12.68 | 12.40 | 0.14 | 5.81 | 9.93 | 2.42 | 0.38 | 0.36 | 95.02 |
| 7 | 47.63 | 2.75 | 12.54 | 13.42 | 0.20 | 5.69 | 9.95 | 2.54 | 0.37 | 0.30 | 95.39 |
| 8 | 47.92 | 2.81 | 12.61 | 12.53 | 0.11 | 5.79 | 10.08 | 2.44 | 0.41 | 0.43 | 95.14 |
| 9 | 47.82 | 2.79 | 12.73 | 13.06 | 0.17 | 5.62 | 9.78 | 2.40 | 0.41 | 0.36 | 95.13 |
| 10 | 47.65 | 2.72 | 12.55 | 13.58 | 0.21 | 5.73 | 9.89 | 2.61 | 0.36 | 0.35 | 95.64 |
| 11 | 47.87 | 2.84 | 12.54 | 13.20 | 0.14 | 5.79 | 9.91 | 2.44 | 0.42 | 0.40 | 95.55 |
| 12 | 47.94 | 2.80 | 12.60 | 13.01 | 0.27 | 5.69 | 10.09 | 2.48 | 0.42 | 0.37 | 95.67 |
| 13 | 47.91 | 2.61 | 12.64 | 13.05 | 0.15 | 5.68 | 9.86 | 2.44 | 0.40 | 0.37 | 95.11 |
| 14 | 47.80 | 2.53 | 12.62 | 13.02 | 0.28 | 5.72 | 9.93 | 2.42 | 0.44 | 0.34 | 95.11 |
| 15 | 48.06 | 2.98 | 12.42 | 14.05 | 0.23 | 5.19 | 9.41 | 2.44 | 0.45 | 0.52 | 95.75 |
| 16 | 48.03 | 2.81 | 12.66 | 13.50 | 0.25 | 5.72 | 10.00 | 2.40 | 0.41 | 0.38 | 96.16 |
| 17 | 47.96 | 2.78 | 12.69 | 13.02 | 0.27 | 5.65 | 10.18 | 2.29 | 0.43 | 0.33 | 95.59 |
| 18 | 48.32 | 2.84 | 12.80 | 12.82 | 0.16 | 5.54 | 9.81 | 2.56 | 0.41 | 0.41 | 95.68 |
| 19 | 48.00 | 2.70 | 12.32 | 12.57 | 0.24 | 6.64 | 10.36 | 2.31 | 0.39 | 0.32 | 95.84 |
| 20 | 47.84 | 2.71 | 12.52 | 13.06 | 0.35 | 5.67 | 10.09 | 2.35 | 0.42 | 0.38 | 95.40 |
| 21 | 48.56 | 3.06 | 12.99 | 13.86 | 0.23 | 4.23 | 9.01 | 2.81 | 0.46 | 0.31 | 95.52 |
| 22 | 48.11 | 3.07 | 12.47 | 13.59 | 0.34 | 5.40 | 9.64 | 2.53 | 0.41 | 0.38 | 95.93 |
| **Mean** | **48.00** | **2.79** | **12.58** | **13.23** | **0.22** | **5.61** | **9.81** | **2.48** | **0.42** | **0.37** | **95.53** |
| St. Dev. | 0.27 | 0.15 | 0.20 | 0.43 | 0.06 | 0.53 | 0.36 | 0.13 | 0.03 | 0.05 | 0.35 |

**Major oxide concentrations of shards from the LINK 14:185 tephra horizon. n = number of shards analysed. Mean and 1 standard deviations are shown. All oxides are presented as weight %. Total iron is expressed as FeO.**

| n | $SiO_2$ | $TiO_2$ | $Al_2O_3$ | FeO | MnO | MgO | CaO | $Na_2O$ | $K_2O$ | $P_2O_5$ | Total |
|---|---|---|---|---|---|---|---|---|---|---|---|
| **LINK 14:185** | | | | | | | | | | | |
| 1 | 48.67 | 2.92 | 12.76 | 14.05 | 0.17 | 5.76 | 10.05 | 2.53 | 0.47 | 0.39 | 97.77 |
| 2a | 49.37 | 3.22 | 12.84 | 14.47 | 0.24 | 5.59 | 10.07 | 2.35 | 0.48 | 0.39 | 99.03 |
| 2b | 48.92 | 3.25 | 12.63 | 14.65 | 0.28 | 5.63 | 10.13 | 2.38 | 0.46 | 0.30 | 98.65 |
| 3a | 48.40 | 3.22 | 12.42 | 14.53 | 0.26 | 5.39 | 9.61 | 2.59 | 0.46 | 0.29 | 97.17 |
| 3b | 48.37 | 3.38 | 12.49 | 14.08 | 0.18 | 5.44 | 9.65 | 2.63 | 0.45 | 0.42 | 97.09 |
| 3c | 48.01 | 3.26 | 12.32 | 14.60 | 0.30 | 5.33 | 9.79 | 2.74 | 0.49 | 0.41 | 97.24 |
| 4a | 48.69 | 2.93 | 12.73 | 14.27 | 0.19 | 5.68 | 10.27 | 2.56 | 0.42 | 0.36 | 98.11 |
| 4b | 48.56 | 3.12 | 12.71 | 14.45 | 0.26 | 5.80 | 10.17 | 2.42 | 0.42 | 0.32 | 98.24 |
| 4c | 48.64 | 2.97 | 12.54 | 13.94 | 0.27 | 5.72 | 10.17 | 2.66 | 0.41 | 0.37 | 97.69 |
| 5a | 47.82 | 2.90 | 12.70 | 14.26 | 0.31 | 5.60 | 9.99 | 2.57 | 0.42 | 0.34 | 96.92 |
| 5b | 48.52 | 2.90 | 12.65 | 13.77 | 0.19 | 5.60 | 10.10 | 2.58 | 0.42 | 0.29 | 97.02 |
| 5c | 48.79 | 2.87 | 12.71 | 13.60 | 0.20 | 5.66 | 10.12 | 2.56 | 0.41 | 0.31 | 97.23 |
| **Mean** | **48.56** | **3.08** | **12.63** | **14.22** | **0.24** | **5.60** | **10.01** | **2.55** | **0.44** | **0.35** | **97.68** |
| St. Dev. | 0.40 | 0.18 | 0.15 | 0.34 | 0.05 | 0.15 | 0.21 | 0.11 | 0.03 | 0.05 | 0.69 |

**Major oxide concentrations of shards from the NGRIP 1848 m tephra horizon. n = number of shards analysed. Mean and 1 standard deviations are shown. All oxides are presented as weight %. Total iron is expressed as FeO.**

| n | $SiO_2$ | $TiO_2$ | $Al_2O_3$ | FeO | MnO | MgO | CaO | $Na_2O$ | $K_2O$ | $P_2O_5$ | Total |
|---|---|---|---|---|---|---|---|---|---|---|---|
| **NGRIP 1848 m Population 1** | | | | | | | | | | | |
| 1 | 51.54 | 3.35 | 12.62 | 14.07 | 0.32 | 4.09 | 8.25 | 3.16 | 0.66 | 0.63 | 98.69 |
| 2 | 50.86 | 3.36 | 11.99 | 14.07 | 0.31 | 4.19 | 8.79 | 2.60 | 0.65 | 0.54 | 97.37 |
| 3 | 50.61 | 3.48 | 12.42 | 13.50 | 0.24 | 4.40 | 8.74 | 2.92 | 0.64 | 0.55 | 97.50 |
| 4 | 49.97 | 3.61 | 12.29 | 14.25 | 0.32 | 4.51 | 8.66 | 3.02 | 0.63 | 0.50 | 97.77 |
| 5 | 49.96 | 3.68 | 12.40 | 14.75 | 0.20 | 4.60 | 9.12 | 2.89 | 0.61 | 0.54 | 98.77 |
| 6 | 49.90 | 3.76 | 12.41 | 15.52 | 0.16 | 4.55 | 8.92 | 2.89 | 0.60 | 0.53 | 99.24 |
| 7 | 49.84 | 3.74 | 12.02 | 15.47 | 0.28 | 4.75 | 9.08 | 2.80 | 0.58 | 0.47 | 99.03 |
| 8 | 49.82 | 3.60 | 12.42 | 14.86 | 0.26 | 4.66 | 8.84 | 2.85 | 0.58 | 0.53 | 98.41 |
| 9 | 49.36 | 3.74 | 12.33 | 14.62 | 0.25 | 4.48 | 9.06 | 2.75 | 0.50 | 0.47 | 97.55 |
| 10 | 49.27 | 3.79 | 12.21 | 14.38 | 0.22 | 4.76 | 9.09 | 2.87 | 0.52 | 0.48 | 97.59 |
| 11 | 49.22 | 3.58 | 12.22 | 14.83 | 0.40 | 4.84 | 9.18 | 2.83 | 0.57 | 0.44 | 98.11 |
| 12 | 49.12 | 3.63 | 12.25 | 14.29 | 0.19 | 4.63 | 9.00 | 2.89 | 0.55 | 0.49 | 97.05 |
| 13 | 48.93 | 3.63 | 12.33 | 15.07 | 0.26 | 4.72 | 9.01 | 2.83 | 0.54 | 0.50 | 97.82 |
| 14 | 48.84 | 3.63 | 12.52 | 15.21 | 0.23 | 4.75 | 9.29 | 2.80 | 0.55 | 0.48 | 98.32 |
| 15 | 48.72 | 3.66 | 12.54 | 15.33 | 0.24 | 4.85 | 9.21 | 2.86 | 0.51 | 0.45 | 98.38 |
| **Mean** | **49.73** | **3.62** | **12.33** | **14.68** | **0.26** | **4.59** | **8.95** | **2.86** | **0.58** | **0.51** | **98.11** |
| St. Dev. | 0.80 | 0.13 | 0.18 | 0.58 | 0.06 | 0.22 | 0.26 | 0.12 | 0.05 | 0.05 | 0.65 |
| **NGRIP 1848 m Population 2** | | | | | | | | | | | |
| 1 | 53.75 | 2.90 | 12.83 | 13.00 | 0.18 | 3.45 | 7.64 | 3.24 | 0.77 | 0.73 | 98.48 |
| 2 | 53.72 | 2.90 | 12.67 | 12.33 | 0.29 | 3.35 | 7.24 | 3.35 | 0.85 | 0.78 | 97.47 |
| 3 | 53.39 | 3.15 | 12.59 | 12.91 | 0.17 | 3.43 | 7.48 | 3.42 | 0.92 | 0.70 | 98.17 |
| 4 | 53.27 | 3.10 | 12.68 | 13.46 | 0.22 | 3.42 | 7.47 | 3.31 | 0.89 | 0.74 | 98.57 |
| 5 | 52.95 | 3.19 | 12.48 | 12.89 | 0.24 | 3.52 | 7.68 | 3.18 | 0.85 | 0.68 | 97.67 |
| 6 | 52.86 | 3.35 | 13.34 | 14.18 | 0.21 | 3.41 | 7.36 | 3.50 | 0.87 | 0.63 | 99.70 |
| **Mean** | **53.32** | **3.10** | **12.76** | **13.13** | **0.22** | **3.43** | **7.48** | **3.33** | **0.86** | **0.71** | **98.35** |
| St. Dev. | 0.37 | 0.18 | 0.30 | 0.63 | 0.04 | 0.06 | 0.17 | 0.12 | 0.05 | 0.05 | 0.79 |

**Major oxide concentrations of shards from the LINK 17:634 tephra horizon. n = number of shards analysed. Mean and 1 standard deviations are shown. All oxides are presented as weight %. Total iron is expressed as FeO.**

| n | $SiO_2$ | $TiO_2$ | $Al_2O_3$ | FeO | MnO | MgO | CaO | $Na_2O$ | $K_2O$ | $P_2O_5$ | Total |
|---|---|---|---|---|---|---|---|---|---|---|---|
| **LINK 17:634** | | | | | | | | | | | |
| 1a | 49.12 | 3.68 | 12.45 | 15.02 | 0.28 | 4.66 | 9.06 | 2.87 | 0.57 | 0.51 | 98.22 |
| 1b | 49.48 | 3.74 | 12.48 | 15.15 | 0.23 | 4.69 | 9.03 | 3.01 | 0.53 | 0.44 | 98.78 |
| 2a | 49.82 | 3.78 | 12.75 | 15.14 | 0.20 | 4.25 | 8.98 | 3.15 | 0.61 | 0.47 | 99.13 |
| 2b | 49.31 | 3.68 | 12.59 | 14.92 | 0.28 | 4.59 | 9.10 | 2.85 | 0.59 | 0.46 | 98.36 |
| 3a | 49.90 | 3.88 | 12.63 | 15.14 | 0.19 | 4.76 | 9.14 | 2.77 | 0.55 | 0.47 | 99.43 |
| 3b | 49.72 | 3.85 | 12.49 | 14.86 | 0.25 | 4.86 | 8.85 | 2.77 | 0.56 | 0.48 | 98.69 |
| 4a | 48.92 | 3.86 | 12.55 | 15.18 | 0.34 | 4.61 | 8.93 | 2.94 | 0.54 | 0.47 | 98.34 |
| 4b | 49.60 | 3.85 | 12.41 | 15.52 | 0.17 | 4.68 | 8.58 | 2.99 | 0.61 | 0.53 | 98.95 |
| 5a | 49.00 | 3.65 | 12.40 | 15.25 | 0.23 | 4.56 | 8.91 | 2.92 | 0.56 | 0.46 | 97.95 |
| 6 | 49.35 | 3.89 | 12.73 | 15.86 | 0.33 | 4.73 | 9.00 | 2.99 | 0.58 | 0.53 | 99.98 |
| 7a | 49.29 | 4.17 | 12.58 | 15.63 | 0.23 | 4.58 | 8.82 | 2.97 | 0.53 | 0.42 | 99.22 |
| 7b | 49.69 | 3.73 | 11.57 | 14.13 | 0.32 | 6.49 | 9.70 | 2.57 | 0.51 | 0.48 | 99.20 |
| 8a | 49.20 | 3.74 | 12.36 | 14.77 | 0.22 | 4.49 | 8.82 | 2.91 | 0.57 | 0.49 | 97.57 |
| 8b | 48.80 | 3.90 | 12.44 | 15.53 | 0.26 | 4.81 | 9.03 | 2.85 | 0.55 | 0.46 | 98.62 |
| 9a | 49.03 | 3.90 | 12.54 | 14.95 | 0.30 | 4.72 | 8.93 | 2.88 | 0.56 | 0.46 | 98.25 |
| 9b | 49.21 | 3.86 | 12.36 | 14.54 | 0.17 | 4.69 | 9.04 | 2.85 | 0.55 | 0.52 | 97.79 |
| 10a | 49.25 | 3.59 | 12.38 | 15.40 | 0.17 | 4.57 | 8.57 | 2.90 | 0.63 | 0.52 | 97.98 |
| 10b | 49.55 | 3.77 | 12.40 | 14.75 | 0.29 | 4.56 | 8.58 | 2.96 | 0.55 | 0.52 | 97.93 |
| **Mean** | **49.35** | **3.80** | **12.45** | **15.10** | **0.25** | **4.74** | **8.95** | **2.90** | **0.56** | **0.48** | **98.58** |
| St. Dev. | 0.32 | 0.13 | 0.25 | 0.42 | 0.06 | 0.46 | 0.26 | 0.12 | 0.03 | 0.03 | 0.65 |

**Trace element concentrations of shards from the GRIP 1528.61 m tephra horizon. n = shard number and relates to the major oxide analyses from this horizon. All concentrations are presented as ppm. Mean and 1 standard deviations are shown.**

**GRIP 1528.61 m**

| n | 4 | 5 | 8 | 10 | 12 | 13 | 14 | 15 | 16 | 18 | 21 | Mean | St. Dev. |
|---|---|---|---|---|---|---|---|---|---|---|---|---|---|
| Sc | 40.35 | 60.66 | 37.80 | 55.64 | 50.24 | 55.43 | 69.12 | 71.80 | 50.29 | 40.79 | 48.99 | 52.8 | 11.2 |
| Rb | 12.05 | 18.79 | 6.73 | 15.50 | 17.21 | 15.84 | 11.28 | 18.94 | 14.27 | 11.04 | 9.20 | 13.7 | 3.98 |
| Sr | 325.51 | 315.43 | 223.12 | 315.66 | 319.88 | 337.63 | 333.28 | 340.68 | 330.40 | 291.35 | 287.68 | 311 | 33.8 |
| Y | 55.21 | 66.36 | 44.22 | 56.56 | 61.67 | 66.53 | 59.76 | 68.44 | 64.78 | 55.17 | 46.93 | 58.7 | 8.00 |
| Zr | 261.47 | 298.68 | 250.98 | 260.87 | 289.52 | 253.32 | 252.50 | 303.67 | 278.73 | 252.30 | 249.37 | 268 | 20.5 |
| Nb | 26.55 | 26.97 | 19.79 | 19.39 | 29.88 | 20.02 | 24.24 | 29.99 | 23.42 | 28.37 | 23.80 | 24.8 | 3.92 |
| Cs | -0.09 | 0.22 | 0.69 | -0.50 | -0.11 | 0.21 | 1.28 | 1.20 | 0.02 | 0.45 | 0.06 | 0.31 | 0.55 |
| Ba | 146.43 | 182.83 | 106.54 | 176.83 | 162.78 | 186.08 | 214.70 | 207.18 | 134.23 | 149.65 | 133.10 | 164 | 33.3 |
| La | 19.47 | 20.08 | 16.79 | 17.97 | 19.94 | 17.74 | 16.01 | 21.72 | 18.37 | 19.78 | 17.34 | 18.7 | 1.69 |
| Ce | 55.98 | 48.01 | 36.76 | 37.83 | 46.45 | 43.08 | 59.61 | 53.05 | 42.62 | 43.64 | 36.47 | 45.8 | 7.79 |
| Pr | 6.96 | 6.73 | 6.19 | 5.57 | 7.32 | 6.21 | 5.31 | 8.03 | 6.37 | 7.24 | 4.63 | 6.41 | 0.99 |
| Nd | 25.08 | 29.25 | 23.51 | 30.65 | 34.99 | 35.70 | 33.64 | 35.17 | 24.12 | 18.22 | 22.21 | 28.4 | 6.09 |
| Sm | 8.26 | 7.38 | 7.54 | 8.53 | 10.17 | 5.31 | 10.81 | 5.56 | 9.26 | 6.28 | 8.61 | 7.97 | 1.78 |
| Eu | 3.14 | 2.76 | 2.94 | 5.79 | 4.05 | 4.66 | 4.04 | 4.36 | 3.42 | 5.00 | 3.69 | 3.99 | 0.93 |
| Gd | 8.08 | 9.51 | 8.34 | 10.28 | 8.10 | 9.26 | 12.01 | 9.89 | 12.21 | 7.76 | 8.51 | 9.45 | 1.54 |
| Tb | 2.03 | 1.94 | 1.63 | 1.80 | 2.09 | 1.40 | 1.59 | 2.09 | 1.20 | 1.86 | 1.13 | 1.71 | 0.34 |
| Dy | 11.99 | 12.54 | 8.82 | 10.72 | 14.72 | 10.88 | 12.65 | 13.79 | 12.19 | 8.57 | 11.06 | 11.6 | 1.88 |
| Ho | 1.73 | 2.78 | 1.18 | 1.80 | 2.54 | 2.13 | 2.11 | 2.09 | 1.91 | 2.00 | 1.61 | 1.99 | 0.43 |
| Er | 5.84 | 7.51 | 3.93 | 3.63 | 5.30 | 7.42 | 5.69 | 7.00 | 5.72 | 6.92 | 4.29 | 5.75 | 1.38 |
| Tm | 0.80 | 0.61 | 0.49 | 0.65 | 0.91 | 0.74 | 0.88 | 0.85 | 0.64 | 0.64 | 0.82 | 0.73 | 0.13 |
| Yb | 6.15 | 5.89 | 3.21 | 5.03 | 5.58 | 5.08 | 6.85 | 6.61 | 5.08 | 4.22 | 3.97 | 5.24 | 1.13 |
| Lu | 0.72 | 1.29 | 0.43 | 0.78 | 1.04 | 1.00 | 1.30 | 0.55 | 0.72 | 0.99 | 0.52 | 0.85 | 0.30 |
| Hf | 7.80 | 7.03 | 3.84 | 7.09 | 7.26 | 5.80 | 6.23 | 6.98 | 7.14 | 9.01 | 6.53 | 6.79 | 1.29 |
| Ta | 1.07 | 1.45 | 1.30 | 1.97 | 1.24 | 1.97 | 1.93 | 2.11 | 1.66 | 1.71 | 1.09 | 1.59 | 0.38 |
| Th | 1.93 | 1.97 | 1.21 | 2.05 | 1.83 | 1.49 | 1.48 | 2.00 | 1.11 | 1.50 | 1.42 | 1.64 | 0.33 |
| U | 0.61 | 0.39 | 0.30 | 0.39 | 0.57 | 0.52 | 0.52 | 0.58 | 0.20 | 0.49 | 0.45 | 0.45 | 0.13 |

**Trace element concentrations of shards from the LINK 14:185 tephra horizon. n = shard number and relates to the major oxide analyses from this horizon. All concentrations are presented as ppm. Mean and 1 standard deviations are shown.**

**LINK 14:185**

| n | 1 | 2a | 2b | 3a | 3c | 4a | 4b | 5a | 5b | **Mean** | St. Dev. |
|---|---|---|---|---|---|---|---|---|---|---|---|
| Sc | 45.34 | 30.24 | 26.43 | 35.37 | 31.53 | 29.90 | 38.67 | 27.36 | 34.60 | **33.3** | 5.98 |
| Rb | 17.79 | 11.07 | 15.17 | 10.16 | 10.26 | 9.33 | 11.46 | 7.53 | 9.46 | **11.4** | 3.18 |
| Sr | 438.74 | 215.70 | 307.78 | 222.02 | 224.48 | 1053.36 | 332.11 | 203.55 | 283.03 | **365** | 269 |
| Y | 49.67 | 39.06 | 38.99 | 48.65 | 47.54 | 47.61 | 47.57 | 38.42 | 44.17 | **44.6** | 4.60 |
| Zr | 214.75 | 182.97 | 184.12 | 224.04 | 205.35 | 209.94 | 211.15 | 181.65 | 197.22 | **201** | 15.5 |
| Nb | 20.32 | 17.51 | 17.17 | 22.35 | 19.71 | 19.46 | 19.50 | 17.11 | 18.85 | **19.1** | 1.69 |
| Cs | 0.33 | 0.54 | 0.20 | 0.15 | 0.10 | -0.11 | 0.18 | 0.13 | 0.16 | **0.18** | 0.17 |
| Ba | 98.89 | 136.43 | 141.03 | 101.93 | 104.28 | 100.64 | 102.42 | 82.46 | 98.43 | **107** | 18.9 |
| La | 19.80 | 16.22 | 16.64 | 19.07 | 16.39 | 16.89 | 20.92 | 14.69 | 16.69 | **17.5** | 2.00 |
| Ce | 46.29 | 36.67 | 42.51 | 45.06 | 43.17 | 45.28 | 47.51 | 37.39 | 51.19 | **43.9** | 4.64 |
| Pr | 7.42 | 4.88 | 4.89 | 6.04 | 5.36 | 6.20 | 8.93 | 5.32 | 6.06 | **6.12** | 1.32 |
| Nd | 21.68 | 25.73 | 26.76 | 29.98 | 28.24 | 24.52 | 29.06 | 25.13 | 29.21 | **26.7** | 2.70 |
| Sm | 7.21 | 8.07 | 7.71 | 7.42 | 8.25 | 8.52 | 6.63 | 5.55 | 8.54 | **7.55** | 0.98 |
| Eu | 2.56 | 2.31 | 2.22 | 2.50 | 1.94 | 2.55 | 2.15 | 2.48 | 2.42 | **2.35** | 0.21 |
| Gd | 8.25 | 5.54 | 5.76 | 9.76 | 9.58 | 10.10 | 9.38 | 7.71 | 8.35 | **8.27** | 1.68 |
| Tb | 1.72 | 1.08 | 1.27 | 1.51 | 1.29 | 1.63 | 1.44 | 1.10 | 1.35 | **1.38** | 0.22 |
| Dy | 9.77 | 9.08 | 8.72 | 10.87 | 9.16 | 9.18 | 10.47 | 8.15 | 9.10 | **9.39** | 0.85 |
| Ho | 1.85 | 1.58 | 1.69 | 2.21 | 2.14 | 1.65 | 1.82 | 1.84 | 2.27 | **1.89** | 0.25 |
| Er | 6.54 | 3.76 | 3.91 | 5.65 | 5.99 | 5.93 | 5.95 | 6.52 | 5.44 | **5.52** | 1.02 |
| Tm | 0.83 | 0.72 | 0.51 | 0.81 | 0.85 | 0.94 | 1.09 | 0.83 | 0.89 | **0.83** | 0.16 |
| Yb | 5.20 | 4.25 | 5.83 | 5.56 | 5.98 | 5.96 | 5.48 | 4.90 | 5.39 | **5.40** | 0.56 |
| Lu | 0.84 | 0.69 | 0.66 | 0.84 | 0.77 | 0.96 | 0.83 | 0.57 | 0.96 | **0.79** | 0.13 |
| Hf | 7.24 | 5.91 | 4.43 | 6.52 | 6.93 | 4.70 | 6.30 | 6.13 | 6.62 | **6.09** | 0.95 |
| Ta | 1.77 | 1.34 | 1.33 | 1.69 | 1.31 | 1.52 | 1.73 | 1.16 | 1.86 | **1.52** | 0.25 |
| Th | 1.93 | 1.69 | 1.56 | 1.81 | 1.53 | 1.86 | 2.21 | 1.54 | 1.95 | **1.79** | 0.23 |
| U | 2.56 | 1.02 | 1.01 | 0.55 | 0.55 | 0.66 | 0.81 | 0.54 | 0.59 | **0.92** | 0.64 |

**Trace element concentrations of shards from the NGRIP 1848 m tephra horizon. n = shard number and relates to the major oxide analyses from this horizon. All concentrations are presented as ppm. Mean and 1 standard deviations are shown.**

| NGRIP 1848 m Population 1 | | | | | | | |
|---|---|---|---|---|---|---|---|
| n | 1 | 2 | 6 | 7 | 12 | **Mean** | St. Dev. |
| Sc | 28.36 | 32.66 | 39.24 | 44.20 | 36.55 | **36.2** | 6.07 |
| Rb | 29.53 | 29.72 | 22.85 | 13.76 | 11.54 | **21.5** | 8.56 |
| Sr | 252.94 | 220.01 | 244.65 | 273.02 | 280.22 | **254** | 24.0 |
| Y | 66.44 | 47.99 | 50.10 | 54.43 | 59.20 | **55.6** | 7.42 |
| Zr | 340.76 | 289.20 | 282.77 | 283.64 | 287.30 | **297** | 24.8 |
| Nb | 30.94 | 23.38 | 22.44 | 26.93 | 28.34 | **26.4** | 3.52 |
| Cs | 0.42 | 0.57 | -0.23 | 0.65 | -0.34 | **0.21** | 0.46 |
| Ba | 230.77 | 275.60 | 216.40 | 175.46 | 166.06 | **213** | 44.3 |
| La | 25.53 | 22.18 | 19.77 | 23.49 | 20.71 | **22.3** | 2.28 |
| Ce | 53.83 | 41.49 | 48.68 | 48.74 | 49.70 | **48.5** | 4.45 |
| Pr | 6.59 | 6.15 | 5.97 | 7.04 | 7.84 | **6.72** | 0.75 |
| Nd | 39.96 | 23.92 | 27.58 | 37.09 | 42.01 | **34.1** | 7.94 |
| Sm | 10.09 | 9.90 | 10.49 | 9.15 | 9.36 | **9.80** | 0.54 |
| Eu | 2.79 | 3.36 | 1.47 | 3.34 | 2.58 | **2.71** | 0.77 |
| Gd | 10.44 | 10.92 | 8.50 | 10.43 | 10.65 | **10.2** | 0.96 |
| Tb | 2.07 | 1.12 | 0.99 | 1.10 | 1.40 | **1.34** | 0.44 |
| Dy | 13.19 | 8.20 | 9.26 | 12.31 | 12.74 | **11.1** | 2.25 |
| Ho | 2.11 | 1.79 | 1.64 | 2.44 | 2.53 | **2.10** | 0.39 |
| Er | 7.73 | 3.51 | 5.75 | 5.18 | 6.23 | **5.68** | 1.54 |
| Tm | 0.71 | 0.60 | 0.57 | 0.84 | 1.02 | **0.75** | 0.19 |
| Yb | 5.44 | 4.44 | 5.61 | 6.77 | 6.20 | **5.69** | 0.87 |
| Lu | 0.73 | 1.91 | 0.80 | 0.52 | 0.47 | **0.89** | 0.59 |
| Hf | 10.69 | 7.28 | 8.45 | 9.56 | 7.90 | **8.77** | 1.36 |
| Ta | 2.22 | 1.76 | 1.85 | 1.55 | 1.85 | **1.85** | 0.24 |
| Th | 2.61 | 1.77 | 1.70 | 1.42 | 2.11 | **1.92** | 0.46 |
| U | 0.49 | 0.55 | 0.51 | 0.59 | 0.75 | **0.58** | 0.10 |

| NGRIP 1848 m Population 2 | | | | | | |
|---|---|---|---|---|---|---|
| n | 2 | 3 | 4 | 6 | **Mean** | St. Dev. |
| Sc | 19.20 | 23.81 | 23.83 | 34.26 | **25.3** | 6.37 |
| Rb | 27.33 | 26.00 | 22.99 | 18.74 | **23.8** | 3.81 |
| Sr | 313.43 | 287.12 | 230.28 | 310.36 | **285** | 38.5 |
| Y | 79.50 | 75.84 | 59.00 | 71.51 | **71.5** | 8.93 |
| Zr | 422.54 | 402.13 | 310.80 | 363.39 | **375** | 49.2 |
| Nb | 42.54 | 38.73 | 30.37 | 35.36 | **36.8** | 5.17 |
| Cs | 0.25 | 0.19 | 0.55 | 0.39 | **0.34** | 0.16 |
| Ba | 271.99 | 249.22 | 312.56 | 218.83 | **263** | 39.5 |
| La | 34.62 | 29.41 | 24.67 | 30.63 | **29.8** | 4.10 |
| Ce | 70.03 | 67.73 | 52.33 | 65.67 | **63.9** | 7.94 |
| Pr | 9.41 | 10.33 | 8.31 | 9.97 | **9.50** | 0.88 |
| Nd | 54.36 | 57.10 | 33.12 | 43.44 | **47.0** | 11.0 |
| Sm | 10.49 | 16.33 | 12.35 | 9.43 | **12.2** | 3.04 |
| Eu | 3.04 | 2.87 | 2.46 | 3.44 | **2.95** | 0.40 |
| Gd | 13.09 | 15.26 | 11.11 | 13.61 | **13.3** | 1.71 |
| Tb | 1.51 | 2.16 | 1.62 | 2.47 | **1.94** | 0.45 |
| Dy | 16.55 | 15.79 | 7.93 | 17.87 | **14.5** | 4.48 |
| Ho | 3.41 | 3.50 | 2.56 | 2.74 | **3.05** | 0.47 |
| Er | 8.08 | 6.71 | 7.17 | 7.53 | **7.37** | 0.58 |
| Tm | 1.28 | 1.04 | 0.89 | 1.30 | **1.13** | 0.20 |
| Yb | 8.57 | 7.98 | 4.61 | 8.99 | **7.54** | 2.00 |
| Lu | 0.85 | 0.79 | 0.62 | 1.05 | **0.83** | 0.18 |
| Hf | 11.21 | 8.56 | 7.15 | 10.10 | **9.26** | 1.77 |
| Ta | 2.86 | 3.36 | 2.23 | 1.43 | **2.47** | 0.83 |
| Th | 3.25 | 2.80 | 2.74 | 2.22 | **2.75** | 0.42 |
| U | 0.95 | 0.89 | 0.83 | 0.64 | **0.83** | 0.13 |

**Trace element concentrations of shards from the LINK 17:634 tephra horizon. n = shard number and relates to the major oxide analyses from this horizon. All concentrations are presented as ppm. Mean and 1 standard deviations are shown.**

| LINK 17:634 | | | | | | | | | | | | | | | | | | | |
|---|---|---|---|---|---|---|---|---|---|---|---|---|---|---|---|---|---|---|---|
| n | 1a | 1b | 2a | 2b | 3a | 3b | 4a | 4b | 6 | 7a | 7b | 8a | 8b | 9a | 9b | 10a | 10b | **Mean** | St. Dev. |
| Sc | 42.36 | 40.27 | 42.06 | 46.24 | 48.97 | 44.38 | 34.05 | 41.23 | 41.52 | 59.37 | 32.17 | 43.89 | 36.30 | 33.96 | 48.05 | 38.91 | 39.45 | **42.0** | 6.57 |
| Rb | 14.02 | 12.90 | 13.71 | 21.69 | 12.85 | 14.62 | 27.07 | 12.74 | 27.56 | 16.00 | 13.11 | 13.68 | 14.72 | 15.06 | 27.46 | 15.57 | 13.33 | **16.8** | 5.44 |
| Sr | 310.37 | 251.18 | 248.45 | 272.05 | 244.23 | 256.31 | 239.51 | 237.14 | 241.68 | 276.42 | 219.98 | 247.54 | 208.94 | 229.97 | 267.59 | 264.22 | 243.01 | **251** | 23.5 |
| Y | 62.87 | 48.11 | 52.77 | 56.18 | 51.16 | 47.06 | 51.80 | 51.59 | 51.81 | 59.01 | 45.61 | 48.31 | 44.66 | 48.48 | 53.77 | 56.13 | 56.10 | **52.1** | 23.5 |
| Zr | 299.47 | 217.28 | 233.99 | 247.02 | 250.52 | 241.88 | 249.48 | 237.73 | 245.18 | 286.52 | 226.77 | 251.36 | 221.72 | 223.26 | 258.29 | 266.49 | 263.10 | **248** | 4.89 |
| Nb | 31.90 | 23.22 | 26.44 | 26.89 | 27.07 | 26.31 | 25.35 | 26.18 | 22.87 | 28.37 | 23.38 | 25.93 | 21.18 | 21.28 | 27.58 | 25.60 | 29.48 | **25.8** | 2.82 |
| Cs | 0.39 | 0.15 | 0.14 | 0.56 | 0.16 | 0.09 | 0.21 | 0.39 | 1.32 | 0.52 | 0.09 | 0.90 | 0.58 | 0.14 | 1.14 | 0.35 | 0.06 | **0.42** | 0.38 |
| Ba | 163.06 | 116.70 | 191.34 | 156.70 | 138.42 | 134.34 | 140.06 | 132.15 | 176.42 | 156.28 | 123.82 | 135.95 | 120.17 | 133.41 | 150.45 | 138.88 | 129.51 | **143** | 20.0 |
| La | 28.05 | 18.81 | 20.15 | 21.17 | 20.40 | 20.23 | 21.74 | 19.42 | 19.12 | 24.62 | 17.60 | 20.37 | 18.31 | 19.50 | 23.21 | 23.66 | 23.03 | **21.1** | 2.66 |
| Ce | 56.96 | 42.57 | 45.68 | 54.33 | 47.04 | 49.92 | 51.56 | 46.36 | 54.03 | 56.83 | 43.20 | 53.76 | 54.70 | 46.32 | 53.19 | 56.35 | 53.71 | **51.0** | 4.83 |
| Pr | 7.34 | 6.30 | 6.86 | 7.10 | 7.68 | 7.52 | 7.93 | 6.81 | 6.38 | 8.08 | 6.08 | 7.03 | 6.27 | 6.78 | 8.24 | 7.47 | 7.94 | **7.17** | 0.68 |
| Nd | 39.31 | 28.44 | 33.41 | 34.39 | 34.57 | 29.74 | 31.04 | 30.01 | 33.33 | 38.32 | 30.34 | 32.05 | 34.32 | 29.38 | 32.57 | 40.29 | 32.85 | **33.2** | 3.47 |
| Sm | 10.31 | 6.76 | 9.04 | 8.21 | 8.72 | 10.09 | 9.32 | 9.14 | 8.41 | 7.29 | 7.79 | 8.89 | 7.23 | 9.93 | 8.71 | 10.98 | 9.67 | **8.85** | 1.16 |
| Eu | 3.18 | 3.40 | 2.89 | 2.52 | 2.92 | 3.37 | 2.56 | 3.57 | 3.42 | 3.53 | 2.49 | 2.69 | 2.34 | 2.62 | 2.96 | 3.23 | 2.64 | **2.96** | 0.41 |
| Gd | 18.38 | 10.59 | 11.04 | 10.24 | 10.56 | 10.56 | 9.08 | 9.98 | 11.19 | 13.59 | 8.94 | 10.32 | 8.36 | 10.26 | 11.12 | 12.33 | 11.63 | **11.1** | 2.25 |
| Tb | 2.08 | 1.11 | 1.69 | 1.69 | 1.70 | 1.37 | 1.82 | 1.72 | 1.52 | 1.77 | 1.05 | 1.47 | 1.74 | 1.72 | 1.56 | 1.56 | 1.78 | **1.61** | 0.25 |
| Dy | 13.25 | 11.21 | 12.21 | 11.12 | 11.96 | 10.90 | 8.77 | 10.61 | 10.38 | 11.06 | 8.96 | 11.94 | 9.63 | 9.59 | 11.00 | 12.12 | 10.39 | **10.9** | 1.21 |
| Ho | 2.57 | 1.72 | 2.48 | 2.14 | 1.97 | 2.10 | 1.80 | 1.61 | 2.33 | 2.55 | 1.67 | 1.78 | 2.14 | 1.78 | 1.73 | 2.44 | 2.33 | **2.07** | 0.33 |
| Er | 6.95 | 4.81 | 6.98 | 5.46 | 5.78 | 5.50 | 7.59 | 5.97 | 5.23 | 5.72 | 4.29 | 5.97 | 5.17 | 5.24 | 7.86 | 6.33 | 6.72 | **5.97** | 0.98 |
| Tm | 0.95 | 0.92 | 0.94 | 0.91 | 0.96 | 0.75 | 0.99 | 0.91 | 0.89 | 0.82 | 0.75 | 0.56 | 1.29 | 0.74 | 0.86 | 0.82 | 0.85 | **0.88** | 0.15 |
| Yb | 5.43 | 3.45 | 4.86 | 6.16 | 5.49 | 3.90 | 4.19 | 5.82 | 5.89 | 6.02 | 3.99 | 4.81 | 4.19 | 4.88 | 5.26 | 5.77 | 6.22 | **5.08** | 0.88 |
| Lu | 1.09 | 0.68 | 1.66 | 1.13 | 1.20 | 1.02 | 0.68 | 0.88 | 0.62 | 1.00 | 0.39 | 0.81 | 0.70 | 0.53 | 0.94 | 0.93 | 0.97 | **0.89** | 0.30 |
| Hf | 6.61 | 6.03 | 7.96 | 8.27 | 6.07 | 6.94 | 7.13 | 6.36 | 7.47 | 7.10 | 6.41 | 7.45 | 5.97 | 6.30 | 6.82 | 7.87 | 8.28 | **7.00** | 0.78 |
| Ta | 2.36 | 1.55 | 2.20 | 2.08 | 2.19 | 2.25 | 2.21 | 2.63 | 1.96 | 1.42 | 1.94 | 1.90 | 1.82 | 1.84 | 2.20 | 2.06 | 2.02 | **2.04** | 0.29 |
| Th | 2.37 | 1.75 | 2.32 | 2.64 | 2.20 | 1.99 | 3.05 | 2.01 | 2.95 | 2.14 | 1.60 | 2.10 | 2.07 | 1.98 | 2.95 | 2.67 | 2.53 | **2.31** | 0.43 |
| U | 0.62 | 0.51 | 0.72 | 0.92 | 0.45 | 0.61 | 0.87 | 0.72 | 0.75 | 0.56 | 0.57 | 0.68 | 0.76 | 0.64 | 0.84 | 0.89 | 0.72 | **0.70** | 0.14 |

**Major oxide concentrations of shards from the GRIP 1716.08 m tephra horizon. n = number of shards analysed. Mean and 1 standard deviations are shown. All oxides are presented as weight %. Total iron is expressed as FeO.**

| n | $SiO_2$ | $TiO_2$ | $Al_2O_3$ | FeO | MnO | MgO | CaO | $Na_2O$ | $K_2O$ | $P_2O_5$ | Total |
|---|---|---|---|---|---|---|---|---|---|---|---|
| **GRIP 1716.08 m** | | | | | | | | | | | |
| 1 | 45.93 | 4.66 | 12.31 | 14.18 | 0.23 | 4.99 | 9.50 | 2.87 | 0.73 | 0.54 | 95.94 |
| 2 | 46.17 | 4.57 | 12.47 | 14.42 | 0.38 | 5.04 | 9.82 | 2.77 | 0.71 | 0.60 | 96.95 |
| 3 | 45.86 | 4.77 | 12.16 | 13.57 | 0.19 | 4.96 | 9.03 | 2.86 | 0.76 | 0.62 | 94.76 |
| 4 | 46.64 | 4.67 | 12.37 | 14.07 | 0.16 | 4.83 | 9.54 | 2.96 | 0.73 | 0.59 | 96.54 |
| 5 | 45.53 | 4.50 | 12.32 | 13.65 | 0.14 | 4.75 | 9.21 | 2.85 | 0.73 | 0.57 | 94.26 |
| 6 | 47.46 | 4.56 | 12.42 | 13.85 | 0.37 | 4.67 | 9.96 | 2.08 | 0.81 | 0.64 | 96.82 |
| 7 | 45.89 | 4.51 | 12.22 | 13.85 | 0.19 | 4.97 | 9.43 | 2.87 | 0.67 | 0.56 | 95.16 |
| 8 | 45.71 | 4.53 | 12.36 | 14.00 | 0.20 | 4.84 | 9.35 | 2.98 | 0.68 | 0.60 | 95.24 |
| 9 | 45.54 | 4.52 | 12.12 | 13.96 | 0.25 | 5.00 | 9.50 | 2.99 | 0.67 | 0.56 | 95.13 |
| 10 | 46.02 | 4.41 | 11.40 | 13.46 | 0.20 | 6.07 | 10.05 | 2.61 | 0.58 | 0.52 | 95.31 |
| 11 | 45.05 | 4.57 | 12.00 | 13.41 | 0.35 | 4.89 | 9.43 | 3.05 | 0.66 | 0.56 | 93.97 |
| 12 | 46.15 | 4.53 | 12.30 | 14.18 | 0.27 | 5.03 | 9.56 | 2.82 | 0.65 | 0.58 | 96.07 |
| 13 | 45.90 | 4.77 | 12.24 | 14.70 | 0.13 | 4.88 | 9.18 | 2.82 | 0.72 | 0.57 | 95.91 |
| 14 | 45.59 | 4.41 | 12.28 | 14.06 | 0.25 | 4.96 | 9.30 | 2.84 | 0.68 | 0.52 | 94.89 |
| 15 | 45.94 | 4.64 | 12.29 | 14.18 | 0.27 | 5.04 | 9.30 | 2.78 | 0.68 | 0.55 | 95.66 |
| 16 | 45.29 | 4.88 | 12.15 | 13.78 | 0.23 | 5.03 | 9.15 | 2.74 | 0.68 | 0.57 | 94.53 |
| 17 | 45.89 | 4.53 | 12.29 | 13.50 | 0.14 | 5.07 | 9.60 | 2.51 | 0.70 | 0.54 | 94.77 |
| 18 | 46.30 | 4.57 | 12.24 | 13.63 | 0.20 | 4.99 | 9.52 | 2.59 | 0.73 | 0.53 | 95.31 |
| 19 | 46.16 | 4.69 | 12.39 | 13.56 | 0.20 | 4.94 | 9.53 | 2.95 | 0.66 | 0.48 | 95.58 |
| 20 | 46.03 | 4.62 | 12.36 | 14.77 | 0.19 | 4.94 | 9.57 | 2.86 | 0.67 | 0.51 | 96.53 |
| 21 | 46.02 | 4.83 | 12.30 | 13.67 | 0.14 | 4.98 | 9.64 | 2.78 | 0.67 | 0.53 | 95.55 |
| 22 | 46.41 | 4.71 | 12.43 | 13.07 | 0.24 | 5.09 | 10.39 | 2.34 | 0.67 | 0.63 | 95.99 |
| 23 | 45.91 | 4.72 | 12.41 | 13.81 | 0.27 | 5.06 | 9.60 | 2.94 | 0.73 | 0.52 | 95.98 |
| **Mean** | **45.97** | **4.62** | **12.25** | **13.88** | **0.23** | **5.00** | **9.53** | **2.78** | **0.69** | **0.56** | **95.51** |
| St. Dev. | 0.48 | 0.13 | 0.22 | 0.41 | 0.07 | 0.26 | 0.31 | 0.22 | 0.04 | 0.04 | 0.79 |

**Major oxide concentrations of shards from the NGRIP 1895.3 m tephra horizon. n = number of shards analysed. Mean and 1 standard deviations are shown. All oxides are presented as weight %. Total iron is expressed as FeO.**

| n | $SiO_2$ | $TiO_2$ | $Al_2O_3$ | FeO | MnO | MgO | CaO | $Na_2O$ | $K_2O$ | $P_2O_5$ | Total |
|---|---|---|---|---|---|---|---|---|---|---|---|
| **NGRIP 1895.3 m** | | | | | | | | | | | |
| 1 | 45.94 | 4.31 | 12.89 | 14.32 | 0.24 | 5.53 | 10.37 | 3.08 | 0.67 | 0.46 | 97.83 |
| 2 | 46.95 | 4.40 | 12.88 | 13.86 | 0.16 | 5.41 | 10.01 | 3.06 | 0.78 | 0.51 | 98.00 |
| 3 | 46.70 | 4.44 | 12.84 | 14.73 | 0.20 | 5.50 | 10.57 | 2.91 | 0.75 | 0.45 | 99.10 |
| 4 | 46.25 | 4.43 | 12.90 | 14.41 | 0.26 | 5.50 | 10.34 | 3.06 | 0.72 | 0.52 | 98.41 |
| 5 | 46.75 | 4.49 | 12.83 | 13.92 | 0.17 | 5.37 | 10.06 | 3.04 | 0.82 | 0.51 | 97.96 |
| 6 | 46.91 | 4.33 | 12.92 | 14.29 | 0.22 | 5.45 | 10.27 | 3.02 | 0.72 | 0.52 | 98.65 |
| 7 | 46.77 | 4.37 | 12.91 | 14.37 | 0.19 | 5.38 | 10.26 | 3.11 | 0.74 | 0.47 | 98.56 |
| 8 | 46.20 | 4.54 | 12.83 | 14.67 | 0.26 | 5.46 | 10.22 | 2.89 | 0.66 | 0.48 | 98.20 |
| 9 | 47.57 | 4.42 | 12.91 | 14.02 | 0.26 | 5.35 | 10.13 | 2.81 | 0.78 | 0.55 | 98.81 |
| 10 | 46.67 | 4.25 | 12.94 | 14.53 | 0.22 | 5.40 | 10.13 | 3.04 | 0.72 | 0.50 | 98.38 |
| 11 | 47.41 | 4.37 | 12.91 | 13.55 | 0.24 | 5.37 | 10.09 | 2.95 | 0.72 | 0.56 | 98.18 |
| 12 | 46.73 | 4.37 | 12.83 | 14.36 | 0.20 | 5.46 | 10.02 | 3.05 | 0.75 | 0.51 | 98.29 |
| 13 | 46.91 | 4.25 | 12.69 | 14.37 | 0.15 | 5.40 | 10.22 | 2.84 | 0.69 | 0.49 | 98.01 |
| 14 | 45.98 | 4.49 | 12.89 | 14.85 | 0.25 | 5.59 | 10.49 | 2.81 | 0.68 | 0.48 | 98.50 |
| 15 | 47.06 | 4.51 | 13.02 | 14.64 | 0.28 | 5.47 | 10.28 | 2.82 | 0.73 | 0.53 | 99.34 |
| 16 | 46.78 | 4.41 | 12.90 | 14.67 | 0.23 | 5.44 | 10.13 | 2.99 | 0.74 | 0.54 | 98.83 |
| 17 | 47.00 | 4.27 | 12.87 | 14.60 | 0.28 | 5.42 | 10.04 | 2.64 | 0.73 | 0.53 | 98.39 |
| 18 | 47.11 | 4.32 | 12.87 | 14.60 | 0.12 | 5.39 | 10.14 | 3.11 | 0.74 | 0.48 | 98.88 |
| 19 | 47.18 | 4.40 | 13.08 | 14.17 | 0.35 | 5.31 | 10.12 | 2.88 | 0.73 | 0.53 | 98.74 |
| 20 | 47.33 | 4.39 | 13.06 | 14.18 | 0.31 | 5.47 | 10.21 | 2.58 | 0.72 | 0.47 | 98.73 |
| 21 | 46.10 | 4.63 | 12.74 | 14.83 | 0.14 | 5.38 | 10.41 | 2.97 | 0.68 | 0.62 | 98.51 |
| 22 | 47.17 | 4.40 | 12.84 | 14.26 | 0.26 | 5.40 | 10.18 | 3.03 | 0.71 | 0.49 | 98.75 |
| **Mean** | **46.79** | **4.40** | **12.89** | **14.37** | **0.23** | **5.43** | **10.21** | **2.94** | **0.73** | **0.51** | **98.50** |
| St. Dev. | 0.46 | 0.10 | 0.09 | 0.33 | 0.06 | 0.07 | 0.15 | 0.15 | 0.04 | 0.04 | 0.38 |

**Major oxide concentrations of shards from the NGRIP 1915.5 m tephra horizon. n = number of shards analysed. Mean and 1 standard deviations are shown. All oxides are presented as weight %. Total iron is expressed as FeO.**

| n | $SiO_2$ | $TiO_2$ | $Al_2O_3$ | FeO | MnO | MgO | CaO | $Na_2O$ | $K_2O$ | $P_2O_5$ | Total |
|---|---|---|---|---|---|---|---|---|---|---|---|
| **NGRIP 1915.5 m** | | | | | | | | | | | |
| 1 | 46.57 | 4.04 | 13.15 | 13.10 | 0.23 | 5.64 | 10.61 | 2.67 | 0.65 | 0.46 | 97.11 |
| 2 | 47.33 | 4.23 | 13.36 | 14.48 | 0.22 | 5.92 | 10.66 | 2.09 | 0.50 | 0.50 | 99.29 |
| 3 | 46.89 | 4.11 | 13.29 | 14.02 | 0.14 | 5.78 | 11.23 | 2.67 | 0.63 | 0.49 | 99.25 |
| 4 | 47.10 | 4.03 | 13.42 | 14.59 | 0.30 | 5.29 | 10.68 | 2.80 | 0.68 | 0.49 | 99.36 |
| 5 | 47.66 | 3.99 | 13.35 | 13.60 | 0.24 | 5.64 | 10.39 | 2.71 | 0.73 | 0.48 | 98.80 |
| 6 | 46.89 | 3.88 | 13.26 | 13.63 | 0.19 | 5.76 | 10.78 | 2.74 | 0.65 | 0.48 | 98.27 |
| 7 | 46.67 | 4.09 | 13.23 | 13.35 | 0.26 | 5.72 | 11.08 | 2.72 | 0.59 | 0.50 | 98.20 |
| 8 | 48.01 | 4.04 | 13.75 | 14.78 | 0.12 | 4.39 | 9.63 | 3.21 | 0.59 | 0.48 | 99.01 |
| 9 | 46.68 | 4.52 | 13.38 | 14.69 | 0.21 | 5.51 | 10.79 | 2.48 | 0.74 | 0.46 | 99.45 |
| 10 | 46.97 | 4.11 | 13.15 | 13.87 | 0.32 | 5.34 | 10.81 | 2.78 | 0.69 | 0.49 | 98.52 |
| 11 | 46.82 | 3.96 | 13.12 | 13.60 | 0.23 | 5.69 | 10.99 | 2.75 | 0.67 | 0.46 | 98.29 |
| 12 | 47.19 | 4.02 | 13.50 | 13.88 | 0.23 | 5.61 | 10.87 | 2.42 | 0.63 | 0.48 | 98.82 |
| 13 | 46.85 | 5.04 | 12.08 | 14.86 | 0.24 | 4.79 | 9.79 | 3.00 | 0.84 | 0.79 | 98.29 |
| 14 | 46.78 | 4.06 | 13.21 | 13.25 | 0.08 | 5.58 | 11.02 | 2.75 | 0.69 | 0.51 | 97.91 |
| 15 | 46.97 | 3.89 | 13.22 | 13.32 | 0.15 | 5.83 | 10.83 | 2.86 | 0.62 | 0.45 | 98.15 |
| 16 | 46.55 | 4.01 | 13.16 | 13.74 | 0.22 | 5.77 | 10.85 | 2.61 | 0.66 | 0.44 | 98.01 |
| 17 | 47.19 | 4.07 | 13.44 | 13.42 | 0.38 | 5.81 | 11.18 | 1.88 | 0.68 | 0.46 | 98.53 |
| 18 | 46.82 | 4.13 | 13.20 | 13.67 | 0.26 | 5.66 | 10.97 | 2.70 | 0.69 | 0.50 | 98.60 |
| 19 | 47.64 | 4.20 | 13.53 | 12.54 | 0.22 | 5.54 | 10.06 | 3.71 | 0.72 | 0.45 | 98.61 |
| 20 | 47.28 | 3.78 | 13.21 | 14.35 | 0.28 | 6.72 | 9.24 | 2.92 | 0.88 | 0.50 | 99.15 |
| 21 | 46.58 | 3.98 | 13.26 | 13.33 | 0.13 | 5.72 | 11.05 | 2.82 | 0.66 | 0.46 | 97.98 |
| 22 | 47.57 | 4.16 | 13.28 | 12.98 | 0.20 | 5.73 | 10.81 | 2.02 | 0.64 | 0.45 | 97.87 |
| **Mean** | **47.05** | **4.11** | **13.25** | **13.78** | **0.22** | **5.61** | **10.65** | **2.69** | **0.67** | **0.49** | **98.52** |
| St. Dev. | 0.40 | 0.25 | 0.30 | 0.63 | 0.07 | 0.43 | 0.52 | 0.38 | 0.08 | 0.07 | 0.59 |

**Major oxide concentrations of shards from the NGRIP 2631.9 m tephra horizon. n = number of shards analysed. Mean and 1 standard deviations are shown. All oxides are presented as weight %. Total iron is expressed as FeO.**

| n | $SiO_2$ | $TiO_2$ | $Al_2O_3$ | FeO | MnO | MgO | CaO | $Na_2O$ | $K_2O$ | $P_2O_5$ | Total |
|---|---|---|---|---|---|---|---|---|---|---|---|
| **NGRIP 2631.9 m** | | | | | | | | | | | |
| 1 | 47.29 | 4.32 | 13.18 | 14.32 | 0.18 | 5.15 | 9.75 | 3.17 | 0.85 | 0.77 | 98.98 |
| 2 | 47.08 | 4.27 | 13.04 | 14.48 | 0.22 | 5.21 | 9.84 | 2.55 | 0.82 | 0.69 | 98.19 |
| 3 | 47.58 | 4.57 | 13.27 | 14.29 | 0.27 | 5.12 | 9.83 | 3.00 | 0.80 | 0.75 | 99.48 |
| 4 | 48.56 | 4.39 | 13.30 | 14.15 | 0.23 | 4.71 | 9.36 | 2.74 | 0.88 | 0.75 | 99.08 |
| 5 | 47.46 | 4.37 | 13.19 | 14.40 | 0.18 | 5.07 | 9.46 | 3.15 | 0.81 | 0.69 | 98.78 |
| 6 | 47.42 | 4.35 | 13.07 | 14.27 | 0.20 | 5.14 | 9.64 | 3.15 | 0.85 | 0.70 | 98.80 |
| 7 | 47.62 | 4.54 | 13.09 | 14.72 | 0.14 | 5.04 | 9.86 | 3.19 | 0.86 | 0.78 | 99.83 |
| 8 | 48.54 | 4.68 | 13.29 | 14.11 | 0.16 | 4.60 | 9.47 | 2.99 | 0.99 | 0.80 | 99.61 |
| 9 | 47.90 | 4.27 | 13.41 | 12.79 | 0.21 | 5.09 | 10.01 | 3.20 | 0.76 | 0.76 | 98.38 |
| 10 | 48.66 | 4.27 | 14.45 | 12.88 | 0.17 | 4.38 | 9.92 | 3.18 | 0.80 | 0.69 | 99.39 |
| 11 | 47.48 | 4.55 | 13.08 | 13.84 | 0.19 | 5.12 | 9.43 | 2.89 | 0.84 | 0.80 | 98.21 |
| 12 | 48.38 | 4.44 | 13.59 | 13.54 | 0.21 | 4.89 | 10.03 | 3.42 | 0.79 | 0.73 | 100.01 |
| 13 | 47.56 | 4.68 | 13.14 | 14.06 | 0.27 | 5.09 | 9.69 | 3.10 | 0.82 | 0.69 | 99.09 |
| 14 | 47.49 | 4.26 | 13.08 | 13.90 | 0.26 | 4.96 | 9.69 | 3.10 | 0.93 | 0.69 | 98.36 |
| 15 | 47.58 | 4.52 | 13.09 | 14.48 | 0.25 | 5.11 | 9.99 | 2.84 | 0.80 | 0.77 | 99.42 |
| 16 | 46.22 | 4.40 | 12.82 | 15.29 | 0.32 | 5.04 | 9.88 | 3.09 | 0.81 | 0.60 | 98.46 |
| 17 | 46.91 | 4.31 | 13.18 | 13.63 | 0.30 | 5.05 | 9.73 | 3.21 | 0.84 | 0.82 | 97.96 |
| 18 | 47.15 | 4.51 | 13.05 | 13.81 | 0.13 | 5.19 | 9.82 | 3.15 | 0.91 | 0.73 | 98.45 |
| 19 | 48.68 | 4.44 | 13.28 | 14.05 | 0.20 | 4.94 | 10.10 | 2.60 | 0.69 | 0.76 | 99.72 |
| 20 | 48.40 | 4.24 | 13.16 | 11.57 | 0.36 | 5.90 | 12.10 | 2.77 | 0.82 | 0.74 | 100.06 |
| 21 | 46.71 | 4.54 | 12.64 | 14.47 | 0.11 | 5.20 | 9.50 | 3.05 | 0.88 | 0.69 | 97.79 |
| 22 | 48.45 | 4.28 | 14.04 | 12.36 | 0.18 | 4.62 | 10.22 | 3.23 | 0.63 | 0.80 | 98.80 |
| 23 | 46.95 | 4.45 | 13.00 | 14.63 | 0.26 | 5.18 | 9.46 | 3.05 | 0.82 | 0.77 | 98.57 |
| **Mean** | **47.66** | **4.42** | **13.24** | **13.91** | **0.22** | **5.03** | **9.86** | **3.04** | **0.83** | **0.74** | **98.93** |
| St. Dev. | 0.68 | 0.13 | 0.37 | 0.83 | 0.06 | 0.29 | 0.54 | 0.21 | 0.07 | 0.05 | 0.66 |

**Trace element concentrations of shards from the GRIP 1716.08 m tephra horizon. n = shard number and relates to the major oxide analyses from this horizon. All concentrations are presented as ppm. Mean and 1 standard deviations are shown.**

| GRIP 1716.08 m | | | | | | | | | | | | | | | | | | |
|---|---|---|---|---|---|---|---|---|---|---|---|---|---|---|---|---|---|---|
| n | 1 | 2 | 3 | 4 | 5 | 6 | 7 | 8 | 10 | 12 | 13 | 14 | 17 | 20 | 21 | 23 | **Mean** | St. Dev. |
| Sc | 17.62 | 16.78 | 21.63 | 23.69 | 17.08 | 14.03 | 6.20 | 13.54 | 10.49 | 20.48 | 21.79 | 11.01 | 7.84 | 37.02 | 20.07 | 23.66 | **17.7** | 7.52 |
| Rb | 24.36 | 15.98 | 26.43 | 29.80 | 24.47 | 21.94 | 28.05 | 23.04 | 26.15 | 20.49 | 18.01 | 24.57 | 20.62 | 19.99 | 18.98 | 21.76 | **22.8** | 3.77 |
| Sr | 275.66 | 162.98 | 344.01 | 318.13 | 185.36 | 233.91 | 165.47 | 149.50 | 180.74 | 416.36 | 256.27 | 85.79 | 100.65 | 459.48 | 248.50 | 300.64 | **243** | 107 |
| Y | 21.32 | 10.84 | 25.95 | 22.03 | 13.21 | 18.61 | 13.97 | 10.63 | 10.72 | 34.20 | 19.57 | 6.10 | 7.65 | 33.99 | 14.51 | 25.53 | **18.1** | 8.67 |
| Zr | 191.68 | 141.50 | 224.39 | 207.91 | 159.24 | 193.28 | 146.16 | 120.41 | 154.88 | 213.08 | 172.48 | 117.42 | 110.24 | 254.44 | 190.72 | 189.45 | **174** | 41.2 |
| Nb | 20.54 | 10.82 | 23.89 | 25.46 | 11.20 | 15.99 | 8.04 | 10.23 | 13.71 | 29.98 | 20.44 | 3.77 | 6.48 | 33.37 | 16.42 | 22.09 | **17.0** | 8.57 |
| Cs | 1.45 | 1.02 | 0.34 | 0.10 | -0.03 | 0.17 | 0.52 | -0.42 | 0.12 | 1.05 | 0.35 | 0.81 | 0.68 | 1.18 | -0.15 | 0.63 | **0.49** | 0.52 |
| Ba | 203.12 | 195.37 | 203.98 | 226.25 | 196.11 | 207.63 | 200.23 | 172.11 | 182.05 | 184.28 | 161.91 | 195.32 | 136.75 | 186.41 | 181.93 | 183.96 | **189** | 20.5 |
| La | 15.94 | 8.06 | 16.97 | 16.38 | 10.00 | 14.13 | 5.96 | 6.11 | 10.00 | 19.66 | 13.96 | 5.31 | 5.79 | 24.46 | 13.83 | 16.07 | **12.7** | 5.61 |
| Ce | 31.05 | 14.06 | 37.44 | 32.57 | 19.08 | 24.85 | 16.04 | 13.18 | 17.24 | 43.72 | 32.58 | 7.78 | 8.67 | 60.97 | 27.58 | 31.75 | **26.2** | 14.1 |
| Pr | 3.57 | 1.96 | 5.56 | 4.84 | 2.81 | 4.59 | 1.86 | 2.40 | 2.09 | 4.72 | 4.94 | 1.13 | 0.75 | 6.35 | 3.63 | 4.65 | **3.49** | 1.68 |
| Nd | 19.52 | 10.10 | 26.44 | 21.54 | 11.03 | 20.75 | 7.75 | 8.79 | 14.07 | 26.07 | 18.75 | 5.45 | 5.85 | 51.33 | 15.47 | 17.79 | **17.5** | 11.2 |
| Sm | 4.61 | 2.90 | 7.84 | 8.73 | 5.59 | 6.09 | 3.44 | 3.28 | 3.51 | 5.88 | 3.70 | 2.89 | 1.43 | 7.67 | 2.06 | 4.56 | **4.64** | 2.15 |
| Eu | 0.74 | 1.38 | 1.96 | 0.79 | 1.78 | 1.01 | 2.01 | 2.68 | 0.54 | 1.39 | 1.12 | 1.96 | 0.79 | 2.52 | 1.44 | 1.76 | **1.49** | 0.64 |
| Gd | 5.42 | 2.73 | 5.52 | 4.46 | 4.05 | 3.57 | 3.18 | 0.76 | 2.92 | 7.48 | 3.44 | 0.40 | 1.77 | 7.47 | 4.37 | 4.31 | **3.87** | 2.02 |
| Tb | 0.87 | 0.11 | 0.88 | 0.92 | 0.31 | 0.77 | 0.60 | 0.32 | 0.58 | 0.87 | 0.68 | 0.29 | 0.33 | 1.66 | 0.58 | 0.79 | **0.66** | 0.37 |
| Dy | 4.90 | 0.89 | 5.32 | 7.24 | 2.54 | 3.78 | 1.00 | 1.77 | 0.92 | 5.28 | 3.87 | 0.99 | 0.66 | 4.99 | 3.35 | 5.20 | **3.29** | 2.08 |
| Ho | 0.70 | 0.29 | 0.31 | 0.93 | 0.56 | 0.81 | 0.63 | 0.29 | 0.52 | 0.98 | 0.83 | 0.16 | 0.48 | 1.42 | 0.82 | 1.27 | **0.69** | 0.36 |
| Er | 1.72 | 0.86 | 3.53 | 3.11 | 0.97 | 1.01 | 0.69 | 2.01 | 1.40 | 2.85 | 1.77 | 0.39 | 0.84 | 3.79 | 1.78 | 2.16 | **1.80** | 1.05 |
| Tm | 0.26 | 0.10 | 0.28 | 0.41 | 0.07 | 0.19 | 0.15 | 0.08 | 0.24 | 0.48 | 0.34 | -0.02 | 0.15 | 0.15 | 0.21 | 0.26 | **0.21** | 0.13 |
| Yb | 2.01 | 0.48 | 2.00 | 2.19 | 0.99 | 1.53 | 1.20 | 0.61 | 0.86 | 2.73 | 1.52 | 0.57 | 0.57 | 1.67 | 1.32 | 2.19 | **1.40** | 0.69 |
| Lu | 0.13 | 0.36 | 0.49 | 0.36 | 0.10 | 0.37 | 0.16 | 0.07 | 0.19 | 0.14 | 0.21 | 0.15 | 0.03 | 0.52 | 0.15 | 0.02 | **0.22** | 0.16 |
| Hf | 3.65 | 3.69 | 5.09 | 4.03 | 3.24 | 3.98 | 2.85 | 2.64 | 3.14 | 5.70 | 3.43 | 3.06 | 2.35 | 6.52 | 4.47 | 4.09 | **3.87** | 1.13 |
| Ta | 1.01 | 0.55 | 1.15 | 1.15 | 0.64 | 0.65 | 0.77 | 0.90 | 0.50 | 1.32 | 1.14 | 0.28 | 0.33 | 2.03 | 1.02 | 1.06 | **0.91** | 0.43 |
| Th | 0.77 | 1.15 | 1.23 | 0.85 | 0.95 | 1.08 | 0.31 | 0.70 | 1.13 | 1.45 | 1.05 | 0.37 | 0.47 | 1.77 | 1.09 | 1.23 | **0.98** | 0.39 |
| U | 0.19 | 0.32 | 0.33 | 0.57 | 0.31 | 0.54 | 0.24 | 0.21 | 0.26 | 0.18 | 0.31 | 0.43 | 0.07 | 0.55 | 0.33 | 0.34 | **0.32** | 0.14 |

**Trace element concentrations of shards from the NGRIP 1895.3 m tephra horizon. n = shard number and relates to the major oxide analyses from this horizon. All concentrations are presented as ppm. Mean and 1 standard deviations are shown.**

| NGRIP 1895.3 m | | | | | | | | | | | | | | | | |
|---|---|---|---|---|---|---|---|---|---|---|---|---|---|---|---|---|
| n | 1 | 3 | 5 | 6 | 7 | 9 | 11 | 12 | 13 | 15 | 16 | 18 | 19 | 21 | **Mean** | St. Dev. |
| Sc | 41.20 | 27.21 | 10.64 | 10.74 | 19.72 | 23.19 | 13.21 | 34.52 | 6.61 | 22.98 | 22.45 | 32.73 | 33.25 | 28.27 | **23.3** | 10.3 |
| Rb | 34.22 | 22.13 | 28.79 | 26.46 | 23.69 | 27.90 | 26.39 | 25.77 | 71.35 | 29.72 | 28.52 | 33.46 | 21.85 | 31.89 | **30.9** | 12.3 |
| Sr | 713.52 | 380.33 | 199.31 | 149.55 | 357.28 | 295.27 | 277.70 | 726.22 | 144.10 | 331.55 | 379.33 | 576.00 | 579.96 | 234.90 | **382** | 195 |
| Y | 51.09 | 26.35 | 10.96 | 12.64 | 25.14 | 16.99 | 16.48 | 38.32 | 12.19 | 22.83 | 23.14 | 42.08 | 38.85 | 20.00 | **25.5** | 12.5 |
| Zr | 288.02 | 183.53 | 148.60 | 130.98 | 194.09 | 166.11 | 197.06 | 244.07 | 128.64 | 189.77 | 215.21 | 288.19 | 255.04 | 179.33 | **201** | 52.0 |
| Nb | 42.38 | 24.47 | 10.64 | 2.74 | 22.64 | 15.57 | 16.13 | 37.40 | 4.21 | 17.88 | 19.49 | 42.85 | 40.55 | 14.37 | **22.2** | 13.6 |
| Cs | 0.54 | 0.44 | 0.34 | 0.52 | 0.98 | 0.66 | 1.20 | 1.64 | 1.37 | 0.32 | 0.77 | 1.11 | 1.06 | 1.67 | **0.90** | 0.46 |
| Ba | 181.19 | 145.51 | 166.89 | 141.90 | 219.46 | 131.01 | 161.09 | 138.44 | 142.08 | 151.84 | 172.43 | 170.91 | 137.02 | 147.97 | **158** | 23.4 |
| La | 28.23 | 13.21 | 8.23 | 7.41 | 22.48 | 13.93 | 11.92 | 20.64 | 8.18 | 15.07 | 19.06 | 26.85 | 29.09 | 12.73 | **16.9** | 7.52 |
| Ce | 60.69 | 30.31 | 15.09 | 20.09 | 35.05 | 24.51 | 23.34 | 50.49 | 18.23 | 33.06 | 36.69 | 53.60 | 55.83 | 23.68 | **34.3** | 15.1 |
| Pr | 8.48 | 4.71 | 2.10 | 2.71 | 5.15 | 4.53 | 3.49 | 6.36 | 1.76 | 3.18 | 6.04 | 6.34 | 7.83 | 2.76 | **4.67** | 2.12 |
| Nd | 45.46 | 16.07 | 8.44 | 8.81 | 21.66 | 8.98 | 9.56 | 37.61 | 15.60 | 19.39 | 18.63 | 32.08 | 44.43 | 14.32 | **21.5** | 13.1 |
| Sm | 9.87 | 4.44 | 2.95 | | 4.72 | 1.18 | 3.54 | 9.82 | 1.05 | 2.73 | 4.14 | 14.09 | 7.50 | 3.07 | **5.32** | 3.89 |
| Eu | 4.26 | 1.92 | 0.64 | -0.43 | 0.52 | 1.56 | 1.11 | 1.33 | 0.19 | -0.36 | 2.81 | 1.43 | 1.80 | -0.89 | **1.13** | 1.37 |
| Gd | 8.89 | 2.28 | 1.33 | 0.95 | 5.17 | 3.09 | 1.60 | 7.23 | -0.06 | 3.40 | 4.63 | 6.89 | 8.86 | 2.44 | **4.05** | 2.95 |
| Tb | 1.07 | 0.93 | 0.11 | 0.09 | -0.04 | 0.69 | 0.09 | 1.08 | 0.04 | -0.01 | 0.29 | 1.31 | 0.66 | 0.30 | **0.47** | 0.47 |
| Dy | 7.75 | 4.93 | 2.70 | 2.41 | 4.16 | 3.94 | 2.40 | 4.60 | 2.98 | 3.91 | 4.59 | 6.56 | 6.55 | 3.57 | **4.36** | 1.64 |
| Ho | 1.26 | 0.87 | 0.38 | 0.22 | 0.69 | 0.95 | 0.70 | 0.60 | 0.38 | 0.63 | 0.76 | 1.43 | 1.25 | 0.28 | **0.74** | 0.38 |
| Er | 3.41 | 2.40 | 0.89 | 0.23 | 1.31 | 2.44 | 2.52 | 2.88 | 0.51 | 2.12 | 2.40 | 3.91 | 3.07 | 1.44 | **2.11** | 1.09 |
| Tm | 0.39 | 0.23 | -0.12 | 0.22 | -0.07 | 0.05 | 0.29 | 0.37 | 0.19 | 0.31 | 0.32 | 0.37 | 0.55 | 0.41 | **0.25** | 0.19 |
| Yb | 2.44 | 1.08 | 1.05 | 1.78 | 2.25 | 0.85 | 1.00 | 3.16 | 1.19 | 1.08 | 1.46 | 2.74 | 2.45 | 0.58 | **1.65** | 0.81 |
| Lu | 0.08 | 0.13 | 0.31 | 0.40 | 0.45 | 0.36 | 0.21 | 0.71 | 0.38 | 0.36 | 0.34 | 0.29 | 0.76 | 0.38 | **0.37** | 0.19 |
| Hf | 4.77 | 5.67 | 2.42 | 4.23 | 6.16 | 2.46 | 4.63 | 5.17 | 2.00 | 5.33 | 5.95 | 6.29 | 3.92 | 5.29 | **4.59** | 1.42 |
| Ta | 2.35 | 1.77 | 0.49 | 0.60 | 1.56 | 1.34 | 0.81 | 1.85 | 1.02 | 1.15 | 0.96 | 1.84 | 1.91 | 1.11 | **1.34** | 0.55 |
| Th | 2.21 | 1.43 | 0.89 | 0.81 | 1.17 | 0.74 | 1.05 | 3.57 | 0.70 | 1.51 | 5.01 | 2.34 | 2.86 | 0.92 | **1.80** | 1.28 |
| U | 0.85 | 0.36 | 0.06 | 0.30 | 0.40 | 0.72 | 0.90 | 0.77 | 0.22 | 0.56 | 0.89 | 0.86 | 0.91 | 0.71 | **0.61** | 0.29 |

**Trace element concentrations of shards from the NGRIP 1915.5 m tephra horizon. n = shard number and relates to the major oxide analyses from this horizon. All concentrations are presented as ppm. Mean and 1 standard deviations are shown.**

| NGRIP 1915.5 m | | | | | | | |
|---|---|---|---|---|---|---|---|
| n | 11 | 17 | 18 | 20 | 21 | **Mean** | St. Dev. |
| Sc | 18.00 | 15.42 | -0.19 | 8.29 | 7.80 | **9.86** | 7.16 |
| Rb | 9.48 | 9.41 | 26.16 | 21.88 | 21.59 | **17.7** | 7.75 |
| Sr | 108.85 | 84.17 | 138.75 | 116.17 | 114.96 | **112.6** | 19.5 |
| Y | 8.59 | 6.24 | 10.14 | 8.89 | 8.19 | **8.41** | 1.42 |
| Zr | 62.33 | 49.58 | 95.07 | 82.35 | 86.37 | **75.1** | 18.7 |
| Nb | 7.38 | 5.58 | 7.48 | 7.09 | 6.18 | **6.74** | 0.83 |
| Cs | 0.13 | 0.15 | 0.46 | 0.15 | 0.29 | **0.24** | 0.14 |
| Ba | 416.18 | 1242.18 | 2601.03 | 230.46 | 127.96 | **924** | 1035 |
| La | 6.96 | 4.87 | 9.21 | 7.99 | 7.81 | **7.37** | 1.61 |
| Ce | 13.85 | 10.57 | 18.75 | 16.26 | 15.97 | **15.1** | 3.06 |
| Pr | 1.68 | 1.39 | 2.45 | 2.11 | 1.99 | **1.92** | 0.40 |
| Nd | 8.65 | 6.32 | 7.41 | 13.21 | 10.89 | **9.30** | 2.77 |
| Sm | 1.62 | 1.39 | 1.03 | 0.34 | 2.14 | **1.30** | 0.68 |
| Eu | 0.11 | 0.43 | 2.58 | 1.46 | 1.22 | **1.16** | 0.97 |
| Gd | 1.50 | 2.00 | | 1.34 | -0.25 | **1.15** | 0.97 |
| Tb | 0.27 | 0.18 | 0.20 | 0.25 | 0.35 | **0.25** | 0.07 |
| Dy | 1.46 | 1.24 | 1.81 | 1.69 | 2.20 | **1.68** | 0.36 |
| Ho | 0.27 | 0.21 | 0.37 | 0.19 | 0.26 | **0.26** | 0.07 |
| Er | 0.58 | 0.75 | 1.14 | 0.86 | 1.13 | **0.89** | 0.25 |
| Tm | 0.09 | 0.07 | 0.27 | 0.12 | 0.12 | **0.13** | 0.08 |
| Yb | 0.63 | 0.43 | 0.72 | 1.37 | 0.70 | **0.77** | 0.05 |
| Lu | 0.12 | 0.04 | 0.17 | 0.07 | 0.09 | **0.10** | 0.05 |
| Hf | 1.38 | 1.49 | 2.00 | 2.28 | 2.51 | **1.93** | 0.49 |
| Ta | 0.35 | 0.36 | 0.74 | 0.30 | 0.83 | **0.51** | 0.25 |
| Th | 1.01 | 0.80 | 1.15 | 1.43 | 1.37 | **1.15** | 0.26 |
| U | 0.26 | 0.20 | 0.29 | 0.43 | 0.35 | **0.31** | 0.09 |

**Trace element concentrations of shards from the NGRIP 2631.9 m tephra horizon. n = shard number and relates to the major oxide analyses from this horizon. All concentrations are presented as ppm. Mean and 1 standard deviations are shown.**

| NGRIP 2631.9 m | | | | | | | | | | | | | | |
|---|---|---|---|---|---|---|---|---|---|---|---|---|---|---|
| n | 3 | 4 | 7 | 8 | 11 | 12 | 14 | 15 | 17 | 19 | 20 | 21 | **Mean** | St. Dev. |
| Sc | 6.66 | 2.98 | -2.35 | -1.28 | -3.45 | -35.50 | 18.96 | 16.44 | 15.21 | 17.00 | 14.87 | 14.97 | **5.38** | 15.3 |
| Rb | 27.66 | 13.36 | 22.17 | 22.40 | 24.13 | 58.35 | 5.56 | 6.11 | 3.37 | 3.94 | 5.01 | 6.64 | **29.0** | 7.10 |
| Sr | 389.99 | 407.65 | 337.81 | 396.02 | | 325.29 | 272.48 | 237.67 | 236.36 | 234.09 | 229.05 | 209.12 | **298** | 75.7 |
| Y | 27.92 | 29.23 | 25.21 | 29.25 | 28.40 | 33.32 | 21.38 | 19.73 | 19.01 | 19.20 | 19.22 | 17.05 | **24.1** | 5.41 |
| Zr | 172.21 | 167.99 | 150.11 | 177.00 | 160.31 | 197.53 | 131.67 | 114.01 | 107.64 | 112.99 | 109.88 | 105.94 | **142** | 32.4 |
| Nb | 27.85 | 28.15 | 25.68 | 27.06 | 26.37 | 30.38 | 22.35 | 18.32 | 18.55 | 17.76 | 16.81 | 16.07 | **22.9** | 5.18 |
| Cs | 0.51 | 0.02 | 0.25 | 0.20 | 0.31 | -0.39 | -0.11 | -0.09 | -0.03 | -0.25 | 0.20 | -0.06 | **0.04** | 0.25 |
| Ba | 350.08 | | 216.74 | 242.40 | 201.44 | 373.43 | 127.26 | 115.46 | 119.69 | 119.72 | 136.01 | 108.28 | **192** | 95.8 |
| La | 21.14 | 20.08 | 18.91 | 23.08 | 19.74 | 28.51 | 15.76 | 15.12 | 14.63 | 13.22 | 14.89 | 12.13 | **18.1** | 4.73 |
| Ce | 45.94 | 53.12 | 46.51 | 46.75 | 49.78 | 60.39 | 36.66 | 32.68 | 30.94 | 29.39 | 29.23 | 27.92 | **40.8** | 11.0 |
| Pr | 6.26 | 6.64 | 5.25 | 7.02 | 5.81 | 6.76 | 5.01 | 4.50 | 3.92 | 3.79 | 3.73 | 3.49 | **5.18** | 1.30 |
| Nd | 28.15 | 29.19 | 25.99 | 30.52 | 25.79 | 36.99 | 22.46 | 24.37 | 17.22 | 18.16 | 20.02 | 19.86 | **24.9** | 5.79 |
| Sm | 4.28 | 7.14 | 5.95 | 5.92 | 5.93 | 8.47 | 6.49 | 4.66 | 4.40 | 4.65 | 4.23 | 3.68 | **5.48** | 1.42 |
| Eu | 4.14 | 2.24 | 2.59 | 3.71 | 2.29 | 4.07 | 1.84 | 1.52 | 1.06 | 1.27 | 1.95 | 1.79 | **2.37** | 1.06 |
| Gd | 11.75 | 8.18 | 8.67 | 10.80 | 7.69 | 12.10 | 6.20 | 5.79 | 4.21 | 4.44 | 3.84 | 4.89 | **7.38** | 2.97 |
| Tb | 0.88 | 0.74 | 0.81 | 0.74 | 0.70 | 1.14 | 0.70 | 0.53 | 0.67 | 0.57 | 0.38 | 0.56 | **0.70** | 0.19 |
| Dy | 5.14 | 5.61 | 4.70 | 5.17 | 5.47 | 6.97 | 4.05 | 3.55 | 3.12 | 3.51 | 3.16 | 2.66 | **4.43** | 1.29 |
| Ho | 0.73 | 1.01 | 0.77 | 0.94 | 0.99 | 0.97 | 0.81 | 0.67 | 0.73 | 0.58 | 0.59 | 0.68 | **0.79** | 0.15 |
| Er | 1.75 | 2.47 | 1.59 | 2.72 | 2.19 | 3.85 | 2.08 | 1.70 | 1.69 | 1.93 | 1.77 | 1.28 | **2.09** | 0.68 |
| Tm | 0.22 | 0.29 | 0.18 | 0.14 | 0.40 | 0.26 | 0.30 | 0.22 | 0.28 | 0.21 | 0.00 | 0.20 | **0.23** | 0.10 |
| Yb | 2.03 | 1.80 | 2.16 | 2.12 | 2.09 | 2.35 | 1.94 | 1.56 | 1.37 | 1.55 | 1.15 | 1.74 | **1.82** | 0.36 |
| Lu | 0.43 | 0.33 | 0.33 | 0.28 | 0.15 | 0.39 | 0.21 | 0.25 | 0.29 | 0.10 | 0.40 | 0.14 | **0.28** | 0.11 |
| Hf | 3.89 | 4.42 | 2.74 | 4.45 | 3.82 | 4.52 | 3.15 | 3.03 | 2.43 | 2.88 | 2.09 | 2.48 | **3.32** | 0.86 |
| Ta | 1.52 | 1.73 | 1.54 | 1.60 | 1.25 | 3.14 | 1.46 | 1.19 | 0.97 | 1.34 | 1.33 | 1.03 | **1.51** | 0.56 |
| Th | 1.63 | 1.62 | 1.30 | 1.68 | 1.36 | 1.58 | 1.46 | 1.33 | 1.31 | 1.25 | 1.09 | 1.11 | **1.39** | 0.20 |
| U | 0.30 | 0.44 | 0.38 | 0.44 | 0.54 | 0.57 | 0.42 | 0.37 | 0.31 | 0.42 | 0.28 | 0.36 | **0.40** | 0.09 |

# Appendix 3 – NGRIP Tephra Shard Counts and Geochemical Data

**Tephra shard counts and depth information for individual ice samples taken from the NGRIP ice-core.**

| Bag Number | Bag Depth Interval | Top depth (m) | Bottom depth (m) | No. of Tephra Shards |
|---|---|---|---|---|
| 4365 | 0-35 | 2400.2 | 2400.55 | 0 |
| 4365 | 35-40 | 2400.55 | 2400.6 | 1 |
| 4365 | 40-45 | 2400.6 | 2400.65 | 0 |
| 4365 | 45-50 | 2400.65 | 2400.7 | 0 |
| 4365 | 50-55 | 2400.7 | 2400.75 | 0 |
| 4366 | 0-5 | 2400.75 | 2400.8 | 1 |
| 4366 | 5-55 | 2400.8 | 2401.3 | 1 |
| 4376 | 0-40 | 2406.25 | 2406.65 | 0 |
| 4376 | 40-45 | 2406.65 | 2406.7 | 0 |
| 4376 | 45-55 | 2406.7 | 2406.8 | 0 |
| 4377 | 0-5 | 2406.8 | 2406.85 | 0 |
| 4377 | 5-15 | 2406.85 | 2406.95 | 1 |
| 4377 | 15-20 | 2406.95 | 2407 | 0 |
| 4377 | 20-30 | 2407 | 2407.1 | 0 |
| 4377 | 30-55 | 2407.1 | 2407.35 | 0 |
| 4380 | 0-20 | 2408.45 | 2408.65 | 0 |
| 4380 | 20-45 | 2408.65 | 2408.9 | 0 |
| 4380 | 45-50 | 2408.9 | 2408.95 | 0 |
| 4380 | 50-55 | 2408.95 | 2409 | 0 |
| 4381 | 0-10 | 2409 | 2409.1 | 0 |
| 4381 | 10-16 | 2409.1 | 2409.16 | 0 |
| 4381 | 16-27 | 2409.16 | 2409.27 | 0 |
| 4381 | 27-32 | 2409.27 | 2409.32 | 0 |
| 4381 | 32-55 | 2409.32 | 2409.55 | 0 |
| 4383 | 0-5 | 2410.1 | 2410.15 | 0 |
| 4383 | 5-10 | 2410.15 | 2410.2 | 0 |
| 4383 | 10-23 | 2410.2 | 2410.33 | 0 |
| 4383 | 23-32 | 2410.33 | 2410.42 | 0 |
| 4383 | 32-40 | 2410.42 | 2410.5 | 0 |
| 4383 | 40-45 | 2410.5 | 2410.55 | 0 |
| 4383 | 45-50 | 2410.55 | 2410.6 | 0 |
| 4383 | 50-55 | 2410.6 | 2410.65 | 0 |
| 4384 | 0-5 | 2410.65 | 2410.7 | 0 |
| 4384 | 5-15 | 2410.7 | 2410.8 | 0 |
| 4384 | 15-25 | 2410.8 | 2410.9 | 0 |
| 4384 | 25-35 | 2410.9 | 2411 | 0 |
| 4384 | 35-45 | 2411 | 2411.1 | 0 |
| 4384 | 45-55 | 2411.1 | 2411.2 | 0 |
| 4385 | 0-10 | 2411.2 | 2411.3 | 0 |
| 4385 | 10-20 | 2411.3 | 2411.4 | 0 |
| 4385 | 20-30 | 2411.4 | 2411.5 | 0 |
| 4385 | 30-40 | 2411.5 | 2411.6 | 0 |
| 4385 | 40-50 | 2411.6 | 2411.7 | 0 |
| 4385 | 50-55 | 2411.7 | 2411.75 | 0 |
| 4386 | 0-5 | 2411.75 | 2411.8 | 0 |
| 4386 | 5-15 | 2411.8 | 2411.9 | 2 |
| 4386 | 15-25 | 2411.9 | 2412 | 0 |
| 4386 | 25-35 | 2412 | 2412.1 | 0 |
| 4386 | 35-45 | 2412.1 | 2412.2 | 0 |
| 4386 | 45-55 | 2412.2 | 2412.3 | 0 |

| Bag Number | Bag Depth Interval | Top depth (m) | Bottom depth (m) | No. of Tephra Shards |
|---|---|---|---|---|
| 4387 | 0-5 | 2412.3 | 2412.35 | 0 |
| 4387 | 5-15 | 2412.35 | 2412.45 | 0 |
| 4387 | 15-25 | 2412.45 | 2412.55 | 0 |
| 4387 | 25-40 | 2412.55 | 2412.6 | 0 |
| 4387 | 30-35 | 2412.6 | 2412.65 | 0 |
| 4387 | 35-41 | 2412.65 | 2412.71 | 0 |
| 4387 | 41-48 | 2412.71 | 2412.78 | 0 |
| 4387 | 48-55 | 2412.78 | 2412.85 | 0 |
| 4388 | 0-5 | 2412.85 | 2412.9 | 0 |
| 4388 | 5-10 | 2412.9 | 2412.95 | 0 |
| 4388 | 10-15 | 2412.95 | 2413 | 0 |
| 4388 | 15-20 | 2413 | 2413.05 | 0 |
| 4388 | 20-25 | 2413.05 | 2413.1 | 0 |
| 4388 | 25-30 | 2413.1 | 2413.15 | 0 |
| 4388 | 30-35 | 2413.15 | 2413.2 | 0 |
| 4388 | 35-40 | 2413.2 | 2413.25 | 0 |
| 4388 | 40-45 | 2413.25 | 2413.3 | 0 |
| 4388 | 45-50 | 2413.3 | 2413.35 | 0 |
| 4388 | 50-55 | 2413.35 | 2413.4 | 0 |
| 4397 | 0-5 | 2417.8 | 2417.85 | 0 |
| 4397 | 5-10 | 2417.85 | 2417.9 | 0 |
| 4397 | 10-15 | 2417.9 | 2417.95 | 0 |
| 4397 | 15-20 | 2417.95 | 2418 | 0 |
| 4397 | 20-50 | 2418 | 2418.3 | 0 |
| 4397 | 50-55 | 2418.3 | 2418.35 | 0 |
| 4398 | 0-10 | 2418.35 | 2418.45 | 2 |
| 4398 | 10-15 | 2418.45 | 2418.5 | 0 |
| 4398 | 15-25 | 2418.5 | 2418.6 | 0 |
| 4398 | 25-35 | 2418.6 | 2418.7 | 0 |
| 4398 | 35-40 | 2418.7 | 2418.75 | 4 |
| 4398 | 40-55 | 2418.75 | 2418.9 | 0 |
| 4404 | 0-4 | 2421.65 | 2421.69 | 0 |
| 4404 | 4-9 | 2421.69 | 2421.74 | 0 |
| 4404 | 9-14 | 2421.74 | 2421.79 | 0 |
| 4404 | 14-19 | 2421.79 | 2421.84 | 0 |
| 4404 | 19-30 | 2421.84 | 2421.95 | 0 |
| 4404 | 30-35 | 2421.95 | 2422 | 0 |
| 4404 | 35-38 | 2422 | 2422.03 | 0 |
| 4404 | 38-43 | 2422.03 | 2422.08 | 0 |
| 4404 | 43-55 | 2422.08 | 2422.2 | 0 |
| 4406 | 0-5 | 2422.75 | 2422.8 | 0 |
| 4406 | 5-10 | 2422.8 | 2422.85 | 0 |
| 4406 | 10-15 | 2422.85 | 2422.9 | 0 |
| 4406 | 15-21 | 2422.9 | 2422.96 | 0 |
| 4406 | 21-26 | 2422.96 | 2423.01 | 0 |
| 4406 | 26-55 | 2423.01 | 2423.3 | 1 |
| 4407 | 0-26 | 2423.3 | 2423.56 | 0 |
| 4407 | 26-31 | 2423.56 | 2423.61 | 0 |
| 4407 | 31-36 | 2423.61 | 2423.66 | 0 |
| 4407 | 36-40 | 2423.66 | 2423.7 | 0 |

| Bag Number | Bag Depth Interval | Top depth (m) | Bottom depth (m) | No. of Tephra Shards |
|---|---|---|---|---|
| 4407 | 40-45 | 2423.7 | 2423.75 | 0 |
| 4407 | 45-55 | 2423.75 | 2423.85 | 0 |
| 4426 | 0-46 | 2433.75 | 2434.21 | 0 |
| 4426 | 46-52 | 2434.21 | 2434.27 | 0 |
| 4426 | 52-55 | 2434.27 | 2434.3 | 0 |
| 4427 | 0-5 | 2434.3 | 2434.35 | 0 |
| 4427 | 5-10 | 2434.35 | 2434.4 | 0 |
| 4427 | 10-15 | 2434.4 | 2434.45 | 0 |
| 4427 | 15-55 | 2434.45 | 2434.85 | 0 |
| 4430 | 0-40 | 2435.95 | 2436.35 | 0 |
| 4430 | 40-45 | 2436.35 | 2436.4 | 0 |
| 4430 | 45-52 | 2436.4 | 2436.47 | 0 |
| 4430 | 52-55 | 2436.47 | 2436.5 | 0 |
| 4431 | 0-1 | 2436.5 | 2436.51 | 0 |
| 4431 | 1-6 | 2436.51 | 2436.56 | 0 |
| 4431 | 6-12 | 2436.56 | 2436.62 | 0 |
| 4431 | 12-20 | 2436.62 | 2436.7 | 0 |
| 4431 | 20-27 | 2436.7 | 2436.77 | 0 |
| 4431 | 27-32 | 2436.77 | 2436.82 | 0 |
| 4431 | 32-37 | 2436.82 | 2436.87 | 0 |
| 4431 | 37-41 | 2436.87 | 2436.91 | 0 |
| 4431 | 41-46 | 2436.91 | 2436.96 | 2 |
| 4431 | 46-51 | 2436.96 | 2437.01 | 0 |
| 4431 | 51-55 | 2437.01 | 2437.05 | 0 |
| 4432 | 0-7 | 2437.05 | 2437.12 | 0 |
| 4432 | 7-13 | 2437.12 | 2437.18 | 0 |
| 4432 | 13-17 | 2437.18 | 2437.22 | 0 |
| 4432 | 17-22 | 2437.22 | 2437.27 | 0 |
| 4432 | 22-27 | 2437.27 | 2437.32 | 0 |
| 4432 | 27-55 | 2437.32 | 2437.6 | 3 |
| 4437 | 0-16 | 2439.8 | 2439.96 | 2 |
| 4437 | 16-21 | 2439.96 | 2440.01 | 0 |
| 4437 | 21-25 | 2440.01 | 2440.05 | 0 |
| 4437 | 25-30 | 2440.05 | 2440.1 | 0 |
| 4437 | 30-39 | 2440.1 | 2440.19 | 0 |
| 4437 | 39-45 | 2440.19 | 2440.25 | 0 |
| 4437 | 45-50 | 2440.25 | 2440.3 | 0 |
| 4437 | 50-55 | 2440.3 | 2440.35 | 0 |
| 4438 | 0-10 | 2440.35 | 2440.45 | 0 |
| 4438 | 10-15 | 2440.45 | 2440.5 | 0 |
| 4438 | 15-23 | 2440.5 | 2440.58 | 0 |
| 4438 | 23-29 | 2440.58 | 2440.64 | 0 |
| 4438 | 29-34 | 2440.64 | 2440.69 | 0 |
| 4438 | 34-39 | 2440.69 | 2440.74 | 0 |
| 4438 | 39-42 | 2440.74 | 2440.77 | 0 |
| 4438 | 42-49 | 2440.77 | 2440.84 | 0 |
| 4438 | 49-55 | 2440.84 | 2440.9 | 0 |
| 4439 | 0-13 | 2440.9 | 2441.03 | 0 |
| 4439 | 13-18 | 2441.03 | 2441.08 | 0 |
| 4439 | 18-24 | 2441.08 | 2441.14 | 15 |
| 4439 | 24-29 | 2441.14 | 2441.19 | 5 |
| 4439 | 29-34 | 2441.19 | 2441.24 | 0 |
| 4439 | 34-38 | 2441.24 | 2441.28 | 24 |
| 4439 | 38-43 | 2441.28 | 2441.33 | 0 |
| 4439 | 43-55 | 2441.33 | 2441.45 | 0 |
| 4441 | 0-50 | 2442 | 2442.5 | 0 |
| 4441 | 50-55 | 2442.5 | 2442.55 | 0 |
| 4442 | 0-5 | 2442.55 | 2442.6 | 0 |
| 4442 | 5-10 | 2442.6 | 2442.65 | 0 |
| 4442 | 10-15 | 2442.65 | 2442.7 | 0 |
| 4442 | 15-40 | 2442.7 | 2442.95 | 0 |
| 4442 | 40-45 | 2442.95 | 2443 | 0 |
| 4442 | 45-50 | 2443 | 2443.05 | 0 |
| 4442 | 50-55 | 2443.05 | 2443.1 | 0 |
| 4443 | 0-5 | 2443.1 | 2443.15 | 0 |
| 4443 | 5-55 | 2443.15 | 2443.65 | 0 |
| 4446 | 0-3 | 2444.75 | 2444.78 | 0 |
| 4446 | 3-8 | 2444.78 | 2444.83 | 0 |
| 4446 | 8-12 | 2444.83 | 2444.87 | 0 |
| 4446 | 12-20 | 2444.87 | 2444.95 | 0 |
| 4446 | 20-28 | 2444.95 | 2445.03 | 0 |
| 4446 | 28-33 | 2445.03 | 2445.08 | 0 |
| 4446 | 33-55 | 2445.08 | 2445.3 | 0 |
| 4447 | 0-5 | 2445.3 | 2445.35 | 0 |
| 4447 | 5-10 | 2445.35 | 2445.4 | 0 |
| 4447 | 10-50 | 2445.4 | 2445.8 | 0 |
| 4447 | 50-55 | 2445.8 | 2445.85 | 0 |
| 4448 | 0-3 | 2445.85 | 2445.88 | 0 |
| 4448 | 3-7 | 2445.88 | 2445.92 | 0 |
| 4448 | 7-12 | 2445.92 | 2445.97 | 0 |
| 4448 | 12-23 | 2445.97 | 2446.08 | 0 |
| 4448 | 23-28 | 2446.08 | 2446.13 | 0 |
| 4448 | 28-33 | 2446.13 | 2446.18 | 0 |
| 4448 | 33-38 | 2446.18 | 2446.23 | 0 |
| 4448 | 38-55 | 2446.23 | 2446.4 | 0 |
| 4449 | 0-10 | 2446.4 | 2446.5 | 1 |
| 4449 | 10-20 | 2446.5 | 2446.6 | 0 |
| 4449 | 20-25 | 2446.6 | 2446.65 | 0 |
| 4449 | 25-55 | 2446.65 | 2446.95 | 0 |
| 4450 | 0-13 | 2446.95 | 2447.08 | 0 |
| 4450 | 13-18 | 2447.08 | 2447.13 | 0 |
| 4450 | 18-26 | 2447.13 | 2447.21 | 0 |
| 4450 | 26-31 | 2447.21 | 2447.26 | 1 |
| 4450 | 31-38 | 2447.26 | 2447.33 | 0 |
| 4450 | 38-43 | 2447.33 | 2447.38 | 0 |
| 4450 | 43-49 | 2447.38 | 2447.44 | 1 |
| 4450 | 49-55 | 2447.44 | 2447.5 | 0 |
| 4451 | 0-17 | 2447.5 | 2447.67 | 0 |
| 4451 | 17-22 | 2447.67 | 2447.72 | 0 |
| 4451 | 22-29 | 2447.72 | 2447.79 | 0 |

| Bag Number | Bag Depth Interval | Top depth (m) | Bottom depth (m) | No. of Tephra Shards |
|---|---|---|---|---|
| 4451 | 29-33 | 2447.79 | 2447.83 | 0 |
| 4451 | 33-38 | 2447.83 | 2447.88 | 0 |
| 4451 | 38-42 | 2447.88 | 2447.92 | 0 |
| 4451 | 42-50 | 2447.92 | 2448 | 0 |
| 4451 | 50-55 | 2448 | 2448.05 | 0 |
| 4458 | 0-5 | 2451.35 | 2451.4 | 0 |
| 4458 | 5-10 | 2451.4 | 2451.45 | 0 |
| 4458 | 10-30 | 2451.45 | 2451.65 | 0 |
| 4458 | 30-35 | 2451.65 | 2451.7 | 0 |
| 4458 | 35-42 | 2451.7 | 2451.77 | 0 |
| 4458 | 42-47 | 2451.77 | 2451.82 | 0 |
| 4458 | 47-55 | 2451.82 | 2451.9 | 0 |
| 4459 | 0-5 | 2451.9 | 2451.95 | 0 |
| 4459 | 5-35 | 2451.95 | 2452.25 | 0 |
| 4459 | 35-40 | 2452.25 | 2452.3 | 0 |
| 4459 | 40-45 | 2452.3 | 2452.35 | 0 |
| 4459 | 45-50 | 2452.35 | 2452.4 | 0 |
| 4459 | 50-55 | 2452.4 | 2452.45 | 0 |
| 4464 | 0-5 | 2454.65 | 2454.7 | 0 |
| 4464 | 5-10 | 2454.7 | 2454.75 | 0 |
| 4464 | 10-15 | 2454.75 | 2454.8 | 0 |
| 4464 | 15-20 | 2454.8 | 2454.85 | 45 |
| 4464 | 20-25 | 2454.85 | 2454.9 | 0 |
| 4464 | 25-30 | 2454.9 | 2454.95 | 0 |
| 4464 | 30-35 | 2454.95 | 2455 | 0 |
| 4464 | 35-55 | 2455 | 2455.2 | 0 |
| 4471 | 0-18 | 2458.5 | 2458.68 | 0 |
| 4471 | 18-23 | 2458.68 | 2458.73 | 0 |
| 4471 | 23-27 | 2458.73 | 2458.77 | 0 |
| 4471 | 27-30 | 2458.77 | 2458.8 | 0 |
| 4471 | 30-35 | 2458.8 | 2458.85 | 0 |
| 4471 | 35-55 | 2458.85 | 2459.05 | 0 |
| 4472 | 0-30 | 2459.05 | 2459.35 | 0 |
| 4472 | 30-35 | 2459.35 | 2459.4 | 0 |
| 4472 | 35-40 | 2459.4 | 2459.45 | 0 |
| 4472 | 40-45 | 2459.45 | 2459.5 | 0 |
| 4472 | 45-55 | 2459.5 | 2459.6 | 0 |
| 4473 | 0-20 | 2459.6 | 2459.8 | 0 |
| 4473 | 20-44 | 2459.8 | 2460.04 | 0 |
| 4473 | 44-49 | 2460.04 | 2460.09 | 0 |
| 4473 | 49-55 | 2460.09 | 2460.15 | 1 |
| 4474 | 0-20 | 2460.15 | 2460.35 | 0 |
| 4474 | 20-40 | 2460.35 | 2460.55 | 0 |
| 4474 | 40-55 | 2460.55 | 2460.7 | 0 |
| 4475 | 0-20 | 2460.7 | 2460.9 | 0 |
| 4475 | 20-40 | 2460.9 | 2461.1 | 1 |
| 4475 | 40-45 | 2461.1 | 2461.15 | 0 |
| 4475 | 45-50 | 2461.15 | 2461.2 | 0 |
| 4475 | 50-55 | 2461.2 | 2461.25 | 0 |
| 4476 | 0-5 | 2461.25 | 2461.3 | 0 |

| Bag Number | Bag Depth Interval | Top depth (m) | Bottom depth (m) | No. of Tephra Shards |
|---|---|---|---|---|
| 4476 | 5-11 | 2461.3 | 2461.36 | 0 |
| 4476 | 11-16 | 2461.36 | 2461.41 | 0 |
| 4476 | 16-40 | 2461.41 | 2461.65 | 0 |
| 4476 | 40-55 | 2461.65 | 2461.8 | 0 |
| 4477 | 0-20 | 2461.8 | 2462 | 0 |
| 4477 | 20-40 | 2462 | 2462.2 | 0 |
| 4477 | 40-55 | 2462.2 | 2462.35 | 0 |
| 4478 | 0-20 | 2462.35 | 2462.55 | 0 |
| 4478 | 20-40 | 2462.55 | 2462.75 | 0 |
| 4478 | 40-55 | 2462.75 | 2462.9 | 2 |
| 4479 | 0-15 | 2462.9 | 2463.05 | 0 |
| 4479 | 15-23 | 2463.05 | 2463.13 | 0 |
| 4479 | 23-30 | 2463.13 | 2463.2 | 0 |
| 4479 | 30-35 | 2463.2 | 2463.25 | 0 |
| 4479 | 35-40 | 2463.25 | 2463.3 | 0 |
| 4479 | 40-55 | 2463.3 | 2463.45 | 0 |
| 4481 | 0-20 | 2464 | 2464.2 | 0 |
| 4481 | 20-40 | 2464.2 | 2464.4 | 2 |
| 4481 | 40-55 | 2464.4 | 2464.55 | 3 |
| 4482 | 0-20 | 2464.55 | 2464.75 | 1 |
| 4482 | 20-40 | 2464.75 | 2464.95 | 0 |
| 4482 | 40-55 | 2464.95 | 2465.1 | 0 |
| 4483 | 0-20 | 2465.1 | 2465.3 | 0 |
| 4483 | 20-40 | 2465.3 | 2465.5 | 0 |
| 4483 | 40-55 | 2465.5 | 2465.65 | 0 |
| 4484 | 0-20 | 2465.65 | 2465.85 | 0 |
| 4484 | 20-40 | 2465.85 | 2466.05 | 0 |
| 4484 | 40-55 | 2466.05 | 2466.2 | 0 |
| 4485 | 0-20 | 2466.2 | 2466.4 | 0 |
| 4485 | 20-40 | 2466.4 | 2466.6 | 0 |
| 4485 | 40-55 | 2466.6 | 2466.75 | 0 |
| 4486 | 0-20 | 2466.75 | 2466.95 | 0 |
| 4486 | 20-25 | 2466.95 | 2467 | 0 |
| 4486 | 25-30 | 2467 | 2467.05 | 0 |
| 4486 | 30-35 | 2467.05 | 2467.1 | 0 |
| 4486 | 35-55 | 2467.1 | 2467.3 | 0 |
| 4487 | 0-20 | 2467.3 | 2467.5 | 0 |
| 4487 | 20-27 | 2467.5 | 2467.57 | 0 |
| 4487 | 27-33 | 2467.57 | 2467.63 | 0 |
| 4487 | 33-38 | 2467.63 | 2467.68 | 0 |
| 4487 | 38-55 | 2467.68 | 2467.85 | 0 |
| 4502 | 0-6 | 2475.55 | 2475.61 | 0 |
| 4502 | 6-10 | 2475.61 | 2475.65 | 0 |
| 4502 | 10-19 | 2475.65 | 2475.74 | 0 |
| 4502 | 19-26 | 2475.74 | 2475.81 | 0 |
| 4502 | 26-31 | 2475.81 | 2475.86 | 0 |
| 4502 | 31-55 | 2475.86 | 2476.1 | 0 |
| 4503 | 0-4 | 2476.1 | 2476.14 | 0 |
| 4503 | 4-9 | 2476.14 | 2476.19 | 0 |
| 4503 | 9-17 | 2476.19 | 2476.27 | 0 |

| Bag Number | Bag Depth Interval | Top depth (m) | Bottom depth (m) | No. of Tephra Shards |
|---|---|---|---|---|
| 4503 | 17-23 | 2476.27 | 2476.33 | 0 |
| 4503 | 23-28 | 2476.33 | 2476.38 | 0 |
| 4503 | 28-42 | 2476.38 | 2476.52 | 0 |
| 4503 | 42-47 | 2476.52 | 2476.57 | 0 |
| 4503 | 47-52 | 2476.57 | 2476.62 | 0 |
| 4503 | 52-55 | 2476.62 | 2476.65 | 0 |
| 4506 | 0-2 | 2477.75 | 2477.77 | 0 |
| 4506 | 2-8 | 2477.77 | 2477.83 | 1 |
| 4506 | 8-13 | 2477.83 | 2477.88 | 0 |
| 4506 | 13-16 | 2477.88 | 2477.91 | 1 |
| 4506 | 16-19 | 2477.91 | 2477.94 | 0 |
| 4506 | 19-22 | 2477.94 | 2477.97 | 0 |
| 4506 | 22-27 | 2477.97 | 2478.02 | 2 |
| 4506 | 27-55 | 2478.02 | 2478.3 | 0 |
| 4507 | 0-39 | 2478.3 | 2478.69 | 1 |
| 4507 | 39-44 | 2478.69 | 2478.74 | 1 |
| 4507 | 44-47 | 2478.74 | 2478.77 | 0 |
| 4507 | 47-50 | 2478.77 | 2478.8 | 0 |
| 4507 | 50-53 | 2478.8 | 2478.83 | 0 |
| 4507 | 53-55 | 2478.83 | 2478.85 | 1 |
| 4508 | 0-3 | 2478.85 | 2478.88 | 0 |
| 4508 | 3-8 | 2478.88 | 2478.93 | 0 |
| 4508 | 8-15 | 2478.93 | 2479 | 0 |
| 4508 | 15-20 | 2479 | 2479.05 | 0 |
| 4508 | 20-26 | 2479.05 | 2479.11 | 0 |
| 4508 | 26-30 | 2479.11 | 2479.15 | 1 |
| 4508 | 30-33 | 2479.15 | 2479.18 | 0 |
| 4508 | 33-40 | 2479.18 | 2479.25 | 1 |
| 4508 | 40-45 | 2479.25 | 2479.3 | 0 |
| 4508 | 45-50 | 2479.3 | 2479.35 | 0 |
| 4508 | 50-55 | 2479.35 | 2479.4 | 0 |
| 4513 | 0-8 | 2481.6 | 2481.68 | 0 |
| 4513 | 8-13 | 2481.68 | 2481.73 | 0 |
| 4513 | 13-20 | 2481.73 | 2481.8 | 0 |
| 4513 | 20-25 | 2481.8 | 2481.85 | 0 |
| 4513 | 25-55 | 2481.85 | 2482.15 | 0 |
| 4523 | 0-5 | 2487.1 | 2487.15 | 0 |
| 4523 | 5-9 | 2487.15 | 2487.19 | 0 |
| 4523 | 9-13 | 2487.19 | 2487.23 | 1 |
| 4523 | 13-16 | 2487.23 | 2487.26 | 0 |
| 4523 | 16-21 | 2487.26 | 2487.31 | 0 |
| 4523 | 21-25 | 2487.31 | 2487.35 | 0 |
| 4523 | 25-29 | 2487.35 | 2487.39 | 0 |
| 4523 | 29-33 | 2487.39 | 2487.43 | 0 |
| 4523 | 33-38 | 2487.43 | 2487.48 | 0 |
| 4523 | 38-43 | 2487.48 | 2487.53 | 0 |
| 4523 | 43-55 | 2487.53 | 2487.65 | 0 |
| 4531 | 0-9 | 2491.5 | 2491.59 | 2 |
| 4531 | 9-14 | 2491.59 | 2491.64 | 0 |
| 4531 | 14-19 | 2491.64 | 2491.69 | 0 |
| 4531 | 19-25 | 2491.69 | 2491.75 | 0 |
| 4531 | 25-32 | 2491.75 | 2491.82 | 0 |
| 4531 | 32-36 | 2491.82 | 2491.86 | 0 |
| 4531 | 36-41 | 2491.86 | 2491.91 | 1 |
| 4531 | 41-46 | 2491.91 | 2491.96 | 0 |
| 4531 | 46-50 | 2491.96 | 2492 | 0 |
| 4531 | 50-55 | 2492 | 2492.05 | 0 |
| 4532 | 0-2 | 2492.05 | 2492.07 | 0 |
| 4532 | 2-7 | 2492.07 | 2492.12 | 0 |
| 4532 | 7-14 | 2492.12 | 2492.19 | 0 |
| 4532 | 14-19 | 2492.19 | 2492.24 | 0 |
| 4532 | 19-55 | 2492.24 | 2492.6 | 0 |
| 4535 | 0-19 | 2493.7 | 2493.89 | 0 |
| 4535 | 19-24 | 2493.89 | 2493.94 | 0 |
| 4535 | 24-30 | 2493.94 | 2494 | 0 |
| 4535 | 30-35 | 2494 | 2494.05 | 0 |
| 4535 | 35-38 | 2494.05 | 2494.08 | 0 |
| 4535 | 38-43 | 2494.08 | 2494.13 | 1 |
| 4535 | 43-47 | 2494.13 | 2494.17 | 0 |
| 4535 | 47-52 | 2494.17 | 2494.22 | 0 |
| 4535 | 52-55 | 2494.22 | 2494.25 | 0 |
| 4546 | 0-45 | 2499.75 | 2500.2 | 0 |
| 4546 | 45-50 | 2500.2 | 2500.25 | 0 |
| 4546 | 50-55 | 2500.25 | 2500.3 | 0 |
| 4547 | 0-4 | 2500.3 | 2500.34 | 0 |
| 4547 | 4-9 | 2500.34 | 2500.39 | 0 |
| 4547 | 9-18 | 2500.39 | 2500.48 | 0 |
| 4547 | 18-23 | 2500.48 | 2500.53 | 0 |
| 4547 | 23-29 | 2500.53 | 2500.59 | 2 |
| 4547 | 29-34 | 2500.59 | 2500.64 | 0 |
| 4547 | 34-46 | 2500.64 | 2500.76 | 0 |
| 4547 | 46-53 | 2500.76 | 2500.83 | 0 |
| 4547 | 53-55 | 2500.83 | 2500.85 | 0 |
| 4548 | 0-5 | 2500.85 | 2500.9 | 24 |
| 4548 | 5-10 | 2500.9 | 2500.95 | 0 |
| 4548 | 10-15 | 2500.95 | 2501 | 0 |
| 4548 | 15-20 | 2501 | 2501.05 | 0 |
| 4548 | 20-55 | 2501.05 | 2501.4 | 0 |
| 4563 | 0-7 | 2509.1 | 2509.17 | 0 |
| 4563 | 7-13 | 2509.17 | 2509.23 | 0 |
| 4563 | 13-18 | 2509.23 | 2509.28 | 0 |
| 4563 | 18-32 | 2509.28 | 2509.42 | 0 |
| 4563 | 32-37 | 2509.42 | 2509.47 | 0 |
| 4563 | 37-41 | 2509.47 | 2509.51 | 0 |
| 4563 | 41-46 | 2509.51 | 2509.56 | 0 |
| 4563 | 46-55 | 2509.56 | 2509.65 | 0 |
| 4566 | 0-50 | 2510.75 | 2511.25 | 0 |
| 4566 | 50-55 | 2511.25 | 2511.3 | 0 |
| 4567 | 0-10 | 2511.3 | 2511.4 | 0 |
| 4567 | 10-15 | 2511.4 | 2511.45 | 0 |

| Bag Number | Bag Depth Interval | Top depth (m) | Bottom depth (m) | No. of Tephra Shards |
|---|---|---|---|---|
| 4567 | 15-20 | 2511.45 | 2511.5 | 0 |
| 4567 | 20-55 | 2511.5 | 2511.85 | 0 |
| 4572 | 0-20 | 2514.05 | 2514.25 | 0 |
| 4572 | 20-25 | 2514.25 | 2514.3 | 0 |
| 4572 | 25-32 | 2514.3 | 2514.37 | 0 |
| 4572 | 32-35 | 2514.37 | 2514.4 | 0 |
| 4572 | 35-40 | 2514.4 | 2514.45 | 0 |
| 4572 | 40-55 | 2514.45 | 2514.6 | 0 |
| 4574 | 0-6 | 2515.15 | 2515.21 | 0 |
| 4574 | 6-11 | 2515.21 | 2515.26 | 0 |
| 4574 | 11-19 | 2515.26 | 2515.34 | 0 |
| 4574 | 11-19 | 2515.34 | 2515.39 | 0 |
| 4574 | 24-46 | 2515.39 | 2515.61 | 0 |
| 4574 | 46-51 | 2515.61 | 2515.66 | 0 |
| 4574 | 51-55 | 2515.66 | 2515.7 | 2 |
| 4575 | 0-2 | 2515.7 | 2515.72 | 0 |
| 4575 | 2-7 | 2515.72 | 2515.77 | 0 |
| 4575 | 7-55 | 2515.77 | 2516.25 | 1 |
| 4581 | 0-3 | 2519 | 2519.03 | 0 |
| 4581 | 3-10 | 2519.03 | 2519.1 | 0 |
| 4581 | 10-16 | 2519.1 | 2519.16 | 0 |
| 4581 | 16-21 | 2519.16 | 2519.21 | 0 |
| 4581 | 21-31 | 2519.21 | 2519.31 | 0 |
| 4581 | 31-36 | 2519.31 | 2519.36 | 0 |
| 4581 | 36-43 | 2519.36 | 2519.43 | 0 |
| 4581 | 43-48 | 2519.43 | 2519.48 | 0 |
| 4581 | 48-55 | 2519.48 | 2519.55 | 0 |
| 4592 | 0-7 | 2525.05 | 2525.12 | 0 |
| 4592 | 7-15 | 2525.12 | 2525.2 | 0 |
| 4592 | 15-19 | 2525.2 | 2525.24 | 0 |
| 4592 | 19-24 | 2525.24 | 2525.29 | 0 |
| 4592 | 24-55 | 2525.29 | 2525.6 | 1 |
| 4597 | 0-5 | 2527.8 | 2527.85 | 0 |
| 4597 | 5-10 | 2527.85 | 2527.9 | 0 |
| 4597 | 10-18 | 2527.9 | 2527.98 | 0 |
| 4597 | 18-25 | 2527.98 | 2528.05 | 0 |
| 4597 | 25-30 | 2528.05 | 2528.1 | 0 |
| 4597 | 30-35 | 2528.1 | 2528.15 | 0 |
| 4597 | 35-55 | 2528.15 | 2528.35 | 0 |
| 4602 | 0-15 | 2530.55 | 2530.7 | 0 |
| 4602 | 15-20 | 2530.7 | 2530.75 | 0 |
| 4602 | 20-25 | 2530.75 | 2530.8 | 0 |
| 4602 | 25-30 | 2530.8 | 2530.85 | 0 |
| 4602 | 30-35 | 2530.85 | 2530.9 | 0 |
| 4602 | 35-40 | 2530.9 | 2530.95 | 0 |
| 4602 | 40-45 | 2530.95 | 2531 | 0 |
| 4602 | 45-50 | 2531 | 2531.05 | 0 |
| 4602 | 50-55 | 2531.05 | 2531.1 | 0 |
| 4603 | 0-5 | 2531.1 | 2531.15 | 0 |
| 4603 | 5-10 | 2531.15 | 2531.2 | 0 |

| Bag Number | Bag Depth Interval | Top depth (m) | Bottom depth (m) | No. of Tephra Shards |
|---|---|---|---|---|
| 4603 | 10-15 | 2531.2 | 2531.25 | 0 |
| 4603 | 15-20 | 2531.25 | 2531.3 | 0 |
| 4603 | 20-25 | 2531.3 | 2531.35 | 0 |
| 4603 | 25-30 | 2531.35 | 2531.4 | 0 |
| 4603 | 30-35 | 2531.4 | 2531.45 | 0 |
| 4603 | 35-55 | 2531.45 | 2531.65 | 0 |
| 4604 | 0-3 | 2531.65 | 2531.68 | 0 |
| 4604 | 3-8 | 2531.68 | 2531.73 | 0 |
| 4604 | 8-15 | 2531.73 | 2531.8 | 0 |
| 4604 | 15-20 | 2531.8 | 2531.85 | 0 |
| 4604 | 20-55 | 2531.85 | 2532.2 | 2 |
| 4605 | 0-20 | 2532.2 | 2532.4 | 0 |
| 4605 | 20-40 | 2532.4 | 2532.6 | 0 |
| 4605 | 40-55 | 2532.6 | 2532.75 | 1 |
| 4606 | 0-28 | 2532.75 | 2533.03 | 0 |
| 4606 | 28-33 | 2533.03 | 2533.08 | 0 |
| 4606 | 33-40 | 2533.08 | 2533.15 | 0 |
| 4606 | 40-45 | 2533.15 | 2533.2 | 0 |
| 4606 | 45-55 | 2533.2 | 2533.3 | 0 |
| 4607 | 0-20 | 2533.3 | 2533.5 | 0 |
| 4607 | 20-40 | 2533.5 | 2533.7 | 0 |
| 4607 | 40-55 | 2533.7 | 2533.85 | 1 |
| 4608 | 0-20 | 2533.85 | 2534.05 | 0 |
| 4608 | 20-40 | 2534.05 | 2534.25 | 0 |
| 4608 | 40-55 | 2534.25 | 2534.4 | 0 |
| 4609 | 0-20 | 2534.4 | 2534.6 | 1 |
| 4609 | 20-40 | 2534.6 | 2534.8 | 0 |
| 4609 | 40-55 | 2534.8 | 2534.95 | 1 |
| 4610 | 0-6 | 2534.95 | 2535.01 | 0 |
| 4610 | 6-13 | 2535.01 | 2535.08 | 0 |
| 4610 | 13-18 | 2535.08 | 2535.13 | 0 |
| 4610 | 18-40 | 2535.13 | 2535.35 | 0 |
| 4610 | 40-55 | 2535.35 | 2535.5 | 0 |
| 4611 | 0-20 | 2535.5 | 2535.7 | 2 |
| 4611 | 20-40 | 2535.7 | 2535.9 | 0 |
| 4611 | 40-55 | 2535.9 | 2536.05 | 0 |
| 4612 | 0-20 | 2536.05 | 2536.25 | 0 |
| 4612 | 20-40 | 2536.25 | 2536.45 | 0 |
| 4612 | 40-55 | 2536.45 | 2536.6 | 0 |
| 4613 | 0-7 | 2536.6 | 2536.67 | 0 |
| 4613 | 7-12 | 2536.67 | 2536.72 | 0 |
| 4613 | 12-17 | 2536.72 | 2536.77 | 1 |
| 4613 | 17-40 | 2536.77 | 2537 | 0 |
| 4613 | 40-55 | 2537 | 2537.15 | 0 |
| 4614 | 0-20 | 2537.15 | 2537.35 | 0 |
| 4614 | 20-40 | 2537.35 | 2537.55 | 0 |
| 4614 | 40-55 | 2537.55 | 2537.7 | 0 |
| 4615 | 0-20 | 2537.7 | 2537.9 | 0 |
| 4615 | 20-40 | 2537.9 | 2538.1 | 0 |
| 4615 | 40-55 | 2538.1 | 2538.25 | 0 |

| Bag Number | Bag Depth Interval | Top depth (m) | Bottom depth (m) | No. of Tephra Shards |
|---|---|---|---|---|
| 4616 | 0-26 | 2538.25 | 2538.51 | 0 |
| 4616 | 26-31 | 2538.51 | 2538.56 | 0 |
| 4616 | 31-37 | 2538.56 | 2538.62 | 0 |
| 4616 | 37-41 | 2538.62 | 2538.66 | 0 |
| 4616 | 41-51 | 2538.66 | 2538.76 | 0 |
| 4616 | 51-55 | 2538.76 | 2538.8 | 0 |
| 4623 | 0-20 | 2542.1 | 2542.3 | 0 |
| 4623 | 20-40 | 2542.3 | 2542.5 | 0 |
| 4623 | 40-55 | 2542.5 | 2542.65 | 0 |
| 4624 | 0-14 | 2542.65 | 2542.79 | 0 |
| 4624 | 14-19 | 2542.79 | 2542.84 | 0 |
| 4624 | 19-23 | 2542.84 | 2542.88 | 0 |
| 4624 | 23-28 | 2542.88 | 2542.93 | 0 |
| 4624 | 28-55 | 2542.93 | 2543.2 | 0 |
| 4625 | 0-23 | 2543.2 | 2543.43 | 0 |
| 4625 | 23-28 | 2543.43 | 2543.48 | 0 |
| 4625 | 28-32 | 2543.48 | 2543.52 | 0 |
| 4625 | 32-37 | 2543.52 | 2543.57 | 0 |
| 4625 | 37-40 | 2543.57 | 2543.6 | 0 |
| 4625 | 40-55 | 2543.6 | 2543.75 | 0 |
| 4626 | 0-20 | 2543.75 | 2543.95 | 0 |
| 4626 | 20-40 | 2543.95 | 2544.15 | 0 |
| 4626 | 40-55 | 2544.15 | 2544.3 | 0 |
| 4627 | 0-20 | 2544.3 | 2544.5 | 1 |
| 4627 | 20-40 | 2544.5 | 2544.7 | 0 |
| 4627 | 40-55 | 2544.7 | 2544.85 | 0 |
| 4628 | 0-27 | 2544.85 | 2545.12 | 0 |
| 4628 | 27-32 | 2545.12 | 2545.17 | 0 |
| 4628 | 32-37 | 2545.17 | 2545.22 | 0 |
| 4628 | 37-42 | 2545.22 | 2545.27 | 0 |
| 4628 | 42-55 | 2545.27 | 2545.4 | 0 |
| 4629 | 0-2 | 2545.4 | 2545.42 | 0 |
| 4629 | 2-10 | 2545.42 | 2545.5 | 0 |
| 4629 | 10-15 | 2545.5 | 2545.55 | 0 |
| 4629 | 15-34 | 2545.55 | 2545.74 | 0 |
| 4629 | 34-39 | 2545.74 | 2545.79 | 0 |
| 4629 | 39-45 | 2545.79 | 2545.85 | 0 |
| 4629 | 45-50 | 2545.85 | 2545.9 | 0 |
| 4629 | 50-55 | 2545.9 | 2545.95 | 0 |
| 4630 | 0-20 | 2545.95 | 2546.15 | 0 |
| 4630 | 20-40 | 2546.15 | 2546.35 | 0 |
| 4630 | 40-55 | 2546.35 | 2546.5 | 2 |
| 4631 | 0-20 | 2546.5 | 2546.7 | 0 |
| 4631 | 20-40 | 2546.7 | 2546.9 | 0 |
| 4631 | 40-55 | 2546.9 | 2547.05 | 0 |
| 4632 | 0-5 | 2547.05 | 2547.1 | 0 |
| 4632 | 5-9 | 2547.1 | 2547.14 | 0 |
| 4632 | 9-14 | 2547.14 | 2547.19 | 0 |
| 4632 | 14-20 | 2547.19 | 2547.25 | 0 |
| 4632 | 20-25 | 2547.25 | 2547.3 | 0 |
| 4632 | 25-55 | 2547.3 | 2547.6 | 0 |
| 4633 | 0-30 | 2547.6 | 2547.9 | 0 |
| 4633 | 30-35 | 2547.9 | 2547.95 | 0 |
| 4633 | 35-40 | 2547.95 | 2548 | 0 |
| 4633 | 40-45 | 2548 | 2548.05 | 0 |
| 4633 | 45-50 | 2548.05 | 2548.1 | 0 |
| 4633 | 50-55 | 2548.1 | 2548.15 | 0 |
| 4634 | 0-20 | 2548.15 | 2548.35 | 33 |
| 4634 | 20-40 | 2548.35 | 2548.55 | 0 |
| 4634 | 40-55 | 2548.55 | 2548.7 | 0 |
| 4635 | 0-9 | 2548.7 | 2548.79 | 0 |
| 4635 | 9-14 | 2548.79 | 2548.84 | 0 |
| 4635 | 14-20 | 2548.84 | 2548.9 | 0 |
| 4635 | 20-25 | 2548.9 | 2548.95 | 0 |
| 4635 | 25-55 | 2548.95 | 2549.25 | 0 |
| 4636 | 0-20 | 2549.25 | 2549.45 | 0 |
| 4636 | 20-40 | 2549.45 | 2549.65 | 0 |
| 4636 | 40-55 | 2549.65 | 2549.8 | 0 |
| 4637 | 0-17 | 2549.8 | 2549.97 | 0 |
| 4637 | 17-22 | 2549.97 | 2550.02 | 0 |
| 4637 | 22-26 | 2550.02 | 2550.06 | 0 |
| 4637 | 26-30 | 2550.06 | 2550.1 | 0 |
| 4637 | 30-33 | 2550.1 | 2550.13 | 0 |
| 4637 | 33-38 | 2550.13 | 2550.18 | 0 |
| 4637 | 38-55 | 2550.18 | 2550.35 | 0 |
| 4638 | 0-19 | 2550.35 | 2550.54 | 0 |
| 4638 | 19-25 | 2550.54 | 2550.6 | 0 |
| 4638 | 25-31 | 2550.6 | 2550.66 | 0 |
| 4638 | 31-36 | 2550.66 | 2550.71 | 0 |
| 4638 | 36-45 | 2550.71 | 2550.8 | 0 |
| 4638 | 45-50 | 2550.8 | 2550.85 | 0 |
| 4638 | 50-55 | 2550.85 | 2550.9 | 0 |
| 4639 | 0-3 | 2550.9 | 2550.93 | 0 |
| 4639 | 3-8 | 2550.93 | 2550.98 | 0 |
| 4639 | 8-13 | 2550.98 | 2551.03 | 0 |
| 4639 | 13-18 | 2551.03 | 2551.08 | 0 |
| 4639 | 18-44 | 2551.08 | 2551.34 | 0 |
| 4639 | 44-49 | 2551.34 | 2551.39 | 1 |
| 4639 | 49-55 | 2551.39 | 2551.45 | 0 |
| 4640 | 0-5 | 2551.45 | 2551.5 | 0 |
| 4640 | 5-10 | 2551.5 | 2551.55 | 0 |
| 4640 | 10-55 | 2551.55 | 2552 | 0 |
| 4641 | 0-20 | 2552 | 2552.2 | 0 |
| 4641 | 20-40 | 2552.2 | 2552.4 | 0 |
| 4641 | 40-55 | 2552.4 | 2552.55 | 0 |
| 4642 | 0-30 | 2552.55 | 2552.85 | 0 |
| 4642 | 30-35 | 2552.85 | 2552.9 | 0 |
| 4642 | 35-40 | 2552.9 | 2552.95 | 0 |
| 4642 | 40-45 | 2552.95 | 2553 | 0 |
| 4642 | 45-50 | 2553 | 2553.05 | 0 |

| Bag Number | Bag Depth Interval | Top depth (m) | Bottom depth (m) | No. of Tephra Shards |
|---|---|---|---|---|
| 4642 | 50-55 | 2553.05 | 2553.1 | 0 |
| 4643 | 0-3 | 2553.1 | 2553.13 | 0 |
| 4643 | 3-6 | 2553.13 | 2553.16 | 0 |
| 4643 | 6-9 | 2553.16 | 2553.19 | 0 |
| 4643 | 9-12 | 2553.19 | 2553.22 | 1 |
| 4643 | 12-17 | 2553.22 | 2553.27 | 0 |
| 4643 | 17-22 | 2553.27 | 2553.32 | 0 |
| 4643 | 22-55 | 2553.32 | 2553.65 | 0 |
| 4644 | 0-25 | 2553.65 | 2553.9 | 0 |
| 4644 | 25-30 | 2553.9 | 2553.95 | 0 |
| 4644 | 30-33 | 2553.95 | 2553.98 | 0 |
| 4644 | 33-36 | 2553.98 | 2554.01 | 2 |
| 4644 | 36-41 | 2554.01 | 2554.06 | 0 |
| 4644 | 41-46 | 2554.06 | 2554.11 | 0 |
| 4644 | 46-51 | 2554.11 | 2554.16 | 0 |
| 4644 | 51-55 | 2554.16 | 2554.2 | 0 |
| 4645 | 0-20 | 2554.2 | 2554.4 | 1 |
| 4645 | 20-40 | 2554.4 | 2554.6 | 0 |
| 4645 | 40-55 | 2554.6 | 2554.75 | 0 |
| 4646 | 0-24 | 2554.75 | 2554.99 | 0 |
| 4646 | 24-29 | 2554.99 | 2555.04 | 0 |
| 4646 | 29-32 | 2555.04 | 2555.07 | 0 |
| 4646 | 32-36 | 2555.07 | 2555.11 | 0 |
| 4646 | 36-41 | 2555.11 | 2555.16 | 0 |
| 4646 | 41-46 | 2555.16 | 2555.21 | 0 |
| 4646 | 46-55 | 2555.21 | 2555.3 | 0 |
| 4647 | 0-4 | 2555.3 | 2555.34 | 0 |
| 4647 | 4-9 | 2555.34 | 2555.39 | 0 |
| 4647 | 9-17 | 2555.39 | 2555.47 | 0 |
| 4647 | 17-22 | 2555.47 | 2555.52 | 0 |
| 4647 | 22-55 | 2555.52 | 2555.85 | 0 |
| 4648 | 0-2 | 2555.85 | 2555.87 | 0 |
| 4648 | 2-7 | 2555.87 | 2555.92 | 0 |
| 4648 | 7-13 | 2555.92 | 2555.98 | 4 |
| 4648 | 13-18 | 2555.98 | 2556.03 | 0 |
| 4648 | 18-55 | 2556.03 | 2556.4 | 0 |
| 4649 | 0-4 | 2556.4 | 2556.44 | 0 |
| 4649 | 4-9 | 2556.44 | 2556.49 | 0 |
| 4649 | 9-14 | 2556.49 | 2556.54 | 0 |
| 4649 | 14-19 | 2556.54 | 2556.59 | 0 |
| 4649 | 19-26 | 2556.59 | 2556.66 | 0 |
| 4649 | 26-31 | 2556.66 | 2556.71 | 0 |
| 4649 | 31-36 | 2556.71 | 2556.76 | 0 |
| 4649 | 36-42 | 2556.76 | 2556.82 | 0 |
| 4649 | 42-47 | 2556.82 | 2556.87 | 0 |
| 4649 | 47-55 | 2556.87 | 2556.95 | 0 |
| 4650 | 0-20 | 2556.95 | 2557.15 | 0 |
| 4650 | 20-40 | 2557.15 | 2557.35 | 0 |
| 4650 | 40-55 | 2557.35 | 2557.5 | 0 |
| 4651 | 0-20 | 2557.5 | 2557.7 | 0 |
| 4651 | 20-40 | 2557.7 | 2557.9 | 0 |
| 4651 | 40-55 | 2557.9 | 2558.05 | 0 |
| 4652 | 0-5 | 2558.05 | 2558.1 | 0 |
| 4652 | 5-10 | 2558.1 | 2558.15 | 0 |
| 4652 | 10-15 | 2558.15 | 2558.2 | 0 |
| 4652 | 15-20 | 2558.2 | 2558.25 | 0 |
| 4652 | 20-25 | 2558.25 | 2558.3 | 0 |
| 4652 | 25-30 | 2558.3 | 2558.35 | 0 |
| 4652 | 30-35 | 2558.35 | 2558.4 | 0 |
| 4652 | 35-40 | 2558.4 | 2558.45 | 0 |
| 4652 | 40-45 | 2558.45 | 2558.5 | 0 |
| 4652 | 45-50 | 2558.5 | 2558.55 | 0 |
| 4652 | 50-55 | 2558.55 | 2558.6 | 0 |
| 4653 | 0-5 | 2558.6 | 2558.65 | 0 |
| 4653 | 5-10 | 2558.65 | 2558.7 | 0 |
| 4653 | 10-14 | 2558.7 | 2558.74 | 0 |
| 4653 | 14-20 | 2558.74 | 2558.8 | 0 |
| 4653 | 20-28 | 2558.8 | 2558.88 | 0 |
| 4653 | 28-33 | 2558.88 | 2558.93 | 0 |
| 4653 | 33-55 | 2558.93 | 2559.15 | 0 |
| 4654 | 0-4 | 2559.15 | 2559.19 | 0 |
| 4654 | 4-9 | 2559.19 | 2559.24 | 0 |
| 4654 | 9-15 | 2559.24 | 2559.3 | 0 |
| 4654 | 15-20 | 2559.3 | 2559.35 | 0 |
| 4654 | 20-35 | 2559.35 | 2559.5 | 0 |
| 4654 | 35-40 | 2559.5 | 2559.55 | 0 |
| 4654 | 40-46 | 2559.55 | 2559.61 | 0 |
| 4654 | 46-51 | 2559.61 | 2559.66 | 0 |
| 4654 | 51-55 | 2559.66 | 2559.7 | 0 |
| 4655 | 0-15 | 2559.7 | 2559.85 | 0 |
| 4655 | 15-35 | 2559.85 | 2560.05 | 0 |
| 4655 | 35-55 | 2560.05 | 2560.25 | 0 |
| 4663 | 0-5 | 2564.1 | 2564.15 | 0 |
| 4663 | 5-10 | 2564.15 | 2564.2 | 0 |
| 4663 | 10-15 | 2564.2 | 2564.25 | 0 |
| 4663 | 15-20 | 2564.25 | 2564.3 | 0 |
| 4663 | 20-27 | 2564.3 | 2564.37 | 0 |
| 4663 | 27-32 | 2564.37 | 2564.42 | 0 |
| 4663 | 32-42 | 2564.42 | 2564.52 | 0 |
| 4663 | 42-47 | 2564.52 | 2564.57 | 0 |
| 4663 | 47-50 | 2564.57 | 2564.6 | 0 |
| 4663 | 50-55 | 2564.6 | 2564.65 | 0 |
| 4664 | 0-5 | 2564.65 | 2564.7 | 0 |
| 4664 | 5-10 | 2564.7 | 2564.75 | 2 |
| 4664 | 10-18 | 2564.75 | 2564.83 | 0 |
| 4664 | 18-23 | 2564.83 | 2564.88 | 0 |
| 4664 | 23-29 | 2564.88 | 2564.94 | 0 |
| 4664 | 29-34 | 2564.94 | 2564.99 | 0 |
| 4664 | 34-39 | 2564.99 | 2565.04 | 0 |
| 4664 | 39-55 | 2565.04 | 2565.2 | 0 |

| Bag Number | Bag Depth Interval | Top depth (m) | Bottom depth (m) | No. of Tephra Shards |
|---|---|---|---|---|
| 4665 | 0-10 | 2565.2 | 2565.3 | 0 |
| 4665 | 10-15 | 2565.3 | 2565.35 | 0 |
| 4665 | 15-20 | 2565.35 | 2565.4 | 0 |
| 4665 | 20-25 | 2565.4 | 2565.45 | 0 |
| 4665 | 25-30 | 2565.45 | 2565.5 | 0 |
| 4665 | 30-35 | 2565.5 | 2565.55 | 0 |
| 4665 | 35-40 | 2565.55 | 2565.6 | 0 |
| 4665 | 40-45 | 2565.6 | 2565.65 | 0 |
| 4665 | 45-55 | 2565.65 | 2565.75 | 0 |
| 4667 | 0-6 | 2566.3 | 2566.36 | 0 |
| 4667 | 6-11 | 2566.36 | 2566.41 | 0 |
| 4667 | 11-18 | 2566.41 | 2566.48 | 0 |
| 4667 | 18-25 | 2566.48 | 2566.55 | 0 |
| 4667 | 25-30 | 2566.55 | 2566.6 | 0 |
| 4667 | 30-35 | 2566.6 | 2566.65 | 0 |
| 4667 | 35-55 | 2566.65 | 2566.85 | 0 |
| 4668 | 0-5 | 2566.85 | 2566.9 | 0 |
| 4668 | 5-10 | 2566.9 | 2566.95 | 0 |
| 4668 | 10-15 | 2566.95 | 2567 | 0 |
| 4668 | 15-20 | 2567 | 2567.05 | 0 |
| 4668 | 20-25 | 2567.05 | 2567.1 | 0 |
| 4668 | 25-30 | 2567.1 | 2567.15 | 0 |
| 4668 | 30-35 | 2567.15 | 2567.2 | 0 |
| 4668 | 35-40 | 2567.2 | 2567.25 | 0 |
| 4668 | 40-45 | 2567.25 | 2567.3 | 0 |
| 4668 | 45-50 | 2567.3 | 2567.35 | 0 |
| 4668 | 50-55 | 2567.35 | 2567.4 | 0 |
| 4676 | 0-20 | 2571.25 | 2571.45 | 0 |
| 4676 | 20-25 | 2571.45 | 2571.5 | 0 |
| 4676 | 25-30 | 2571.5 | 2571.55 | 0 |
| 4676 | 30-36 | 2571.55 | 2571.61 | 0 |
| 4676 | 36-40 | 2571.61 | 2571.65 | 0 |
| 4676 | 40-45 | 2571.65 | 2571.7 | 0 |
| 4676 | 45-50 | 2571.7 | 2571.75 | 0 |
| 4676 | 50-55 | 2571.75 | 2571.8 | 0 |
| 4677 | 0-5 | 2571.8 | 2571.85 | 0 |
| 4677 | 5-10 | 2571.85 | 2571.9 | 0 |
| 4677 | 10-15 | 2571.9 | 2571.95 | 0 |
| 4677 | 15-20 | 2571.95 | 2572 | 0 |
| 4677 | 20-25 | 2572 | 2572.05 | 0 |
| 4677 | 25-30 | 2572.05 | 2572.1 | 0 |
| 4677 | 30-35 | 2572.1 | 2572.15 | 0 |
| 4677 | 35-40 | 2572.15 | 2572.2 | 0 |
| 4677 | 40-45 | 2572.2 | 2572.25 | 0 |
| 4677 | 45-50 | 2572.25 | 2572.3 | 0 |
| 4677 | 50-55 | 2572.3 | 2572.35 | 0 |
| 4678 | 0-18 | 2572.35 | 2572.53 | 0 |
| 4678 | 18-23 | 2572.53 | 2572.58 | 0 |
| 4678 | 23-27 | 2572.58 | 2572.62 | 0 |
| 4678 | 27-31 | 2572.62 | 2572.66 | 1 |

| Bag Number | Bag Depth Interval | Top depth (m) | Bottom depth (m) | No. of Tephra Shards |
|---|---|---|---|---|
| 4678 | 31-35 | 2572.66 | 2572.7 | 0 |
| 4678 | 35-40 | 2572.7 | 2572.75 | 0 |
| 4678 | 40-55 | 2572.75 | 2572.9 | 0 |
| 4679 | 0-20 | 2572.9 | 2573.1 | 0 |
| 4679 | 20-40 | 2573.1 | 2573.3 | 1 |
| 4679 | 40-55 | 2573.3 | 2573.45 | 0 |
| 4681 | 0-20 | 2574 | 2574.2 | 0 |
| 4681 | 20-40 | 2574.2 | 2574.4 | 0 |
| 4681 | 40-49 | 2574.4 | 2574.49 | 0 |
| 4681 | 49-55 | 2574.49 | 2574.55 | 20 |
| 4682 | 0-20 | 2574.55 | 2574.75 | 0 |
| 4682 | 20-40 | 2574.75 | 2574.95 | 1 |
| 4682 | 40-50 | 2574.95 | 2575.05 | 0 |
| 4682 | 50-55 | 2575.05 | 2575.1 | 0 |
| 4683 | 0-25 | 2575.1 | 2575.35 | 2 |
| 4683 | 25-30 | 2575.35 | 2575.4 | 0 |
| 4683 | 30-35 | 2575.4 | 2575.45 | 0 |
| 4683 | 35-40 | 2575.45 | 2575.5 | 0 |
| 4683 | 40-55 | 2575.5 | 2575.65 | 0 |
| 4684 | 0-20 | 2575.65 | 2575.85 | 0 |
| 4684 | 20-40 | 2575.85 | 2576.05 | 0 |
| 4684 | 40-55 | 2576.05 | 2576.2 | 0 |
| 4685 | 0-23 | 2576.2 | 2576.43 | 0 |
| 4685 | 23-28 | 2576.43 | 2576.48 | 0 |
| 4685 | 28-35 | 2576.48 | 2576.55 | 0 |
| 4685 | 35-40 | 2576.55 | 2576.6 | 0 |
| 4685 | 40-55 | 2576.6 | 2576.75 | 0 |
| 4686 | 0-20 | 2576.75 | 2576.95 | 0 |
| 4686 | 20-40 | 2576.95 | 2577.15 | 0 |
| 4686 | 40-55 | 2577.15 | 2577.3 | 0 |
| 4687 | 0-20 | 2577.3 | 2577.5 | 1 |
| 4687 | 20-40 | 2577.5 | 2577.7 | 0 |
| 4687 | 40-45 | 2577.7 | 2577.75 | 0 |
| 4687 | 45-55 | 2577.75 | 2577.85 | 0 |
| 4688 | 0-20 | 2577.85 | 2578.05 | 0 |
| 4688 | 20-40 | 2578.05 | 2578.25 | 0 |
| 4688 | 40-55 | 2578.25 | 2578.4 | 0 |
| 4689 | 0-20 | 2578.4 | 2578.6 | 0 |
| 4689 | 20-40 | 2578.6 | 2578.8 | 0 |
| 4689 | 40-55 | 2578.8 | 2578.95 | 0 |
| 4690 | 0-20 | 2578.95 | 2579.15 | 0 |
| 4690 | 20-40 | 2579.15 | 2579.35 | 0 |
| 4690 | 40-55 | 2579.35 | 2579.5 | 0 |
| 4691 | 0-20 | 2579.5 | 2579.7 | 0 |
| 4691 | 20-40 | 2579.7 | 2579.9 | 0 |
| 4691 | 40-55 | 2579.9 | 2580.05 | 0 |
| 4692 | 0-25 | 2580.05 | 2580.3 | 0 |
| 4692 | 25-30 | 2580.3 | 2580.35 | 0 |
| 4692 | 30-35 | 2580.35 | 2580.4 | 0 |
| 4692 | 35-40 | 2580.4 | 2580.45 | 0 |

| Bag Number | Bag Depth Interval | Top depth (m) | Bottom depth (m) | No. of Tephra Shards |
|---|---|---|---|---|
| 4692 | 40-55 | 2580.45 | 2580.6 | 0 |
| 4693 | 0-20 | 2580.6 | 2580.8 | 0 |
| 4693 | 20-40 | 2580.8 | 2581 | 2 |
| 4693 | 40-45 | 2581 | 2581.05 | 0 |
| 4693 | 45-55 | 2581.05 | 2581.15 | 0 |
| 4694 | 0-20 | 2581.15 | 2581.35 | 0 |
| 4694 | 20-40 | 2581.35 | 2581.55 | 0 |
| 4694 | 40-55 | 2581.55 | 2581.7 | 0 |
| 4695 | 0-20 | 2581.7 | 2581.9 | 1 |
| 4695 | 20-40 | 2581.9 | 2582.1 | 0 |
| 4695 | 40-55 | 2582.1 | 2582.25 | 0 |
| 4696 | 0-20 | 2582.25 | 2582.45 | 0 |
| 4696 | 20-40 | 2582.45 | 2582.65 | 0 |
| 4696 | 40-55 | 2582.65 | 2582.8 | 0 |
| 4697 | 0-20 | 2582.8 | 2583 | 0 |
| 4697 | 20-40 | 2583 | 2583.2 | 0 |
| 4697 | 40-55 | 2583.2 | 2583.35 | 0 |
| 4698 | 0-20 | 2583.35 | 2583.55 | 0 |
| 4698 | 20-40 | 2583.55 | 2583.75 | 0 |
| 4698 | 40-55 | 2583.75 | 2583.9 | 0 |
| 4699 | 0-15 | 2583.9 | 2584.05 | 0 |
| 4699 | 15-20 | 2584.05 | 2584.1 | 0 |
| 4699 | 20-25 | 2584.1 | 2584.15 | 0 |
| 4699 | 25-30 | 2584.15 | 2584.2 | 0 |
| 4699 | 30-55 | 2584.2 | 2584.45 | 0 |
| 4700 | 0-20 | 2584.45 | 2584.65 | 0 |
| 4700 | 20-40 | 2584.65 | 2584.85 | 0 |
| 4700 | 40-55 | 2584.85 | 2585 | 0 |
| 4708 | 0-5 | 2588.85 | 2588.9 | 0 |
| 4708 | 5-8 | 2588.9 | 2588.93 | 0 |
| 4708 | 8-13 | 2588.93 | 2588.98 | 0 |
| 4708 | 13-19 | 2588.98 | 2589.04 | 0 |
| 4708 | 19-23 | 2589.04 | 2589.08 | 0 |
| 4708 | 23-27 | 2589.08 | 2589.12 | 0 |
| 4708 | 27-32 | 2589.12 | 2589.17 | 0 |
| 4708 | 32-42 | 2589.17 | 2589.27 | 0 |
| 4708 | 42-47 | 2589.27 | 2589.32 | 0 |
| 4708 | 47-55 | 2589.32 | 2589.4 | 0 |
| 4709 | 0-8 | 2589.4 | 2589.48 | 0 |
| 4709 | 8-14 | 2589.48 | 2589.54 | 0 |
| 4709 | 14-19 | 2589.54 | 2589.59 | 0 |
| 4709 | 19-22 | 2589.59 | 2589.62 | 0 |
| 4709 | 22-28 | 2589.62 | 2589.68 | 0 |
| 4709 | 28-33 | 2589.68 | 2589.73 | 0 |
| 4709 | 33-55 | 2589.73 | 2589.95 | 0 |
| 4710 | 0-7 | 2589.95 | 2590.02 | 0 |
| 4710 | 7-13 | 2590.02 | 2590.08 | 0 |
| 4710 | 13-17 | 2590.08 | 2590.12 | 0 |
| 4710 | 17-22 | 2590.12 | 2590.17 | 0 |
| 4710 | 22-55 | 2590.17 | 2590.5 | 0 |

| Bag Number | Bag Depth Interval | Top depth (m) | Bottom depth (m) | No. of Tephra Shards |
|---|---|---|---|---|
| 4711 | 0-35 | 2590.5 | 2590.85 | 0 |
| 4711 | 35-40 | 2590.85 | 2590.9 | 0 |
| 4711 | 40-45 | 2590.9 | 2590.95 | 0 |
| 4711 | 45-47 | 2590.95 | 2590.97 | 0 |
| 4711 | 47-55 | 2590.97 | 2591.05 | 0 |
| 4714 | 0-10 | 2592.15 | 2592.25 | 0 |
| 4714 | 10-15 | 2592.25 | 2592.3 | 0 |
| 4714 | 15-20 | 2592.3 | 2592.35 | 0 |
| 4714 | 20-25 | 2592.35 | 2592.4 | 0 |
| 4714 | 25-31 | 2592.4 | 2592.46 | 0 |
| 4714 | 31-39 | 2592.46 | 2592.54 | 0 |
| 4714 | 39-44 | 2592.54 | 2592.59 | 0 |
| 4714 | 44-55 | 2592.59 | 2592.7 | 0 |
| 4716 | 0-5 | 2593.25 | 2593.3 | 0 |
| 4716 | 5-13 | 2593.3 | 2593.38 | 0 |
| 4716 | 13-18 | 2593.38 | 2593.43 | 0 |
| 4716 | 18-30 | 2593.43 | 2593.55 | 0 |
| 4716 | 30-35 | 2593.55 | 2593.6 | 0 |
| 4716 | 35-40 | 2593.6 | 2593.65 | 0 |
| 4716 | 40-45 | 2593.65 | 2593.7 | 0 |
| 4716 | 45-50 | 2593.7 | 2593.75 | 0 |
| 4716 | 50-55 | 2593.75 | 2593.8 | 0 |
| 4717 | 0-5 | 2593.8 | 2593.85 | 0 |
| 4717 | 5-10 | 2593.85 | 2593.9 | 0 |
| 4717 | 10-15 | 2593.9 | 2593.95 | 0 |
| 4717 | 15-25 | 2593.95 | 2594.05 | 0 |
| 4717 | 25-30 | 2594.05 | 2594.1 | 0 |
| 4717 | 30-35 | 2594.1 | 2594.15 | 0 |
| 4717 | 35-40 | 2594.15 | 2594.2 | 0 |
| 4717 | 40-44 | 2594.2 | 2594.24 | 0 |
| 4717 | 44-49 | 2594.24 | 2594.29 | 0 |
| 4717 | 49-55 | 2594.29 | 2594.35 | 0 |
| 4720 | 0-9 | 2595.45 | 2595.54 | 0 |
| 4720 | 9-14 | 2595.54 | 2595.59 | 0 |
| 4720 | 14-20 | 2595.59 | 2595.65 | 0 |
| 4720 | 20-25 | 2595.65 | 2595.7 | 0 |
| 4720 | 25-32 | 2595.7 | 2595.77 | 0 |
| 4720 | 32-36 | 2595.77 | 2595.81 | 0 |
| 4720 | 36-41 | 2595.81 | 2595.86 | 0 |
| 4720 | 41-55 | 2595.86 | 2596 | 0 |

**Major oxide concentrations of shards from the NGRIP 2441.14 m tephra horizon. n = number of shards analysed. Mean and 1 standard deviations are shown. All oxides are presented as weight %. Total iron is expressed as FeO.**

| n | $SiO_2$ | $TiO_2$ | $Al_2O_3$ | FeO | MnO | MgO | CaO | $Na_2O$ | $K_2O$ | $P_2O_5$ | Cl | Total |
|---|---|---|---|---|---|---|---|---|---|---|---|---|
| **NGRIP 2441.14 m** | | | | | | | | | | | | |
| 1 | 54.90 | 1.32 | 15.57 | 9.55 | 0.22 | 3.98 | 7.52 | 3.97 | 1.24 | 0.12 | 0.10 | 98.49 |
| 2 | 54.80 | 1.61 | 14.34 | 12.59 | 0.22 | 3.60 | 6.84 | 3.50 | 1.09 | 0.20 | 0.12 | 98.91 |
| 3 | 54.47 | 1.21 | 15.51 | 10.35 | 0.20 | 4.32 | 8.47 | 2.16 | 0.92 | 0.18 | 0.08 | 97.87 |
| 4 | 54.44 | 1.30 | 15.51 | 11.47 | 0.35 | 4.01 | 8.33 | 1.62 | 0.96 | 0.22 | 0.08 | 98.30 |
| 5 | 54.95 | 1.36 | 15.66 | 9.42 | 0.22 | 4.27 | 8.56 | 3.13 | 0.68 | 0.25 | 0.11 | 98.62 |
| 6 | 54.21 | 1.06 | 16.25 | 8.96 | 0.19 | 4.43 | 9.12 | 3.46 | 0.66 | 0.25 | 0.06 | 98.64 |
| 7 | 54.26 | 1.28 | 15.77 | 9.87 | 0.23 | 4.19 | 8.58 | 2.69 | 0.90 | 0.22 | 0.09 | 98.09 |
| 8 | 54.59 | 1.26 | 15.56 | 9.70 | 0.20 | 3.90 | 8.06 | 3.82 | 0.90 | 0.20 | 0.09 | 98.29 |
| 9 | 54.96 | 1.03 | 16.50 | 9.42 | 0.15 | 4.31 | 8.58 | 2.76 | 0.67 | 0.22 | 0.04 | 98.65 |
| **Mean** | **54.62** | **1.27** | **15.88** | **10.31** | **0.22** | **4.18** | **8.36** | **3.06** | **0.91** | **0.21** | **0.09** | **98.43** |
| St. Dev. | 0.29 | 0.17 | 0.62 | 1.18 | 0.05 | 0.27 | 0.70 | 0.79 | 0.20 | 0.04 | 0.02 | 0.32 |

**Major oxide concentrations of shards from the NGRIP 2441.28 m tephra horizon. n = number of shards analysed. Mean and 1 standard deviations are shown. All oxides are presented as weight %. Total iron is expressed as FeO.**

| n | $SiO_2$ | $TiO_2$ | $Al_2O_3$ | FeO | MnO | MgO | CaO | $Na_2O$ | $K_2O$ | $P_2O_5$ | Total |
|---|---|---|---|---|---|---|---|---|---|---|---|
| **NGRIP 2441.28 m** | | | | | | | | | | | |
| 1 | 75.05 | 0.34 | 12.03 | 1.74 | 0.21 | 0.33 | 1.71 | 4.04 | 2.11 | 0.06 | 97.62 |
| 2 | 76.68 | 0.39 | 12.39 | 1.55 | 0.02 | 0.33 | 1.78 | 4.04 | 2.04 | 0.01 | 99.23 |
| 3 | 76.52 | 0.36 | 12.44 | 1.61 | 0.12 | 0.35 | 1.74 | 4.00 | 2.14 | 0.04 | 99.32 |
| 4 | 76.54 | 0.37 | 12.38 | 1.88 | 0.13 | 0.37 | 1.74 | 3.87 | 2.18 | 0.00 | 99.46 |
| 5 | 76.85 | 0.35 | 12.37 | 1.88 | 0.09 | 0.34 | 1.81 | 4.11 | 2.10 | 0.04 | 99.94 |
| 6 | 76.68 | 0.34 | 12.38 | 1.64 | 0.01 | 0.34 | 1.71 | 4.28 | 2.09 | 0.04 | 99.51 |
| 7 | 76.17 | 0.31 | 12.20 | 1.74 | -0.03 | 0.32 | 1.72 | 3.95 | 2.06 | -0.02 | 98.47 |
| 8 | 75.64 | 0.34 | 12.15 | 1.78 | 0.09 | 0.34 | 1.78 | 4.05 | 2.06 | 0.02 | 98.23 |
| 9 | 74.71 | 0.37 | 12.05 | 1.53 | 0.08 | 0.33 | 1.81 | 4.03 | 2.16 | 0.01 | 97.08 |
| 10 | 77.44 | 0.31 | 12.23 | 1.66 | 0.14 | 0.28 | 1.46 | 4.14 | 2.12 | -0.03 | 99.78 |
| 11 | 75.35 | 0.35 | 12.37 | 1.82 | 0.08 | 0.43 | 2.02 | 3.83 | 2.01 | 0.01 | 98.27 |
| 12 | 75.76 | 0.40 | 12.30 | 1.45 | 0.08 | 0.36 | 1.76 | 3.94 | 2.00 | 0.02 | 98.06 |
| 13 | 76.88 | 0.39 | 12.34 | 1.90 | 0.14 | 0.36 | 1.78 | 4.13 | 2.22 | 0.02 | 100.17 |
| 14 | 76.81 | 0.44 | 12.38 | 1.66 | 0.09 | 0.36 | 1.84 | 3.97 | 2.11 | 0.06 | 99.70 |
| 15 | 77.14 | 0.31 | 12.21 | 1.69 | 0.07 | 0.33 | 1.74 | 4.05 | 2.21 | 0.04 | 99.78 |
| 16 | 76.44 | 0.35 | 12.28 | 1.71 | 0.13 | 0.35 | 1.74 | 4.20 | 2.07 | 0.02 | 99.28 |
| **Mean** | **76.29** | **0.36** | **12.28** | **1.70** | **0.09** | **0.35** | **1.76** | **4.04** | **2.10** | **0.02** | **98.99** |
| St. Dev. | 0.78 | 0.04 | 0.13 | 0.13 | 0.06 | 0.03 | 0.11 | 0.12 | 0.07 | 0.02 | 0.92 |

**Major oxide concentrations of shards from the NGRIP 2454.9 m tephra horizon. n = number of shards analysed. Mean and 1 standard deviations are shown. All oxides are presented as weight %. Total iron is expressed as FeO.**

| | $SiO_2$ | $TiO_2$ | $Al_2O_3$ | FeO | MnO | MgO | CaO | $Na_2O$ | $K_2O$ | $P_2O_5$ | Total |
|---|---|---|---|---|---|---|---|---|---|---|---|
| **NGRIP 2454.9 m** | | | | | | | | | | | |
| 1 | 48.22 | 2.78 | 13.65 | 9.92 | 0.22 | 9.08 | 10.70 | 2.51 | 2.00 | 0.49 | 99.59 |
| 2 | 47.39 | 2.77 | 13.64 | 10.01 | 0.30 | 6.61 | 13.54 | 2.17 | 1.87 | 0.53 | 98.84 |
| 3 | 47.56 | 2.91 | 13.40 | 8.65 | 0.09 | 7.49 | 14.01 | 2.27 | 1.81 | 0.55 | 98.74 |
| 4 | 47.40 | 3.00 | 13.62 | 8.46 | 0.22 | 7.11 | 14.19 | 2.26 | 1.86 | 0.49 | 98.62 |
| 5 | 47.17 | 2.90 | 13.47 | 9.47 | 0.15 | 7.07 | 13.56 | 2.38 | 1.94 | 0.51 | 98.60 |
| 6 | 47.56 | 2.66 | 12.93 | 9.60 | 0.02 | 7.85 | 13.50 | 2.04 | 1.77 | 0.51 | 98.45 |
| 7 | 47.24 | 2.73 | 12.83 | 10.06 | 0.19 | 7.53 | 13.77 | 1.97 | 1.73 | 0.48 | 98.52 |
| 8 | 47.31 | 2.65 | 12.63 | 10.48 | 0.19 | 7.42 | 13.55 | 2.40 | 1.90 | 0.46 | 98.99 |
| 9 | 46.26 | 2.94 | 13.02 | 10.42 | 0.15 | 7.09 | 13.29 | 2.53 | 1.70 | 0.48 | 97.88 |
| 10 | 47.82 | 2.85 | 13.47 | 9.11 | 0.12 | 6.79 | 13.01 | 2.73 | 1.94 | 0.48 | 98.33 |
| 11 | 47.34 | 2.70 | 13.93 | 9.77 | 0.23 | 6.41 | 12.38 | 2.91 | 2.06 | 0.48 | 98.22 |
| 12 | 47.67 | 2.96 | 14.02 | 9.51 | 0.11 | 6.22 | 12.48 | 2.34 | 2.04 | 0.50 | 97.85 |
| 13 | 47.11 | 3.08 | 13.85 | 9.28 | 0.19 | 6.91 | 13.14 | 2.55 | 2.01 | 0.51 | 98.62 |
| 14 | 47.19 | 3.13 | 13.64 | 9.39 | 0.15 | 6.75 | 13.12 | 2.51 | 1.86 | 0.53 | 98.27 |
| 15 | 46.38 | 2.90 | 13.86 | 9.98 | 0.24 | 6.43 | 12.85 | 2.80 | 2.14 | 0.55 | 98.12 |
| 16 | 47.22 | 2.68 | 15.56 | 9.23 | 0.19 | 5.88 | 12.21 | 3.03 | 1.94 | 0.47 | 98.41 |
| 17 | 46.20 | 2.93 | 13.72 | 10.23 | 0.31 | 6.59 | 12.84 | 2.34 | 2.01 | 0.51 | 97.68 |
| 18 | 47.28 | 2.79 | 14.00 | 9.85 | 0.11 | 6.41 | 13.04 | 1.93 | 2.26 | 0.47 | 98.15 |
| 19 | 47.71 | 2.94 | 13.90 | 9.43 | 0.10 | 6.59 | 13.47 | 2.12 | 2.00 | 0.51 | 98.78 |
| 20 | 47.40 | 2.83 | 13.74 | 8.74 | 0.15 | 7.81 | 14.18 | 1.98 | 1.63 | 0.47 | 98.93 |
| 21 | 47.11 | 2.72 | 12.62 | 9.67 | 0.17 | 7.60 | 13.56 | 2.31 | 1.73 | 0.49 | 97.99 |
| 22 | 47.26 | 2.80 | 12.71 | 10.05 | 0.17 | 7.47 | 13.61 | 2.23 | 1.81 | 0.47 | 98.57 |
| 23 | 47.42 | 3.01 | 13.77 | 10.21 | 0.16 | 6.31 | 13.21 | 1.90 | 1.79 | 0.48 | 98.24 |
| 24 | 47.17 | 2.99 | 13.41 | 9.54 | 0.19 | 7.21 | 13.84 | 1.86 | 1.72 | 0.54 | 98.47 |
| 25 | 47.97 | 2.94 | 13.86 | 10.17 | 0.12 | 6.48 | 12.77 | 2.17 | 1.92 | 0.49 | 98.89 |
| 26 | 47.25 | 2.78 | 13.46 | 9.76 | 0.20 | 6.71 | 13.31 | 2.46 | 1.93 | 0.44 | 98.28 |
| **Mean** | **47.29** | **2.86** | **13.56** | **9.65** | **0.17** | **6.99** | **13.20** | **2.33** | **1.90** | **0.50** | **98.46** |
| St. Dev. | 0.46 | 0.13 | 0.59 | 0.53 | 0.06 | 0.67 | 0.72 | 0.31 | 0.15 | 0.03 | 0.42 |

**Major oxide concentrations of shards from the NGRIP 2500.9 m tephra horizon. n = number of shards analysed. Mean and 1 standard deviations are shown. All oxides are presented as weight %. Total iron is expressed as FeO.**

| n | $SiO_2$ | $TiO_2$ | $Al_2O_3$ | FeO | MnO | MgO | CaO | $Na_2O$ | $K_2O$ | $P_2O_5$ | Total |
|---|---|---|---|---|---|---|---|---|---|---|---|
| **NGRIP 2500.9 m** | | | | | | | | | | | |
| 1 | 48.31 | 3.05 | 12.44 | 14.95 | 0.38 | 3.70 | 8.66 | 3.60 | 0.92 | 1.51 | 97.54 |
| 2 | 47.92 | 3.12 | 12.64 | 15.64 | 0.31 | 3.71 | 8.60 | 3.59 | 0.92 | 1.54 | 97.99 |
| 3 | 49.51 | 3.15 | 12.91 | 15.01 | 0.30 | 3.36 | 8.62 | 3.48 | 1.05 | 1.62 | 99.01 |
| 4 | 48.33 | 3.24 | 10.92 | 16.32 | 0.42 | 3.72 | 8.83 | 2.73 | 1.13 | 1.78 | 97.41 |
| 5 | 48.79 | 2.92 | 12.66 | 15.88 | 0.22 | 3.75 | 8.37 | 3.18 | 0.94 | 1.56 | 98.27 |
| 6 | 48.43 | 3.25 | 12.69 | 15.21 | 0.46 | 3.76 | 8.48 | 3.31 | 0.93 | 1.59 | 98.10 |
| 7 | 48.99 | 2.94 | 12.58 | 14.59 | 0.29 | 3.66 | 8.16 | 3.40 | 1.00 | 1.73 | 97.33 |
| 8 | 48.75 | 3.23 | 12.59 | 15.37 | 0.24 | 3.66 | 8.13 | 3.58 | 1.02 | 1.51 | 98.07 |
| 9 | 49.06 | 3.10 | 13.03 | 15.14 | 0.30 | 3.74 | 8.37 | 3.42 | 0.95 | 1.57 | 98.68 |
| 10 | 48.63 | 3.10 | 12.74 | 15.49 | 0.32 | 3.68 | 8.54 | 3.34 | 0.92 | 1.68 | 98.43 |
| 11 | 48.64 | 3.06 | 12.55 | 15.10 | 0.34 | 3.76 | 8.78 | 3.24 | 1.04 | 1.57 | 98.07 |
| 12 | 48.27 | 3.15 | 12.85 | 15.15 | 0.26 | 3.55 | 8.40 | 3.31 | 0.93 | 1.60 | 97.47 |
| 13 | 48.45 | 3.27 | 12.75 | 15.16 | 0.39 | 3.84 | 8.75 | 3.34 | 0.90 | 1.58 | 98.43 |
| 14 | 48.83 | 3.29 | 12.88 | 15.65 | 0.33 | 3.86 | 8.48 | 3.24 | 0.98 | 1.64 | 99.19 |
| 15 | 49.11 | 3.42 | 12.47 | 14.66 | 0.49 | 3.91 | 8.59 | 3.55 | 1.01 | 1.75 | 98.97 |
| 16 | 47.65 | 3.14 | 12.57 | 14.53 | 0.27 | 3.66 | 8.35 | 3.81 | 0.93 | 1.66 | 96.58 |
| 17 | 48.57 | 3.16 | 12.69 | 15.77 | 0.32 | 3.73 | 8.56 | 3.21 | 0.95 | 1.61 | 98.56 |
| 18 | 48.46 | 3.26 | 12.64 | 14.88 | 0.29 | 3.69 | 8.32 | 3.52 | 0.95 | 1.67 | 97.69 |
| 19 | 48.88 | 3.12 | 12.73 | 15.12 | 0.45 | 3.72 | 8.41 | 3.15 | 0.90 | 1.66 | 98.13 |
| **Mean** | **48.61** | **3.16** | **12.60** | **15.24** | **0.34** | **3.71** | **8.49** | **3.37** | **0.97** | **1.62** | **98.10** |
| St. Dev. | 0.43 | 0.12 | 0.43 | 0.46 | 0.08 | 0.12 | 0.19 | 0.23 | 0.06 | 0.08 | 0.66 |

**Major oxide concentrations of shards from the NGRIP 2548.35 m tephra horizon. n = number of shards analysed. Mean and 1 standard deviations are shown. All oxides are presented as weight %. Total iron is expressed as FeO.**

| n | $SiO_2$ | $TiO_2$ | $Al_2O_3$ | FeO | MnO | MgO | CaO | $Na_2O$ | $K_2O$ | $P_2O_5$ | Total |
|---|---|---|---|---|---|---|---|---|---|---|---|
| **NGRIP 2548.35 m** | | | | | | | | | | | |
| 1 | 49.10 | 2.20 | 13.53 | 12.76 | 0.30 | 6.62 | 11.47 | 2.59 | 0.27 | 0.28 | 99.13 |
| 2 | 49.25 | 2.03 | 13.33 | 12.79 | 0.22 | 6.64 | 11.34 | 2.57 | 0.29 | 0.25 | 98.69 |
| 3 | 48.69 | 2.16 | 13.33 | 12.32 | 0.19 | 6.76 | 11.26 | 2.47 | 0.29 | 0.27 | 97.74 |
| 4 | 48.96 | 2.20 | 13.32 | 12.88 | 0.08 | 6.67 | 11.45 | 2.52 | 0.25 | 0.24 | 98.58 |
| 5 | 49.22 | 2.03 | 13.52 | 11.95 | 0.17 | 7.54 | 11.38 | 2.60 | 0.25 | 0.24 | 98.91 |
| 6 | 49.01 | 2.11 | 13.35 | 12.68 | 0.25 | 6.74 | 11.31 | 2.56 | 0.24 | 0.22 | 98.48 |
| 7 | 48.34 | 2.19 | 13.30 | 13.65 | 0.17 | 6.46 | 11.49 | 2.54 | 0.23 | 0.25 | 98.64 |
| 8 | 48.59 | 2.12 | 13.19 | 13.06 | 0.11 | 6.33 | 11.22 | 2.56 | 0.28 | 0.19 | 97.64 |
| 9 | 48.85 | 2.17 | 13.25 | 12.83 | 0.17 | 6.61 | 11.26 | 2.49 | 0.25 | 0.23 | 98.10 |
| 10 | 48.64 | 2.21 | 13.11 | 12.23 | 0.11 | 6.78 | 11.40 | 2.37 | 0.28 | 0.24 | 97.36 |
| 11 | 47.16 | 2.13 | 13.00 | 11.80 | 0.17 | 6.29 | 10.78 | 2.48 | 0.24 | 0.25 | 94.30 |
| 12 | 49.11 | 2.09 | 13.41 | 11.53 | 0.22 | 6.88 | 11.38 | 2.31 | 0.24 | 0.28 | 97.46 |
| 13 | 49.27 | 2.14 | 13.36 | 12.87 | 0.20 | 6.78 | 11.40 | 2.30 | 0.23 | 0.22 | 98.76 |
| 14 | 48.63 | 2.04 | 13.35 | 12.51 | 0.27 | 6.69 | 11.55 | 2.51 | 0.27 | 0.24 | 98.04 |
| 15 | 48.62 | 2.18 | 13.32 | 12.76 | 0.06 | 6.65 | 11.29 | 2.38 | 0.24 | 0.22 | 97.72 |
| 16 | 48.96 | 2.12 | 13.25 | 12.70 | 0.22 | 6.70 | 11.49 | 2.54 | 0.29 | 0.25 | 98.52 |
| 17 | 48.62 | 2.03 | 13.33 | 12.80 | 0.23 | 6.78 | 11.40 | 2.53 | 0.24 | 0.22 | 98.18 |
| 18 | 48.82 | 2.18 | 13.27 | 12.56 | 0.39 | 6.68 | 11.38 | 2.41 | 0.23 | 0.23 | 98.16 |
| 19 | 48.57 | 2.12 | 13.17 | 12.51 | 0.28 | 6.71 | 11.27 | 2.52 | 0.28 | 0.21 | 97.65 |
| 20 | 48.23 | 2.19 | 13.09 | 13.31 | 0.35 | 6.35 | 11.04 | 2.40 | 0.29 | 0.22 | 97.46 |
| 21 | 48.53 | 2.09 | 13.02 | 12.80 | 0.27 | 6.83 | 11.37 | 2.53 | 0.26 | 0.21 | 97.91 |
| 22 | 49.36 | 2.17 | 13.66 | 14.13 | 0.13 | 5.76 | 11.00 | 1.75 | 0.28 | 0.22 | 98.46 |
| **Mean** | **48.75** | **2.13** | **13.29** | **12.70** | **0.21** | **6.65** | **11.32** | **2.45** | **0.26** | **0.23** | **98.00** |
| St. Dev. | 0.47 | 0.06 | 0.16 | 0.57 | 0.08 | 0.32 | 0.18 | 0.18 | 0.02 | 0.02 | 0.97 |

**Major oxide concentrations of shards from the NGRIP 2574.55 m tephra horizon. n = number of shards analysed. Mean and 1 standard deviations are shown. All oxides are presented as weight %. Total iron is expressed as FeO.**

| n | $SiO_2$ | $TiO_2$ | $Al_2O_3$ | FeO | MnO | MgO | CaO | $Na_2O$ | $K_2O$ | $P_2O_5$ | Cl | Total |
|---|---|---|---|---|---|---|---|---|---|---|---|---|
| **NGRIP 2574.55 m** | | | | | | | | | | | | |
| 1 | 46.30 | 4.85 | 12.24 | 13.65 | 0.27 | 4.86 | 9.55 | 2.96 | 0.74 | 0.55 | 0.07 | 96.02 |
| 2 | 46.40 | 4.43 | 12.09 | 14.18 | 0.23 | 4.91 | 9.51 | 3.22 | 0.75 | 1.03 | 0.05 | 96.80 |
| 3 | 46.35 | 4.75 | 12.24 | 14.05 | 0.16 | 4.86 | 9.45 | 3.20 | 0.76 | 0.85 | 0.07 | 96.74 |
| 4 | 47.14 | 4.27 | 12.07 | 14.29 | 0.26 | 4.70 | 9.38 | 2.95 | 0.81 | 1.57 | 0.06 | 97.52 |
| 5 | 46.72 | 4.98 | 12.24 | 14.41 | 0.26 | 4.76 | 9.58 | 3.04 | 0.78 | 0.68 | 0.05 | 97.51 |
| 6 | 45.89 | 4.82 | 12.03 | 14.40 | 0.29 | 4.85 | 9.50 | 3.20 | 0.78 | 0.85 | 0.10 | 96.70 |
| 7 | 45.86 | 4.79 | 12.06 | 14.41 | 0.25 | 4.85 | 9.57 | 3.01 | 0.75 | 0.68 | 0.04 | 96.29 |
| 8 | 46.37 | 5.02 | 12.31 | 15.01 | 0.27 | 4.89 | 9.59 | 3.10 | 0.73 | 0.49 | 0.04 | 97.82 |
| 9 | 46.13 | 4.95 | 12.34 | 14.26 | 0.22 | 4.92 | 9.68 | 3.13 | 0.76 | 0.87 | 0.06 | 97.32 |
| 10 | 46.32 | 4.63 | 12.21 | 15.21 | 0.28 | 4.84 | 9.63 | 2.89 | 0.75 | 0.81 | 0.05 | 97.62 |
| **Mean** | **46.35** | **4.75** | **12.18** | **14.39** | **0.25** | **4.85** | **9.54** | **3.07** | **0.76** | **0.84** | **0.06** | **97.03** |
| St. Dev. | 0.38 | 0.24 | 0.11 | 0.45 | 0.04 | 0.07 | 0.09 | 0.12 | 0.02 | 0.30 | 0.02 | 0.62 |

**Trace element concentrations of shards from the NGRIP 2441.14 m tephra horizon. n = shard number and relates to the major oxide analyses from this horizon. All concentrations are presented as ppm. Mean and 1 standard deviations are shown.**

| NGRIP 2441.14 m | | | | | | | | |
|---|---|---|---|---|---|---|---|---|
| n | 2 | 5 | 6 | 7 | 8 | 9 | **Mean** | St. Dev. |
| Sc | -5.21 | 9.21 | 24.17 | 6.49 | 15.50 | 22.06 | **12.0** | 10.9 |
| Rb | 25.88 | 31.84 | 22.48 | 29.77 | 26.01 | 34.21 | **28.4** | 4.35 |
| Sr | 118.52 | 134.16 | 208.88 | 184.79 | 320.34 | 240.79 | **201** | 74.0 |
| Y | 7.71 | 9.73 | 11.09 | 12.53 | 20.23 | 16.69 | **13.0** | 4.66 |
| Zr | 95.80 | 87.58 | 84.92 | 92.36 | 99.67 | 102.12 | **93.7** | 6.74 |
| Nb | 4.03 | 2.67 | 1.07 | 1.75 | 2.69 | 1.89 | **2.35** | 1.03 |
| Ba | 569.00 | 509.93 | 320.62 | 454.76 | 415.16 | 457.56 | **455** | 84.5 |
| La | 6.06 | 6.38 | 4.42 | 4.12 | 5.52 | 6.36 | **5.48** | 0.99 |
| Ce | 8.32 | 9.25 | 8.60 | 10.28 | 12.82 | 11.22 | **10.1** | 1.72 |
| Pr | 0.95 | 1.35 | 1.36 | 1.51 | 1.90 | 1.84 | **1.48** | 0.35 |
| Nd | 6.46 | 3.83 | 13.01 | 5.51 | 8.36 | 6.95 | **7.35** | 3.16 |
| Sm | | 1.67 | 2.05 | | 2.90 | 1.47 | **2.02** | 0.63 |
| Eu | 1.52 | 1.32 | 1.10 | 1.29 | 1.22 | 2.22 | **1.45** | 0.40 |
| Gd | -0.18 | 0.43 | 1.81 | 1.23 | 1.96 | 1.43 | **1.11** | 0.83 |
| Tb | 0.06 | 0.11 | 0.07 | 0.16 | 0.41 | -0.05 | **0.13** | 0.15 |
| Dy | 0.42 | 1.56 | 1.63 | 1.80 | 4.16 | 2.79 | **2.06** | 1.27 |
| Ho | 0.39 | 0.18 | 0.46 | 0.38 | 0.41 | 0.40 | **0.37** | 0.09 |
| Er | 0.72 | 0.59 | 0.68 | 1.27 | 1.58 | 1.10 | **0.99** | 0.39 |
| Tm | 0.17 | 0.20 | 0.17 | 0.21 | 0.14 | 0.22 | **0.19** | 0.03 |
| Yb | 0.53 | 0.32 | 0.65 | 0.62 | 1.41 | 1.76 | **0.88** | 0.57 |
| Lu | 0.18 | | 0.35 | 0.20 | 0.13 | 0.33 | **0.24** | 0.10 |
| Hf | 1.18 | 2.09 | 1.64 | 2.59 | 2.03 | 2.53 | **2.01** | 0.54 |
| Ta | 0.13 | 0.19 | 0.28 | 0.22 | 0.12 | 0.25 | **0.20** | 0.06 |
| Th | 1.84 | 1.47 | 1.15 | 1.27 | 1.76 | 1.62 | **1.52** | 0.27 |
| U | 0.64 | 0.61 | 0.41 | 0.34 | 1.40 | 0.57 | **0.66** | 0.38 |

**Trace element concentrations of shards from the NGRIP 2441.28 m tephra horizon. n = shard number and relates to the major oxide analyses from this horizon. All concentrations are presented as ppm. Mean and 1 standard deviations are shown.**

| NGRIP 2441.28 m | | | | | | | | | | | |
|---|---|---|---|---|---|---|---|---|---|---|---|
| n | 2 | 3 | 5 | 7 | 9 | 11 | 13 | 14 | 15 | **Mean** | St. Dev. |
| *Sc* | *20.53* | *-3.98* | *1.63* | *-2.55* | *-0.83* | *-1.09* | *2.74* | *1.76* | *3.10* | ***6.66*** | *9.25* |
| Rb | 28.11 | 42.69 | 27.59 | 41.75 | 30.71 | 40.99 | 41.79 | 38.26 | 37.42 | **36.5** | 6.55 |
| Sr | 64.40 | 65.04 | 88.72 | 76.77 | 110.34 | 85.19 | 97.87 | 68.36 | 68.49 | **82.1** | 16.6 |
| Y | 5.95 | 5.91 | 14.39 | 6.29 | 20.07 | 7.30 | 19.07 | 8.90 | 5.12 | **11.0** | 5.98 |
| Zr | 124.26 | 119.36 | 144.85 | 141.10 | 153.78 | 203.06 | 152.84 | 120.63 | 131.20 | **145** | 27.3 |
| *Nb* | *-1.13* | *-1.07* | *-0.67* | *0.37* | *0.33* | *2.63* | *1.48* | *0.16* | *1.14* | ***0.99*** | *1.06* |
| Ba | 849.65 | 777.33 | 798.45 | 824.47 | 743.28 | 847.99 | 708.74 | 750.85 | 844.43 | **788** | 51.6 |
| La | 5.27 | 5.77 | 9.22 | 6.48 | 8.92 | 9.01 | 8.21 | 5.91 | 5.99 | **7.35** | 1.65 |
| Ce | 9.91 | 10.09 | 12.81 | 10.81 | 16.87 | 22.08 | 14.76 | 10.28 | 11.61 | **13.5** | 4.30 |
| Pr | 1.24 | 1.14 | 1.55 | 1.65 | 2.18 | 2.94 | 1.67 | 1.07 | 1.02 | **1.68** | 0.62 |
| Nd | 4.51 | 8.60 | 6.21 | 6.39 | 9.27 | 11.12 | 10.07 | 6.70 | 10.31 | **7.86** | 2.25 |
| Sm | 0.49 | 1.43 | 1.11 | 3.10 | 1.18 | 2.71 | 2.36 | 1.34 | 0.25 | **1.71** | 0.90 |
| Eu | | | | | 1.08 | 1.42 | 1.92 | | | **1.17** | 0.69 |
| Gd | 0.44 | 0.52 | | 0.25 | 1.53 | 4.18 | 2.50 | 2.97 | | **1.77** | 1.50 |
| Tb | 0.09 | 0.21 | 0.35 | 0.03 | 0.18 | | 0.04 | 0.08 | 0.27 | **0.14** | 0.11 |
| Dy | 0.30 | 0.24 | 0.85 | 0.52 | 2.01 | 2.20 | 1.44 | 0.70 | 0.94 | **1.03** | 0.76 |
| Ho | 0.32 | 0.16 | 0.44 | 0.36 | 0.81 | 0.19 | 0.75 | 0.42 | | **0.43** | 0.24 |
| Er | 0.66 | 0.27 | 1.58 | 0.57 | 2.45 | | 1.80 | | | **1.22** | 0.85 |
| Tm | | | 0.23 | | 0.27 | 0.16 | 0.32 | 0.11 | 0.08 | **0.19** | 0.11 |
| Yb | 0.25 | 0.95 | 1.94 | 1.30 | 1.82 | 0.21 | 2.30 | 0.81 | 0.51 | **1.20** | 0.78 |
| Lu | 0.16 | | 0.12 | | 0.30 | 0.11 | 0.42 | 0.19 | | **0.22** | 0.12 |
| Hf | 4.25 | 1.99 | 4.07 | 3.14 | 3.35 | 4.54 | 3.28 | 4.45 | 1.95 | **3.63** | 0.86 |
| Ta | 0.50 | 0.00 | 0.32 | 0.26 | 0.01 | 0.01 | | 0.34 | 0.12 | **0.36** | 0.11 |
| Th | 2.65 | 2.21 | 2.39 | 2.00 | 2.60 | 2.62 | 3.28 | 2.41 | 1.82 | **2.52** | 0.38 |
| U | 0.34 | 0.60 | 1.03 | 1.03 | 0.77 | 0.70 | 0.74 | 0.71 | 0.69 | **0.74** | 0.22 |

**Trace element concentrations of shards from the NGRIP 2454.9 m tephra horizon. n = shard number and relates to the major oxide analyses from this horizon. All concentrations are presented as ppm. Mean and 1 standard deviations are shown.**

| NGRIP 2454.9 m | | | | | | | | | | |
|---|---|---|---|---|---|---|---|---|---|---|
| n | 5 | 6 | 9 | 15 | 18 | 21 | 23 | 25 | **Mean** | St. Dev. |
| Sc | 16.75 | 22.43 | 17.81 | 25.35 | 13.45 | 27.46 | 35.01 | 25.84 | **23.0** | 6.92 |
| Rb | 23.79 | 28.23 | 26.83 | 32.56 | 24.03 | 32.78 | 39.23 | 32.86 | **30.0** | 5.28 |
| Sr | 136.41 | 196.39 | 233.90 | 233.92 | 148.51 | 287.38 | 292.54 | 250.26 | **222** | 58.2 |
| Y | 6.28 | 9.13 | 8.92 | 12.82 | 7.36 | 12.03 | 12.59 | 12.25 | **10.2** | 2.57 |
| Zr | 89.18 | 96.58 | 101.43 | 112.10 | 100.74 | 120.62 | 131.90 | 110.08 | **108** | 13.8 |
| Nb | 12.22 | 19.54 | 21.43 | 24.71 | 17.26 | 32.43 | 36.22 | 25.28 | **23.6** | 7.86 |
| Ba | 503.30 | 484.36 | 489.02 | 516.14 | 499.36 | 526.48 | 520.42 | 494.80 | **504** | 15.3 |
| La | 10.39 | 12.25 | 15.29 | 17.09 | 10.85 | 19.20 | 21.57 | 17.75 | **15.5** | 4.08 |
| Ce | 19.00 | 24.15 | 31.13 | 32.20 | 19.49 | 38.57 | 40.34 | 30.39 | **29.4** | 8.01 |
| Pr | 2.25 | 3.34 | 3.62 | 3.92 | 2.52 | 5.66 | 4.43 | 3.52 | **3.66** | 1.07 |
| N | 10.00 | 11.73 | 12.62 | 20.48 | 9.08 | 15.48 | 15.59 | 16.15 | **13.9** | 3.75 |
| Sm | 1.89 | 1.47 | 2.54 | 2.22 | 2.88 | 3.22 | 2.33 | 3.09 | **2.46** | 0.60 |
| Eu | 0.69 | 1.20 | | 1.39 | 0.37 | 0.45 | 1.10 | 0.69 | **0.84** | 0.39 |
| Gd | 1.17 | 2.21 | 2.23 | 1.51 | 2.28 | 3.73 | 2.33 | 1.70 | **2.14** | 0.77 |
| Tb | 0.34 | 0.20 | 0.44 | 0.29 | 0.21 | 0.30 | 0.64 | 0.52 | **0.37** | 0.15 |
| Dy | | 1.50 | 1.94 | 1.69 | 1.34 | 2.59 | 1.81 | 1.55 | **1.78** | 0.41 |
| Ho | 0.27 | 0.24 | 0.23 | 0.26 | 0.27 | 0.47 | 0.51 | 0.33 | **0.32** | 0.11 |
| Er | 0.67 | 0.87 | 0.93 | 0.81 | 0.39 | 1.26 | 1.25 | 0.91 | **0.89** | 0.29 |
| Tm | 0.19 | 0.12 | 0.20 | 0.23 | 0.22 | 0.23 | 0.34 | 0.05 | **0.20** | 0.09 |
| Yb | 0.92 | 0.79 | 0.88 | 1.17 | 0.40 | 0.72 | 1.52 | 1.05 | **0.93** | 0.33 |
| Lu | 0.08 | | 0.13 | 0.11 | 0.15 | 0.23 | | 0.04 | **0.12** | 0.07 |
| Hf | 2.37 | 2.27 | 1.91 | 2.68 | 1.58 | 3.04 | 3.31 | 1.86 | **2.38** | 0.60 |
| Ta | 1.12 | 0.86 | 1.08 | 1.11 | 0.80 | 1.94 | 1.91 | 1.32 | **1.27** | 0.43 |
| Th | 1.89 | 2.11 | 2.45 | 2.25 | 1.82 | 2.58 | 2.90 | 2.75 | **2.35** | 0.39 |
| U | 0.44 | 0.67 | 0.59 | 0.68 | 0.54 | 0.43 | 0.80 | 0.80 | **0.62** | 0.15 |

**Trace element concentrations of shards from the NGRIP 2500.9 m tephra horizon. n = shard number and relates to the major oxide analyses from this horizon. All concentrations are presented as ppm. Mean and 1 standard deviations are shown.**

| NGRIP 2500.9 m | | | | | | | | | | | | |
|---|---|---|---|---|---|---|---|---|---|---|---|---|
| n | 4 | 5 | 9 | 11 | 13 | 14 | 15 | 17 | 18 | 19 | **Mean** | St. Dev. |
| Sc | -2.77 | -0.31 | 1.51 | 17.44 | 13.19 | 18.51 | 10.54 | 18.69 | 12.77 | 17.00 | **10.7** | 8.90 |
| Rb | 22.81 | 24.56 | 29.04 | 33.03 | 29.31 | 30.71 | 26.02 | 36.50 | 28.23 | 32.95 | **29.3** | 4.25 |
| Sr | 249.34 | 136.62 | 222.13 | 638.69 | 431.60 | 411.62 | 176.28 | 528.07 | 528.98 | 537.77 | **386** | 199 |
| Y | 26.08 | 12.70 | 21.82 | 71.55 | 42.49 | 38.34 | 22.17 | 50.06 | 56.72 | 62.16 | **40.4** | 21.4 |
| Zr | 215.34 | 130.51 | 169.91 | 454.24 | 281.53 | 274.22 | 148.84 | 359.25 | 374.40 | 367.51 | **278** | 121 |
| Nb | 22.86 | 8.05 | 20.47 | 58.05 | 35.79 | 33.77 | 15.72 | 38.44 | 46.40 | 45.33 | **32.5** | 17.2 |
| Ba | 186.46 | 132.91 | 174.37 | 292.24 | 190.37 | 199.89 | 153.39 | 233.40 | 270.75 | 269.00 | **210** | 55.0 |
| La | 18.01 | 10.09 | 16.69 | 41.08 | 26.08 | 21.06 | 12.15 | 28.61 | 31.43 | 35.50 | **24.1** | 11.4 |
| Ce | 36.86 | 24.48 | 31.87 | 91.48 | 59.82 | 46.40 | 26.31 | 64.68 | 70.76 | 71.07 | **52.4** | 24.9 |
| Pr | 4.80 | 3.00 | 3.81 | 11.74 | 7.66 | 6.87 | 3.94 | 8.94 | 11.59 | 10.94 | **7.33** | 3.71 |
| Nd | 27.06 | 13.36 | 19.87 | 59.88 | 40.76 | 26.22 | 11.28 | 51.01 | 51.00 | 43.61 | **34.4** | 18.6 |
| Sm | 10.97 | 1.61 | 3.24 | 15.94 | 10.05 | 4.97 | 4.37 | 9.55 | 16.36 | 17.05 | **9.41** | 5.89 |
| Eu | 1.10 | 1.94 | 1.85 | 4.38 | 5.20 | 3.80 | 2.18 | 5.00 | 4.81 | 4.38 | **3.46** | 1.77 |
| Gd | 7.71 | 1.41 | 3.66 | 10.21 | 8.80 | 5.35 | 3.50 | 9.22 | 9.42 | 14.10 | **7.34** | 4.21 |
| Tb | 1.39 | 0.60 | 0.80 | 1.69 | 0.83 | 0.93 | 0.32 | 1.33 | 2.25 | 1.69 | **1.18** | 0.66 |
| Dy | 4.02 | 2.36 | 3.59 | 9.46 | 6.78 | 6.49 | 2.79 | 9.39 | 11.75 | 6.51 | **6.32** | 3.34 |
| Ho | 0.74 | 0.22 | 0.66 | 2.10 | 1.16 | 0.87 | 0.48 | 1.03 | 1.79 | 1.35 | **1.04** | 0.59 |
| Er | 2.28 | 0.64 | 0.68 | 4.69 | 1.89 | 1.71 | 2.40 | 2.44 | 4.01 | 4.73 | **2.55** | 1.53 |
| Tm | 0.24 | 0.11 | 0.19 | 0.47 | 0.49 | 0.22 | | 0.52 | 0.32 | 0.42 | **0.33** | 0.15 |
| Yb | 1.77 | 1.05 | 1.01 | 3.62 | 1.80 | 2.21 | 0.82 | 2.53 | 2.24 | 4.09 | **2.11** | 1.11 |
| Lu | 0.20 | | 0.27 | 0.49 | 0.20 | | | 0.81 | 0.59 | 0.33 | **0.41** | 0.24 |
| Hf | 3.65 | 1.85 | 3.75 | 6.08 | 5.12 | 4.66 | 2.21 | 3.95 | 5.59 | 5.66 | **4.25** | 1.57 |
| Ta | 0.52 | 0.43 | 0.74 | 2.75 | 1.14 | 1.17 | 0.29 | 1.08 | 2.30 | 2.36 | **1.28** | 0.89 |
| Th | 1.78 | 1.59 | 1.53 | 3.50 | 2.52 | 1.96 | 1.80 | 2.77 | 2.74 | 2.25 | **2.24** | 0.63 |
| U | 0.46 | 0.39 | 0.41 | 0.58 | 0.70 | 0.50 | 0.23 | 0.75 | 0.62 | 0.89 | **0.55** | 0.19 |

**Trace element concentrations of shards from the 2548.35 m tephra horizon. n = shard number and relates to the major oxide analyses from this horizon. All concentrations are presented as ppm. Mean and 1 standard deviations are shown.**

| NGRIP 2548.35 m | | | | | | | | | |
|---|---|---|---|---|---|---|---|---|---|
| n | 2 | 7 | 14 | 15 | 18 | 21 | 22 | **Mean** | St. Dev. |
| Sc | 15.13 | 33.21 | 17.01 | 14.47 | 8.71 | 24.88 | 14.67 | **18.3** | 8.14 |
| Rb | 15.31 | 11.33 | 13.16 | 18.18 | 23.04 | 15.34 | 11.34 | **15.4** | 4.17 |
| Sr | 57.47 | 99.11 | 78.80 | 74.48 | 43.08 | 101.66 | 76.64 | **75.9** | 20.9 |
| Y | 4.98 | 16.43 | 7.98 | 11.22 | 3.87 | 16.58 | 8.83 | **9.99** | 5.07 |
| Zr | 84.09 | 97.83 | 93.40 | 97.81 | 101.86 | 113.49 | 102.64 | **98.7** | 9.01 |
| Nb | 0.80 | 5.13 | 2.89 | 1.54 | 0.26 | 2.85 | 2.35 | **2.26** | 1.62 |
| Ba | 199.34 | 127.99 | 142.25 | 163.72 | 255.59 | 194.93 | 141.12 | **175** | 44.8 |
| La | 3.47 | 4.68 | 3.16 | 2.77 | 3.20 | 5.17 | 2.95 | **3.63** | 0.92 |
| Ce | 7.15 | 8.47 | 7.51 | 7.25 | 5.56 | 10.04 | 6.33 | **7.47** | 1.46 |
| Pr | 0.87 | 1.41 | 0.94 | 0.62 | 0.74 | 1.56 | 1.01 | **1.02** | 0.35 |
| Nd | 1.43 | 8.09 | 4.18 | 6.21 | 2.06 | 5.17 | 1.52 | **4.09** | 2.56 |
| Sm | 0.27 | 1.83 | 0.40 | 1.74 | 1.11 | 2.82 | 0.58 | **1.25** | 0.93 |
| Eu | 0.57 | 1.86 | 0.08 | 0.50 | 0.61 | 1.89 | 0.63 | **0.88** | 0.71 |
| Gd | 0.43 | 1.34 | 0.36 | 1.06 | 0.65 | 2.57 | 0.27 | **0.96** | 0.81 |
| Tb | 0.17 | 0.46 | 0.31 | 0.30 | 0.10 | 0.36 | 0.15 | **0.26** | 0.13 |
| Dy | 1.01 | 3.33 | 1.71 | 0.63 | | 1.59 | 1.15 | **1.57** | 0.95 |
| Ho | 0.24 | 0.46 | 0.30 | 0.08 | 0.13 | 0.31 | 0.14 | **0.24** | 0.13 |
| Er | 0.21 | 0.74 | 0.86 | 0.35 | 0.40 | 1.33 | 0.68 | **0.65** | 0.38 |
| Tm | 0.02 | 0.12 | 0.04 | 0.08 | 0.11 | | | **0.07** | 0.04 |
| Yb | 0.34 | 0.98 | 0.44 | 0.96 | 0.69 | 1.59 | 0.55 | **0.79** | 0.43 |
| Lu | 0.12 | 0.10 | 0.11 | 0.16 | 0.09 | 0.22 | 0.07 | **0.12** | 0.05 |
| Hf | 1.91 | 1.50 | 1.87 | 2.40 | 2.70 | 1.37 | 2.13 | **1.98** | 0.47 |
| Ta | 0.11 | 0.60 | 0.01 | 0.07 | 0.00 | 0.38 | 0.37 | **0.22** | 0.23 |
| Th | 1.06 | 0.52 | 0.91 | 1.10 | 1.39 | 1.02 | 1.10 | **1.01** | 0.26 |
| U | 0.41 | 0.37 | 0.40 | 0.36 | 0.32 | 0.49 | 0.38 | **0.39** | 0.05 |

**Trace element concentrations of shards from the NGRIP 2574.55 m tephra horizon. n = shard number and relates to the major oxide analyses from this horizon. All concentrations are presented as ppm. Mean and 1 standard deviations are shown.**

| NGRIP 2574.55 m | | | | | | | | |
|---|---|---|---|---|---|---|---|---|
| n | 1 | 3 | 6 | 7 | 8 | 10 | **Mean** | St. Dev. |
| Sc | 13.78 | 5.61 | 7.27 | 12.25 | 1.89 | 17.72 | **9.75** | 5.85 |
| Rb | 8.56 | 6.20 | 9.27 | 6.48 | 4.08 | 7.12 | **6.95** | 1.84 |
| Sr | 198.92 | 143.82 | 271.11 | 205.64 | 137.62 | 233.04 | **198** | 51.4 |
| Y | 20.70 | 14.21 | 21.99 | 18.50 | 10.91 | 19.83 | **17.7** | 4.26 |
| Zr | 112.95 | 61.78 | 118.67 | 87.70 | 78.90 | 103.80 | **94.0** | 21.8 |
| Nb | 20.60 | 9.37 | 16.28 | 14.02 | 8.54 | 14.28 | **13.8** | 4.47 |
| Ba | 103.27 | 71.01 | 110.67 | 86.52 | 76.60 | 89.81 | **89.6** | 15.2 |
| La | 13.06 | 7.47 | 15.68 | 10.95 | 8.29 | 9.28 | **10.8** | 3.12 |
| Ce | 26.90 | 16.48 | 31.33 | 20.96 | 15.42 | 22.93 | **22.3** | 6.10 |
| Pr | 3.35 | 1.91 | 4.10 | 2.72 | 1.88 | 2.53 | **2.75** | 0.86 |
| Nd | 14.88 | 9.81 | 19.67 | 16.14 | 9.42 | 11.55 | **13.6** | 4.02 |
| Sm | 4.28 | 1.07 | 3.45 | 2.69 | 1.81 | 2.89 | **2.70** | 1.14 |
| Eu | 0.96 | 0.77 | 1.90 | 0.12 | 0.16 | 1.70 | **0.93** | 0.75 |
| Gd | 5.66 | 1.71 | 5.59 | 2.95 | 1.82 | 1.50 | **3.21** | 1.94 |
| Tb | 0.45 | 0.45 | 0.42 | 0.24 | | 0.31 | **0.37** | 0.10 |
| Dy | 4.24 | 2.59 | 4.76 | 1.60 | 1.47 | 1.52 | **2.70** | 1.14 |
| Ho | 0.76 | 0.46 | 0.68 | 0.67 | 0.32 | 0.48 | **0.56** | 0.17 |
| Er | 1.67 | 0.72 | 2.21 | 1.11 | 1.49 | 1.23 | **1.40** | 0.51 |
| Tm | 0.25 | 0.11 | 0.29 | 0.15 | | 0.12 | **0.18** | 0.08 |
| Yb | 1.82 | 0.89 | 2.11 | 0.96 | 0.46 | 1.01 | **1.21** | 0.62 |
| Lu | 0.25 | 0.14 | 0.10 | 0.23 | 0.18 | 0.21 | **0.18** | 0.06 |
| Hf | 3.00 | 1.34 | 1.76 | 1.73 | 1.93 | 1.60 | **1.89** | 0.57 |
| Ta | 0.74 | 0.81 | 1.09 | 0.69 | 0.44 | 1.04 | **0.80** | 0.24 |
| Th | 1.42 | 1.02 | 1.08 | 1.18 | 0.84 | 1.29 | **1.14** | 0.21 |
| U | 0.47 | 0.43 | 0.52 | 0.63 | 0.52 | 0.45 | **0.50** | 0.07 |

# Appendix 4 – GRIP Tephra Shard Counts and Geochemical Data

**Tephra shard counts and depth information for individual ice samples taken from the GRIP ice-core.**

| Bag Number | Bag Depth Interval | Top depth (m) | Bottom depth (m) | No. of Tephra Shards |
|---|---|---|---|---|
| 4525 | 0-20 | 2488.2 | 2488.4 | 1 |
| 4525 | 20-40 | 2488.4 | 2488.6 | 1 |
| 4525 | 40-55 | 2488.6 | 2488.75 | 1 |
| 4526 | 0-20 | 2488.75 | 2488.95 | 0 |
| 4526 | 20-40 | 2488.95 | 2489.15 | 0 |
| 4526 | 40-55 | 2489.15 | 2489.3 | 0 |
| 4527 | 0-20 | 2489.3 | 2489.5 | 0 |
| 4527 | 20-25 | 2489.5 | 2489.55 | 0 |
| 4527 | 25-30 | 2489.55 | 2489.6 | 0 |
| 4527 | 30-35 | 2489.6 | 2489.65 | 0 |
| 4527 | 35-55 | 2489.65 | 2489.85 | 1 |
| 4528 | 0-20 | 2489.85 | 2490.05 | 1 |
| 4528 | 20-40 | 2490.05 | 2490.25 | 2 |
| 4528 | 40-55 | 2490.25 | 2490.4 | 0 |
| 4529 | 0-20 | 2490.4 | 2490.6 | 0 |
| 4529 | 20-40 | 2490.6 | 2490.8 | 0 |
| 4529 | 40-55 | 2490.8 | 2490.95 | 2 |
| 4530 | 0-20 | 2490.95 | 2491.15 | 0 |
| 4530 | 20-40 | 2491.15 | 2491.35 | 0 |
| 4530 | 40-55 | 2491.35 | 2491.5 | 0 |
| 4531 | 0-20 | 2491.5 | 2491.7 | 0 |
| 4531 | 20-40 | 2491.7 | 2491.9 | 0 |
| 4531 | 40-55 | 2491.9 | 2492.05 | 0 |
| 4543 | 0-20 | 2498.1 | 2498.3 | 0 |
| 4543 | 20-40 | 2498.3 | 2498.5 | 60 |
| 4543 | 40-55 | 2498.5 | 2498.65 | 0 |
| 4544 | 0-20 | 2498.65 | 2498.85 | 0 |
| 4544 | 20-40 | 2498.85 | 2499.05 | 0 |
| 4544 | 40-55 | 2499.05 | 2499.2 | 1 |
| 4545 | 0-20 | 2499.2 | 2499.4 | 1 |
| 4545 | 20-40 | 2499.4 | 2499.6 | 0 |
| 4545 | 40-55 | 2499.6 | 2499.75 | 43 |
| 4546 | 0-15 | 2499.75 | 2499.9 | 0 |
| 4546 | 15-20 | 2499.9 | 2499.95 | 0 |
| 4546 | 20-25 | 2499.95 | 2500 | 1 |
| 4546 | 25-30 | 2500 | 2500.05 | 0 |
| 4546 | 30-55 | 2500.05 | 2500.3 | 0 |
| 4547 | 0-20 | 2500.3 | 2500.5 | 1 |
| 4547 | 20-40 | 2500.5 | 2500.7 | 0 |
| 4547 | 40-55 | 2500.7 | 2500.85 | 0 |
| 4548 | 0-20 | 2500.85 | 2501.05 | 31 |
| 4548 | 20-40 | 2501.05 | 2501.25 | 0 |
| 4548 | 40-55 | 2501.25 | 2501.4 | 1 |
| 4549 | 0-20 | 2501.4 | 2501.6 | 1 |
| 4549 | 20-40 | 2501.6 | 2501.8 | 0 |
| 4549 | 40-55 | 2501.8 | 2501.95 | 0 |
| 4601 | 0-20 | 2530 | 2530.2 | 0 |
| 4601 | 20-40 | 2530.2 | 2530.4 | 0 |
| 4601 | 40-55 | 2530.4 | 2530.55 | 0 |
| 4602 | 0-20 | 2530.55 | 2530.75 | 1 |

| Bag Number | Bag Depth Interval | Top depth (m) | Bottom depth (m) | No. of Tephra Shards |
|---|---|---|---|---|
| 4602 | 20-40 | 2530.75 | 2530.95 | 0 |
| 4602 | 40-55 | 2530.95 | 2531.1 | 0 |
| 4603 | 0-3 | 2531.1 | 2531.13 | 0 |
| 4603 | 3-8 | 2531.13 | 2531.18 | 0 |
| 4603 | 8-13 | 2531.18 | 2531.23 | 1 |
| 4603 | 13-40 | 2531.23 | 2531.5 | 0 |
| 4603 | 40-55 | 2531.5 | 2531.65 | 0 |
| 4604 | 0-5 | 2531.65 | 2531.7 | 0 |
| 4604 | 5-10 | 2531.7 | 2531.75 | 0 |
| 4604 | 10-15 | 2531.75 | 2531.8 | 40 |
| 4604 | 15-20 | 2531.8 | 2531.85 | 0 |
| 4604 | 20-40 | 2531.85 | 2532.05 | 0 |
| 4604 | 40-55 | 2532.05 | 2532.2 | 0 |
| 4605 | 0-20 | 2532.2 | 2532.4 | 1 |
| 4605 | 20-40 | 2532.4 | 2532.6 | 0 |
| 4605 | 40-55 | 2532.6 | 2532.75 | 0 |
| 4606 | 0-20 | 2532.75 | 2532.95 | 31 |
| 4606 | 20-40 | 2532.95 | 2533.15 | 0 |
| 4606 | 40-55 | 2533.15 | 2533.3 | 0 |
| 4607 | 0-20 | 2533.3 | 2533.5 | 0 |
| 4607 | 20-40 | 2533.5 | 2533.7 | 0 |
| 4607 | 40-55 | 2533.7 | 2533.85 | 0 |
| 4608 | 0-20 | 2533.85 | 2534.05 | 0 |
| 4608 | 20-40 | 2534.05 | 2534.25 | 0 |
| 4608 | 40-55 | 2534.25 | 2534.4 | 0 |
| 4663 | 0-20 | 2564.1 | 2564.3 | 21 |
| 4663 | 20-40 | 2564.3 | 2564.5 | 0 |
| 4663 | 40-50 | 2564.5 | 2564.6 | 0 |
| 4663 | 50-55 | 2564.6 | 2564.65 | 0 |
| 4664 | 0-5 | 2564.65 | 2564.7 | 0 |
| 4664 | 5-10 | 2564.7 | 2564.75 | 0 |
| 4664 | 10-30 | 2564.75 | 2564.95 | 0 |
| 4664 | 30-35 | 2564.95 | 2565 | 0 |
| 4664 | 35-40 | 2565 | 2565.05 | 0 |
| 4664 | 40-45 | 2565.05 | 2565.1 | 0 |
| 4664 | 45-50 | 2565.1 | 2565.15 | 0 |
| 4664 | 50-55 | 2565.15 | 2565.2 | 0 |
| 4665 | 0-5 | 2565.2 | 2565.25 | 0 |
| 4665 | 5-10 | 2565.25 | 2565.3 | 0 |
| 4665 | 10-30 | 2565.3 | 2565.5 | 1 |
| 4665 | 30-55 | 2565.5 | 2565.75 | 0 |
| 4666 | 0-20 | 2565.75 | 2565.95 | 0 |
| 4666 | 20-40 | 2565.95 | 2566.15 | 0 |
| 4666 | 40-55 | 2566.15 | 2566.3 | 0 |

**Major oxide concentrations of shards from the GRIP 2498.5 m tephra horizon. n = number of shards analysed. Mean and 1 standard deviations are shown. All oxides are presented as weight %. Total iron is expressed as FeO.**

| n | $SiO_2$ | $TiO_2$ | $Al_2O_3$ | FeO | MnO | MgO | CaO | $Na_2O$ | $K_2O$ | $P_2O_5$ | Cl | Total |
|---|---|---|---|---|---|---|---|---|---|---|---|---|
| **GRIP 2498.5 m** | | | | | | | | | | | | |
| 1 | 46.55 | 2.79 | 13.73 | 10.52 | 0.30 | 7.42 | 12.80 | 2.06 | 0.32 | 0.50 | 0.01 | 97.01 |
| 2 | 46.63 | 2.69 | 13.46 | 10.98 | 0.21 | 6.80 | 11.66 | 2.48 | 0.44 | 0.38 | 0.04 | 95.75 |
| 3 | 46.61 | 2.81 | 12.52 | 11.39 | 0.17 | 6.62 | 11.40 | 2.45 | 0.49 | 0.33 | 0.04 | 94.84 |
| 4 | 46.19 | 2.59 | 13.83 | 11.59 | 0.17 | 6.80 | 11.99 | 2.31 | 0.35 | 1.63 | 0.02 | 97.47 |
| 5 | 47.00 | 2.65 | 13.63 | 10.97 | 0.09 | 6.63 | 11.68 | 2.27 | 0.41 | 0.77 | 0.02 | 96.12 |
| 6 | 46.75 | 2.81 | 13.19 | 11.12 | 0.21 | 6.68 | 11.75 | 2.42 | 0.42 | 0.44 | 0.04 | 95.81 |
| 7 | 46.63 | 2.66 | 13.44 | 11.38 | 0.23 | 6.52 | 11.84 | 2.50 | 0.47 | 0.39 | 0.03 | 96.08 |
| 8 | 46.74 | 2.79 | 13.12 | 11.10 | 0.21 | 6.63 | 11.66 | 2.38 | 0.42 | 0.35 | 0.04 | 95.44 |
| 9 | 49.62 | 2.42 | 12.26 | 11.94 | 0.10 | 6.10 | 10.76 | 2.39 | 0.32 | 0.28 | 0.02 | 96.22 |
| 10 | 46.60 | 2.48 | 13.19 | 10.94 | 0.11 | 7.03 | 11.39 | 2.39 | 0.41 | 0.36 | 0.02 | 94.93 |
| 11 | 46.88 | 2.60 | 13.75 | 10.48 | 0.23 | 6.87 | 11.82 | 2.29 | 0.40 | 0.35 | 0.04 | 95.72 |
| 12 | 46.74 | 2.75 | 12.87 | 11.37 | 0.19 | 6.49 | 11.90 | 2.38 | 0.48 | 0.38 | 0.03 | 95.57 |
| 13 | 46.78 | 2.56 | 13.56 | 12.46 | 0.18 | 6.11 | 11.35 | 2.53 | 0.48 | 0.37 | 0.03 | 96.40 |
| 14 | 46.98 | 2.62 | 13.58 | 10.89 | 0.27 | 6.61 | 11.90 | 2.45 | 0.43 | 0.40 | 0.03 | 96.14 |
| 15 | 47.44 | 2.88 | 13.45 | 9.89 | 0.25 | 7.79 | 13.15 | 1.96 | 0.21 | 0.43 | 0.01 | 97.47 |
| 16 | 47.00 | 2.59 | 13.57 | 11.10 | 0.19 | 6.89 | 11.58 | 2.43 | 0.43 | 0.37 | 0.04 | 96.20 |
| 17 | 47.01 | 2.74 | 13.06 | 12.34 | 0.29 | 5.63 | 10.91 | 2.93 | 0.70 | 0.36 | 0.04 | 96.03 |
| 18 | 46.84 | 2.83 | 13.44 | 11.23 | 0.17 | 6.66 | 11.88 | 2.44 | 0.44 | 0.37 | 0.03 | 96.35 |
| 19 | 46.88 | 2.61 | 13.58 | 11.28 | 0.30 | 6.59 | 11.86 | 2.46 | 0.42 | 0.37 | 0.02 | 96.36 |
| 20 | 46.60 | 2.82 | 13.63 | 11.12 | 0.22 | 6.65 | 11.69 | 2.36 | 0.45 | 0.48 | 0.03 | 96.05 |
| 21 | 47.01 | 2.61 | 13.36 | 11.19 | 0.24 | 6.55 | 11.91 | 2.41 | 0.44 | 0.36 | 0.02 | 96.10 |
| 22 | 46.55 | 2.71 | 13.58 | 10.99 | 0.17 | 6.60 | 11.84 | 2.33 | 0.44 | 0.52 | 0.03 | 95.75 |
| 23 | 46.58 | 2.38 | 13.95 | 11.45 | 0.26 | 6.55 | 12.04 | 2.39 | 0.44 | 0.39 | 0.04 | 96.46 |
| 24 | 46.71 | 2.66 | 13.85 | 11.24 | 0.16 | 6.97 | 11.78 | 2.36 | 0.40 | 0.36 | 0.03 | 96.52 |
| **Mean** | **46.89** | **2.67** | **13.40** | **11.21** | **0.21** | **6.67** | **11.77** | **2.39** | **0.43** | **0.46** | **0.03** | **96.12** |
| St. Dev. | 0.63 | 0.13 | 0.41 | 0.54 | 0.06 | 0.42 | 0.49 | 0.17 | 0.09 | 0.27 | 0.01 | 0.63 |

**Major oxide concentrations of shards from the GRIP 2499.75 m tephra horizon. n = number of shards analysed. Mean and 1 standard deviations are shown. All oxides are presented as weight %. Total iron is expressed as FeO.**

| n | $SiO_2$ | $TiO_2$ | $Al_2O_3$ | FeO | MnO | MgO | CaO | $Na_2O$ | $K_2O$ | $P_2O_5$ | Cl | Total |
|---|---|---|---|---|---|---|---|---|---|---|---|---|
| **GRIP 2499.75 m-1** | | | | | | | | | | | | |
| 1 | 46.92 | 2.92 | 13.51 | 11.13 | 0.26 | 6.11 | 12.31 | 2.34 | 1.85 | 0.55 | 0.07 | 97.96 |
| 2 | 48.71 | 3.00 | 15.35 | 10.67 | 0.21 | 3.86 | 9.66 | 2.81 | 2.41 | 0.57 | 0.10 | 97.35 |
| 3 | 47.38 | 2.89 | 13.42 | 9.82 | 0.18 | 7.04 | 13.20 | 2.13 | 1.87 | 0.49 | 0.07 | 98.50 |
| 4 | 47.33 | 2.66 | 13.33 | 9.78 | 0.19 | 6.63 | 12.58 | 2.31 | 1.70 | 0.53 | 0.07 | 97.11 |
| 5 | 47.93 | 2.46 | 13.74 | 9.78 | 0.31 | 6.03 | 12.02 | 2.17 | 1.99 | 0.49 | 0.09 | 97.02 |
| 6 | 46.65 | 2.51 | 13.59 | 9.78 | 0.28 | 6.64 | 13.21 | 2.46 | 1.96 | 0.53 | 0.06 | 97.68 |
| 7 | 45.22 | 2.64 | 13.16 | 9.67 | 0.14 | 6.81 | 12.97 | 2.32 | 1.85 | 0.49 | 0.21 | 95.48 |
| 8 | 47.07 | 2.69 | 13.57 | 9.40 | 0.13 | 6.75 | 13.34 | 2.40 | 1.87 | 0.51 | 0.07 | 97.80 |
| 9 | 47.60 | 2.72 | 12.72 | 9.39 | 0.25 | 7.16 | 13.33 | 2.20 | 1.75 | 0.55 | 0.07 | 97.72 |
| 10 | 46.65 | 2.56 | 13.68 | 9.35 | 0.24 | 6.61 | 13.11 | 2.36 | 1.89 | 0.52 | 0.08 | 97.06 |
| 11 | 47.25 | 2.67 | 13.29 | 9.30 | 0.19 | 7.09 | 13.46 | 2.04 | 1.89 | 0.50 | 0.06 | 97.75 |
| 12 | 47.26 | 2.96 | 13.97 | 9.28 | 0.21 | 6.03 | 12.82 | 2.52 | 1.95 | 0.50 | 0.09 | 97.59 |
| 13 | 47.30 | 2.86 | 13.49 | 9.27 | 0.13 | 6.89 | 13.33 | 2.16 | 1.83 | 0.53 | 0.08 | 97.87 |
| 14 | 47.51 | 2.68 | 13.39 | 9.13 | 0.26 | 6.85 | 13.22 | 2.24 | 1.83 | 0.51 | 0.07 | 97.70 |
| 15 | 48.28 | 2.97 | 14.22 | 9.04 | 0.15 | 5.75 | 11.79 | 3.13 | 2.24 | 0.51 | 0.08 | 98.18 |
| 16 | 47.40 | 2.81 | 13.12 | 8.94 | 0.20 | 7.28 | 13.46 | 1.91 | 1.85 | 0.50 | 0.07 | 97.57 |
| 17 | 47.35 | 2.95 | 13.75 | 8.88 | 0.20 | 6.86 | 12.05 | 2.87 | 2.09 | 0.52 | 0.09 | 97.60 |
| 18 | 47.71 | 2.54 | 12.12 | 8.66 | 0.03 | 8.62 | 15.04 | 1.71 | 1.63 | 0.48 | 0.06 | 98.58 |
| 19 | 48.89 | 2.50 | 14.72 | 8.60 | 0.16 | 6.17 | 12.13 | 2.49 | 2.39 | 0.51 | 0.09 | 98.65 |
| 20 | 49.14 | 2.55 | 14.58 | 8.02 | 0.20 | 5.70 | 11.78 | 2.86 | 2.18 | 0.51 | 0.08 | 97.61 |
| **Mean** | **47.48** | **2.73** | **13.64** | **9.39** | **0.20** | **6.55** | **12.74** | **2.37** | **1.95** | **0.51** | **0.08** | **97.64** |
| St. Dev. | 0.87 | 0.18 | 0.71 | 0.69 | 0.06 | 0.91 | 1.05 | 0.35 | 0.21 | 0.02 | 0.03 | 0.68 |
| **GRIP 2499.75 m-2** | | | | | | | | | | | | |
| 1 | 48.95 | 3.09 | 12.10 | 13.95 | 0.27 | 5.32 | 10.13 | 2.55 | 0.43 | 0.36 | 0.04 | 97.17 |
| 2 | 48.60 | 2.90 | 12.55 | 13.32 | 0.19 | 5.75 | 10.55 | 2.58 | 0.38 | 0.35 | 0.01 | 97.19 |
| 3 | 48.97 | 2.88 | 12.71 | 13.30 | 0.28 | 5.75 | 10.54 | 2.64 | 0.37 | 0.34 | 0.02 | 97.79 |
| 4 | 48.82 | 2.88 | 12.59 | 13.18 | 0.21 | 5.69 | 10.53 | 2.63 | 0.37 | 0.35 | 0.03 | 97.29 |
| 5 | 48.98 | 2.62 | 12.56 | 13.17 | 0.26 | 5.75 | 10.64 | 2.65 | 0.37 | 0.35 | 0.04 | 97.38 |
| 6 | 48.79 | 2.79 | 12.53 | 13.12 | 0.23 | 5.61 | 10.64 | 2.45 | 0.38 | 0.35 | 0.02 | 96.91 |
| 7 | 50.01 | 2.73 | 13.05 | 13.11 | 0.25 | 5.84 | 10.86 | 2.59 | 0.24 | 0.38 | 0.04 | 99.09 |
| 8 | 48.19 | 2.71 | 12.54 | 13.03 | 0.27 | 5.83 | 10.60 | 2.60 | 0.35 | 0.38 | 0.05 | 96.57 |
| 9 | 49.56 | 2.72 | 12.72 | 12.49 | 0.23 | 6.33 | 11.35 | 1.34 | 0.37 | 0.37 | 0.04 | 97.50 |
| **Mean** | **48.99** | **2.81** | **12.59** | **13.18** | **0.24** | **5.76** | **10.65** | **2.45** | **0.36** | **0.36** | **0.03** | **97.43** |
| St. Dev. | 0.53 | 0.14 | 0.25 | 0.38 | 0.03 | 0.26 | 0.33 | 0.42 | 0.05 | 0.02 | 0.01 | 0.71 |

**Major oxide concentrations of shards from the GRIP 2501.05 m tephra horizon. n = number of shards analysed. Mean and 1 standard deviations are shown. All oxides are presented as weight %. Total iron is expressed as FeO.**

| n | $SiO_2$ | $TiO_2$ | $Al_2O_3$ | FeO | MnO | MgO | CaO | $Na_2O$ | $K_2O$ | $P_2O_5$ | Cl | Total |
|---|---|---|---|---|---|---|---|---|---|---|---|---|
| **GRIP 2501.05 m** | | | | | | | | | | | | |
| 1 | 47.67 | 2.70 | 15.19 | 10.78 | 0.20 | 5.75 | 13.00 | 2.66 | 0.41 | 0.35 | 0.04 | 98.74 |
| 2 | 46.61 | 2.90 | 13.93 | 11.49 | 0.20 | 7.66 | 12.19 | 2.40 | 0.36 | 0.38 | 0.03 | 98.14 |
| 3 | 45.97 | 2.86 | 14.16 | 11.95 | 0.13 | 6.98 | 12.18 | 2.12 | 0.39 | 0.35 | 0.03 | 97.10 |
| 4 | 46.18 | 2.98 | 13.89 | 13.24 | 0.26 | 6.63 | 11.64 | 2.50 | 0.44 | 0.37 | 0.05 | 98.17 |
| 5 | 45.98 | 2.93 | 13.55 | 12.08 | 0.22 | 6.96 | 12.18 | 2.43 | 0.37 | 0.35 | 0.03 | 97.08 |
| 6 | 45.73 | 2.97 | 13.70 | 12.10 | 0.23 | 6.95 | 12.03 | 2.34 | 0.37 | 0.38 | 0.03 | 96.83 |
| 7 | 45.59 | 2.83 | 14.27 | 11.23 | 0.17 | 7.03 | 11.98 | 2.43 | 0.36 | 0.36 | 0.04 | 96.29 |
| 8 | 45.76 | 2.84 | 14.22 | 11.67 | 0.12 | 7.03 | 12.24 | 2.55 | 0.35 | 0.37 | 0.03 | 97.19 |
| 9 | 45.96 | 2.93 | 14.32 | 11.23 | 0.12 | 6.99 | 12.10 | 2.35 | 0.36 | 0.33 | 0.03 | 96.72 |
| 10 | 46.47 | 2.89 | 13.73 | 12.18 | 0.15 | 6.70 | 12.06 | 2.45 | 0.35 | 0.34 | 0.04 | 97.36 |
| 11 | 45.95 | 2.80 | 14.22 | 11.90 | 0.19 | 6.94 | 12.04 | 2.49 | 0.38 | 0.36 | 0.09 | 97.35 |
| 12 | 46.09 | 3.34 | 13.74 | 13.50 | 0.11 | 5.85 | 11.11 | 2.74 | 0.50 | 0.34 | 0.05 | 97.37 |
| 13 | 47.37 | 2.95 | 15.02 | 10.87 | 0.24 | 5.99 | 12.29 | 2.66 | 0.35 | 0.37 | 0.04 | 98.17 |
| 14 | 45.47 | 3.04 | 13.68 | 11.38 | 0.20 | 6.82 | 12.22 | 2.47 | 0.38 | 0.36 | 0.03 | 96.06 |
| 15 | 47.63 | 2.84 | 15.11 | 9.63 | 0.17 | 6.47 | 13.52 | 2.55 | 0.27 | 0.34 | 0.02 | 98.56 |
| 16 | 45.59 | 3.04 | 14.01 | 11.29 | 0.18 | 6.86 | 12.04 | 2.42 | 0.36 | 0.33 | 0.03 | 96.16 |
| 17 | 46.47 | 2.91 | 13.99 | 11.98 | 0.24 | 6.49 | 12.11 | 2.49 | 0.34 | 0.37 | 0.06 | 97.43 |
| 18 | 45.69 | 2.89 | 13.63 | 11.90 | 0.14 | 6.35 | 11.80 | 2.43 | 0.42 | 0.38 | 0.09 | 95.73 |
| 19 | 46.17 | 3.02 | 14.16 | 11.70 | 0.20 | 6.82 | 12.13 | 2.47 | 0.35 | 0.36 | 0.04 | 97.42 |
| 20 | 46.24 | 2.81 | 14.04 | 11.12 | 0.09 | 6.96 | 12.29 | 2.05 | 0.33 | 0.38 | 0.04 | 96.35 |
| 21 | 46.56 | 2.91 | 14.55 | 10.90 | 0.26 | 6.20 | 12.50 | 2.55 | 0.31 | 0.36 | 0.04 | 97.13 |
| 22 | 45.70 | 2.93 | 14.11 | 11.59 | 0.17 | 7.09 | 12.12 | 2.37 | 0.35 | 0.35 | 0.03 | 96.81 |
| 23 | 46.38 | 3.04 | 14.31 | 11.03 | 0.10 | 7.68 | 13.47 | 1.90 | 0.23 | 0.35 | 0.03 | 98.53 |
| **Mean** | **46.23** | **2.93** | **14.15** | **11.60** | **0.18** | **6.75** | **12.23** | **2.43** | **0.36** | **0.36** | **0.04** | **97.25** |
| St. Dev. | 0.62 | 0.13 | 0.46 | 0.80 | 0.05 | 0.49 | 0.52 | 0.19 | 0.05 | 0.02 | 0.02 | 0.84 |

**Major oxide concentrations of shards from the GRIP 2531.8 m tephra horizon. n = number of shards analysed. Mean and 1 standard deviations are shown. All oxides are presented as weight %. Total iron is expressed as FeO.**

| n | $SiO_2$ | $TiO_2$ | $Al_2O_3$ | FeO | MnO | MgO | CaO | $Na_2O$ | $K_2O$ | $P_2O_5$ | Cl | Total |
|---|---|---|---|---|---|---|---|---|---|---|---|---|
| **GRIP 2531.8 m** | | | | | | | | | | | | |
| 1 | 49.31 | 3.12 | 12.72 | 14.30 | 0.34 | 3.59 | 8.46 | 2.81 | 0.91 | 1.51 | 0.07 | 97.14 |
| 2 | 48.67 | 3.15 | 12.69 | 14.19 | 0.36 | 3.89 | 8.70 | 2.95 | 0.89 | 1.74 | 0.08 | 97.32 |
| 3 | 49.44 | 3.00 | 12.67 | 14.59 | 0.37 | 3.66 | 8.40 | 3.24 | 0.94 | 1.54 | 0.05 | 97.89 |
| 4 | 48.65 | 2.87 | 12.53 | 14.76 | 0.45 | 3.68 | 8.49 | 3.58 | 0.93 | 1.65 | 0.07 | 97.66 |
| 5 | 50.31 | 3.02 | 11.29 | 14.98 | 0.44 | 3.63 | 8.51 | 2.64 | 1.28 | 1.89 | 0.06 | 98.06 |
| 6 | 48.89 | 3.11 | 12.43 | 14.29 | 0.36 | 3.79 | 8.43 | 2.72 | 0.88 | 1.66 | 0.07 | 96.62 |
| 7 | 49.19 | 3.29 | 12.63 | 14.18 | 0.26 | 3.66 | 8.30 | 3.13 | 1.05 | 1.66 | 0.07 | 97.42 |
| 8 | 49.21 | 3.02 | 12.47 | 14.48 | 0.29 | 3.96 | 8.70 | 3.85 | 0.62 | 1.59 | 0.05 | 98.25 |
| 9 | 49.24 | 2.95 | 12.73 | 14.70 | 0.28 | 3.57 | 8.32 | 3.05 | 0.92 | 1.60 | 0.06 | 97.43 |
| 10 | 48.92 | 3.14 | 12.67 | 14.89 | 0.26 | 3.58 | 8.36 | 3.10 | 0.91 | 1.61 | 0.07 | 97.51 |
| 11 | 49.17 | 2.79 | 12.68 | 13.64 | 0.27 | 3.56 | 8.38 | 3.20 | 0.95 | 1.58 | 0.08 | 96.31 |
| 12 | 48.57 | 2.89 | 12.58 | 14.05 | 0.30 | 3.69 | 8.65 | 3.21 | 0.91 | 1.59 | 0.06 | 96.50 |
| 13 | 48.48 | 3.47 | 12.44 | 13.74 | 0.24 | 3.29 | 8.67 | 3.92 | 0.75 | 1.20 | 0.06 | 96.27 |
| 14 | 48.30 | 3.09 | 11.43 | 14.30 | 0.33 | 3.77 | 8.13 | 3.46 | 0.88 | 1.44 | 0.08 | 95.20 |
| 15 | 49.26 | 2.82 | 12.14 | 14.16 | 0.32 | 3.54 | 8.09 | 3.24 | 0.94 | 1.48 | 0.07 | 96.06 |
| 16 | 48.83 | 2.87 | 11.81 | 14.86 | 0.31 | 3.58 | 8.27 | 3.36 | 0.93 | 1.50 | 0.06 | 96.38 |
| 17 | 48.87 | 2.81 | 12.53 | 14.12 | 0.41 | 3.44 | 8.31 | 3.21 | 0.96 | 1.78 | 0.05 | 96.49 |
| 18 | 49.44 | 2.74 | 12.18 | 14.11 | 0.36 | 3.48 | 8.25 | 3.33 | 0.95 | 1.54 | 0.08 | 96.46 |
| 19 | 49.03 | 3.02 | 11.80 | 14.30 | 0.35 | 3.51 | 7.93 | 3.27 | 0.96 | 1.40 | 0.06 | 95.62 |
| 20 | 49.11 | 2.95 | 12.12 | 14.68 | 0.26 | 3.45 | 8.19 | 3.44 | 0.98 | 1.54 | 0.05 | 96.79 |
| 21 | 48.97 | 3.03 | 12.06 | 14.48 | 0.23 | 3.55 | 8.22 | 3.28 | 0.92 | 1.52 | 0.06 | 96.32 |
| 22 | 48.98 | 3.04 | 12.32 | 14.06 | 0.32 | 3.47 | 8.08 | 3.40 | 0.93 | 1.58 | 0.06 | 96.24 |
| **Mean** | **49.04** | **3.01** | **12.31** | **14.36** | **0.32** | **3.61** | **8.36** | **3.25** | **0.93** | **1.57** | **0.06** | **96.81** |
| St. Dev. | 0.42 | 0.17 | 0.42 | 0.36 | 0.06 | 0.15 | 0.21 | 0.31 | 0.11 | 0.14 | 0.01 | 0.80 |

**Major oxide concentrations of shards from the GRIP 2532.95 m tephra horizon. n = number of shards analysed. Mean and 1 standard deviations are shown. All oxides are presented as weight %. Total iron is expressed as FeO.**

| n | $SiO_2$ | $TiO_2$ | $Al_2O_3$ | FeO | MnO | MgO | CaO | $Na_2O$ | $K_2O$ | $P_2O_5$ | Cl | Total |
|---|---|---|---|---|---|---|---|---|---|---|---|---|
| **GRIP 2532.95 m** | | | | | | | | | | | | |
| 1 | 48.88 | 2.84 | 12.02 | 12.46 | 0.25 | 5.68 | 10.07 | 2.65 | 0.50 | 0.47 | 0.05 | 95.88 |
| 2 | 49.39 | 3.69 | 12.05 | 14.45 | 0.22 | 4.46 | 9.25 | 2.73 | 0.79 | 0.44 | 0.03 | 97.51 |
| 3 | 49.02 | 2.84 | 12.22 | 13.01 | 0.16 | 5.48 | 9.97 | 2.60 | 0.50 | 0.34 | 0.05 | 96.19 |
| 4 | 48.90 | 3.17 | 12.59 | 13.31 | 0.26 | 4.96 | 9.50 | 2.71 | 0.57 | 0.41 | 0.06 | 96.45 |
| 5 | 48.80 | 2.91 | 12.04 | 13.13 | 0.19 | 5.47 | 9.89 | 2.68 | 0.50 | 2.01 | 0.03 | 97.65 |
| 6 | 48.79 | 3.30 | 12.32 | 13.73 | 0.31 | 4.64 | 9.22 | 2.96 | 0.68 | 0.47 | 0.05 | 96.45 |
| 7 | 49.43 | 3.22 | 12.28 | 13.60 | 0.24 | 4.75 | 9.22 | 2.83 | 0.68 | 0.46 | 0.05 | 96.76 |
| 8 | 49.81 | 3.23 | 12.68 | 13.05 | 0.31 | 5.14 | 9.82 | 2.42 | 0.68 | 0.42 | 0.04 | 97.60 |
| 9 | 48.98 | 3.39 | 12.04 | 14.19 | 0.12 | 4.77 | 9.10 | 2.90 | 0.74 | 0.50 | 0.03 | 96.77 |
| 10 | 49.55 | 3.02 | 12.52 | 13.99 | 0.25 | 5.29 | 10.26 | 2.41 | 0.73 | 0.42 | 0.03 | 98.47 |
| 11 | 50.12 | 3.44 | 13.16 | 15.18 | 0.25 | 3.80 | 8.53 | 2.61 | 0.64 | 0.45 | 0.06 | 98.23 |
| 12 | 49.00 | 3.25 | 12.70 | 13.38 | 0.21 | 4.65 | 9.24 | 2.81 | 0.66 | 0.46 | 0.04 | 96.40 |
| 13 | 49.43 | 3.07 | 12.41 | 13.61 | 0.25 | 4.61 | 9.17 | 2.77 | 0.73 | 0.55 | 0.04 | 96.64 |
| 14 | 49.29 | 3.19 | 12.25 | 13.99 | 0.25 | 4.73 | 8.91 | 2.90 | 0.72 | 0.54 | 0.04 | 96.82 |
| 15 | 49.17 | 2.80 | 12.66 | 13.43 | 0.15 | 5.48 | 10.21 | 2.68 | 0.48 | 0.38 | 0.04 | 97.48 |
| 16 | 49.06 | 2.98 | 12.06 | 13.54 | 0.32 | 5.06 | 9.45 | 2.83 | 0.63 | 0.40 | 0.04 | 96.37 |
| 17 | 49.21 | 2.72 | 12.47 | 12.60 | 0.22 | 5.52 | 10.01 | 2.57 | 0.52 | 0.35 | 0.04 | 96.23 |
| 18 | 48.58 | 2.71 | 11.86 | 12.73 | 0.29 | 5.57 | 9.58 | 2.66 | 0.52 | 0.32 | 0.03 | 94.85 |
| 19 | 50.16 | 3.37 | 11.55 | 13.74 | 0.18 | 4.33 | 8.45 | 2.64 | 0.78 | 0.44 | 0.06 | 95.70 |
| 20 | 49.64 | 3.48 | 11.63 | 13.98 | 0.29 | 4.37 | 8.69 | 2.98 | 0.75 | 0.44 | 0.05 | 96.32 |
| 21 | 48.94 | 3.13 | 11.95 | 13.84 | 0.21 | 4.71 | 8.85 | 2.78 | 0.70 | 0.42 | 0.05 | 95.58 |
| 22 | 48.85 | 2.67 | 12.45 | 12.72 | 0.21 | 5.58 | 10.08 | 2.65 | 0.45 | 0.33 | 0.02 | 96.02 |
| 23 | 50.23 | 3.23 | 12.61 | 13.71 | 0.27 | 4.67 | 8.81 | 3.25 | 0.89 | 0.60 | 0.05 | 98.31 |
| **Mean** | **49.27** | **3.12** | **12.28** | **13.54** | **0.23** | **4.95** | **9.40** | **2.74** | **0.65** | **0.51** | **0.04** | **96.73** |
| St. Dev. | 0.46 | 0.27 | 0.38 | 0.64 | 0.05 | 0.50 | 0.56 | 0.19 | 0.12 | 0.34 | 0.01 | 0.93 |

**Major oxide concentrations of shards from the GRIP 2564.3 m tephra horizon. n = number of shards analysed. Mean and 1 standard deviations are shown. All oxides are presented as weight %. Total iron is expressed as FeO.**

| n | $SiO_2$ | $TiO_2$ | $Al_2O_3$ | FeO | MnO | MgO | CaO | $Na_2O$ | $K_2O$ | $P_2O_5$ | Cl | Total |
|---|---|---|---|---|---|---|---|---|---|---|---|---|
| **GRIP 2564.3 m-1** | | | | | | | | | | | | |
| 1 | 51.15 | 3.06 | 12.54 | 12.29 | 0.34 | 3.60 | 7.80 | 3.41 | 1.06 | 1.73 | 0.07 | 97.04 |
| 2 | 50.97 | 3.20 | 12.66 | 11.82 | 0.25 | 3.55 | 7.98 | 3.36 | 1.10 | 1.52 | 0.06 | 96.48 |
| 3 | 50.96 | 2.96 | 12.54 | 11.97 | 0.27 | 3.57 | 7.87 | 3.29 | 1.10 | 1.52 | 0.06 | 96.11 |
| 4 | 50.89 | 3.10 | 12.17 | 12.06 | 0.32 | 3.72 | 7.87 | 2.94 | 1.06 | 1.41 | 0.05 | 95.58 |
| 5 | 50.79 | 3.12 | 11.93 | 12.34 | 0.24 | 3.66 | 7.54 | 3.28 | 1.09 | 1.48 | 0.05 | 95.50 |
| 6 | 50.73 | 3.22 | 12.47 | 11.80 | 0.29 | 3.56 | 7.97 | 3.19 | 1.08 | 1.79 | 0.07 | 96.17 |
| **Mean** | **50.92** | **3.11** | **12.38** | **12.05** | **0.28** | **3.61** | **7.84** | **3.25** | **1.08** | **1.57** | **0.06** | **96.15** |
| St. Dev. | 0.15 | 0.10 | 0.28 | 0.23 | 0.04 | 0.07 | 0.16 | 0.17 | 0.02 | 0.15 | 0.01 | 0.57 |
| **GRIP 2564.3 m-2** | | | | | | | | | | | | |
| 1 | 49.65 | 3.28 | 12.44 | 12.82 | 0.29 | 3.97 | 8.35 | 3.16 | 0.98 | 1.36 | 0.07 | 96.38 |
| 2 | 49.60 | 3.54 | 12.21 | 12.48 | 0.24 | 4.01 | 8.28 | 3.22 | 0.99 | 1.29 | 0.05 | 95.91 |
| 3 | 49.38 | 3.54 | 12.11 | 13.12 | 0.29 | 4.10 | 8.25 | 3.48 | 0.95 | 1.26 | 0.05 | 96.53 |
| 4 | 49.32 | 3.52 | 12.02 | 12.31 | 0.29 | 3.79 | 8.35 | 3.08 | 1.04 | 1.34 | 0.08 | 95.14 |
| 5 | 48.93 | 3.64 | 12.09 | 12.67 | 0.24 | 4.14 | 8.62 | 3.34 | 0.92 | 1.28 | 0.06 | 95.93 |
| 6 | 48.56 | 3.71 | 11.49 | 12.88 | 0.27 | 4.24 | 8.00 | 3.66 | 0.94 | 1.19 | 0.05 | 94.98 |
| **Mean** | **49.24** | **3.54** | **12.06** | **12.71** | **0.27** | **4.04** | **8.31** | **3.32** | **0.97** | **1.29** | **0.06** | **95.81** |
| St. Dev. | 0.42 | 0.14 | 0.32 | 0.29 | 0.02 | 0.16 | 0.20 | 0.21 | 0.04 | 0.06 | 0.01 | 0.63 |

**Trace element concentrations of shards from the GRIP 2498.5 m tephra horizon. n = shard number and relates to the major oxide analyses from this horizon. All concentrations are presented as ppm. Mean and 1 standard deviations are shown.**

| GRIP 2498.5 m | | | | | | | | | | | | | | | | | | |
|---|---|---|---|---|---|---|---|---|---|---|---|---|---|---|---|---|---|---|
| n | 1 | 2 | 4 | 5 | 6 | 8 | 9 | 10 | 13 | 14 | 15 | 16 | 18 | 19 | 21 | 24 | **Mean** | St. Dev. |
| Sc | 11.23 | 6.88 | 15.94 | 16.21 | 20.83 | 26.17 | 24.33 | 27.59 | 10.24 | 12.42 | 15.17 | 12.18 | 15.93 | 19.88 | 15.31 | 16.11 | **16.7** | 5.81 |
| Rb | 7.64 | 4.13 | 22.35 | 7.12 | 10.27 | 8.40 | 9.59 | 7.85 | 12.91 | 8.66 | 7.05 | 5.32 | 3.35 | 3.87 | 3.19 | 11.47 | **8.32** | 4.72 |
| Sr | 103.38 | 83.63 | 194.79 | 207.22 | 305.77 | 354.21 | 147.09 | 443.97 | 135.30 | 242.53 | 255.49 | 208.63 | 246.99 | 352.33 | 232.27 | 251.77 | **235** | 96.1 |
| Y | 10.56 | 9.12 | 15.43 | 15.91 | 26.06 | 23.22 | 29.51 | 24.73 | 12.17 | 18.99 | 18.05 | 17.36 | 17.59 | 23.60 | 18.09 | 18.83 | **18.7** | 5.63 |
| Zr | 56.18 | 46.15 | 89.04 | 92.58 | 117.10 | 120.17 | 115.98 | 154.18 | 51.82 | 104.91 | 101.99 | 93.40 | 102.65 | 132.51 | 96.73 | 97.24 | **98.3** | 28.7 |
| Nb | 5.97 | 3.05 | 10.19 | 12.12 | 13.95 | 15.28 | 8.52 | 21.82 | 6.10 | 10.90 | 13.36 | 9.16 | 8.92 | 15.01 | 8.15 | 13.53 | **11.0** | 4.54 |
| Ba | 67.32 | 60.57 | 177.88 | 90.68 | 112.19 | 136.12 | 107.37 | 139.64 | 124.76 | 106.19 | 120.03 | 108.90 | 115.16 | 136.62 | 99.99 | 113.32 | **114** | 28.0 |
| La | 6.13 | 7.06 | 12.03 | 12.12 | 13.78 | 15.81 | 9.82 | 17.88 | 9.44 | 12.28 | 13.25 | 11.15 | 15.40 | 16.40 | 11.63 | 12.98 | **12.3** | 3.22 |
| Ce | 13.91 | 11.92 | 24.81 | 25.02 | 30.54 | 40.11 | 23.88 | 40.77 | 19.04 | 26.72 | 30.49 | 24.81 | 29.05 | 32.05 | 26.95 | 27.81 | **26.7** | 7.75 |
| Pr | 1.75 | 1.15 | 3.14 | 2.75 | 3.38 | 4.47 | 2.68 | 5.98 | 2.59 | 3.13 | 3.36 | 3.07 | 3.52 | 4.90 | 3.52 | 3.30 | **3.29** | 1.14 |
| Nd | 7.66 | 3.71 | 11.98 | 17.38 | 17.05 | 19.89 | 15.53 | 18.50 | 10.76 | 17.20 | 14.77 | 15.28 | 15.21 | 16.52 | 14.46 | 14.51 | **14.4** | 4.14 |
| Sm | 0.85 | 1.98 | 5.67 | 2.83 | 4.58 | 5.60 | 3.41 | 9.62 | 1.48 | 4.35 | 6.19 | 3.26 | 3.50 | 3.32 | 4.47 | 2.84 | **4.00** | 2.11 |
| Eu | 0.35 | 0.82 | 1.79 | 0.76 | 2.41 | 1.07 | 0.89 | 2.39 | 0.87 | 1.16 | 0.96 | 0.30 | 0.43 | 0.75 | -0.33 | 1.73 | **1.02** | 0.74 |
| Gd | 1.05 | 0.79 | 3.42 | 2.41 | 3.60 | 3.99 | 2.98 | 5.57 | 2.55 | 3.10 | 2.87 | 2.72 | 5.60 | 4.21 | 6.07 | 5.81 | **3.55** | 1.60 |
| Tb | 0.24 | 0.39 | 0.44 | 0.49 | 0.76 | 0.79 | 0.64 | 0.93 | 0.34 | 0.53 | 0.82 | 0.35 | 0.53 | 0.79 | 0.82 | 0.46 | **0.58** | 0.21 |
| Dy | 1.12 | 1.94 | 3.32 | 3.16 | 3.96 | 5.85 | 4.33 | 3.40 | 2.02 | 3.70 | 5.65 | 3.93 | 2.36 | 3.15 | 3.39 | 4.45 | **3.48** | 1.27 |
| Ho | 0.42 | 0.33 | 0.35 | 0.86 | 0.86 | 0.95 | 0.79 | 0.76 | 0.45 | 0.66 | 0.53 | 0.82 | 0.62 | 0.91 | 0.46 | 0.75 | **0.66** | 0.21 |
| Er | 0.74 | 0.77 | 1.91 | 1.79 | 2.05 | 2.15 | 1.93 | 2.98 | 0.99 | 1.88 | 1.43 | 1.10 | 1.66 | 1.82 | 1.11 | 1.65 | **1.62** | 0.58 |
| Tm | 0.07 | 0.00 | 0.16 | 0.32 | 0.28 | 0.36 | 0.38 | 0.33 | 0.07 | 0.30 | 0.23 | 0.15 | 0.28 | 0.25 | 0.20 | 0.19 | **0.22** | 0.11 |
| Yb | 1.19 | 0.56 | 1.26 | 1.27 | 1.44 | 1.33 | 2.36 | 2.59 | 1.00 | 1.10 | 2.37 | 1.37 | 1.76 | 2.36 | 1.67 | 1.97 | **1.60** | 0.58 |
| Lu | 0.13 | 0.22 | 0.36 | 0.26 | 0.27 | 0.34 | 0.36 | 0.30 | 0.12 | 0.21 | 0.20 | 0.14 | 0.09 | 0.30 | 0.20 | 0.20 | **0.23** | 0.09 |
| Hf | 1.94 | 1.23 | 3.55 | 2.67 | 4.02 | 3.75 | 3.37 | 5.83 | 1.04 | 2.99 | 3.20 | 2.14 | 4.21 | 1.81 | 2.86 | 2.80 | **2.96** | 1.21 |
| Ta | 0.23 | 0.20 | 0.89 | 0.53 | 1.13 | 0.97 | 0.52 | 1.31 | 0.96 | 0.62 | 0.67 | 0.54 | 0.61 | 1.07 | 0.52 | 0.67 | **0.72** | 0.31 |
| Th | 1.30 | 1.24 | 1.91 | 1.52 | 1.74 | 1.52 | 1.23 | 1.27 | 1.75 | 1.38 | 1.67 | 1.96 | 2.04 | 2.61 | 1.61 | 1.54 | **1.64** | 0.36 |
| U | 0.90 | 0.88 | 1.74 | 0.60 | 0.55 | 0.58 | 0.56 | 0.53 | 0.53 | 0.52 | 0.61 | 0.77 | 0.65 | 0.63 | 1.03 | 0.69 | **0.74** | 0.31 |

**Trace element concentrations of shards from the GRIP 2499.75 m-1 tephra horizon. n = shard number and relates to the major oxide analyses from this horizon. All concentrations are presented as ppm. Mean and 1 standard deviations are shown.**

| GRIP 2499.75 m-1 | | | | | | | | | | | | |
|---|---|---|---|---|---|---|---|---|---|---|---|---|
| n | 1 | 3 | 4 | 6 | 8 | 13 | 16 | 18 | 19 | 20 | **Mean** | St. Dev. |
| Sc | 7.98 | -0.74 | -3.31 | 5.01 | 0.31 | 8.00 | 9.39 | -1.58 | 4.70 | -5.06 | **2.47** | 5.18 |
| Rb | 22.87 | 12.47 | 14.47 | 22.04 | 5.92 | 18.91 | 30.08 | 15.13 | 12.45 | 10.69 | **16.5** | 7.04 |
| Sr | 349.86 | 140.37 | 159.75 | 275.19 | 56.69 | 272.31 | 259.31 | 158.68 | 184.45 | 78.57 | **194** | 93.6 |
| Y | 17.51 | 10.59 | 9.44 | 14.06 | 9.03 | 13.99 | 15.16 | 9.66 | 11.42 | 7.92 | **11.9** | 3.13 |
| Zr | 123.62 | 66.98 | 103.61 | 96.65 | 42.81 | 93.36 | 99.92 | 65.78 | 79.29 | 46.18 | **81.8** | 26.2 |
| Nb | 29.46 | 10.27 | 12.58 | 23.54 | 0.37 | 22.08 | 23.98 | 10.77 | 16.29 | 2.58 | **15.2** | 9.59 |
| Ba | 441.43 | 196.60 | 226.77 | 336.88 | 98.50 | 362.27 | 362.86 | 201.32 | 246.97 | 95.11 | **257** | 116 |
| La | 27.30 | 13.35 | 13.21 | 20.17 | 6.85 | 20.91 | 23.27 | 12.74 | 16.91 | 8.31 | **16.3** | 6.59 |
| Ce | 48.93 | 22.81 | 27.71 | 43.21 | 12.10 | 44.18 | 43.23 | 24.09 | 29.78 | 13.59 | **31.0** | 13.3 |
| Pr | 6.04 | 2.67 | 2.93 | 4.70 | 1.73 | 4.09 | 4.35 | 2.27 | 2.65 | 1.46 | **3.29** | 1.46 |
| Nd | 16.41 | 7.81 | 9.36 | 21.52 | 4.11 | 16.20 | 20.15 | 8.54 | 13.89 | 4.71 | **12.3** | 6.23 |
| Sm | 4.22 | 1.71 | 3.41 | 4.04 | 1.00 | 4.55 | 4.63 | 2.81 | 2.67 | 1.06 | **3.01** | 1.39 |
| Eu | 0.99 | | 0.25 | 0.54 | 0.29 | 1.34 | | 0.48 | | | **0.65** | 0.43 |
| Gd | 4.50 | 2.73 | 1.28 | 0.50 | 1.56 | 1.95 | 4.04 | 2.44 | 3.08 | 1.77 | **2.38** | 1.24 |
| Tb | 0.42 | 0.25 | 0.13 | 0.26 | 0.05 | 0.49 | 0.58 | 0.17 | 0.33 | 0.24 | **0.29** | 0.17 |
| Dy | 2.96 | 1.56 | 1.65 | 2.23 | 1.11 | 2.70 | 3.70 | 1.38 | 1.77 | 1.72 | **2.08** | 0.81 |
| Ho | 0.52 | 0.32 | 0.36 | 0.33 | 0.22 | 0.49 | 0.58 | 0.30 | 0.36 | 0.26 | **0.38** | 0.12 |
| Er | 1.32 | 0.70 | 0.89 | 1.83 | 0.67 | 1.56 | 0.94 | 0.61 | 1.12 | 0.75 | **1.04** | 0.41 |
| Tm | 0.10 | 0.14 | 0.22 | 0.15 | 0.13 | 0.22 | 0.10 | 0.09 | 0.14 | 0.09 | **0.14** | 0.05 |
| Yb | 1.56 | 0.69 | 1.58 | 1.46 | 0.29 | 1.83 | 1.74 | 0.42 | 0.79 | 0.94 | **1.13** | 0.57 |
| Lu | 0.16 | 0.15 | 0.11 | 0.11 | 0.03 | 0.15 | 0.12 | 0.17 | 0.40 | 0.16 | **0.16** | 0.09 |
| Hf | 3.62 | 1.63 | 1.51 | 3.79 | 1.30 | 2.67 | 2.48 | 2.59 | 2.33 | 1.92 | **2.39** | 0.84 |
| Ta | 2.37 | 0.57 | 0.54 | 1.65 | 0.25 | 1.21 | 1.47 | 0.89 | 0.94 | 0.09 | **1.00** | 0.70 |
| Th | 3.32 | 1.92 | 1.51 | 3.00 | 1.25 | 2.96 | 3.07 | 1.89 | 2.38 | 1.84 | **2.31** | 0.73 |
| U | 1.18 | 0.96 | 0.58 | 0.74 | 0.78 | 1.11 | 1.39 | 0.81 | 1.02 | 0.96 | **0.95** | 0.24 |

**Trace element concentrations of shards from the GRIP 2501.05 m tephra horizon. n = shard number and relates to the major oxide analyses from this horizon. All concentrations are presented as ppm. Mean and 1 standard deviations are shown.**

| GRIP 2501.05 m | | | | | | | | | | | | | | | | |
|---|---|---|---|---|---|---|---|---|---|---|---|---|---|---|---|---|
| n | 1 | 2 | 5 | 7 | 10 | 11 | 12 | 13 | 14 | 15 | 18 | 21 | 22 | 23 | **Mean** | St. Dev. |
| Sc | 14.75 | 20.78 | 19.23 | -2.80 | 33.52 | 9.77 | 27.60 | 10.12 | 19.44 | 26.45 | 30.86 | 27.98 | 39.71 | 29.15 | **21.9** | 11.2 |
| Rb | 12.76 | 16.59 | 10.54 | 13.21 | 6.28 | 6.08 | 5.41 | 5.16 | 8.12 | 6.05 | 8.04 | 7.64 | 4.92 | 7.86 | **8.48** | 3.53 |
| Sr | 498.25 | 423.75 | 680.95 | 297.09 | 327.88 | 125.33 | 323.41 | 161.81 | 207.30 | 351.71 | 383.00 | 356.27 | 408.06 | 385.14 | **352** | 139 |
| Y | 36.52 | 26.92 | 32.87 | 18.48 | 21.10 | 9.29 | 24.16 | 12.15 | 15.33 | 18.63 | 24.89 | 18.95 | 20.92 | 24.21 | **21.7** | 7.38 |
| Zr | 168.38 | 140.81 | 169.25 | 117.97 | 107.38 | 48.13 | 100.96 | 55.89 | 83.45 | 97.23 | 124.32 | 105.69 | 110.90 | 111.96 | **110** | 34.9 |
| Nb | 25.95 | 18.67 | 29.30 | 10.11 | 16.43 | 5.00 | 18.40 | 6.65 | 8.50 | 12.04 | 17.52 | 16.22 | 16.58 | 19.95 | **15.8** | 6.92 |
| Ba | 136.57 | 144.13 | 195.90 | 144.10 | 92.80 | 63.49 | 100.29 | 68.15 | 102.51 | 96.23 | 131.04 | 130.85 | 105.30 | 146.40 | **118** | 35.3 |
| La | 20.16 | 15.41 | 15.76 | 13.11 | 15.24 | 7.28 | 14.05 | 8.07 | 10.48 | 14.83 | 13.53 | 13.00 | 16.02 | 13.83 | **13.6** | 3.31 |
| Ce | 44.59 | 34.02 | 32.83 | 31.77 | 34.26 | 15.14 | 30.79 | 17.07 | 23.40 | 27.84 | 35.39 | 38.03 | 33.19 | 36.84 | **31.1** | 7.99 |
| Pr | 6.53 | 5.12 | 4.55 | 4.58 | 4.35 | 1.91 | 4.77 | 2.59 | 3.34 | 3.51 | 4.20 | 4.46 | 4.49 | 5.56 | **4.28** | 1.17 |
| Nd | 28.66 | 24.92 | 32.92 | 15.17 | 22.46 | 9.82 | 18.30 | 9.52 | 15.80 | 18.40 | 18.29 | 28.47 | 29.40 | 19.53 | **20.8** | 7.26 |
| Sm | 9.40 | 2.72 | 5.93 | 3.00 | 5.35 | 2.24 | 3.48 | 2.32 | 3.93 | 3.45 | 3.35 | 4.17 | 7.77 | 5.02 | **4.44** | 2.09 |
| Eu | 2.26 | 2.75 | 2.91 | 2.40 | 1.84 | 0.37 | 1.90 | 1.29 | 1.64 | 1.82 | 1.29 | 1.17 | 1.23 | 2.64 | **1.82** | 0.72 |
| Gd | 5.59 | 4.49 | 5.83 | 0.83 | 5.53 | 2.61 | 5.61 | 3.65 | 3.36 | 6.53 | 7.70 | 4.82 | 4.88 | 6.80 | **4.87** | 1.80 |
| Tb | 1.11 | 0.43 | 0.49 | 0.51 | 0.81 | 0.26 | 0.65 | 0.32 | 0.94 | 0.71 | 0.66 | 0.59 | 1.23 | 0.83 | **0.68** | 0.28 |
| Dy | 7.80 | 5.84 | 3.90 | 5.29 | 3.80 | 2.30 | 5.28 | 2.14 | 4.43 | 4.33 | 5.81 | 4.55 | 4.03 | 4.63 | **4.58** | 1.44 |
| Ho | 1.79 | 0.71 | 0.92 | 0.46 | 0.97 | 0.41 | 1.22 | 0.34 | 0.54 | 0.72 | 0.79 | 0.58 | 0.82 | 0.92 | **0.80** | 0.37 |
| Er | 3.10 | 3.11 | 3.05 | 2.16 | 3.26 | 1.31 | 2.39 | 1.21 | 1.35 | 2.78 | 2.81 | 2.42 | 1.71 | 2.02 | **2.33** | 0.72 |
| Tm | 0.74 | 0.37 | 0.33 | 0.44 | 0.33 | 0.11 | 0.20 | 0.34 | 0.39 | 0.44 | 0.21 | 0.17 | 0.34 | 0.33 | **0.34** | 0.15 |
| Yb | 3.48 | 1.39 | 1.30 | 1.63 | 2.81 | 0.75 | 1.64 | 0.64 | 0.74 | 1.30 | 1.26 | 2.46 | 1.98 | 2.93 | **1.74** | 0.88 |
| Lu | 0.29 | 0.30 | 0.56 | 0.34 | 0.37 | 0.07 | 0.21 | 0.15 | 0.15 | 0.28 | 0.32 | 0.47 | 0.23 | 0.24 | **0.28** | 0.13 |
| Hf | 3.06 | 3.00 | 6.14 | 2.37 | 4.08 | 1.59 | 2.45 | 1.38 | 2.72 | 2.99 | 3.50 | 2.93 | 3.27 | 3.14 | **3.04** | 1.13 |
| Ta | 1.58 | 0.64 | 1.29 | 0.65 | 0.85 | 0.40 | 0.99 | 0.24 | 0.66 | 0.93 | 1.53 | 0.78 | 1.12 | 1.44 | **0.93** | 0.42 |
| Th | 1.51 | 1.29 | 1.02 | 1.44 | 0.92 | 1.21 | 1.24 | 1.48 | 1.48 | 1.44 | 1.25 | 0.93 | 1.12 | 1.30 | **1.26** | 0.20 |
| U | 0.29 | 0.26 | 0.59 | 0.53 | 0.29 | 0.78 | 0.35 | 0.53 | 0.44 | 0.50 | 0.33 | 0.38 | 0.31 | 0.37 | **0.43** | 0.14 |

**Trace element concentrations of shards from the GRIP 2531.8 m tephra horizon. n = shard number and relates to the major oxide analyses from this horizon. All concentrations are presented as ppm. Mean and 1 standard deviations are shown.**

| GRIP 2531.8 m | | | | | | | | | | | | | | | | |
|---|---|---|---|---|---|---|---|---|---|---|---|---|---|---|---|---|
| n | 3 | 4 | 7 | 10 | 11 | 12 | 13 | 14 | 17 | 18 | 19 | 20 | 21 | 22 | **Mean** | St. Dev. |
| Sc | 18.75 | 19.71 | 14.17 | 19.69 | 15.14 | 7.11 | 46.74 | 12.51 | 12.56 | 5.88 | 23.90 | 23.13 | 20.93 | 19.12 | **18.5** | 9.80 |
| Rb | 19.57 | 18.88 | 20.18 | 22.88 | 29.46 | 30.67 | 24.34 | 28.16 | 28.78 | 35.79 | 33.91 | 20.41 | 19.80 | 19.16 | **25.1** | 5.88 |
| Sr | 670.33 | 670.57 | 746.13 | 815.47 | 698.05 | 731.16 | 709.29 | 731.89 | 725.64 | 528.08 | 759.62 | 508.96 | 424.95 | 562.41 | **663** | 113 |
| Y | 62.87 | 70.36 | 68.73 | 69.69 | 64.44 | 65.15 | 71.25 | 76.97 | 70.01 | 52.03 | 79.32 | 56.05 | 39.34 | 59.41 | **64.7** | 10.4 |
| Zr | 419.87 | 436.58 | 445.02 | 473.49 | 452.46 | 435.27 | 468.57 | 462.97 | 448.95 | 337.51 | 520.60 | 322.05 | 260.57 | 342.43 | **416** | 72.2 |
| Nb | 55.90 | 54.87 | 53.52 | 60.50 | 53.58 | 53.00 | 55.36 | 59.35 | 59.00 | 42.59 | 63.61 | 38.33 | 28.92 | 37.73 | **51.2** | 10.2 |
| Ba | 405.89 | 393.84 | 329.98 | 347.78 | 426.17 | 342.39 | 357.31 | 399.03 | 365.43 | 299.62 | 369.99 | 261.08 | 239.38 | 272.75 | **344** | 57.2 |
| La | 59.05 | 59.81 | 46.72 | 61.02 | 49.01 | 52.55 | 53.01 | 66.53 | 53.52 | 38.82 | 58.26 | 37.62 | 28.23 | 39.78 | **50.3** | 10.9 |
| Ce | 129.44 | 141.52 | 136.87 | 153.99 | 118.09 | 136.36 | 119.65 | 138.11 | 125.98 | 118.45 | 132.88 | 85.09 | 66.90 | 102.83 | **122** | 23.3 |
| Pr | 17.83 | 19.92 | 15.09 | 21.69 | 21.43 | 14.38 | 21.56 | 21.29 | 19.98 | 11.34 | 17.85 | 11.42 | 12.19 | 15.46 | **17.2** | 3.90 |
| Nd | 101.17 | 83.69 | 87.94 | 94.59 | 111.95 | 71.41 | 92.15 | 101.59 | 81.58 | 52.38 | 93.63 | 60.03 | 46.56 | 66.06 | **81.8** | 19.7 |
| Sm | 23.74 | 18.81 | 13.53 | 30.38 | 18.54 | 19.00 | 20.68 | 18.37 | 19.90 | 13.70 | 19.68 | 14.16 | 12.04 | 14.86 | **18.4** | 4.79 |
| Eu | 7.06 | 4.37 | 6.97 | 11.18 | 8.24 | 7.05 | 10.24 | 8.58 | 9.29 | 5.42 | 8.42 | 5.31 | 4.95 | 4.93 | **7.29** | 2.13 |
| Gd | 17.25 | 23.69 | 16.63 | 17.83 | 19.20 | 18.53 | 18.08 | 19.36 | 23.99 | 11.28 | 16.21 | 16.25 | 12.21 | 15.27 | **17.6** | 3.55 |
| Tb | 3.32 | 2.80 | 2.08 | 3.08 | 2.71 | 2.45 | 2.16 | 2.29 | 3.30 | 1.95 | 2.89 | 2.47 | 2.37 | 1.96 | **2.56** | 0.47 |
| Dy | 11.67 | 18.69 | 12.13 | 15.97 | 18.61 | 11.13 | 12.83 | 16.50 | 17.00 | 10.20 | 17.66 | 11.09 | 8.23 | 11.21 | **13.8** | 3.48 |
| Ho | 2.02 | 2.44 | 3.49 | 2.86 | 3.00 | 2.75 | 2.63 | 3.06 | 2.85 | 2.25 | 4.92 | 1.26 | 1.20 | 2.37 | **2.65** | 0.92 |
| Er | 5.91 | 7.43 | 5.30 | 5.82 | 7.15 | 8.34 | 7.08 | 7.69 | 6.80 | 5.07 | 5.70 | 5.62 | 3.45 | 5.07 | **6.17** | 1.30 |
| Tm | 0.70 | 1.16 | 0.61 | 0.96 | 0.69 | 1.34 | 0.73 | 0.80 | 0.64 | 0.63 | 0.70 | 0.80 | 0.49 | 0.36 | **0.76** | 0.25 |
| Yb | 3.51 | 8.97 | 5.47 | 6.08 | 5.85 | 5.23 | 4.80 | 5.09 | 4.27 | 4.30 | 5.45 | 3.64 | 3.10 | 5.65 | **5.10** | 1.44 |
| Lu | 0.93 | 0.55 | 0.69 | 0.90 | 0.77 | 0.51 | 0.78 | 1.33 | 1.02 | 0.54 | 0.68 | 0.66 | 0.48 | 0.46 | **0.74** | 0.24 |
| Hf | 11.46 | 13.91 | 7.85 | 11.20 | 10.15 | 11.37 | 12.79 | 11.69 | 9.19 | 5.70 | 10.16 | 8.43 | 5.94 | 6.79 | **9.76** | 2.54 |
| Ta | 3.50 | 2.89 | 3.48 | 3.40 | 3.68 | 2.48 | 3.61 | 3.46 | 4.44 | 2.06 | 3.51 | 2.26 | 1.57 | 2.85 | **3.09** | 0.77 |
| Th | 3.98 | 3.17 | 3.93 | 3.59 | 4.11 | 4.19 | 3.90 | 3.19 | 4.36 | 2.80 | 5.09 | 4.17 | 2.44 | 3.81 | **3.77** | 0.68 |
| U | 1.09 | 1.02 | 0.72 | 1.39 | 1.20 | 1.67 | 1.41 | 1.57 | 0.96 | 1.00 | 1.66 | 1.09 | 1.14 | 1.27 | **1.23** | 0.28 |

**Trace element concentrations of shards from the 2532.95 m tephra horizon. n = shard number and relates to the major oxide analyses from this horizon. All concentrations are presented as ppm. Mean and 1 standard deviations are shown.**

| GRIP 2532.95 m | | | | | | | | | | | | | | | | |
|---|---|---|---|---|---|---|---|---|---|---|---|---|---|---|---|---|
| n | 2 | 5 | 6 | 7 | 9 | 10 | 12 | 13 | 14 | 15 | 16 | 18 | 20 | 22 | **Mean** | St. Dev. |
| Sc | 48.12 | 26.25 | 51.51 | 25.20 | 11.85 | 0.15 | -4.43 | 19.06 | 11.59 | 17.13 | 6.90 | 3.83 | 32.45 | 14.68 | **18.9** | 16.6 |
| Rb | 22.90 | 20.90 | 13.37 | 24.92 | 20.49 | 21.26 | 29.84 | 31.74 | 21.23 | 19.57 | 24.42 | 11.99 | 28.78 | 12.98 | **21.7** | 6.10 |
| Sr | 250.01 | 345.68 | 225.14 | 490.39 | 325.31 | 289.24 | 285.29 | 416.91 | 301.97 | 292.41 | 158.68 | 70.67 | 363.18 | 404.06 | **301** | 107 |
| Y | 41.34 | 50.63 | 28.80 | 65.48 | 44.04 | 36.74 | 35.41 | 57.07 | 42.55 | 42.21 | 23.96 | 7.20 | 61.15 | 24.40 | **40.1** | 15.8 |
| Zr | 240.15 | 233.24 | 189.41 | 387.88 | 231.09 | 177.46 | 198.18 | 294.05 | 206.67 | 250.25 | 121.22 | 57.26 | 327.65 | 119.53 | **217** | 86.1 |
| Nb | 23.67 | 25.08 | 17.78 | 45.06 | 25.53 | 18.66 | 27.41 | 30.86 | 25.65 | 19.32 | 7.88 | 2.55 | 35.98 | 13.23 | **22.8** | 10.9 |
| Ba | 191.42 | 177.20 | 138.78 | 286.85 | 227.46 | 186.04 | 210.28 | 253.69 | 219.92 | 190.87 | 176.18 | 109.80 | 246.57 | 100.90 | **194** | 53.0 |
| La | 22.76 | 24.74 | 18.68 | 32.43 | 22.21 | 19.04 | 22.84 | 32.17 | 25.09 | 14.43 | 9.50 | 6.94 | 33.28 | 10.72 | **21.1** | 8.47 |
| Ce | 50.33 | 52.80 | 38.30 | 98.30 | 50.13 | 36.20 | 72.70 | 63.66 | 47.27 | 54.71 | 26.63 | 12.04 | 67.40 | 30.02 | **50.0** | 21.6 |
| Pr | 7.00 | 7.87 | 5.62 | 9.43 | 6.67 | 5.59 | 6.21 | 7.43 | 9.21 | 5.34 | 2.82 | 4.19 | 8.82 | 4.26 | **6.46** | 1.99 |
| Nd | 33.47 | 31.70 | 26.88 | 44.18 | 43.38 | 24.71 | 47.26 | 40.45 | 29.80 | 41.93 | 22.86 | 5.49 | 43.26 | 14.08 | **32.1** | 12.4 |
| Sm | 10.90 | 13.99 | 5.52 | 16.82 | 6.83 | 8.11 | 11.19 | 5.74 | 11.55 | 9.18 | 2.29 | 0.38 | 15.59 | 3.97 | **8.72** | 4.93 |
| Eu | 2.59 | 2.42 | 3.25 | 7.50 | 1.79 | 4.22 | 4.82 | 5.35 | 4.98 | 3.84 | 1.49 | 1.16 | 3.31 | 3.30 | **3.57** | 1.72 |
| Gd | 8.64 | 9.48 | 3.92 | 17.23 | 5.30 | 6.03 | 8.00 | 12.78 | 7.57 | 10.39 | 3.71 | 2.52 | 15.68 | 12.01 | **8.80** | 4.46 |
| Tb | 0.82 | 1.97 | 1.16 | 2.61 | 1.66 | 1.13 | 1.68 | 2.22 | 1.66 | 1.95 | 1.04 | 0.07 | 1.34 | 0.74 | **1.43** | 0.67 |
| Dy | 8.19 | 9.88 | 6.59 | 15.20 | 10.57 | 8.27 | 6.18 | 15.48 | 8.88 | 11.86 | 3.84 | 1.29 | 11.51 | 5.23 | **8.78** | 4.05 |
| Ho | 1.70 | 2.08 | 1.29 | 1.82 | 1.27 | 1.43 | 1.67 | 1.67 | 1.04 | 2.02 | 0.94 | 0.11 | 1.71 | 1.42 | **1.44** | 0.51 |
| E | 3.71 | 5.12 | 2.74 | 9.76 | 6.59 | 2.98 | 2.73 | 5.14 | 3.22 | 3.55 | 2.89 | 0.68 | 5.34 | 3.72 | **4.15** | 2.17 |
| Tm | 0.84 | 0.91 | 0.37 | 1.54 | 0.74 | 0.60 | 0.92 | 0.74 | 0.66 | 0.45 | 0.21 | 0.12 | 1.25 | 0.58 | **0.71** | 0.38 |
| Yb | 3.71 | 4.75 | 2.61 | 4.83 | 2.39 | 5.50 | 4.38 | 4.36 | 4.34 | 5.14 | 3.60 | 0.35 | 5.88 | 3.24 | **3.94** | 1.45 |
| Lu | 0.40 | 0.86 | 0.48 | 1.17 | 0.54 | 1.19 | 0.90 | 1.02 | 0.53 | 0.58 | 0.15 | 0.21 | 0.69 | 0.09 | **0.63** | 0.36 |
| Hf | 6.18 | 5.44 | 3.53 | 8.63 | 5.82 | 3.45 | 4.36 | 6.93 | 4.67 | 6.52 | 2.71 | 1.56 | 7.15 | 4.24 | **5.08** | 1.94 |
| Ta | 1.59 | 1.58 | 1.11 | 3.18 | 2.15 | 1.14 | 1.82 | 2.01 | 2.25 | 1.36 | 1.45 | 0.32 | 2.38 | 2.12 | **1.75** | 0.69 |
| Th | 2.60 | 2.44 | 1.35 | 3.04 | 2.63 | 2.79 | 2.83 | 2.45 | 2.43 | 1.65 | 2.64 | 2.12 | 3.31 | 1.44 | **2.41** | 0.58 |
| U | 1.02 | 1.04 | 0.32 | 1.05 | 1.12 | 0.93 | 1.00 | 1.04 | 1.15 | 0.78 | 1.03 | 0.76 | 0.85 | 0.09 | **0.87** | 0.31 |

# Appendix 5 – MD04-2822 Tephra Shard Counts and Geochemical Data

**Tephra shards per 0.5 g of dry weight sediment from the 25-80 µm grain size fraction of samples from the MD04-2822 marine core. Samples split into 2.3-2.5g/cm$^3$ and >2.5 g/cm$^3$ density fractions using heavy liquid density separation.**

| Sample Depth (cm) | 2.3-2.5 g/cm$^3$ (Colourless shards) | >2.5 g/cm$^3$ (Brown Shards) |
|---|---|---|
| 2201-2202 | 2 | 0 |
| 2203-2204 | 2 | 3 |
| 2205-2206 | 2 | 2 |
| 2207-2208 | 3 | 3 |
| 2209-2210 | 0 | 1 |
| 2211-2212 | 3 | 0 |
| 2213-2214 | 1 | 4 |
| 2215-2216 | 1 | 0 |
| 2217-2218 | 0 | 0 |
| 2219-2220 | 0 | 0 |
| 2221-2222 | 0 | 0 |
| 2223-2224 | 2 | 1 |
| 2225-2226 | 1 | 0 |
| 2227-2228 | 2 | 3 |
| 2229-2230 | 1 | 0 |
| 2231-2232 | 0 | 0 |
| 2233-2234 | 2 | 1 |
| 2235-2236 | 0 | 0 |
| 2237-2238 | 0 | 0 |
| 2239-2240 | 0 | 0 |
| 2241-2242 | 1 | 3 |
| 2243-2244 | 0 | 0 |
| 2245-2246 | 0 | 0 |
| 2247-2248 | 2 | 0 |
| 2249-2250 | 1 | 0 |
| 2251-2252 | 0 | 4 |
| 2253-2254 | 1 | 0 |
| 2255-2256 | 1 | 2 |
| 2257-2258 | 0 | 0 |
| 2259-2260 | 0 | 1 |
| 2261-2262 | 0 | 0 |
| 2263-2264 | 0 | 1 |
| 2265-2266 | 0 | 1 |
| 2267-2268 | 0 | 1 |
| 2269-2270 | 0 | 1 |
| 2271-2272 | 0 | 0 |
| 2273-2274 | 3 | 2 |
| 2275-2276 | 0 | 1 |
| 2277-2278 | 1 | 1 |
| 2279-2280 | 0 | 0 |
| 2281-2282 | 0 | 0 |
| 2283-2284 | 0 | 0 |
| 2285-2286 | 3 | 0 |
| 2287-2288 | 1 | 0 |
| 2289-2290 | 0 | 0 |
| 2291-2292 | 0 | 1 |

| Sample Depth (cm) | 2.3-2.5 g/cm$^3$ (Colourless shards) | >2.5 g/cm$^3$ (Brown Shards) |
|---|---|---|
| 2293-2294 | 0 | 0 |
| 2295-2296 | 1 | 2 |
| 2297-2298 | 0 | 2 |
| 2299-2300 | 0 | 0 |
| 2301-2302 | 0 | 1 |
| 2303-2304 | 0 | 0 |
| 2305-2306 | 0 | 0 |
| 2307-2308 | 0 | 0 |
| 2309-2310 | 0 | 1 |
| 2311-2312 | 0 | 2 |
| 2313-2314 | 0 | 0 |
| 2315-2316 | 1 | 1 |
| 2317-2318 | 13 | 0 |
| 2319-2320 | 17 | 0 |
| 2321-2322 | 5 | 1 |
| 2323-2324 | 15 | 1 |
| 2325-2326 | 5 | 0 |
| 2327-2328 | 531 | 1 |
| 2329-2330 | 2 | 0 |
| 2331-2332 | 5 | 1 |
| 2333-2334 | 4 | 0 |
| 2335-2336 | 4 | 1 |
| 2337-2338 | 9 | 0 |
| 2339-2340 | 18 | 1 |
| 2341-2342 | 5 | 0 |
| 2343-2344 | 4 | 0 |
| 2345-2346 | 10 | 0 |
| 2347-2348 | | 0 |
| 2349-2350 | 5 | 0 |
| 2351-2352 | 3 | 1 |
| 2353-2354 | 13 | 0 |
| 2355-2356 | 24 | 1 |
| 2357-2358 | 41 | 0 |
| 2359-2360 | 189 | 0 |
| 2361-2362 | 220 | 0 |
| 2363-2364 | 197 | 0 |
| 2365-2366 | 222 | 0 |
| 2367-2368 | 123 | 2 |
| 2369-2370 | 28 | 0 |
| 2371-2372 | 3 | 1 |
| 2373-2374 | 13 | 0 |
| 2375-2376 | 6 | 0 |
| 2377-2378 | 30 | 0 |
| 2379-2380 | 29 | 0 |

**Tephra shards per 0.5 g of dry weight sediment from the 80-125 μm and > 125 μm grain size fractions of samples from the MD04-2822 marine core. Samples were not density separated.**

| | 80-125 μm | | >125 μm | |
|---|---|---|---|---|
| Sample Depth (cm) | Colourless Shards | Brown Shards | Colourless Shards | Brown Shards |
| 2225-2226 | 0 | 0 | 0 | 0 |
| 2227-2228 | 0 | 0 | 0 | 0 |
| 2229-2230 | 1 | 0 | 0 | 0 |
| 2231-2232 | 0 | 0 | 0 | 0 |
| 2233-2234 | 0 | 0 | 0 | 0 |
| 2235-2236 | 0 | 0 | 0 | 0 |
| 2237-2238 | 0 | 0 | 0 | 0 |
| 2239-2240 | 0 | 0 | 0 | 0 |
| 2241-2242 | 0 | 0 | 0 | 0 |
| 2243-2244 | 0 | 0 | 0 | 0 |
| 2245-2246 | 0 | 0 | 1 | 0 |
| 2247-2248 | 0 | 0 | 0 | 0 |
| 2249-2250 | 0 | 0 | 0 | 0 |
| 2251-2252 | 0 | 0 | 0 | 0 |
| 2253-2254 | 0 | 0 | 0 | 0 |
| 2255-2256 | 0 | 0 | 0 | 0 |
| 2257-2258 | 0 | 0 | 0 | 0 |
| 2259-2260 | 0 | 0 | 0 | 0 |
| | | | | |
| 2315-2316 | 0 | 0 | 0 | 0 |
| 2317-2318 | 0 | 0 | 0 | 0 |
| 2319-2320 | 0 | 0 | 0 | 0 |
| 2321-2322 | 0 | 0 | 0 | 0 |
| 2323-2324 | 1 | 0 | 0 | 0 |
| 2325-2326 | 0 | 0 | 0 | 0 |
| 2327-2328 | 10 | 0 | 4 | 0 |
| 2329-2330 | 0 | 0 | 0 | 0 |
| 2331-2332 | 0 | 0 | 0 | 0 |
| 2333-2334 | 0 | 0 | 0 | 0 |
| 2335-2336 | 0 | 0 | 1 | 0 |
| | | | | |
| 2355-2356 | 0 | 0 | 0 | 0 |
| 2357-2358 | 0 | 0 | 0 | 0 |
| 2359-2360 | 2 | 0 | 0 | 0 |
| 2361-2362 | 0 | 0 | 0 | 0 |
| 2363-2364 | 1 | 0 | 0 | 0 |
| 2365-2366 | 0 | 0 | 0 | 0 |
| | | | | |
| 2371-2372 | 1 | 0 | 0 | 0 |
| 2373-2374 | 0 | 0 | 0 | 0 |
| 2375-2376 | 0 | 0 | 0 | 0 |
| 2377-2378 | 0 | 0 | 0 | 0 |
| 2379-2380 | 0 | 0 | 0 | 0 |

**Major oxide concentrations of shards from the MD04-2822 2327-2328 cm sample. n = number of shards analysed. Mean and 1 standard deviations are shown. All oxides are presented as weight %. Total iron is expressed as FeO.**

| n | $SiO_2$ | $TiO_2$ | $Al_2O_3$ | FeO | MnO | MgO | CaO | $Na_2O$ | $K_2O$ | $P_2O_5$ | Cl | Total |
|---|---|---|---|---|---|---|---|---|---|---|---|---|
| **MD04-2822 2327-2328 cm – Population 1** | | | | | | | | | | | | |
| 1 | 70.31 | 0.28 | 11.74 | 2.66 | 0.18 | 0.04 | 0.56 | 4.41 | 3.41 | -0.01 | 0.14 | 93.73 |
| 2 | 70.72 | 0.17 | 11.70 | 2.48 | 0.12 | 0.04 | 0.54 | 4.45 | 3.41 | 0.01 | 0.14 | 93.77 |
| 3 | 70.37 | 0.04 | 11.71 | 2.53 | 0.23 | 0.02 | 0.56 | 4.68 | 3.60 | 0.00 | 0.13 | 93.87 |
| 4 | 69.82 | 0.34 | 11.66 | 2.81 | 0.16 | 0.03 | 0.56 | 4.52 | 3.45 | -0.03 | 0.13 | 93.49 |
| 5 | 70.41 | 0.32 | 11.68 | 2.49 | 0.07 | 0.04 | 0.53 | 4.65 | 3.54 | -0.02 | 0.12 | 93.85 |
| 6 | 70.36 | 0.25 | 11.64 | 2.46 | 0.21 | 0.03 | 0.59 | 4.61 | 3.32 | 0.00 | 0.12 | 93.60 |
| 7 | 69.82 | 0.25 | 11.60 | 2.62 | 0.16 | 0.05 | 0.55 | 4.65 | 3.49 | 0.00 | 0.14 | 93.33 |
| 8 | 71.33 | 0.19 | 11.61 | 2.56 | 0.24 | 0.03 | 0.54 | 4.53 | 3.52 | 0.02 | 0.15 | 94.73 |
| 9 | 70.51 | 0.19 | 11.49 | 2.90 | -0.06 | 0.05 | 0.51 | 4.63 | 3.61 | -0.02 | 0.16 | 94.03 |
| 10 | 67.55 | 0.24 | 11.99 | 2.49 | 0.10 | 0.04 | 0.54 | 4.56 | 3.36 | 0.01 | 0.14 | 91.02 |
| **Mean** | **70.12** | **0.23** | **11.68** | **2.60** | **0.14** | **0.04** | **0.55** | **4.57** | **3.47** | **0.00** | **0.14** | **93.54** |
| St. Dev. | 1.00 | 0.09 | 0.13 | 0.15 | 0.09 | 0.01 | 0.02 | 0.09 | 0.10 | 0.02 | 0.01 | 0.96 |
| **MD04-2822 2327-2328 cm – Population 2** | | | | | | | | | | | | |
| 1 | 70.39 | -0.12 | 12.55 | 2.24 | 0.10 | 0.11 | 0.80 | 4.20 | 3.65 | 0.01 | 0.21 | 94.26 |
| 2 | 70.51 | 0.09 | 12.53 | 1.91 | 0.16 | 0.09 | 0.70 | 4.02 | 3.82 | 0.02 | 0.19 | 94.03 |
| 3 | 70.05 | 0.04 | 12.39 | 2.00 | 0.03 | 0.11 | 0.74 | 3.93 | 3.86 | -0.02 | 0.17 | 93.32 |
| 4 | 70.20 | 0.20 | 12.50 | 2.04 | 0.00 | 0.14 | 0.79 | 4.35 | 3.66 | 0.02 | 0.22 | 94.11 |
| 5 | 70.54 | 0.15 | 12.51 | 2.21 | 0.08 | 0.13 | 0.77 | 4.29 | 3.73 | 0.00 | 0.19 | 94.60 |
| 6 | 70.36 | 0.25 | 12.08 | 2.09 | -0.02 | 0.10 | 0.72 | 3.99 | 3.56 | 0.05 | 0.18 | 93.38 |
| 7 | 68.28 | 0.16 | 11.93 | 2.01 | 0.14 | 0.15 | 0.73 | 4.19 | 3.62 | 0.06 | 0.26 | 91.52 |
| Mean | 70.05 | 0.11 | 12.35 | 2.07 | 0.07 | 0.12 | 0.75 | 4.14 | 3.70 | 0.02 | 0.20 | 93.60 |
| St. Dev. | 0.80 | 0.12 | 0.25 | 0.12 | 0.07 | 0.02 | 0.04 | 0.16 | 0.11 | 0.03 | 0.03 | 1.03 |

**Major oxide concentrations of shards from the MD04-2822 2359-2360 cm sample. n = number of shards analysed. Mean and 1 standard deviations are shown. All oxides are presented as weight %. Total iron is expressed as FeO.**

| n | $SiO_2$ | $TiO_2$ | $Al_2O_3$ | FeO | MnO | MgO | CaO | $Na_2O$ | $K_2O$ | $P_2O_5$ | Cl | Total |
|---|---|---|---|---|---|---|---|---|---|---|---|---|
| **MD04-2822 2359-2360 cm** | | | | | | | | | | | | |
| 1 | 74.75 | 0.06 | 11.12 | 1.17 | -0.13 | 0.01 | 0.72 | 3.94 | 3.03 | -0.01 | 0.04 | 94.84 |
| 2 | 74.63 | -0.07 | 11.38 | 1.29 | 0.20 | -0.01 | 0.76 | 3.97 | 3.04 | 0.00 | 0.06 | 95.33 |
| 3 | 74.30 | 0.02 | 11.33 | 1.35 | -0.02 | 0.00 | 0.77 | 4.11 | 2.98 | 0.00 | 0.07 | 94.93 |
| 4 | 74.04 | 0.03 | 11.41 | 1.34 | 0.17 | -0.02 | 0.93 | 4.10 | 2.89 | 0.00 | 0.05 | 94.96 |
| 5 | 73.93 | 0.14 | 11.42 | 1.20 | 0.04 | 0.00 | 0.81 | 4.09 | 3.01 | 0.01 | 0.06 | 94.69 |
| 6 | 73.89 | 0.06 | 11.30 | 1.36 | -0.02 | 0.00 | 0.88 | 3.93 | 2.95 | 0.00 | 0.08 | 94.45 |
| 7 | 73.88 | 0.19 | 11.53 | 0.30 | 0.11 | -0.02 | 0.58 | 3.91 | 2.79 | -0.03 | 0.04 | 93.32 |
| 8 | 73.87 | 0.11 | 11.30 | 1.17 | 0.28 | 0.00 | 0.89 | 3.89 | 2.96 | -0.02 | 0.06 | 94.53 |
| 9 | 73.67 | 0.12 | 11.32 | 1.72 | 0.12 | 0.01 | 0.91 | 4.05 | 3.11 | 0.00 | 0.05 | 95.08 |
| 10 | 73.66 | 0.04 | 11.55 | 1.29 | 0.09 | 0.00 | 0.89 | 3.74 | 2.93 | 0.00 | 0.07 | 94.26 |
| 11 | 73.62 | 0.21 | 11.26 | 1.43 | 0.02 | 0.01 | 0.85 | 3.83 | 2.87 | -0.01 | 0.04 | 94.13 |
| 12 | 73.60 | 0.00 | 11.31 | 1.26 | 0.08 | 0.00 | 0.81 | 3.74 | 2.99 | 0.02 | 0.05 | 93.87 |
| 13 | 73.50 | 0.07 | 11.60 | 1.36 | -0.03 | 0.00 | 0.91 | 3.93 | 2.97 | -0.01 | 0.07 | 94.41 |
| 14 | 73.41 | 0.19 | 11.57 | 1.30 | 0.10 | 0.01 | 0.79 | 3.75 | 2.85 | 0.01 | 0.05 | 94.03 |
| 15 | 73.39 | 0.08 | 11.36 | 1.32 | 0.08 | 0.01 | 0.86 | 3.96 | 2.92 | 0.00 | 0.04 | 94.02 |
| 16 | 73.29 | 0.07 | 11.40 | 1.65 | 0.01 | 0.02 | 0.87 | 3.68 | 2.83 | 0.01 | 0.06 | 93.89 |
| **Mean** | **73.84** | **0.08** | **11.39** | **1.28** | **0.07** | **0.00** | **0.83** | **3.91** | **2.95** | **0.00** | **0.05** | **94.42** |
| St.Dev. | 0.42 | 0.07 | 0.13 | 0.30 | 0.10 | 0.01 | 0.09 | 0.14 | 0.08 | 0.01 | 0.01 | 0.53 |

**Major oxide concentrations of shards from the MD04-2822 2361-2362 cm sample. n = number of shards analysed. Mean and 1 standard deviations are shown. All oxides are presented as weight %. Total iron is expressed as FeO.**

| n | $SiO_2$ | $TiO_2$ | $Al_2O_3$ | FeO | MnO | MgO | CaO | $Na_2O$ | $K_2O$ | $P_2O_5$ | Cl | Total |
|---|---|---|---|---|---|---|---|---|---|---|---|---|
| **MD04-2822 2361-2362 cm** | | | | | | | | | | | | |
| 1 | 73.57 | 0.15 | 11.21 | 1.18 | 0.04 | 0.00 | 0.88 | 3.96 | 3.01 | 0.00 | 0.06 | 94.05 |
| 2 | 73.30 | 0.00 | 11.44 | 1.15 | 0.10 | 0.01 | 0.85 | 3.93 | 3.00 | -0.02 | 0.06 | 93.83 |
| 3 | 72.45 | 0.23 | 11.05 | 1.26 | 0.13 | 0.00 | 0.91 | 3.96 | 2.95 | -0.04 | 0.05 | 92.98 |
| 4 | 73.78 | 0.05 | 11.46 | 1.09 | 0.06 | 0.00 | 0.87 | 4.06 | 3.00 | 0.00 | 0.05 | 94.42 |
| 5 | 73.65 | 0.13 | 11.18 | 1.49 | -0.02 | 0.00 | 0.84 | 4.00 | 2.91 | 0.00 | 0.06 | 94.28 |
| 6 | 73.96 | 0.02 | 11.43 | 1.18 | 0.00 | 0.01 | 0.86 | 3.93 | 3.26 | -0.01 | 0.07 | 94.71 |
| 7 | 74.22 | 0.11 | 11.35 | 1.10 | -0.08 | -0.01 | 0.82 | 3.81 | 3.19 | -0.01 | 0.07 | 94.66 |
| 8 | 73.95 | 0.04 | 11.27 | 0.95 | -0.10 | 0.00 | 0.70 | 3.95 | 3.07 | 0.00 | 0.05 | 93.97 |
| 9 | 73.54 | 0.13 | 11.09 | 1.14 | 0.20 | -0.01 | 0.73 | 3.91 | 3.09 | -0.02 | 0.06 | 93.88 |
| 10 | 73.77 | 0.15 | 11.24 | 1.34 | 0.05 | 0.01 | 0.90 | 4.02 | 3.04 | -0.04 | 0.04 | 94.56 |
| 11 | 73.76 | 0.03 | 11.26 | 1.24 | -0.02 | 0.01 | 0.78 | 4.02 | 3.13 | -0.01 | 0.04 | 94.26 |
| 12 | 73.97 | 0.15 | 11.27 | 1.29 | 0.22 | 0.00 | 0.62 | 3.97 | 3.22 | 0.00 | 0.04 | 94.74 |
| 13 | 73.28 | 0.11 | 11.08 | 1.21 | -0.06 | 0.01 | 0.93 | 3.90 | 2.96 | 0.02 | 0.08 | 93.56 |
| 14 | 74.08 | 0.12 | 11.44 | 1.22 | -0.06 | 0.01 | 0.81 | 4.10 | 3.07 | -0.02 | 0.04 | 94.88 |
| 15 | 73.04 | 0.07 | 11.37 | 1.11 | 0.07 | 0.01 | 0.92 | 4.06 | 2.96 | 0.02 | 0.06 | 93.67 |
| 16 | 73.65 | 0.05 | 11.11 | 1.17 | -0.03 | 0.01 | 0.93 | 4.07 | 2.95 | 0.00 | 0.08 | 94.03 |
| 17 | 72.63 | 0.11 | 11.00 | 1.38 | 0.08 | -0.01 | 1.00 | 4.03 | 2.94 | -0.03 | 0.05 | 93.23 |
| 18 | 74.16 | 0.05 | 11.29 | 1.34 | -0.06 | 0.00 | 0.94 | 4.02 | 3.04 | -0.02 | 0.03 | 94.88 |
| 19 | 73.79 | 0.06 | 11.33 | 1.40 | -0.06 | 0.00 | 0.95 | 4.07 | 2.91 | 0.02 | 0.06 | 94.58 |
| 20 | 73.02 | 0.12 | 11.21 | 1.41 | 0.20 | 0.02 | 0.93 | 3.88 | 2.91 | -0.01 | 0.06 | 93.75 |
| 21 | 73.21 | 0.20 | 11.30 | 1.52 | 0.10 | 0.00 | 0.84 | 3.80 | 2.95 | 0.03 | 0.06 | 94.01 |
| 22 | 73.84 | 0.04 | 11.30 | 1.57 | 0.12 | -0.01 | 0.85 | 4.13 | 3.00 | 0.00 | 0.04 | 94.90 |
| 23 | 73.86 | 0.17 | 11.23 | 1.39 | -0.07 | 0.00 | 0.83 | 3.92 | 3.17 | -0.02 | 0.06 | 94.63 |
| 24 | 73.27 | 0.01 | 11.13 | 1.35 | -0.08 | 0.00 | 0.96 | 4.14 | 2.97 | -0.02 | 0.04 | 93.88 |
| 25 | 73.74 | 0.08 | 11.54 | 1.54 | 0.13 | -0.01 | 0.92 | 4.06 | 2.98 | 0.00 | 0.05 | 95.06 |
| **Mean** | **73.58** | **0.09** | **11.26** | **1.28** | **0.03** | **0.00** | **0.86** | **3.99** | **3.03** | **-0.01** | **0.05** | **94.22** |
| St. Dev. | 0.46 | 0.06 | 0.14 | 0.16 | 0.10 | 0.01 | 0.09 | 0.09 | 0.10 | 0.02 | 0.01 | 0.55 |

**Major oxide concentrations of shards from the MD04-2822 2363-2364 cm sample. n = number of shards analysed. Mean and 1 standard deviations are shown. All oxides are presented as weight %. Total iron is expressed as FeO.**

| n | $SiO_2$ | $TiO_2$ | $Al_2O_3$ | FeO | MnO | MgO | CaO | $Na_2O$ | $K_2O$ | $P_2O_5$ | Cl | Total |
|---|---|---|---|---|---|---|---|---|---|---|---|---|
| **MD04-2822 2363-2364 cm** | | | | | | | | | | | | |
| 1 | 73.96 | 0.10 | 11.31 | 1.53 | 0.14 | -0.01 | 0.90 | 4.15 | 3.14 | -0.01 | 0.05 | 95.30 |
| 2 | 73.19 | 0.07 | 11.44 | 1.31 | 0.06 | 0.01 | 0.94 | 3.92 | 2.97 | -0.03 | 0.07 | 93.99 |
| 3 | 73.29 | 0.00 | 11.44 | 1.07 | 0.01 | 0.02 | 0.68 | 3.89 | 3.03 | -0.01 | 0.07 | 93.48 |
| 4 | 74.56 | 0.08 | 11.20 | 0.72 | -0.08 | 0.00 | 0.74 | 4.34 | 2.70 | 0.00 | 0.07 | 94.40 |
| 5 | 73.35 | 0.08 | 11.27 | 1.23 | -0.03 | 0.00 | 0.75 | 3.80 | 3.21 | -0.03 | 0.07 | 93.77 |
| 6 | 73.49 | 0.08 | 11.18 | 1.48 | 0.02 | -0.01 | 0.93 | 4.06 | 2.86 | 0.02 | 0.09 | 94.20 |
| 7 | 72.39 | 0.10 | 11.11 | 1.20 | 0.15 | 0.00 | 0.95 | 4.04 | 3.00 | -0.01 | 0.09 | 93.03 |
| 8 | 73.96 | 0.07 | 11.15 | 1.22 | 0.03 | 0.01 | 0.84 | 4.18 | 3.10 | -0.03 | 0.06 | 94.62 |
| 9 | 74.33 | 0.13 | 11.30 | 1.28 | 0.17 | 0.00 | 0.81 | 4.00 | 3.14 | -0.01 | 0.05 | 95.23 |
| 10 | 73.88 | 0.08 | 11.23 | 0.92 | 0.00 | 0.00 | 0.82 | 4.12 | 3.02 | 0.03 | 0.05 | 94.14 |
| 11 | 73.32 | 0.11 | 11.10 | 1.40 | 0.03 | 0.00 | 0.93 | 3.91 | 3.02 | 0.00 | 0.06 | 93.88 |
| 12 | 73.93 | 0.03 | 11.43 | 1.25 | 0.11 | 0.00 | 0.88 | 4.10 | 2.94 | -0.02 | 0.06 | 94.74 |
| 13 | 74.34 | 0.15 | 11.23 | 1.22 | 0.13 | -0.01 | 0.91 | 3.91 | 3.01 | 0.02 | 0.06 | 94.98 |
| 14 | 73.66 | 0.06 | 11.36 | 1.55 | -0.02 | 0.00 | 0.90 | 4.17 | 3.06 | -0.02 | 0.06 | 94.81 |
| 15 | 72.12 | 0.12 | 11.05 | 2.09 | 0.25 | 0.01 | 1.37 | 3.92 | 3.14 | -0.01 | 0.08 | 94.16 |
| 16 | 72.75 | 0.09 | 11.23 | 1.57 | 0.02 | 0.00 | 0.92 | 3.80 | 2.93 | -0.01 | 0.08 | 93.39 |
| 17 | 72.96 | -0.02 | 11.29 | 1.16 | 0.06 | 0.02 | 0.85 | 4.00 | 2.95 | 0.00 | 0.05 | 93.34 |
| 18 | 73.24 | 0.22 | 11.21 | 1.29 | -0.01 | 0.01 | 0.77 | 4.17 | 3.14 | 0.00 | 0.08 | 94.14 |
| 19 | 72.10 | 0.04 | 11.08 | 1.11 | 0.03 | 0.01 | 0.92 | 4.25 | 3.12 | 0.02 | 0.07 | 92.76 |
| 20 | 73.31 | 0.11 | 11.32 | 1.08 | -0.03 | -0.01 | 0.86 | 3.99 | 3.00 | -0.02 | 0.06 | 93.73 |
| 21 | 73.30 | 0.13 | 11.26 | 1.47 | 0.04 | 0.00 | 0.93 | 3.93 | 3.00 | -0.03 | 0.05 | 94.13 |
| 22 | 73.96 | 0.11 | 11.15 | 0.78 | -0.10 | 0.00 | 0.68 | 4.09 | 3.22 | -0.01 | 0.08 | 94.08 |
| 23 | 73.31 | 0.07 | 11.36 | 1.28 | 0.07 | 0.00 | 0.82 | 4.07 | 3.05 | -0.02 | 0.08 | 94.12 |
| 24 | 73.45 | 0.03 | 11.28 | 1.41 | -0.02 | 0.00 | 0.87 | 4.01 | 3.13 | -0.02 | 0.05 | 94.22 |
| **Mean** | **73.42** | **0.09** | **11.25** | **1.28** | **0.04** | **0.00** | **0.87** | **4.03** | **3.04** | **-0.01** | **0.07** | **94.11** |
| St. Dev. | 0.65 | 0.05 | 0.11 | 0.28 | 0.08 | 0.01 | 0.13 | 0.14 | 0.12 | 0.02 | 0.01 | 0.64 |

**Major oxide concentrations of shards from the MD04-2822 2365-2366 cm sample. n = number of shards analysed. Mean and 1 standard deviations are shown. All oxides are presented as weight %. Total iron is expressed as FeO.**

| n | $SiO_2$ | $TiO_2$ | $Al_2O_3$ | FeO | MnO | MgO | CaO | $Na_2O$ | $K_2O$ | $P_2O_5$ | Cl | Total |
|---|---|---|---|---|---|---|---|---|---|---|---|---|
| **MD04-2822 2365-2366 cm** | | | | | | | | | | | | |
| 1 | 74.02 | 0.03 | 11.58 | 1.21 | 0.01 | 0.00 | 0.97 | 3.97 | 3.01 | -0.04 | 0.06 | 94.87 |
| 2 | 73.58 | 0.06 | 11.28 | 1.40 | -0.08 | 0.01 | 0.94 | 3.99 | 2.86 | 0.01 | 0.07 | 94.21 |
| 3 | 73.55 | 0.05 | 11.45 | 1.52 | 0.09 | 0.00 | 0.97 | 4.03 | 3.11 | -0.01 | 0.06 | 94.82 |
| 4 | 73.41 | -0.02 | 11.40 | 1.33 | 0.00 | -0.01 | 0.88 | 4.06 | 3.08 | -0.03 | 0.08 | 94.24 |
| 5 | 74.27 | 0.08 | 11.44 | 1.32 | 0.06 | -0.01 | 0.74 | 3.96 | 3.17 | -0.02 | 0.05 | 95.09 |
| 6 | 73.67 | 0.05 | 11.46 | 1.36 | 0.02 | 0.01 | 0.88 | 4.06 | 3.12 | -0.02 | 0.03 | 94.66 |
| 7 | 71.87 | 0.20 | 11.05 | 1.13 | 0.01 | -0.01 | 0.91 | 3.97 | 3.02 | -0.03 | 0.08 | 92.23 |
| 8 | 73.47 | 0.05 | 11.30 | 1.48 | -0.05 | 0.00 | 0.90 | 4.03 | 2.97 | 0.00 | 0.06 | 94.26 |
| 9 | 73.46 | 0.18 | 11.23 | 1.34 | -0.07 | 0.01 | 0.91 | 3.93 | 3.12 | -0.01 | 0.07 | 94.25 |
| 10 | 74.03 | 0.08 | 11.25 | 1.41 | 0.00 | 0.02 | 0.98 | 4.07 | 3.02 | -0.02 | 0.06 | 94.91 |
| 11 | 73.83 | -0.06 | 11.39 | 1.31 | 0.00 | 0.01 | 0.89 | 4.00 | 3.01 | -0.04 | 0.06 | 94.49 |
| 12 | 73.25 | 0.14 | 11.40 | 1.44 | 0.00 | 0.01 | 0.92 | 3.97 | 2.99 | 0.01 | 0.05 | 94.17 |
| 13 | 73.73 | 0.05 | 11.30 | 1.33 | 0.18 | 0.01 | 0.86 | 3.91 | 3.09 | 0.00 | 0.06 | 94.52 |
| 14 | 74.09 | 0.17 | 11.48 | 1.45 | 0.06 | 0.00 | 0.92 | 4.03 | 3.02 | 0.01 | 0.06 | 95.29 |
| 15 | 73.45 | 0.07 | 11.43 | 1.24 | 0.09 | 0.00 | 0.88 | 4.04 | 2.97 | 0.00 | 0.04 | 94.20 |
| 16 | 73.83 | 0.07 | 11.27 | 1.19 | 0.08 | -0.01 | 0.92 | 4.02 | 3.06 | -0.01 | 0.06 | 94.51 |
| 17 | 73.16 | 0.16 | 11.44 | 1.60 | 0.06 | 0.00 | 0.87 | 4.03 | 3.03 | 0.00 | 0.05 | 94.40 |
| 18 | 73.97 | 0.14 | 11.53 | 1.35 | 0.07 | 0.01 | 0.76 | 3.94 | 3.36 | 0.00 | 0.07 | 95.20 |
| **Mean** | **73.59** | **0.08** | **11.37** | **1.36** | **0.03** | **0.00** | **0.90** | **4.00** | **3.06** | **-0.01** | **0.06** | **94.46** |
| St. Dev. | 0.53 | 0.07 | 0.13 | 0.12 | 0.06 | 0.01 | 0.06 | 0.05 | 0.11 | 0.02 | 0.01 | 0.67 |

**Trace element concentrations of shards from the MD04-2822 2327-2328 cm sample. n = shard number and relates to the major oxide analyses from this horizon. All concentrations are presented as ppm. Mean and 1 standard deviations are shown.**

| MD04-2822 2327-2328 cm – Population 1 | | | | | |
|---|---|---|---|---|---|
| n | 4 | 5 | 7 | **Mean** | St. Dev. |
| Sc | 25.37 | 10.45 | 12.00 | **15.9** | 8.21 |
| Rb | 139.81 | 180.13 | 144.94 | **155** | 22.0 |
| Sr | 54.00 | 56.05 | 61.88 | **57.3** | 4.09 |
| Y | 142.20 | 166.70 | 161.93 | **157** | 13.0 |
| Zr | 942.72 | 1156.04 | 1118.76 | **1073** | 114 |
| Nb | 189.21 | 236.17 | 211.95 | **212** | 23.5 |
| Cs | 3.39 | 2.90 | 2.09 | **2.80** | 0.66 |
| Ba | 926.82 | 1126.83 | 1097.96 | **1051** | 108 |
| La | 150.72 | 186.19 | 173.75 | **170** | 18.0 |
| Ce | 288.51 | 348.09 | 326.21 | **321** | 30.1 |
| Pr | 36.30 | 42.54 | 39.01 | **39.3** | 3.13 |
| Nd | 142.43 | 164.37 | 176.77 | **161** | 17.4 |
| Sm | 28.63 | 36.83 | 28.19 | **31.2** | 4.87 |
| Eu | 3.89 | 6.30 | 3.82 | **4.67** | 1.41 |
| Gd | 24.27 | 30.69 | 26.00 | **27.0** | 3.32 |
| Tb | 3.39 | 4.83 | 4.73 | **4.31** | 0.80 |
| Dy | 21.94 | 28.59 | 29.14 | **26.6** | 4.01 |
| Ho | 5.95 | 6.31 | 6.03 | **6.09** | 0.19 |
| Er | 12.78 | 17.85 | 18.49 | **16.4** | 3.13 |
| Tm | 2.25 | 2.61 | 2.04 | **2.30** | 0.29 |
| Yb | 13.37 | 18.47 | 16.22 | **16.0** | 2.56 |
| Lu | 2.02 | 2.62 | 1.93 | **2.19** | 0.37 |
| Hf | 24.98 | 34.48 | 32.05 | **30.5** | 4.94 |
| Ta | 12.42 | 15.52 | 13.45 | **13.8** | 1.58 |
| Th | 18.71 | 22.12 | 23.39 | **21.4** | 2.42 |
| U | 4.49 | 5.87 | 8.05 | **6.14** | 1.79 |

| MD04-2822 2327-2328 cm – Population 2 | | | | |
|---|---|---|---|---|
| n | 2 | 4 | **Mean** | St. Dev. |
| Sc | 23.53 | 10.15 | **16.8** | 9.46 |
| Rb | 167.09 | 155.33 | **161** | 8.32 |
| Sr | 77.58 | 62.03 | **69.8** | 11.0 |
| Y | 115.70 | 128.47 | **122** | 9.03 |
| Zr | 532.24 | 574.19 | **553** | 30.0 |
| Nb | 92.41 | 96.02 | **94.2** | 2.55 |
| Cs | 1.47 | 0.98 | **1.22** | 0.34 |
| Ba | 1423.52 | 1550.02 | **1487** | 89.4 |
| La | 105.54 | 115.71 | **111** | 7.20 |
| Ce | 211.08 | 226.24 | **219** | 10.7 |
| Pr | 23.78 | 26.60 | **25.2** | 2.00 |
| Nd | 95.29 | 112.21 | **104** | 12.0 |
| Sm | 24.69 | 25.14 | **24.9** | 0.32 |
| Eu | 4.46 | 5.33 | **4.89** | 0.62 |
| Gd | 17.75 | 21.42 | **19.6** | 2.59 |
| Tb | 2.97 | 3.14 | **3.06** | 0.12 |
| Dy | 18.68 | 24.06 | **21.4** | 3.81 |
| Ho | 4.08 | 3.94 | **4.01** | 0.10 |
| Er | 11.65 | 13.69 | **12.7** | 1.44 |
| Tm | 1.67 | 1.68 | **1.67** | 0.01 |
| Yb | 12.07 | 14.13 | **13.1** | 1.46 |
| Lu | 1.57 | 1.74 | **1.66** | 0.12 |
| Hf | 16.94 | 15.90 | **16.4** | 0.73 |
| Ta | 6.40 | 6.69 | **6.54** | 0.21 |
| Th | 16.69 | 18.29 | **17.5** | 1.14 |
| U | 3.85 | 4.44 | **4.15** | 0.42 |

**Trace element concentrations of shards from the MD04-2822 2359-2360 cm sample. n = shard number and relates to the major oxide analyses from this horizon. All concentrations are presented as ppm. Mean and 1 standard deviations are shown.**

| MD04-2822 2359-2360 cm | | | | | | | | | | | | |
|---|---|---|---|---|---|---|---|---|---|---|---|---|
| n | 2 | 3 | 4 | 6 | 7 | 9 | 10 | 11 | 13 | 15 | **Mean** | St. Dev. |
| Rb | 120.16 | 120.25 | 116.33 | 123.21 | 167.67 | 139.92 | 128.71 | 119.75 | 129.67 | 239.30 | **141** | 37.9 |
| Sr | 110.21 | 112.71 | 108.97 | 112.72 | 118.47 | 115.32 | 114.74 | 109.77 | 104.37 | | **112** | 4.14 |
| Y | 145.15 | 138.37 | 146.84 | 152.31 | 140.76 | 151.66 | 156.33 | 181.31 | 156.46 | 125.35 | **149** | 14.6 |
| Zr | 273.14 | 263.88 | 269.77 | 270.59 | 303.99 | 310.74 | 279.23 | 336.74 | 282.09 | 303.60 | **289** | 23.3 |
| Nb | 94.56 | 92.26 | 104.30 | 90.56 | 94.80 | 94.38 | 93.56 | 100.46 | 92.85 | 69.13 | **92.7** | 9.23 |
| Cs | 1.68 | 0.89 | 6.15 | 2.13 | 2.11 | 2.69 | 2.41 | 1.54 | 1.92 | 14.75 | **3.63** | 4.16 |
| Ba | 1009.65 | | 1055.59 | | 1357.87 | 1076.15 | 1191.22 | 1178.65 | 1089.34 | 1168.99 | **1141** | 109 |
| La | 71.03 | 70.26 | 70.51 | 72.03 | 71.47 | 83.48 | 72.79 | 93.21 | 75.42 | 76.77 | **75.7** | 7.35 |
| Ce | 144.50 | 138.32 | 150.29 | 167.96 | 144.70 | 175.64 | 152.08 | 194.66 | 155.18 | 145.91 | **157** | 17.4 |
| Pr | 18.39 | 18.15 | 18.18 | 21.09 | 17.01 | 21.22 | 19.48 | 22.42 | 19.35 | 17.71 | **19.3** | 1.76 |
| Nd | 86.74 | 70.40 | 84.38 | 92.56 | 62.06 | 88.07 | 89.29 | 99.40 | 81.61 | 68.02 | **82.3** | 11.8 |
| Sm | 18.92 | 17.49 | 17.95 | 19.56 | 21.28 | 23.10 | 20.87 | 24.25 | 22.02 | 14.05 | **19.9** | 3.01 |
| Eu | 3.93 | 4.25 | 4.74 | 4.47 | 4.85 | 4.13 | 5.82 | 5.43 | 5.29 | 5.17 | **4.81** | 0.62 |
| Gd | 25.39 | 18.11 | 24.00 | 23.08 | 21.23 | 23.83 | 21.73 | 26.71 | 24.74 | 18.33 | **22.7** | 2.86 |
| Tb | 3.08 | 3.26 | 4.00 | 3.56 | 2.72 | 4.64 | 4.11 | 4.16 | 3.49 | 3.16 | **3.62** | 0.59 |
| Dy | 22.46 | 20.47 | 25.97 | 28.00 | 24.95 | 25.95 | 26.96 | 27.68 | 26.43 | 17.77 | **24.7** | 3.36 |
| Ho | 4.82 | 4.54 | 5.61 | 4.69 | 4.22 | 5.81 | 5.03 | 5.83 | 6.36 | 4.08 | **5.10** | 0.77 |
| Er | 15.20 | 12.21 | 15.16 | 15.93 | 14.21 | 14.58 | 16.25 | 16.92 | 16.23 | 10.67 | **14.7** | 1.95 |
| Tm | 2.58 | 1.97 | 2.02 | 1.85 | 2.24 | 2.14 | 2.38 | 2.51 | 2.16 | 2.03 | **2.19** | 0.24 |
| Yb | 15.58 | 13.07 | 14.08 | 16.84 | 13.58 | 15.68 | 15.19 | 19.05 | 15.12 | 10.55 | **14.9** | 2.28 |
| Lu | 1.81 | 2.09 | 2.11 | 2.47 | 2.30 | 2.81 | 2.38 | 2.82 | 2.50 | 1.48 | **2.28** | 0.42 |
| Hf | 10.83 | 10.22 | 10.75 | 12.44 | 11.72 | 13.77 | 11.14 | 13.42 | 10.20 | 18.27 | **12.3** | 2.45 |
| Ta | 7.64 | 5.89 | 6.08 | 6.15 | 7.75 | 7.58 | 7.01 | 7.03 | 6.67 | 6.47 | **6.83** | 0.68 |
| Th | 15.19 | 15.89 | 17.27 | 16.29 | 16.26 | 16.01 | 16.53 | 18.26 | 15.78 | 32.57 | **18.0** | 5.19 |
| U | 3.65 | 3.79 | 4.15 | 3.49 | 4.24 | 4.47 | 4.70 | 3.97 | 3.62 | 7.76 | **4.38** | 1.25 |

**Trace element concentrations of shards from the MD04-2822 2361-2362 cm sample. n = shard number and relates to the major oxide analyses from this horizon. All concentrations are presented as ppm. Mean and 1 standard deviations are shown.**

| MD04-2822 2361-2362 cm | | | | | | | | | | | | | | | |
|---|---|---|---|---|---|---|---|---|---|---|---|---|---|---|---|
| n | 5 | 8 | 9 | 10 | 12 | 14 | 15 | 16 | 18 | 19 | 20 | 21 | 24 | **Mean** | St. Dev. |
| Rb | 116.24 | 149.34 | 121.13 | 133.27 | 150.22 | 119.92 | 116.79 | 113.38 | 122.41 | 135.98 | 110.79 | 81.84 | 67.05 | **118** | 23.4 |
| Sr | 132.55 | 144.47 | 115.90 | 120.86 | 151.46 | 119.02 | 101.51 | 106.98 | 118.60 | 132.35 | 111.77 | 98.48 | 106.78 | **120** | 16.2 |
| Y | 99.89 | 144.00 | 103.41 | 115.05 | 109.53 | 144.24 | 131.52 | 163.65 | 131.74 | 136.32 | 141.91 | 105.64 | 86.32 | **124** | 22.4 |
| Zr | 199.72 | 287.28 | 210.30 | 237.54 | 223.85 | 263.52 | 255.15 | 287.10 | 260.21 | 288.53 | 265.79 | 201.45 | 173.47 | **243** | 37.9 |
| Nb | 55.09 | 86.96 | 76.73 | 75.58 | 69.73 | 86.02 | 85.54 | 92.54 | 78.24 | 82.14 | 85.07 | 62.20 | 46.81 | **75.6** | 13.6 |
| Cs | 0.98 | 1.87 | 1.18 | 2.41 | 4.73 | 1.61 | 1.84 | 1.93 | 2.39 | 1.58 | 1.22 | 1.62 | 0.85 | **1.86** | 0.99 |
| Ba | 860.33 | 1133.25 | 859.61 | 910.81 | 1055.54 | 984.91 | 907.92 | 1013.86 | 938.91 | 993.34 | 909.75 | 718.73 | 637.88 | **917** | 132 |
| La | 47.42 | 70.77 | 56.13 | 58.91 | 56.12 | 65.63 | 62.74 | 76.15 | 69.56 | 73.22 | 65.65 | 52.92 | 43.53 | **61.4** | 9.99 |
| Ce | 102.60 | 139.23 | 125.15 | 122.06 | 113.80 | 135.88 | 132.91 | 170.21 | 137.88 | 148.35 | 141.19 | 101.08 | 85.26 | **127** | 22.6 |
| Pr | 13.44 | 17.73 | 13.86 | 15.55 | 14.98 | 17.06 | 17.32 | 23.86 | 16.21 | 17.62 | 16.83 | 13.01 | 9.25 | **15.9** | 3.39 |
| Nd | 55.11 | 71.30 | 55.57 | 62.09 | 54.71 | 70.91 | 70.59 | 89.16 | 71.13 | 81.14 | 68.80 | 59.99 | 44.00 | **65.7** | 12.1 |
| Sm | 8.48 | 19.76 | 14.07 | 16.44 | 15.90 | 16.91 | 16.96 | 17.81 | 13.91 | 18.25 | 19.41 | 13.49 | 8.35 | **15.4** | 3.65 |
| Eu | 5.30 | 6.13 | 3.77 | 5.36 | 6.34 | 4.08 | 3.71 | 6.75 | 3.28 | 4.67 | 4.13 | 2.33 | 3.40 | **4.56** | 1.33 |
| Gd | 13.73 | 24.24 | 17.48 | 16.97 | 13.00 | 24.51 | 20.95 | 23.78 | 20.21 | 24.07 | 21.77 | 15.15 | 12.89 | **19.1** | 4.48 |
| Tb | 1.94 | 3.52 | 2.46 | 2.44 | 2.74 | 3.11 | 3.06 | 3.46 | 3.23 | 3.39 | 3.35 | 2.36 | 1.53 | **2.81** | 0.63 |
| Dy | 13.32 | 18.63 | 19.70 | 19.24 | 17.25 | 22.44 | 23.53 | 24.70 | 17.68 | 21.27 | 20.30 | 16.62 | 12.27 | **19.0** | 3.66 |
| Ho | 2.92 | 4.37 | 3.22 | 4.24 | 3.80 | 3.89 | 4.46 | 5.34 | 4.65 | 4.25 | 5.53 | 3.69 | 2.84 | **4.09** | 0.83 |
| Er | 8.25 | 12.41 | 9.80 | 10.64 | 9.80 | 12.25 | 12.60 | 14.45 | 12.05 | 15.80 | 11.51 | 8.32 | 7.05 | **11.1** | 2.51 |
| Tm | 1.23 | 2.16 | 1.45 | 1.46 | 1.76 | 2.03 | 2.03 | 2.20 | 1.87 | 1.61 | 2.51 | 1.10 | 1.23 | **1.74** | 0.44 |
| Yb | 8.46 | 11.56 | 9.46 | 13.24 | 11.47 | 15.14 | 11.65 | 15.04 | 13.66 | 14.00 | 13.32 | 8.91 | 7.28 | **11.8** | 2.58 |
| Lu | 1.58 | 1.92 | 1.81 | 1.78 | 1.80 | 2.04 | 2.26 | 2.01 | 1.94 | 1.94 | 2.53 | 1.64 | 1.25 | **1.88** | 0.31 |
| Hf | 7.76 | 10.34 | 7.60 | 10.06 | 7.42 | 10.87 | 10.65 | 10.21 | 9.62 | 10.83 | 9.85 | 6.61 | 5.40 | **9.02** | 1.82 |
| Ta | 4.19 | 6.29 | 5.22 | 4.62 | 5.60 | 6.04 | 6.02 | 6.26 | 5.81 | 5.07 | 5.37 | 4.58 | 3.27 | **5.26** | 0.90 |
| Th | 9.23 | 15.02 | 11.07 | 11.87 | 12.51 | 14.92 | 13.93 | 16.68 | 13.27 | 14.50 | 15.16 | 10.76 | 8.41 | **12.9** | 2.49 |
| U | 4.00 | 5.44 | 4.89 | 4.24 | 3.82 | 5.35 | 4.93 | 5.11 | 4.44 | 4.09 | 5.25 | 6.63 | 3.21 | **4.73** | 0.88 |

**Trace element concentrations of shards from the MD04-2822 2363-2364 cm sample. n = shard number and relates to the major oxide analyses from this horizon. All concentrations are presented as ppm. Mean and 1 standard deviations are shown.**

| MD04-2822 2363-2364 cm | | | | | | | | | | | | | | | | |
|---|---|---|---|---|---|---|---|---|---|---|---|---|---|---|---|---|
| n | 2 | 4 | 5 | 6 | 9 | 11 | 13 | 14 | 15 | 18 | 19 | 22 | 23 | 24 | **Mean** | St. Dev. |
| Rb | 116.14 | 115.87 | 130.46 | 124.42 | 115.73 | 112.89 | 104.12 | 126.64 | 140.59 | 125.92 | 129.65 | 134.67 | 127.07 | 140.84 | **125** | 10.7 |
| Sr | 112.61 | 98.60 | 113.61 | 121.81 | 104.29 | 101.80 | 104.80 | 124.93 | 106.10 | 102.55 | 90.95 | 162.52 | 108.59 | 121.97 | **113** | 17.3 |
| Y | 148.44 | 150.52 | 177.46 | 164.53 | 155.10 | 122.50 | 139.08 | 156.94 | 180.73 | 150.84 | 117.93 | 128.35 | 154.54 | 176.75 | **152** | 19.7 |
| Zr | 273.44 | 278.32 | 329.60 | 373.31 | 303.23 | 233.21 | 262.15 | 334.58 | 331.90 | 302.02 | 242.11 | 256.21 | 310.34 | 318.63 | **296** | 40.3 |
| Nb | 90.57 | 99.81 | 104.04 | 101.44 | 90.37 | 76.16 | 85.19 | 93.78 | 110.84 | 96.94 | 82.64 | 91.31 | 98.83 | 122.31 | **96.0** | 11.8 |
| Cs | 1.19 | 1.01 | 2.24 | 1.59 | 1.36 | 1.52 | 1.01 | 1.48 | 2.86 | 1.30 | 2.15 | 1.36 | 1.03 | 2.53 | **1.62** | 0.59 |
| Ba | 1002.80 | 982.07 | 1244.72 | 1049.74 | 1030.89 | 899.90 | 947.94 | 1099.11 | 1253.70 | 1057.25 | 937.66 | 1106.90 | 1051.19 | 1226.55 | **1064** | 113 |
| La | 73.48 | 69.69 | 86.08 | 91.19 | 73.20 | 61.99 | 68.68 | 81.14 | 83.42 | 70.89 | 57.98 | 67.65 | 71.50 | 81.97 | **74.2** | 9.40 |
| Ce | 149.27 | 144.72 | 179.55 | 180.55 | 155.65 | 122.24 | 140.39 | 159.77 | 177.08 | 167.67 | 130.20 | 126.06 | 154.56 | 171.35 | **154** | 19.7 |
| Pr | 17.52 | 17.88 | 21.07 | 22.87 | 16.30 | 14.77 | 16.09 | 20.80 | 22.12 | 18.39 | 15.49 | 15.83 | 17.13 | 19.76 | **18.3** | 2.62 |
| Nd | 82.25 | 72.68 | 92.93 | 94.65 | 86.37 | 67.61 | 79.05 | 81.81 | 92.34 | 78.80 | 66.53 | 68.34 | 81.14 | 90.37 | **81.1** | 9.62 |
| Sm | 16.21 | 22.07 | 21.57 | 23.27 | 23.89 | 14.86 | 19.99 | 18.43 | 24.33 | 24.70 | 14.98 | 15.05 | 21.27 | 20.82 | **20.1** | 3.60 |
| Eu | 4.25 | 4.42 | 6.73 | 4.11 | 4.08 | 3.58 | 4.14 | 3.97 | 6.79 | 5.53 | 3.38 | 4.20 | 3.52 | 4.38 | **4.51** | 1.08 |
| Gd | 25.81 | 21.26 | 26.59 | 23.87 | 24.66 | 20.47 | 21.59 | 22.90 | 26.45 | 25.15 | 16.90 | 20.02 | 22.17 | 23.28 | **22.9** | 2.76 |
| Tb | 3.92 | 3.35 | 3.86 | 3.75 | 3.52 | 2.51 | 3.29 | 4.06 | 4.18 | 3.45 | 3.52 | 2.72 | 3.50 | 4.05 | **3.55** | 0.49 |
| Dy | 24.88 | 23.04 | 25.12 | 26.50 | 25.92 | 15.69 | 25.25 | 24.23 | 30.70 | 27.47 | 20.40 | 17.41 | 25.12 | 28.14 | **24.3** | 4.06 |
| Ho | 5.88 | 3.93 | 5.61 | 5.21 | 5.13 | 3.92 | 4.73 | 4.67 | 6.49 | 5.61 | 3.42 | 5.73 | 5.60 | 5.32 | **5.09** | 0.86 |
| Er | 12.85 | 16.43 | 15.97 | 12.31 | 16.80 | 11.79 | 13.11 | 14.46 | 18.26 | 14.81 | 11.99 | 11.90 | 14.88 | 16.41 | **14.4** | 2.13 |
| Tm | 1.89 | 1.87 | 2.86 | 2.21 | 1.96 | 1.13 | 1.87 | 2.57 | 2.26 | 2.60 | 1.59 | 1.83 | 1.70 | 2.34 | **2.05** | 0.46 |
| Yb | 14.92 | 14.17 | 19.62 | 16.57 | 16.80 | 13.08 | 14.64 | 15.62 | 17.24 | 15.85 | 13.83 | 13.35 | 16.82 | 18.06 | **15.8** | 1.89 |
| Lu | 2.15 | 2.03 | 2.53 | 2.17 | 2.47 | 1.84 | 1.77 | 2.04 | 2.55 | 2.41 | 1.82 | 1.95 | 2.18 | 2.31 | **2.16** | 0.27 |
| Hf | 11.55 | 12.15 | 13.57 | 12.96 | 12.26 | 8.83 | 10.25 | 11.79 | 13.17 | 11.68 | 10.09 | 10.37 | 11.74 | 11.92 | **11.6** | 1.31 |
| Ta | 5.85 | 5.91 | 6.33 | 6.80 | 7.00 | 4.69 | 6.39 | 6.38 | 7.15 | 7.12 | 6.13 | 8.67 | 7.05 | 7.30 | **6.63** | 0.91 |
| Th | 15.38 | 15.01 | 18.30 | 17.10 | 17.74 | 13.11 | 14.51 | 16.68 | 18.26 | 16.14 | 14.10 | 15.09 | 15.34 | 19.18 | **16.1** | 1.79 |
| U | 4.21 | 4.38 | 5.02 | 4.62 | 4.33 | 3.71 | 3.81 | 4.40 | 4.45 | 4.76 | 4.33 | 4.18 | 4.42 | 4.18 | **4.34** | 0.34 |

**Trace element concentrations of shards from the MD04-2822 2365-2366 cm. n = shard number and relates to the major oxide analyses from this horizon. All concentrations are presented as ppm. Mean and 1 standard deviations are shown.**

| MD04-2822 2365-2366 cm | | | | | | | | | | | | | |
|---|---|---|---|---|---|---|---|---|---|---|---|---|---|
| n | 2 | 4 | 5 | 6 | 8 | 10 | 10 | 11 | 12 | 15 | 16 | **Mean** | St. Dev. |
| Rb | 135.56 | 123.78 | | 101.51 | 127.31 | 128.59 | 105.71 | 121.58 | 126.32 | 125.69 | 125.50 | **122** | 10.5 |
| Sr | 121.55 | 117.16 | 124.42 | 113.41 | 127.48 | 122.90 | 106.45 | 111.74 | 114.72 | 124.56 | 115.56 | **118** | 6.49 |
| Y | 168.22 | 156.71 | 140.06 | 112.01 | 158.95 | 170.68 | 137.40 | 165.34 | 161.79 | 179.36 | 156.40 | **155** | 18.9 |
| Zr | 302.75 | 288.17 | 254.88 | 233.74 | 300.23 | 340.03 | 286.20 | 316.70 | 314.77 | 314.56 | 291.30 | **295** | 30.0 |
| Nb | 106.38 | 96.96 | 77.92 | 68.56 | 96.59 | 105.44 | 91.91 | 103.07 | 112.51 | 106.24 | 102.60 | **97.1** | 13.2 |
| Cs | 1.89 | 1.34 | 1.04 | 1.31 | 2.91 | 1.71 | 1.21 | 1.68 | 2.23 | 2.71 | 1.52 | **1.78** | 0.61 |
| Ba | 1103.20 | -394.89 | 882.88 | 848.97 | 1109.51 | 1118.08 | 997.52 | 1103.74 | 1096.36 | 1180.23 | 1083.50 | **921** | 448 |
| La | 77.70 | 71.85 | 65.83 | 53.23 | 72.64 | 81.15 | 69.50 | 77.30 | 83.00 | 79.40 | 74.01 | **73.2** | 8.39 |
| Ce | 159.49 | 157.45 | 136.10 | 116.35 | 152.37 | 164.80 | 154.93 | 156.86 | 164.24 | 166.53 | 153.84 | **153** | 14.7 |
| Pr | 19.09 | 19.85 | 17.19 | 17.16 | 23.33 | 21.28 | 18.22 | 18.44 | 21.12 | 22.37 | 19.00 | **19.7** | 2.05 |
| Nd | 93.63 | 93.24 | 75.41 | 67.26 | 77.91 | 97.74 | 80.53 | 87.85 | 85.20 | 94.67 | 83.94 | **85.2** | 9.40 |
| Sm | 21.50 | 20.26 | 19.43 | 13.69 | 14.10 | 20.72 | 18.05 | 22.03 | 18.66 | 26.25 | 24.93 | **20.0** | 3.88 |
| Eu | 4.97 | 5.53 | 4.62 | 4.07 | 3.94 | 5.58 | 4.30 | 4.19 | 5.69 | 5.18 | 4.66 | **4.79** | 0.64 |
| Gd | 22.76 | 22.34 | 20.58 | 16.54 | 23.08 | 25.09 | 20.65 | 22.00 | 20.57 | 24.96 | 25.53 | **22.2** | 2.61 |
| Tb | 4.23 | 3.29 | 3.60 | 2.50 | 4.64 | 4.26 | 3.63 | 3.94 | 4.52 | 3.84 | 3.32 | **3.80** | 0.63 |
| Dy | 28.04 | 27.16 | 22.08 | 18.20 | 24.16 | 30.77 | 24.61 | 26.51 | 31.50 | 31.64 | 30.01 | **26.8** | 4.26 |
| Ho | 6.70 | 5.30 | 5.03 | 4.29 | 5.44 | 6.57 | 4.75 | 6.06 | 6.80 | 6.51 | 5.67 | **5.74** | 0.86 |
| Er | 17.56 | 16.00 | 15.42 | 10.94 | 14.34 | 16.90 | 14.64 | 16.95 | 18.58 | 19.69 | 14.76 | **16.0** | 1.90 |
| Tm | 2.58 | 2.56 | 1.82 | 1.56 | 2.36 | 2.88 | 2.33 | 2.31 | 2.52 | 2.63 | 2.21 | **2.34** | 0.38 |
| Yb | 16.13 | 15.60 | 13.07 | 13.04 | 18.97 | 17.58 | 15.18 | 18.25 | 16.19 | 17.28 | 15.84 | **16.1** | 1.90 |
| Lu | 2.38 | 2.44 | 2.30 | 1.50 | 1.94 | 2.13 | 1.90 | 2.24 | 2.51 | 2.86 | 2.34 | **2.23** | 0.36 |
| Hf | 12.56 | 11.82 | 9.43 | 9.40 | 12.48 | 13.83 | 10.78 | 13.61 | 14.09 | 16.49 | 13.53 | **12.5** | 2.12 |
| Ta | 6.90 | 6.73 | 4.75 | 4.98 | 7.61 | 6.66 | 5.41 | 7.48 | 7.13 | 8.30 | 6.81 | **6.61** | 1.12 |
| Th | 16.67 | 17.02 | 14.73 | 12.53 | 16.08 | 19.16 | 15.34 | 17.84 | 17.86 | 19.05 | 16.83 | **16.6** | 1.94 |
| U | 4.27 | 3.88 | 3.27 | 3.00 | 4.24 | 6.48 | 4.42 | 4.15 | 4.23 | 4.35 | 4.02 | **4.21** | 0.88 |

**Major oxide concentrations of shards from the MD04-2822 2317-2318 cm, 2319-2320 cm, 2339-2340 cm, 2359-2360 cm, 2365-2366 cm and 2373-2374 cm samples. n = number of shards analysed. Mean and 1 standard deviations are shown. All oxides are presented as weight %. Total iron is expressed as FeO.**

| n | $SiO_2$ | $TiO_2$ | $Al_2O_3$ | FeO | MnO | MgO | CaO | $Na_2O$ | $K_2O$ | $P_2O_5$ | Cl | Total |
|---|---|---|---|---|---|---|---|---|---|---|---|---|
| **MD04-2822 2317-2318 cm** | | | | | | | | | | | | |
| 1 | 71.94 | 0.21 | 11.40 | 2.46 | 0.14 | 0.01 | 0.41 | 4.87 | 3.9 | -0.01 | 0.15 | 95.59 |
| **MD04-2822 2319-2320 cm (Population 1)** | | | | | | | | | | | | |
| 1 | 68.09 | 0.13 | 11.10 | 2.19 | -0.03 | 0.04 | 0.39 | 4.44 | 3.61 | -0.01 | 0.17 | 90.18 |
| 2 | 71.47 | 0.21 | 11.46 | 2.34 | 0.05 | 0.03 | 0.36 | 4.67 | 3.94 | 0.00 | 0.13 | 94.66 |
| **Mean** | **69.78** | **0.17** | **11.28** | **2.27** | **0.01** | **0.04** | **0.38** | **4.56** | **3.77** | **0.00** | **0.16** | **92.43** |
| St. Dev. | 2.39 | 0.06 | 0.25 | 0.10 | 0.06 | 0.01 | 0.02 | 0.16 | 0.23 | 0.01 | 0.03 | 3.17 |
| **MD04-2822 2319-2320 cm (Population 2)** | | | | | | | | | | | | |
| 1 | 69.95 | 0.10 | 12.50 | 1.76 | 0.09 | 0.13 | 0.84 | 4.43 | 3.86 | 0.00 | 0.22 | 93.89 |
| 2 | 68.52 | 0.08 | 12.31 | 2.06 | 0.09 | 0.11 | 0.88 | 4.23 | 3.50 | 0.01 | 0.21 | 92.00 |
| 3 | 68.58 | 0.16 | 12.14 | 2.35 | 0.12 | 0.11 | 0.83 | 4.23 | 3.51 | 0.03 | 0.25 | 92.33 |
| 4 | 69.20 | 0.01 | 12.46 | 1.95 | 0.08 | 0.13 | 0.86 | 4.48 | 3.79 | -0.02 | 0.23 | 93.19 |
| **Mean** | **69.06** | **0.09** | **12.35** | **2.03** | **0.10** | **0.12** | **0.85** | **4.34** | **3.66** | **0.01** | **0.23** | **92.85** |
| St. Dev. | 0.67 | 0.06 | 0.16 | 0.25 | 0.02 | 0.01 | 0.02 | 0.13 | 0.19 | 0.02 | 0.02 | 0.85 |
| **MD04-2822 2339-2340 cm** | | | | | | | | | | | | |
| 1 | 73.40 | 0.09 | 11.43 | 1.05 | -0.01 | 0.01 | 0.87 | 4.11 | 2.94 | 0.00 | 0.10 | 94.00 |
| 2 | 70.37 | 0.14 | 11.20 | 2.13 | 0.22 | 0.04 | 0.54 | 4.44 | 3.83 | 0.02 | 0.31 | 93.26 |
| 3 | 70.44 | 0.16 | 11.39 | 2.44 | 0.08 | 0.02 | 0.50 | 4.52 | 3.82 | -0.03 | 0.31 | 93.67 |
| 4 | 69.79 | 0.38 | 11.93 | 2.14 | 0.10 | 0.15 | 0.58 | 4.51 | 3.63 | 0.01 | 0.11 | 93.35 |
| **MD04-2822 2359-2360 cm (Outliers)** | | | | | | | | | | | | |
| 1 | 70.86 | 0.11 | 12.49 | 1.99 | 0.00 | 0.05 | 0.64 | 4.50 | 3.76 | 0.02 | 0.21 | 94.62 |
| 2 | 70.41 | 0.47 | 12.03 | 2.12 | 0.07 | 0.17 | 0.53 | 4.34 | 4.04 | 0.02 | 0.11 | 94.30 |
| **MD04-2822 2365-2366 cm (Outlier)** | | | | | | | | | | | | |
| 1 | 70.44 | 0.12 | 12.22 | 1.89 | 0.07 | 0.05 | 0.71 | 4.53 | 3.75 | 0.00 | 0.21 | 93.99 |
| **MD04-2822 2373-2374 cm (Main Population)** | | | | | | | | | | | | |
| 1 | 69.11 | 0.16 | 12.12 | 1.78 | 0.11 | 0.07 | 0.67 | 4.39 | 3.42 | 0.00 | 0.22 | 92.05 |
| 2 | 69.49 | 0.42 | 12.22 | 2.17 | 0.02 | 0.25 | 0.72 | 4.94 | 3.68 | 0.02 | 0.12 | 94.04 |
| 3 | 69.60 | 0.15 | 12.15 | 2.05 | 0.12 | 0.06 | 0.64 | 4.52 | 3.30 | 0.01 | 0.26 | 92.85 |
| 4 | 70.41 | 0.08 | 12.13 | 2.05 | 0.20 | 0.06 | 0.70 | 4.55 | 3.66 | 0.02 | 0.22 | 94.09 |
| 5 | 70.41 | 0.14 | 12.11 | 1.96 | -0.11 | 0.05 | 0.66 | 4.57 | 3.62 | 0.01 | 0.25 | 93.77 |
| 6 | 70.56 | 0.16 | 12.06 | 2.05 | 0.16 | 0.06 | 0.67 | 4.66 | 3.73 | -0.04 | 0.20 | 94.31 |
| **Mean** | **69.93** | **0.18** | **12.13** | **2.01** | **0.08** | **0.09** | **0.68** | **4.61** | **3.57** | **0.00** | **0.21** | **93.52** |
| St. Dev. | 0.60 | 0.12 | 0.05 | 0.13 | 0.11 | 0.08 | 0.03 | 0.19 | 0.17 | 0.02 | 0.05 | 0.88 |
| **MD04-2822 2373-2374 cm (Correlatives to MD04-2822 2359-2366 cm)** | | | | | | | | | | | | |
| 1 | 73.34 | 0.09 | 11.23 | 0.89 | -0.11 | 0.00 | 0.83 | 3.89 | 2.92 | -0.02 | 0.06 | 93.25 |
| 2 | 73.93 | 0.03 | 11.26 | 1.16 | 0.05 | 0.01 | 0.85 | 3.95 | 3.04 | -0.04 | 0.05 | 94.33 |

**Major oxide concentrations of shards from the MD04-2822 2377-2378 cm sample. n = number of shards analysed. Mean and 1 standard deviations are shown. All oxides are presented as weight %. Total iron is expressed as FeO.**

| n | $SiO_2$ | $TiO_2$ | $Al_2O_3$ | FeO | MnO | MgO | CaO | $Na_2O$ | $K_2O$ | $P_2O_5$ | Cl | Total |
|---|---|---|---|---|---|---|---|---|---|---|---|---|
| **MD04-2822 2377-2378 cm (Main Population)** | | | | | | | | | | | | |
| 1 | 70.04 | 0.13 | 11.82 | 2.23 | 0.26 | 0.05 | 0.60 | 4.30 | 3.79 | 0.02 | 0.20 | 93.44 |
| 2 | 70.09 | 0.26 | 12.04 | 2.09 | 0.04 | 0.18 | 0.62 | 4.74 | 3.75 | 0.05 | 0.11 | 93.95 |
| 3 | 71.20 | 0.26 | 12.22 | 1.90 | 0.05 | 0.20 | 0.64 | 5.00 | 3.96 | -0.01 | 0.09 | 95.52 |
| 4 | 70.29 | 0.21 | 12.03 | 1.92 | 0.03 | 0.02 | 0.67 | 4.60 | 3.68 | -0.03 | 0.26 | 93.70 |
| 5 | 69.76 | 0.47 | 12.24 | 2.01 | 0.21 | 0.20 | 0.72 | 4.81 | 3.73 | 0.02 | 0.10 | 94.26 |
| **Mean** | **70.28** | **0.27** | **12.07** | **2.03** | **0.12** | **0.13** | **0.65** | **4.69** | **3.78** | **0.01** | **0.15** | **94.18** |
| St. Dev. | 0.55 | 0.12 | 0.17 | 0.14 | 0.11 | 0.09 | 0.05 | 0.26 | 0.11 | 0.03 | 0.07 | 0.81 |
| **MD04-2822 2377-2378 cm (Correlatives to MD04-2822 2359-2366 cm)** | | | | | | | | | | | | |
| 1 | 72.55 | 0.09 | 11.15 | 1.33 | 0.04 | -0.01 | 0.92 | 3.85 | 2.88 | 0.02 | 0.06 | 92.88 |
| 2 | 72.22 | 0.20 | 11.21 | 1.38 | 0.19 | 0.01 | 0.96 | 3.89 | 2.84 | 0.00 | 0.07 | 92.98 |
| **MD04-2822 2377-2378 cm (Outliers)** | | | | | | | | | | | | |
| 1 | 74.61 | 0.02 | 11.22 | 0.92 | 0.04 | 0.03 | 0.48 | 3.80 | 4.09 | 0.02 | 0.13 | 95.36 |
| 2 | 73.73 | 0.04 | 11.41 | 0.82 | -0.02 | 0.04 | 0.47 | 3.88 | 3.93 | 0.00 | 0.11 | 94.43 |
| 3 | 70.15 | -0.01 | 10.57 | 2.04 | 0.11 | 0.05 | 0.74 | 3.13 | 3.39 | -0.01 | 0.04 | 90.23 |
| 4 | 71.67 | 0.20 | 10.99 | 2.18 | 0.23 | 0.02 | 0.95 | 2.83 | 3.45 | 0.01 | 0.06 | 92.60 |
| 5 | 70.59 | 0.15 | 11.20 | 2.33 | -0.03 | 0.01 | 0.50 | 4.34 | 3.78 | 0.03 | 0.27 | 93.22 |
| 6 | 69.13 | 0.12 | 12.22 | 2.27 | 0.02 | 0.06 | 0.86 | 4.68 | 3.56 | -0.01 | 0.18 | 93.09 |
| 7 | 69.83 | 0.13 | 12.35 | 2.65 | 0.10 | 0.08 | 0.87 | 4.83 | 3.66 | 0.00 | 0.19 | 94.69 |

# Appendix 6 – Similarity Coefficient Comparisons to Previously Identified MIS 2-5e North Atlantic Tephra Horizons

**Similarity coefficients for comparisons between Icelandic basaltic horizons identified within the MIS 4 sections of the NGRIP and GRIP ice cores and the composition of North Atlantic basaltic tephra horizons deposited during MIS 2, 3 and 5. Average concentrations of $SiO_2$, $TiO_2$, $Al_2O_3$, FeO, MgO, CaO and $Na_2O$ utilised within the comparisons. Values in bold exceed 0.95.**

| Tephra Horizon | NGRIP 2500.9 m | NGRIP 2548.35 m | NGRIP 2574.55 m | GRIP 2498.5 m | GRIP 2499.75 m-2 | GRIP 2501.05 m | GRIP 2531.8 m | GRIP 2532.95 m | GRIP 2564.3 m-2 | Reference |
|---|---|---|---|---|---|---|---|---|---|---|
| Fugloyarbanki Tephra | 0.92 | 0.82 | 0.93 | 0.81 | 0.88 | 0.81 | 0.92 | 0.94 | 0.93 | Rasmussen et al. (2003) |
| FMAZ III | 0.85 | 0.92 | 0.85 | 0.92 | **0.96** | 0.91 | 0.85 | 0.92 | 0.85 | |
| Ash Zone 2 (II-THOL-2) | 0.87 | 0.89 | 0.88 | 0.89 | **0.95** | 0.87 | 0.88 | **0.95** | 0.87 | |
| Ash Zone 2 (II-TAB-1) | 0.90 | 0.80 | 0.94 | 0.80 | 0.85 | 0.80 | 0.89 | 0.91 | 0.91 | |
| Pop. 5d-1 | 0.91 | 0.84 | 0.91 | 0.83 | 0.89 | 0.83 | 0.91 | **0.96** | 0.92 | Fronval et al. (1998) |
| Pop. 5d-2 | 0.87 | 0.89 | 0.88 | 0.89 | 0.94 | 0.89 | 0.87 | **0.95** | 0.88 | |
| Pop. 5d-3 | 0.76 | 0.94 | 0.77 | 0.93 | 0.88 | 0.92 | 0.77 | 0.83 | 0.77 | |
| Pop. 5ebase-1 | 0.90 | 0.86 | 0.89 | 0.86 | 0.91 | 0.86 | 0.91 | **0.95** | 0.89 | |
| Pop. 5ebase-2 | 0.70 | 0.89 | 0.71 | 0.89 | 0.82 | 0.88 | 0.71 | 0.76 | 0.71 | |
| 5a (~83ka) | 0.89 | 0.82 | **0.95** | 0.82 | 0.88 | 0.82 | 0.88 | 0.94 | 0.90 | Lacasse et al. (1998) |
| 5a (~84ka) | 0.87 | 0.83 | **0.96** | 0.82 | 0.87 | 0.82 | 0.87 | 0.92 | 0.89 | |
| 5c (~103ka) | 0.84 | 0.85 | 0.93 | 0.84 | 0.90 | 0.85 | 0.84 | 0.90 | 0.85 | |
| 5d (~113ka) | 0.92 | 0.82 | 0.90 | 0.82 | 0.89 | 0.82 | 0.91 | **0.95** | 0.91 | |
| 5a-Top/BAS-I | 0.87 | 0.89 | 0.88 | 0.89 | **0.96** | 0.88 | 0.88 | 0.94 | 0.86 | Wastegård and Rasmussen (2001) |
| 5a-Low/BAS-I | 0.75 | **0.96** | 0.77 | 0.93 | 0.89 | 0.92 | 0.76 | 0.82 | 0.76 | |
| 5c-Midt/BAS-I | 0.83 | 0.94 | 0.84 | 0.91 | **0.96** | 0.89 | 0.84 | 0.91 | 0.83 | |
| 5e-Top/BAS | 0.85 | 0.91 | 0.87 | 0.89 | 0.94 | 0.87 | 0.86 | 0.93 | 0.87 | |
| 5e-Low/BAS-IV | 0.85 | 0.91 | 0.86 | 0.90 | **0.96** | 0.88 | 0.86 | 0.93 | 0.86 | |

| Tephra Horizon | NGRIP 2500.9 m | NGRIP 2548.35 m | NGRIP 2574.55 m | GRIP 2498.5 m | GRIP 2499.75 m-2 | GRIP 2501.05 m | GRIP 2531.8 m | GRIP 2532.95 m | GRIP 2564.3 m-2 | Reference |
|---|---|---|---|---|---|---|---|---|---|---|
| VZ 2 | 0.78 | **0.96** | 0.80 | 0.94 | 0.93 | 0.92 | 0.80 | 0.86 | 0.80 | Lackschewitz and Wallrabe-Adams (1997) |
| VZ 3 | 0.77 | **0.96** | 0.78 | 0.93 | 0.91 | 0.91 | 0.78 | 0.84 | 0.78 | |
| VZ 4 | 0.72 | 0.91 | 0.73 | 0.90 | 0.84 | 0.89 | 0.72 | 0.78 | 0.73 | |
| VZ 5 | 0.82 | 0.93 | 0.84 | 0.93 | **0.96** | 0.91 | 0.84 | 0.91 | 0.84 | |
| NGRIP 1895.3 m | 0.86 | 0.83 | **0.95** | 0.83 | 0.89 | 0.84 | 0.86 | 0.91 | 0.87 | S. Davies (unpublished) |
| NGRIP 1915.5 m | 0.84 | 0.87 | 0.91 | 0.87 | 0.92 | 0.87 | 0.84 | 0.92 | 0.86 | |
| NGRIP 2620.05 m | 0.83 | 0.92 | 0.83 | 0.92 | **0.97** | 0.90 | 0.84 | 0.90 | 0.83 | |
| NGRIP 2631.9 m | 0.87 | 0.83 | **0.96** | 0.82 | 0.87 | 0.82 | 0.87 | 0.93 | 0.89 | |

**Similarity coefficients for comparisons between MD04-2822 rhyolitic tephra horizons and the composition of North Atlantic rhyolitic tephra horizons deposited during MIS 3 and 5. II-RHY-1, 5d-Low/RHY and 5e-Top/RHY identified within the ENAM33 core from Faroe Islands region (Wastegård et al., 2006; Wastegård and Rasmussen, 2001). 5e-Midt/RHY data from shards within the HM71-19 core from the Nordic Seas (Fronvold et al., 1998). Average concentrations of $SiO_2$, $Al_2O_3$, FeO, $Na_2O$ and $K_2O$ utilised within the comparisons. Values highlighted in red exceed 0.95.**

| Tephra Horizon | MD04-2822 2327-2328 cm Population 1 | MD04-2822 2327-2328 cm Population 2 | MD04-2822 2359-2366 cm |
|---|---|---|---|
| II-RHY-1 (NAAZ II) | 0.932 | 0.947 | 0.853 |
| 5d-Low/RHY-I | 0.927 | **0.963** | 0.842 |
| 5d-Low/RHY-II | 0.895 | 0.884 | 0.798 |
| 5d-Low/RHY-III | 0.872 | 0.857 | 0.800 |
| 5e-Top/RHY | 0.901 | **0.973** | 0.847 |
| 5e-Midt/RHY | 0.786 | 0.746 | 0.745 |